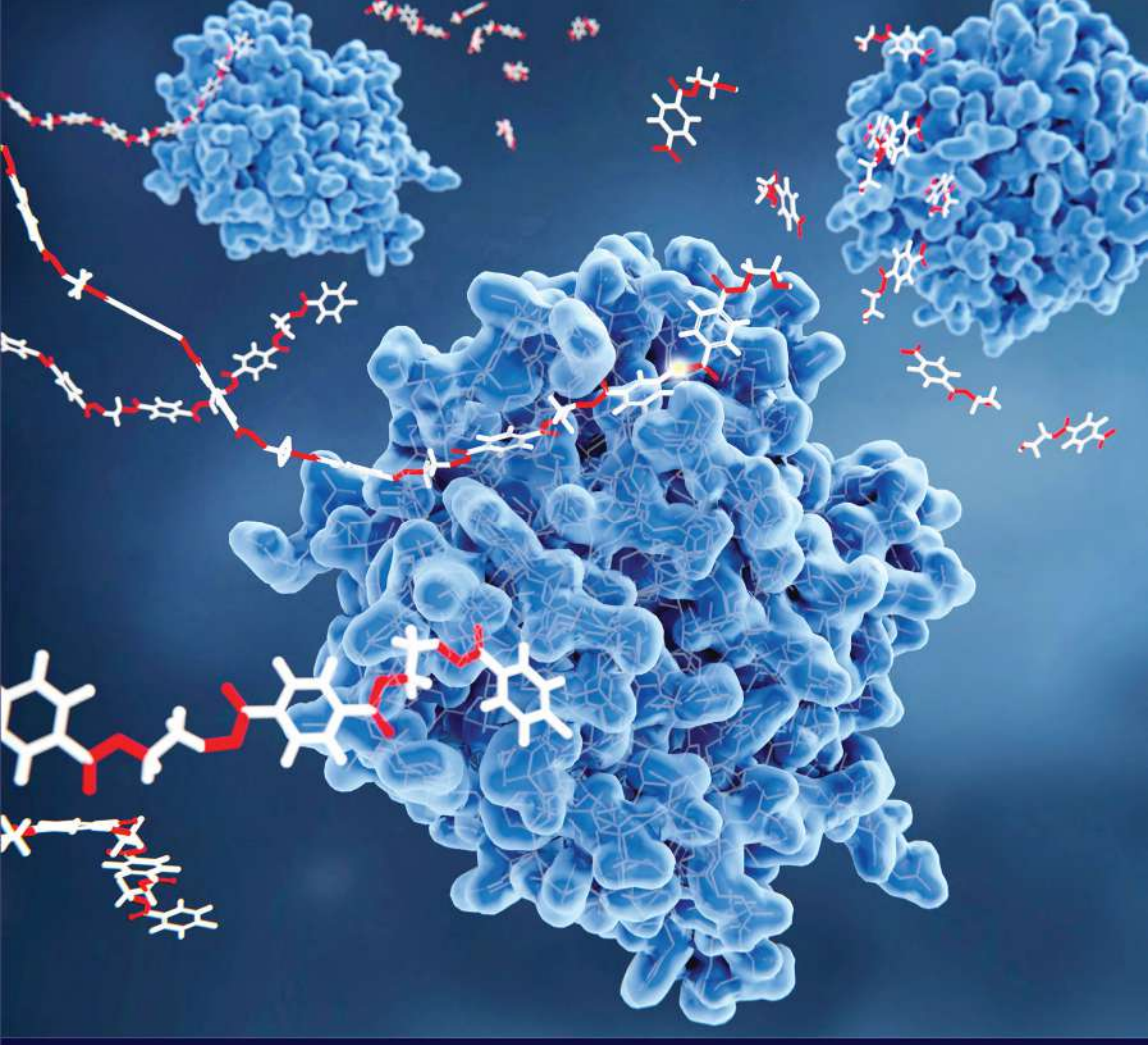

Supramolecular Coordination Complexes

Design, Synthesis, and Applications

Edited by
Sankarasekaran Shanmugaraju

ELSEVIER

Supramolecular Coordination Complexes

Supramolecular Coordination Complexes

Design, Synthesis, and Applications

Edited by

Sankarasekaran Shanmugaraju
Department of Chemistry, Indian Institute of Technology Palakkad (IIITPKD), Palakkad, Kerala, India

ELSEVIER

Elsevier
Radarweg 29, PO Box 211, 1000 AE Amsterdam, Netherlands
The Boulevard, Langford Lane, Kidlington, Oxford OX5 1GB, United Kingdom
50 Hampshire Street, 5th Floor, Cambridge, MA 02139, United States

Notices

Knowledge and best practice in this field are constantly changing. As new research and experience broaden our understanding, changes in research methods, professional practices, or medical treatment may become necessary.

Practitioners and researchers must always rely on their own experience and knowledge in evaluating and using any information, methods, compounds, or experiments described herein. In using such information or methods they should be mindful of their own safety and the safety of others, including parties for whom they have a professional responsibility.

To the fullest extent of the law, neither the Publisher nor the authors, contributors, or editors, assume any liability for any injury and/or damage to persons or property as a matter of products liability, negligence or otherwise, or from any use or operation of any methods, products, instructions, or ideas contained in the material herein.

ISBN: 978-0-323-90582-4

For Information on all Elsevier publications visit our website at https://www.elsevier.com/books-and-journals

Publisher: Susan Dennis
Acquisitions Editor: Charles Bath
Editorial Project Manager: Kyle Gravel
Production Project Manager: Rashmi Manoharan
Cover Designer: Greg Harris

Typeset by Aptara, New Delhi, India

Contents

Contributors

Murugan Arunachalam, Department of Chemistry, The Gandhigram Rural Institute (Deemed to be University), Gandhigram, Dindigul, India

Renitta Benny, School of Chemistry, Indian Institute of Science Education and Research Thiruvananthapuram (IISER-TVM), Thiruvananthapuram, India

Muniyappan Boominathan, Department of Chemistry, The Gandhigram Rural Institute (Deemed to be University), Gandhigram, Dindigul, India

Reema Borkar, School of Chemistry, University of Hyderabad, Hyderabad, India

Arivazhagan Chinnappa, Department of Chemistry, National Institute of Technology, Tiruchirappalli, Tamil Nadu, India

Aniket Chowdhury, Department of Industrial Chemistry, School of Physical Sciences, Mizoram University, Aizawl, Mizoram, India

Neeladri Das, Department of Chemistry, Indian Institute of Technology Patna, Patna, Bihar, India

Soumen De, School of Chemistry, Indian Institute of Science Education and Research Thiruvananthapuram (IISER-TVM), Thiruvananthapuram, India

Gustavo Fernández, Organisch Chemisches Institut, Universität Münster, Corrensstraße 36, 48149 Münster, Germany

Sushobhan Ghosh, Department of Chemistry, Alipurduar University, Alipurduar, India

Ruchika Gupta, Department of Chemistry, University of Delhi, Delhi, India

Rajeev Gupta, Department of Chemistry, University of Delhi, Delhi, India

Nithish Kumar KS, School of Chemistry, Indian Institute of Science Education and Research Thiruvananthapuram (IISER-TVM), Thiruvananthapuram, India

Krishnan Kartha Kalathil, Organisch Chemisches Institut, Universität Münster, Corrensstraße 36, 48149 Münster, Germany

Moon Kedia, School of Chemistry, University of Hyderabad, Hyderabad, India

Saurabh Kumar, Department of Chemistry, Indian Institute of Technology Patna, Patna, Bihar, India

Hong-Yu Lin, Shanghai Key Laboratory of Green Chemistry and Chemical Processes, School of Chemistry and Molecular Engineering, East China Normal University, Shanghai, China

Huidrom Mangalsana, Inorganic and Physical Chemistry Laboratory (IPCL), Council of Scientific and Industrial Research (CSIR)-Central Leather Research Institute (CLRI),

Adyar, Chennai, India; Academy of Scientific and Innovative Research (AcSIR), Ghaziabad, Uttar Pradesh, India

Isha Mishra, School of Chemistry, University of Hyderabad, Hyderabad, India

Binduja Mohan, Department of Chemistry, Indian Institute of Technology Palakkad (IITPKD), Palakkad, Kerala, India

Abhijeet Mohanty, Inorganic and Physical Chemistry Laboratory (IPCL), Council of Scientific and Industrial Research (CSIR)-Central Leather Research Institute (CLRI), Adyar, Chennai, India; Academy of Scientific and Innovative Research (AcSIR), Ghaziabad, Uttar Pradesh, India

Bijnaneswar Mondal, Department of Chemistry, Guru Ghasidas Vishwavidyalaya, Bilaspur, Chhattisgarh, India

Pandurangan Nanjan, School of Physical Sciences, Amrita Vishwa Vidyapeetham, Mysuru Campus, Karnataka, India

Prakash P. Neelakandan, Institute of Nano Science and Technology, Knowledge City, Mohali, Punjab, India

Sanya Pachisia, Department of Chemistry, University of Delhi, Delhi, India

Upasana Phukon, School of Chemistry, University of Hyderabad, Hyderabad, India

Diptiprava Sahoo, School of Chemistry, Indian Institute of Science Education and Research Thiruvananthapuram (IISER-TVM), Thiruvananthapuram, India

Dipanjana Sarkar, Department of Chemistry, Indian Institute of Technology Palakkad (IITPKD), Palakkad, Kerala, India

Malaichamy Sathiyendiran, School of Chemistry, University of Hyderabad, Hyderabad, India

Jeyabalan Shanmugapriya, Department of Chemistry, Madura College, Madurai, Tamil Nadu, India

Sankarasekaran Shanmugaraju, Department of Chemistry, Indian Institute of Technology Palakkad (IITPKD), Palakkad, Kerala, India

Ananthu Shanmughan, Department of Chemistry, Indian Institute of Technology Palakkad (IITPKD), Palakkad, Kerala, India

Gandhi Sivaraman, Department of Chemistry, Gandhigram Rural Institute-Deemed to be University, Dindigul, Tamil Nadu, India

K.R. Soumya, School of Chemistry, University of Hyderabad, Hyderabad, India

Nidhi Tyagi, Institute of Nano Science and Technology, Knowledge City, Mohali, Punjab, India

Amit A. Vernekar, Inorganic and Physical Chemistry Laboratory (IPCL), Council of Scientific and Industrial Research (CSIR)-Central Leather Research Institute (CLRI), Adyar, Chennai, India; Academy of Scientific and Innovative Research (AcSIR), Ghaziabad, Uttar Pradesh, India

Yu-Te Wang, Shanghai Key Laboratory of Green Chemistry and Chemical Processes, School of Chemistry and Molecular Engineering, East China Normal University, Shanghai, China

Lin Xu, Shanghai Key Laboratory of Green Chemistry and Chemical Processes, School of Chemistry and Molecular Engineering, East China Normal University, Shanghai, China

Dawei Zhang, Shanghai Key Laboratory of Green Chemistry and Chemical Processes, School of Chemistry and Molecular Engineering, East China Normal University, Shanghai, China

Chapter 1

Supramolecular coordination self-assembly—A general introduction

Binduja Mohan and Sankarasekaran Shanmugaraju
Department of Chemistry, Indian Institute of Technology Palakkad (IITPKD), Palakkad, Kerala, India

1.1 Introduction

"The snake biting its tail"—a life-changing dream of August Kekulé paved the way to a new world of cyclic configuration that evolved from small molecules to giant macrocyclic structures [1]. A keen observation into the essence of nature raises the question about the formation of complex natural systems from simple building blocks such as filament formation by the aggregation of actin monomers in the cytoplasm of the cell, the generation of viral coat in various viruses through the self-assembly process [1]. The curiosity to understand nature's wonders led to the emergence of new areas of science called supramolecular chemistry. The discovery of "Crown Ethers" by Pedersen [2], "Cryptands" by Lehn [3], and "Spherands" by Cram [4] in early 1960 were the stepping stones to the incredible world of supramolecular chemistry. The synthesis of large macromolecules through the use of conventional covalent bonds involves multistep reactions and is thus time-consuming and laborious [5]. Therefore, for the past few decades, the supramolecular self-assembly process has flourished as an alternative and efficient synthetic method for the synthesis of targeted macrocyclic structures [6]. Self-assembly is a process of generation of intricate supramolecular structures from preprogrammed synthetic constructs that recognize each other through noncovalent interactions. Among the various noncovalent interactions, metal–ligand coordination bonding interaction has been considered a favorite chemical force and used extensively in the molecular self-assembly processes for the design of targeted supramolecular structures. This is because of their high directionality which helps to predict the geometry of final structures and the moderate bond enthalpy of 15–50 kcal/mol, which lies in between the strong covalent bond and other weak noncovalent interactions [7]. This chapter highlights the importance

Supramolecular Coordination Complexes: Design, Synthesis, and Applications.
DOI: https://doi.org/10.1016/B978-0-323-90582-4.00012-9

of coordination-driven self-assembly covering different design principles formulated for the synthesis of functional supramolecular coordination complexes. From this chapter, readers will gain insights into the general introduction to the design, synthesis, and exploration of supramolecular coordination complexes (SCC) of varied structures and functions.

1.2 Coordination-driven molecular self-assembly

Among the numerous noncovalent self-assembly processes, metal–ligand coordination driven self-assembly become an efficient and the powerful route for the synthesis of complex supramolecular architectures; this is owing to their (i) high bonding directionality that helps to design desired molecular architectures from the predesigned building units, (ii) the moderate bond enthalpy of metal–ligand coordination bonds results in the isolation of thermodynamically stable at the same stimuli-responsive supramolecular structures, (iii) variety of precursors of different bite-angles can easily be designed through the functionalization of coordinatively unsaturated metal cations [8]. The kinetic lability of the metal–ligand (M–L) bond is the characteristic of supramolecular bonding, that is, only those M–L bonds which are kinetically labile are considered supramolecular self-assembly processes [9,10]. The formation of metal-containing supramolecular assemblies majorly depends on the judicious choice of metal-based acceptors and organic donor ligands; these building units are self-assembled to generate the finite supramolecular complexes. As far as the acceptor units are concerned, the square planar Pt(II) and Pd(II)-based metal complexes or the octahedral Ru(II), Re(I), and Ir(I)-based metal complexes with vacant or easily accessible coordination sites have been used extensively in supramolecular coordination self-assembly process because of their stable coordination geometry which retains throughout the self-assembly reactions (see Figs. 1.1A and B) [1, 8–9].

On the contrary, the donor ligands are mostly organic moieties with bite angles ranging from 0° to 180° that could readily donate lone pairs of electrons to the complementary metal-acceptors to form a coordination bond and thus generate chemically stable supramolecular structures [11]. Polypyridyl or polyimidazolyl ligands were the most commonly used organic donors because of their strong coordinating ability as well as their predictable bonding directionality (see Fig. 1.1C) [12]. The subsequent sections highlight various design principles formulated for coordination-based self-assembly approaches.

1.3 Background and design principles

As alluded to above, the main advantages of coordination-driven self-assemblies lie in the high directionality and bond-enthalpy of M–L bonding interactions. In general, the molecular geometry and physicochemical properties of final supramolecular complexes are engendered by the characteristic nature of the

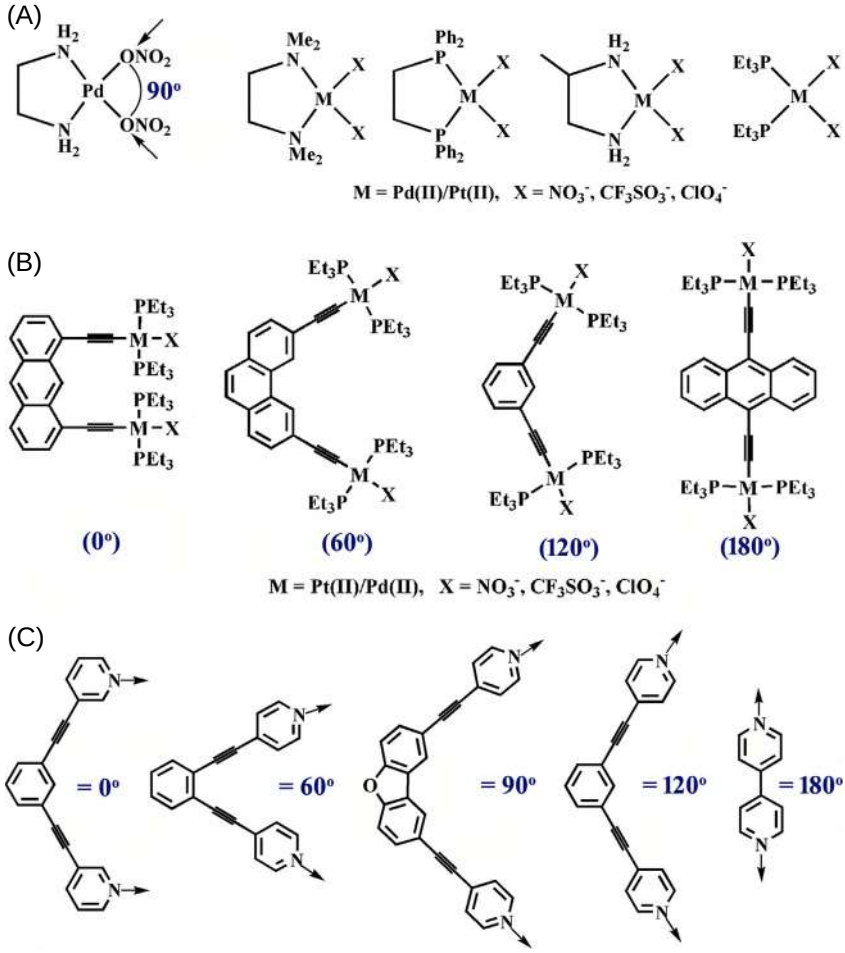

FIGURE 1.1 (A) Few selected examples of cis-blocked Pt(II)/Pd(II) 90° acceptors, (B) shape-selective organometallic acceptors, and (C) shape-selective polypyridyl donors having different bite angles.

corresponding building blocks [13]. Because of the numerous interdisciplinary applications of the supramolecular structures, various synthetic strategies have been formulated to achieve the desired products. Among the different strategies, this chapter converges on some well-established approaches such as directional bonding, symmetry interaction, weak link approach, dimetallic building block approach, and molecular paneling approaches [14–24]. Amidst these, the weak link approach relies on both thermodynamic and kinetically controlled pathways for the design of both two-dimensional (2D) and three-dimensional (3D) flexible architectures whereas all other strategies follow only the thermodynamically controlled pathway [14–24].

1.3.1 Directional bonding approach

This approach promises the synthesis of diverse 2D and 3D supramolecular assemblies as it is the most relevant synthetic strategy used largely for the development of a surplus amount of supramolecular architectures isolated in excellent yield [8]. The fundamental structural necessities for the development of discrete supramolecular ensembles using this approach are (i) structural rigidity of the complementary building block with preprogrammed bite angles, (ii) symmetry, and the proper stoichiometric ratio of the precursors. Hence, by the careful selection of donor and acceptor pairs, one can construct distinct supramolecular structures with the desired functions. For instance, a [4+4] molecular square can be formed from the stoichiometric combination of a cis-blocked 90° acceptor with a linear 180° complementary donor. Similarly, the self-assembly reaction of a 60° acceptor with a linear 180° complementary donor yield a [3+3] molecular triangular structure. Likewise, a wide variety of 2D metallacycles and 3D metallocages were designed and synthesized by the right combination of complementary donors and acceptors (Fig. 1.2A) [8]. Also, a variety of 3D supramolecular cages can be designed by the right choice of complementary building units where at least one of the building units must have more than two-reactive sites to form 3D structures with a large internal cavity. The collection of various supramolecular architectures designed using the directional bonding approach is summarized in Fig. 1.2B.

1.3.2 Symmetry interaction approach

This design strategy focuses on the construction of higher symmetry coordination clusters self-assembled by metal–ligand coordination interactions. The symmetry and rigidity of the available coordination sites on the metal center as well as the symmetry and binding affinity of multibranched chelating ligands are the key factors in this self-assembly approach [8]. The rigidly fixed binding sites of the chelating ligand restrict the possibility of the formation of any oligomers or polymers and mostly results in the formation of desired supramolecular coordination complexes. With the expected topology, a surplus variety of 2D and 3D supramolecular complexes mainly the helicates, adamantoids, catenanes, and several intricate supramolecular structures have been generated using this approach [14–16,23,24]. For instance, the formation of M_2L_3 triple helicates with idealized D_3h symmetry by Raymond et al. is a perfect example of this strategy [17,18]. This kind of helicates possess orthogonal C_3 and C_2 axes and can efficiently be synthesized by the self-assembly of two pseudo-octahedral metal centers which share a C_3 axis and three C_2 symmetric chelating ligands (Fig. 1.3).

1.3.3 Paneling approach

Fujita et al. introduced this phenomenal approach for the design and synthesis of amazing 3D molecular architectures with vast variation in functionalities and

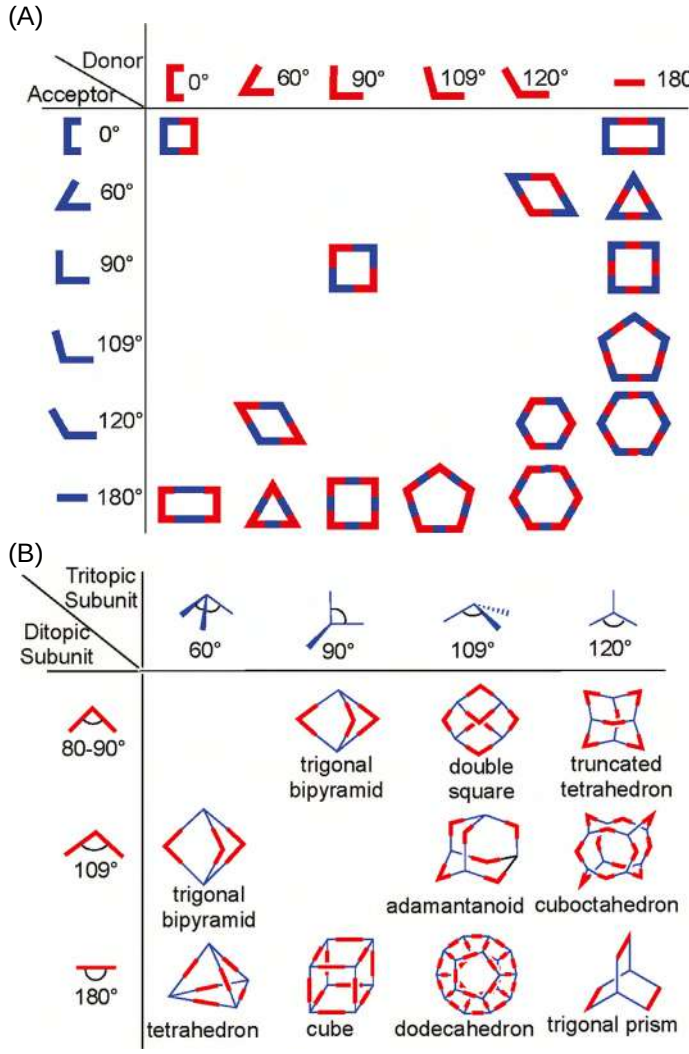

FIGURE 1.2 A molecular library for the rational design of (A) 2D metallomacrocycles and (B) 3D metallocages. Reprinted with permission from Ref. [8]. Copyright 2011 American Chemical Society.

applications [25–27]. Using this approach, even complex 3D architectures can easily be made from the reaction of simple molecular components. This strategy relies on the selection of an appropriate paneling unit and the complementary connecting part (corner unit). The corner units are mostly *cis*-blocked metal centers and the panel units are multidentate organic ligands. For instance, paneling of four triangles with a *cis*-blocked 90° metal acceptor yields a molecular tetrahedron whereas eight triangular surfaces associated with cis-blocked 90° corner units generate a molecular octahedron (Figs. 1.4A and B). The main benefits of

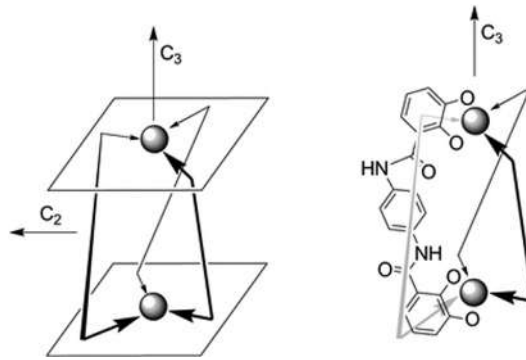

FIGURE 1.3 Schematic representation of the formation of D_3h symmetry triple helicate using symmetry interaction approach.

this strategy are (i) the *cis*-blocked metal centers help to avoid undesired binding and increase the possibility of forming the expected architectures with specific geometry, (ii) generation of complexes with large internal cavities that can be exploited for a variety of applications including molecular recognition, reversible host–guest interactions, cavity-controlled catalysis and stabilization of reactive species [8].

1.3.4 Weak-link approach

The weak-link approach established by Mirkin and coworkers gained much popularity due to the facile construction of intricate 2D and 3D supramolecular ensembles by assembling hemilabile ligand-based donors and transition metal-based acceptors [20,28,29]. As mentioned in the above section, unlike all other approaches, the weak-link approach is kinetically controlled. The ligands are hemilabile and flexible with a bidentate donor site for coordination and the metal acceptors usually possess free or easily accessible coordination sites. The hemilabile nature of the ligand results in a unique type of coordination where one of the metal–ligand bonds would be relatively weaker than the other. Thus, combining the hemilabile ligand with the acceptor metal unit results in an intermediate that is kinetically controlled and stabilized by the π–π stacking interaction within the two central bridging units and the chelating effect of hemilabile ligands. Further reaction of intermediate with small ancillary ligands, weak ligands are displaced by small ancillary ligands which have the strong coordinating ability with transition metal acceptors. This eventually results in the formation of extended macrocyclic architectures (Fig. 1.5). The significance of this approach is (i) the self-assembly process of the intermediate step is kinetically controlled, (ii) the flexibility of hemilabile ligands helps in the formation of polymeric supramolecular entities as the directionality is unpredictable [20,28,29].

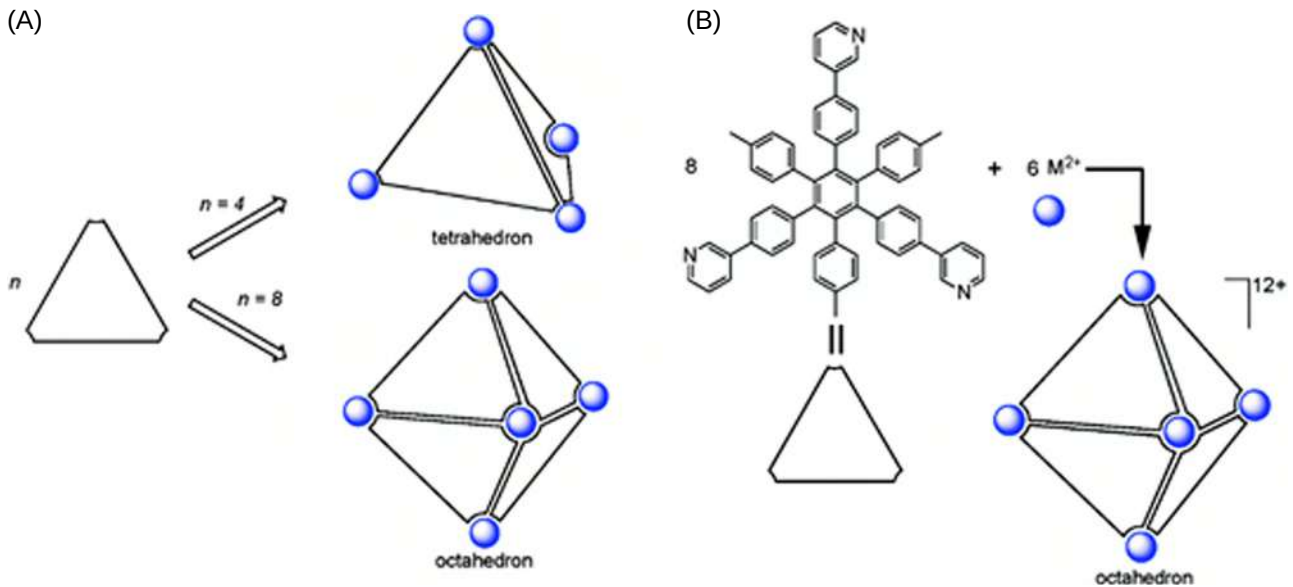

FIGURE 1.4 (A) Schematic representation for assembling a tetrahedron and an octahedron using triangular panels. (B) Formation of a molecular octahedron from a tripyridyl donor which acts as a triangular panel.

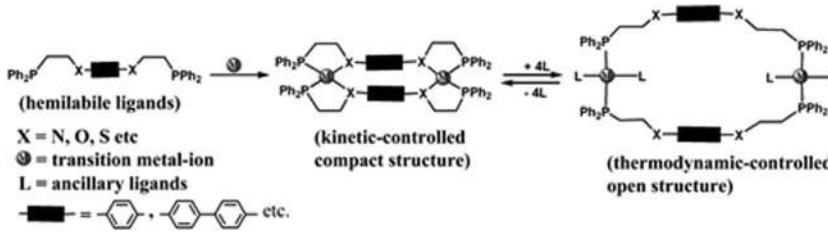

FIGURE 1.5 Schematic representation of the formation of conformationally flexible supramolecular architectures via weak–link approach.

1.3.5 Dimetallic building block approach

This design strategy was first developed by Cotton and his group for the design of aesthetic supramolecular ensembles with structural neutrality [21,22]. The interesting part of this approach is the construction of complexes possessing dimetallic paddle wheels or lantern-like frameworks. The popularly used dimetallic paddle units are Mo_2^{4+} and Rh_2^{4+} based complex and the linking units belong to the class of various organic linkers. The substituents present on the dimetallic unit play an important role in the self-assembly process. Nonlabile chelating ligands such as amidinate are present on one or more edges of the dimetallic units which resist the unnecessary coordination and oligomerization reaction and the remaining sites are filled by labile ligands like chloride ions, acetonitriles, etc. An example of equatorial and axial organic linker units is polycarboxylate and polypyridyl organic ligands, respectively. Depending upon the selection of the organic linkers, the mode of interactions between the linkers and dimetallic units can be classified as (i) the face-to-face approach with the axial linker, (ii) end-to-end with the equatorial linker, and iii) the mixture of both equatorial as well as axial linkers (Fig. 1.6) [21,22].

1.4 Characterization of supramolecular coordination complexes

Advancements in analytical techniques have a remarkable impact on the swift development of coordination-driven self-assembly. The common characterization techniques used for the analysis of supramolecular coordination complexes are mass spectrometry (MS), nuclear magnetic resonance spectroscopy (NMR), and X-ray diffraction (XRD) analysis. NMR spectroscopy has been used as the primary characterization technique to understand the ligand to metal coordination interactions by observing the chemical shift changes before and after the self-assembly reaction. NMR also reveals the number of products that form in the self-assembly reaction [13].

For example, Stang et al. prepared a heterometallic trigonal bipyramidal cage via [2+3] self-assembly reaction between a Pt(II) 90° acceptor and a predesigned

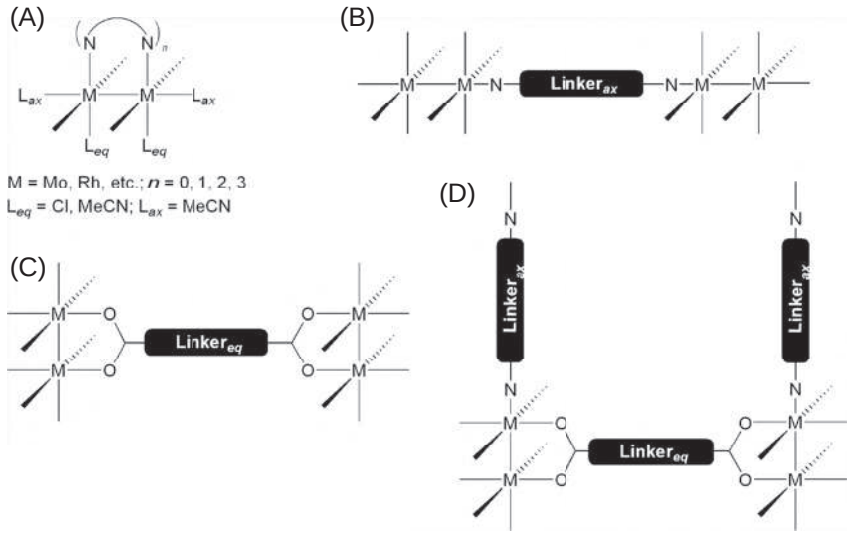

FIGURE 1.6 Different modes (a–d) of assembly of dinuclear units in dimetallic building block approach.

Ga(III) based tri-4-pyridyl donor in a CD_2Cl_2–CD_3NO_2 medium after 5 h of stirring at room temperature (Fig. 1.7A) [50]. The metal–ligand coordination interaction in the formation of the bipyramidal cage was supported by NMR analysis. The $^{31}P\{^1H\}$ NMR spectrum of the cage appeared as a sharp singlet at -1.4 ppm along with ^{195}Pt satellite peaks, which is upfield shifted by 14 ppm compared to the starting 90° acceptor; this upfield shift is due to the increased electron-density at Pt(II) centers and subsequent shielding of ^{31}P nuclei upon coordination of pyridyl to platinum (Fig. 1.7B). The metal–ligand coordination was further supported by the ^1H NMR spectrum in which the peaks corresponding to the pyridyl unit were significantly downfield shifted due to the loss of electron density upon coordination. Even though NMR analysis delivers a general idea of the complex formation, it is often not to be considered adequate proof of the structural characterization of supramolecular complexes. In the last decades, several advanced analytical techniques have emerged for the precise determination of the structure of self-assembled supramolecular complexes with great ease and improved resolution. The high-resolution mass spectrometric analysis of the supramolecular complexes provides information about the chemical composition of supramolecular structures. Soft ionization techniques like electrospray ionization mass spectrometry (ESI-MS) usually lower the internal energy of the ions, thus subduing the massive fragmentation without disturbing the easy ionization of noncovalent supramolecular coordination assemblies. For instance, further proof of the formation of the aforesaid trigonal-bipyramidal cage was obtained from the ESI-MS analysis. The ESI-MS spectrum displayed two well-resolved peaks at $m/z = 1500.2$ and 950.8, corresponding to $[M-2OTf]^{2+}$ and

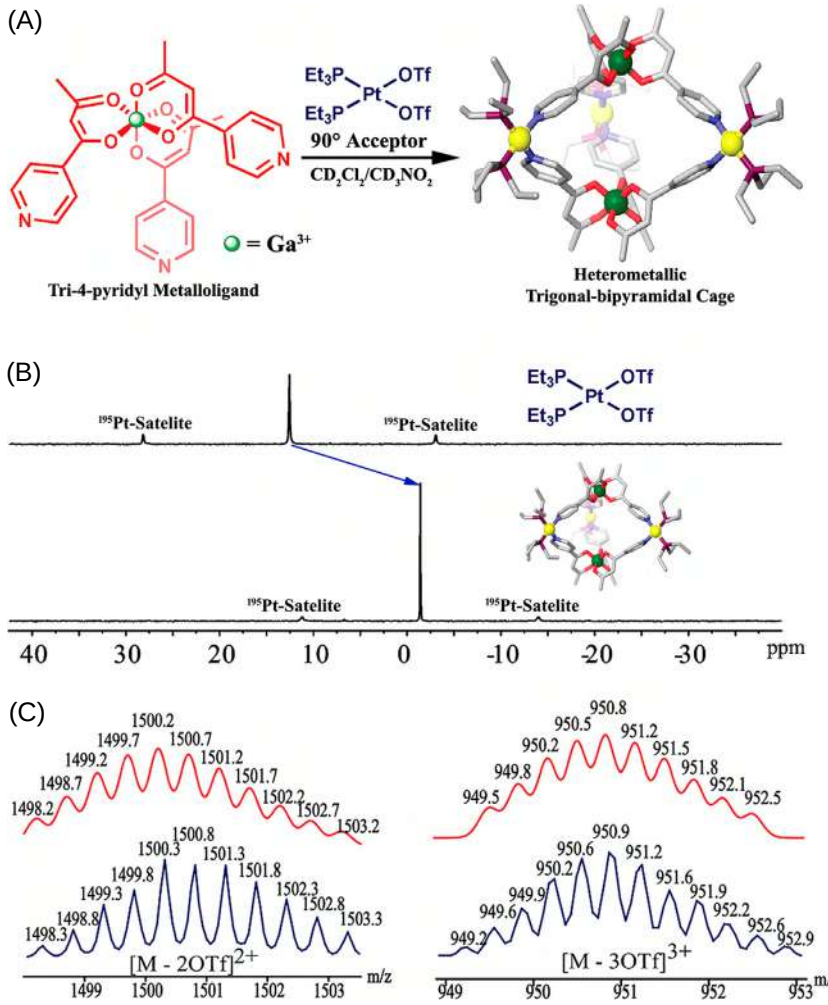

FIGURE 1.7 (A) [2+3] self-assembly formation of the heterometallic trigonal-bipyramidal cage from the reaction of a 90° acceptor with Ga^{3+} based tri-4-pyridyl donor in CD_2Cl_2–CD_3NO_2; (B) $^{31}P\{^1H\}$ NMR spectra the trigonal–bipyramidal cage compared with the starting 90° Pt(II) acceptor; (C) Calculated (red) and experimental (blue) ESI-MS spectrum of the trigonal-bipyramidal cage corresponding to the $[M-2OTf]^{2+}$ and $[M-3OTf]^{3+}$ charged species. Reprinted with permission from Ref. [50]. Copyright 2012 American Chemical Society.

$[M-3OTf]^{3+}$, respectively. These charged peaks were isotopically resolved and they were in good agreement with the calculated distributions (Fig. 1.7C). In addition to ESI-MS, several other mass-spectrometric techniques were also used for the identification of supramolecular ensembles. For instance, Yang and Li et al. developed novel 2D ring-in-ring complexes as well as 3D sphere-in-sphere

supramolecular entities by the self-assembly of pyridyl-based tetratopic ligand with two different Pt(II) metal acceptors with 180° bite angle and naked Pd(II) metal acceptor units, separately [31]. The self-assembled structures were characterized by using different techniques like multidimensional mass spectrometry, atomic force microscopy (AFM), transmission electron microscopy (TEM), and diffusion-ordered NMR spectroscopy (DOSY), two-dimensional (COSY and NOESY) as well as multinuclear NMR spectroscopy [13]. Amidst all these techniques, multidimensional MS data provided more precise information about the structure of the complexes. The qualitative conformational data was obtained using conventional ESI-MS, and the structural isomers or conformers were identified using ion mobility mass spectroscopy (IM–MS) [31]. Finally, the difference in stability of the supramolecular complexes was analyzed using gradient tandem-mass spectrometry (gMS) (Fig. 1.8). Lately, several complex supramolecular architectures were reported from the same group and they were characterized using a combination of MS techniques.

The X-ray diffraction (XRD) technique is a well-founded characterization method for the self-assembled supramolecular coordination systems as the molecular structure can unambiguously be comprehended by single-crystal XRD analysis. Despite that, the XRD method has been considered the most convenient technique for the characterization of supramolecular coordination complexes, usage of conventional single-crystal XRD approaches is restrained due to the complication in crystallization because of the intricate and flexible nature of self-assembled structures [13]. To surmount these issues, in the recent past, a novel solution-phase XRD technique has emerged that delivers information about the shape and structural features of the metallo-assemblies in the solution phase. This exceptional quality makes the new XRD method much more useful compared to the traditional crystallographic methods. The solution-phase X-ray machine has two different scatterings namely, small-angle (SAXS) and wide-angle (WAXS) scattering in which SAXS is utilized for low-resolution characterization whereas WAXS allows high-resolution data collection [32]. The combination of both generates a clear structural and conformational picture of the sample in solution. As a comparison, the Tiede group analyzed the solution as well as the solid-state X-ray crystallography method [33]. The observations obtained from solution phase XRD analysis were in good agreement with the molecular modeling analysis.

1.5 Functionalization of supramolecular coordination complexes

The properties of supramolecular coordination complexes depend on the functional groups present in them. Therefore, the functional properties of supramolecular complexes can accurately be modified through the proper selection and the introduction of desired functional groups within the system [8]. There are two well-established methods by which the desired functionality

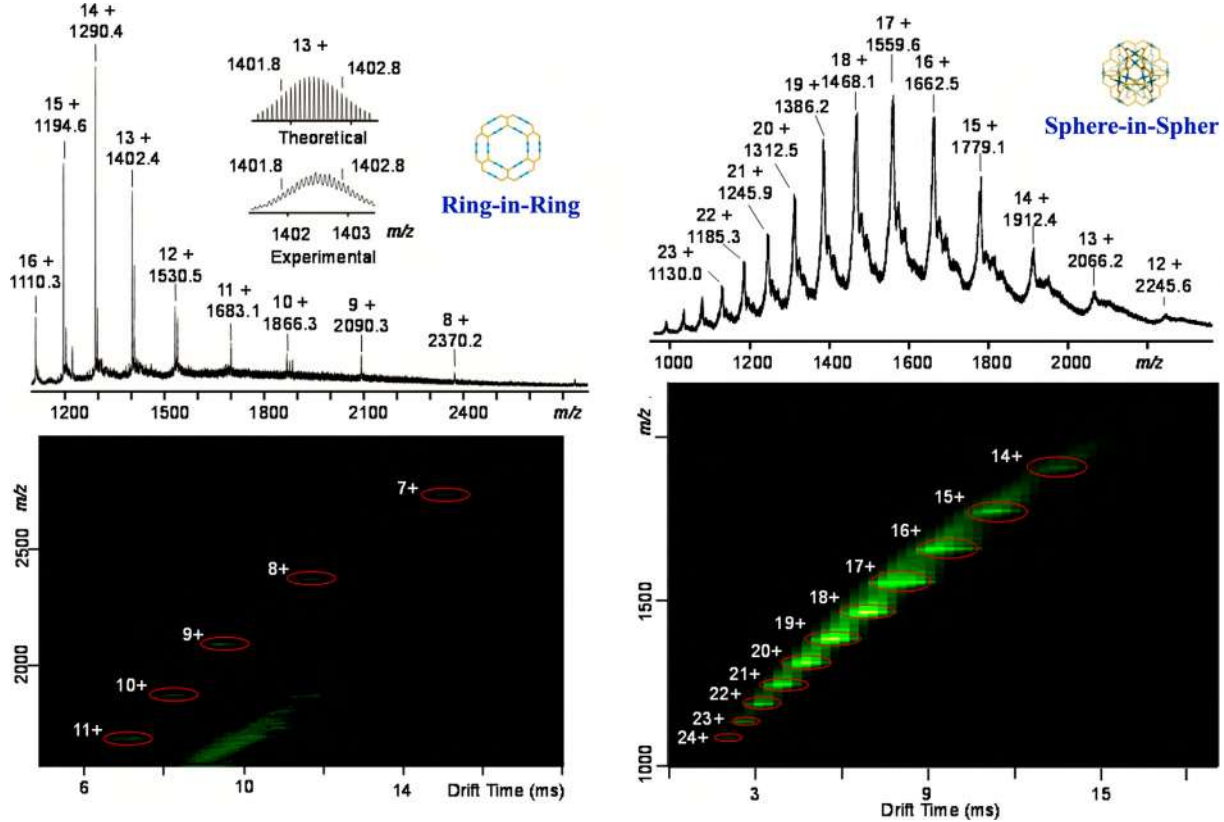

FIGURE 1.8 ESI-MS spectrum of ring-in-ring structure (with an inset showing the calculated and experimental isotopic patterns for the 13^+ charged species) (top left) and 2D ESI-IM-MS plot (*m/z* vs. drift time) of ring-in-ring structure (left-bottom); ESI-MS (top-right) and 2D ESI-IM-MS plot (*m/z* vs. drift time) of sphere-in-sphere structure with BF_4^- as the counterion (bottom-right). Reprinted with permission from Ref. [31]. Copyright 2015 American Chemical Society.

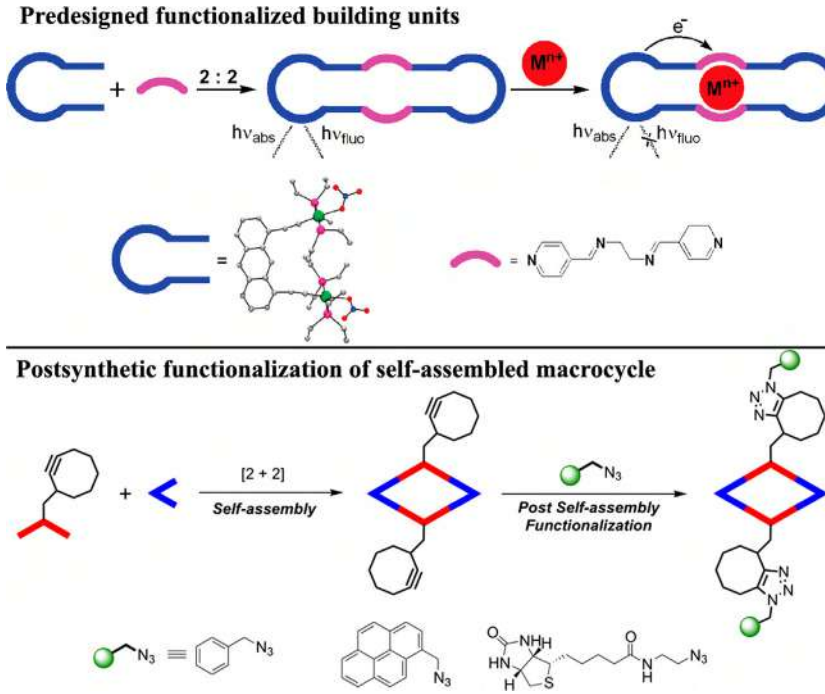

FIGURE 1.9 Examples of predesigned anthracene functionalized [2+2] molecular rectangle used as a fluorescence sensor for the discriminative sensing of metal cations (top). The post–self-assembly functionalization of organoplatinum(II) metallacycles bearing cyclooctynes underwent Huisgen cycloaddition reaction with a varied of azides to yield postfunctionalized supramolecular ensembles (bottom). Reprinted with permission from Refs. [11] and [12]. Copyright 2009, 2012 American Chemical Society.

can be introduced within the supramolecular system (i) using the predesigned precursors functionalized with desired functionality and (ii) postsynthetic functionalization of already self-assembled structures with desired functional groups (Fig. 1.9) [8, 11–12]. Some of the common functional groups introduced into the systems are porphyrin, ferrocene, anthracene, pyrene, etc. One of the finest examples of functional supramolecular architecture is the assemblies formed from the transition metal building blocks with unsaturated ethynyl moiety within the backbone [8, 11–12]. In the past decades, a plethora of functional supramolecular coordination complexes have been designed and used for their various applications including optoelectronics, chemical sensing, host–guest chemistry, etc. (see Fig. 1.9). The supramolecular structures with Pt(II)-ethynyl moieties are highly emissive due to the efficient metal-to-ligand charge transfer (MLCT) transition and thus, those complexes have been realized for optoelectronic material applications. The triethyl phosphine (PEt_3) is another commonly used moiety in the supramolecular design. The attachment of the bulky PEt_3 group increases the

stability of complexes by restricting the generation of possible excimers between the macrocyclic systems and limiting the number of available coordination sites on the metal center and also helps to improve the solubility of self-assembled structures in common organic solvents.

1.6 Self-sorting and self-selection in supramolecular coordination complex formation

Various natural systems such as proteins, nucleic acids, and lipids employ supramolecular noncovalent interactions to generate large biomolecules and to perform various biological functions. In other words, self-organization can be considered as one of the potential forces that led to the growth of the biological era [8]. The easiness in the synthesis of desired supramolecular assemblies depends mainly on the kinetic reversible nature of metal–ligand coordination that ultimately results in thermodynamically stable complexes [8]. However, a few other characteristic features such as the association constant of the building blocks, concentration, and temperature are also integral aspects of governing the degree of self-organization. The formation of varieties of supramolecular assemblies mainly depends on the extent to which the self-association was successful. In some cases, the process would be an absolute association that results in the generation of distinct supramolecular ensembles, other possibilities include the formation of statistical mixtures of complexes and amplified supramolecular systems with few structures in higher proportion (Fig. 1.10A) [34]. The self-selection and self-sorting phenomena can be comprehended by the coordination-driven directional self-assembly of numerous donor and acceptor building blocks. Self-selection is an amazing characteristic feature of supramolecular architecture that permits the formation of self-assembled complexes from a mixture of intricate constituents [8]. In 1993, the Lehn group demonstrated the earliest example of the self-selection process [35]. They reported the construction of metal helices via the combination of various ligand moieties to a metal ion. For instance, a mixture of bipyridine units when treated with Cu(II) ions generated double helicates. Similarly, when two separate tris-bipyridine donor units were reacted with two metal ions (Cu(I) and Ni(II) ions), the reaction favored the generation of a double helicate and a triple helicate exclusively. This example designates the discriminative binding of like-metal ions with like-donor ligands to generate a mixture of selectively combined supramolecular ensembles. Hupp and his team illustrated an example of self-sorting phenomena [36]. The self-assembly of a metal-acceptor with two different linear donor units with varying lengths usually results in the generation of mixed products having two differently sized molecular squares and one rectangular geometry. However, the self-assembly process of $Re(CO)_5Cl$ with two different pyridyl-based rigid donor units (pyrazine and 4,4-bipyridine) resulted in the generation of only two kinds of molecular squares instead of squares and a rectangle.

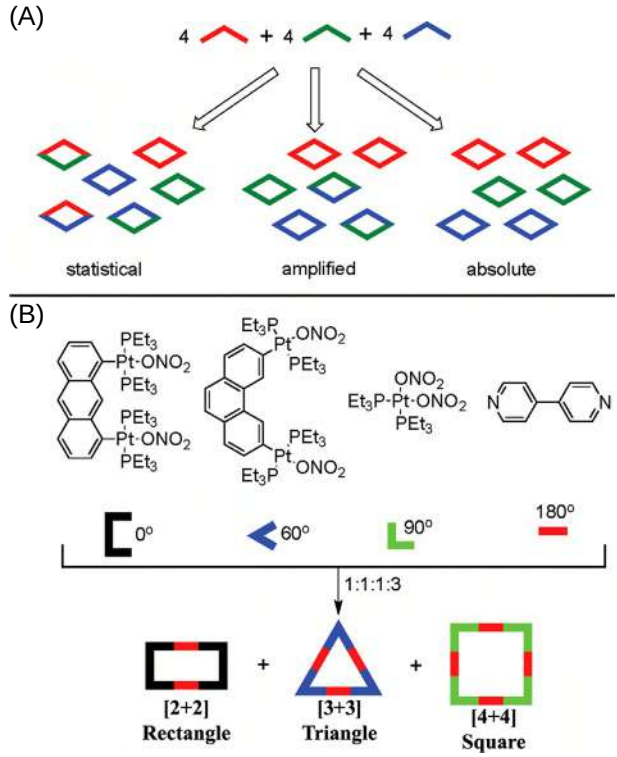

FIGURE 1.10 (A) Schematic representation of different extents of molecular self-organization that can occur within a complex mixture of building units. (B) The absolute self-organization of different Pt(II)-acceptors having 0°, 60°, and 90° bite angles between their accepting sites with a linear 4,4′-bipyridine in 1:1:1:3 molar ratio results in the formation of a discrete rectangle, a triangle, and a square, respectively. Reprinted with permission from Refs. [34] and [37]. Copyright 2009 American Chemical Society, Copyright 2004 American Chemical Society.

Stang group has extensively studied the self-organization and self-sorting phenomena of Pt(II)-based 2D and 3D supramolecular coordination complexes formations [37]. They have analyzed and demonstrated that by the judicious selection and modification of subunits parameters (such as size, bite-angle, and position of coordinating sites), absolute self-organization could be realized without applying any external forces and diverse kinds of supramolecular coordination complexes can be designed following this strategy. For instance, the combination of a linear dipyridyl donor, 4,4′-bipyridine, in a 3:1:1:1 molar ratio with three different Pt(II) acceptors led to the absolute self-organized product formation such as a [2+2] rectangle, a [3+3] triangle and a [4+4] molecular square in quantitative yield (Fig. 1.10B) [37].

1.7 Selected examples of 2D and 3D supramolecular coordination complexes

Generally, 2D metallacycles are synthesized via the linear combination of suitable building units mixing them in an appropriate molar ratio. The journey of the 2D world of supramolecular chemistry began with Fujitha's group's first report on the development of a metal-cornered [4+4] molecular square complex [38]. After this seminal contribution, the research interests in the development of 2D metallacycles vary from simple molecular rhomboids to complicated polygonal structures have gained significant attention, and evolved very rapidly. In the following passage, we exemplified various selected examples of 2D supramolecular architectures. The simple and easy to synthesize 2D supramolecular macrocycle is molecular rhomboid. The rhomboid structure of the metallacycles can be obtained by the directional self-assembly of the metal-based 90° acceptor unit and organic donor with an angular shape and a bite angle of ∼120° [8]. One such example of a molecular rhomboid (**SCC-1**) was obtained via a [2+2] self-assembly reaction of a novel carbazole-functionalized angular dipyridyl donor, 3,6-di(4-pyridylethynyl)carbazole (**D_1**), and *cis*-(dppf)Pd(OTf)$_2$ 90° acceptor (**A_1**) mixed them in 1:1 stoichiometry ratio and stirred at 50°C for 5 h [30]. **SCC-1** formation was fully supported by the multinuclear NMR and the molecular structure was unambiguously proved by the x-ray diffraction analysis. Due to the large internal cavity, the π-electron-rich **SCC-1** was further employed as a potential host forming a stable 1:1 host–guest complex with electron-poor fullerene C_{60} guest, and this complex was stabilized by the strong donor–acceptor type of π–π interactions (Fig. 1.11A). The host–guest binding was probed using fluorescence titration studies. The initial strong emission of **SCC-1** was attenuated upon the addition of C_{60} in increasing concentration and the calculated binding constant (K_{SV}) was 1.0×10^5 M^{-1} [30].

Another interesting category of 2D supramolecular architecture is molecular triangles. Molecular triangular structures are in general formed through the directional bonding approach either by the combination of three linear building units having 180° bite angle and complementary three 60° donor ligand units or by joining a contorted metal-based acceptor unit with three flexible as well as linear donor moiety [1,8]. However, the second approach is practically difficult due to the lack of distorted 60° metal-based acceptor units. Another self-assembly strategy involves the combination of metal acceptors with octahedral geometry such as Fe(II) or Ru(II) complexes with 60° ligand units having two different coordinating sites like terpyridine-based donor ligands [39]. Another prime example is the synthesis of a single linkage isomeric molecular triangular architecture through the self-assembly of 90° cis-blocked Pd(II)/Pt(II) based metal acceptors with various ambidendate complementary donors [40]. In 2007, Mukherjee et al. synthesized a heterometallic (Fe^{2+} and Pd^{2+}) [3+3] molecular triangle from the self-assembly reaction of a cis-blocked 90° acceptor (**A_1**) with an ambidentate donor, sodium nicotinate (**D_2**) [41]. Due to the different bonding

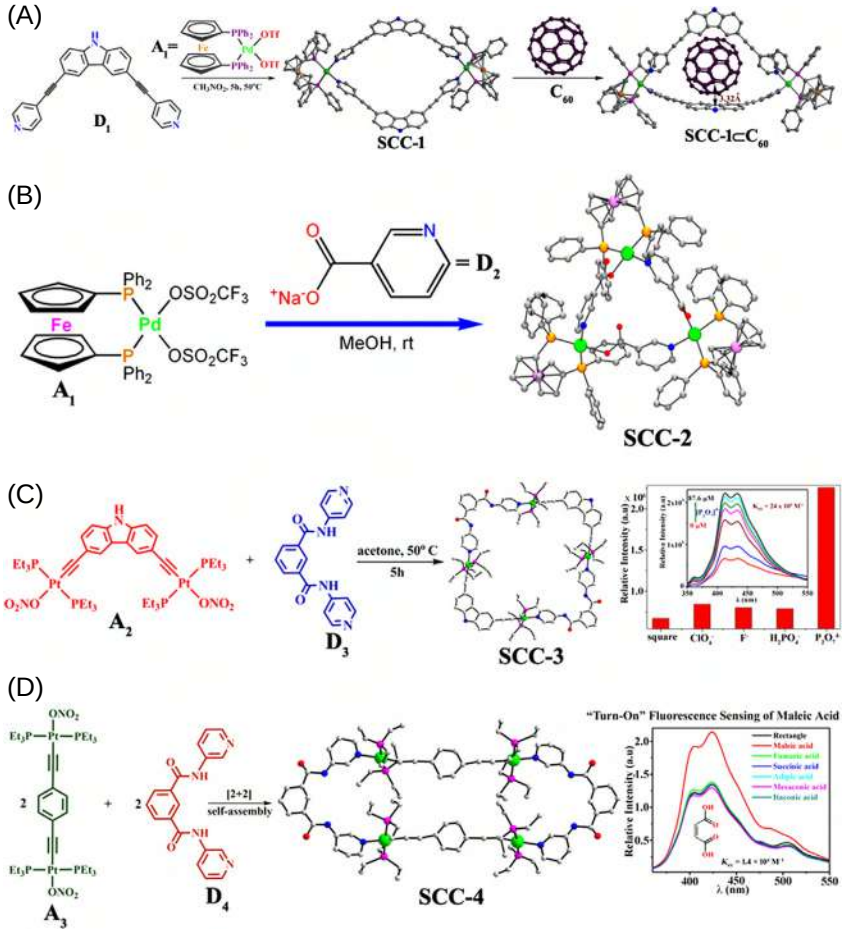

FIGURE 1.11 Schematic representation of (A) carbazole-containing molecular rhomboid (**SCC-1**) and its host–guest complex with C_{60}, (B) self-selective self-assembly formation of the heterometallic single isomeric molecular triangle (**SCC-2**), (C) carbazole-based organometallic [2+2] molecular square (**SCC-3**) and its application as a chemosensor for pyrophosphate anion, (D) two-component self-assembly formation of a molecular rectangle (**SCC-4**) for selective turn-on fluorescence sensing maleic acid. Reprinted with permission from Refs. [30,41,45], and [47]. Copyright 2012, 2010 American Chemical Society, Copyright 2007, 2013 Royal Society of Chemistry.

connectivity, different linkage isomeric molecular triangles were expected, however, the self-assembly reaction resulted in the isolation of one single-linkage isomeric triangle formation. The formation of the self-selection single triangle was supported by the ^{31}P NMR spectrum which showed two sharp signals corresponding to indicating the formation of a symmetrical triangular structure and further confirmed that no other isomeric products or oligomers were present

in the isolated product. The symmetrical triangle formation was proved by the single diffraction analysis (Fig. 1.11B).

The next dominant category of 2D assemblies is molecular squares. Because of the stable conformation and remarkable structural characteristics, molecular squares are more common compared to other 2D supramolecular entities [1,8]. The molecular square can easily be built by the self-assembly of four *cis*-block metal acceptors having 90° bite angles with complementary four linear donor building units. Another synthetic pathway involves the combination of four linear metal-based acceptors and corresponding four 90° corner units [8]. In 1991, Fujita and his group designed the first molecular square using the combination of cis-blocked palladium (II)-based metal acceptor with 90^0 bite angle $[Pd(en)(NO_3)_2]$ and 4,4 bipyridyl donor moiety [42]. Similarly, numerous varieties of functional molecular squares with different functional modifications were generated using this synthetic approach [1,8]. For instance, a series of neutral chiral metalla-squares were designed by Hupp's group via the self-assembly of Re(I) metal-based acceptor by reacting with numerous organic donors [43]. Würthner group has reported several electrochemically active molecular squares derived from perylene bisimide-based organic donors [44]. We have developed a series of [2+2] molecular squares via the two-component self-assembly processes. For example, a novel carbazole functionalized [2+2] molecular square (**SCC-3**) was designed by employing Pt^{II}_2 organometallic 90° acceptor, 3,6-bis[*trans*-platinum(triethylphosphine)$_2$(nitrate)(ethynyl)] carbazole (**A_2**), combined in a stoichiometric ratio with a flexible amide-based ditopic donor, 1,3-bis(4-pyridyl)isophthalamide (**D_3**) (Fig. 1.11C) [45]. **SCC-3** is an interesting square composed of amide-based receptor sites and carbazole-based luminescent moieties which can act as an indicator for chemosensor applications. **SCC-3** exhibited a moderate emission intensity and upon the addition of pyrophosphate ($P_2O_7^{4-}$) anions, significant enhancement in emission intensity was observed due to the strong binding of molecular square with anion in solution. Notable, the addition of other anions including F^-, ClO_4^-, and $H_2PO_4^-$ showed negligible effects on the emission properties. Hence, **SCC-3** could be used as a potential chemosensor for selective detection of pyrophosphate anion with strong binding efficiency.

Molecular rectangles are one of the 2D assemblies with synthetic difficulties due to the counter formation of molecular squares [8]. Typically, these 2D architectures are generated by the three-component [4+2+2] self-combination of cis-blocked 90° acceptor with two separate donors with linear geometry. However, this type of self-association would usually result in the formation of two diverse molecular squares rather than molecular rectangles due to the dearth of discriminative recognition between the two organic donor building units [8]. As an alternative to this approach, a new two-component self-assembly strategy was introduced by Stang and Mukherjee groups. In this approach, a molecular clip type-units with a 0° bite angle reacted in a 1:1 molar ratio with linear complementary building units to quantitatively isolate a [2+2] molecular rectangle [46].

As an example, we designed a [2+2] molecular rectangle (**SCC-4**) employing a linear Pt^{II}_2 acceptor which was reacted with a clip-type pyridyl donor, 1,3-bis(3-pyridyl)isophthalamide (**D_4**), with a 0° bite angle (Fig. 1.11D) [47]. Owing to the intrinsic fluorescence nature and the presence of amide-functional moieties, **SCC-4** was used as a potential chemosensor for the selective detection of maleic acid. The moderate emission intensity of **SCC-4** was drastically enhanced upon the addition of maleic acid while other interfering acids did not show any effect on the fluorescence properties. Similarly, numerous metalla-rectangles with application in supramolecular host–guest chemistry were designed and synthesized through this facile and easy pathway.

A large number of 2D supramolecular assemblies with higher-order polygonal structures have been reported in recent years [7,8]. Within the higher-order category, 5-membered and 6-membered molecular architectures are a common class of metallomacrocycles. As per the directional approach, a pentagonal macrocycle can be obtained by the self-assembly of five linear precursors combine with five angular complementary building units. In 2005, Hwang and coworkers reported a molecular pentagon (**SCC-5**) by the self-assembly of an octahedral Fe(II) ion with a terpyridine-based donor unit, 9-hexyl-3,6-bis(terpyridine)carbazole (**D_5**) (Fig. 1.12A) [48]. The hexagonal assemblies can be generated by the coordination-driven assembly of six 120° building moieties with six complimentary units with linear geometry or vice versa [8]. For example, a [6+6] molecular hexagonal (**SCC-6**) assembly was obtained by the self-assembly of a bimetallic Pt(II) based linear acceptor (**A_6**) with 120° angular dipyridyl donor unit (**D_6**) after stirring for 12 h at room temperature (Fig. 1.12B) [49].

The design approaches for 3D supramolecular metallocages are challenging because of their inherent structural intricacy and they require a judicious design strategy for the construction of 3D architectures [1,8]. A basic necessity of 3D cages is the presence of a building block with three or more coordination units. A molecular trigonal prism can be designed through the combination of a tritopic donor unit with 120° bite angles with a clip-type complementary acceptor unit. One such example is the formation of Ru(II) based M_3L_2 molecular trigonal prism (**SCC-7**) from the self-assembly reaction of a tri-pyridyl donor, 1,3,5-tris(4-pyridylethynyl)benzene (**D_7**), and dinuclear half-sandwich octahedral Ru(II) acceptor (**A_7**) (Fig. 1.13A) [50]. The presence of the arene-ethynyl moieties engenders **SCC-7** being strongly emissive and thus, it was employed as a fluorescence chemosensor for the ultra-trace detection of 1,3,5-trinitrotoluene (TNT) in solution. Following this two-component self-assembly method, Mukherjee, Stang, and several other research groups have reported a variety of trigonal prismatic cages and used them for various applications starting from chemo-sensing to stimuli-responsive drug delivery in biomedicine [8]. Similarly, the construction of supramolecular tetragonal prisms is difficult to achieve from multicomponent self-assembly reactions. However, by the careful design of appropriate building units and following the two-component

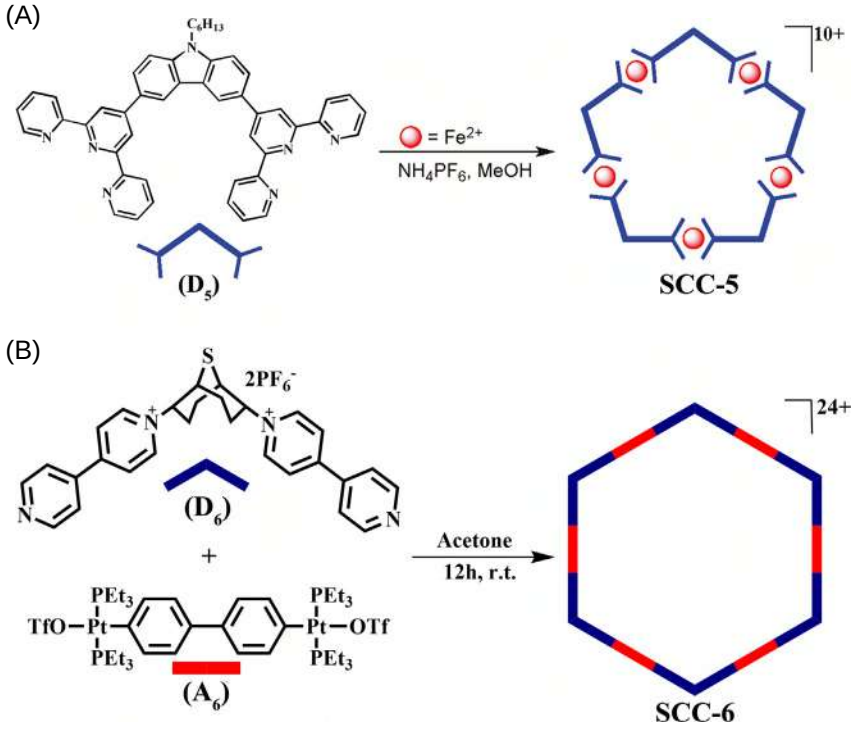

FIGURE 1.12 Schematic representation of (A) carbazole–terpyridine-based molecular pentagonal assembly (**SCC-5**) and (B) [6+6] self-assembly formation of a molecular hexagon (**SCC-6**). Reprinted with permission from Refs. [48] and [49]. Copyright 2005 Royal Society of Chemistry; Copyright 2006 American Chemical Society.

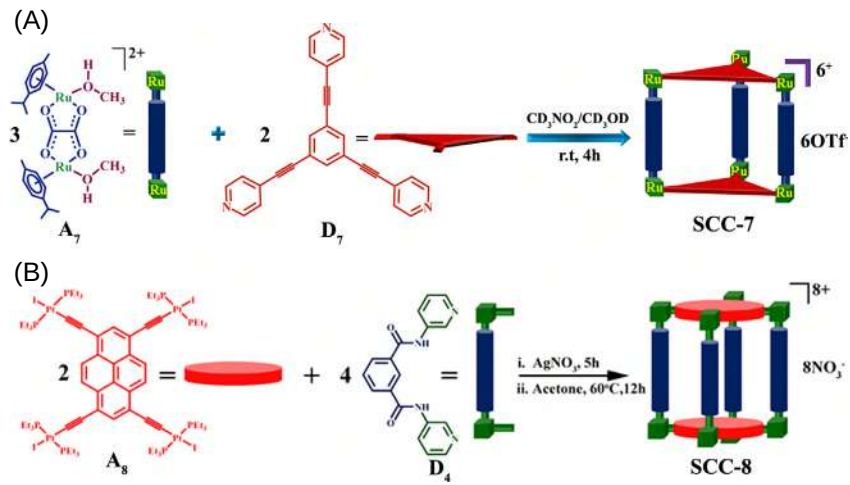

FIGURE 1.13 Schematic representation of (A) coordination-self-assembly formation of M_3L_2 trigonal prism **SCC-7**; (B) tetragonal prism (**SCC-8**) self-assembled from a pyrene-containing start-shaped Pt(II) acceptor ($\mathbf{A_8}$) with a clip-type dipyridyl donor ($\mathbf{D_4}$).

self-assembly strategy, the molecular tetragonal prism can easily be designed in quantitative yield [8]. For example, Shanmugaraju et al. have reported a cationic pyrene-based Pt^{II}_8 tetragonal prism **SCC-8** (Fig. 1.13B); this prismatic cage was obtained by reacting a pyrene-based star-shaped Pt(II) acceptor ($\mathbf{A_8}$) with dipyridyl donor $\mathbf{D_4}$. The π-electron-rich prism **SCC-8** was used as a host molecule that formed an efficient host–guest complex with electron-deficient nitroaromatic guests both in solution and vapor phase [51].

1.8 Conclusion

In this chapter, we have mainly focused on the background and various design principles of coordination-driven self-assembly processes. We have also highlighted the significant advancement in analytical methods for the characterization of self-assembled complexes including the self-sorting and self-selection in supramolecular coordination self-assembly. At last, we have exemplified a few selected examples of various two-dimensional and three-dimensional metallosupramolecular architecture; their synthesis, characterization, and in some cases applications also have been briefly mentioned. Coordination-driven self-assembly is a rapidly growing research area with amazing applications in various fields of science. A variety of supramolecular assemblies ranging from simple molecular triangles to complex three-dimensional cages can be generated by carefully selecting suitable complementary building units. High-resolution NMR spectroscopy and ESI-MS analysis are the fundamental characterization tools used for the structural elucidation of supramolecular complexes. Even though myriads of supramolecular architectures with various practical applications are developed, the structural characterizations of the assemblies are quite complicated due to the difficulty in the generation of single crystals of these intricate supramolecular ensembles through the XRD technique. Recently, an expensive synchrotron-based technique is utilized for the structural characterization of coordination assemblies. In the coming chapters, numerous applications of the two-dimensional and three-dimensional supramolecular structures are discussed in detail.

Acknowledgment

We gratefully acknowledge the Science and Engineering Research Board (EMEQ Award EEQ/2018/000799 to S.S.), India, and the Indian Institute of Technology Palakkad (IITPKD) for financial support.

References

[1] B. Mohan, S. Shanmugaraju, Self-assembled metallo-assemblies, published in Supramol, Chem. Corros. Biofouling Prot. (2021) 103–128.

[2] C.J. Pedersen, The discovery of crown ethers (Noble Lecture), Angew. Chem. Int. Ed. Engl. 27 (1988) 1021–1027.

[3] J. Lehn, Supramolecular chemistry—scope and perspectives molecules, supermolecules, and molecular devices (Nobel Lecture), Angew. Chem. Int. Ed. Engl. 27 (1988) 89–112.
[4] D.J. Cram, The design of molecular hosts, guests, and their complexes (Nobel lecture), Angew. Chem. Int. Ed. Engl. 27 (1988) 1009–1020.
[5] P.J. Stang, B. Olenyuk, Self-assembly, symmetry, and molecular architecture: coordination as the motif in the rational design of supramolecular metallacyclic polygons and polyhedra, Acc. Chem. Res. 30 (1997) 502–518.
[6] J.W. Steed, D.R. Turner, K. Wallace, Core concepts in Supramolecular Chemistry and Nanochemistry, Wiley, Hoboken, New Jersey, U.S., 2007.
[7] P.J. Stang, Molecular architecture: coordination as the motif in the rational design and assembly of discrete supramolecular species—self-assembly of metallacyclic polygons and polyhedra, Chem. Eur. J. 4 (1998) 19–27.
[8] R. Chakrabarty, P.S. Mukherjee, P.J. Stang, Supramolecular coordination: self-assembly of finite two-and three-dimensional ensembles, Chem. Rev. 111 (2011) 6810–6918.
[9] P.J. Stang, From solvolysis to self-assembly, J. Org. Chem. 74 (2009) 2–20.
[10] B. Therrien, Arene ruthenium cages: boxes full of surprises, Eur. J. Inorg. Chem. 2009 (2009) 2445–2453.
[11] R. Chakrabarty, P.J. Stang, Post-assembly functionalization of organoplatinum(II) metallacycles via copper-free click chemistry, J. Am. Chem. Soc. 134 (2012) 14738–14741.
[12] S. Ghosh, R. Chakrabarty, P.S. Mukherjee, Design, synthesis, and characterizations of a series of Pt4 macrocycles and fluorescent sensing of Fe^{3+}/Cu^{2+}/Ni^{2+} through metal coordination, Inorg. Chem. 48 (2009) 549–556.
[13] H.-B. Yang, Metallomacrocycles: From Structures to Applications, Royal Society of Chemistry, 2018.
[14] P.N.W. Baxter, J. Lehn, B.O. Kneisel, G. Baum, D. Fenske, The designed self-assembly of multicomponent and multicompartmental cylindrical nanoarchitectures, Chem. Eur. J. 5 (1999) 113–120.
[15] P.N.W. Baxter, J. Lehn, G. Baum, D. Fenske, The design and generation of inorganic cylindrical cage architectures by metal-ion-directed multicomponent self-assembly, Chem. Eur. J. 5 (1999) 102–112.
[16] R.W. Saalfrank, R. Burak, S. Reihs, N. Löw, F. Hampel, H. Stachel, J. Lentmaier, K. Peters, E. Peters, H.G. von Schnering, Synthesis and structure of tetra-and octanuclear chelate complexes—exohedral guest exchange in tetrahemispheraplexes, Angew. Chem. Int. Ed. Engl. 34 (1995) 993–995.
[17] D.L. Caulder, K.N. Raymond, The rational design of high symmetry coordination clusters, J. Chem. Soc. Dalt. Trans. (1999) 1185–1200.
[18] D.L. Caulder, K.N. Raymond, Supermolecules by design, Acc. Chem. Res. 32 (1999) 975–982.
[19] M. Fujita, M. Tominaga, A. Hori, B. Therrien, Coordination assemblies from a Pd (II)-cornered square complex, Acc. Chem. Res. 38 (2005) 369–378.
[20] C.G. Oliveri, P.A. Ulmann, M.J. Wiester, C.A. Mirkin, Heteroligated supramolecular coordination complexes formed via the halide-induced ligand rearrangement reaction, Acc. Chem. Res. 41 (2008) 1618–1629.
[21] F.A. Cotton, C. Lin, C.A. Murillo, The use of dimetal building blocks in convergent syntheses of large arrays, Proc. Natl. Acad. Sci. 99 (2002) 4810–4813.
[22] F.A. Cotton, C. Lin, C.A. Murillo, Supramolecular arrays based on dimetal building units, Acc. Chem. Res. 34 (2001) 759–771.

[23] B.H. Northrop, D. Chercka, P.J. Stang, Carbon-rich supramolecular metallacycles and metallacages, Tetrahedron 64 (2008) 11495–11503.
[24] R.W. Saalfrank, I. Bernt, E. Uller, F. Hampel, Template-mediated self assembly of six-and eight-membered iron coronates, Angew. Chem. Int. Ed. Engl. 36 (1997) 2482–2485.
[25] M. Fujita, Metal-directed self-assembly of two-and three-dimensional synthetic receptors, Chem. Soc. Rev. 27 (1998) 417–425.
[26] M. Fujita, Molecular paneling through metal-directed self-assembly, Molecular Self-Assembly Organic Versus Inorganic Approaches, Angeliki Athanasopoulou, Springer, Springer Nature Switzerland, 2000, pp. 177–201.
[27] M. Fujita, K. Umemoto, M. Yoshizawa, N. Fujita, T. Kusukawa, K. Biradha, Molecular paneling via coordination, Chem. Commun. (2001) 509–518.
[28] N.C. Gianneschi, M.S. Masar, C.A. Mirkin, Development of a coordination chemistry-based approach for functional supramolecular structures, Acc. Chem. Res. 38 (2005) 825–837.
[29] B.J. Holliday, C.A. Mirkin, Strategies for the construction of supramolecular compounds through coordination chemistry, Angew. Chem. Int. Ed. 40 (2001) 2022–2043.
[30] S. Shanmugaraju, V. Vajpayee, S. Lee, K.-W. Chi, P.J. Stang, P.S. Mukherjee, Coordination-driven self-assembly of 2D-metallamacrocycles using a new carbazole-based dipyridyl donor: synthesis, characterization, and C_{60} binding study, Inorg. Chem. 51 (2012) 4817–4823.
[31] B. Sun, M. Wang, Z. Lou, M. Huang, C. Xu, X. Li, L.-J. Chen, Y. Yu, G.L. Davis, B. Xu, From ring-in-ring to sphere-in-sphere: self-assembly of discrete 2D and 3D architectures with increasing stability, J. Am. Chem. Soc. 137 (2015) 1556–1564.
[32] L. Makowski, Characterization of proteins with wide-angle X-ray solution scattering (WAXS), J. Struct. Funct. Genom. 11 (2010) 9–19.
[33] J.L. O'Donnell, X. Zuo, A.J. Goshe, L. Sarkisov, R.Q. Snurr, J.T. Hupp, D.M. Tiede, Solution-phase structural characterization of supramolecular assemblies by molecular diffraction, J. Am. Chem. Soc. 129 (2007) 1578–1585.
[34] B.H. Northrop, Y.-R. Zheng, K.-W. Chi, P.J. Stang, Self-organization in coordination-driven self-assembly, Acc. Chem. Res. 42 (2009) 1554–1563.
[35] R. Kramer, J.-M. Lehn, A. Marquis-Rigault, Self-recognition in helicate self-assembly: spontaneous formation of helical metal complexes from mixtures of ligands and metal ions, Proc. Natl. Acad. Sci. 90 (1993) 5394–5398.
[36] R.V Slone, K.D. Benkstein, S. Bélanger, J.T. Hupp, I.A. Guzei, A.L. Rheingold, Luminescent transition-metal-containing cyclophanes ("molecular squares"): covalent self-assembly, host-guest studies and preliminary nanoporous materials applications, Coord. Chem. Rev. 171 (1998) 221–243.
[37] C. Addicott, N. Das, P.J. Stang, Self-recognition in the coordination driven self-assembly of 2-D polygons, Inorg. Chem. 43 (2004) 5335–5338.
[38] M. Fujita, J. Yazaki, K. Ogura, Preparation of a macrocyclic polynuclear complex,[(en) Pd (4, 4'-bpy)]$_4$(NO_3)$_8$ (en = ethylenediamine, bpy = bipyridine), which recognizes an organic molecule in aqueous media, J. Am. Chem. Soc. 112 (1990) 5645–5647.
[39] S.-H. Hwang, C.N. Moorefield, F.R. Fronczek, O. Lukoyanova, L. Echegoyen, G.R. Newkome, Construction of triangular metallomacrocycles:[M 3 (1, 2-bis (2, 2′: 6′, 2″-terpyridin-4-yl-ethynyl) benzene)$_3$][M= Ru (II), Fe (II), 2Ru(II)Fe(II)], Chem. Commun. (2005) 713–715.
[40] A.K. Bar, R. Chakrabarty, K.-W. Chi, S.R. Batten, P.S. Mukherjee, Synthesis and characterisation of heterometallic molecular triangles using ambidentate linker: self-selection of a single linkage isomer, Dalt. Trans. (2009) 3222–3229.

[41] S. Ghosh, D.R. Turner, S.R. Batten, P.S. Mukherjee, Self-assembly of a heterometallic molecular triangle using an ambidentate ligand and self-selection for a single linkage isomer, Dalt. Trans. (2007) 1869–1871.

[42] M. Fujita, J. Yazaki, K. Ogura, Spectroscopic observation of self-assembly of a macrocyclic tetranuclear complex composed of Pt^{2+} and 4, 4′-bipyridine, Chem. Lett. 20 (1991) 1031–1032.

[43] R.V Slone, J.T. Hupp, C.L. Stern, T.E. Albrecht-Schmitt, Self-assembly of luminescent molecular squares featuring octahedral rhenium corners, Inorg. Chem. 35 (1996) 4096–4097.

[44] F. Würthner, A. Sautter, Highly fluorescent and electroactive molecular squares containing perylene bisimide ligands, Chem. Commun. (2000) 445–446.

[45] S. Shanmugaraju, A.K. Bar, K.-W. Chi, P.S. Mukherjee, Coordination-driven self-assembly of metallamacrocycles via a new Pt^{II}_2 organometallic building block with 90° geometry and optical sensing of anions, Organometallics 29 (2010) 2971–2980.

[46] P.S. Mukherjee, N. Das, Y.K. Kryschenko, A.M. Arif, P.J. Stang, Design, synthesis, and crystallographic studies of neutral platinum-based macrocycles formed via self-assembly, J. Am. Chem. Soc. 126 (2004) 2464–2473.

[47] S. Shanmugaraju, A.K. Bar, H. Jadhav, D. Moon, P.S. Mukherjee, Coordination self-assembly of tetranuclear Pt (II) macrocycles with an organometallic backbone for sensing of acyclic dicarboxylic acids, Dalt. Trans. 42 (2013) 2998–3008.

[48] S.-H. Hwang, P. Wang, C.N. Moorefield, L.A. Godínez, J. Manríquez, E. Bustos, G.R. Newkome, Design, self-assembly, and photophysical properties of pentameric metallomacrocycles:[M 5 (N-hexyl [1, 2-bis (2, 2′: 6′, 2″-terpyridin-4-yl)] carbazole)$_5$][M= Fe (II), Ru (II), and Zn (II)], Chem. Commun. (2005) 4672–4674.

[49] H.-B. Yang, N. Das, F. Huang, A.M. Hawkridge, D.D. Díaz, A.M. Arif, M.G. Finn, D.C. Muddiman, P.J. Stang, Incorporation of 2, 6-di (4, 4 '-dipyridyl)-9-thiabicyclo [3.3. 1] nonane into discrete 2d supramolecules via coordination-driven self-assembly, J. Org. Chem. 71 (2006) 6644–6647.

[50] M. Wang, V. Vajpayee, S. Shanmugaraju, Y.-R. Zheng, Z. Zhao, H. Kim, P.S. Mukherjee, K.-W. Chi, P.J. Stang, Coordination-driven self-assembly of M3L2 trigonal cages from preorganized metalloligands incorporating octahedral metal centers and fluorescent detection of nitroaromatics, Inorg. Chem. 50 (2011) 1506–1512.

[51] S. Shanmugaraju, H. Jadhav, Y.P. Patil, P.S. Mukherjee, Self-assembly of an octanuclear platinum (II) tetragonal prism from a new Pt^{II}_4 organometallic star-shaped acceptor and its nitroaromatic sensing study, Inorg. Chem. 51 (2012) 13072–13074.

Chapter 2

Supramolecular coordination complexes from metalloligands: Hydrogen bonding-based self-assemblies

Ruchika Gupta, Sanya Pachisia and Rajeev Gupta
Department of Chemistry, University of Delhi, Delhi, India

2.1 Introduction

Nature utilizes simple self-assembly concepts to create challenging structures. In this strategy, weak yet directional bonding interactions play significant roles to develop highly ordered structures [1–5]. Supramolecular chemistry, taking inspiration from nature, has emerged as a fascinating field that relies on the concepts of directional bonding interactions [3,6]. Out of various such interactions, *hydrogen bonding* (H-bonding) interactions have been particularly important due to their ability to afford well-defined and highly ordered self-assembled structures [1,3,4]. Synthetic chemists have also successfully integrated H-bonding sensitive functional groups in a variety of compounds and have studied their self-assembly [1,2,5]. These examples have not only provided aesthetically appealing supramolecular architectures but also many functional materials that are solely manifested by the *hydrogen bonds* (H-bonds) [5,7]. The incorporation of H-bonds has also assisted in the development of rational design strategies that have aided researchers to control the topology and functionality of the resulting supramolecular architectures [8].

A continuing challenge in the field of supramolecular chemistry is the design and construction of architectures having predictable architectures and tailor-made properties [9,10]. In this context, considerable efforts have been made to incorporate H-bonding sensitive functional groups in comparatively rigid organic compounds [1,5]. Alternatively, well-defined coordination complexes have also been developed and employed as the structure-directing building blocks, referred to as the metalloligands, for the synthesis of predictable supramolecular architectures [11–15]. A metalloligand can be defined as a

Supramolecular Coordination Complexes: Design, Synthesis, and Applications.
DOI: https://doi.org/10.1016/B978-0-323-90582-4.00017-8

metal-containing complex offering additional binding sites which can either coordinate to a secondary metal ion (cf. Chapter 3) or involve in H-bonding interactions (this chapter) which can aid in the construction of supramolecular architecture [12–19].

2.2 Coordination complexes as the metalloligands containing appended H-bonding functional groups

A metalloligand is developed by the coordination of one or more multidentate chelating ligand(s) to a metal ion (mostly transition metals). The involvement of a metal ion having a particular geometrical preference induces structural rigidity to the associated multidentate chelating ligand(s) [12–15]. As a result, a metalloligand is inherently rigid in contrast to its multidentate ligand counterpart which is flexible in nature. By the virtue of the structural rigidity of a metalloligand, the auxiliary functional groups are oriented in limited confirmations. Such a feature of a metalloligand has been shown to afford predictable architectures [12–15].

Inspired by the success of the H-bonding assisted self-assembly process in organic compounds, efforts have also been made to integrate H-bonding functional groups to the well-defined metalloligands [3,16–19]. The idea is that the inherent rigidness of a metalloligand will result in limited orientation(s) of the appended functional groups emerging from a metalloligand. Such a strategy may result in the design and synthesis of predictable architectures.

Pyridine-2,6-dicarboxamide-based ligands have been effectively utilized for the synthesis of a variety of metalloligands [16–27]. In such ligands, while the pincer part coordinates to a primary metal ion; the appended groups remain free and available for the subsequent purposes [16–21,23,26]. Such a strategy also allows integrating a variety of functional groups that could participate in H-bonding interactions. Out of various functional groups, phenol and carboxylic acid functionalities have been particularly successful for the H-bonding assisted self-assembly [16–19].

The present chapter discusses design strategies and synthetic approaches for the development of assorted metalloligands based on pyridine-2,6-dicarboxamide-based multidentate ligands while containing appended functional groups featuring phenol, catechol, and aryl carboxylic acid groups. While amide-O groups from a metalloligand functioned as the H-bond acceptors; the appended functional groups act both as the H-bond donors and H-bond acceptors. As a result of the presence of complementary functionalities within a single molecule; such metalloligands have been shown to be involved in *intermolecular* H-bonding for the construction of H-bonded self-assembled architectures [3,16–19]. This chapter has been primarily divided into two sections: while the first part discusses metalloligands offering phenol and catechol functional groups; the second part elaborates metalloligands appended with assorted aryl carboxylic acid groups. In both sections, design concepts, crystal structures of metalloligands, and their self-assembled architectures have been discussed.

2.3 Synthesis and characterization of metalloligands

Our research group has synthesized a diversified range of metalloligands by utilizing pyridine-2,6-dicarboxamide-based multidentate ligands containing assorted appended functional groups [14,16–27]. Such ligands, in their di-deprotonated form, on treatment with suitable Co(II) salts followed by aerial oxidation furnish the corresponding metalloligands [16,18–27]. Importantly, such metalloligands can be synthesized by adapting two different routes which vary in terms of a base and a metal salt being used. In the first strategy, NaH was used as a base for the deprotonation of a ligand followed by a reaction with $[Co(H_2O)_6](ClO_4)_2$ further followed by the addition of excess dioxygen which resulted in the synthesis of metalloligands **ML1^P–ML6^P** (Schemes 2.1 and 2.2) [16,18,19]. Under such reaction conditions, the monoanionic charge on a metalloligand is balanced by the presence of a sodium cation. In the second strategy, K_2CO_3 was used as a base followed by the reaction with $Co(OAc)_2$ in the presence of Et_4NCl and dioxygen which produced metalloligands **ML4^P–ML6^P** (Scheme 2.2) [16,18,19]. In such cases, Et_4N^+ cation balanced the monoanionic charge on a metalloligand. The aforementioned routes afforded metalloligands containing protected phenol/catechol and ester functionalities. In order to explore the H-bonding capabilities of such metalloligands, deprotection was required [16–19]. While metalloligands containing protected phenol/catechol were deprotected using BBr_3 providing free phenol and catechol groups (**1–3**) [16]; metalloligands having ester functionalities were deprotected by base-assisted hydrolysis to afford free aryl carboxylic acid groups (**4–12**) [18,19]. Metalloligands **4–12** differed by the strategic position and number of the carboxylic acid groups on an arene ring; counter cation and the solvents of crystallization (Table 2.1) [18,19]. Although our research group has reported H-bonding assisted self-assembly of all such metalloligands; for the sake of simplicity; this chapter has only discussed the self-assembly of metalloligands containing Et_4N^+ as the counter cation (**4–6**) [18,19].

These deep-green to yellowish-green metalloligands were thoroughly characterized using different spectroscopic techniques, microanalyses, conductivity, thermal studies and single-crystal X-ray diffraction analysis [16–27]. For example, FTIR spectra of these metalloligands illustrated the absence of N–H stretches in addition to red-shifted $C{=}O_{amide}$ bands. Both these points established that the amidic groups are not only deprotonated but are coordinated to a metal ion through anionic $N_{amidate}$ groups [16,18,21,26]. NMR spectral analyses ascertained the formation of a symmetrical bis-ligated Co(III) complexe while the conductivity measurements revealed their 1:1 electrolyte nature [22–25,27].

The crystallographic studies of all metalloligands (**1–12**) showcased that a central Co(III) adopts a compressed octahedral geometry receiving four coordinations from the deprotonated $N_{amidate}$ groups in the distorted equatorial basal plane while the axial positions were occupied by two $N_{pyridine}$ groups [16,18,21,26]. Importantly, the $Co–N_{amidate}$ bond distances were significantly longer than that of $Co–N_{pyridine}$ bonds [16,18,21,26]. The appended

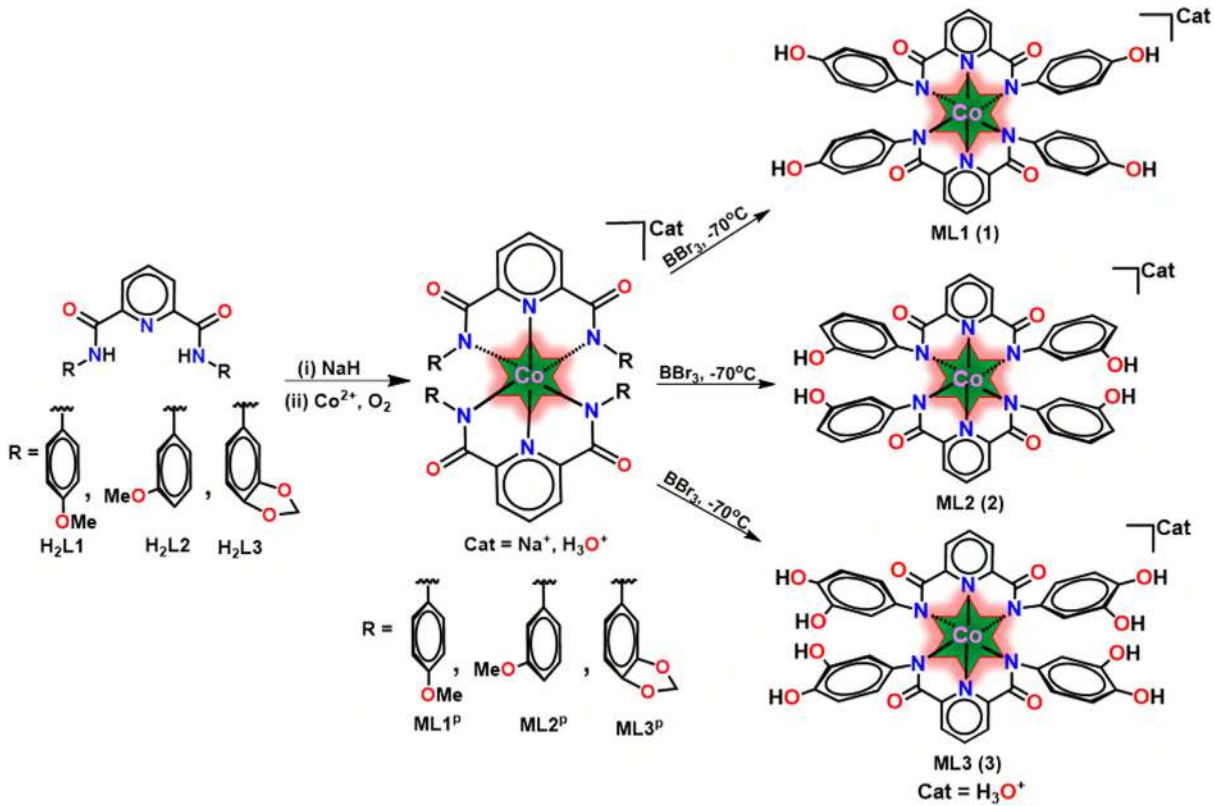

SCHEME 2.1 Preparative route for the synthesis of metalloligands **1**–**3**.

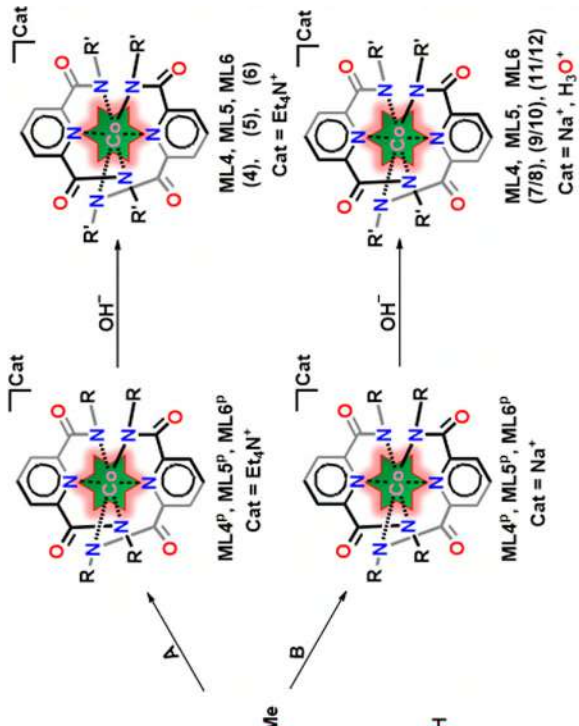

SCHEME 2.2 Preparative route for the synthesis of metalloligands **4–12**.

TABLE 2.1 Solvents used for the recrystallization and counter cations required for the charge balance of monoanionic metalloligands **1–12**.

Metalloligand	Solvent used for recrystallization	Cation
1	Methanol	H_3O^+
2	Methanol	H_3O^+
3	Methanol	H_3O^+
4	Water	Et_4N^+
5	Water	Et_4N^+
6	Methanol/methyl *tert*-butyl ether	Et_4N^+
7	Water	H_3O^+
8	DMF/ether	H_3O^+
9	Water	H_3O^+
10	DMF/ether	H_3O^+
11	DMF/ether	Na^+
12	Water	H_3O^+

functional groups (phenol/catechol and aryl carboxylic acid) rendering both H-bond donors and acceptors remain freely available and can thus involve in forming H-bonded self-assembled architectures involving complementary H-bonding groups [16,18,19].

2.4 Metalloligands offering different appended functional groups

2.4.1 Metalloligands offering appended phenol and catechol groups

The Co-based metalloligands bearing appended phenol and catechol groups provided a significant opportunity to study their self-assembly as they incorporated both H-bond donors (O–H groups of phenol and catechol) and H-bond acceptors ($C{=}O_{amide}$ groups) in a single molecule [3,16]. In particular, metalloligands **1** (*para*-phenol donor) and **2** (*meta*-phenol donor) provided a complementary number of *four* H-bond donors and *four* H-bond acceptors in a single molecule. As a result, both these metalloligands resulted in a straight-forward 4 × 4 self-assembly as a consequence of complementary H-bonding interactions [16]. However, both these metalloligands differed by the position of a hydroxide group on an arene ring; *para*- versus *meta* in **1** and **2**, respectively, which also affected the self-assembly process. On the other hand, catechol-based metalloligand (**3**) was designed to understand the effect of inconsistency between the number of H-bond donors (8 O–H groups) and acceptors (4 $C{=}O_{amide}$ groups) on the self-assembly process [16]. The next few sections have discussed the H-bonding-based self-assemblies generated by the above-stated metalloligands bearing phenol and catechol groups.

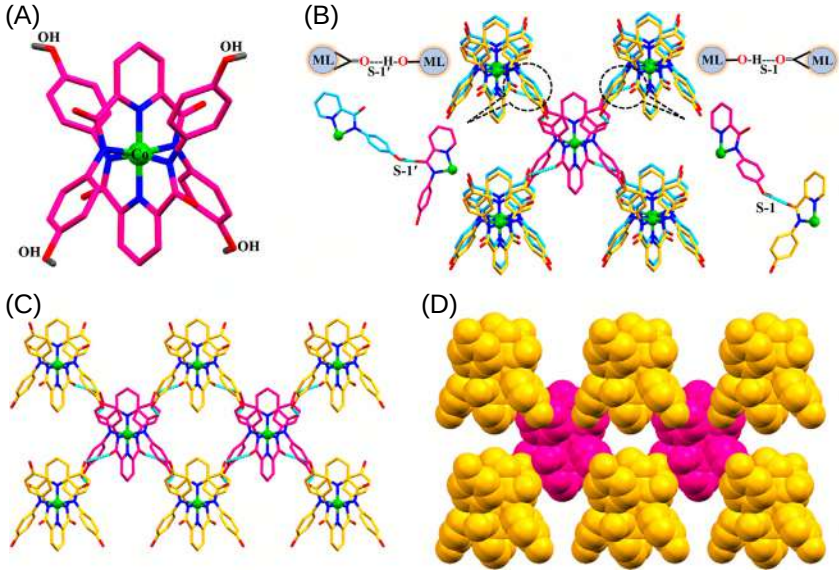

FIGURE 2.1 (A) Crystal structure of metalloligand **1**; (B) H-bonding interactions between different metalloligands involving **S-1** and **S-1′** synthons in an offset view along the *a-axis*; (C) a view of packing diagram along the *a-axis*; (D) space-filling model of the packing diagram along the *a-axis*. Hydronium ions have been omitted for clarity in all panels. Adapted from Ref. [16][1].

2.4.1.1 Para-*phenol groups*

The metalloligand **1**, appended with *para*-phenol groups, provided a space-filling complementary number of *four* H-bond donors (phenolic-OH groups) and *four* H-bond acceptors (O_{amide} groups). In the crystal structure, the H-bond donors and the H-bond acceptors from a single metalloligand were positioned above and below from a plane (Fig. 2.1(A) and (B)). As a result, a central metalloligand was able to interact with eight neighboring metalloligands via *four* O–H…O_{amide} synthons (**S-1**; metalloligands are shown in golden color) and *four* O_{amide}…H–O synthons (**S-1′**; metalloligands are shown in aqua-blue color). It is important to note that both **S-1** and **S-1′** are identical synthons but differ by the order of functional groups. A combination of both such synthons generated a highly symmetrical [4 × 4] array of metalloligands if viewed along the *a*-axis (Fig. 2.1(C) and (D)) [16]. The heteroatom separation between any such synthon (**S-1** or **S-1′**) varied between 2.58 and 2.68 Å, while the O–H—O_{amide} angle was found to be in the range of 148°–171°. Both these parameters indicated a moderately strong nature of the intermolecular H-bond.

1. Throughout the chapter, following colour codes have been used: primary metal atom, dark green; nitrogen atom, blue; oxygen atom, red; carbon atom, pink, aqua blue and golden; hydrogen atom, grey.

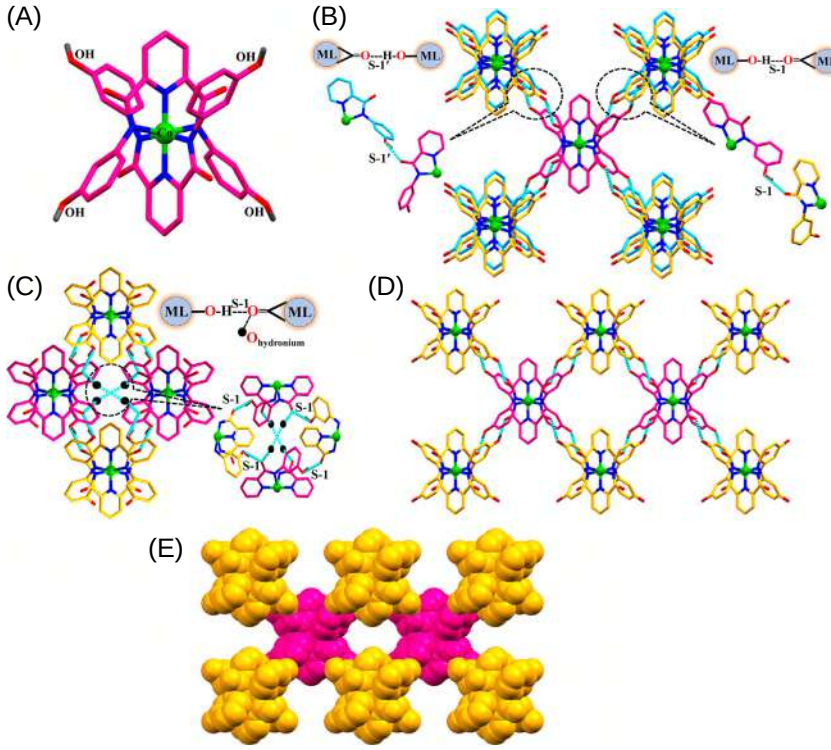

FIGURE 2.2 (A) Crystal structure of metalloligand **2**; (B) H-bonding interactions between different metalloligands involving **S-1** and **S-1′** synthons in an offset view along the *a-axis*; (C) a view of H-bonded network including hydronium ions (shown in black color) along the *ac* plane; (D) a view of packing diagram along the *a-axis*; (E) space-filling model of the packing diagram along the *a-axis*. Hydronium ions have been omitted for clarity in panels D and E. Adapted from Ref. [16].

The hydronium ions, balancing the monoanionic charge present on a metalloligand, were present between these H-bonded networks. Notably, due to the highly symmetrical nature of intermolecular H-bonding interactions between different metalloligands; such hydronium ions did not participate in any meaningful H-bonding interactions with the metalloligands [16]. Consequently, such disordered hydronium ions occupied the large solvent-accessible volume (SAV) of 1282 $Å^3$ offered by these self-assembled metalloligands (Fig. 2.1(D)).

2.4.1.2 Meta-*phenol groups*

The metalloligand **2** with *meta*-phenol groups also offered the complimentary number of *four* H-bond donors (phenolic-OH groups) and *four* H-bond acceptors (O_{amide} groups) (Fig. 2.2(A)). As a result, metalloligand **2** also manifested intermolecular H-bonding interactions between the phenolic–OH and the amidic–O (–C=O_{amide}) groups via OH…O_{amide} (**S-1**; metalloligands are shown in golden

color) and O_{amide}…H–O (**S-1′**; metalloligands are shown in aqua-blue color) synthons leading to a [4 × 4] array if viewed along the *a*-axis (Fig. 2.2(B)) [16]. In contrast to **1**, metalloligand **2** exhibited significant H-bonding interactions of the hydronium ions to the O_{amide} groups [16]. The heteroatom separation for O_{amide}…$O_{hydronium}$ motifs were between 2.78 and 2.86 Å, while $O_{hydronium}$… $O_{hydronium}$ motif displayed *a*-axis separation of 2.89 Å. Such interactions led to the connection of metalloligands together (displayed in pink color) and the generation of a chain along the *ac* plane (Fig. 2.2(C)). The hydronium ion bonded metalloligands and therefore the resultant chains were further connected to two alternate chains created via **S-1** synthons between metalloligands (displayed in golden color) which formed a 2D network along the *a*-axis (Fig. 2.2(D)). The strategic placement of a –OH group at the *meta* position in **2** enabled the O_{amide} groups to appropriately interact with the hydronium ions and therefore accommodate them within the voids. This particular characteristic emphasized that the placement of a hydroxyl group on an arene ring is a noteworthy parameter for constructing a distinct H-bonding self-assembled network. Metalloligand **2** exhibited a much lower SAV (277 $Å^3$) in comparison to **1** as it furnished a compact H-bonded network (Fig. 2.2(E)).

Metalloligands **1** and **2**, although offering the identical numbers of H-bond donors and H-bond acceptors, resulted in different self-assembled structures. While metalloligand appended with *para*-phenol rings (**1**) resulted in a highly symmetrical and complementary H-bonding network; metalloligand **2**, on the other hand, featuring *meta*-phenol rings induced a little asymmetry due to the relative twisting of the appended phenol rings. Such a fact allowed hydronium ions to act as the "spacers" connecting different metalloligand units and thus reducing the void space. The difference in the symmetry-led self-assembly is further evident from their respective SAVs: 1282 $Å^3$ and 277 $Å^3$ offered by metalloligands **1** and **2**, respectively.

2.4.1.3 Catechol groups

The H-bonding assisted self-assembly of metalloligands **1** and **2** encouraged us to incorporate appended catechol groups in place of phenol groups. Metalloligand **3** rendered four auxiliary catechol groups located at the periphery. This complex offered *eight* H-bond donors (–OH) while only *four* H-bond acceptors (O_{amide}) groups in a single metalloligand (Fig. 2.3(A)). Such a mismatch between the number of H-bond donors and H-bond acceptors resulted in *a*-axis interesting self-assembly [16]. This metalloligand illustrated two different types of intermolecular H-bonds: first, between a catechol–OH and an O_{amide} group; and the second, between a *meta*-OH group of a catechol ring to that of a *para*-OH group of a catechol ring [16]. In the first case, an O–H group present at the *meta*-position of a catechol ring forms an intermolecular H-bond with the O_{amide} group via O_m–H…O_{amide} synthon (**S-1**; metalloligands are shown in golden color) as well as O_{amide}…H–O_m synthon (**S-1′**; metalloligands are shown in aqua-blue

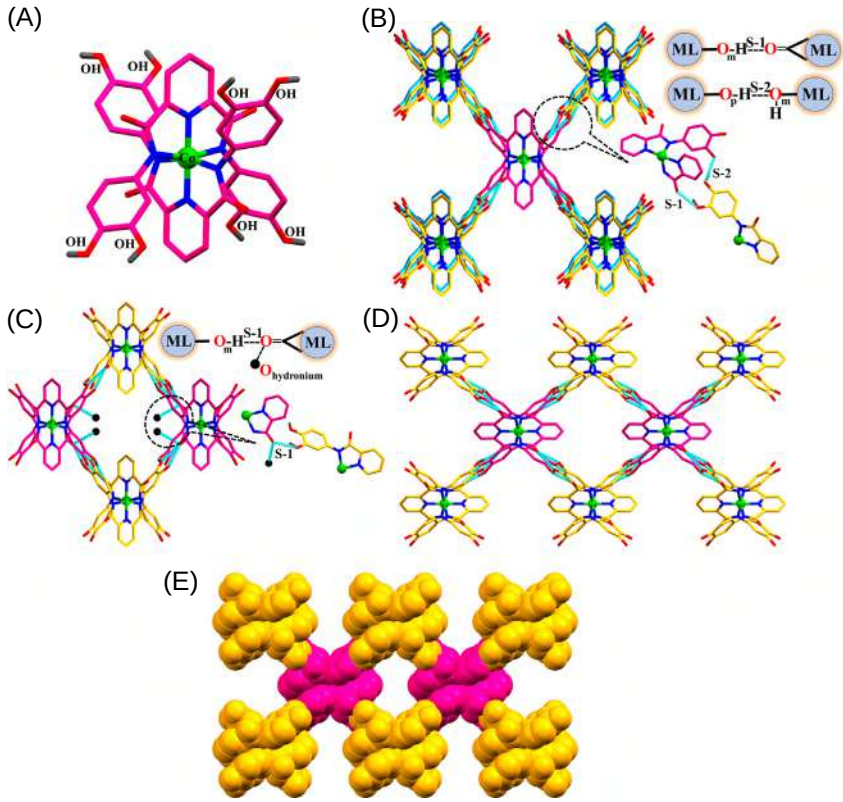

FIGURE 2.3 (A) Crystal structure of metalloligand **3**; (B) H-bonding interactions between different metalloligands involving **S-1**, **S-1′**, and **S-2** synthons in an offset view along the *a-axis*; (C) a view of H-bonded network including hydronium ions (shown in black color) along the *ac* plane; (D) a view of packing diagram along the *a-axis*; (E) space-filling model of the packing diagram along the *a-axis*. For panels (D) and (E) hydronium ions have been omitted for clarity. Adapted from Ref. [16].

color) with a heteroatom separation of 1.83 Å and O–H…O_{amide} bond angle of 148°. While the second intermolecular H-bond was observed between the –OH group present at the *para*-position to that of O-atom of –OH group at the *meta*-position of a catechol ring resulting in an O_p–H…O_m synthon (**S-2**) with a heteroatom separation of 2.58 Å and O–H…O bond angle of 163° (Figs. 2.3(B) and (D)). Consequently, both O–H groups of a catechol ring were involved as H-bond donors as well as H-bond acceptors. As noted for **2**, metalloligand **3** also revealed H-bonding interactions between the hydronium ions and O_{amide} groups (Fig. 2.3(C)) thus suggesting that both these complexes are isomorphous in nature. A comparison of SAVs revealed that metalloligand **3** offered a slightly larger SAV (371 $Å^3$) (Fig. 2.3(E)) in comparison to **2** (277 $Å^3$) while much smaller than that of **1** (1282 $Å^3$) which is justified by the rational design of all the three complexes.

In essence, it can be inferred that metalloligands **2** and **3** behaved in a very similar manner and displayed offset self-assembly due to the twisted nature of the phenol and catechol rings respectively which oriented the amidic–O groups in such a way that they were effectively involved in H-bonding interactions with the hydronium ions. As a result, such hydronium ions comfortably resided within the voids offered by both these metalloligands. On the contrary, an almost un-twisted nature of *para*-phenol rings in **1** offered a highly symmetrical self-assembly which restricted the interactions of amidic–O groups to that of hydronium ions. A symmetrical nature of H-bonding-based self-assembly and noninvolvement of hydronium ions in H-bonding resulted in much larger SAVs in the case of metalloligand **1**.

2.4.2 Metalloligands offering appended aryl carboxylic acid groups

A carboxylic acid is an interesting functional group as it concurrently offers both an H-bond donor (through its –OH unit) and an H-bond acceptor (through its –C=O unit) [3]. As a result, a carboxylic acid group is self-complementary in nature and tends to form an inter-molecularly linked $[–COOH]_2$ dimers [3,18]. Thus, a carboxylic acid group presents a more challenging H-bonding scenario in comparison to a phenol donor which typically serves as an H-bond donor [3,18,19]. Cobalt-based metalloligands bearing aryl carboxylic acid groups offer a combination of H-bond donors (in O−H groups of carboxylic acid) and H-bond acceptors (in $C=O_{amide}$ groups as well $C=O_{acid}$ of carboxylic acid) within a single molecule. The simultaneous presence of both H-bond donor and acceptor groups within the same metalloligand creates noteworthy self-assembly possibilities via an array of both inter- and intramolecular H-bonding [3]. However, in our case, the self-assembly process of such complementary functional groups was found to be remarkably influenced by the position of a carboxylic acid group on an arene ring, a number of the carboxylic acid group(s) on an arene ring, type of associated counter cation, and solvent of crystallization [18,19]. Such self-assembly becomes more challenging when lattice/cocrystallized solvent molecules (e.g., water or DMF) were also found to engage in H-bonding. In a few cases, such lattice solvent molecules acted as the "spacers" which further elongated the H-bonding network [18,19]. In this section, we discuss the H-bonding-based self-assemblies of Co(III) complexes **4**–**6** appended with monoaryl carboxylic acid groups (*para*- and *meta*-) as well as di-aryl carboxylic space-filling acid groups. Out of various combinations (cations and solvents), for simplicity, metalloligands offering Et_4N^+ group as the counter cation have only been discussed.

2.4.2.1 Para-*aryl carboxylic acid groups*

Metalloligand **4** offering *para*-aryl carboxylic acid groups is monoanionic in nature where Et_4N^+ cation balanced the charge. Metalloligand **4** offered four peripheral H-bond donor groups (–COOH) which were capable of self-assembly via H-bond acceptors (from O_{acid} and O_{amide} groups) (Fig. 2.4(A)). However, for

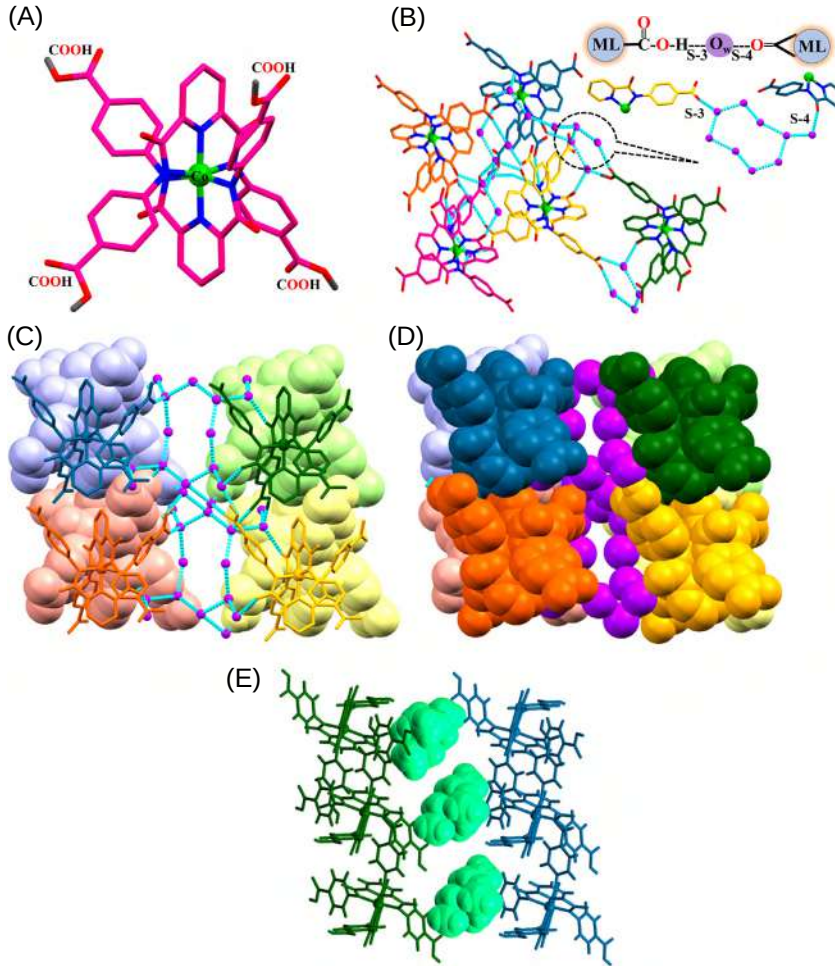

FIGURE 2.4 (A) Crystal structure of metalloligand **4**; (B) H-bonding interactions between different metalloligands involving **S-3** and **S-4** synthons via a set of nine lattice water molecules (shown in purple color); (C) a view of packing diagram along the *c*-axis; (D) space-filling model of the packing diagram along the *c*-axis; (E) space-filling model of a portion of the network showing the presence of Et_4N^+ cations (shown in green color). Et_4N^+ cations (in panel C and D) and hydronium ions (in panel E) have been omitted for clarity. Adapted from Ref. [18].

such H-bond donors, lattice water molecules behaved as the H-bond acceptors instead of amide–O atoms ($C{=}O_{amide}$) [18]. Each acid group (via O–H) from a *para*-aryl carboxylic acid group was H-bonded to two lattice water molecules forming an O_{acid}–H…O_W synthon (**S-3**). For **S-3** synthon, heteroatom separation was between 2.59 and 2.72, while the O–H…O_W angle was larger than 163° (Fig. 2.4(B)). Such lattice water molecules were further H-bonded to O_{amide}

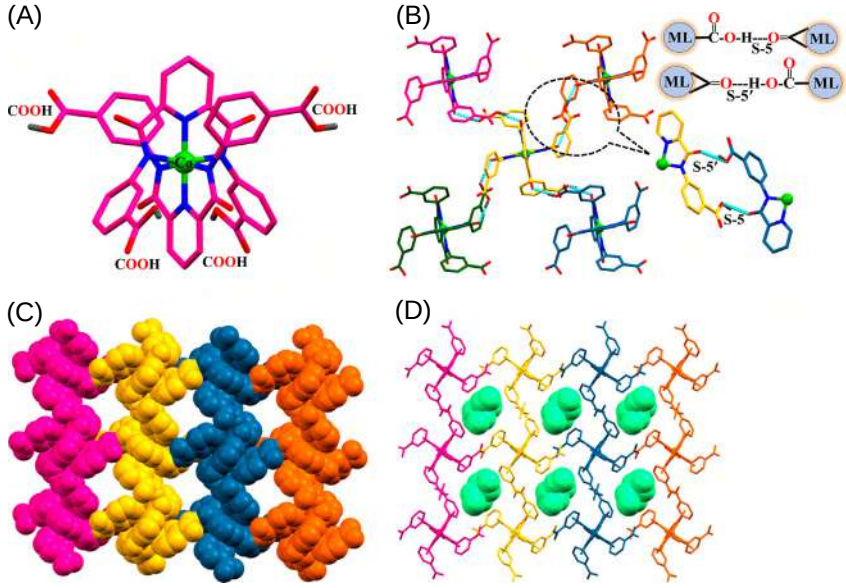

FIGURE 2.5 (A) Crystal structure of metalloligand **5**; (B) H-bonding interactions between different metalloligands involving **S-5** and **S-5′** synthons; (C) space-filling model of the packing diagram in a view along the *c*-axis; (D) a view of the packing diagram showing the presence of Et_4N^+ cations (shown in green color). Et_4N^+ cations have been omitted for clarity in panel C. Adapted from Ref. [18].

groups on the other side via $O_w \ldots O_{amide}$ synthon (**S-4**). Collectively, both **S-3** and **S-4** synthons were holding a total of nine water molecules between them. These H-bonded lattice water molecules were arranged in the form of an octagon and acted as the spacers to further propagate the H-bonding network along the *c*-axis (Fig. 2.4(C)) [18]. Metalloligand **4** offered negligible SAVs as the void space was occupied with the lattice water molecules and charge balancing Et_4N^+ cations (Figs. 2.4(D) and (E)).

2.4.2.2 Meta-*aryl carboxylic acid groups*

The crystal structure of metalloligand **5** illustrated the presence of four appended aryl carboxylic acid groups where –COOH groups were located at the *meta* position of arene rings (Fig. 2.5(A)). This compound was also monoanionic in nature and Et_4N^+ cation balanced the charge. Notably, metalloligand **5** resulted in a highly symmetrical H-bonding-based self-assembly [18]. Each metalloligand was H-bonded to four neighboring metalloligands via O_{acid}–H…O_{amide} (**S-5**) and O_{amide}…H–O_{acid} (**S-5′**) synthons with heteroatom separations varying in the range of 2.58–2.66 and O_{acid}–H…O_{amide} angle between 159° and 172° (Fig. 2.5(B)). It is pertinent to mention that both **S-5** and **S-5′** are identical synthons but differ by the order of the functional groups. Such H-bonding

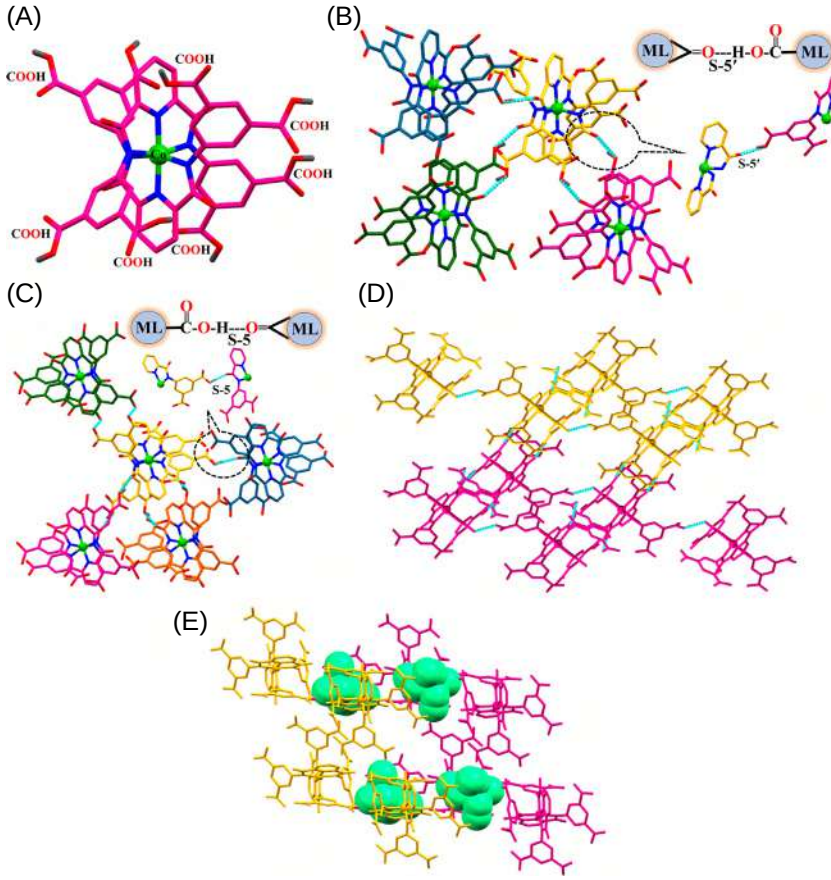

FIGURE 2.6 (A) Crystal structure of metalloligand **6**; (B) H-bonding interactions between different metalloligands involving **S-5′** synthon; (C) H-bonding interactions between different metalloligands involving **S-5** synthon; (D) a view of packing diagram along the *c*-axis involving H-bonding interactions via both O_{amide} and O_{acid} groups; (E) a view of a portion of the network showing the presence of Et_4N^+ cations (shown in green color). Et_4N^+ cations have been omitted for clarity in panel D. Adapted from Ref. [19].

interactions led to the generation of a 2D sheet (Fig. 2.5(C)). Due to a space-filling closely packed network, lattice water molecules did not cocrystallize in this case and thus minimized the competition of H-bond donors/acceptors in the process of H-bonding-based self-assembly [18]. Metalloligand **5** offered small SAVs (277 $Å^3$) which were occupied by the Et_4N^+ cations (Fig. 2.5(D)).

2.4.2.3 3,5-Aryldicarboxylic acid groups

Metalloligand **6** was an interesting case as it offered four appended arene rings where a total of eight –COOH groups were located at 3- and 5-positions

(Fig. 2.6(A)). The metalloligand **6**, bearing 3,5-aryldicarboxylic acid groups, was also monoanionic with an Et_4N^+ cation balancing the charge. Metalloligand **6** offered eight –COOH groups leading to the complicated H-bonding-based self-assembly [3,19].

In this case, each metalloligand was H-bonded to three neighboring metalloligands via O_{amide}–H…O_{acid} synthon (**S-5′**) where three O_{amide} groups interacted to O_{acid} groups while the fourth –C=O_{amide} group remained free (Fig. 2.6(B)). Further, every metalloligand was found to create H-bond to four proximal metalloligands via O_{acid}–H…O_{amide} (**S-5**) synthon, where four O_{acid} groups were found to be associated with four O_{amide} atoms originating from four different metalloligands (Fig. 2.6(C)). Collectively, such interactions led to the generation of a 2D sheet along the *c*-axis (Fig. 2.6(D)) [19]. Complex **6** offered negligible SAVs as voids were mostly occupied by the Et_4N^+ cations (Fig. 2.6(E)).

Metalloligands **4**–**6** offering aryl carboxylic acid groups presented noteworthy structural and self-assembly outcomes. In these metalloligands, the geometrical placement of a –COOH group on an arene ring played a notable role. Similarly, the number of aryl carboxylic acid groups being offered by a metalloligand was also a significant parameter. In addition to these dominating parameters, the choice of a cation and the selection of a solvent of crystallization were also equally notable points that remarkably controlled the self-assembly process.

2.5 Conclusions

This chapter has discussed the H-bonding-based self-assembly of assorted metalloligands presenting phenol, catechol, and aryl carboxylic acid groups. These examples have illustrated that how the position of a hydroxyl group on an arene ring (*para* versus *meta*) and the number of the hydroxyl group(s) on an arene ring (phenol versus catechol) influenced the self-assembly and consequently the network formation. The metalloligands offering aryl carboxylic acid groups presented a far more challenging self-assembly situation by virtue of their dual character to act both as the H-bond donor(s) and H-bond acceptor(s). This particular category of metalloligands provided an opportunity to study the effect of the position of carboxylic group, type of cation, and lattice solvent molecules on the process of H-bonding-based self-assembly.

A comparison of metalloligands offering aryl carboxylic acid groups to that of the ones presenting phenol groups infers that if an H-bonding sensitive functional group is composed of multiatoms (e.g., –COOH); a greater number of atoms are available to act as the H-bond donor(s) and H-bond acceptor(s) and the resultant H-bonding-based self-assembly becomes quite challenging. These are important design parameters that are likely to assist the supramolecular chemistry community to select the required functional groups for the design of the next-generation metalloligands. Taking inspiration from nature together with relying on the concepts of geometrical parameters, rational design and

self-assembly; fascinating and intricate H-bonding-based self-assembled architectures will be achieved.

Acknowledgments

Rajeev Gupta gratefully acknowledges the continous financial assistance from the Science and Engineering Research Board, New Delhi including the present Core Research Grant project (CRG/2021/001700).

References

[1] L. Adriaenssens, P. Ballester, Hydrogen bonded supramolecular capsules with functionalized interiors: the controlled orientation of included guests, Chem. Soc. Rev. 42 (2013) 3261–3277.

[2] B.H. Northrop, Y.-R. Zheng, K.-W. Chi, P.J. Stang, Self-organization in coordination-driven self-assembly, Acc. Chem. Res. 42 (10) (2009) 1554–1563.

[3] G.R. Desiraju, Supramolecular synthons in crystal engineering – a new organic synthesis, Angew. Chem. Int. Ed. 34 (21) (1995) 2311–2327.

[4] S.I. Stupp, L.C. Palmer, Supramolecular chemistry and self-assembly in organic materials design, Chem. Mater. 26 (1) (2014) 507–518.

[5] R. Chakrabarty, P.S. Mukherjee, P.J. Stang, Supramolecular coordination: self-assembly of finite two- and three-dimensional ensembles, Chem. Rev. 111 (11) (2011) 6810–6918.

[6] L.J. Marshall, J. de Mendoza, Self-assembled squares and triangles by simultaneous hydrogen bonding and metal coordination, Org. Lett. 15 (7) (2013) 1548–1551.

[7] K. Ariga, J.P. Hill, M.V. Lee, A. Vinu, R. Charvet, S. Acharya, Challenges and breakthroughs in recent research on self-assembly, Sci. Technol. Adv. Mater. 9 (2008) 1–96.

[8] N. Nasser, R.J. Puddephatt, A diphosphine ligand with amide functionality and its complexes with gold(I) and silver(I): self-assembly of sheet structures, Cryst. Growth Des. 12 (8) (2012) 4275–4282.

[9] J.-M. Lehn, Toward complex matter: supramolecular chemistry and self-organization, Proc. Natl. Acad. Sci. U.S.A. 99 (8) (2002) 4763–4768.

[10] M.Y. Masoomi, A. Morsali, A. Dhakshinamoorthy, H. Garcia, Mixed-metal MOFs: unique opportunities in metal-organic framework (MOF) functionality and design, Angew Chem. Int. Ed. 58 (43) (2019) 15188–15205.

[11] S.R. Halper, L. Do, J.R. Stork, S.M. Cohen, Topological control in heterometallic metal−organic frameworks by anion templating and metalloligand design, J. Am. Chem. Soc. 128 (47) (2006) 15255–15268.

[12] G. Kumar, R. Gupta, Molecularly designed architectures – the metalloligand way, Chem. Soc. Rev. 42 (2013) 9403–9453.

[13] G. Kumar, R. Gupta, Coordination driven architectures based on metalloligands offering appended carboxylic acid groups, J. Chem. Sci. 130 (2018) 86.

[14] S. Pachisia, R. Gupta, Architectural and catalytic aspects of designer materials built using metalloligands of pyridine-2,6-dicarboxamide based ligands, Dalton Trans. 49 (2020) 14731–14748.

[15] G. Kumar, G. Kumar, R. Gupta, Effect of pyridyl donors from organic ligands versus metalloligands on material design, Inorg. Chem. Front. 8 (2021) 1334–1373.

[16] A. Ali, G. Hundal, R. Gupta, Co^{3+}-based building blocks with appended phenol and catechol groups: examples of placing hydrogen-bond donors and acceptors in a single molecule, Cryst. Growth Des. 12 (3) (2012) 1308–1319.

[17] A. Ali, D. Bansal, R. Gupta, Synthesis, characterization and self-assembly of Co^{3+} complexes appended with phenol and catechol groups, J. Chem. Sci. 126 (5) (2014) 1535–1546.

[18] G. Kumar, H. Aggarwal, R. Gupta, Cobalt complexes appended with para- and meta-arylcarboxylic acids: influence of cation, solvent, and symmetry on hydrogen-bonded assemblies, Crystal Growth Des. 13 (1) (2013) 74–90.

[19] S. Srivastava, R. Gupta, Cobalt complexes offering aryldicarboxylic acid groups: hydrogen bonding assemblies and the resultant topologies, ChemistrySelect 1 (19) (2016) 6167–6178.

[20] A. Mishra, A. Ali, S. Upreti, R. Gupta, Cobalt coordination induced functionalized molecular clefts: isolation of $\{Co^{III}–Zn^{II}\}$ heterometallic complexes and their applications in Beckmann rearrangement reactions, Inorg. Chem. 47 (1) (2008) 154–161.

[21] A.P. Singh, A. Ali, R. Gupta, Cobalt complexes as the building blocks: $\{Co^{3+}–Zn^{2+}\}$ heterobimetallic networks and their properties, Dalton Trans. 39 (2010) 8135–8138.

[22] G. Kumar, R. Gupta, A novel Co^{3+}-based asymmetrical building block: heterobimetallic metallacycles versus coordination networks, Inorg. Chem. Commun. 23 (2012) 103–108.

[23] D. Bansal, S. Pandey, G. Hundal, R. Gupta, Heterometallic coordination polymers: syntheses, structures and heterogeneous catalytic applications, New J. Chem. 39 (2015) 9772–9781.

[24] D. Bansal, G. Hundal, R. Gupta, A. Metalloligand, Appended with thiazole rings: heterometallic $Co^{3+}–Zn^{2+}$ and $Co^{3+}–Cd^{2+}$ complexes and their heterogeneous catalytic applications, Eur. J. Inorg. Chem. (2015) 1022–1032.

[25] S. Pandey, D. Bansal, R. Gupta, A metalloligand appended with benzimidazole rings: tetranuclear $[CoZn_3]$ and $[CoCd_3]$ complexes and their catalytic applications, New J. Chem. 42 (2018) 9847–9856.

[26] G. Kumar, R. Gupta, Cobalt complexes appended with p- and m-carboxylates: two unique $\{Co^{3+}–Cd^{2+}\}$ networks and their regioselective and size-selective heterogeneous catalysis, Inorg. Chem. 51 (10) (2012) 5497–5499.

[27] S. Srivastava, V. Kumar, R. Gupta, A carboxylate-rich metalloligand and its heterometallic coordination polymers: syntheses, structures, topologies, and heterogeneous catalysis, Cryst. Growth Des. 16 (5) (2016) 2874–2886.

Chapter 3

Supramolecular coordination complexes from metalloligands: Heteronuclear complexes and coordination polymers and their applications in catalysis

Ruchika Gupta, Sanya Pachisia and Rajeev Gupta
Department of Chemistry, University of Delhi, Delhi, India

3.1 Introduction

In recent times, the field of coordination-driven supramolecular chemistry has emerged as a promising platform for the development of novel materials with tunable structural and functional properties [1–5]. The immense growth in this field is not only driven by the high stability, chemical robustness, porosity, and tunable properties of such materials but also due to their noteworthy applications in various fields including sorption, storage, separation, ion conduction, catalysis, photonics, recognition, and sensing [6–10]. The fundamental knowledge accessible from coordination chemistry regarding organic ligands, metal ions, and their geometrical aspects paved the foundation for the coordination-driven supramolecular chemistry while firmly establishing the concept of rational design [1,4,5,8]. Out of various supramolecular architectures, metal-organic frameworks (MOFs) and coordination polymers (CPs) have shown substantial development [9,10].

The potential of coordination-driven self-assembly and directional bonding approach led to the realization of new materials with increasing complexity and functionality [1,9,10]. However, as the scale and the complexity of materials increases, the spontaneous self-assembly of large supramolecular architectures becomes increasingly difficult. Thus, it became necessary to explore alternate rational design strategies to control the topology and the functionality of the resultant materials [1,4,5,8,10,12]. One such alternate strategy to obtain

Supramolecular Coordination Complexes: Design, Synthesis, and Applications.
DOI: https://doi.org/10.1016/B978-0-323-90582-4.00011-7

predictable supramolecular architectures is to utilize well-defined metalloligands [11,12].

A metalloligand is defined as a metal containing coordination complex offering additional binding sites which can either coordinate to the secondary metal ions or interact via hydrogen bonding (H-bonding) interactions to form supramolecular architectures [13–18]. In particular, the former strategy can produce highly ordered supramolecular architectures by the repetition of the coordination of metalloligands to that of secondary metals. The metalloligand-based synthetic approach allows the development of somewhat predictable architectures due to the limited orientation of the appended functional groups to coordinate to secondary metal ions as a result of the inherent structural rigidity of a coordination complex [13–15]. Depending upon the selection of the multidentate ligands offering assorted appended functional groups and the primary metals, a large number of metalloligands could be synthesized. Subsequently, reaction of such metalloligands with different secondary metals will lead to the generation of a large number of supramolecular architectures [19–41].

The rigid nature of a metalloligand controls the geometrical placement of the appended functional groups to limited orientation. Such a fact could be precisely used for the synthesis of discrete supramolecular complexes versus multidimensional CPs [13,15,19,25]. The metalloligand strategy offers several benefits including nonpenetrating architectures and the ability to place two or more metal ions in close proximity [13–15]. While the former strategy results in porous architectures; the later point potentially generates novel functional materials, which are otherwise difficult to synthesize [13–16].

The present chapter discusses the design strategies involved for the construction of supramolecular architectures by utilizing assorted metalloligands based on pyridine-2,6-dicarboxamide fragment-based multidentate ligands. Such metalloligands offer assorted appended functional groups for binding to different metal ions and thus generate various supramolecular architectures. This chapter has been divided into three sections. While the first section discusses the synthesis and characterization of metalloligands; the second one presents the utilization of such metalloligands for the synthesis of various supramolecular architectures. The last section illustrates the catalytic aspects of various supramolecular architectures in assorted organic transformation reactions.

3.2 Synthesis and characterization of metalloligands

Our research group has synthesized various metalloligands by treating the respective pyridine-2,6-dicarboxamide fragment-based ligands in their di-deprotonated form with an appropriate metal salt. The metalloligands can be synthesized by two different approaches which differ by the selection of a base and a metal salt. In the first approach (route **A**), sodium hydride (NaH) was used as a base for the deprotonation of the amidic groups in DMF followed by

the addition of $[Co(H_2O)_6](ClO_4)_2$ which is further followed by the purging of dioxygen which oxidizes a labile Co(II) ion to an inert Co(III) ion. This resulted in the synthesis of the corresponding metalloligands; **ML1**, **ML4,** and **ML6** (Scheme 3.1) [19–25,31,33]. In this method, a sodium ion serves as a cation to balance the mono-anionic charge on a complex. The second method (route **B**) involves the use of K_2CO_3 as a base for the deprotonation of amidic groups in CH_2Cl_2 followed by the addition of $[Co(OAc)_2]$ in the presence of dioxygen and excess of Et_4NClwhich yielded metalloligands **ML1**, **ML1'**, **ML2**, **ML3,** and **ML5** (Scheme 3.1) [19–30,32]. In this case, Et_4N^+ cation balances the mono-anionic charge on a metalloligand. Notably, metalloligand **ML1** can be synthesized by either of the two methods.

Metalloligands **ML7P**–**ML9P** were also synthesized in a similar manner as explained above. In particular, **ML7P** and **ML8P** were synthesized according to route **B** [34–39] while metalloligand **ML9P** was synthesized following route **A** (Scheme 3.2) [40,41]. Notably, carboxylic acid appended metalloligands further required an additional step of base-assisted hydrolysis of an ester groups to yield free carboxylic acid groups (Scheme 3.2) [18,34–41]. Such a strategy was essential so that a metal ion only binds to the intended $N_{pyridyl}$ and $N_{amidate}$ groups of a pincer cavity ligand while leaving the ester groups uncoordinated.

Such Co-based metalloligands were characterized by assorted spectroscopic techniques and X-ray crystallography [19–41]. The FTIR spectra of such metalloligands exhibited the absence of N–H stretches accompanied by the red-shifted $C{=}O_{amide}$ bands. Both these features not only asserted that an amide group has been deprotonated but coordinated to a metal ion via anionic $N_{amidate}$ groups. The UV–Vis spectra of these deep green to yellowish-green cobalt complexes displayed λ_{max} at ca. 650 nm due to d–d transitions while the high energy features, observed between 350 and 500 nm, are probably due to ligand-to-metal charge transfer. The spectral features below 350 nm were tentatively assigned to intra-ligand transitions. The diamagnetic nature of these Co(III) complexes facilitated their characterization using both ^1H and ^{13}C NMR spectra which confirmed the formation of symmetrical bis-ligated cobalt(III) complex. The conductivity measurements manifested these complexes as 1:1 electrolytes.

X-ray crystallographic analysis of these Co-based metalloligands (**ML1–ML9**) disclosed that a central Co(III) atom is coordinated by four deprotonated $N_{amidate}$ groups in the equatorial basal plane while two $N_{pyridyl}$ groups occupy the axial positions. The meridional coordination of a potentially tridentate ligand to a metal atom resulted in a compressed octahedral geometry. Importantly, Co–$N_{amidate}$ bond distances were considerably longer than that of Co–$N_{pyridyl}$ bonds. Notably, the unusual coordination mode of a ligand leaves two appended groups per ligand uncoordinated which can potentially coordinate to other secondary metal ions. Such a strategy allows the synthesis of both discrete complexes and multidimensional CPs depending upon the directionality of the appended functional groups [19–41].

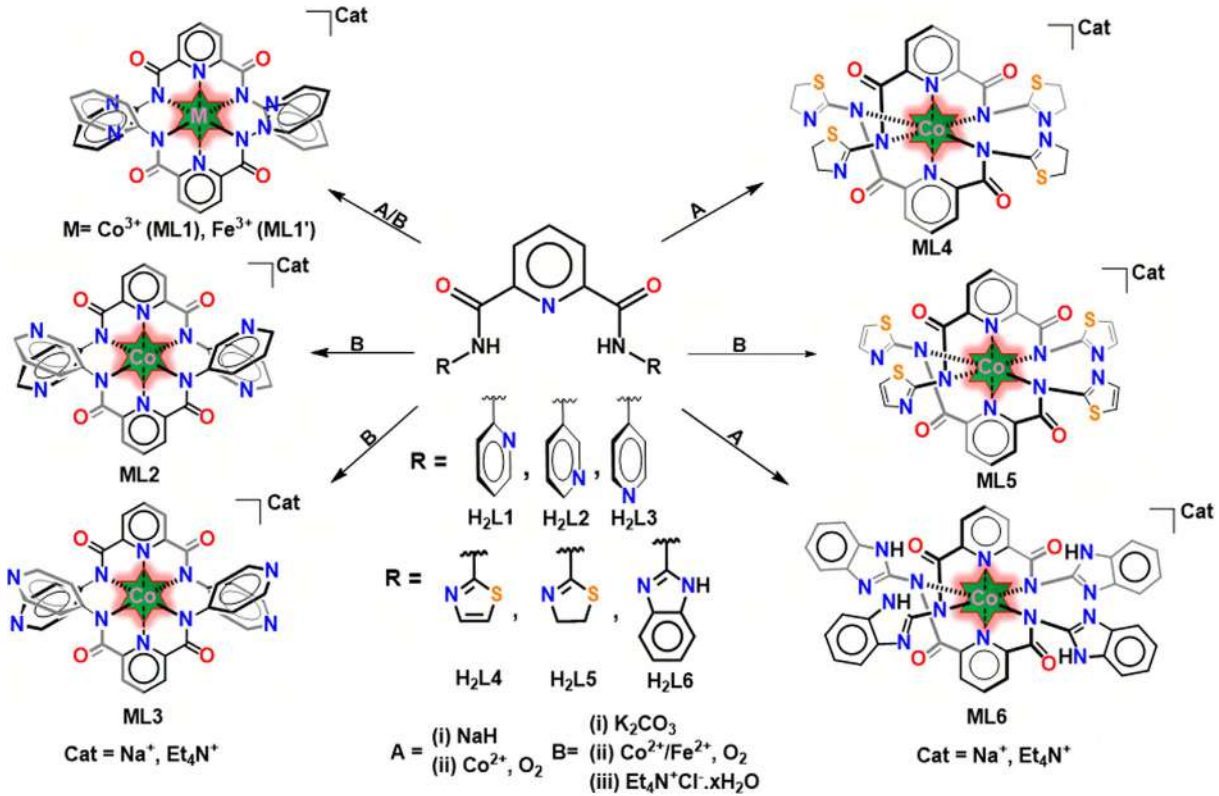

SCHEME 3.1 Preparative route for the synthesis of metalloligands **ML1**–**ML6** using either route **A** or **B**.

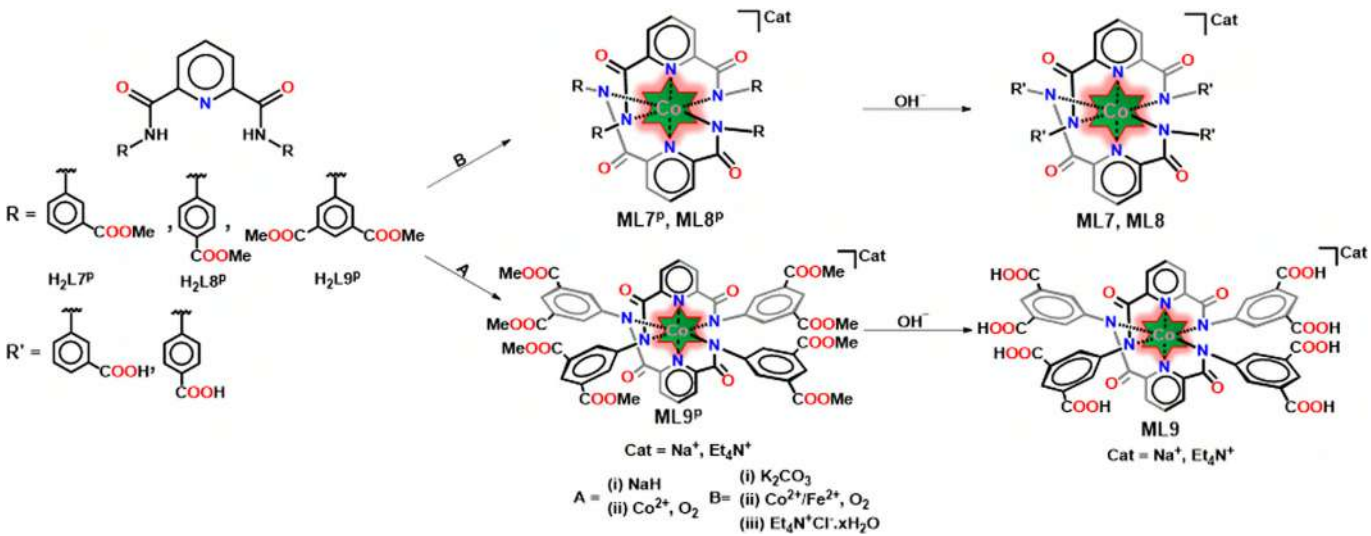

SCHEME 3.2 Preparative route for the synthesis of metalloligands **ML7–ML9** using either route **A** or **B**.

3.3 Metalloligands offering different appended functional groups

3.3.1 Metalloligands offering appended pyridyl rings

A pyridyl ring is one of the copious functionalities that has been effectively used for the synthesis of assorted self-assembled architectures including CPs due to its versatile coordination ability [15,16,19–30]. A pyridyl ring offers a single N-donor site varying by its ring position thus furnishing isomeric 2-pyridyl, 3-pyridyl, and 4-pyridyl varieties. Such pyridyl isomers coordinate with the secondary metals in different directions due to geometrical reasons. As a result, altering the position of the N-atom in an appended pyridyl ring can have a remarkable effect on the synthetic outcome and consequently on the material design. Such metalloligands can result in the formation of either discrete zero-dimensional (0D) complexes or multidimensional (1D, 2D, or 3D) architectures [19–30]. The next few sections will provide a comparative account of several metalloligands offering 2-, 3-, and 4-pyridyl rings and their impact on the design of discrete complexes versus multidimensional (1D, 2D, or 3D) CPs.

3.3.1.1 2-Pyridyl rings

3.3.1.1.1 Design aspects

Metalloligand **ML1** offers 2-pyridyl rings as the appended groups wherein two pyridyl rings from a ligand make angles of varying degrees (31.11–52.87°) with each other while they also make significant angles (14.56–82.95°) with the central pyridine ring. Such a fact indicates that the appended pyridyl rings are not appropriately preorganized in the absence of a secondary metal ion. Such appended pyridyl rings from two ligands converge to form a cleft which is well-suited to accommodate a secondary metal ion [19–25]. The geometry of the central metal ion plays a critical role in giving a unique orientation to the appended pyridyl rings that created the cleft. On reaction with a suitable secondary metal ion, such metalloligands formed 0D homo- and heterometallic complexes depending on the choice of the secondary metal used. **ML1** produced noteworthy linear [M2–M1–M2] trimetallic complexes where M1 and M2 are primary and secondary metals, respectively [19–25]. Such rationally designed molecular building blocks provided a unique way to restrict the dimensionality of the resultant materials to afford discrete 0D complexes.

3.3.1.1.2 Discrete homo- and heterometallic complexes

Metalloligand **ML1** generated a number of homo- and heterometallic complexes on reaction with different secondary metal ions, M2 = Zn^{2+}, Cd^{2+}, Hg^{2+}, Co^{2+}, Cu^{+}, and Cu^{2+} [19–25]. These heterometallic complexes were synthesized by treating **ML1** with the respective metal salts in an appropriate solvent (e.g., CH_3OH, DMF). In such heterometallic complexes, the coordination environment around a secondary metal was quite similar where two ligation sites were occupied by the $N_{pyridyl}$ atoms whereas the remaining sites were occupied

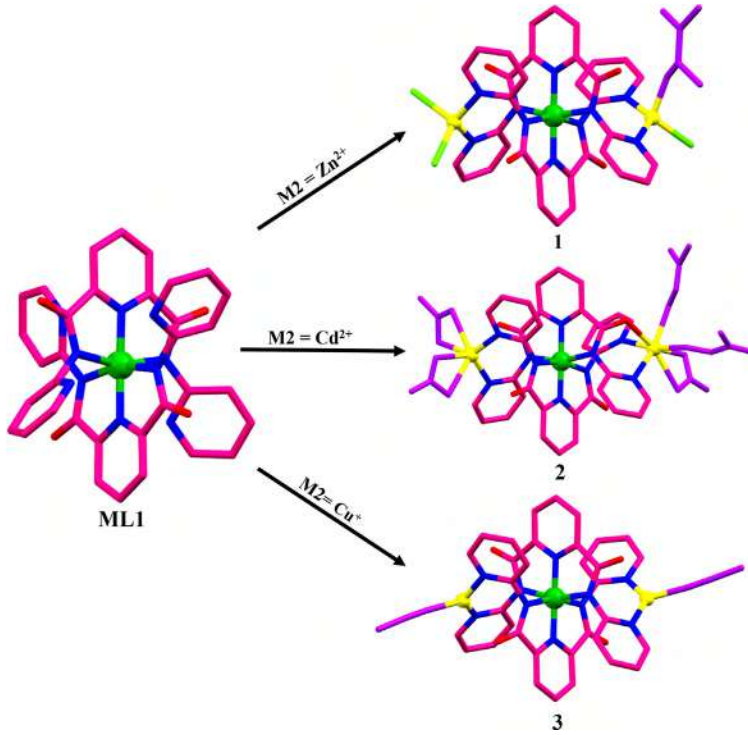

FIGURE 3.1 Crystal structures of metalloligand **ML1** and linear trinuclear complexes **1–3** synthesized using **ML1**. Adapted from Refs. [19, 20, 21].[1]

by the anions and/or solvent molecules. For instance, **ML1** on reaction with $ZnCl_2$ in DMF afforded complex **1** [Zn_2(**ML1**)(Cl_3)(DMF)]. In this complex, two secondary Zn(II) ions were situated in two clefts while additionally ligated by chloride ions and a DMF molecule [19]. Both zinc atoms illustrated a tetrahedral geometry (Fig. 3.1). Similarly, complex **2**, [Cd_2(**ML1**)(NO_3)$_3$($DMF)_2$], exhibited the coordination of a bidentate nitrate ion in addition to a DMF to every cadmium ion (Fig. 3.1) [20]. In contrast, complex **3** with the molecular formula [Cu_2(**ML1**)($CH_3CN)_2$](ClO_4) displayed a trigonal planar geometry around a secondary Cu(I) ion where two coordination sites were occupied by the $N_{pyridyl}$ atoms while the third one was satisfied by a CH_3CN molecule (Fig. 3.1) [21]. Notably, the analogous Fe(III)-based metalloligand **ML1'** also resulted in similar 0D complexes [23,24]. Such a fact asserts that the role of a central metal ion is primarily limited to structural in nature and it does not influence the overall structures of the resulting architectures.

1. Throughout the chapter, following colour codes have been used: primary metal atom, dark green; secondary metal atom, yellow; sodium metal atom, metallic blue; sulfur atom, orange; nitrogen atom, blue; oxygen atom, red; chloride anion, light green; coordinated solvent molecule(s) and anion(s), purple; carbon atom, pink and golden; hydrogen atom, grey.

3.3.1.2 3- and 4-Pyridyl donors

3.3.1.2.1 Design aspects

Changing the position of the nitrogen atom from 2-pyridyl to 3-pyridyl and 4-pyridyl resulted in a substantial effect on the outcome of the resulting architectures [25–30]. Such a fact is related to the opening of the pyridyl-based molecular cleft as observed by the 2-pyridyl appended groups as both appended 3-/4-pyridyl rings are divergent in nature. As a result, metalloligands offering either 3-pyridyl or 4-pyridyl rings afforded materials of higher dimensionalities in complete contrast to discrete 0D heterometallic complexes obtained from metalloligands with 2-pyridyl rings [26–30]. The contrasting architectures, that is, discrete complexes versus multidimensional architectures as a result of the position of the substituted pyridyl ring illustrate the decisive role played by the appended groups in controlling the dimensionality of the resultant materials.

3.3.1.2.2 3-Pyridyl donors

Reaction of metalloligand **ML2** with different secondary metals resulted in the synthesis of various heterometallic CPs with following compositions: $[(Zn(\mathbf{ML2})(H_2O)(DMF)(NO_3)]_n$ (**4**), $[Cd(\mathbf{ML2})(H_2O)(DMF)_2(NO_3)]_n$ (**5**) and $[Ag_2(\mathbf{ML2})_2]_n$ (**6**). In all three cases, secondary metal ions depicted different coordination environments around them depending upon their charge, coordination number, and geometrical preference. Due to the meridional nature of the ligand, appended 3-pyridyl rings coordinated to four different secondary metal ions to form the 2D architectures [25,26,30]. In all cases, the remaining coordination sites were satisfied by the solvent molecules. In case of CP **4**, six secondary Zn^{2+} ions were arranged in a chair conformation (Fig. 3.2) while the adjacent 2D sheets were further connected through H-bonding involving O_{amide} groups, lattice water molecules and nitrate ions to generate a 3D network [25,26]. Similarly, in CP **5**, metalloligands were connected to each other via Cd^{2+} ions to create a 2D sheet (Fig. 3.2). Interestingly, in **5**, out of four 3-pyridyl rings, only three rings were found to coordinate to three different Cd^{2+} ions whereas the remaining pyridyl ring was involved in H-bonding interactions. CP **5** showcased a ladder type arrangement of Co^{3+} and Cd^{2+} ions [26]. The adjacent 2D sheets in **5** were additionally connected to each other via H-bonding interactions involving O_{amide} atom, coordinated water molecules and $N_{pyridyl}$ atom of the uncoordinated pyridyl rings. In CP **6**, silver atoms displayed two different types of coordination geometries: a three-coordinated distorted triangular planar geometry and a two-coordinated linear geometry (Fig. 3.2). In this case, all coordination sites around the Ag(I) ions were satisfied by the $N_{pyridyl}$ atoms. Three-coordinated Ag(I) ions were connected to form a 2D sheet like structure and such 2D sheets were perpendicularly connected to each other via two-coordinated Ag(I) ions to produce a 3D network [30].

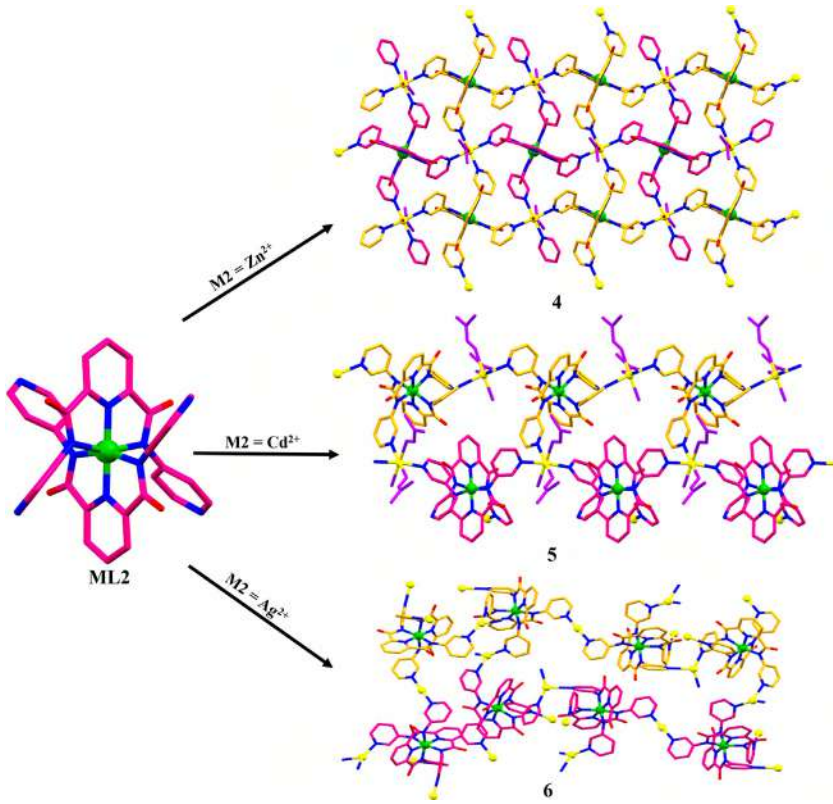

FIGURE 3.2 Crystal structures of metalloligand **ML2** and CPs **4–6** synthesized using **ML2**. Adapted from Refs. [25, 26, 30].

3.3.1.2.3 4-Pyridyl donors

The metalloligand **ML3** upon reaction with secondary metals furnished 2D and 3D CPs with the following formulae: $[Zn_5(\mathbf{ML3})_6(H_2O)_7(NO_3)_4]_n$ (**7**), $[Cd(\mathbf{ML3})(H_2O)_3(NO_3)]_n$ (**8**), and $[(Ag(\mathbf{ML3})(H_2O)]$ (**9**) [26,30]. In CP **7**, six metalloligands were combined via six Zn^{2+} ions to form a hexagonal ring wherein Zn^{2+} ions adopted two different coordination geometries; octahedral (Oh) and trigonal-mono-pyramidal (TMP). While Oh Zn^{2+} ions were located at the periphery of the hexagonal ring; TMP Zn^{2+} ions were situated at the center of the ring (Fig. 3.3) [26]. Similar to **4**, Oh Zn^{2+} ions were arranged in a chair conformation which were connected together to form a honeycomb structure.

In CP **8**, metalloligands were connected to each other through secondary Cd^{2+} ions where Co^{3+} and Cd^{2+} ions were arranged in chair conformations to generate a 2D CP (Fig. 3.3). The adjacent 2D sheets were further connected to each other through H-bonding interactions involving coordinated and lattice

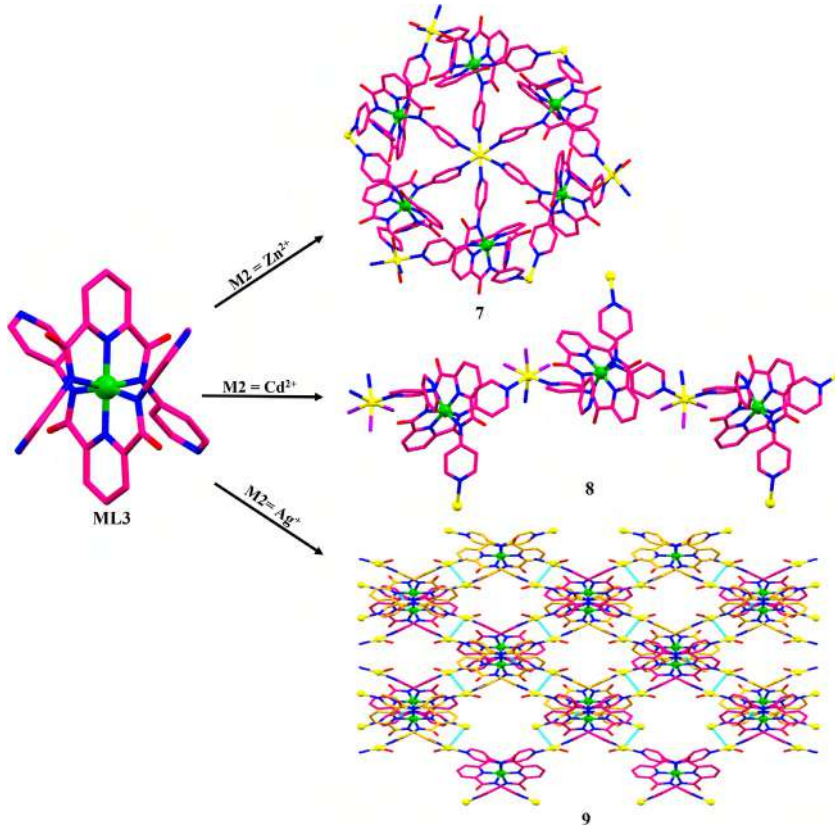

FIGURE 3.3 Crystal structures of metalloligand **ML3** and CPs **7–9** synthesized using **ML3**. Adapted from Refs. [26, 30].

solvent molecules as well as anions [26]. In **9**, Ag(I) ions were coordinated by the appended pyridyl rings from different metalloligands to form a 2D network (Fig. 3.3). The Ag(I) ions exhibited a T-shaped geometry in which two coordination sites were occupied by two pyridyl groups emanating from two different metalloligands whereas the remaining one site was occupied by a water molecule. Importantly, CP **9** exhibited prominent argentophilic interactions ($d_{Ag...Ag}$ ~3.375 Å) between the silver ions from two parallel sheets, thus generating a 3D architecture [30].

3.3.2 Metalloligands offering other appended heterocyclic rings

Substantial amount of research has been done on the architectures arising from pyridyl donors due to their versatile coordination abilities [15,16]. In contrast, limited work has been accomplished utilizing other heterocyclic rings as the

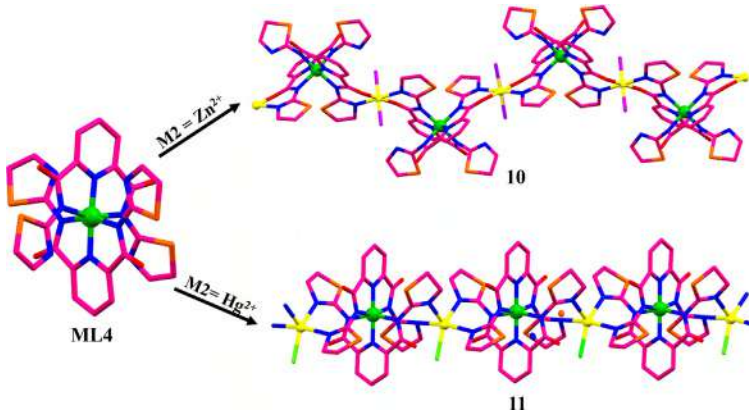

FIGURE 3.4 Crystal structures of metalloligand **ML4** and CPs **10** and **11** synthesized using **ML4**. Adapted from Ref. [31].

donors [15]. As an extension to our ongoing research program, we became interested in the replacement of the appended pyridyl group(s) by other heterocyclic ring(s) such as thiazoline, thiazole, and benzimidazole and to evaluate their role in the secondary-metal-assisted self-assembly process [31–33].

3.3.2.1 Thiazoline donors

3.3.2.1.1 Design aspects and coordination polymers

Metalloligand **ML4** offers four appended thiazoline rings for coordinating to various secondary metal ions. In comparison to a pyridyl ring, a thiazoline ring is unique due to the presence of both hard N-donor and soft S-donor [15,31]. Such a fact creates novel opportunities for coordinating different secondary metal ions via these donor atoms. **ML4** upon reaction with Zn(II) and Hg(II) ions produced 1D CPs with the following compositions: $[Zn(\mathbf{ML4})(H_2O)_2]_n(ClO_4)$ (**10**) and $[Hg(\mathbf{ML4})Cl]_n$ (**11**). Interestingly, both these CPs nicely justified versatile coordination abilities of the thiazoline rings by coordinating to both hard and soft metal atoms. **ML4** on reaction with a hard metal ion, such as Zn^{2+}, led to the formation a 1D chain. Herein, an octahedral Zn(II) ion illustrated coordination both via N-atoms of the thiazoline rings and O-atoms of the amidic groups in the basal plane while axial sites were occupied by the solvent molecules (Fig. 3.4) [31]. In contrast, a softer Hg^{2+} ion showcased coordination from both the donor atoms present in a thiazoline ring viz. nitrogen and sulfur. Interestingly, Hg^{2+} ion in **11** exhibited a distorted square–pyramidal geometry wherein two shorter bonds were formed by the thiazoline-N donors while two longer bonds were rendered by the thiazoline-S donors and the fifth site was occupied by a chloride ion. Notably, in order to allow coordination through thiazoline-S atoms, two out of four thiazoline rings flipped in the resultant CP (Fig. 3.4) [31].

3.3.2.2 Thiazole donors

3.3.2.2.1 Design aspects

Metalloligand **ML5** was designed to offer appended thiazole rings in a similar manner as that of **ML4**. However, a thiazole ring contains an extra double bond when compared to a thiazoline ring. The presence of a double bond makes a thiazole donor even weaker than that of a thiazoline ring and thus provides an interesting case study to understand its effect on the resultant architectures [15,32]. Metalloligand **ML5** was found to coordinate a secondary metal ion either through thiazole-N or amidic-O atom apparently due to the weaker strength of a thiazole donor. Thus, **ML5** on reaction with various secondary metal ions (Zn^{2+}, Cd^{2+}, and Hg^{2+}) resulted in both fascinating discrete complexes as well as 1D CPs [32]. Notably, in all heterometallic complexes, thiazole-S atom was always directed toward an amidic-O atom which resulted in the intramolecular S…O interaction. As a result, only $N_{thiazole}$ groups were freely accessible to bind with the secondary metal ions. The poor electron density at a secondary metal was compensated by the amidic-O donors. Remarkably, all heterometallic complexes exhibited profound H-bonding interactions involving appended yet uncoordinated thiazole rings. In contrast to metalloligands offering appended pyridyl groups which on coordination to the secondary metal ions resulted in heterotrimetallic complexes or multidimensional CPs; thiazole appended metalloligands presented their unique ability to present H-bonds in close proximity to the secondary metals in the resultant CPs.

3.3.2.2.2 Coordination polymers and discrete complexes

The metalloligand **ML5** on reaction with Zn(II) ion afforded both the discrete complex and a 1D CP with the following compositions: $[Zn(\mathbf{ML5})_2(CH_3OH)_2]$ (**12**) and $[Zn(\mathbf{ML5})(CH_3OH)(H_2O)(NO_3)]_n$ (**13**) [32]. Interestingly, on minor changes in the reaction condition during the synthesis, **ML5** afforded two different types of complexes (**12** and **13**) with an identical metal, Zn (Fig. 3.5). Herein, a Zn^{2+} ion was octahedrally coordinated to both thiazole-N and amidic-O atoms while the remaining sites were satisfied by the solvent molecules. In **12**, a Zn^{2+} ion was sandwiched between two metalloligands to yield a discrete compound. In contrast, metalloligands were connected through Zn^{2+} ions furnishing a 1D CP in **13**. Such 1D chains were further connected through H-bonding interactions involving solvent molecules and anions to form a 2D structure.

3.3.2.3 Benzimidazole donors

3.3.2.3.1 Design aspects and tetranuclear complexes

The metalloligand **ML6** was designed to introduce benzimidazole rings as the appendages. In comparison to a pyridyl ring, a benzimidazole ring is a poor donor. But at the same time, a benzimidazole ring can coordinate via both its nitrogen atoms situated on the opposite side of the ring [15,32]. **ML6** decorated

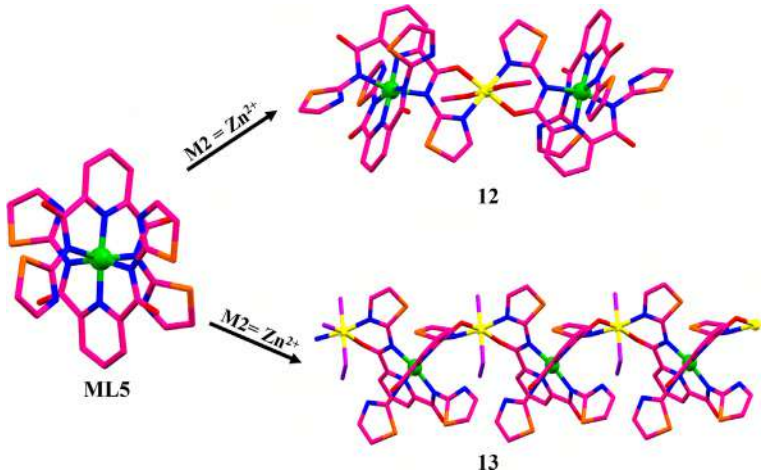

FIGURE 3.5 Crystal structures of metalloligand **ML5** and complex **12** and CP **13** synthesized using **ML5**. Adapted from Ref. [32].

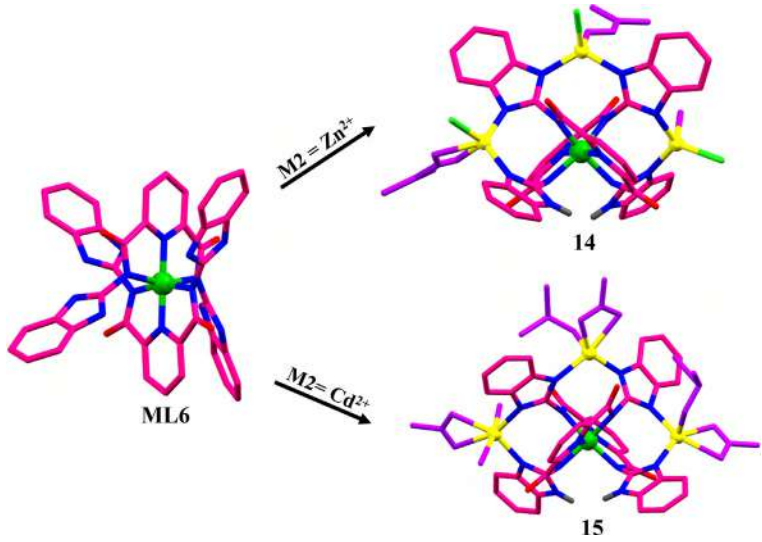

FIGURE 3.6 Crystal structures of metalloligand **ML6** and tetranuclear complexes **14** and **15** synthesized using **ML6**. Adapted from Ref. [33].

with benzimidazole rings on reaction with secondary metal ions (Zn^{2+} and Cd^{2+}) resulted in the isolation of interesting tetranuclear complexes: $[Zn_3(\mathbf{ML6}\text{-}2H^+)Cl_3(DMF)_2(H_2O)]$ (**14**) and $[Cd_3(\mathbf{ML6}\text{-}2H^+)Cl_3(DMF)_2(H_2O)]$ (**15**). It was fascinating to note that both the complexes differed only by the type of solvents/anions coordinated to the secondary metal ions (Fig. 3.6). Notably, secondary metals in both the tetranuclear complexes were tetra-coordinated

wherein two coordination sites were received from the $N_{benzimidazole}$ groups whereas the remaining two sites were occupied by an anion and a solvent. Notably, all four appended benzimidazole rings were involved in coordination to the secondary metal ions. The constrained geometry of the appended benzimidazole rings prevented the insertion of the fourth secondary metal and as a result such benzimidazole rings were protonated and were involved in the H-bonding interactions with the solvent molecules [32]. Thus, metalloligand **ML6** proved to be unique as it was able to incorporate three secondary metal ions in a single complex.

3.3.3 Metalloligands offering appended arylcarboxylic acid groups

The earlier sections have elaborated on the significance of assorted heterocyclic rings in the construction of discrete complexes as well as multidimensional architectures. In addition to the heterocyclic rings, carboxylic acid functional group has also been extensively explored for the synthesis of assorted architectures [13–16,18,34–41]. The incorporation of carboxylic acid groups in metalloligands has unveiled noteworthy avenues for the construction of framework materials due to their ability to coordinate with an array of metal ions while supporting different coordination geometries. This section showcases the effect of number, strategic ring position, and the orientation of an arylcarboxylate group emerging from a metalloligand on the synthetic outcome of molecular architectures [34–41]. The architectures so developed utilizing such metalloligands demonstrated several intriguing features including well-defined pores and channels as well as noninterpenetrated nature of the 2D and 3D networks.

3.3.3.1 Meta-arylcarboxylic acid donors

3.3.3.1.1 Design aspects and coordination polymers

Metalloligand **ML7** offered four *meta*-arylcarboxylic acids as the auxiliary groups. Such appended arylcarboxylic acid groups were found to bind different secondary metal ions to furnish heterometallic CPs [34–39]. Metalloligand **ML7** on reaction with Zn^{2+} and Cd^{2+} ions resulted in the generation of following CPs: $[Zn_3(\mathbf{ML7})(\mu\text{-OH})(H_2O)_6]_n$ (**16**) and $[Cd_{2.5}(\mathbf{ML7})(H_2O)_{15}]_n$ (**17**) [34,35]. In both these cases, a metalloligand was present in its tetra-anionic form and was connected to other metalloligands through the secondary metal ions. While the primary coordination sites on the secondary metal ions were occupied by the arylcarboxylate groups; the remaining sites were satisfied either by the water molecules or bridging hydroxide ions (Fig. 3.7). CP **16**, having secondary building unit (SBU)$[Zn_3(\mu\text{-OH})(\text{–COO})_4]$, featured secondary Zn^{2+} ions in two different coordination geometries: five-coordinated and six-coordinated. In an SBU, three Zn^{2+} ions were bridged by a hydroxide group while the remaining sites were occupied by $O_{carboxylate}$ from different metalloligands and water molecules. Fascinatingly, CP **17** revealed the presence of two different networks,

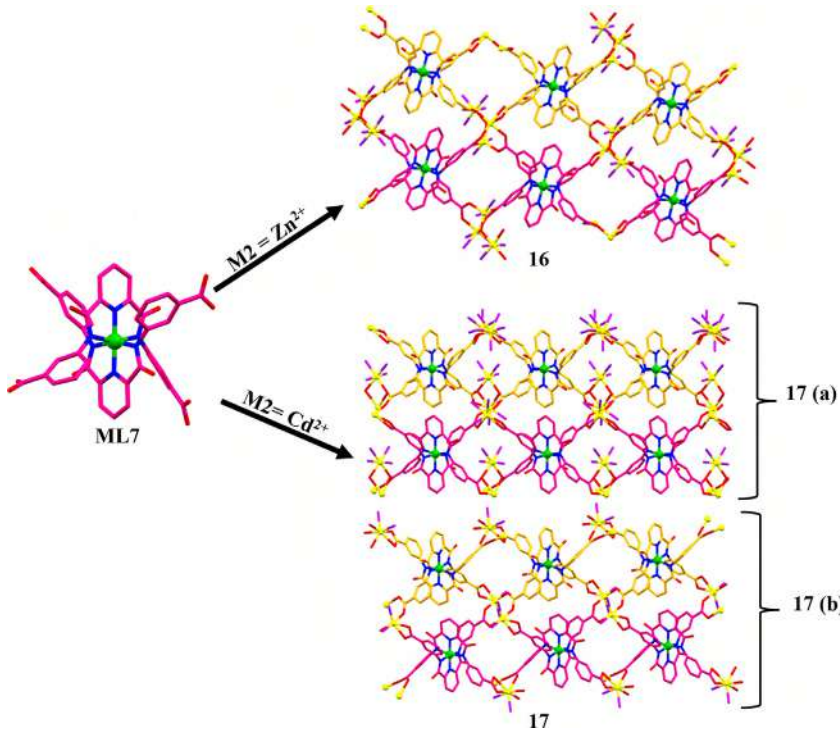

FIGURE 3.7 Crystal structures of metalloligand **ML7** and CPs **16** and **17** synthesized using **ML7**. Adapted from Refs. [34, 35].

17(a) and **17(b)**, within the same unit cell. The two networks differ from each other by means of coordination environment around the secondary metal ions. CP **17(a)** with SBU $[Cd_3(–COO)_4]$ contained three seven-coordinated Cd^{2+} ions while the remaining ones were six-coordinated. In contrast, in **17(b)**, two Cd^{2+} ions were bridged by two arylcarboxylate groups arising from two different metalloligands with SBU of composition $[Cd_2(–COO)_4]$. In both CPs, SBUs were connected through metalloligands producing the resultant 3D networks which offered pores of varying dimensions: 11.9×10.3 Å^2 (**16**), 13.6×10.4 Å^2 (**17a**), and 11.0×10.9 Å^2 (**17b**). Authors illustrated that various substrates and/or reagents could easily diffuse through such pores and channels during the heterogeneous catalysis.

3.3.3.2 Para-arylcarboxylic acid donors

3.3.3.2.1 Design aspects and coordination polymers

Similar to **ML7**, metalloligand **ML8** also furnished four arylcarboxylic acid groups; however, the –COOH moiety is now located at the *para*-position of an arene ring. **ML8** on reaction with secondary Zn^{2+} and Cd^{2+} ions led to

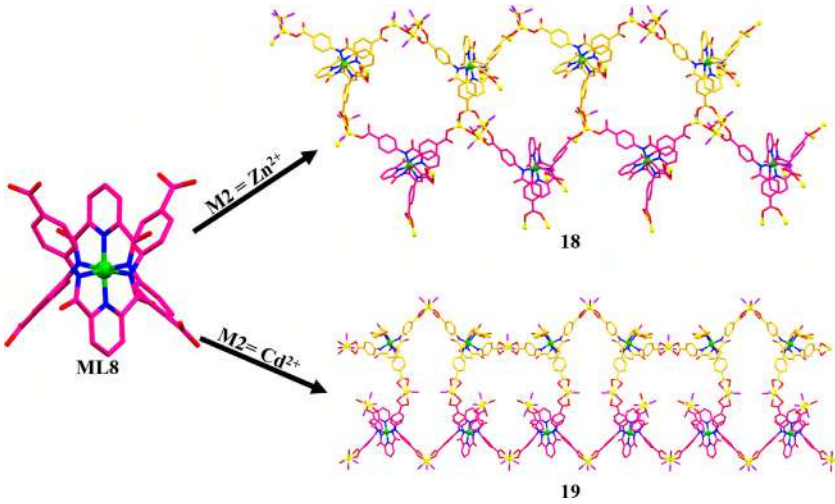

FIGURE 3.8 Crystal structures of metalloligand **ML8** and CPs **18** and **19** synthesized using **ML8**. Adapted from Refs. [34, 35].

the generation of CPs with the following molecular formulae: $[(\mathbf{ML8})_2Zn_6(\mu\text{-}OH)_2(H_2O)_{10}]_n$ (**18**) and $[(\mathbf{ML8})Cd_{2.5}(H_2O)_{10}]_n$ (**19**) [34,35]. CP **18** revealed SBUs with the following composition, $[Zn_5(\mu\text{-}OH)_2(\mu\text{-}H_2O)(\text{–}COO)_8]$ while displayed different coordination environments around the Zn^{2+} ions; two Zn^{2+} ions were six-coordinated, two were five-coordinated while the last one was four-coordinated. Each Zn^{2+} ion was coordinated via a combination of $O_{carboxylate}$ donors, hydroxide groups, and a bridging water molecule depending upon the coordination geometry around the secondary zinc ions (Fig. 3.8). A combination of SBUs and metalloligands resulted in the generation of a 3D CP. CP **19** with SBU composition of $[Cd(\text{–}COO)_2]$ displayed coordination of each metalloligand to four different Cd^{2+} ions. Herein, three Cd(II) ions exhibited seven-coordinated geometry while the fourth one displayed eight-coordinated geometry. Depending upon the geometrical preference around the Cd^{2+} ions, the coordination sites were primarily occupied by $O_{carboxylate}$ groups while the remaining sites were satisfied by the aqua ligands. In this case as well, a 3D CP was formed by a combination of SBUs and metalloligands. Both CPs offered well-defined pores and channels with cross-sections of 12.5×9.9 and 17.4×14.7 Å^2 (**18**) and 17.9×16.3 and 21.5×7.5 Å^2 (**19**). Such pores allowed facile accessibility of the substrates and/or reagents to the Lewis acidic metals during the organic transformation reactions.

3.3.3.3 3,5-Aryldicarboxylic acid donors

3.3.3.1.1 Design aspects and coordination polymers

Metalloligand **ML9** was unique in providing eight free carboxylic acid groups in comparison to the earlier metalloligands **ML7** and **ML8** which offered only four carboxylic acid groups. Interestingly, metalloligand **ML9** exhibited two different

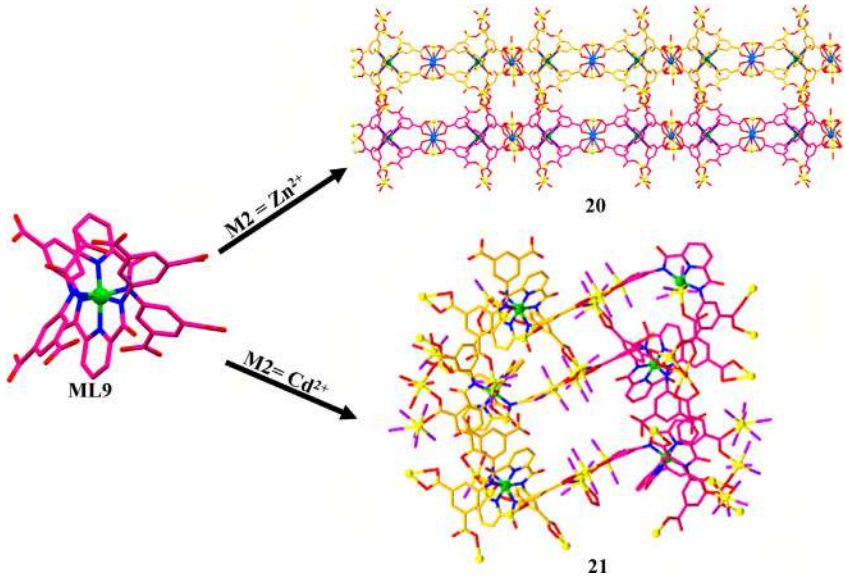

FIGURE 3.9 Crystal structures of metalloligand **ML9** and CPs **20** and **21** synthesized using **ML9**. Adapted from Ref. [41].

coordination modes with the secondary metal ions. While **ML9'** coordinated through all its eight anionic arylcarboxylate groups; **ML9"** ligated only through its six arylcarboxylate groups thus leaving two arylcarboxylic acid groups intact [41]. The reaction of **ML9** with Zn^{2+} and Cd^{2+} ions resulted in the generation of 3D CPs with the following compositions: $[Zn_8(\mathbf{ML9'})_2\{Na_2(H_2O)_{21}\}]_n$ (**20**) and $[Cd_8(\mathbf{ML9'})(\mathbf{ML9''})(H_2O)_{21}]_n$ (**21**) (Fig. 3.9) [41]. In **20**, metalloligands coordinated to the secondary metal ions via all eight anionic arylcarboxylate groups while in **21** Cd^{2+} ions were found to only coordinate via six arylcarboxylate groups leaving two –COOH groups uncoordinated.

In both CPs, metal ions were essentially coordinated through $O_{carboxylate}$ atoms from different metalloligands while the remaining sites were ligated by the water molecules depending upon the geometrical preference of a secondary metal ion. In CP **20**, Zn^{2+} ions demonstrated two different types of coordination geometries: six-coordinated and seven-coordinated. In contrast, CP **21** exhibited a rather complicated structure illustrating different coordination environments around every Cd^{2+} ion. Both the CPs showcased densely packed structures and thus only favored diffusion of smaller substrates in comparison to the bulkier ones during the catalytic reactions.

3.4 Catalytic aspects

Discrete tri- and tetra-nuclear complexes, as well as multidimensional CPs, discussed in this article, not only provided interesting structural aspects but also presented noteworthy catalytic properties. Their catalytic properties were

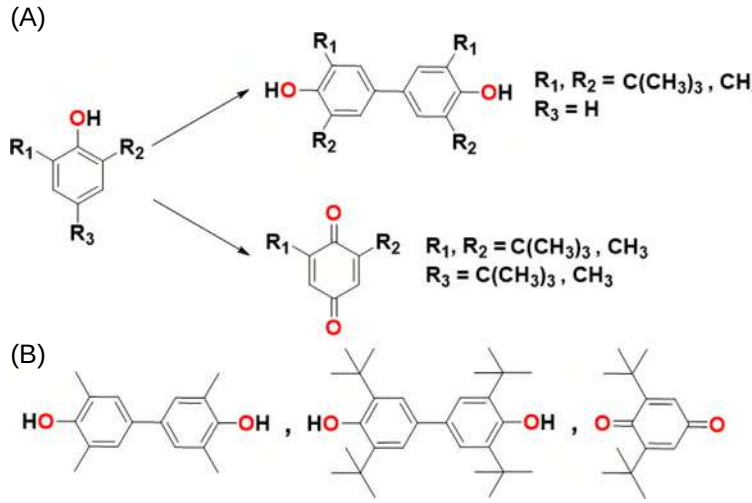

SCHEME 3.3 (A) Coupling and dealkylation reactions of hindered alcohols. (B) Examples of various C–C coupled and dealkylated products.

primarily due to the presence of either Lewis acidic or the redox nature of the secondary metals [15,19–42].

3.4.1 Oxidation and dealkylation reactions of substituted phenols

Notably, both Cu^{+} ions in complex **3** not only offered labile solvent molecules (i.e., CH_3CN) but also exhibited a facile Cu^{2+}/Cu^{+} redox potential. Both these features suggested its potential application in oxidation reactions [15,21,23,43]. Complex **3** illustrated oxidation of hindered phenols to yield C–C coupled products employing molecular oxygen as an exclusive oxidant (Scheme 3.3) [21]. Interestingly, the reaction with 2,4,6-trisubstituted phenols resulted in the dealkylation reaction. The authors explained that the presence of substituents both at *ortho* and *para* positions did not allow such substrates to interact with the redox active Cu^{+} ions present in the molecular clefts to give the expected oxidation products but rather promoted dealkylation reaction. Control reactions with H_2O_2 as the oxidant did not result in dealkylation proving the exclusive role of the $Cu–O_2$ species in such reactions [21,23].

3.4.2 A^3-coupling reactions

Lower coordination numbers around the Ag(I) ions in CPs **6** and **9** as well as a potential exchange of the coordinated solvent molecules validated the possibility of interaction of a substrate/reagent with these metal centers [30]. These points intrigued the authors to test such CPs as the catalysts for the one-pot synthesis of propargylamines via A^3-coupling using assorted amines, aldehydes

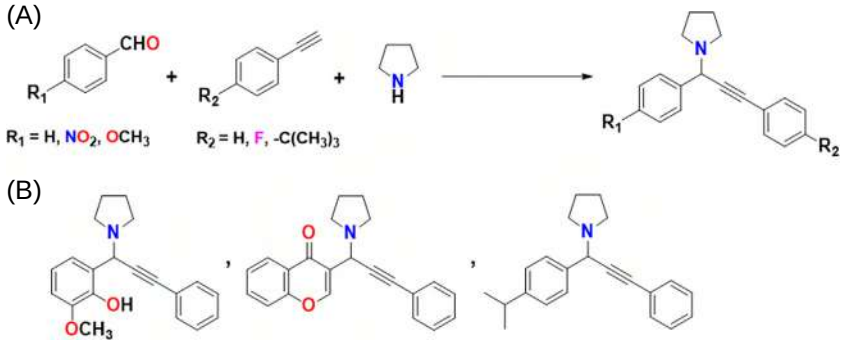

SCHEME 3.4 (A) The A^3-coupling reaction of substituted aldehydes, substituted alkynes, and proline. (B) Examples of various A^3-coupled products.

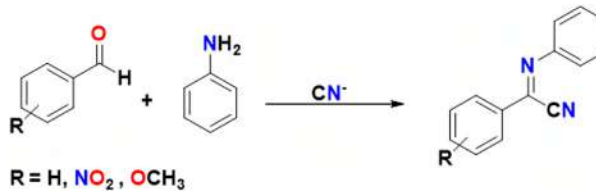

SCHEME 3.5 Strecker reaction of substituted aldehydes with aniline in presence of a cyanide source.

and alkynes (Scheme 3.4) [15,30]. Satisfyingly, a lower catalyst loading as well as shorter reaction duration resulted in high product yields. Well-defined pores and channels in CP **6** permitted facile access to both substrates and reagents and thus produced the corresponding products in high yield in comparison to CP **9** which exhibited a densely packed structure which potentially hindered their diffusion and thus reducing the product yield [30]. Gratifyingly, these catalysts were also active for the conversion of a few biologically relevant aldehydes.

3.4.3 Strecker reactions

Strecker reaction is an easy strategy for the synthesis of aminonitriles which are essential intermediates for the preparation of amino acids via hydrolysis of nitriles. Such reactions are usually catalyzed by the Lewis acid catalysts [15,44]. Discrete heterometallic complexes **1** and **2** as well as CPs **4** and **5** were effectively employed as the catalysts for the Strecker reaction (Scheme 3.5) [15,19,20,25,26]. Out of two different types of materials, CPs **4** and **5** outperformed discrete complexes **1** and **2** for such reactions. Such a noteworthy catalytic performance of CPs can be attributed to their heterogeneous nature which offered advantages including reusability and recyclability. Interestingly, all such catalysts were able to convert a variety of substituted imines bearing both electron-realizing and electron-withdrawing substituents to their corresponding aminonitriles.

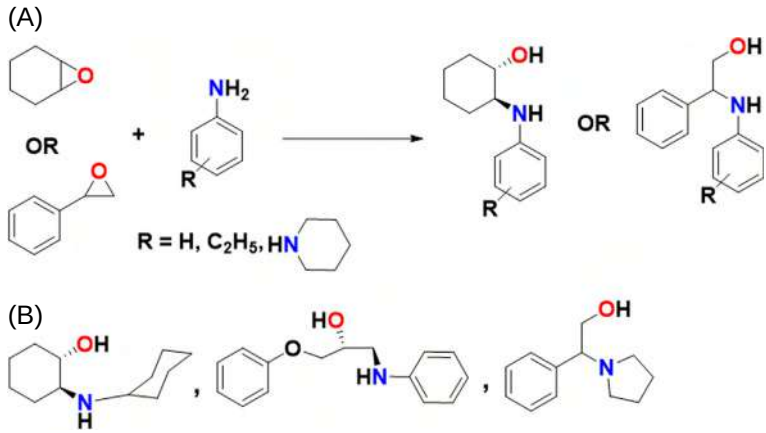

SCHEME 3.6 (A) Ring-opening reaction of oxiranes. (B) Examples of various ring-opened products.

3.4.4 Ring-opening reactions (RORs)

Compounds **1**, **2**, **4**, **7**, **8,** and **10** were utilized as the catalysts for the regioselective RORs of various oxiranes to produce pharmaceutically relevant products (Scheme 3.6) [15,19,20,25,26,31,45]. From the abovementioned compounds, CPs **4**, **7**, **8,** and **10** proved to be superior catalysts in comparison to discrete complexes **1** and **2**. The enhanced catalytic performance of CPs was attributed to the existence of coordinated solvent molecules which were labile and therefore promoted easy accessibility of the epoxides to the Lewis acidic metals.

CPs **16–19** also exhibited facile RORs of various epoxides with assorted nucleophiles [15,34,35]. Products were obtained with perfect regioselectivity. It was believed that the catalytic sites were orderly embedded in the crystalline polymeric network and thus a nucleophile could only attack from limited direction to a metal-bound epoxide which resulted in regioselective ring-opened products. The heterogeneous nature of catalysis allowed facile separation of CPs by filtration and therefore multiple catalytic cycles. CPs isolated after several catalytic cycles were characterized by various techniques such as FTIR spectra, powder XRD, and SEM which established the stability of CPs and further validated the true heterogeneous nature of these catalysts.

3.4.5 Knoevenagel condensation reactions

Metal complexes **10–15**, obtained by metalloligands offering heterocyclic rings (**ML4**-**ML6**), behaved as the efficient heterogeneous catalysts for the Knoevenagel condensation reactions (KCRs) (Scheme 3.7) [15, 31–33,46]. All these complexes showcased excellent yields for the C–C coupled products. Notably, Hg-containing complex **11** furnished higher yield for the sulfur-containing

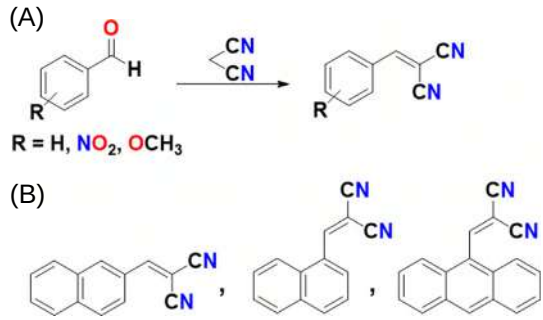

SCHEME 3.7 (A) Knoevenagel condensation reaction of substituted aldehydes. (B) Examples of various Knoevenagel condensation products.

aldehydes thus validating the concept of binding of a softer substrate to a softer metal during its activation to undergo the desired catalytic transformation [31]. Tetranuclear complexes **14** and **15** also proved to be efficient catalysts as a lower catalyst loading as well as a shorter reaction duration was required for the desired organic transformation. The enhanced catalytic performance of **14** and **15** was attributed to the presence of three exposed secondary metal centers in these complexes [33].

CPs **20** and **21** were also employed for KCRs with various active methylene compounds and substituted carbonyl compounds [15,41]. Interestingly, the presence of various electronic substituents in substrates did not influence the yield of the products. In contrast, molecular size of the substrates greatly influenced the product outcome. Yields were compromised for the bulkier substrates which could be explained due to their hindered diffusion through smaller pores and channels of the moderately porous CPs.

3.5 Conclusions

The chapter has explained the utilization of judiciously selected metalloligands offering coordination-sensitive functional groups for the synthesis of discrete heterometallic complexes as well as highly ordered multidimensional heterometallic CPs. In both categories, metalloligands were offering two major types of functional groups; heterocyclic rings and arylcarboxylic acid groups. In the first category, we have shown the use of pyridyl, thiazole, thiazoline, and benzimidazole rings for illustrating a variety of discrete heterometallic complexes. The variation of 2-, 3-, and 4-pyridyl rings emerging from a metalloligand provided a significant strategy to control the dimensionality of the resultant architectures. In the second category, the use of metalloligands offering arylcarboxylate groups provided 2D and 3D architectures with porous and robust network structures. The metalloligand approach excelled in generating noninterpenetrated architectures while providing the opportunity of placing a variety of secondary metals at desirable sites.

Such coordination-driven discrete complexes, as well as CPs, were notable catalysts for assorted organic transformation reactions. The metalloligand approach allowed for placing both Lewis acidic and redox-sensitive secondary metals which created noteworthy opportunities for targeting a variety of catalytic reactions. While discrete complexes acted as the homogenous catalysts for a number of challenging organic transformations; the multidimensional CPs were blessed as the reusable and recyclable heterogeneous catalysts.

While we illustrated a few functional groups that were integrated with a metalloligand; a wide variety of functional groups and therefore metalloligands could be easily envisioned. As a result, a plethora of coordination-driven supramolecular assemblies is waiting to be designed and utilized as the next-generation materials for novel functional properties and applications.

Acknowledgments

Acknowledgment: Rajeev Gupta gratefully acknowledges the continuous financial assistance from the Science and Engineering Research Board, New Delhi including the Core Research Grant Project (CRG/2021/001700).

References

[1] H.-C. Joe Zhou, S. Kitagawa, Metal–organic frameworks (MOFs), Chem. Soc. Rev. 43 (2014) 5415–5418.

[2] J.R. Long, O.M. Yaghi, The pervasive chemistry of metal–organic frameworks, Chem. Soc. Rev. 38 (2009) 1213–1214.

[3] D.J. Tranchemontagne, J.L. Mendoza-Cortés, M. O'Keeffe, O.M. Yaghi, Secondary building units, nets and bonding in the chemistry of metal–organic frameworks, Chem. Soc. Rev. 38 (2009) 1257–1283.

[4] J.-M. Lehn, Toward complex matter: supramolecular chemistry and self-organization, Proc. Natl. Acad. Sci. U.S.A. 99 (8) (2002) 4763–4768.

[5] B. Li, H.-M. Wen, W. Zhou, B. Chen, Porous metal–organic frameworks for gas storage and separation: what, how, and why? J. Phys. Chem. Lett. 5 (20) (2014) 3468–3479.

[6] A.H. Chughtai, N. Ahmad, H.A. Younus, A. Laypkov, F. Verpoort, Metal–organic frameworks: versatile heterogeneous catalysts for efficient catalytic organic transformations, Chem. Soc. Rev. 44 (2015) 6804–6849.

[7] K. Sumida, D.L. Rogow, J.A. Mason, T.M. McDonald, E.D. Bloch, Z.R. Herm, T.-H. Bae, J.R. Long, Carbon dioxide capture in metal–organic frameworks, Chem. Rev. 112 (2) (2012) 724–781.

[8] N. Huang, K. Wang, H. Drake, P. Cai, J. Pang, J. Li, S. Che, L. Huang, Q. Wang, H.-C. Zhou, Tailor-made pyrazolide-based metal–organic frameworks for selective catalysis, J. Am. Chem. Soc. 140 (120) (2018) 6383–6390.

[9] Ü. Kökçam-Demir, A. Goldman, L. Esrafili, M. Gharib, A. Morsali, O. Weingart, C. Janiak, Coordinatively unsaturated metal sites (open metal sites) in metal–organic frameworks: design and applications, Chem. Soc. Rev. 49 (2020) 2751–2798.

[10] M.Y. Masoomi, A. Morsali, A. Dhakshinamoorthy, H. Garcia, Mixed-metal MOFs: unique opportunities in metal–organic framework (MOF) functionality and design, Angew Chem. Int. Ed. 58 (43) (2019) 15188–15205.

[11] S.R. Halper, L. Do, J.R. Stork, S.M. Cohen, Topological control in heterometallic metal−organic frameworks by anion templating and metalloligand design, J. Am. Chem. Soc. 128 (47) (2006) 15255–15268.

[12] E. Pardo, R. Ruiz-García, J. Cano, X. Ottenwaelder, R. Lescouëzec, Y. Journaux, F. Lloret, M. Julve, Ligand design for multidimensional magnetic materials: a metallosupramolecular perspective, Dalton Trans. (2008) 2780–2805.

[13] G. Kumar, R. Gupta, Molecularly designed architectures – the metalloligand way, Chem. Soc. Rev. 42 (2013) 9403–9453.

[14] G. Kumar, R. Gupta, Coordination driven architectures based on metalloligands offering appended carboxylic acid groups, J. Chem. Sci. 130 (2018) 86.

[15] S. Pachisia, R. Gupta, Architectural and catalytic aspects of designer materials built using metalloligands of pyridine-2,6-dicarboxamide based ligands, Dalton Trans. 49 (2020) 14731–14748.

[16] G. Kumar, G. Kumar, R. Gupta, Effect of pyridyl donors from organic ligands versus metalloligands on material design, Inorg. Chem. Front. 8 (2021) 1334–1373.

[17] A. Ali, G. Hundal, R. Gupta, Co^{3+}-based building blocks with appended phenol and catechol groups: examples of placing hydrogen-bond donors and acceptors in a single molecule, Cryst. Growth Des. 12 (3) (2012) 1308–1319.

[18] G. Kumar, H. Aggarwal, R. Gupta, Cobalt complexes appended with para- and meta-arylcarboxylic acids: influence of cation, solvent, and symmetry on hydrogen-bonded assemblies, Crystal Growth Des. 13 (1) (2013) 74–90.

[19] A.A Mishra, S. Upreti, R. Gupta, Cobalt coordination induced functionalized molecular clefts: isolation of $\{Co^{III}-Zn^{II}\}$ heterometallic complexes and their applications in Beckmann rearrangement reactions, Inorg. Chem. 47 (1) (2008) 154–161.

[20] A.A Mishra, S. Upreti, M.S. Whittingham, R. Gupta, Cobalt complex as building blocks: synthesis, characterization, and catalytic applications of $\{Cd^{2+}$-Co^{3+}-$Cd^{2+}\}$ and $\{Hg^{2+}$-Co^{3+}-$Hg^{2+}\}$ heterobimetallic complexes, Inorg. Chem. 48 (12) (2009) 5234–5243.

[21] A.P. Singh, R. Gupta, Copper(I) in the cleft: syntheses, structures and catalytic properties of $\{Cu^{+}$-Co^{3+}-$Cu^{+}\}$ and $\{Cu^{+}$-Fe^{3+}-$Cu^{+}\}$ heterobimetallic complexes, Eur. J. Inorg. Chem. (2010) 4546–4554.

[22] G. Kumar, A. Singh, R. Gupta, Syntheses, structures and heterogeneous catalytic application of $\{Co^{3+}$–$Eu^{3+}\}$ and $\{Co^{3+}$– $Tb^{3+}\}$ coordination polymers, Eur. J. Inorg. Chem. (2010) 5103–5112.

[23] S. Srivastava, A. Ali, A. Tyagi, R. Gupta, $\{Cu^{2+}$–Co^{3+}–$Cu^{2+}\}$ and $\{Cu^{2+}$–Fe^{3+}–$Cu^{2+}\}$ heterobimetallic complexes and their catalytic properties, Eur. J. Inorg. Chem (2014) 2113–2123.

[24] S. Srivastava, M.S. Dagur, A. Ali, R. Gupta, Trinuclear $\{Co^{2+}$–M^{3+}–$Co^{2+}\}$ complexes catalyze reduction of nitro compounds, Dalton Trans. 44 (2015) 17453–17461.

[25] A.P. Singh, A. Ali, R. Gupta, Cobalt complexes as the building blocks: $\{Co^{3+}$–$Zn^{2+}\}$ heterobimetallic networks and their properties, Dalton Trans. 39 (2010) 8135–8138.

[26] A.P. Singh, G. Kumar, R. Gupta, Two-dimensional $\{Co^{3+}$–$Zn^{2+}\}$ and $\{Co^{3+}$–$Cd^{2+}\}$ networks and their applications in heterogeneous and solvent-free ring opening reactions, Dalton Trans. 40 (2011) 12454–12461.

[27] S. Srivastava, M.S. Dagur, R. Gupta, Two-dimensional Co^{3+}–Co^{2+} and Fe^{3+}–Co^{2+} networks and their heterogeneous catalytic activities, Eur. J. Inorg. Chem. (2014) 4966–4974.

[28] G. Kumar, R. Gupta, A novel Co^{3+}-based asymmetrical building block: heterobimetallic metallacycles versus coordination networks, Inorg. Chem. Commun. 23 (2012) 103–108.

[29] G. Kumar, G. Kumar, R. Gupta, Asymmetrical metalloligands based $\{Co^{3+}$–$Cd^{2+}\}$ and $\{Co^{3+}$–$Ag^{+}\}$ coordination polymers: syntheses and characterization, Inorg. Chim. Acta 425 (2015) 260–268.

[30] G. Kumar, S. Pandey, R. Gupta, Ag-based coordination polymers based on metalloligands and their catalytic performance in multicomponent A^3-coupling reactions, Cryst. Growth Des. 18 (9) (2018) 5501–5511.

[31] D. Bansal, S. Pandey, G. Hundal, R. Gupta, Heterometallic coordination polymers: syntheses, structures and heterogeneous catalytic applications, New J. Chem. 39 (2015) 9772–9781.

[32] D. Bansal, G. Hundal, R. Gupta, A. Metalloligand, Appended with thiazole rings: heterometallic Co^{3+}–Zn^{2+} and Co^{3+}–Cd^{2+} complexes and their heterogeneous catalytic applications, Eur. J. Inorg. Chem. (2015) 1022–1032.

[33] S. Pandey, D. Bansal, R. Gupta, A metalloligand appended with benzimidazole rings: tetranuclear $[CoZn_3]$ and $[CoCd_3]$ complexes and their catalytic applications, New J. Chem. 42 (2018) 9847–9856.

[34] G. Kumar, R. Gupta, Three-dimensional $\{Co^{3+}$–$Zn^{2+}\}$ and $\{Co^{3+}$–$Cd^{2+}\}$ networks originated from carboxylate-rich building blocks: syntheses, structures, and heterogeneous catalysis, Inorg. Chem. 52 (19) (2013) 10773–10787.

[35] G. Kumar, R. Gupta, Cobalt complexes appended with p- and m-carboxylates: two unique $\{Co^{3+}$–$Cd^{2+}\}$ networks and their regioselective and size-selective heterogeneous catalysis, Inorg. Chem. 51 (10) (2012) 5497–5499.

[36] G. Kumar, G. Kumar, R. Gupta, Manganese- and cobalt-based coordination networks as promising heterogeneous catalysts for olefin epoxidation reactions, Inorg. Chem. 54 (2015) 2603–2615.

[37] G. Kumar, G. Kumar, R. Gupta, Lanthanide-based coordination polymers as promising heterogeneous catalysts for ring-opening reactions, RSC Adv. 6 (2016) 21352–21361.

[38] G. Kumar, F. Hussain, R. Gupta, Carbon-sulphur cross coupling reactions catalyzed by nickel-based coordination polymers based on metalloligands, Dalton Trans. 46 (2017) 15023–15031.

[39] G. Kumar, F. Hussain, R. Gupta, Copper based coordination polymers based on metalloligands: utilization as heterogeneous oxidation catalysts, Dalton Trans. 47 (2018) 16985–16994.

[40] S. Srivastava, H. Aggarwal, R. Gupta, Three-dimensional heterometallic coordination networks: syntheses, crystal structures, topologies, and heterogeneous catalysis, Cryst. Growth Des. 15 (8) (2015) 4110–4122.

[41] S. Srivastava, V. Kumar, R. Gupta, A carboxylate-rich metalloligand and its heterometallic coordination polymers: syntheses, structures, topologies, and heterogeneous catalysis, Cryst. Growth Des. 16 (5) (2016) 2874–2886.

[42] N.K Bavykina, I.S. Khan, J.A. Bau, A. Ramirez, J. Gascon, Metal–organic frameworks in heterogeneous catalysis: recent progress, new trends, and future perspectives, Chem. Rev. 120 (16) (2020) 8468–8535.

[43] K.J.H Lucchese, D.-H. Lee, C.D. Incarvito, R.D. Sommer, A.L. Rheingold, K.D. Karlin, Mono-, bi-, and trinuclear CuII-Cl containing products based on the tris(2-pyridylmethyl)amine chelate derived from copper(I) complex dechlorination reactions of chloroform, Inorg. Chem. 43 (19) (2004) 5987–5998.

[44] J. Wang, X. Liu, X. Feng, Asymmetric strecker reactions, Chem. Rev. 111 (11) (2011) 6947–6983.

[45] D. Britt, C. Lee, F.J. Uribe-Romo, H. Furukawa, O.M. Yaghi, Ring-opening reactions within porous metal−organic frameworks, Inorg. Chem. 49 (2010) 6387–6389.

[46] J.N. Appaturi, R. Ratti, B.L. Phoon, S.M. Batagarawa, I.U. Din, M. Selvaraj, R.J. Ramalingam, A review of the recent progress on heterogeneous catalysts for Knoevenagel condensation, Dalton Trans. 50 (2021) 4445–4469.

Chapter 4

Platinum-containing heterometallic metallacycles and metallacages

Hong-Yu Lin, Yu-Te Wang, Dawei Zhang and Lin Xu
Shanghai Key Laboratory of Green Chemistry and Chemical Processes, School of Chemistry and Molecular Engineering, East China Normal University, Shanghai, China

4.1 Introduction

Coordination-driven self-assembly is powerful tool to construct discrete metallacycles and metallacages due to their considerable synthetic advantages including fast and facile construction, inherent self-correction, and defect-free assembly [1–5]. Besides the pure aesthetics, these 2D and 3D-supramolecular architectures have found useful applications in molecular recognition, chemical sensing, catalysis, drug delivery, and separation [6].

Many advances have been achieved to make the self-assembly process more predictable and the assembled structure more sophisticated. To this end, heterometallic coordination complexes are of great interest [7–9]. Compared with the homometallic coordination strategy, the introduction of a second metal can improve the topological complexity and structural diversity of the final assemblies, enabling the access to larger or more complicated architectures. The combination of two different metal cations in a single discrete structure also offers the chance to combine properties of two different metals, potentially expanding its electrochemical, photophysical, or magnetic properties.

Among the metal cations used in the coordination-driven self-assembly, the relatively inert platinum(II) has evolved to be one of the most attractive cations due to the high stability and accessibility of square-planar platinum(II) coordination geometries [10]. In this chapter, we will thus focus on the construction of platinum-containing heterometallic metallacycles and metallacages. These assemblies were mainly constructed by the metalloligand approach, in which a metalloligand was prepared prior to the final self-assembly with another different metal. The self-sorting strategy was also occasionally used, enabling the one-pot synthesis of the final product from a multicomponent mixture containing

Supramolecular Coordination Complexes: Design, Synthesis, and Applications.
DOI: https://doi.org/10.1016/B978-0-323-90582-4.00013-0

different metals. The functions and applications of these 2D and 3D-supramolecular architectures will be briefly described as well.

4.2 Platinum-containing heterometallic metallacycles

Metallacycles with various sizes, shapes, and coordination geometries could be regulated by changing the category of coordinated metal ions, the design of the building blocks and metal/ligand ratios. Particularly, platinum-based metallacycles have attracted much interest due to their synthetic superiority. Among these metallacycles, heterometallic metallacycles possess rich photophysical and electrochemical characteristics, leading to applications in several fields, such as sensing and catalysis [11, 12]. Hence, in this section, we focus on the recent advances in the construction and application of platinum-containing heterometallic metallacycles.

4.2.1 Pt–Pd heterometallic metallacycles

The history of human development is a process of imitating nature. Most biological substances are chiral, such as carbohydrates, amino acids, and nucleic acids. The inspiration of supramolecular chemistry originates mainly from biological molecules, such as proteins and lipids, and their interactions [13]. Hence, it is important to explore the function of chiral elements in artificial supramolecular structures, which could assist to realize the effect of chiral components in biological systems. In 1998, Stang and coworkers reported ten different air-stable, chiral, neutral-charged Pt/Pt and Pt/Pd metallacycles **1**–**10** based on 2,3-*O*-isopropylidene-2,3-dihydroxy-1,4-bis(diphenylphosphino)-butane (DIOP) units and 2,2′-bis(diphenylphosphino)-1,1′-binaphthyl (BINAP) units (Scheme 4.1) [14]. In particular, the BINAP unit has C_2 symmetry and is well known as a chiral transition-metal-chelating reagent in asymmetric catalysis. As a result, the chirality and the corresponding special chiroptical properties were endowed to the metallacycles. Then, silver complexes **11**–**15** were obtained by adding 2 equivalents of silver triflate to metallacycles **1, 3, 4, 9**, and **10** via π-tweezer effect (Scheme 4.2). This was followed by catching neutral guests tetramethylpyrazine or phenazine by coordination to the π-coordinated silver atoms at the respective neutral corners, leading to complexes **16**–**22**. The formation of metallacycles, silver coordination, and guest inclusion were demonstrated by NMR spectroscopy showing significant chemical shift differences. Due to the orbital overlap perturbation resulted from the coordination effect between neutral Pt(DIOP)(4-ethynylpyridine)$_2$ moieties and Pt/Pd(II)(BINAP) moieties, large cotton effects were observed between 320 and 350 nm in circular dichroism (CD) spectra upon metallacycles formation. Particularly, comparing the CD spectra of **3** and **4** shown in Fig. 4.1, it revealed that the chiroptical properties were mainly ascribed to the BINAP units. Besides, the most intense band maxima shift and intensity changes in CD spectra were caused by the coordination of silver

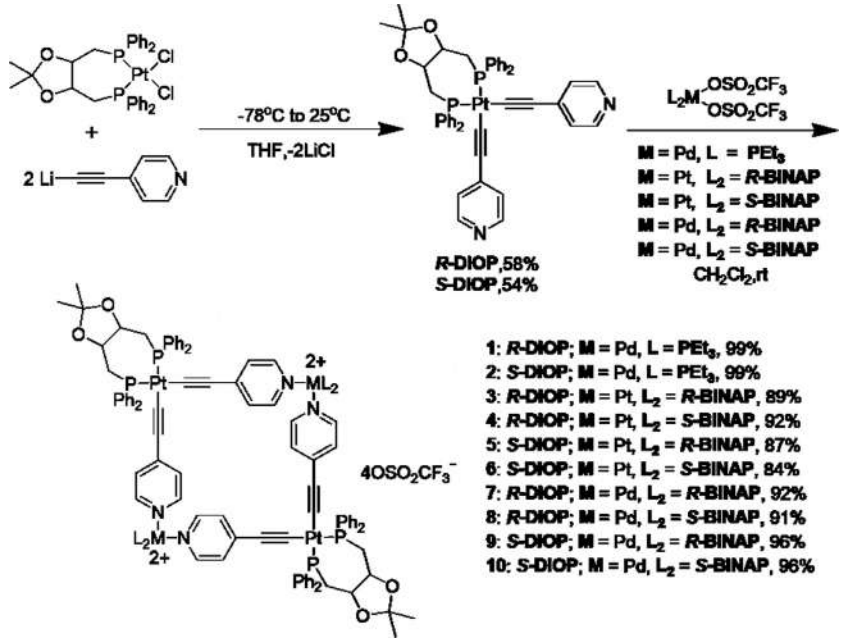

SCHEME 4.1 Self-assembly of metallacycles 1–10.

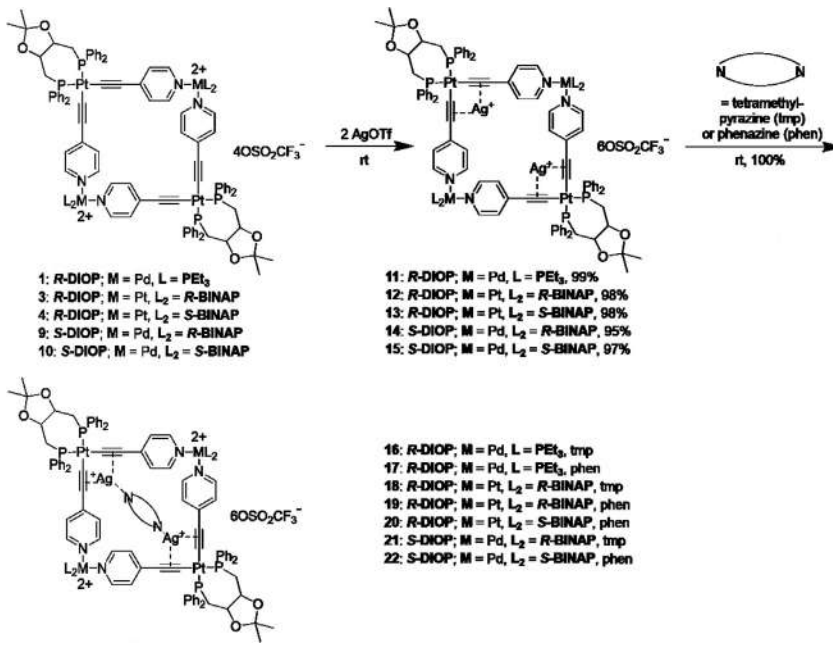

SCHEME 4.2 Self-assembly of silver complexes 11–15 and coordination complexes 16–22.

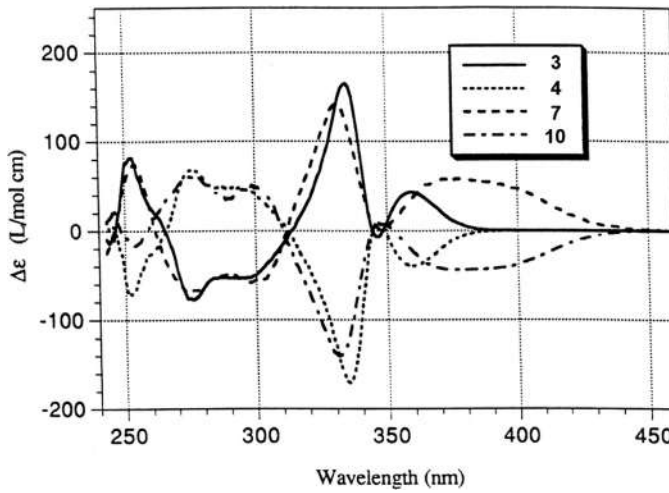

FIGURE 4.1 CD spectra of chiral metallacycles **3, 4, 7**, and **10**. *Reproduced with permission [14]. Copyright © 1998, American Chemical Society.*

and the subsequent neutral guest inclusion. This work identified that circular dichroism can serve as a powerful tool to study host–guest systems for Lewis acid/base receptors. Two other platinum-containing heterometallic metallacycles with palladium ions were provided by Findlay, Crowley and coworkers [15]. Square and triangular-shaped metallacycles were obtained by self-assembly between Pt(II) containing metalloligands and $PdCl_2$ linker moieties. Meanwhile, the triangular-shaped metallacycle can yield singlet oxygen under the irradiation of a 250 W sun lamp and catalyze anthracene.

4.2.2 Pt–Zn heterometallic metallacycles

Metallosalen complexes always attracted huge attention due to their versatile properties and wide applications in several fields, such as heterogeneous catalysis, environmental protection, chemical sensors, and sustainable energy [16]. For the catalytic chemical transformation reactions, cooperative bimetallic processes are always involved. Supramolecular coordination self-assembly containing two or more reactive metal centers is promising candidates as efficient catalysts for these reactions. In order to achieve this target, Hupp, Nguyen, and coworkers designed and constructed several platinum-containing heterometallic metallacycles with zinc ions in different methods [17]. Initially, loop metallacycles were prepared by the reaction of the equimolar amounts of cis-$(Pet_3)_2Pt(OTf)_2$ and bis(4-pyridyl)-functionalized free-base salen-type ligands **23–26** (Scheme 4.3). It is important to note that the thermodynamic stable products are linker-strained dimetallic loops but not the less strained tetrametallic squares confirmed by X-ray crystallography. This result indicated the significance of entropy in

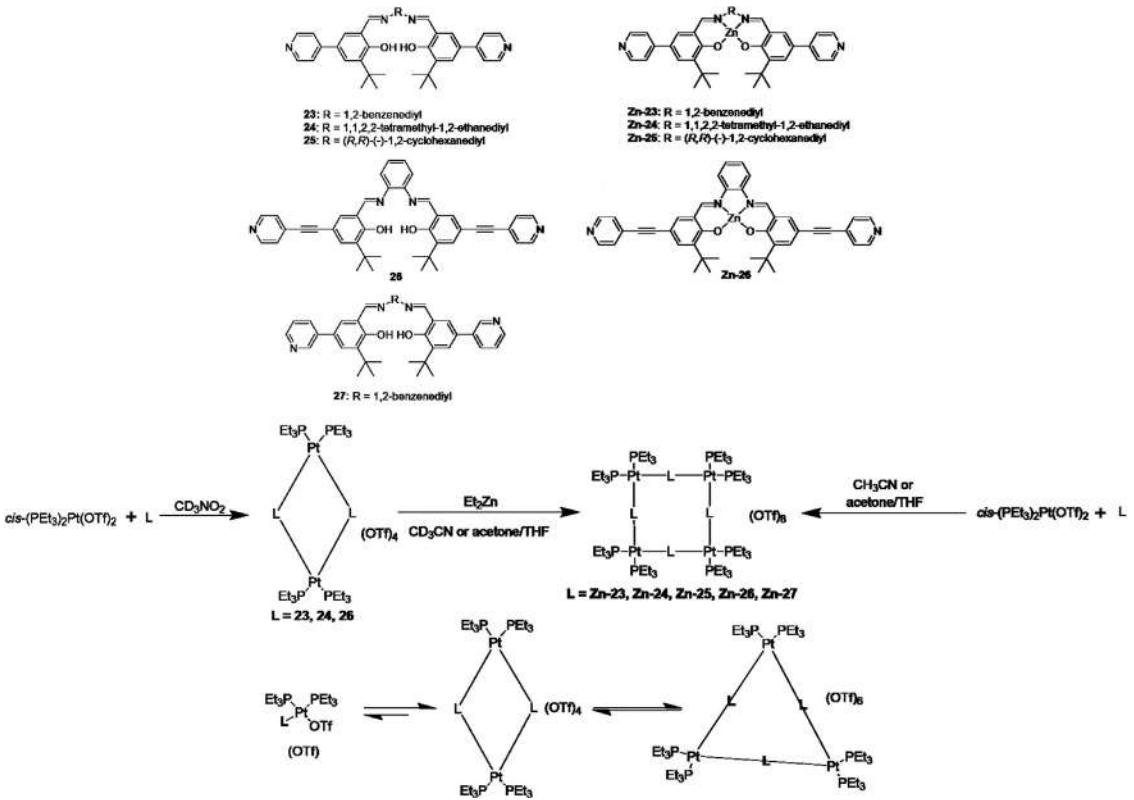

SCHEME 4.3 Functionalized salen-type ligands 23–27, Zn23–27, and self-assembly of various metallacycles with different shapes.

supramolecular self-assembly process, which is also identified in some other systems [18, 19]. Zinc salen ligands (**Zn23–26**) were prepared to rigidify the ligand framework, resulting in preferential formation of less strained square structures instead of loops. Notably, coordinating cosolvents THF or CH_3CN were indispensable to obtain single desired square products rather than complicated mixture products. Meanwhile, this study gave the first instance of quantitative structural rearrangements involving metal nuclearity changes without a template effect, illustrated by Zn metalation of the free-base salen units in loops and getting a square product (Scheme 4.3). Then, bis(3-pyridyl)-functionalized free-base salen-type ligand **27** was utilized to replace 4-pyridyl entities to construct different assemblies. A concentration-based dynamic equilibrium between predominant trinuclear triangular species and dinuclear loops was observed (Scheme 4.3). Nevertheless, a single loop assembly was achieved after rigidifying bridging salen ligands by Zn metalation. This study provided a typical example to demonstrate the diversity and the capability of accurate regulation of coordination chemistry in supramolecular self-assembly.

4.2.3 Pt–Fe heterometallic metallacycles

Under rational design and precise construction, supramolecular self-assemblies with desired numbers of electroactive or photoactive units can be realized readily in a few steps and high yields. Meanwhile, the effect of structural factors on electrochemistry was of interest to electrochemists. To gain profound insight into this, Stang, White, and coworkers prepared a group of multiferrocenyl rhomboidal and hexagonal metallacycles **32–34** by combining equimolar amounts of 120° bispyridyl donor moieties **28** decorated by a ferrocene group and different degrees (60°, 120°, or 180°) Pt(II) acceptors **29–31** (Scheme 4.4) [20]. The diffusion coefficients and the number of ferrocene sites per molecule in metallacycles **32** and **33** were obtained from cyclic voltammetry experiments. The results indicated that the ferrocene groups attached to the metallacycles were stable, independent, and electrochemically active. Besides, the diffusion coefficient was inversely proportional to the size of the assemblies.

Later, two other groups of charged and neutral dendritic rhomboidal metallacycles containing ferrocene moieties were reported by Yang and coworkers [21]. As shown in Scheme 4.5, metallacycles **38a–c** and **39a–c** were composed of 60° bis(ferrocenyl) di-Pt(II) acceptors **35** and corresponding complementary 120° dipyridyl donors **36a–c** and dicarboxylate donors **37a–c**. The cyclic voltammetry results indicated that both charged and neutral moieties contributed similar effects to the electrochemical behavior of the assemblies. The reduction of the diffusion coefficients resulted from an increase of molecular size, which is consistent with the reported cases [20, 22].

Metallopharmaceutical is well known for anticancer or antimicrobial agents, such as carboplatin and cisplatin. However, many platinum drugs have a series of side effects containing low blood cell levels, nausea, and electrolyte problems

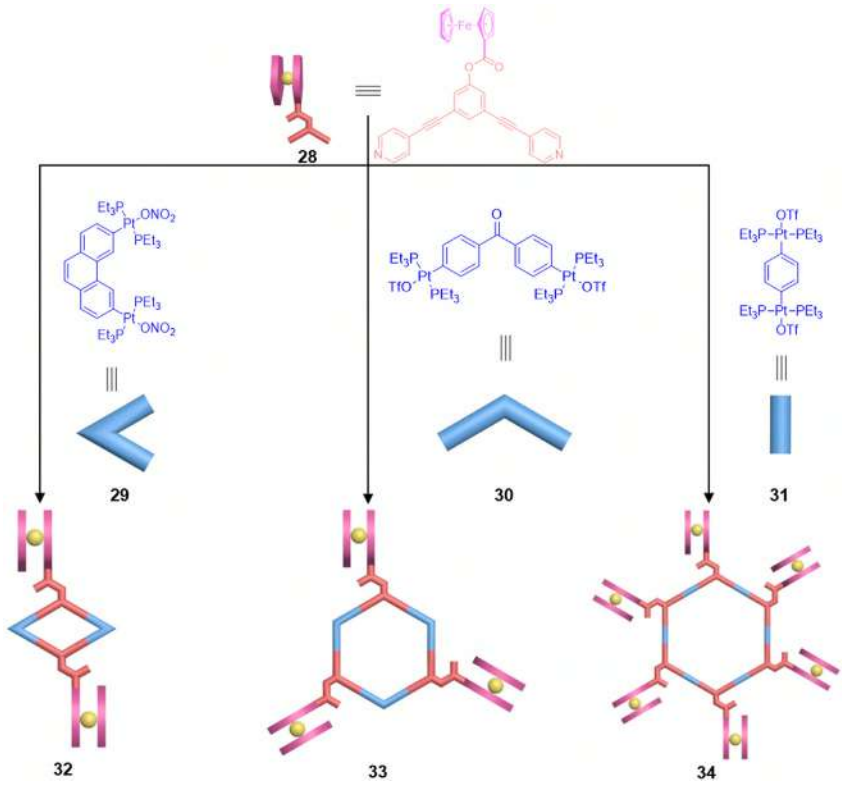

SCHEME 4.4 Self-assembly of metallacycles 32–34 and chemical structures of building blocks 28–31.

[23]. Hence, the exploration of efficient and safe platinum drugs is of great interest to biologists. In the previous study, Chi and coworkers found that larger metallacycles displayed higher levels compared with small metallacycles since they stay more readily inside cancer cells due to their bigger size [24]. In view of this, they designed and constructed a Pt–Fe heterometallic metallacycle **42** by merging bis(4-(pyridin-4-ylethynyl)phenyl)pyridine-2,6-dicarboxamide)) donor ligands **40** and heterometallic cis-Pt-[(dppf)$(OTf)_2$] acceptors **41** (Scheme 4.6) [25]. The results from in vitro anticancer activity tests demonstrated that metallacycle **42** could bring considerable inhibitory effect to T98G (brain tumor) human cancer cell lines, but much less cytotoxic to nonmalignant HEK-293 cells. Furthermore, cell growth was also significantly inhibited by metallacycle **42**, illustrated by cell growth inhibitory experiments, apoptosis, MMP change, and caspase assay consequences. The cellular-uptake and fluorescence detection experiments revealed that metallacycle **42** still had a catching ability to guest molecules after being engulfed by cells. This study presented a representative example of employing metallacycles as promising candidates for anticancer agents with less side effects.

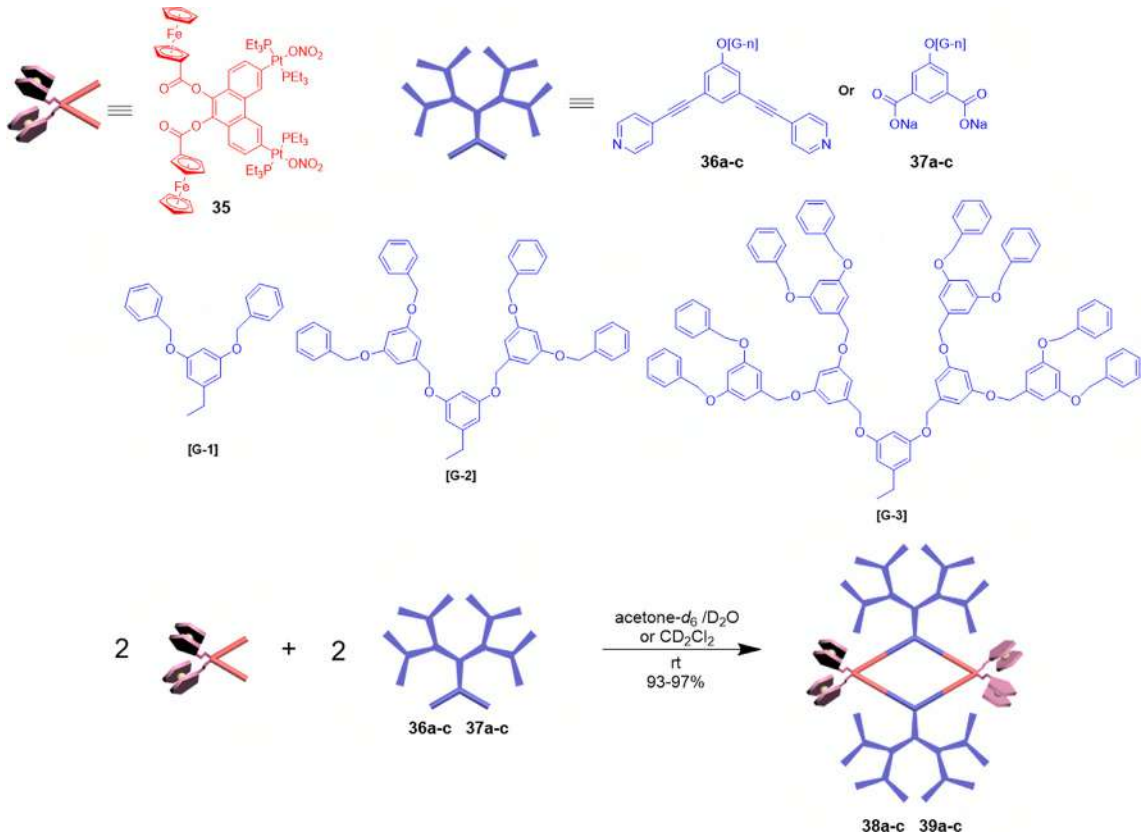

SCHEME 4.5 Chemical structures of building blocks 35, 36a–c, 37a–c, and G1–G3, and self-assembly of metallacycles 38a–c and 39a–c.

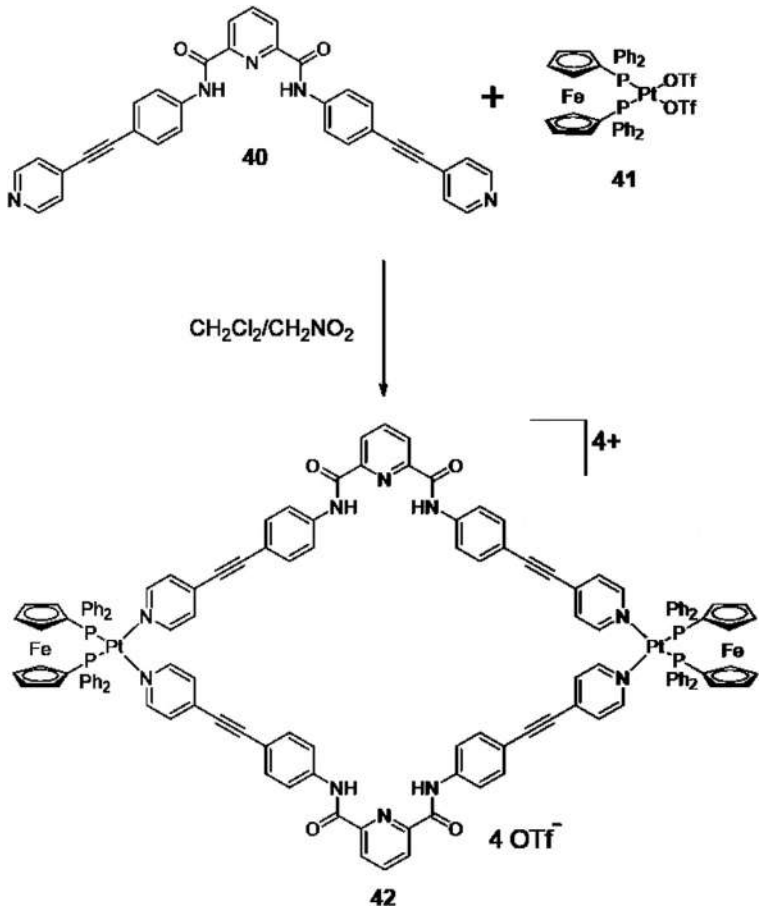

SCHEME 4.6 Self-assembly of heterometallic metallacycle 42.

Although bicyclic molecules are common and play a significant role in the biological field [26], artificial bicyclic supramolecular molecules are still rare. Recently, Stang and coworkers offered a novel vertex-overlapping strategy to design and synthesis twisted heterometallic bicyclic supramolecules using one multitopic donor as the common vertice of two compositions [27]. As shown in Scheme 4.7, the heterometallic bicyclic metallacycles **47a** and **47b** were constituted by the mutually orthogonal interactions of [organo−Pt(II)←Py] coordination and [terpyridine→Fe(II)←terpyridine] coordination. In the practical work, initially, Fe(II) ion was selected as the center of the hinge for heterometallic bicyclic metallacycles due to its particular features of octahedral arrangement by six donor atoms and considerable rigidity after coordination. Following the generation of the hinge **44** by merging the terpyridine–pyridine hybrid ligand **43** and $Fe(BF_4)_2 \bullet 6H_2O$ in a molar ratio of 2:1, the Pt(II) acceptor **46a**/**46b** and

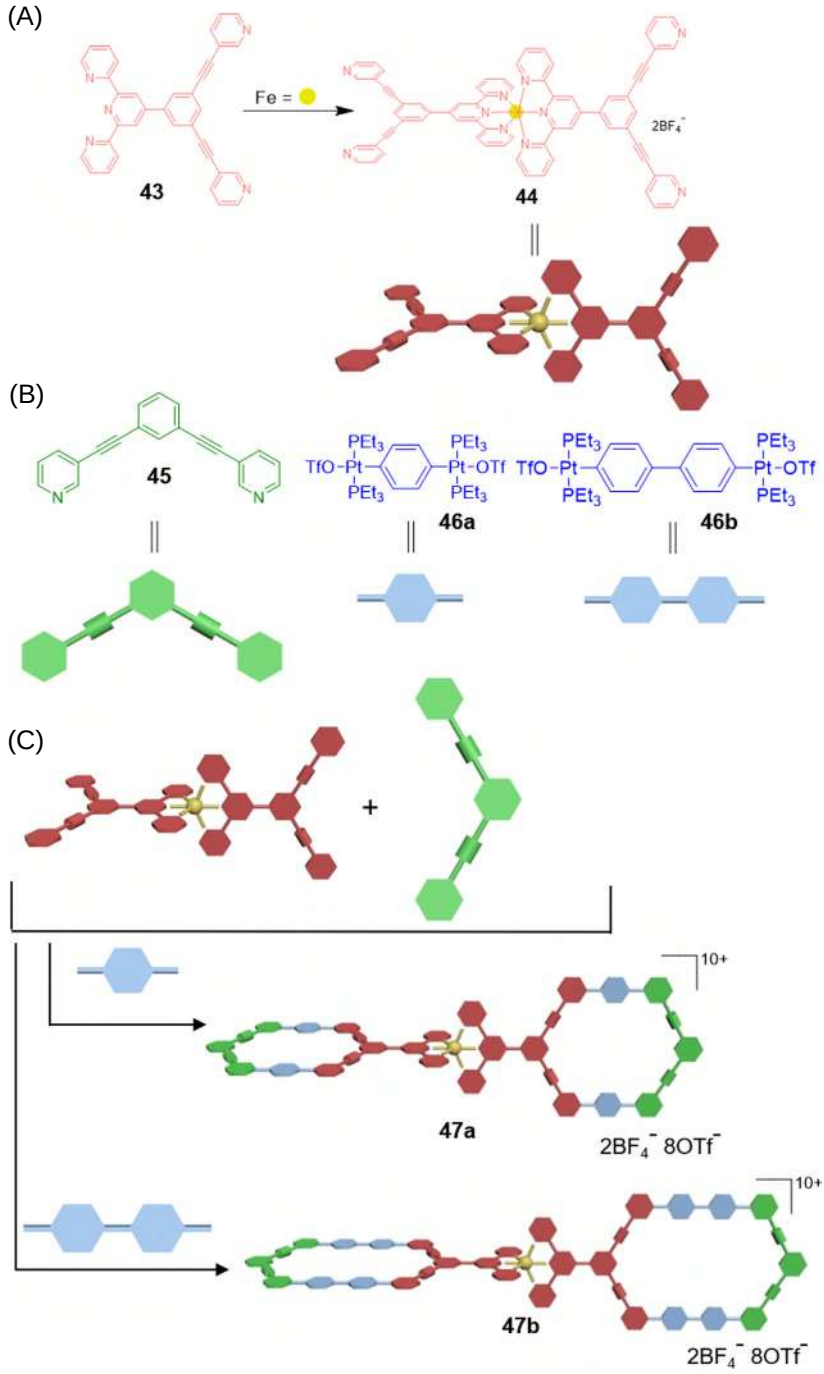

SCHEME 4.7 Self-assembly of hinge 44, twisted heterometallic bicyclic metallacycles 47a and 47b, and chemical structures of building blocks 43, 45, 46a, and 46b.

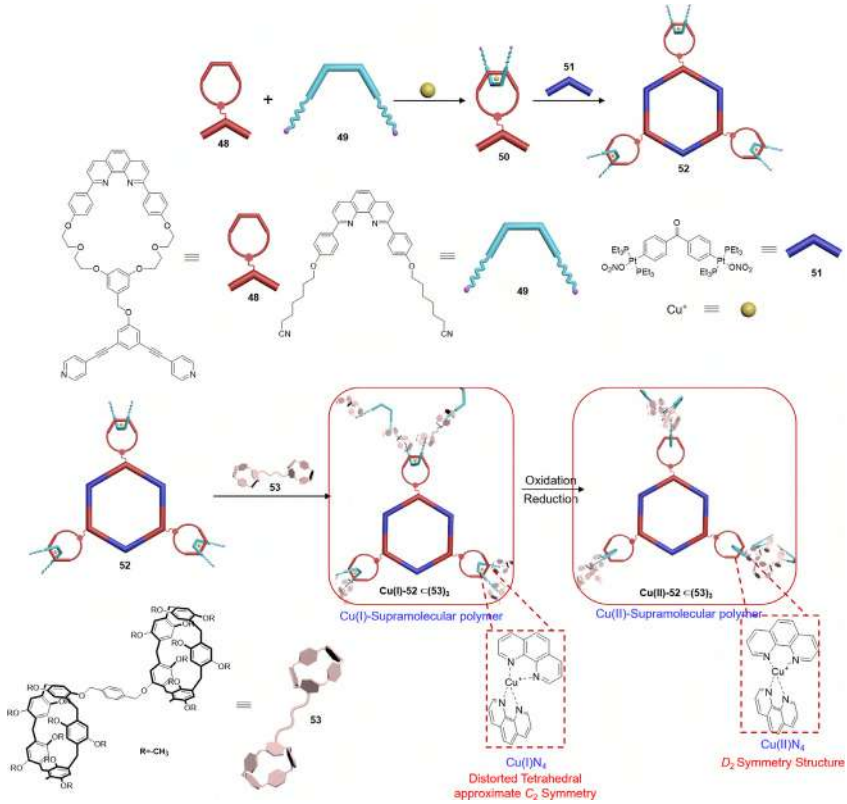

SCHEME 4.8 Self-assembly of hexagonal metallacycle 52 and polymer $52\supset(53)_3$, reversible redox process of polymer $52\supset(53)_3$, and chemical structures of building blocks 48, 49, 51, and 53.

the ligand **45** were added to self-assemble the twisted heterometallic bicyclic metallacycles **47a/47b** with a yield of 70%. Metallacycles **47a** and **47b** were fully characterized by multinuclear NMR, 2D NMR, electrospray ionization time-of-flight mass, and UV−vis spectroscopies.

4.2.4 Pt–Cu heterometallic metallacycles

A stimuli-responsive supramolecular polymer containing discrete tris-[2] pseudorotaxane metallacycles was constructed by merging coordination-driven self-assembly, host–guest interactions, and supramolecular polymerization in Yang's group [28]. In the beginning, pseudorotaxane precursor **50** was synthesized from a Cu(I) template reaction between macrocycle **48** and phen derivative **49** (Scheme 4.8). This was followed by coordination-driven self-assembly of hexagonal metallacycle **52** with an addition of 120° di-Pt(II) acceptors **51**. Then, pillar [n]arene derivative **53** was added to bind dinitrile groups in the pseudorotaxanes,

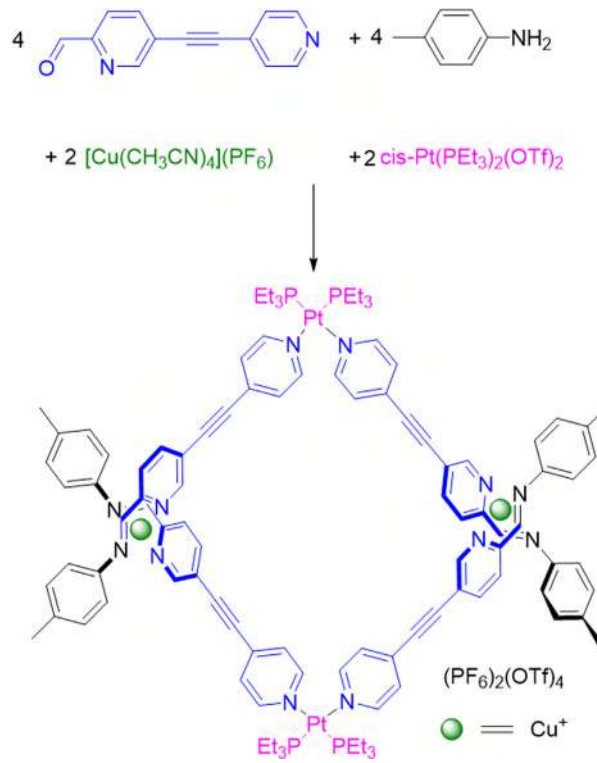

SCHEME 4.9 Self-assembly of heterometallic metallacycle 58.

forming cross-linked supramolecular polymers **52⊃(53)$_3$**. Interestingly, polymer **52⊃(53)$_3$** possesses a reversibly redox-responsive property, which is contributed by multiple valences of copper. Then, $NOBF_4$ was used as an oxidant to form tetrahedral complex Cu(II)N_4, which can be recovered by ascorbic acid. This chemically redox-responsive behavior was illustrated by ^{1}H NMR and UV–vis spectroscopies. Above all, a reversible change of weight-average diffusion coefficients upon redox stimuli was monitored by 2D DOSY NMR spectroscopy. Compared with a loose network from Cu(I)N_4 complex, a compact network from Cu(II)N_4 complex had a larger diffusion coefficient.

Meanwhile, another platinum-containing heterometallic metallacycle with copper ions was designed and synthesized via self-sorting [29]. As displayed in Scheme 4.9, heterometallic metallacycle **58** was prepared by the reaction of building blocks **54, 55, 56**, and **57** in the ratio of 4:4:2:2. The preference of the square planar arrangement of two donors from phosphine-capped Pt(II) acceptors and the favor of a tetrahedral arrangement of four donors from Cu(I) acceptors resulted in a single thermodynamic product metallacycle **58** instead of the mixture product, which was demonstrated by multinuclear NMR and 2D NMR spectroscopies. This self-sorting technology provided a simple but efficient strategy to obtain complicated multicomponent assemblies.

4.2.5 Pt–Ir heterometallic metallacycles

Supramolecular coordination metallacycles have been demonstrated as a versatile platform for precise positions and numbers of incorporated functional groups, leading to several application systems, such as catalysis and Förster resonance energy transfer (FRET) systems [30]. Yang and coworkers designed a photoswitchable fluorescent system with a FRET behavior based on a Pt–Ir heterometallic metallacycle [31]. The ring-open form metallacycle **o-61** was composed of photo stimuli-responsive acceptors **o-60** containing a diarylethene unit and Ir complex bearing donors **59** (Scheme 4.10). Notably, a large overlap between the emission spectrum of **59** and the absorption spectrum of ring-closed state acceptor **60** or metallacycle **61** was observed, leading to the possibility of FRET. In the practical study, the appearance of a new peak in the absorption spectrum and the color change of the solution from light-yellow to purple under irradiation at 365 nm in a nitrogen atmosphere (Fig. 4.2A), indicated the formation of ring-closed state metallacycle **c-61**. Meanwhile, a fluorescence quenching phenomenon was displayed with a decreased emission peak at 630 nm (Fig. 4.2C), which illustrated the FRET behavior from the Ir complex to the ring-closed state diarylethene. The fatigue resistance experiments in nitrogen atmosphere for both absorption and emission spectra revealed exceptional stimuli-responsive reversibility (Fig. 4.2B and D). Moreover, the dramatically decreased photoluminescence quantum yields from ring-open form metallacycle **o-61** to ring-closed form metallacycle **c-61** and the change of emission lifetime gave another strong evidence for the photoswitchable FRET.

4.2.6 Pt–Ln heterometallic metallacycles

Lanthanide ions have considerable luminescent properties due to their unique 4f orbitals. Sun and coworkers reported a heterometallic metallacycle containing lanthanide ions with postassembly modification, resulting in a notable luminescence enhancement and a notable sensing selectivity toward toxic thiophosphonates [32]. As shown in Scheme 4.11, initially, heterometallic metallacycle **63** was synthesized by a reaction of Pt(II) ligand **62** and lanthanide ions. Compared with ligand **62**, the metallacycle **63** revealed a distinguished enhancement of ^{1}MLCT absorption at 366 nm and several distinct emission peaks at the visible light region. It also showed a strong binding ability to thiophosphonates with a remarkable binding constant of 1.06×10^{10} M^{-2} for omethoate molecules in a 1:2 binding manner. Heterometallic metallacycle **63** features open metal sites and its lanthanide ions are nine-coordinated by two tridentate pyridine-2,6-dicarboxamide chelating units from two ligands, two outside water molecules and one oxygen atom from the thiophosphonate anion, observed from the single-crystal X-ray diffraction experiment. Sequentially, a postassembly modification with an incorporation of bis(2-(diphenylphosphino) phenyl) ether oxide ligand **64**, which can sensitize lanthanide luminescence, was carried out to obtain final metallacycle **65**. The metallacycle **65** displayed a dramatical improvement of

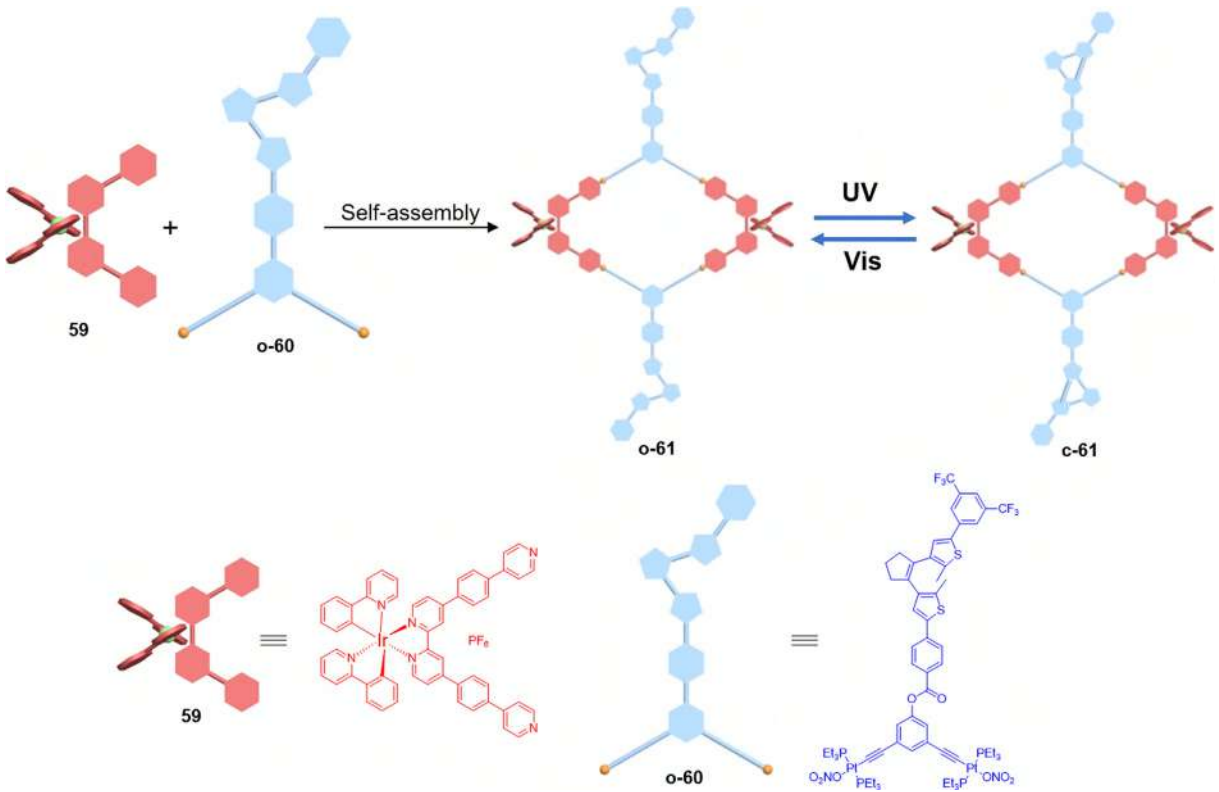

SCHEME 4.10 Self-assembly of o-61, photo stimuli-responsive behavior of metallacycle 61, and chemical structures of building blocks 59 and o-60.

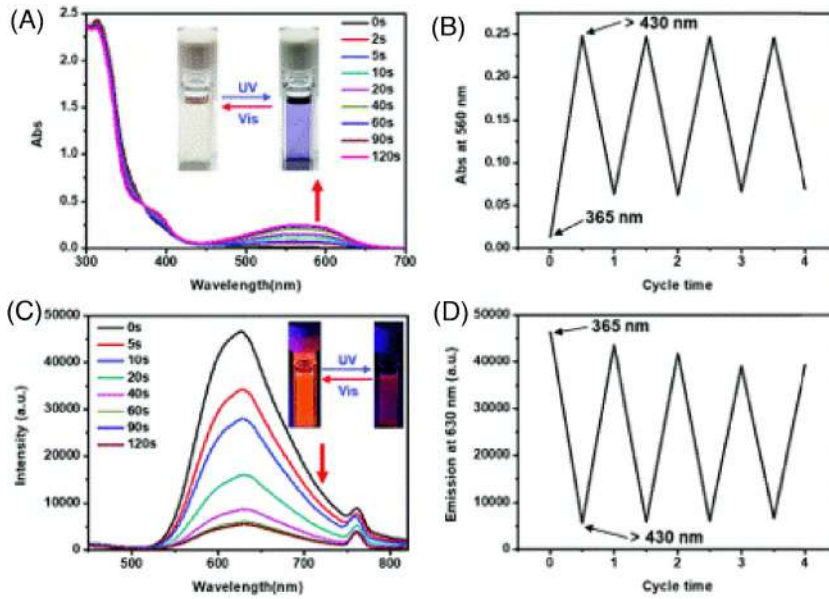

FIGURE 4.2 (A) Absorption spectral changes of heterometallic metallacycle **61** upon irradiation at 365 nm in a nitrogen atmosphere. (B) Fatigue resistance absorption spectral results of heterometallic metallacycle **61** under alternating cycles of UV and visible light radiation. (C) Emission spectral changes of heterometallic metallacycle **61** upon irradiation at 365 nm. (D) Fatigue resistance emission spectral results of heterometallic metallacycle **61** under alternating cycles of UV and visible light irradiation. Reproduced with permission [31]. *Copyright © 2019, The Royal Society of Chemistry.*

photoluminescence quantum yield, from 1.4% of ligand **62** to 79.4%, which was contributed by the decreased nonradiative quenching.

4.3 Platinum-containing heterometallic metallacages

Discrete self-assembled metallacages have received considerable attention because of their wide range of applications based on their well-defined cavities. In particular, sophisticated platinum-containing heterometallic capsules have been reported, the shapes of which range from trigonal-bipyramids, trigonal, tetragonal, and hexagonal prisms, spheres to cubes.

4.3.1 Pt–Al/Ga heterometallic metallacages

In 2011, Stang and coworkers reported the design and preparation of several trigonal-bipyramidal heterometallic cages via the coordination-driven self-assembly of preorganized metalloligands containing octahedral aluminum(III) or gallium(III), with complementary platinum(II)-containing subunits [33]. As shown in Fig. 4.3, the preparation of heterometallic trigonal-bipyramidal cages **69** and **70** was achieved by the [2+3] self-assembly of metalloligands **65** and **66**,

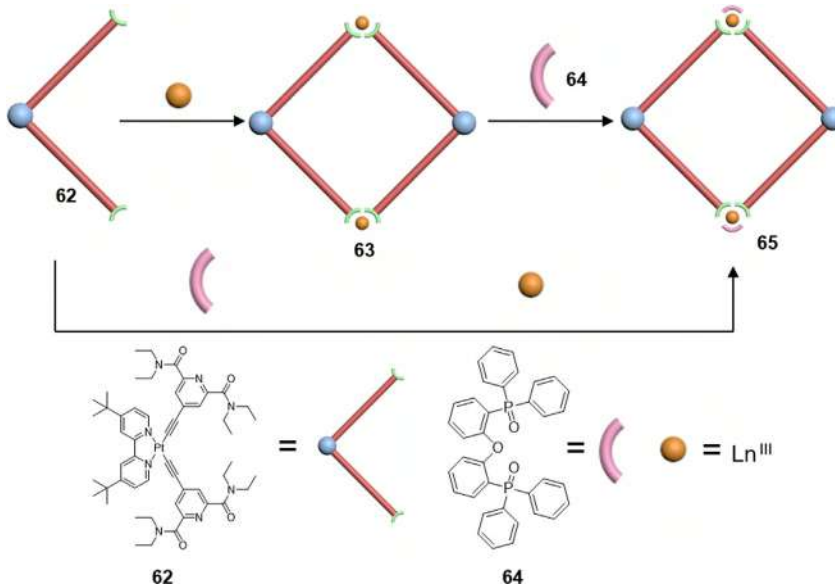

SCHEME 4.11 Self-assembly of the metallacycles 63 and 65, and chemical structures of building blocks 62 and 64.

respectively, with 90° platinum acceptor **67**. Upon addition of a CD_2Cl_2 solution of ligand **65** or **66** into 1.5 equiv. of **67** in CD_3NO_2, **69** and **70** were obtained after stirring at room temperature (r.t.) for 5 h. Similarly, for the self-assembly of **71** and **72**, metalloligands **65** and **66** were treated with the 60° acceptor **68** in an acetone-d_6 and D_2O (1:1, v/v) solution for 15 h at 65°C. These cages were characterized using NMR spectroscopy and ESI-MS spectrometry.

4.3.2 Pt–Ru heterometallic metallacages

The metalloligand synthetic approach has been also efficiently used to construct various heterometallic prismatic cages. Mukherjee and coworkers reported the coordination-driven self-assembly of two Ru_6–Pt_6 trigonal prismatic cages **75a** and **75b** comprising arene-ruthenium(II) clips and a tritopic platinum(II) metalloligand (Fig. 4.4) [34]. Due to the restricted coordination sites as a result of the fixed position of the *p*-cymene moiety, dinuclear arene-ruthenium(II) acceptor building blocks **73** were designed to coordinate with triplatinum metalloligand **74**, which was synthesized through a four-step reaction involving a Sonogashira coupling. The self-assembly of methanolic solutions of **73a(NO$_3$)$_2$**, or **73b(NO$_3$)$_2$** with **74** in a ratio of 3:2 at r.t. yielded the trigonal prismatic cages in high yields. The isolated cages were soluble in common organic solvents such as methanol, acetonitrile, acetone, nitromethane, and dimethyl sulfoxide. The formation of these cages was ascertained by multinuclear NMR experiments and ESI-MS analyses, and their structures were rationalized by PM6 models.

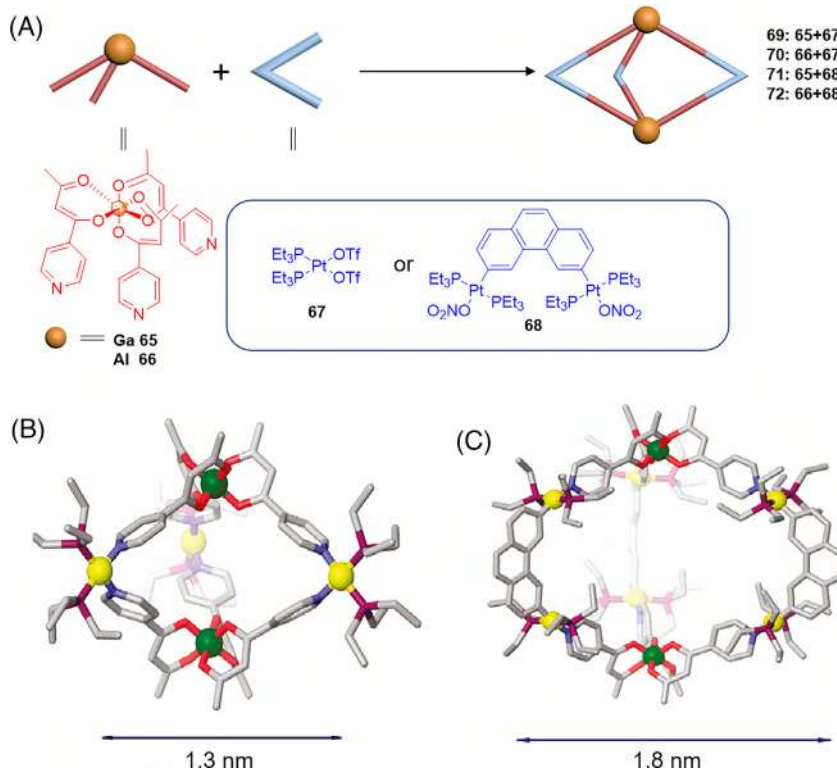

FIGURE 4.3 (A) Coordination-driven self-assembly of trigonal-bipyramidal cages **69**–**72**. MM2-optimized molecular models of **69** (B) and **71** (C). Reproduced with permission [33]. *Copyright © 2011, American Chemical Society.*

4.3.3 Pt–Zn heterometallic metallacages

As platinum(II) ions showed a thermodynamic preference for mixed pyridyl/carboxylate coordination environments, the Stang group reported tetragonal–prismatic cages constructed from ligands respectively containing pyridyl and carboxylate moieties (Scheme 4.12) [35]. Zn^{II}-free prisms **78a–78e** were obtained by mixing 90° Pt^{II} acceptor **67**, carboxylate ligand **76** with tetrapyridylporphyrin (TPyP) in a ratio of 8:4:2. Stirring the mixture at 65°C for 1 h in a solvent mixture of CH_2Cl_2, nitromethane, and acetonitrile (1:1:1, v/v/v) allowed the quantitative formation to occur with **78a–78e** as the sole products. Preparation of the Zn^{II}-metalated analogs **79a–79e** could be achieved by (i) direct metalation of the free-base prisms **78a–78e** in a postassembly modification fashion, (ii) the self-assembly using the direct Zn^{II}-TPyP ligands, or (iii) supramolecular-to-supramolecular transformation through mixing an open trigonal prism containing Zn^{II}-TPyP moieties with free dicarboxylate ligands and additional Pt^{II}-based acceptors. All prisms were characterized

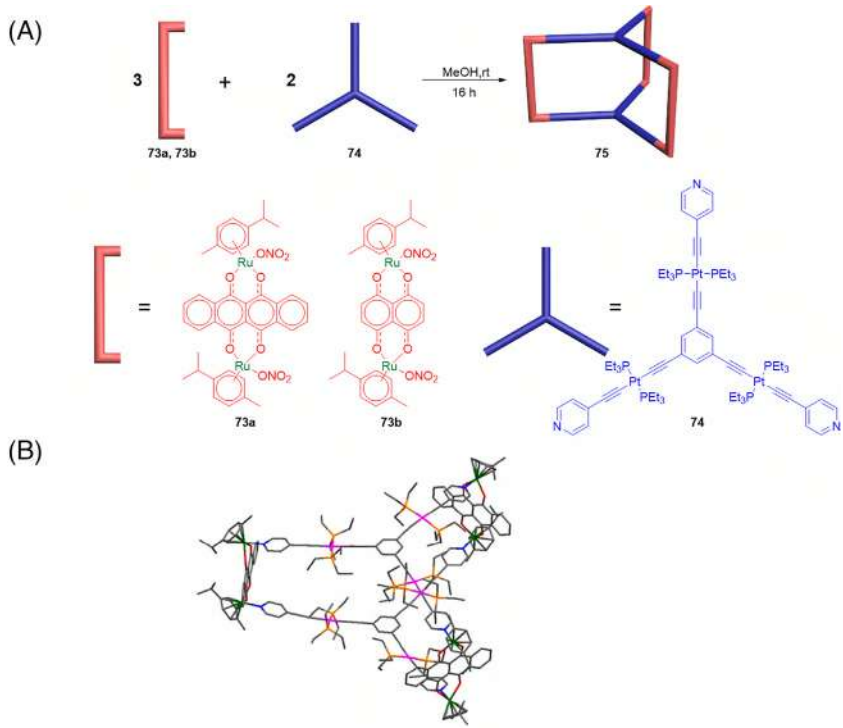

FIGURE 4.4 (A) Coordination-driven self-assembly of trigonal-prismaticcages **75a** and **75b**. (B) PM6-optimized molecular model of **75a**. Reproduced with permission [34]. *Copyright © 2018, American Chemical Society.*

by ^{31}P and ^{1}H NMR spectroscopy and ESI-MS, confirming the structures of each assembly. The photophysical properties of these cages were investigated revealing that the adsorption and emission properties of the free-base and Zn^{II}-metalated porphyrin prisms preserved the spectral features of free TPyP.

4.3.4 Pt–Fe heterometallic metallacages

Using the same strategy, the Stang group also synthesized two metallo-supramolecular hexagonal prisms from hexakis [4-(4-pyridyl)phenyl]benzene, **67**, and amine- or maleimide-functionalized isophthalate [36]. The amino and maleimide groups decorating the isophthalate pillars of prisms provided reactive sites for postassembly modifications under mild conditions. In particular, this postsynthetic modification allowed the incorporation of ferrocene moieties into the hexagonal prism to form a heterometallic cage bearing redox properties.

Mukherjee and coworkers reported the design and synthesis of a $Pt_{12}Fe_{12}$ heterometallic open hexagonal prism **81** containing six faces occupied by 5,10,15,20-tetrakis(4-pyridyl)porphyrin **77a** [37]. Prism **81** was obtained in 94%

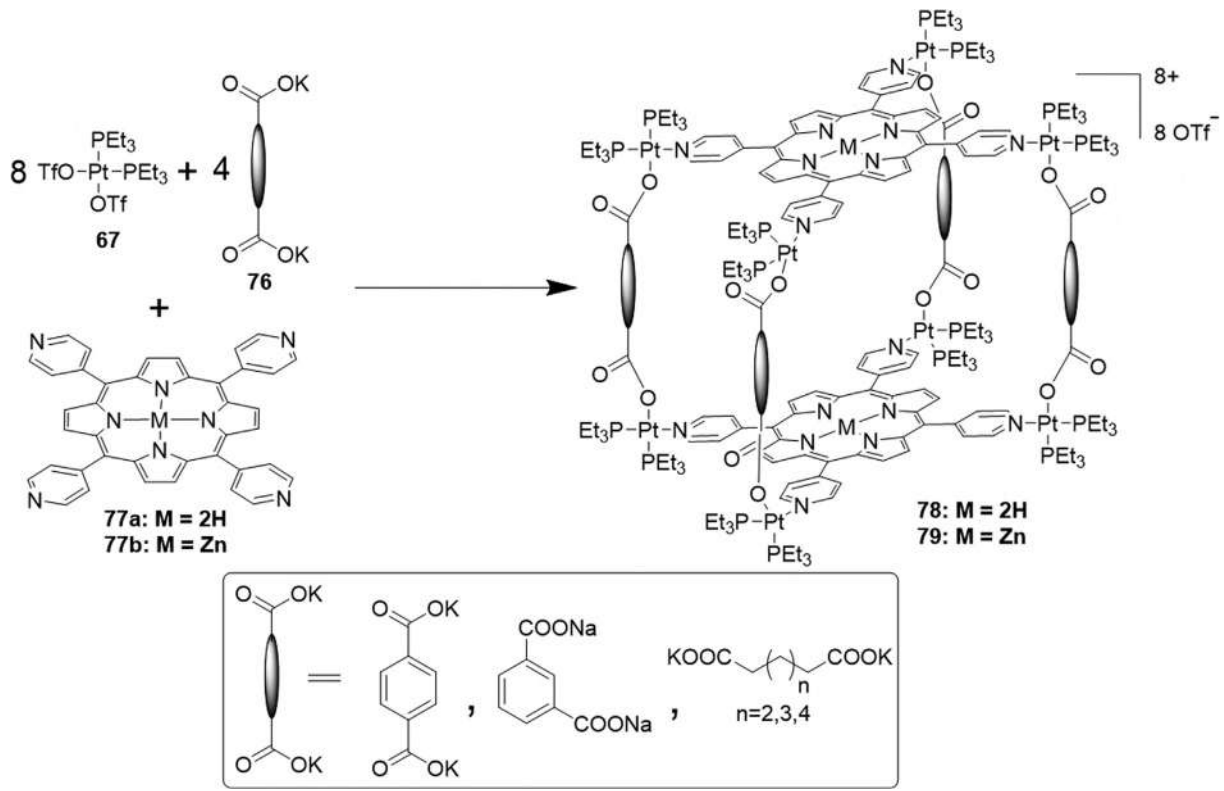

SCHEME 4.12 Coordination-driven self-assembly of tetragonal–prismatic cages **78** and **79**.

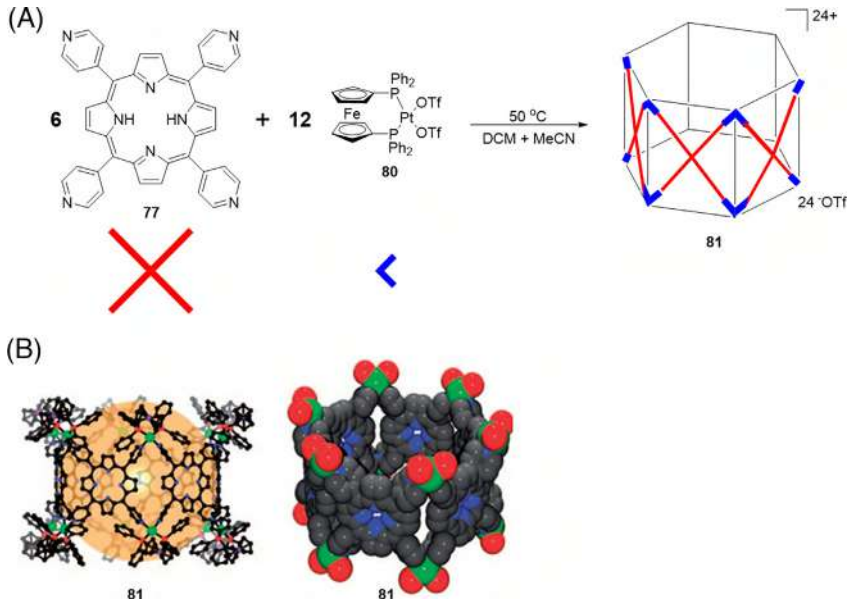

FIGURE 4.5 (A) Coordination-driven self-assembly of hexagonal–prismatic cage **81**. (B) Crystal structure of **81**. Reproduced with permission [37]. *Copyright © 2008, Wiley-VCH Verlag GmbH & Co. KGaA.*

yield by reaction of a solution of tetratopic **77a** in CH_2Cl_2 with 2 equiv. of ferrocene-based 90° Pt^{II} acceptor **80** in nitromethane for 2 h (Fig. 4.5). In fact, several discrete open or closed architectures bearing **77a** as faces and **81** as vertices may form in solution, while the formation of structure **81** was first confirmed by multinuclear NMR experiments and ESI-MS. The crystal structure of **81** further demonstrated that the six porphyrin-based units were hinged by twelve Pt^{II} linkers to form Pt_6 hexameric rings on the top and bottom of the prism. The structure of **81** was rigid, and the inner cavity was large, the volume of which was estimated to be approximately 43,550 $Å^3$. The six porphyrin pockets of **81** provided ideal binding sites for zinc(II) ions. Titration of prism **81** with zinc(II) acetate showed a dramatic change in color from red brown to dark green. Absorption, fluorescence, and NMR spectroscopic studies indicated the encapsulation of Zn^{II} ions into the N_4 pocket of the porphyrin rings.

In 2012, Nitschke and coworkers reported the synthesis and characterization of a $Fe_8Pt_6L_{24}$ cubic cage based on subcomponent self-assembly [38]. Subcomponent self-assembly is a powerful tool for the construction of diverse architectures, in which its building blocks (generally aldehydes and amines) come together through the formation of coordinative (N→metal) and covalent (N=C) bonds and simultaneously coordinate with metal ions [6, 39]. As shown in Scheme 4.13, the reaction of presynthesized square-planar Pt^{II} subcomponent

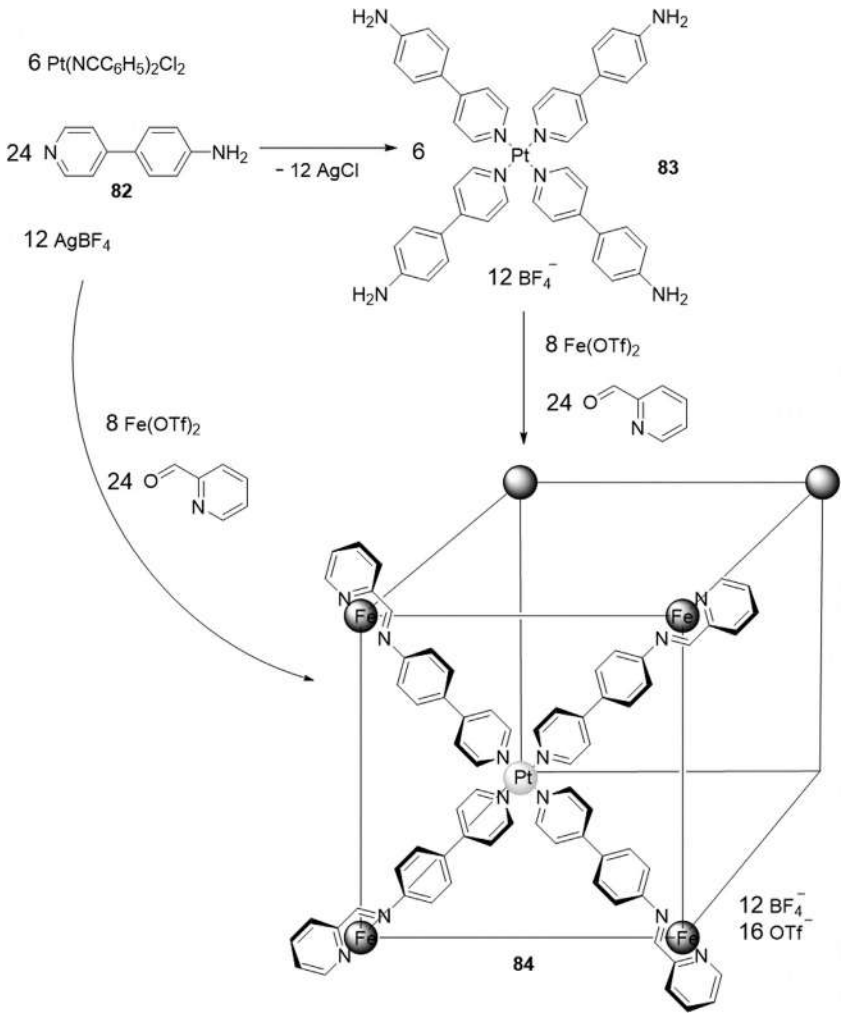

SCHEME 4.13 Coordination-driven self-assembly of cubic cage **84**.

83 (6 equiv.), Fe^{2+} salts (8 equiv.), and 2-formylpyridine (24 equiv.) in acetonitrile resulted in the formation of cube **84** as the unique product, as evidenced by NMR spectroscopy, ESI-MS, and elemental analysis. This cage contained eight iron(II) centers coordinated with pyridylimine binding sites from the six square-planar platinum(II) faces of the cube. In addition, the one-pot synthesis of **84** from a mixture of 4-(4′-pyridyl)aniline **82** (24 equiv.), $Pt(C_5H_5CN)_2Cl_2$ (6 equiv.), $AgBF_4$ (12 equiv.), Fe^{2+} salts (8 equiv.), and 2-formylpyridine in acetonitrile at 338 K was also successful. In this process, a total of 62 building blocks were brought together, demonstrating the potential of self-sorting in the fabrication of large and complex structures. The dynamic nature of the

pyridylimine bonds of **84** also enabled cage-to-cage conversions through a subcomponent displacement strategy.

Following the investigation of the above work, a longer aniline subcomponent, that is 4-(10-(pyridine-4-yl)anthracene-9-yl)aniline, was also introduced in the self-assembly by the same group, generating a larger but more enclosed cubic cage with a cavity volume of 4200 $Å^3$ [40]. Anionic species such as $Mo_6O_{19}{}^{2-}$, $B_{12}F_{12}{}^{2-}$, $BPh_4{}^-$, $CB_{11}H_{12}{}^-$, and $B(C_6F_5)_4{}^-$ were able to bind inside the cavity of the new cube, while no such binding phenomena was observed for cube **30**, demonstrating the important role of cavity enclosure.

By changing the aldehyde subcomponent and based on the same square-planar Pt^{II} subcomponent **83**, Lützen and coworkers reported three different Fe_8Pt_6-cubes and their corresponding Zn_8Pt_6 analogs through subcomponent self-assembly (Scheme 4.14) [41]. The use of zinc(II) salts gave rise to three diamagnetic cages, while iron(II) salts yielded three metallosupramolecular cages that displayed spin-crossover behavior in solution. Results showed that incorporation of 4-thiazolecarbaldehyde or N-methyl-2-imidazole-carbaldehyde yielded iron(II) cages that underwent spin-crossover around r.t., whereas the iron(II) cage obtained using 1H-4-imidazolecarbaldehyde showed a spin-transition at low temperatures. Three new structures were characterized by X-ray diffraction and all of these heterometallic cubic cages were characterized by ESI-MS and NMR spectroscopy.

4.3.5 Pt–Co heterometallic metallacages

Based on tetrapyridyl metalloligands, Lee et al. [42] reported the preparation and characterization of heterobimetallic tetragonal–prismatic cages. Prisms **94** and **95** were obtained by mixing C_4 symmetric Co^{II}-containing tetrapyridyl **92** with 60° diplatinum(II) acceptors **68** or **93** in a ratio of 2:4 (Scheme 4.15). The exclusive formation of **94** and **95** was established by ^1H and $^{31}P\{^1H\}$ NMR spectroscopy, ESI-MS, and elemental analysis.

In contrast, the self-assembly of Co^{II}-containing tetrapyridyl **92** with 90° platinum acceptor **96** in a ratio of 3:6 in nitromethane resulted in a new open trigonal prism **97**, in which the tetratopic ligands spanned the side panels while the linkers occupied the vertices (Scheme 4.16) [43]. The use of cobalt metallocene ligand **98** with longer tetrapyridyl arms and linker **96** produced similar open trigonal prism **99**. These cages were fully characterized by multinuclear and DOSY NMR spectroscopy, and mass spectrometry. The use of tetratopic tetrapyridyl ligands also offered opportunities for investigation of chiral prisms due to the propeller-shaped orientation of pyridyl groups relative to the central core, which had a strongly corrected twist sense and imparted conformational *P* or *M* helical chirality to each cage face. Molecular mechanics results suggested that in the smaller prism **97** collective effects dominated and the all-*P* and all-*M* conformers are strongly favored.

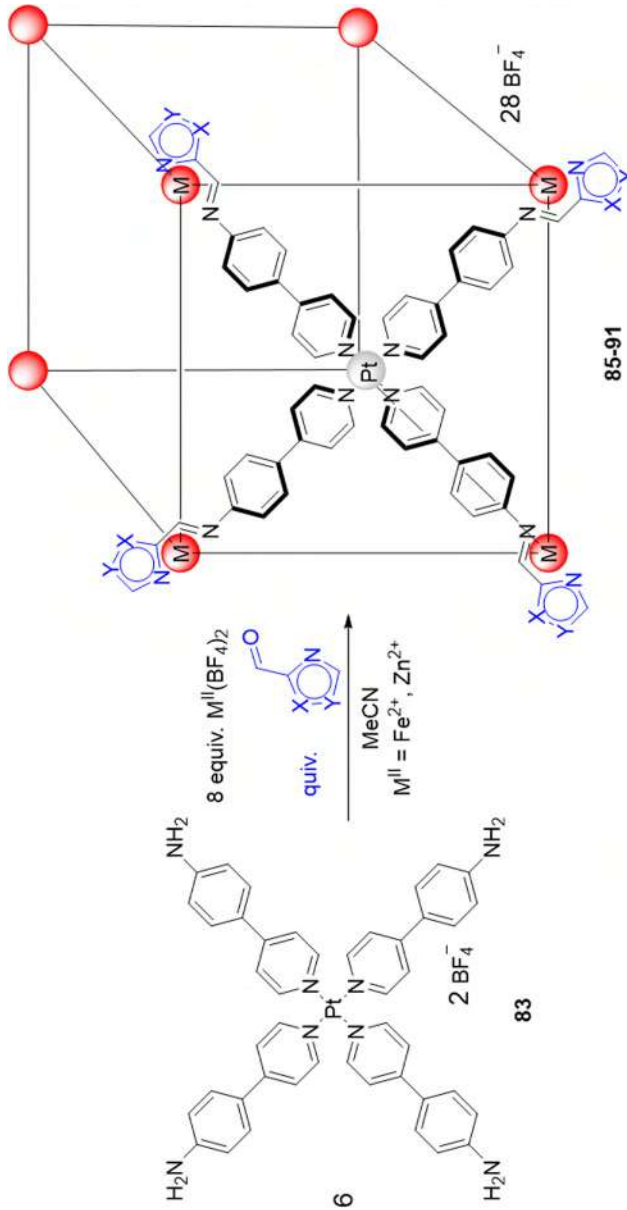

SCHEME 4.14 Coordination-driven self-assembly of cubic cages **85–91**.

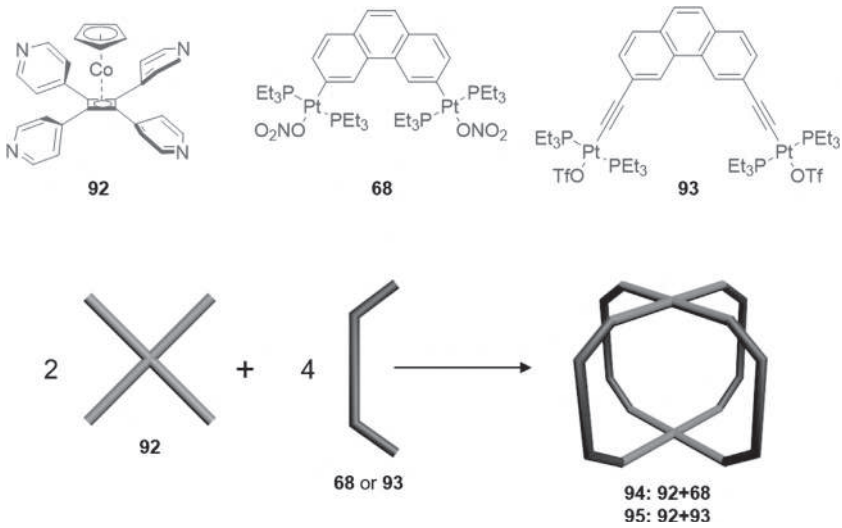

SCHEME 4.15 Coordination-driven self-assembly of tetragonal–prismatic cages **94** and **95**.

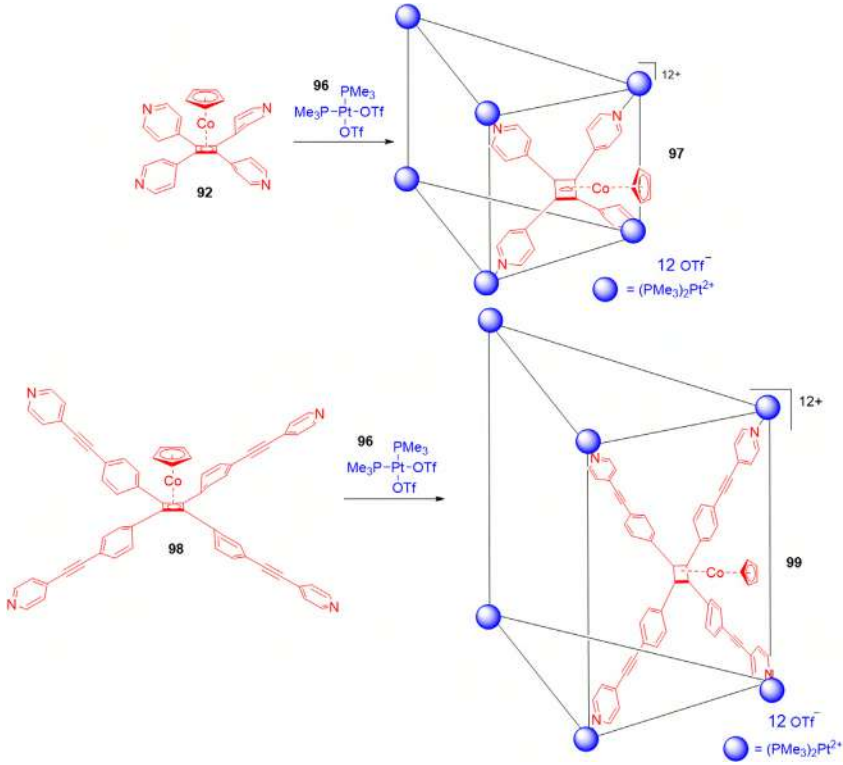

SCHEME 4.16 Coordination-driven self-assembly of trigonal-prismatic cages **97** (A) and **99** (B).

4.3.6 Pt–Pd heterometallic metallacages

The M_2L_4 cage-like system (where M is a square-planar metal ion, commonly palladium(II)) is one of the most studied types of metallacages [44]. Since the early work of McMorran and Steel [45], there have been many Pd_2L_4 cages synthesized, changing from size to functionalization. Yang and coworkers reported a Pd_2L_4 cage functionalized with an alkynylplatinum(II) 2,6-bis-(benzimidazole-2′-yl)-pyridine (bzimpy) moiety [46]. Cage **101** was prepared by mixing the donor ligand **100** with the corresponding palladium(II) acceptor in a 2:1 ratio in DMF at 80°C (Fig. 4.6). The obtained metallacage displayed switchable emission in different DMF/H_2O compositions induced by the formation of intermolecular Pt●●●Pt and $\pi-\pi$ interactions. In particular these interactions also enabled the cage to spontaneously self-assemble into a stable metallogel at r.t. without a heating-cooling process.

Most investigations on the M_2L_4 system have been conducted using Pd_2L_4 cages. Similar cages involving Pt^{II} are less common, presumably because the relatively inert nature of Pt^{II} makes the self-assembly process more difficult. Crowley and coworkers developed a method that enabled the quantitative assembly of a reduced-symmetry, heterobimetallic $PdPtL_4$ cage **102** (Scheme 4.17) [47], which were fully characterized by ^1H and DOSY NMR spectroscopy, ESI-MS, and X-ray crystallography. Heterobimetallic $PdPtL_4$ cage **102** displayed a similarly sized cavity to known homometallic Pd_2L_4 cages, thus showing the binding properties of quinone derivatives. The encapsulation of the 2,6-diaminoanthraquinone guest was also demonstrated by X-ray crystallography. Importantly, the deliberate design of the cage with inert Pt^{II}–pyridyl donor bonds at one end and relatively labile Pd^{II}–pyridyl donor bonds at the other end enabled the cage to be open and closed in a controlled manner. Addition of base N,N′-dimethylaminopyridine (DMAP) resulted in the cage opening at the Pd coordination part, while the subsequent addition of *p*-toluenesulfonic acid (TsOH) recovered the cage. When this process was carried out in the presence of the guest, the sequential addition of DMAP and TsOH allowed the function of guest uptake and release from the cage to occur.

Preston, Crowley, and coworkers also reported the synthesis and characterization of a nona-nuclear heterometallic Pd_3Pt_6 "donut"-shaped cage based on a low symmetry 2-(1-(pyridine-4-methyl)-1H-1,2,3-triazol-4-yl)pyridine ligand [48]. The cage possessed three clefts comprised of planar cationic panels. This structure feature enabled the binding of planar anthracene. In particular, the heterometallic assembly was also able to catalyze the light-induced [4+2] cycloaddition of anthracene with singlet oxygen.

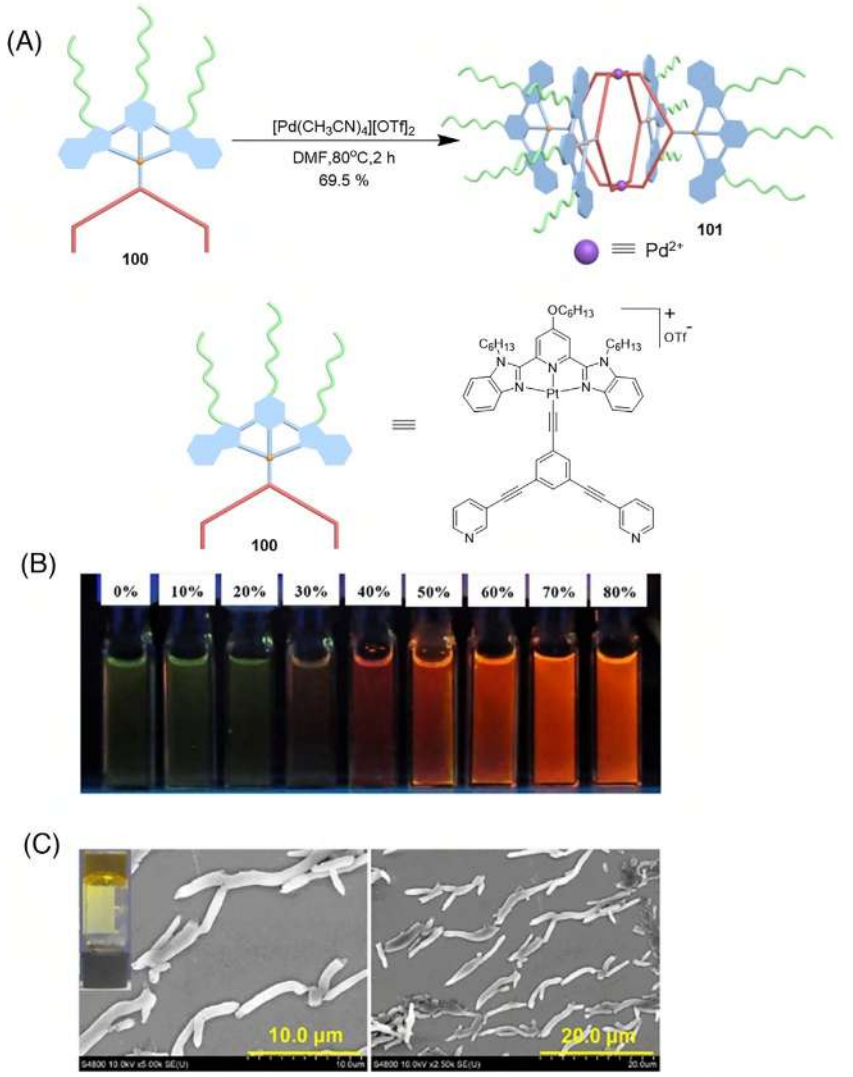

FIGURE 4.6 (A) Coordination-driven self-assembly of cage **101**. (B) Photographs of **101** in mixtures of H_2O/DMF with different ratios under irradiation by a UV lamp at 365 nm. (C) SEM images of xerogel of **101**. Reproduced with permission [46]. *Copyright © 2018, American Chemical Society.*

4.4 Conclusion and perspective

As described above, coordination-driven self-assembly is one of the most powerful and efficient strategies to construct two- or three-dimensional discrete metallacycles and metallacages. Particularly, platinum(II)-based coordination

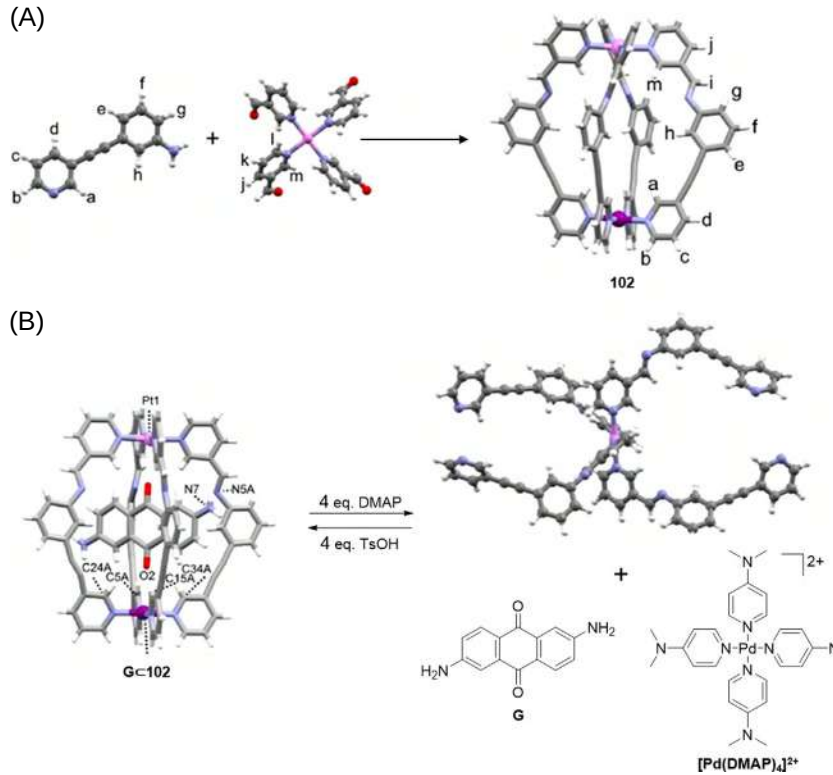

SCHEME 4.17 (A) Coordination-driven self-assembly of cage **102**. (B) Guest release and uptake from cage **102** by the sequential addition of DMAP and TsOH. Reproduced with permission [47]. *Copyright © 2020, Wiley-VCH Verlag GmbH & Co. KGaA.*

has become one of the most considerable methods to forge the supramolecular systems because of its high stability and ready accessibility. Besides, the incorporation of a second metal into a discrete assembly can bring superiorities of the topological complexity and the structural diversity. In this chapter, we summarized the representative cases of platinum-containing heterometallic metallacycles and metallacages and their potential applications. Compared with the homometallic assemblies, the heterometallic metallacycles and metallacages offer rich photophysical, electrochemical, and magnetic characteristics, enabling access to the advantages of sensing and catalysis.

Although extraordinary progress has been carried out in the construction of heterometallic metallacycles and metallacages, there are still several aspects that should be improved. Cooperative bimetallic catalysis is a powerful tool to achieve in modern synthetic chemistry [49]. Although supramolecular structures incorporating two or more active metal sites can be readily synthesized and as promising candidates for asymmetric transformation catalysis,

there are still few examples reported [17]. Besides, fluorescence detection is a fundamental approach in modern analytical chemistry [50−52], while the heavy-atom effect arising from the platinum(II)-containing self-assemblies is always an obstacle. According to several recent reports, the introduction of fluorophores into supramolecular systems decorated with photo-induced electron transfer properties may be a feasible way [53−55]. Moreover, it is worth noting that platinum(II)-containing metallacycles and metallacages have already been widely used in biomedical applications, especially for heterometallic supramolecular systems due to their highly positively charged properties and the synergistic effect of heterometals [56, 57]. Meanwhile, cytotoxicity and solubility of supramolecular systems should be focused on, which are fundamental requirements for biomedical applications.

References

[1] G.Y. Wu, L.J. Chen, L. Xu, X.L. Zhao, H.B. Yang, Construction of supramolecular hexagonal metallacycles via coordination-driven self-assembly: structure, properties and application, Coord. Chem. Rev. 369 (2018) 39–75.

[2] Y. Sun, C.Y. Chen, J.B. Liu, P.J. Stang, Recent developments in the construction and applications of platinum-based metallacycles and metallacages via coordination, Chem. Soc. Rev. 49 (12) (2020) 3889–3919.

[3] M. Yoshizawa, J.K. Klosterman, M. Fujita, Functional molecular flasks: new properties and reactions within discrete, self-assembled hosts, Angew. Chem. Int. Ed. Engl. 48 (19) (2009) 3418–3438.

[4] N.C. Gianneschi, M.S. Masar, C.A. Mirkin, Development of a coordination chemistry-based approach for functional supramolecular structures, Acc. Chem. Res. 38 (11) (2005) 825–837.

[5] T.R. Cook, P.J. Stang, Recent developments in the preparation and chemistry of metallacycles and metallacages via coordination, Chem. Rev. 115 (15) (2015) 7001–7045.

[6] D. Zhang, T.K. Ronson, J.R. Nitschke, Functional capsules via subcomponent self-assembly, Acc. Chem. Res. 51 (10) (2018) 2423–2436.

[7] Y.-Y. Zhang, W.-X. Gao, L. Lin, G.-X. Jin, Recent advances in the construction and applications of heterometallic macrocycles and cages, Coord. Chem. Rev. 344 (2017) 323–344.

[8] H. Li, Z.-J. Yao, D. Liu, G.-X. Jin, Multi-component coordination-driven self-assembly toward heterometallic macrocycles and cages, Coord. Chem. Rev. 293-294 (2015) 139–157.

[9] M. Hardy, A. Lutzen, Better together: functional heterobimetallic macrocyclic and cage-like assemblies, Chem. Eur. J. 26 (59) (2020) 13332–13346.

[10] Y. Sun, C. Chen, J. Liu, P.J. Stang, Recent developments in the construction and applications of platinum-based metallacycles and metallacages via coordination, Chem. Soc. Rev. 49 (12) (2020) 3889–3919.

[11] M.L. Saha, X.Z. Yan, P.J. Stang, Photophysical properties of organoplatinum(II) compounds and derived self-assembled metallacycles and metallacages: fluorescence and its applications, Acc. Chem. Res 49 (11) (2016) 2527–2539.

[12] P. Buchwalter, J. Rose, P. Braunstein, Multimetallic catalysis based on heterometallic complexes and clusters, Chem. Rev. 115 (1) (2015) 28–126.

[13] D.A. Uhlenheuer, K. Petkau, L. Brunsveld, Combining supramolecular chemistry with biology, Chem. Soc. Rev. 39 (8) (2010) 2817–2826.

[14] C. Müller, J.A. Whiteford, P.J. Stang, Self-assembly, chiroptical properties, and host-guest chemistry of chiral Pt-Pt and Pt-Pd tetranuclear macrocycles. Circular dichroism studies on neutral guest inclusion phenomena, J. Am. Chem. Soc. 120 (38) (1998) 9827–9837.

[15] N.R. Lagesse, K.Y.L. Tan, J.D. Crowley, J.A. Findlay, Planar 2-pyridyl-1,2,3-triazole derived metallo-ligands: self-assembly with $PdCl_2$ and photocatalysis, Chem. Asian J. 15 (10) (2020) 1567–1573.

[16] C. Freire, M. Nunes, C. Pereira, D.M. Fernandes, A.F. Peixoto, M. Rocha, Metallo(salen) complexes as versatile building blocks for the fabrication of molecular materials and devices with tuned properties, Coord. Chem. Rev. 394 (2019) 104–134.

[17] S.S. Sun, C.L. Stern, S.T. Nguyen, J.T. Hupp, Directed assembly of transition-metal-coordinated molecular loops and squares from salen-type components. Examples of metalation-controlled structural conversion, J. Am. Chem. Soc. 126 (20) (2004) 6314–6326.

[18] R.A. Bilbeisi, J.K. Clegg, N. Elgrishi, X.D. Hatten, M. Devillard, B. Breiner, P. Mal, J.R. Nitschke, Subcomponent self-assembly and guest-binding properties of face-capped Fe 4L 48+ capsules, J. Am. Chem. Soc. 134 (11) (2012) 5110–5119.

[19] D.A. Roberts, A.M. Castilla, T.K. Ronson, J.R. Nitschke, Post-assembly modification of kinetically metastable FeII2L3 triple helicates, J. Am. Chem. Soc. 136 (23) (2014) 8201–8204.

[20] H.B. Yang, K. Ghosh, Y. Zhao, B.H. Northrop, M.M. Lyndon, D.C. Muddiman, H.S. White, P.J. Stang, A new family of multiferrocene complexes with enhanced control of structure and stoichiometry via coordination-driven self-assembly and their electrochemistry, J. Am. Chem. Soc. 130 (3) (2008) 839–841.

[21] Q.J. Li, G.Z. Zhao, L.J. Chen, H. Tan, C.H. Wang, D.X. Wang, D.A. Lehman, D.C. Muddiman, H.B. Yang, Coordination-driven self-assembly of charged and neutral dendritic tetrakis(ferrocenyl) rhomboids, Organometallics 31 (20) (2012) 7241–7247.

[22] G.Z. Zhao, Q.J. Li, L.J. Chen, H. Tan, C.H. Wang, D.A. Lehman, D.C. Muddiman, H.B. Yang, Facile self-assembly of supramolecular hexakisferrocenyl triangles via coordination-driven self-assembly and their electrochemical behavior, Organometallics 30 (13) (2011) 3637–3642.

[23] R. Oun, Y.E. Moussa, N.J. Wheate, The side effects of platinum-based chemotherapy drugs: a review for chemists, Dalton Trans. 47 (19) (2018) 6645–6653.

[24] A. Mishra, Y.J. Jeong, J.-H. Jo, S.C. Kang, M.S. Lah, K.-W. Chi, Anticancer potency studies of coordination driven selfassembled arene-Ru-based metalla-bowls, ChemBioChem 15 (5) (2014) 695–700.

[25] A. Mishra, S.C. Lee, N. Kaushik, T.R. Cook, E.H. Choi, N.K. Kaushik, P.J. Stang, K.-W. Chi, Self-assembled supramolecular hetero-bimetallacycles for anticancer potency by intracellular release, Chem. Eur. J. 20 (44) (2014) 14410–14420.

[26] R.J. Nash, A. Kato, C.-Y. Yu, G.W.J. Fleet, Iminosugars as therapeutic agents: recent advances and promising trends, Future Med. Chem. 3 (12) (2011) 1513–1521.

[27] H. Sepehrpour, M.L. Saha, P.J. Stang, Fe-Pt twisted heterometallic bicyclic supramolecules via multicomponent self-assembly, J. Am. Chem. Soc. 139 (7) (2017) 2553–2556.

[28] G.Y. Wu, X.Q. Wang, L.J. Chen, Y.X. Hu, G.Q. Yin, L. Xu, B. Jiang, H.B. Yang, Supramolecular polymer cross-linked by discrete tris-2 pseudorotaxane metallacycles and its redox-responsive behavior, Inorg. Chem. 57 (24) (2018) 15414–15420.

[29] M.L. Saha, Z.X. Zhou, P.J. Stang, A four-component heterometallic Cu-Pt quadrilateral via self-sorting, Chem. 11 (19) (2016) 2662–2666.

[30] H.-Y. Lin, L.-Y. Zhou, L. Xu, Photocatalysis in supramolecular fluorescent metallacycles and metallacages, Chem. Asian J. (2021) 3805–3816.

[31] Y. Qin, L.J. Chen, Y. Zhang, Y.X. Hu, W.L. Jiang, G.Q. Yin, H.W. Tan, X.P. Li, L. Xu, H.B. Yang, Photoswitchable Forster resonance energy transfer (FRET) within a heterometallic Ir-Pt macrocycle, Chem. Commun. 55 (74) (2019) 11119–11122.

[32] Q.Y. Zhu, L.P. Zhou, Q.F. Sun, Strongly luminescent 5d/4f heterometal-organic macrocycles with open metal sites: post-assembly modification and sensing, Dalton Trans. 48 (14) (2019) 4479–4483.

[33] M. Wang, V. Vajpayee, S. Shanmugaraju, Y.R. Zheng, Z. Zhao, H. Kim, P.S. Mukherjee, K.W. Chi, P.J. Stang, Coordination-driven self-assembly of M_3L_2 trigonal cages from pre-organized metalloligands incorporating octahedral metal centers and fluorescent detection of nitroaromatics, Inorg. Chem. 50 (4) (2011) 1506–1512.

[34] A.A. Adeyemo, P.S. Mukherjee, Coordination-driven self-assembly of discrete Ru_6-Pt_6 prismatic cages, Beilstein J. Org. Chem. 14 (2018) 2242–2249.

[35] Y. Shi, I. Sanchez-Molina, C. Cao, T.R. Cook, P.J. Stang, Synthesis and photophysical studies of self-assembled multicomponent supramolecular coordination prisms bearing porphyrin faces, Proc. Natl. Acad. Sci. U. S. A. 111 (26) (2014) 9390–9395.

[36] M. Wang, W.J. Lan, Y.R. Zheng, T.R. Cook, H.S. White, P.J. Stang, Post-self-assembly covalent chemistry of discrete multicomponent metallosupramolecular hexagonal prisms, J. Am. Chem. Soc. 133 (28) (2011) 10752–10755.

[37] A.K. Bar, R. Chakrabarty, G. Mostafa, P.S. Mukherjee, Self-assembly of a nanoscopic $Pt_{12}Fe_{12}$ heterometallic open molecular box containing six porphyrin walls, Angew. Chem. Int. Ed. 47 (44) (2008) 8455–8459.

[38] M.M. Smulders, A. Jimenez, J.R. Nitschke, Integrative self-sorting synthesis of a $Fe_8Pt_6L_{24}$ cubic cage, Angew. Chem. Int. Ed. 51 (27) (2012) 6681–6685.

[39] T.K. Ronson, S. Zarra, S.P. Black, J.R. Nitschke, Metal-organic container molecules through subcomponent self-assembly, Chem. Commun. 49 (25) (2013) 2476–2490.

[40] W.J. Ramsay, F.T. Szczypinski, H. Weissman, T.K. Ronson, M.M. Smulders, B. Rybtchinski, J.R. Nitschke, Designed enclosure enables guest binding within the 4200 A^3 cavity of a self-assembled cube, Angew. Chem. Int. Ed. 54 (19) (2015) 5636–5640.

[41] M. Hardy, J. Tessarolo, J.J. Holstein, N. Struch, N. Wagner, R. Weisbarth, M. Engeser, J. Beck, S. Horiuchi, G.H. Clever, A. Lutzen, A family of heterobimetallic cubes shows spin-crossover behaviour near room temperature, Angew. Chem. Int. Ed. 60 (41) (2021) 22562–22569.

[42] J.Y. Ryu, S. Lee, M.H. Lee, J. Lee, Hetero-multinuclear Co_2Pt_8 supramolecular cages having D4 symmetry from tetrapyridyl metalloligands, Bull. Korean Chem. Soc. 40 (4) (2019) 389–392.

[43] D.C. Caskey, T. Yamamoto, C. Addicott, R.K. Shoemaker, J. Vacek, A.M. Hawkridge, D.C. Muddiman, G.S. Kottas, J. Michl, P.J. Stang, Coordination-driven face-directed self-assembly of trigonal prisms. Face-based conformational chirality, J. Am. Chem. Soc. 130 (24) (2008) 7620–7628.

[44] M. Han, D.M. Engelhard, G.H. Clever, Self-assembled coordination cages based on banana-shaped ligands, Chem. Soc. Rev. 43 (6) (2014) 1848–1860.

[45] D.A. McMorran, P.J. Steel, The first coordinatively saturated, quadruply stranded helicate and its encapsulation of a hexafluorophosphate anion, Angew. Chem. Int. Ed. 37 (23) (1998) 3295–3297.

[46] Y. Zhang, Q.F. Zhou, G.F. Huo, G.Q. Yin, X.L. Zhao, B. Jiang, H. Tan, X. Li, H.B. Yang, Hierarchical self-assembly of an alkynylplatinum(ll) bzimpy-functionalized metallacage via Pt.Pt and pi-pi interactions, Inorg. Chem. 57 (7) (2018) 3516–3520.

[47] L.S. Lisboa, J.A. Findlay, L.J. Wright, C.G. Hartinger, J.D. Crowley, A reduced-symmetry heterobimetallic $[PdPtL_4]^{4+}$ cage: assembly, guest binding, and stimulus-induced switching, Angew. Chem. Int. Ed. 59 (27) (2020) 11101–11107.

[48] D. Preston, J.J. Sutton, K.C. Gordon, J.D. Crowley, A nona-nuclear heterometallic Pd_3Pt_6 "donut"-shaped cage: molecular recognition and photocatalysis, Angew. Chem. Int. Ed. 57 (28) (2018) 8659–8663.

[49] J. Park, S. Hong, Cooperative bimetallic catalysis in asymmetric transformations, Chem. Soc. Rev. 41 (21) (2012) 6931–6943.

[50] A.P. de Silva, H.Q.N. Gunaratne, T. Gunnlaugsson, A.J.M. Huxley, C.P. McCoy, J.T. Rademacher, T.E. Rice, Signaling recognition events with fluorescent sensors and switches, Chem. Rev. 97 (5) (1997) 1515–1566.

[51] J.L. Zhu, X. Liu, J.H. Huang, L. Xu, Our expedition in the construction of fluorescent supramolecular metallacycles, Chin. Chem. Lett. 30 (10) (2019) 1767–1774.

[52] C.Y. Yao, H.Y. Lin, H.S.N. Crory, A.P. de Silva, Supra-molecular agents running tasks intelligently (SMARTI): recent developments in molecular logic-based computation, Mol. Syst. Des. Eng. 5 (8) (2020) 1325–1353.

[53] Y. Qin, X. Liu, P.P. Jia, L. Xu, H.B. Yang, BODIPY-based macrocycles, Chem. Soc. Rev. 49 (16) (2020) 5678–5703.

[54] H. Lin, Z. Xu, Comment on "acid-induced tunable white light emission based on triphenylamine derivatives", Chin. Chem. Lett. 33 (2) (2021) 573–574.

[55] J.L. Zhu, L. Xu, Y.Y. Ren, Y. Zhang, X. Liu, G.Q. Yin, B. Sun, X. Cao, Z. Chen, X.L. Zhao, H. Tan, J. Chen, X. Li, H.B. Yang, Switchable organoplatinum metallacycles with high quantum yields and tunable fluorescence wavelengths, Nat. Commun. 10 (1) (2019) 4285.

[56] G.Y. Wu, X.L. Shi, H. Phan, H. Qu, Y.X. Hu, G.Q. Yin, X.L. Zhao, X.P. Li, L. Xu, Q.L. Yu, H.B. Yang, Efficient self-assembly of heterometallic triangular necklace with strong antibacterial activity, Nat. Commun. 11 (3178) (2020) 1–11.

[57] G. Gupta, Y. You, R. Hadiputra, J. Jung, D.K. Kang, C.Y. Lee, Heterometallic BODIPY-based molecular squares obtained by self-assembly: synthesis and biological activities, ACS Omega 4 (8) (2019) 13200–13208.

Chapter 5

Self-assembly of pyrazine-based metallamacrocycles: Design, synthesis, and applications

Saurabh Kumar and Neeladri Das
Department of Chemistry, Indian Institute of Technology Patna, Patna, Bihar, India

Abbreviations

ACN	acetonitrile
Cp*	η^5-C_5Me_5, pentamethylcyclopentadienyl
1D	one-dimensional
2D	two-dimensional
DFT	density functional theory
dmso	dimethylsulfoxide
DNA	deoxyribonucleic acid
DNT	2,4-dinitrotoluene
DOSY NMR	diffusion ordered spectroscopy NMR
fac	facial (stereochemistry)
Hz	hertz
IC_{50}	half-maximal inhibitory concentration
ITC	isothermal titration calorimetry
NMR	nuclear magnetic resonance
OTf^-	triflate anion, $CF_3SO_3^-$
PA	picric acid
PM6	parameterized model number 6
ppm	parts per million
pyz	pyrazine
SCC	supramolecular coordination complex
TUNEL	terminal deoxynucleotidyl transferase dUTP

5.1 Introduction

Pyrazine is an azaheterocycle that is aromatic and contains two nitrogen atoms. Specifically, pyrazine is a diazine and is isomeric with pyrimidine and pyridazine. Pyrazine is an electron-deficient molecule due to the presence of two electronegative N-atoms that withdraw electron density from the aromatic ring.

Supramolecular Coordination Complexes: Design, Synthesis, and Applications.
DOI: https://doi.org/10.1016/B978-0-323-90582-4.00004-X

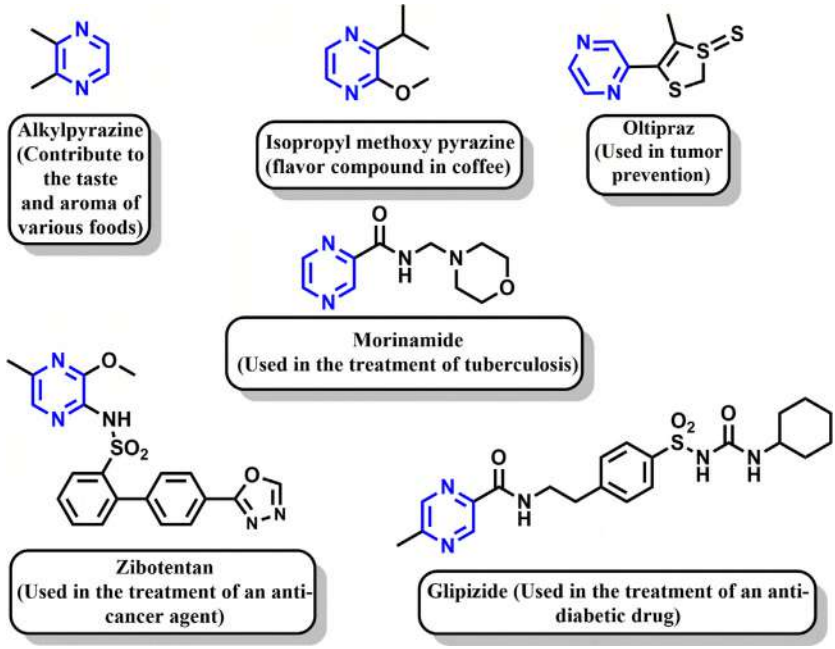

CHART 5.1 Pyrazine derivatives and their uses.

Pyrazine derivatives are well known to exist in natural products and are reported to have medicinal and biological significances. In laboratory, it was first synthesized in 1876 [1]. Pyrazine is an important pharmacophore since it constitutes the integral scaffold in several types of drugs. Precisely, due to the biological activities of pyrazine derivatives, this motif is present in anti-inflammatory, anticancer, antidiabetic, and diuretic drugs [2,3]. Substituted pyrazine derivatives are also effective in the treatment of tuberculosis [4]. Furthermore, pyrazine derivatives are also reported to possess high antimicrobial activities [5]. In addition to the importance of pyrazine derivatives in pharmaceutical sector, these molecules have immense commercial importance in flavor [6], fragrance [7], and food industries [8]. Representative examples showing that the diverse application of pyrazine (pyz) derivatives is presented in Chart 5.1 [6,7,9–12].

In recent past, there has been a keen interest in exploring the supramolecular chemistry of pyz-based linkers. Thus, in this present chapter, the focus is on the development of various pyz-based building blocks with potential to act as tectons (acceptor and/or donor) in supramolecular chemistry. Further, this chapter also highlights their application as synthons in the self-assembly processes, wherein supramolecular frameworks are held tightly via coordination bonds.

In the context of supramolecular chemistry of self-assembled macrocycles held by coordination bonds, two basic structural factors are most important. First,

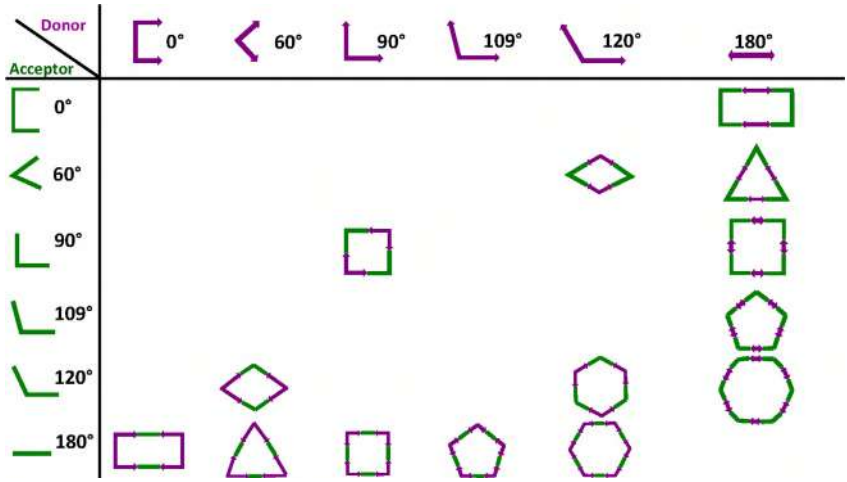

FIGURE 5.1 Arrangement of various building units to produce preferred polygons and canonical polyhedra.

it is desired that precursor entities be structurally rigid. Second, the precursors must have two or more binding sites with the angular separation of the reactive centers ranging from 0° to 180°. Further, the precursors are classified as either donor or acceptor tectons. The donor tectons feature reactive units that are Lewis basic moieties and are able to form coordination bonds with metal centers by donating electrons. On the other hand, the acceptor tectons contain Lewis acidic metal centers that bind (by accepting electrons) with reactive functional groups present in complementary donor tectons. Thus, stoichiometric combination of donor and acceptor tectons (each with two reactive centers) are expected to yield metallacycles, the shape of which is dictated by the bite angle of the employed acceptor/donor tectons. A cartoon representation of metallacycles of different shapes based on bond angle variation is shown in Fig. 5.1.

The evolution of this chapter is based on a systematic survey of literature and highlights through the relevant examples, the macrocycles of various shapes that have been constructed via coordination-driven self-assembly protocol. These include various kinds of supramolecular architectures such as molecular triangles, squares, rectangles, hexagons, and other higher polygonal frameworks. The potential and interesting applications of some of these metallamacrocycles are also elaborated in this chapter which indicates the most recent research trends in this field of supramolecular chemistry.

5.2 Molecular triangles

A triangular macrocycle, consisting of three edges and three vertices, can be self-assembled by reacting appropriate combination of ditopic donor and acceptor

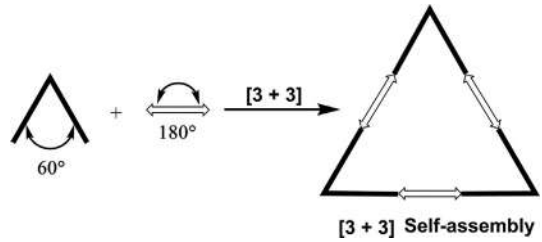

FIGURE 5.2 Schematic representation of molecular triangle formation by [3 + 3] self-assembly.

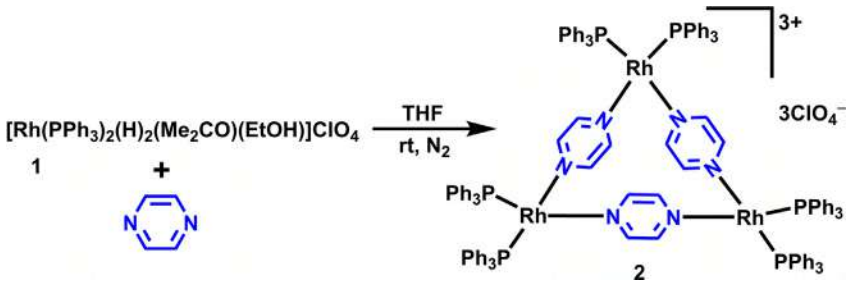

SCHEME 5.1 Synthesis of Rh-based triangular metallacycle **2**.

tectons (Fig. 5.2). One of the tectons (may be acceptor/donor) must have a ~60° angle flanked by its two reactive sites which would define the three vertices. On the other hand, a rigid complementary tecton (donor/acceptor) having a 180° angle between its reactive sites is the other reactant that defines the three edges of the triangular framework [13].

The exclusive formation of molecular triangles containing pyrazine building blocks is still rare. Three examples are included here to show the self-assembly of triangular macrocycles. In 2001, Kitagawa and coworkers reported Rh-based molecular triangles $[Rh_3(PPh_3)_6(\mu\text{-pyz})_3](ClO_4)_3 \cdot EtOH$ (**2**) with pyz as a donor tecton [14]. To obtain **2**, $[Rh(PPh_3)_2(H)_2(Me_2CO)(EtOH)]ClO_4$ (**1**) is reacted with pyz ligand in THF solvent (Scheme 5.1). The molecular structure of **2** confirms the formation of a unique triangular Rh_3 core, which consists of three Rh(I) atoms bridged via three pyz ligands that act as rigid and linear donor tectons. During the self-assembly process, two hydrides ligated to Rh(III) center are lost by reductive elimination process. The geometry around each Rh center is that of a distorted square-planar and is satisfied by coordination of N centers of two bridging pyz and PPh_3 ligands. **2** is a cationic macrocycle bearing three units of charge with noncoordinating perchlorate anions present in the outer sphere. **2** may also be described as a [3 + 3] macrocycle since its formation requires three units each of the donor and acceptor tectons. The selective formation of triangular Rh complex instead of square (a [4 + 4] macrocycle) is ascribed to the lesser steric repulsion between the bulky PPh_3 groups in this [3 + 3] macrocycle.

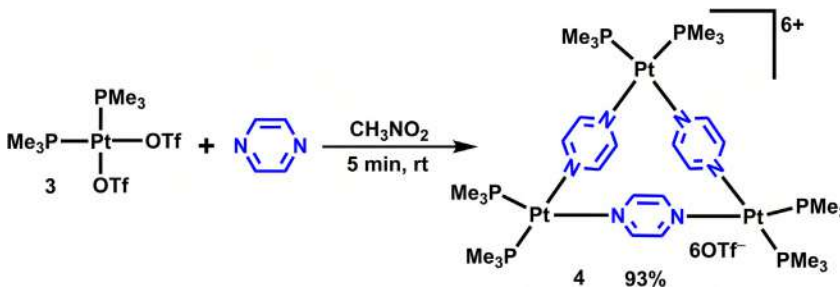

SCHEME 5.2 Synthesis of unexpected Pt triangular species **4** using rigid and small pyz subunits.

Other structurally related, supramolecular triangle **4** was self-assembled unexpectedly as reported by Stang and coworkers [15]. Again, **4** was obtained by the stoichiometric reaction between equimolar concentrations of a ditopic platinum acceptor **3** and pyz (a ditopic donor) in nitromethane as a solvent (Scheme 5.2). Considering the square planar coordination environment around Pt(II) center (reactive sites oriented in roughly 90° angle with respect to each other), it was anticipated that its self-assembly with pyz (a short, inflexible, and linear tecton) would yield a molecular square. However, smaller triangular species **4** was obtained as the major product and isolated in 93% yield. In this case, the authors invoke a combination of entropy factors and the electronic effects of two platinum centers at each pyz unit [16] to rationalize the formation of observed triangular macrocycles. Notwithstanding, due to the strain present in **4**, the geometry around the platinum centers deviates from that expected in an ideal square planar coordination environment. The Pt···Pt distances present in the triangular cage are measured to be around ~6.9 Å.

Another very interesting example of molecular triangle **6** with pyz as one of the tectons was reported by Zangrando and coworkers [17]. Unlike the previous two examples of pyz containing ionic macrocycles, **6** is a neutral metallacycles that is derived from Ru(II)-based acceptor tectons. Two approaches were employed for the synthesis of **6** (Scheme 5.3). In the first method, **6** was self-assembled via direct reaction between *trans*-[$RuCl_2$(dmso-S)$_4$] (**5**) and an equivalent amount of pyz donor linker in chloroform. The molecular triangle [{*trans,cis*-$RuCl_2$(dmso-S)$_2$(μ-pyz)}$_3$] (**6**) could also be obtained by the treatment of *trans*-[$RuCl_2$(dmso-S)$_4$] (**5**) with *trans,cis,cis*-[$RuCl_2$(dmso-S)$_2$(pyz)$_2$] (**7**). In both approaches, a transient species, that is, expected molecular square [{*trans,cis*-$RuCl_2$(dmso-S)$_2$(μ-pyz)}$_4$] was witnessed as an intermediate species. The X-ray structure of **6** reveals the distorted octahedral geometry around the ruthenium centers, due to the smaller pyz–Ru–pyz bond angles (< 90°)—a requirement for obtaining triangular macrocycles. A possible reason for the preferred formation of molecular triangles over the expected molecular squares is associated with unique characteristics of Ru(II)-based corner acceptor fragments with an octahedral coordination environment. The Ru(II) tectons

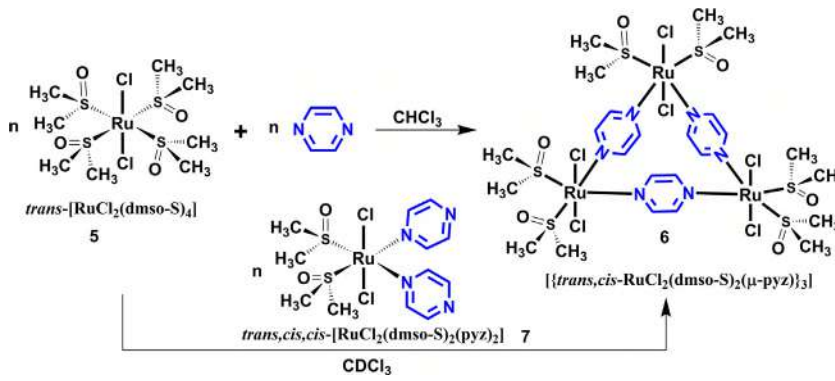

SCHEME 5.3 Synthesis of Ru-based triangular species **6** using rigid and small pyz subunits.

spontaneously favor smaller pyz–Ru–pyz bond angles (<90°) in a molecular triangle that assist in releasing the steric congestion created due to the existence of ancillary ligands on the metal sphere.

From the above examples, it has emerged that the nuclearity of the preferred metallacycle (triangle/square) is often influenced by various factors such solvent, temperature, stoichiometric ratio of reagents, nature of the metal center as well as ancillary ligands bound to it. Slight alteration within the same class of ligands can yield different products [13].

5.3 Molecular squares

A metallosupramolecular assembly having a square shape can be constructed by the combination of four angular ditopic acceptor units (with 90° angle between reactive sites) and four rigid, linear donor linkers (with 180° angle between reactive sites) as shown in Fig. 5.3. The versatile use of this method was explored by Stang and Fujita. This self-assembly protocol was also useful to obtain organosoluble chiral squares [18]. All such molecular squares are designated as [4 + 4] ensembles.

Molecular squares may also be obtained using another approach that employs a lesser number of tectons. In this approach, two ditopic angular tectons with right angles between the two binding sites are combined with two complementary bent tectons with the same bite angles. The resultant assembles are [2 + 2] molecular square (Fig. 5.3). While a [4 + 4] square-shaped macrocycle may be obtained by using a pyz as the donor tecton, the possibility of obtaining a [2 + 2] square is ruled out since it is rigid in nature and its donor centers are at an angle of 180° with respect to each other.

In 2012, Manimaran et al. reported the one-pot synthesis of a molecular square via self-assembly of four units of $Mn(CO)_5Br$ (**8**) and pyz tecton to afford $[Mn(CO)_3Br(\mu\text{-pyz})]_4$ (**10**) (Scheme 5.4) [19]. As evident from the scheme, the

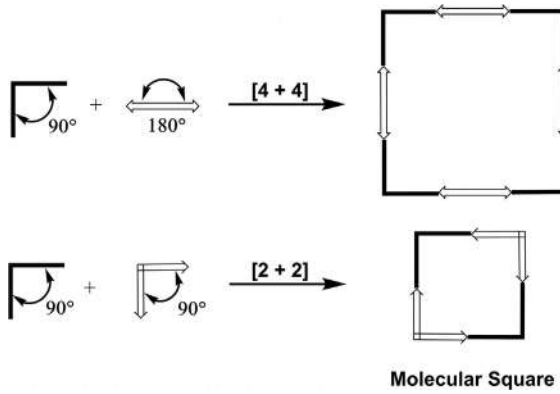

FIGURE 5.3 Schematic representation of molecular square formation by [4 + 4] and [2 + 2] self-assembly.

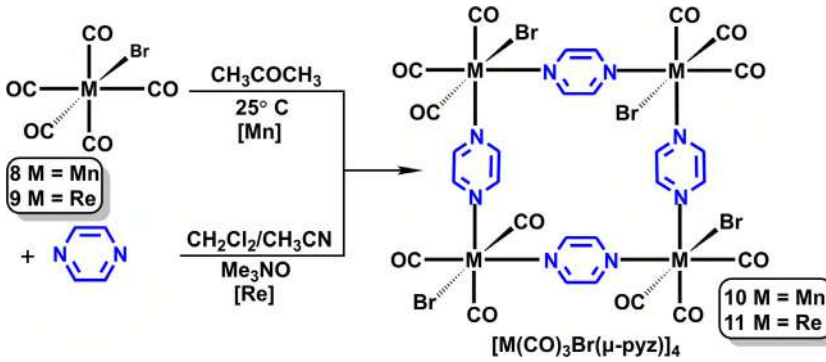

SCHEME 5.4 Synthesis of manganese- and rhenium-based molecular square $[M(CO)_3Br(\mu\text{-pyz})]_4$ [M = Mn, Re] using pyz donor tecton.

Mn(I)-based molecular square is neutral and is formed by the loss of two CO that are *cis* to each other. Loss of the CO that is *trans* to Br is ruled out since the "*trans* effect" of bromide is lesser than that of CO. Various spectroscopic techniques were used to ratify the structure of molecular square, including single-crystal X-ray diffraction study. The molecular structure of **10** reveals a square framework with each manganese ion situated at the four corners. The geometry around Mn(I) is distorted octahedral and is achieved by the coordination of three CO groups, two pyz molecules, and a bromide ion. The molecular square framework is held by the pyz tectons that bridge two manganese corners. The Mn···Mn distance in molecular square is 6.92 Å.

Another fascinating tetranuclear square complex $[Re(CO)_3Br(\mu\text{-pyz})]_4$ (**11**) was synthesized by the self-assembly reaction of $Re(CO)_5Br$ (**9**) and pyz in the presence of Me_3NO as a solvent (Scheme 5.4) [20]. ^1H NMR and ES-MS data were used to investigate the mechanistic pathway that revealed the formation

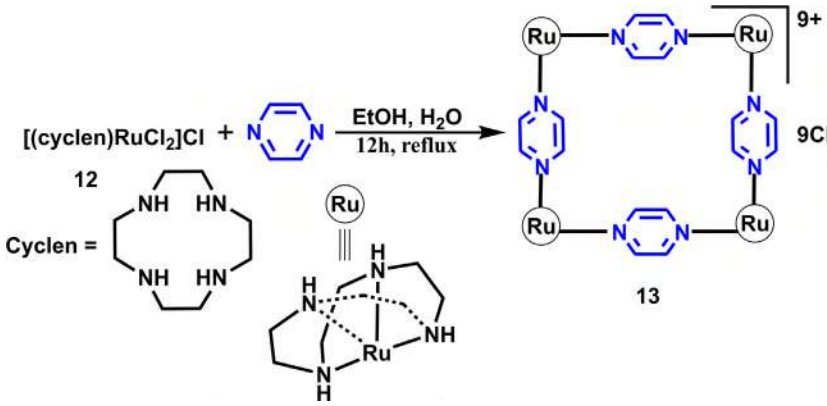

SCHEME 5.5 Synthesis of ruthenium-based molecular square $[(cyclen)_4Ru_4(\mu\text{-}pyz)_4]Cl_9{\cdot}17H_2O$ (**13**).

of other rhenium-based intermediates during the self-assembly process. The uniform Re···Re distance in the tetranuclear square complex is 7.18 Å. The Re-based square has longer edges than its Mn-analogue due to the bigger size of Re(I) cation relative to Mn(I).

In the early 2000s, Long and coworkers reported an interesting pyz containing mixed-valence Ru-based square complex, $[(cyclen)_4Ru_4(\mu\text{-}pyz)_4]Cl_9{\cdot}17H_2O$ (cyclen = 1,4,7,10-tetraazacyclododecane) (**13**), as shown in Scheme 5.5 [21]. Cyclen was chosen as the ancillary ligand due to its ability to act as a tetradentate blocking ligand. The conformational preference of cyclen provided for the *cis*-coordination geometry of the reactive centers, which is a condition requisite for the formation of molecular square. The molecular structure of **13** was unambiguously verified by single-crystal X-ray analysis, which reveals the four Ru centers are connected through pyz linker to generate a regular square with an edge dimension of 6.95 Å. All four pyz rings in the square are equivalent by symmetry, and each is tilted away from the Ru_4 plane by an angle of 55.9°. Other structurally analogous molecular square using Pt(II)-based acceptor tecton was reported by Fujita and coworkers in the form of a highly charged ionic complex $[Pt(en)(\mu\text{-}pyz)]_4{\cdot}8NO_3$ [22].

5.4 Molecular rectangles

Both rectangle and square are quadrilaterals having four right angles. However, unlike a square that has all sides of equal length, in a rectangle only the pairs of opposite sides are of equal length. Therefore, the self-assembly protocol for construction of a molecular rectangle is different from that of a square, even though both are four-sided polygons. A convenient method to obtain a rectangular macrocycle would employ a self-assembly reaction between an acceptor clip with 0° angle between the reactive sites and a linear ditopic donor

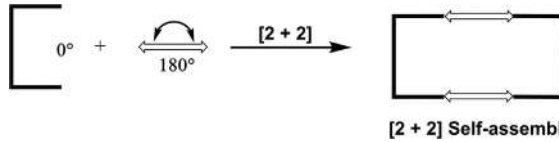

FIGURE 5.4 Schematic representation of molecular rectangle formation by [2 + 2] self-assembly.

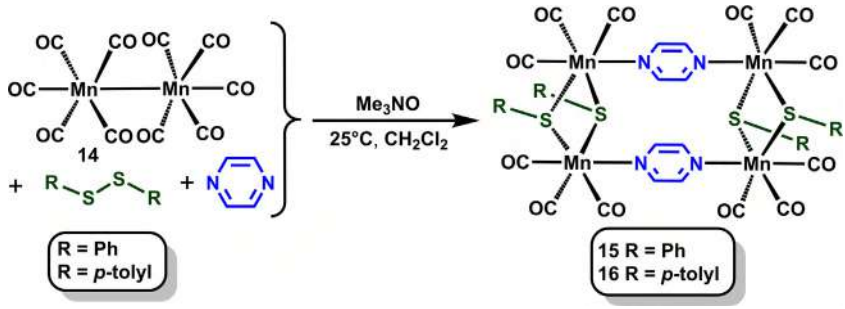

SCHEME 5.6 Self-assembly of Mn(I)-based metallarectangles **15** and **16**.

molecule (such as pyz) in an equimolar ratio (Fig. 5.4). This strategy has been used to design numerous macrocycles and is widely recognized as "molecular rectangles" [23]. Herein, we highlight the molecular rectangles that feature pyz moieties.

In 2015, manganese-based macrocycles [{$(CO)_3$}Mn(μ-SR)$_2$Mn$(CO)_3$}$_2$(μ-pyz)$_2$] [**15**, R = Ph; **16**, R = *p*-tolyl] were reported by Manimaran and coworkers [24] that have a rectangular shape. To accomplish the synthesis of **15** and **16**, three-component self-assembly reactions were carried in the absence of light by employing $Mn_2(CO)_{10}$ (**14**), diaryl disulfides, and pyz tecton in the presence of Me_3NO (solvent) at room temperature (Scheme 5.6). Molecular structure of **15** was endorsed by various spectroscopic techniques, including single-crystal X-ray diffraction study. The later study shows that the four corners of the rectangular architecture are occupied by *fac*-Mn$(CO)_3$ units, which in turn are bridged by two thiolato groups (along the shorter edges) and a pyz ring (along the longer edges). The Mn···Mn distances along the shorter, and longer edges are ~3.63 and ~7.02 Å, respectively. A distorted octahedral geometry around each manganese center in four *fac*-Mn$(CO)_3$ units was witnessed.

Other pyz bearing tetranuclear rectangular complexes [$Cp^*_4M_4$(μ-DHNA)$_2$(μ-pyz)$_2$](OTf)$_4$ [**21**, M = Ir; or **22**, M = Rh] were reported by Jin and coworkers [25]. Treatment of 6,11-dihydroxy-5,12-naphthacenedione (H_2DHNA) with [Cp^*MCl(μ-Cl)]$_2$ (M = Ir or Rh) in the presence of base (CH_3ONa) in 1:1:2 ratio in MeOH yielded complexes [$Cp^*_2M_2$(μ-DHNA)Cl_2] (**17**, M = Ir; **18**, M = Rh), respectively. Further, reactions of **17** and **18** with AgOTf in CH_3OH yielded their corresponding triflate salts **19** and **20**, followed by the addition of ditopic and rigid pyz linker afforded the tetranuclear

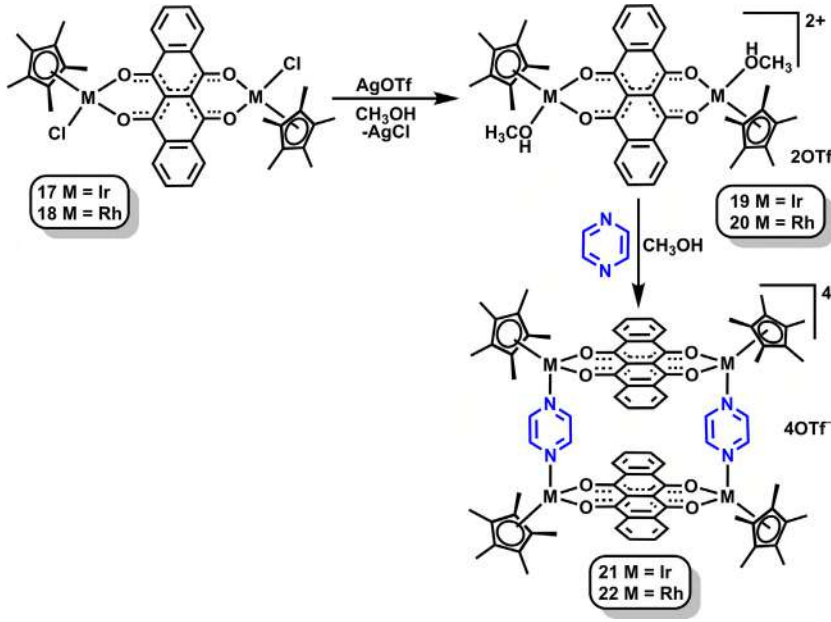

SCHEME 5.7 Synthesis of tetranuclear organometallic boxes **21** and **22**.

complexes $[Cp^*_4M_4(\mu\text{-DHNA})_2(\mu\text{-pyz})_2](OTf)_4$ [**21**, M = Ir; or **22**, M = Rh] (Scheme 5.7). The single-crystal X-ray analyses of **21** and **22** ratified the rectangular framework for these self-assembly complexes. Moreover, the half-sandwich metal centers situated at each corner of the rectangular framework are linked by other bis-bidentate bridging ligands to build the rectangular cavity of different sizes. Additionally, the strong π–π interactions between discrete molecules were perceived, which facilitate the formation of rectangular channels in the solid state.

Yet another interesting method for obtaining molecular rectangles was reported by Lu and coworkers, wherein the dirhenium complex **23** was reacted with pyz under solvothermal conditions [26]. The molecular rectangle $[\{(CO)_3Re(\mu\text{-}H_6bpym)Re(CO)_3\}_2(\mu\text{-pyz})_2]$ (**24**) was obtained in good yield from $Re_2(CO)_{10}$ (**23**), 2,2′-bipyrimidine (bpym), and pyz at 160°C (Scheme 5.8). During the self-assembly process, a rare partial reduction of bpym moiety was observed. The partial reduction of bpym was supported by ^{1}H NMR spectrum, which indicates the disappearance of aromatic proton signals and simultaneously the appearance of new peaks corresponding to aliphatic protons in the upfield region of the spectrum. This confirmed that the uncommon reduction of bpym possibly took place during the course of reaction.

To obtain more insight about the reduction of bpym during the self-assembly route, $Re_2(CO)_{10}$ was treated with bpym in the absence of pyz ligand. Under the same reaction condition, the dirhenium compound **25** (Scheme 5.8) was

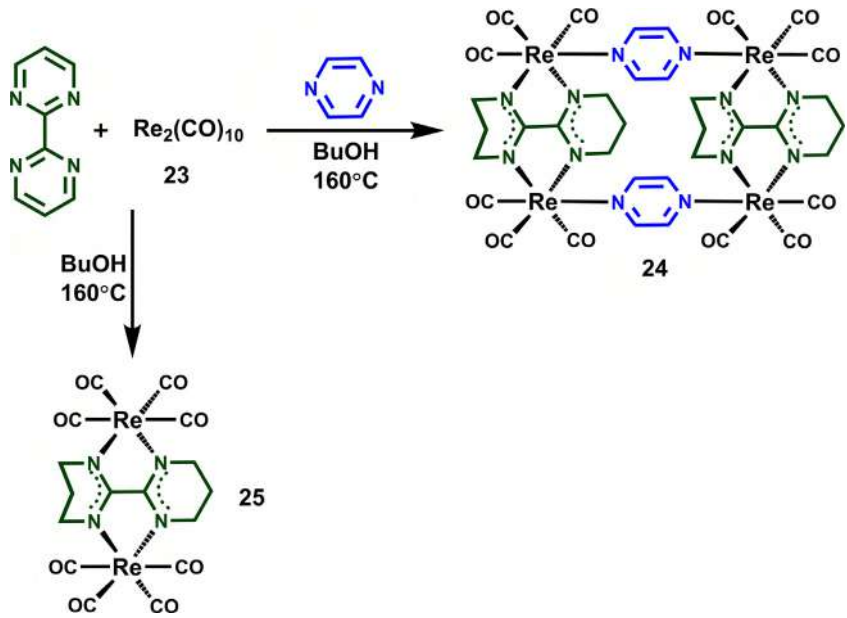

SCHEME 5.8 Self-assembly of Re(I)-based rectangle **24** and bimetallic **25** complexes by trapping a partially reduced bpym to nonaromatic bicycle.

obtained. This reaction certifies the claims of partial reduction of bpym in an early stage of the reaction to give compound **25**. The inspection of molecular structure of **24** reveals a rectangular architecture. Herein, two $(CO)_3Re$–(pyz)–$Re(CO)_3$ edges are joined by two partially reduced bpym moieties with a cavity dimension of 5.79 × 7.31 Å. Further, photophysical and electrochemical properties of rhenium complexes were probed.

5.5 Molecular hexagons

There are fewer examples of larger polygonal frameworks since the formation of such a large framework requires self-assembly of a large number of tectons. Therefore, the self-assembly of a [6 + 6] molecular hexagon using six angular tectons (bite angle 120°) and six linear and rigid tectons (bite angle 180°) is entropically and hence thermodynamically disfavored. From a literature survey, two approaches were commonly employed for the construction of molecular hexagons via directional bonding method [27]. The first approach is the reaction between two complementary ditopic bent tectons involving 120° angles between their respective binding/reactive sites. This would a [3 + 3] molecular hexagon. The second approach requires self-assembly of twelve tectons, and the macrocycle anticipated would be aptly described as a [6 + 6] molecular hexagon (Fig. 5.5).

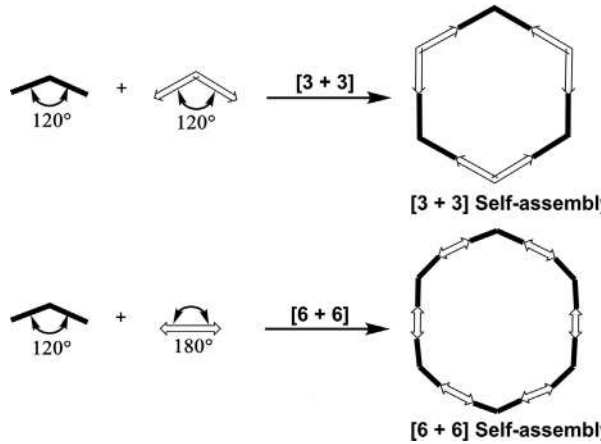

FIGURE 5.5 Schematic representation of molecular hexagons formation by [3 + 3] and [6 + 6] self-assembly.

In the context of molecular hexagons bearing pyz motif, several platinum-based hexagonal metallacycles have been reported in the last decade by Das and coworkers [28–30]. For example, using a pyz-based organometallic complex having an obtuse binding angle (120°) as a synthon, a cationic molecular polygon with a hexagonal shape [29] was conveniently obtained. This donor synthon provides an opportunity to self-assemble a variety of pyz-based metallamacrocycles with hexagonal cavity with different donor tectons. Further their influence in host–guest chemistry was studied. Depending on the nature (neutral or ionic) of the complementary "donor" linker, the resulting self-assembled ensemble is either ionic or neutral. The following section has been systematically divided into two subsections, separating ionic and neutral macrocycles, and is illustrated with representative examples of each type.

5.5.1 Ionic hexagonal macrocycles

A well-recognized strategy to construct an ionic macrocycle is to use neutral bridging linkers (as donors) together with complementary cationic metal-containing tectons (as acceptors). For example, the pyz-based diplatinum acceptor tecton **26** was first reacted with two equivalents of silver nitrate to increase the reactivity of the Pt(II) center followed by the treatment with an appropriate ditopic donor tecton (3,3′-bipyridine or 4,4′-bipyridine) in an equimolar ratio (Scheme 5.9) [29].

This afforded the desired molecular hexagons **27** and **28** which are aptly described as [2 + 2] and [6 + 6] self-assembled ionic/charged ensembles. Thus, it was shown through that macrocycles with hexagonal cavities may also be obtained by using lesser number of tectons of appropriate design. The [6 + 6] ensemble **28** is especially interesting because it is associated with

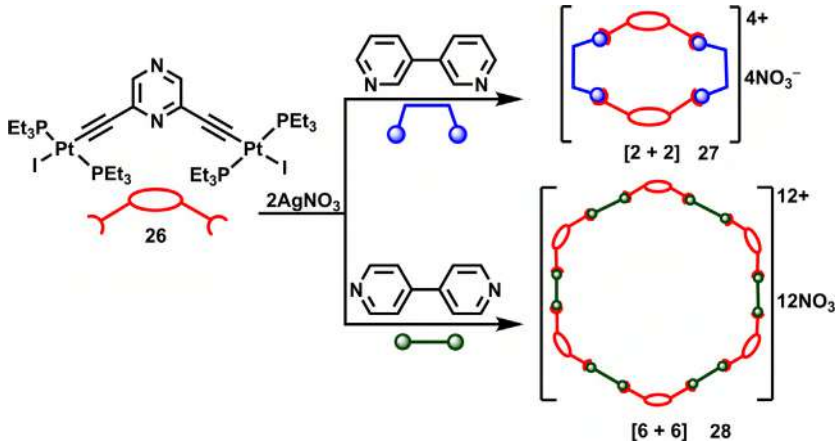

SCHEME 5.9 Self-assembly of hexagonal macrocycles using a pyz-based diplatinum acceptor tecton **26**.

twelve units of positive charge, which are balanced by an equal number of weakly coordinating nitrate counteranions. Needless to say, the [6 + 6] macrocycle **28** has a relatively larger sized hexagonal cavity as compared to other [2 + 2] polygon **27** described in Scheme 5.9. Though in both hexagons, the same acceptor linker (~120° ditopic platinum(II)-based acceptor) is utilized, the difference in size between the two frameworks arises merely from the difference in bite angle of donor units that are employed. Unfortunately, good quality single crystals of the macrocycles **27** and **28** could not be obtained in which case, the structure of these macrocycles was confirmed by molecular modeling method. *In silico* analysis indicated the existence of hexagonal cavities for both **27** and **28**. Further, **27** and **28** are π–electron rich macrocycles, and hence these were tested as hosts for the relatively electron-deficient nitroaromatic molecules such as DNT and PA. Such host–guest chemistry was studied using isothermal titration calorimetry (ITC) as an analytical tool. The presence of platinum ethynyl motifs and conjugated π–electron framework were indeed responsible for the detection of nitroaromatic materials [31,32]. Further, insight about the binding interaction between ionic macrocycles and nitroaromatic guest molecules (DNT/PA) were accomplished by molecular dynamics simulation.

Later (2019), Das and coworkers designed another set of two cationic supramolecular frameworks with pyz motif and studied their biomedical applications. Two new isomeric pyz-based molecules **29** and **30** were developed that had two pendent pyridyl units. **29** and **30** are isomeric but they differ from each other with respect to directionality of the reactive centers. These (**29** and **30**) were used as ditopic donor tectons along with diplatinum acceptor tecton **26** to yield two supramolecular metallacycles **31** and **32** (Scheme 5.10) [33]. The presence of nano-dimensional hexagonal cavities in these metallacycles was concluded

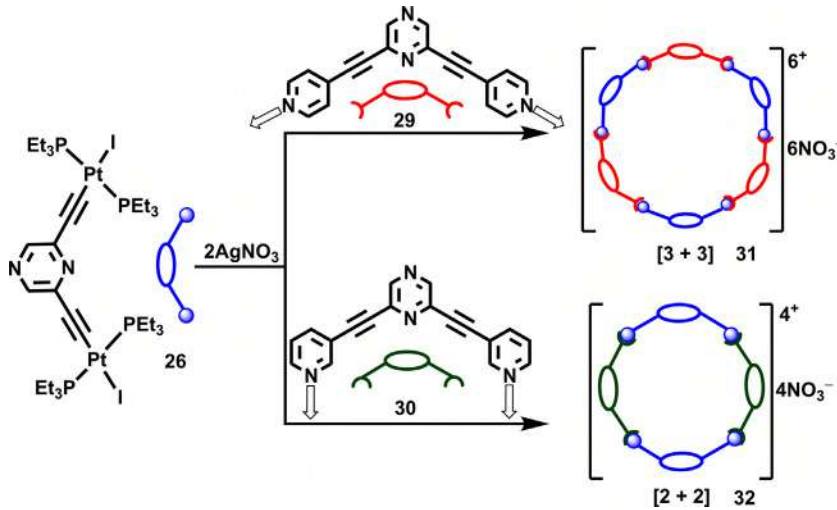

SCHEME 5.10 [3 + 3] and [2 + 2] macrocycles (**31** and **32**) made by self-assembly approach using the pyz-based molecular acceptor clip **26** with the organic donor linkers **29** and **30**. (Arrows indicate the direction of ligation.)

from molecular modeling data that used PM6 semiempirical molecular orbital method [34].

Further, in order to investigate the biological application of these metallacycles, their interactions with different carcinoma cell lines were examined. The cell proliferation activity of different cancer lines (A549, HepG2, and HeLa) was greatly reduced in presence of the nano-dimensional **31** and **32** with their IC_{50} values being comparable with that of cisplatin. Experimental data results also indicated that anticancer efficacy of the highly charged supramolecular metallacycles was superior than their neutral organometallic precursor(s). It was observed that the larger macrocycle (**31**) showed highest anticancer activity even at lower concentration. TUNEL assay suggested that these macrocycles encouraged cell death by apoptosis. These preliminary findings indicate that the nanoscalar supramolecular metallacycles **31** and **32** could find potential biomedical applications as inorganic therapeutic agents.

Das and coworkers also reported the facile syntheses of four novel cationic hexagons (**35**–**38**) using the above-mentioned two different synthetic approaches (as shown in Scheme 5.11) [35].

Contrary to the previous examples, in this set of pyz-based metallamacrocycles, while the acceptor tecton is linear, the donor tecton comprises of the complementary angular subunit required to form the hexagonal macrocycles. In line with the directional-bonding approach, coordination-driven self-assembly reactions of **29** and **30** were carried out with linear (180°) ditopic acceptor linkers **33** and **34** in 1:1 ratio, which yielded [6 + 6] (**35** and **36**) and [2 + 2] (**37** and **38**) hexagonal metallamacrocycles, respectively. PM6 semiempirical molecular

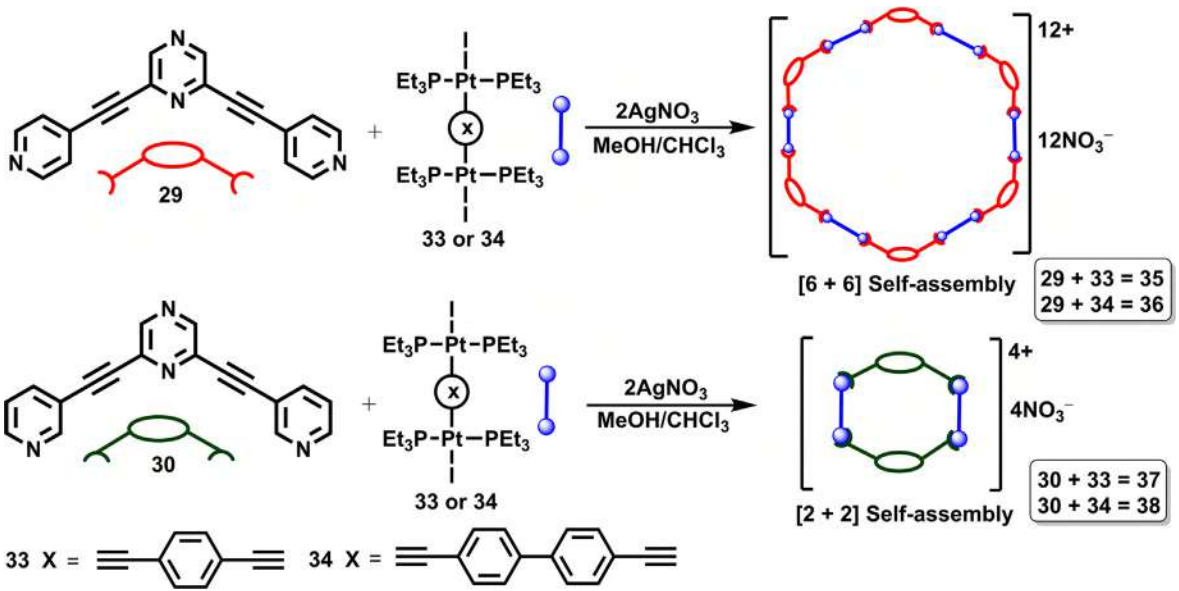

SCHEME 5.11 [6 + 6] (**35** and **36**) and [2 + 2] macrocycles (**37** and **38**) made by self-assembly strategy using the pyz-based organic donor linkers (**29** and **30**) and organometallic linear acceptor tectons (**33** and **34**).

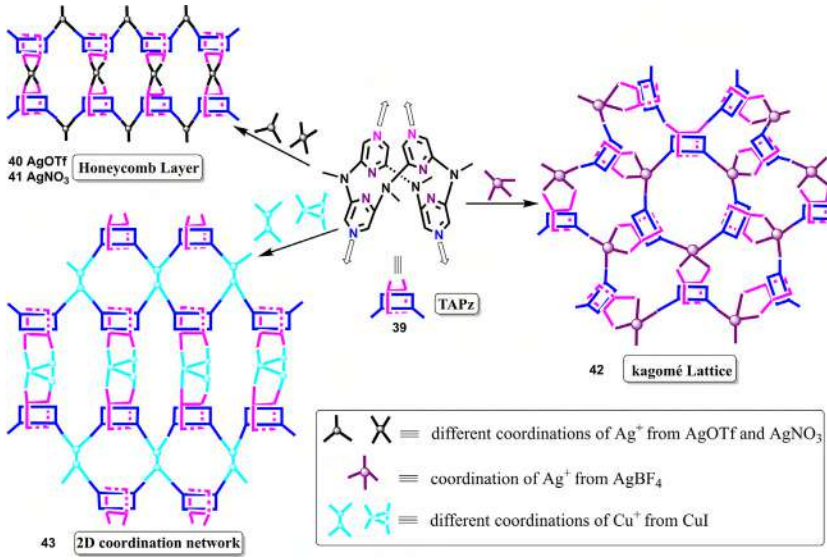

SCHEME 5.12 Synthesis of various cavity-containing coordination networks **40**–**43** using TAPz. Coordinating molecules (ACN and OTf^-) and counteranions (NO_3^- and BF_4^-) have been omitted for clarity. (Arrows indicate the direction of ligation.)

orbital method indicated the presence of hexagonal shaped cavities in these macrocycles. It must be noted that while the macrocycles **35** and **36** are regular hexagons (all sides of equal length), the ensembles **37** and **38** have an irregular hexagonal shape. However, the common feature of these macrocycles is their nanoscalar dimensions.

An interesting pyz-based heteracalixaromatic ligand, tetramethylazacalix[4]pyrazine (TAPz) (**39**), was reported by Zhao et al. in 2012. Its coordinating ability with metal and metal cluster, respectively, were subsequently explored [36]. TAPz has a macrocyclic skeleton comprising of four pyrazinyl rings, which enabled it to exhibit a novel multimodal coordination mode. As expected for flexible macrocycles such as calix[n]arenes, the structural characterization of TAPz revealed a similar fluxional behavior (interconversion between different conformations) in solution. In the solid state, the 1,3-alternate configuration was observed. Interestingly, its convergent chelating coordination sites (two pyrazinyl rings) are orthogonal to 120°-angled bridging sites (remaining two pyrazinyl rings) and thus offer an uncommon multidentate ligand framework (as shown in Scheme 5.12).

Reactions of TAPz with silver (viz. AgOTf, $AgNO_3$, and $AgBF_4$) and copper (Cu_xI_x) salts yielded different self-assembled architectures **40**–**43**, such as honeycomb, kagomé, and cavity-containing 2D layers (Scheme 5.12), respectively. The preorganized 1,3-alternate conformation of the TAPz ligand thus exhibited

good coordinating ability and stiffness, which assisted in its application in construction of unique cavity-involved coordination networks.

Recently, using pyz-based donor and acceptor tectons, Singh et al. reported a unique [1 + 1] platinum metallacycle **46**, which has hexagonal cavity and nanodimensional in size [37]. The self-assembly reaction (Scheme 5.13) utilized a Pt(II)-based organometallic clip **44** and a complementary ditopic donor molecule **45**. Both tectons are semirigid in nature due to possible conformations in which the reactive centers have different angular orientations with respect to each other. The self-assembled product **46** was characterized by various spectroscopic techniques, including $^{31}P\{^{1}H\}$ NMR and mass-spectrometry experiments. The presence of a single peak at δ 15.59 ppm ($^{1}J_{PPt} = 1151$ Hz) implied the yield of a unique highly symmetrical species. The structural information of the [1 + 1] platinum metallacycle **46** was obtained by PM6 semiempirical molecular orbital method.

Thus, **46** was a rare example of a macrocycle with hexagonal cavity that was self-assembled by using only two tectons. Further, the ionic platinum metallacycle **46** was found to interact considerably with DNA molecule and exhibited positive nuclease activity with DNA relative to its neutral donor/acceptor partners. Another unique [1 + 1] platinum metallacycle (**48**) was obtained by using a new donor tecton **47** having two pendant pyridine rings flanked by a central pyz ring is reported by Singh et al. [38]. Herein, both (donor and acceptor) tectons are ditopic with 0° angular orientations with respect to their two reactive sites (Scheme 5.14), and both were derived from 2,6-disubstitued pyz derivatives. The self-assembled product **48** was isolated as an off-white and pristine microcrystalline solid that was characterized by multinuclear NMR, mass spectrometry, and elemental analyses.

For example, in $^{31}P\{^{1}H\}$ NMR spectrum, **48** showed a sharp singlet centered at $\delta = 15.70$ ppm, flanked by a pair of ^{195}Pt satellite peaks ($^{1}J_{PPt} = 1162$ Hz). The hexagonal shaped cavity of the metallamacrocycle was confirmed from PM6 molecular modeling study. *In silico* data suggested the formation of a nanoscalar hexagonal framework. **48** is thus another unique example of a discrete hexagonal framework fabricated from self-assembly of just two tectons—one donor and one acceptor. It must be mentioned that Pt(II)-based hexagonal macrocycles described in earlier literature reports required either six or twelve tectons. **44** and **48** are cytotoxic against three cancer cell lines [A549 (human lung cancer cell line), KB (human oral cancer cell line), and HaCaT (human skin keratinocyte cell line)].

In recent past, Das and coworkers have also designed other molecular hexagons **50** and **51** with pyz motif. Herein, the dimensions of the hexagonal cavities were modulated by using ditopic and linear donor tectons of different lengths in the form of pyrazine and 4,4′-bipyridine. The ditopic Pt(II)-based acceptor tecton (**49**) was same in both the cases (Scheme 5.15) [30]. Coordination-driven self-assembly reactions yielded discrete macrocycles (**50** and **51**) with hexagonal cavities as the exclusive product, which were characterized by

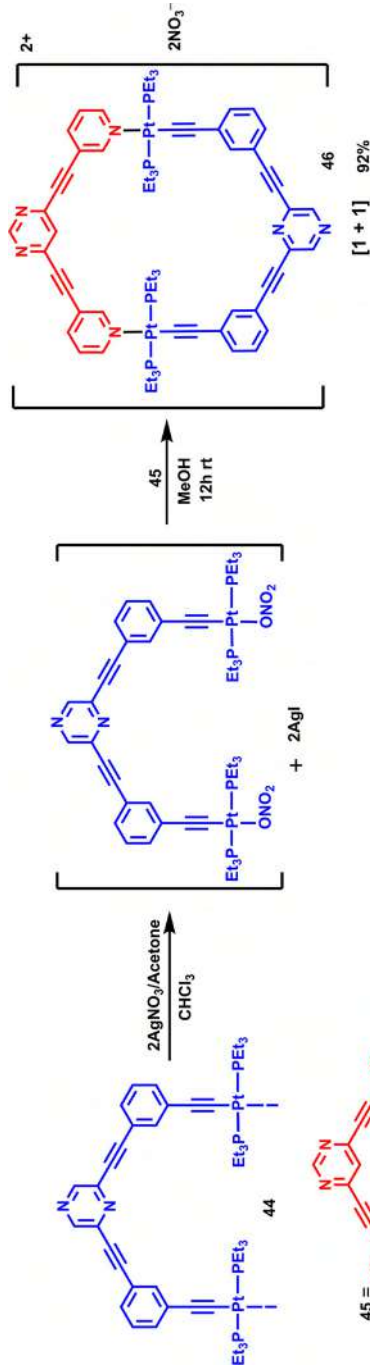

SCHEME 5.13 Design of macrocycle **46**.

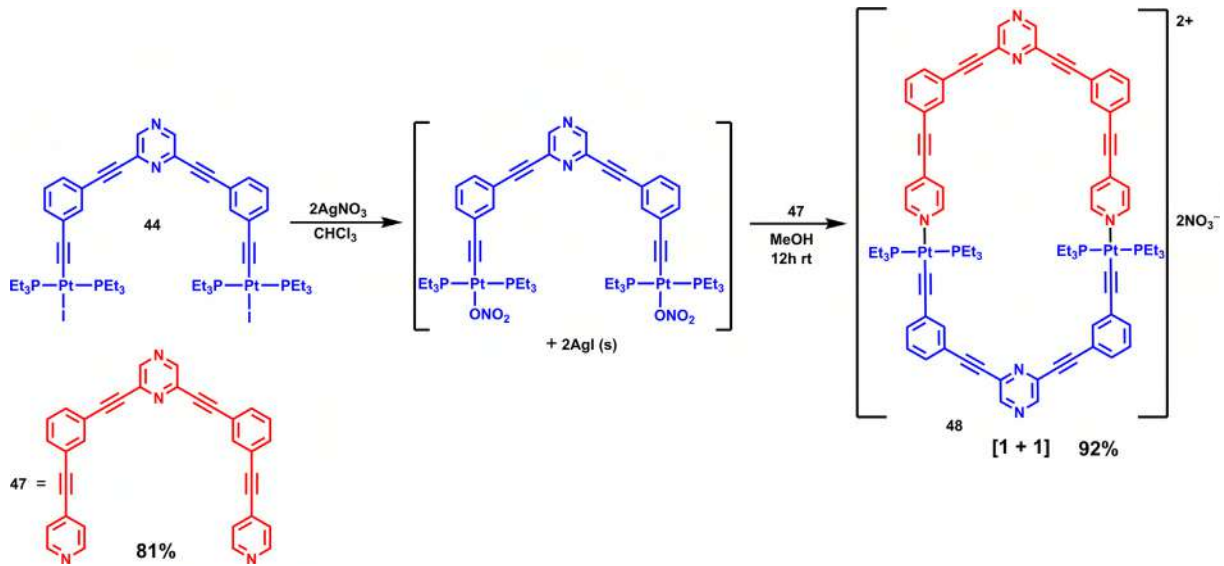

SCHEME 5.14 Synthesis of a hexagonal macrocycle **48** by using merely two molecular tectons.

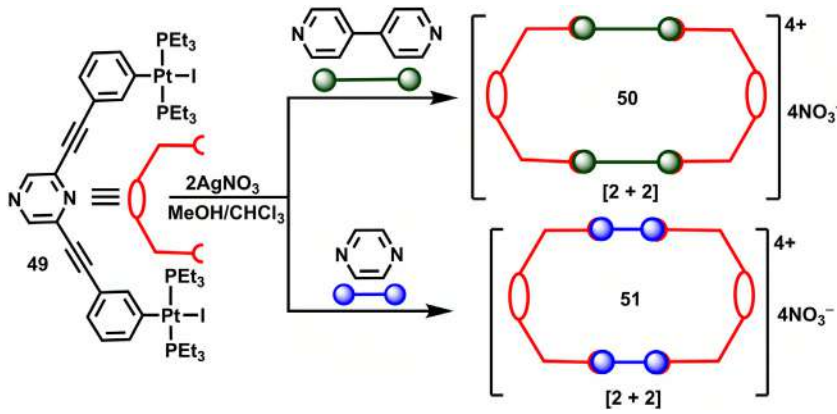

SCHEME 5.15 Synthesis of irregular hexagonal macrocycles **50** and **51** using pyz-based organometallic clip **49**.

multinuclear NMR, mass spectrometry, as well as elemental analyses. **50** was also structurally characterized by single-crystal X-ray analysis. Interestingly, these [2 + 2] self-assembled ensembles macrocycles can be aptly described as irregular hexagons since all sides are not of equal length in these polygonal frameworks. This makes them unique examples of Pt(II)-pyz-based macrocycles of irregular shapes.

Cytotoxic properties of **50** and **51** were tested against various cancer cell lines, such as A549 (human lung carcinoma), KB (human oral cancer), MCF7 (human breast cancer), and HaCaT (human skin keratinocyte). Data obtained were compared with Pt(II)-based cisplatin. Between these two macrocycles, the smaller one was more potent against cancer cell lines screened in this report. From the IC_{50} data, the authors conclude that the activity of macrocycles and cisplatin were comparable when tested against A549 and MCF7 cancer cells.

A unique tris-pyrazinyl-pillared prismatic ligand **52** was reported in 2013 by Wen and coworkers [39] that exhibits both bi- and tridentate modes of coordination. Coordination-driven self-assembly reactions with different metal cations (Ag^+/Cu^{2+}) yielded structurally different coordination polymers **53** and **54**. In a mixture of solvents (benzene and ACN), **52** reacted with $AgBF_4$ to yield a 2D coordination polymer **53** (Scheme 5.16) that was confirmed by single-crystal X-ray diffraction analysis. The ligand **52** and Ag^+ ion were present in 4:3 stoichiometry ratio in **53**. Interestingly, the molecular structure of **53** consists of metallomacrocyclic cage of two shapes, that is, rhomboidal $[Ag_2(\mathbf{52})_2]$ and hexagonal $[Ag_3(\mathbf{52})_3]$ (**52**: tridentate ligand). The rhomboidal $[Ag_2(\mathbf{52})_2]$ framework is defined by two **52** ligands that bridge two Ag^+ cations. The Ag···Ag distance in the rhomboidal $[Ag_2(\mathbf{52})_2]$ cages vary in the range of 12.52–12.82 Å. Similarly, the hexagonal $[Ag_3(\mathbf{52})_3]$ cage was created by coordination of three **52** units with three Ag^+ cations. Both the crystallographically independent silver centers were observed in the same polymeric structure. The geometry around

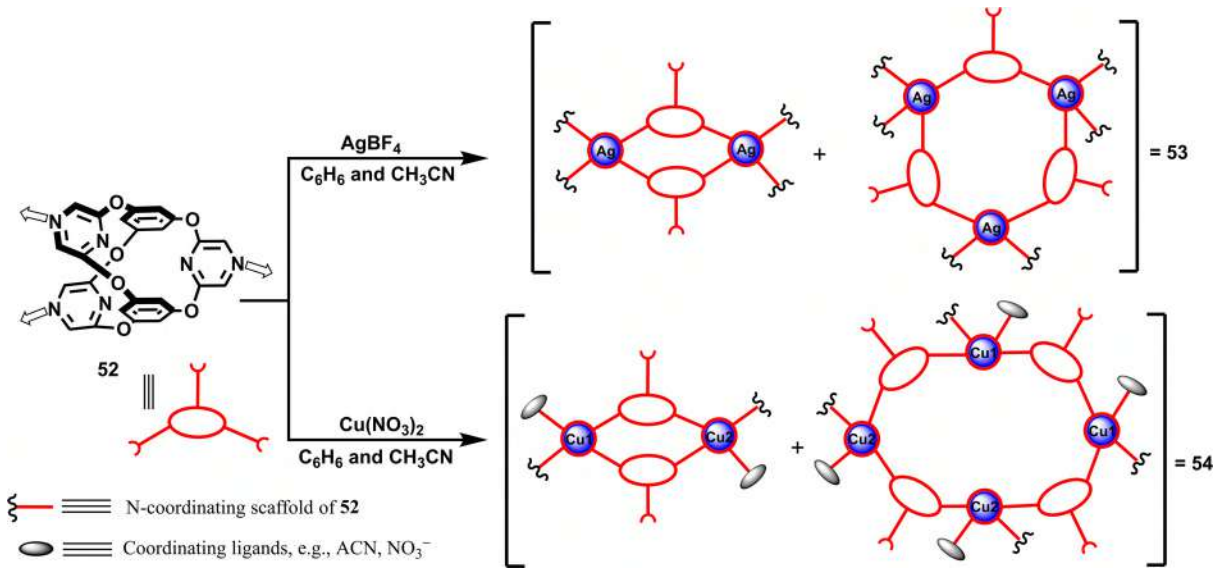

SCHEME 5.16 Synthesis of silver (**53**) and copper (**54**) macrocycles by using pyz scaffold **52**. Counteranions (BF_4^- and NO_3^-) and guest species (benzene and **52**) involved in the macrocycles are omitted for clarity. (Arrows indicate the direction of ligation.)

each silver center in this 2D coordination polymer is distorted square planar. Such a coordination environment is achieved by the coordination of four exo-pyrazinyl nitrogen atoms of four units of **52** with silver cation. The Ag–N bond distances and N_{pyz}–Ag–N_{pyz} bond angles vary in the range of 2.29−2.61 Å and 83.0–103.0°, respectively. The dimensions of the voids (empty space), created due to the rhomboidal [Ag_2(**52**)$_2$] and [Ag_3(**52**)$_3$] hexagonal macrocycles, are suitable for host–guest complexation with benzene and ligand **52**, respectively. An analogous reaction between **52** and $Cu(NO_3)_2$ in the same solvent mixture yielded two crystalline compounds **54** (major) and **55** (minor, 1D polymeric chain), having distinctly different color, that is, green and yellow, respectively. The structure of the 2D coordination polymeric network in **54** was analyzed using single-crystal X-ray diffraction data, in which **52** and Cu^{2+} ions were present in equimolar ratio. Complex **54** too consists of rhomboidal [Cu_2(**52**)$_2$] and hexagonal [Cu_4(**52**)$_4$] cage units as shown in Scheme 5.16.

Close inspection of rhomboidal [Cu_2(**52**)$_2$] cage in **54** reveals that the presence of two crystallographically nonequivalent copper centers (Cu1 and Cu2). Both the copper centers feature highly distorted octahedral environments. The Cu1 center is coordinated with three pyz nitrogen atoms each from a different neighboring **52** moiety. The remaining three coordination sites are fulfilled by two nitrate counteranions displaying monodentate and bidentate modes of coordination. An identical coordination environment around Cu2 center was observed in which four nitrogen (three from **52** moiety and one from coordinated ACN molecule) and two oxygen (bidentate nitrate) centers are present. The two copper centers (Cu1···Cu2) in the rhomboidal cage [Cu_2(**52**)$_2$] of **54** are separated by a distance of 12.04 Å.

Finally, the hexagonal [Cu_4(**52**)$_4$] cavity in this coordination polymer **54** was defined by two types of Cu^{2+} centers (Cu1 and Cu2) and four **52** moieties, that occupy the six corners. The six concave sides of the hexagonal cage are described by the four pyrazinyl ring planes from the four **52** moieties and the remaining two from N_{pyz}–Cu–N_{pyz} planes. The separation between Cu1 and Cu2 centers positioned in opposite corners of the hexagonal cage and two N_{pyz}–Cu–N_{pyz} planes are 24.23 and 10.83 Å, respectively. The void present in the hexagonal cage [Cu_4(**52**)$_4$] is able to accommodate four disordered benzenes as a guest molecule.

5.5.2 Neutral hexagonal macrocycles

As far as the synthesis of neutral macrocycles is concerned, a well-accepted strategy is to use anionic bridging linkers (as donors) along with complementary cationic metal-containing subunits (as acceptors). In recent years, Das and coworkers have also described several pyz motif-containing neutral metallasupramolecular macrocycles that were conveniently synthesized using a ditopic dicationic acceptor tecton along with a ditopic and dianionic donor such

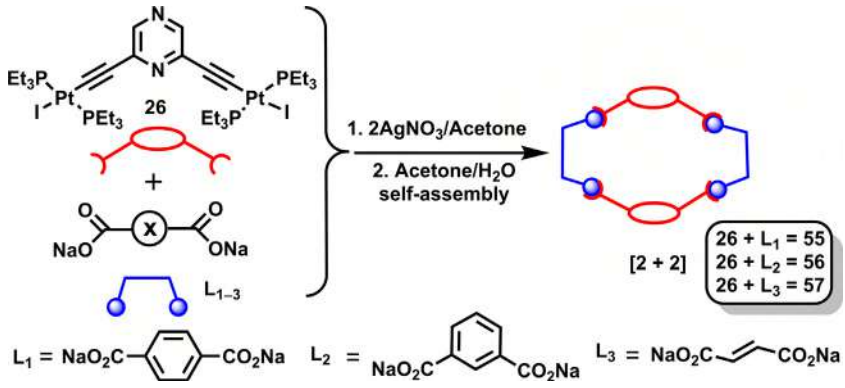

SCHEME 5.17 Self-assembly reactions for the synthesis of neutral metallasupramolecular macrocycles **55**–**57**.

as various dicarboxylates [28]. Considering the directional bonding approach, [40,41] reaction between **26** and anionic ditopic donor species (**L_1**–**L_3**) in equal stoichiometric ratio yielded neutral 2D macrocycles **55**–**57** (Scheme 5.17).

The dicarboxylates used in these reactions were either terephthalate, isophthalate, or fumarate in the form of their sodium salts dissolved in water. These products (**55**−**57**) were obtained as white solids that were characterized using multinuclear NMR and mass spectrometry. ^{1}H-DOSY NMR confirmed the exclusively formation of a single product in each self-assembly reaction. Further, shape and size of each macrocycle were predicted by PM6 semiempirical molecular orbital method. These pyz containing macrocycles act as a host for the nitroaromatic guests such as DNT and PA molecules. Host–guest chemistry was studied using ITC.

Another fascinating example of a set of three neutral and discrete hexagonal [2 + 2] macrocycles **58**–**60** obtained from using the semirigid and ditopic Pt(II)-based acceptor tecton **44** as shown in Scheme 5.18 [42].

These macrocyclic species **58**–**60** with hexagonal cavities are nanoscalar dimensional. The authors examined the nature and extent of interactions of these neutral metallacycles (**58**–**60**) with DNA. Experimental data lead to the conclusion that **58**–**60** were not able to intercalate into DNA or exhibit any noticeable nuclease activity. The authors propose shielding of Pt(II) centers in the neutral discrete macrocyclic species as the reason for the poor/negligible interaction. The examples described so far are those of pyz-based macrocycles obtained from rigid or semirigid tectons. In the next paragraph, few examples of flexible pyz-based tectons will be mentioned along with their applications in coordination-driven self-assembly reactions.

Molecule **61** is an example of a flexible pyz-based ditopic platinum(II) organometallic tecton and is structurally flexible compared to other pyz derived

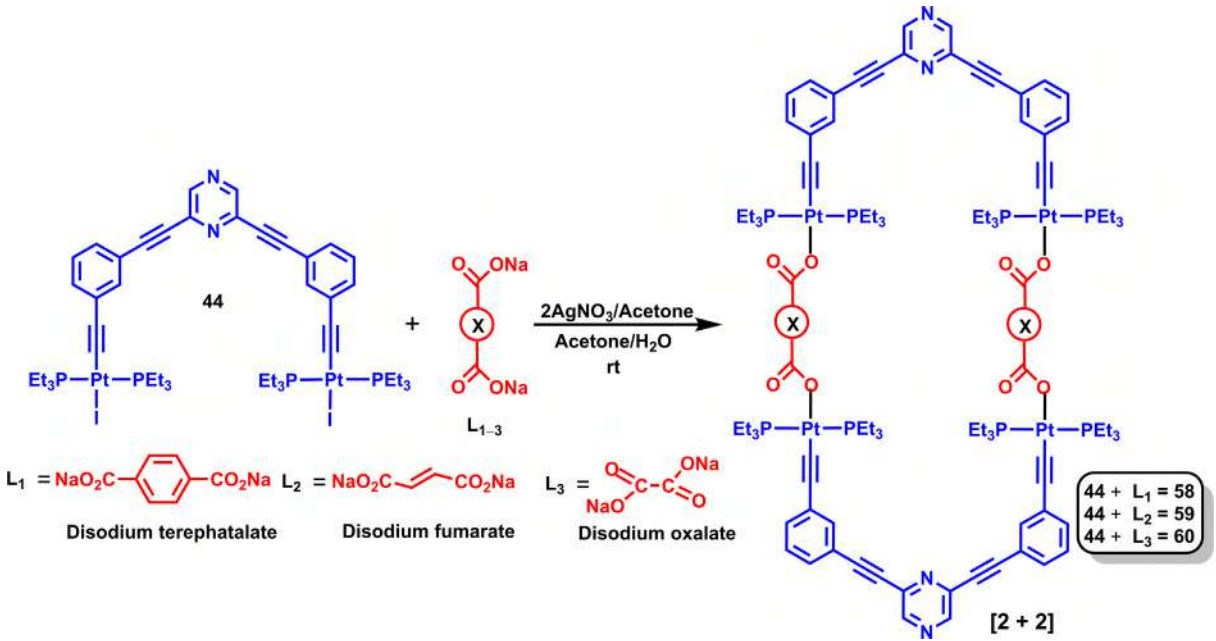

SCHEME 5.18 [2 + 2] self-assembly of neutral metallamacrocycles **58–60** using pyz-based Pt(II) acceptor tecton and dicarboxylate anions ($\mathbf{L_1}$–$\mathbf{L_3}$).

Pt(II)-tectons mentioned earlier in the chapter [43]. The presence of ether functional group joining the pyz core and peripheral entity, introduces the flexibility in the resultant molecules. In case of flexible ligands, the bite angle between the reactive sites of the multitopic tecton is not fixed due to bond rotations involving sp^3 hybridized centers (such as ethereal oxygen). The use of flexible tectons is rare in coordination-driven self-assembly reactions, and only a handful of examples exist, wherein discrete supramolecules have been synthesized using flexible linkers. This is because the inherent flexibility of these linkers renders them less predictable in such reactions. Therefore, it is difficult to predict the dimensions of the resulting supramolecular framework. The use of flexible linkers may lead to the formation of discrete as well as infinite/nondiscrete structures. Therefore, it is more challenging to use flexible subunits in self-assembly of finite structures. The ability of **61** to yield discrete macrocycles in self-assembly reactions was tested by reacting it with various dicarboxylates $\mathbf{L_1}$–$\mathbf{L_3}$ in equimolar concentrations (Scheme 5.19).

In each reaction, a single product was formed in high isolated yields. Using NMR and MS, the products were identified as neutral [2 + 2] pyz incorporated platinacycles **62**–**64**. Using DFT method, the shape and dimensions of **62**–**64** could be predicted. Further, host–guest chemistry of **61** was tested with PA using ITC data. Other analogous examples of a flexible molecule are reported in literature [44] for obtaining discrete pyz-based and Pt(II)-incorporated metallacycles.

5.6 Rings and cages

Few representative examples have been chosen for this section. Jana et al. reported synthesis and characterization of three discrete and neutral Fe(II)/Pt(II) heterobimetallic SCCs **65**–**67** by employing Pt(II) acceptor tectons of different bite angles (0°, 120°, and 180°) in conjugation with 1,1′-ferrocenedicarboxylate as a flexible donor tecton (Fig. 5.6) [45].

The ditopic donor is rotationally flexible due to the presence of ferrocene unit. In each reaction, most entropically favored ensemble was formed as the exclusive product in high yields. Cyclic voltammetry experiments were carried out to investigate the electrochemical response of Fe(II)/Pt(II) heterobimetallic SCCs. Moreover, authors have studied the interaction of tectons and the macrocycles with carbon quantum dots (CD). Experimental data suggested that macrocycles affected the fluorescence quenching of CDs, which was an evidence of their interaction with CDs. Authors also conclude that the Pt(II) bite angles of the acceptor tectons (which is different in the organometallic clips used) in these SCCs play a crucial role in the inefficient quenching of fluorescence property of CD.

Several interesting “pillar-based Pt-cage” compounds were reported by Fujita et al., wherein pyz is an important component [46,47]. The cages **68** and **69**

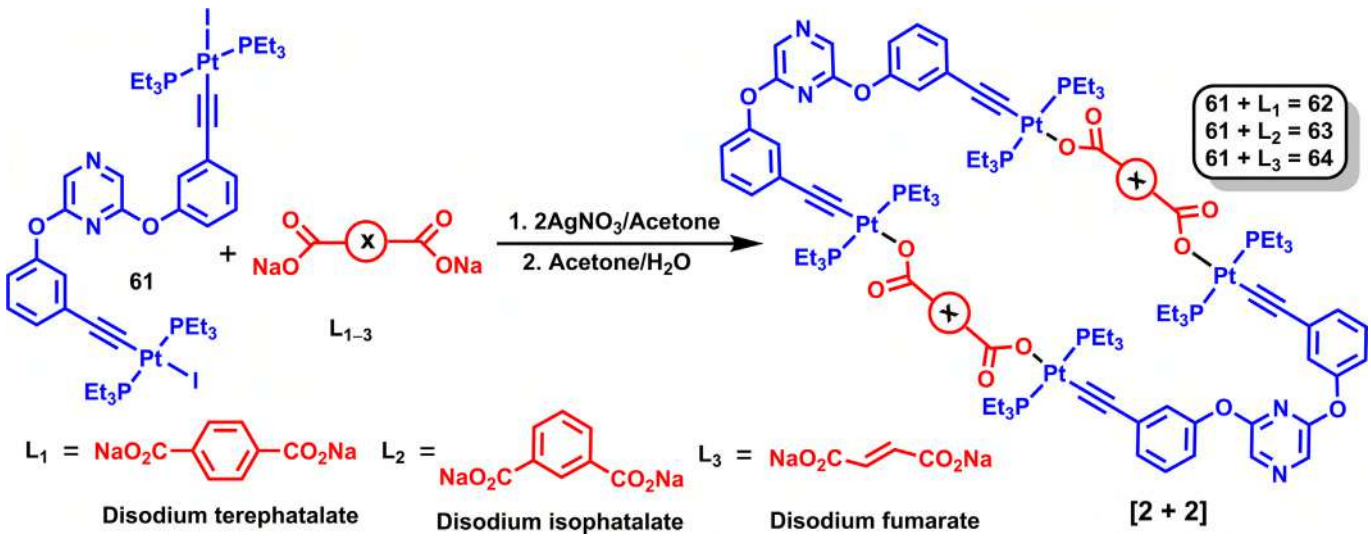

SCHEME 5.19 [2 + 2] self-assembly of macrocycles **62–64** using pyz-based Pt(II) acceptor tecton.

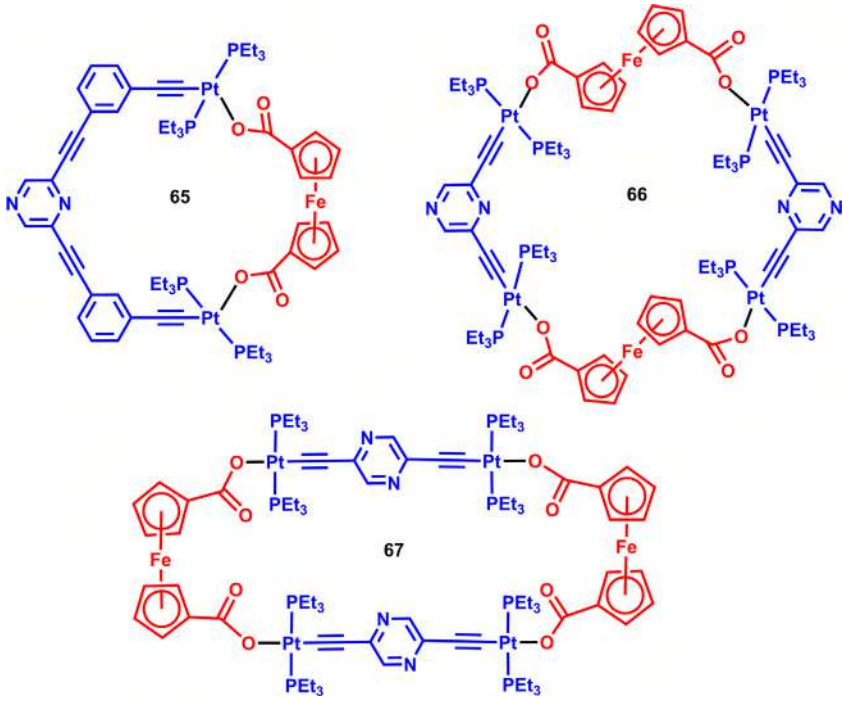

FIGURE 5.6 Ferrocene-based macrocycles **65**–**67**.

were self-assembled using three-component, namely tris(4-pyridyl)triazine, pyz, and [Pt(diamine)]$(NO_3)_2$ in 2:3:6 ratio in an aqueous medium (Scheme 5.20).

In these metallacages, pyz acts as the connecting pillar between the two panels/discs formed by the planar triazine derivative. Pt(II) units coordinate with N atoms of both pyz- and triazine-based connectors. The cage **68** acts as hosts by accommodating a nucleotide base pair (AMP•UMP) in its confined environment resulting in the formation of a complex **68**⊃(AMP·UMP) (⊃ denotes enclathration) in an aqueous solution (Scheme 5.21). An upfield shift of the nucleobase hydrogens in the ^{1}H NMR spectrum indicated that the presence of nucleobase moieties inside the cavity. The observed upfield shift of these hydrogens is due to their shielding by the aromatic panels. Favorable supramolecular interactions (electrostatic interactions, π–π stacking, and hydrophobic interactions) between the anionic nucleotides (guests) and the cationic metallacage are responsible for the facile enclathration of AMP·UMP base pair.

5.7 Conclusions and outlook

In the last two decades, substantial progress has been made in the field of coordination-driven self-assembly. In the early stages, Pd(II)- and Pt(II)-based

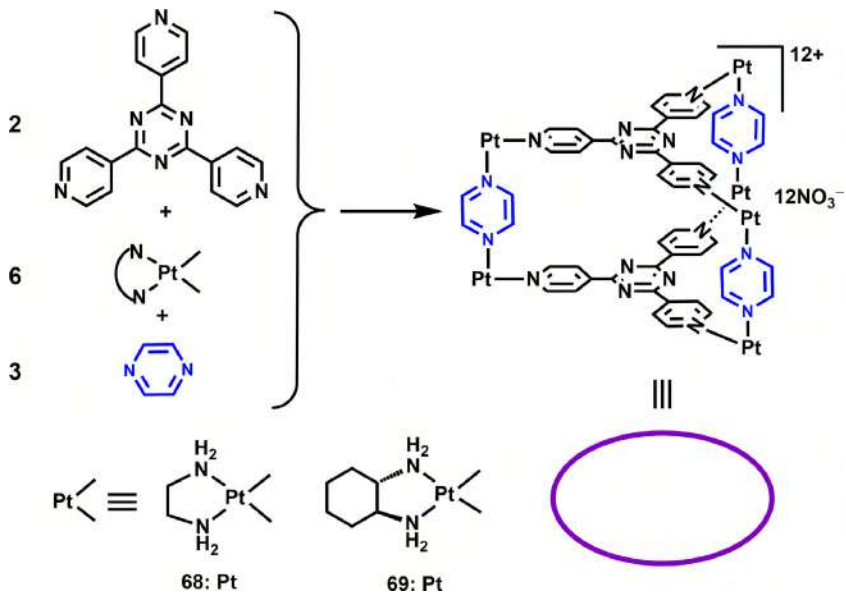

SCHEME 5.20 Synthesis of Pt-based pillared coordination cages **68** and **69**.

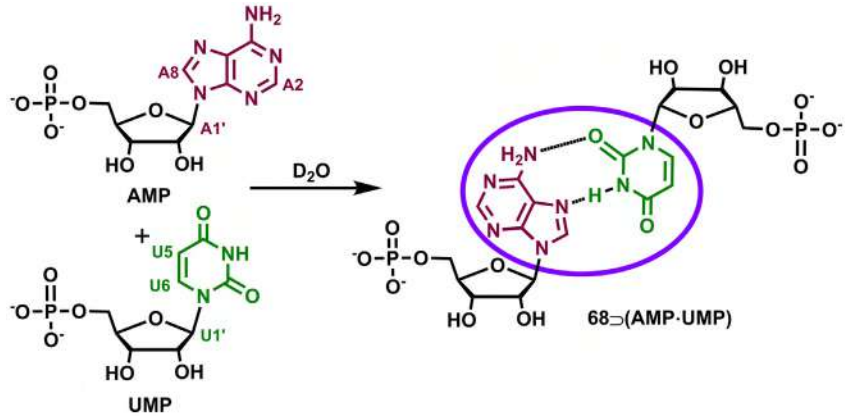

SCHEME 5.21 Formation of host–guest complex **68⊃(AMP·UMP)**.

acceptor tectons were most popular for the design of discrete supramolecular ensembles (macrocycles and cages). However, as the field progressed, other transition metals as well as diverse structural motifs were introduced in the design of acceptor and donor tectons, respectively. Pyrazine is one such motif that was incorporated in both donor and acceptor tectons. The use of pyrazine and its derivatives in the design of molecular tectons for supramolecular self-assembly reactions is a rapidly emerging field in contemporary research, as witnessed from literature reports. In this chapter, the reader is made aware of

the self-assembly protocol used in the design of finite closed systems of various shapes (viz. triangles, squares, rectangles, and hexagons, etc.). However, the main theme of this chapter is to highlight the use of pyrazine in such reactions. Overall, this chapter is framed in such a way as to deliver a flavor of both early-stage work to the recent development with its underlying principles. The potential application of these pyrazine motif-containing supramolecular systems has also been discussed. Although several structures have been synthesized so far, the focus of future research must be to explore their practical applications to a greater extent. Anticipating the research growth in the domain of coordination-driven self-assembly, this chapter aims to motivate readers to make a significant contribution in the interesting field of supramolecular chemistry in the near future.

Acknowledgments

This chapter is dedicated to Peter J. Stang, who is the David P. Gardner Distinguish Professor of Chemistry at the University of Utah. He also served as the editor of *J. Am. Chem. Soc.* S.K. is grateful to CSIR (New Delhi) for Research Associate fellowship (File # 09/1023(0036)/2020-EMR-I).

References

[1] W. Staedel, L. Rügheimer, Ueber die Einwirkung von Ammoniak auf Chloracetylbenzol, Ber. deutsch. chem. Gesellschaft 9 (1876) 563–564.

[2] M. Dolezal, J. Zitko, Pyrazine derivatives: a patent review (June 2012–present), Exp. Opin. Ther. Pat. 25 (2015) 33–47.

[3] S.B. Ferreira, C.R. Kaiser, Pyrazine derivatives: a patent review (2008–present), Exp. Opin. Ther. Pat. 22 (2012) 1033–1051.

[4] C.H.S. Lima, M.G.M.O. Henriques, A.L.P. Candea, M.C.S. Lourenco, F.A.F.M. Bezerra, M.L. Ferreira, C.R. Kaiser, M.V.N.d. Souza, Synthesis and antimycobacterial evaluation of N-(*E*)-heteroaromaticpyrazine-2-carbohydrazide derivatives, Med. Chem. 7 (2011) 245–249.

[5] L.E. Seitz, W.J. Suling, R.C. Reynolds, Synthesis and antimycobacterial activity of pyrazine and quinoxaline derivatives, J. Med. Chem. 45 (2002) 5604–5606.

[6] M. Czerny, W. Grosch, Potent odorants of raw Arabica coffee. Their changes during roasting, J. Agric. Food Chem. 48 (2000) 868–872.

[7] J. Marais, J.J. Hunter, P.D. Haasbroek, Effect of canopy microclimate season and region on Sauvignon blanc grape composition and wine quality, South Afr. J. Enol. Viticult. 20 (1999) 19–30.

[8] F.B. Mortzfeld, C. Hashem, K. Vranková, M. Winkler, F. Rudroff, Pyrazines: synthesis and industrial application of these valuable flavor and fragrance compounds, Biotechnol. J. 15 (2020) 2000064.

[9] K. Iida, K. Itoh, Y. Kumagai, R. Oyasu, K. Hattori, K. Kawai, T. Shimazui, H. Akaza, M. Yamamoto, Nrf2 is essential for the chemopreventive efficacy of oltipraz against urinary bladder carcinogenesis, Cancer Res. 64 (2004) 6424–6431.

[10] G. Bonanni, M. Ciccariello, P. Mancini, V. Pace, G. Sagliaschi, Concomitant ceco-appendicular and urinary tuberculosis. Description of two rare cases: physiopathological and diagnostic remarks, Riv. Eur. Sci. Med. Farmacol. 15 (1993) 171–174.

[11] D.L. Trump, H. Payne, K. Miller, J.S. de Bono, J. Stephenson Iii, H.A. Burris Iii, F. Nathan, M. Taboada, T. Morris, A. Hubner, Preliminary study of the specific endothelin a receptor antagonist zibotentan in combination with docetaxel in patients with metastatic castration-resistant prostate cancer, J. Prostate 71 (2011) 1264–1275.

[12] K.D. Tripathy, Essentials of Medical Pharmacology, sixth ed., Jaypee Brothers Medical Publishers (P) Ltd., New Delhi, 2008.

[13] B. Lippert, P.J. Sanz Miguel, Metallatriangles and metallasquares: the diversity behind structurally characterized examples and the crucial role of ligand symmetry, Chem. Soc. Rev. 40 (2011) 4475–4487.

[14] X.-Y. Yu, M. Maekawa, M. Kondo, S. Kitagawa, G.-X. Jin, Syntheses and crystal structures of novel di- and trinuclear rhodium complexes bridged by pyrazine, Chem. Lett. 30 (2001) 168–169.

[15] M. Schweiger, S.R. Seidel, A.M. Arif, P.J. Stang, The self-assembly of an unexpected, unique supramolecular triangle composed of rigid subunits, Angew. Chem. Int. Ed. 40 (2001) 3467–3469.

[16] E. Zangrando, M. Casanova, E. Alessio, Trinuclear metallacycles: metallatriangles and much more, Chem. Rev. 108 (2008) 4979–5013.

[17] S. Derossi, M. Casanova, E. Iengo, E. Zangrando, M. Stener, E. Alessio, Self-assembled metallacycles with pyrazine edges: a new example in which the unexpected molecular triangle prevails over the expected molecular square, Inorg. Chem. 46 (2007) 11243–11253.

[18] P.J. Stang, D.H. Cao, Transition metal based cationic molecular boxes. Self-assembly of macrocyclic platinum(II) and palladium(II) tetranuclear complexes, J. Am. Chem. Soc. 116 (1994) 4981–4982.

[19] S. Karthikeyan, K. Velavan, R. Sathishkumar, B. Varghese, B. Manimaran, Self-assembly of manganese(I)-based molecular squares: synthesis and spectroscopic and structural characterization, Organometallics 31 (2012) 1953–1957.

[20] T. Rajendran, B. Manimaran, F.-Y. Lee, P.-J. Chen, S.-C. Lin, G.-H. Lee, S.-M. Peng, Y.-J. Chen, K.-L. Lu, Self-assembly of tetrametallic square $[Re_4(CO)_{12}Br_4(\mu\text{-}pz)_4]$ (pz = pyrazine) from $[Re(CO)_4Br(pz)]$. A mechanistic approach, J. Chem. Soc. Dalton Trans. (2001) 3346–3351.

[21] V.C. Lau, L.A. Berben, J.R. Long, $[(Cyclen)_4Ru_4(pz)_4]^{9+}$: a Creutz−Taube square, J. Am. Chem. Soc. 124 (2002) 9042–9043.

[22] K. Kumazawa, K. Biradha, T. Kusukawa, T. Okano, M. Fujita, Multicomponent assembly of a pyrazine-pillared coordination cage that selectively binds planar guests by intercalation, Angew. Chem. Int. Ed. 42 (2003) 3909–3913.

[23] A. Pitto-Barry, N.P.E. Barry, V. Russo, B. Heinrich, B. Donnio, B. Therrien, R. Deschenaux, Designing supramolecular liquid-crystalline hybrids from pyrenyl-containing dendrimers and arene ruthenium metallacycles, J. Am. Chem. Soc. 136 (2014) 17616–17625.

[24] C. Ashok Kumar, R. Nagarajaprakash, B. Ramakrishna, B. Manimaran, Self-assembly of thiolato-bridged manganese(I)-based metallarectangles: one-pot synthesis and structural characterization, Inorg. Chem. 54 (2015) 8406–8414.

[25] Y.-F. Han, Y. Fei, G.-X. Jin, Self-assembled half-sandwich Ir, Rh-based organometallic molecular boxes for reversible trapping of halocarbon molecules, Dalton Trans. 39 (2010) 3976–3984.

[26] J.-Y. Wu, P. Thanasekaran, Y.-W. Cheng, C.-C. Lee, B. Manimaran, T. Rajendran, R.-T. Liao, G.-H. Lee, S.-M. Peng, K.-L. Lu, Unprecedented reduction of 2,2′-bipyrimidine in a one-pot synthesis of neutral rhenium(I)-based molecular rectangles, Organometallics 27 (2008) 2141–2144.

[27] G.-Y. Wu, L.-J. Chen, L. Xu, X.-L. Zhao, H.-B. Yang, Construction of supramolecular hexagonal metallacycles via coordination-driven self-assembly: structure, properties and application, Coord. Chem. Rev. 369 (2018) 39–75.

[28] S. Bhowmick, S. Chakraborty, A. Das, P.R. Rajamohanan, N. Das, Pyrazine-based organometallic complex: synthesis, characterization, and supramolecular chemistry, Inorg. Chem. 54 (2015) 2543–2550.

[29] S. Bhowmick, S. Chakraborty, A. Das, S. Nallapeta, N. Das, Pyrazine motif containing hexagonal macrocycles: synthesis, characterization, and host–guest chemistry with nitro aromatics, Inorg. Chem. 54 (2015) 8994–9001.

[30] S. Bhowmick, A. Jana, K. Singh, P. Gupta, A. Gangrade, B.B. Mandal, N. Das, Coordination-driven self-assembly of ionic irregular hexagonal metallamacrocycles via an organometallic clip and their cytotoxicity potency, Inorg. Chem. 57 (2018) 3615–3625.

[31] S. Shanmugaraju, S.A. Joshi, P.S. Mukherjee, Self-assembly of metallamacrocycles using a dinuclear organometallic acceptor: synthesis, characterization, and sensing study, Inorg. Chem. 50 (2011) 11736–11745.

[32] S. Shanmugaraju, D. Samanta, B. Gole, P.S. Mukherjee, Coordination-driven self-assembly of 2D-metallamacrocycles using a shape-selective Pt^{II}2-organometallic 90° acceptor: design, synthesis and sensing study, Dalton Trans. 40 (2011) 12333–12341.

[33] A. Jana, S. Bhowmick, S. Kumar, K. Singh, P. Garg, N. Das, Self-assembly of Pt(II) based nanoscalar ionic hexagons and their anticancer potencies, Inorg. Chim. Acta 484 (2019) 19–26.

[34] J.J.P. Stewart, Optimization of parameters for semiempirical methods V: modification of NDDO approximations and application to 70 elements, J. Mol. Model. 13 (2007) 1173–1213.

[35] S. Bhowmick, S. Chakraborty, S.R. Marri, J.N. Behera, N. Das, Pyrazine-based donor tectons: synthesis, self-assembly and characterization, RSC Adv. 6 (2016) 8992–9001.

[36] J.-C. Wu, L. Zhao, D.-X. Wang, M.-X. Wang, Structural diversity in coordination self-assembled networks of a multimodal ligand azacalix[4]pyrazine, Inorg. Chem. 51 (2012) 3860–3867.

[37] K. Singh, S. Kumari, A. Jana, P. Das, N. Das, A Pt(II)-based hexagonal ionic supramolecular coordination complex and its DNA interactions, ChemistrySelect 4 (2019) 8255–8262.

[38] K. Singh, A. Gangrade, S. Bhowmick, A. Jana, B.B. Mandal, N. Das, Self-assembly of a [1 + 1] ionic hexagonal macrocycle and its antiproliferative activity, Front. Chem. 6 (2018) 87.

[39] W.-J. Hu, L.-Q. Liu, M.-L. Ma, X.-L. Zhao, Y.A. Liu, X.-Q. Mi, B. Jiang, K. Wen, A trigonal prismatic ligand in the metal-mediated self-assembly of one- and two-dimensional metallosupramolecular polymers, Inorg. Chem. 52 (2013) 9309–9319.

[40] R. Chakrabarty, P.S. Mukherjee, P.J. Stang, Supramolecular coordination: self-assembly of finite two- and three-dimensional ensembles, Chem. Rev. 111 (2011) 6810–6918.

[41] S. Leininger, B. Olenyuk, P.J. Stang, Self-assembly of discrete cyclic nanostructures mediated by transition metals, Chem. Rev. 100 (2000) 853–908.

[42] K. Singh, S. Kumari, A. Jana, S. Bhowmick, P. Das, N. Das, Self-assembled neutral [2+2] platinacycles showing minimal DNA interactions, Polyhedron 157 (2019) 267–275.

[43] A. Jana, S. Bhowmick, S. Kaur, H.K. Kashyap, N. Das, Design of a flexible organometallic tecton: host–guest chemistry with picric acid and self-assembly of platinum macrocycles, Dalton Trans. 46 (2017) 1986–1995.

[44] A. Jana, N. Das, Self-assembly of [2+2] platina macrocycles using a flexible organometallic clip, ChemistrySelect 2 (2017) 4099–4105.

[45] A. Jana, S. Mandal, K. Singh, P. Das, N. Das, Heterobimetallic (Fe^{II}/Pt^{II})-based supramolecular coordination complexes using 1,1′-ferrocene dicarboxylate: self-assembly and interaction with carbon dots, Inorg. Chem. 58 (2019) 2042–2053.

[46] T. Sawada, M. Yoshizawa, S. Sato, M. Fujita, Minimal nucleotide duplex formation in water through enclathration in self-assembled hosts, Nat. Chem. 1 (2009) 53–56.

[47] T. Sawada, M. Fujita, A single Watson−Crick G·C base pair in water: aqueous hydrogen bonds in hydrophobic cavities, J. Am. Chem. Soc. 132 (2010) 7194–7201.

Chapter 6

Rhenium (I)-based supramolecular coordination complexes: Synthesis and functional properties

K.R. Soumya*, Isha Mishra*, Moon Kedia*, Upasana Phukon*, Reema Borkar* and Malaichamy Sathiyendiran*
School of Chemistry, University of Hyderabad, Hyderabad, India

6.1 Introduction

Supramolecular coordination complexes (SCCs) assembled using coordination-driven self-assembly approaches are well-defined discrete cyclic 2D and/or 3D architectures that can have widespread applications in various fields of chemistry and biology due to the presence of metal complex unit and the arrangement of organic building frameworks [1–28]. The spontaneous formation of metal–ligand bond between metal acceptors and organic donors provides several synthetic methodologies to develop these SCCs. Until now, a series of rationally designed discrete SCCs with various shapes including polygonal triangle, square, rectangle, higher polygonal 2D architectures and polyhedral 3D architectures via coordination-driven self-assembly are reported by several research groups. The partially protected *fac*-$Re(CO)_3$ core-based SCCs represent a unique class of cyclic assemblies. The key properties associated with these complexes are thermal, kinetic and photo-stability, robustness and metal to ligand charge transfer absorptions and emissions. Re(I)-based cyclic supramolecular architectures with various shapes including dinuclear, trinuclear, tetranuclear squares, rectangles, gondolas, bowls, calixarene, bicycles, hexanuclear prisms, spheroids, wheel, and octanuclear prisms are found in the literature [10–28]. The dimension, flexibility, shape, and intrinsic properties of these SCCs can be easily tuned by modifying the organic ligand framework. The complexes often serve as promising candidates for applications in molecular recognition, catalysis, bioimaging, sensors,

* All authors contributed equally.

Supramolecular Coordination Complexes: Design, Synthesis, and Applications.
DOI: https://doi.org/10.1016/B978-0-323-90582-4.00014-2

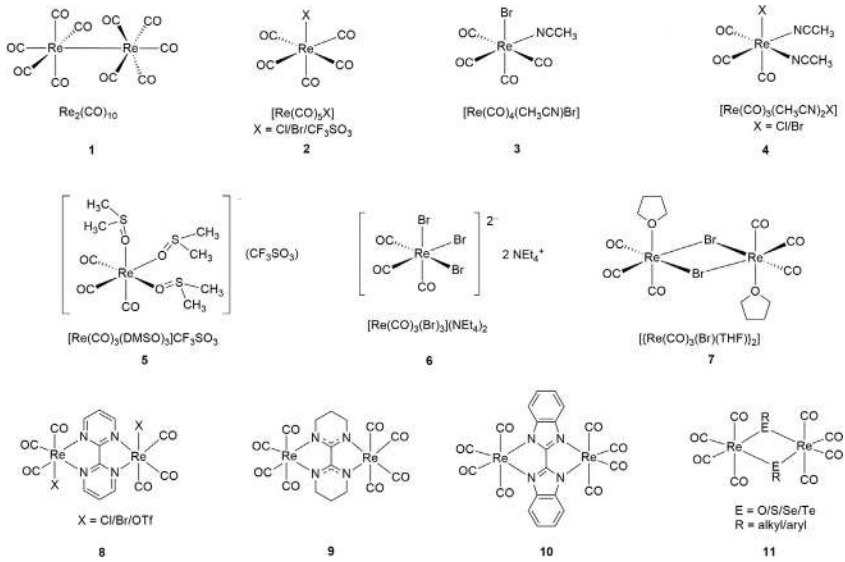

CHART 6.1 Metal precursors for construction of SCCs.

anticancer agents, and molecular devices [1–9]. Herein, the developments of coordination-driven self-assembly using *fac*-$Re(CO)_3$ core and organic building blocks are discussed. The chapter highlights recent reports on well-defined cyclic structures, key design principles, and functional properties with the aim to show their utility in building new SCCs using predesigned organic ligands and their potential for various scientific fields. In addition, few synthetic methodologies known earlier are also included here as those approaches can have potential for making new complexes with interesting properties and applications.

6.2 Metal precursors for supramolecular architectures

The rhenium carbonyl complexes shown in Chart 6.1 can be used to self-assemble ionic, neutral, homoleptic, and/or heteroleptic supramolecular coordination complexes. Complexes **1–6** are commercially available, whereas, complexes **2–9** can be easily prepared from $Re_2(CO)_{10}$ using either one-step or two-steps synthetic approach [3,29–33]. In general, high reaction temperature is required while using $Re_2(CO)_{10}$ as metal precursor. Treatment of mononuclear complexes **2–6** and dinuclear complexes **1** and **7–11** with ligands in the presence of solvents (acetone/THF/toluene) results in the formation of desired SCCs with the elimination of carbon monoxide [10–28]. While using halide-based complexes, silver trifluoromethanesulfonate is added, this provides silver halide precipitate with the labile triflate ancillary ligands coordinated to the metal center [30]. Bromide bridged complexes, triflate-based coordination complexes, and

DMSO coordinated complexes can serve as good metal precursors for making SCCs at room temperature and/or when the thermally unstable ligands are used [29–33].

6.3 Organic ligands as sources for anionic building frameworks

The ligands having –N, –O, or –S donor sites as shown in Chart 6.2 can be used as sources of anionic building units in making *fac*-$[Re(CO)_3]^+$ core-based SCCs [18,34–45]. Among bis-chelating ligands, L^1–L^{20}; L^1–L^9, and L^{15} are good candidates for constructing cavity containing SCCs whereas, L^{10}–L^{14}, L^{16}–L^{20}, and L^{24}–L^{29} can be used for $\pi\cdots\pi$ stacked SCCs [34–45]. Multiple cavity containing SCCs can also be obtained from L^{21}–L^{23} [21–26,28]. The topology and properties of SCCs such as cavity size, solubility, and

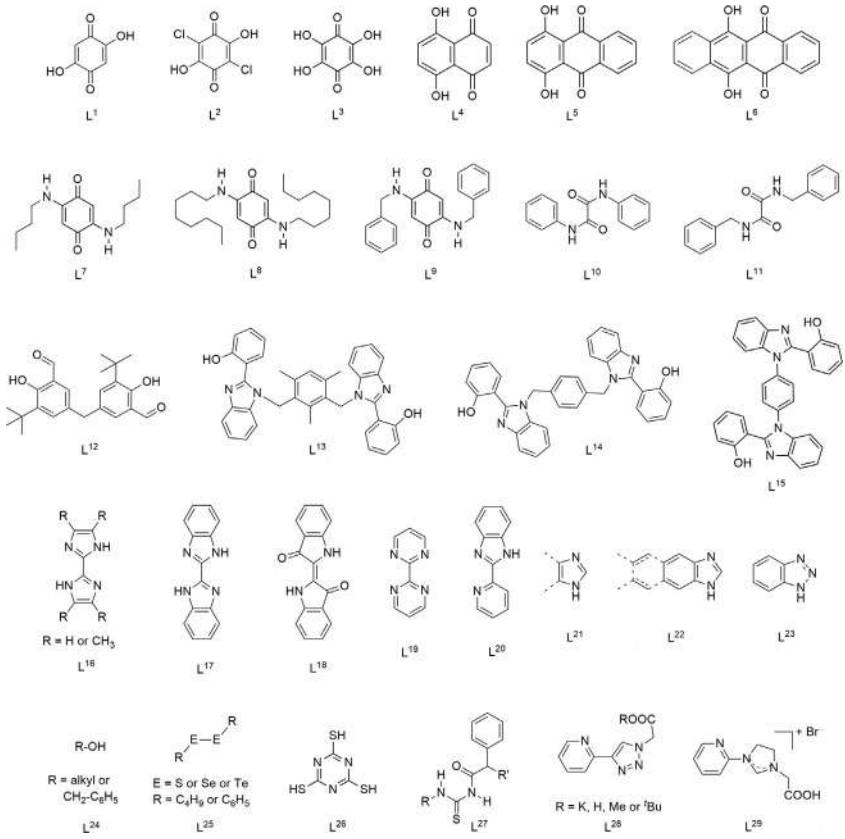

CHART 6.2 Organic building blocks for ligand framework.

luminescence can be tuned by modulating the organic functionalities on ligand motifs.

6.4 Flexible bidentate N,N donors with ether, ester, or amide functionalities and its SCCs

The ligands containing polyether, ester or amide functionalities along with alkyl or aryl spacer motifs bearing pyridyl pendant for coordination to metal centers are ideal choice to construct macrocyclic architectures having various shapes and size. Ligands, L^{30}–L^{32} can provide crown ether type SCCs [35,46,47], whereas ligands L^{33}–L^{40} have been utilized to synthesize hammock shaped, rectangular or square like metallacycles [41,48,49]. In addition, partial rigidity can be imparted to SCCs by incorporating additional rigid framework (phenyl or biphenyl units) along with polyether, amide, or ester functionalities Chart 6.3. The incorporation of functional groups and/or spacer that anchors the functional groups in the ligands may play a crucial role in modulating the shape, size, and properties of the final assembly. The intrinsic properties associated with *fac*-$[Re(CO)_3]^+$ and *fac*-$[Re(CO)_3X]$ (where X = Cl/Br) core are suitable to make luminescent SCCs analogous to crown ether type self-assembly which can have potential utility as sensors, catalysts, in host–guest chemistry and can mimic the natural systems [1–28].

Five types of SCCs, *fac*-$[\{Re(CO)_3Br\}_2L']$ (**12**), *fac*-$[\{Re(CO)_3(BCL)\}_2L']$ (**13, 14**), *fac*-$[\{Re(CO)_3Br\}_2L'_2]$ (**15**), *fac*-$[\{Re(CO)_3(ER)\}_4L'_2]$ (**16**), and *fac*-$[\{Re(CO)_3(BCL)\}_2L'_2]$ (**17**) (where BCL = bis-chelating ligand (N^O) and L′ = X-L-X = N,N donors with ether, ester or amide groups), can be self-assembled by simple combination of tricarbonylrhenium(I) complexes and dipyridyl ligands with or without anionic ancillary ligands [46–49]. The bridging

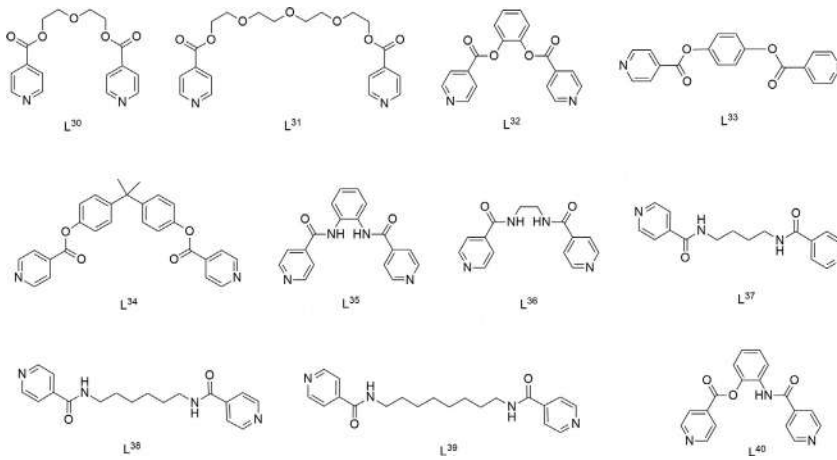

CHART 6.3 Flexible bidentate ligands with ether, ester, and/or amide functionalities.

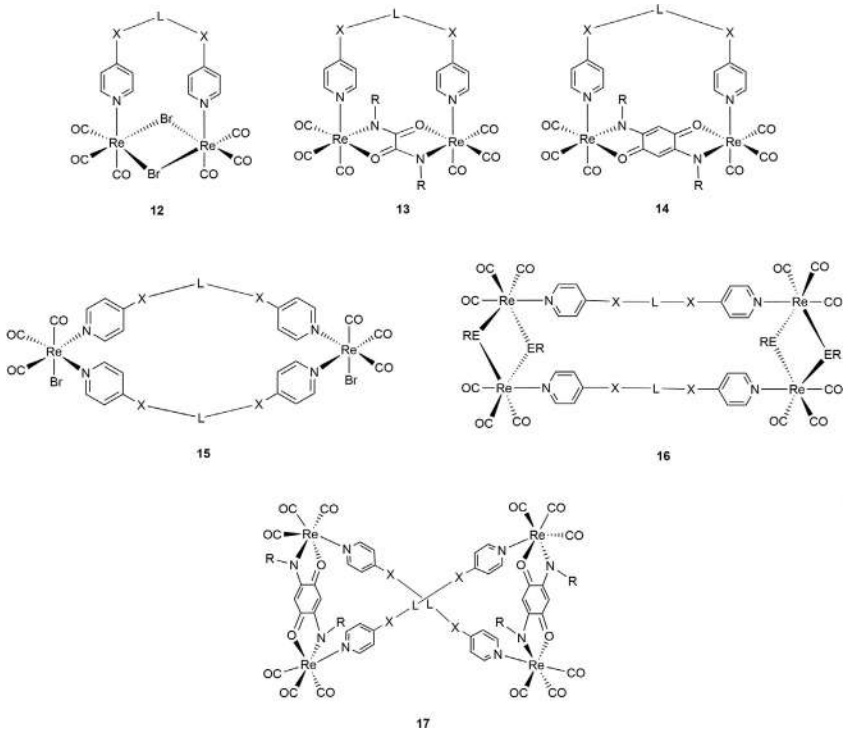

FIGURE 6.1 Chem draw representation of complexes **12–17**.

ligands dictate the size of the cavity of SCCs **12–14** [46–49]. The halide-bridged ligands provide the $\pi\cdots\pi$ stacked SCC (**12**) without any inner cavity whereas the quinone-based bridging ligands provide SCCs (**13,14**) with cavity suitable to accommodate the solvent/guest molecules/ions. The cavity containing SCCs with recognition units (ether, ester or amide groups) display effective host–guest interactions with aromatic amines via noncovalent contacts. The size, shape, and properties of the complexes containing alkyl spacers can be varied upon changing the chain length. The complex **15** synthesized using L^{37}–L^{39} exhibits good photophysical properties with MLCT in the region 544–558 nm. The anticancer studies for these complexes suggested that upon increasing the chain length, the hydrophobicity increases which results in enhanced anticancer activity [49] (Fig. 6.1).

6.5 Neutral rigid pyridine-based ditopic- and tritopic ligands and its SCCs

Neutral rigid ditopic nitrogen donor ligands (Chart 6.4) are highly used as organic building blocks for making molecular squares, $\pi\cdots\pi$ stacked molecular

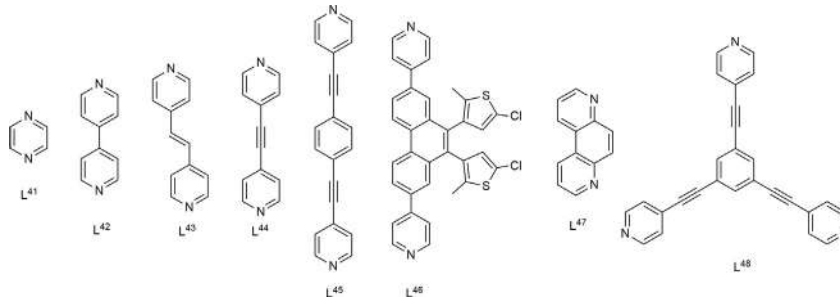

CHART 6.4 Neutral ditopic and tritopic ligands with pyridyl motifs [41,42,50].

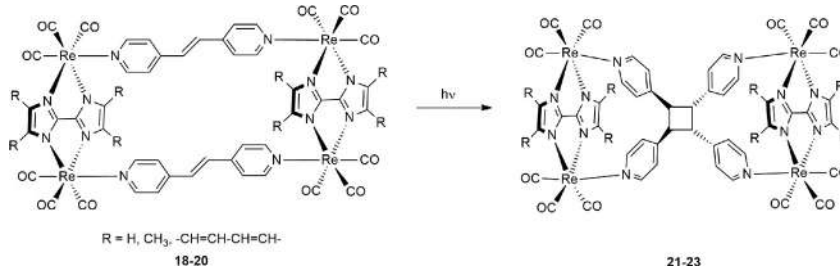

SCHEME 6.1 Photo responsive [2+2] cycloaddition reaction on molecular rectangles, **18–20** [39].

rectangles, cavity containing rectangles, prisms, and other 3D-architectures [18,19,24–26]. These SCCs can be obtained by the treatment of suitable orthogonal tritopic rhenium acceptor and ditopic nitrogen donors with other rigid ditopic ligands, hydroxyl/chalcogenalato bridge, and bis-chelating ligands.

The strategy of synthesizing $\pi\cdots\pi$ stacked molecular rectangles is a good method to bring two double bonds in close proximity for undergoing photo-induced [2+2] cycloaddition reactions without using any solvent [39]. This was nicely demonstrated in the molecular rectangles (**18–20**) (Scheme 6.1) containing two *trans*-1,2-bis(4-pyridyl)ethylene motif lying parallel to each other. Photo responsive molecular rectangle (**24**) can be obtained by using rigid photochromic ditopic nitrogen donors possessing photoactive unit as spacer or decorated on the spacer motif [51]. 1,2-Dithienylethene (DTE) motif containing molecular rectangle displays reversible photochromic rearrangement in solution and can be interconverted by UV and visible light (Scheme 6.2).

Trithiocyanuric acid (H_3-L^{49}) is recently introduced as organic framework unit for neutral heteroleptic SCCs [43]. Unlike dihydroxyquinone-based bis-chelating ligands, fully deprotonated trianion L^{3-} acts as tris-chelating motif having four membered chelating cycles. The preparation of the SCCs can be achieved in two-steps synthetic approach. The treatment of H_3L with $Re_2(CO)_{10}$ in benzene at 160°C yields trinuclear tetracarbonylrhenium(I) complex [{$Re(CO)_4$}$_3$L] (**26**). The combination of the complex **26** (Scheme 6.3) with

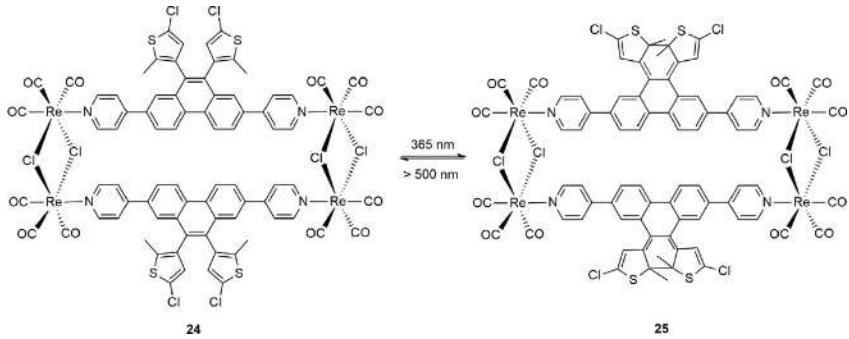

SCHEME 6.2 Photochromic arrangement in rectangle **24** upon irradiating UV–Vis light [51].

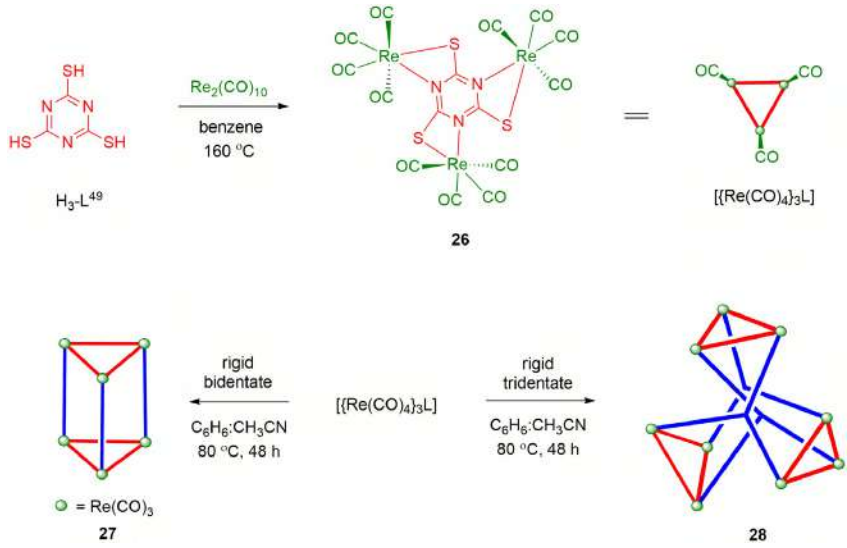

SCHEME 6.3 Synthetic approach for trinuclear tetracarbonylrhenium complex **26** and schematic representation of trigonal prism **27** and nona-nuclear cage **28** [43].

rigid bidentate N-donor in the mixture of benzene and acetonitrile at elevated temperature (~80°C) resulted in hexanuclear trigonal prism (**27**) [43]. The width of the prism can be easily tuned by varying the length of the bidentate donor. The advantage of this precursor is that three aromatic units can be arranged in an edge-to-face fashion in the trigonal prism structure.

Neutral heteroleptic mononuclear complex **28** hitherto unknown cage can be prepared when the assembly unit is rigid tridentate ligand with coordination angle of 120° with complex **26** under same reaction conditions. Due to triple decker arrangement of the rigid tridentate ligands, the complex **28** acquires triangular star shape (Fig. 6.2) [43].

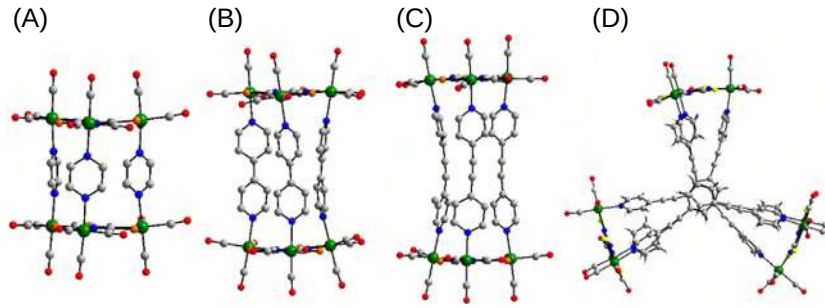

FIGURE 6.2 Molecular structure (ball and stick model); (A–C) Prisms, (D) Triangular star.

6.6 Neutral flexible ditopic P=O donor ligands and its SCCs

Phosphine oxide (P=O) donor-based neutral ditopic and tetratopic ligands are rarely used for making *fac*-$Re(CO)_3$-core-based SCCs. Recently, countable number of SCCs including binuclear and tetranuclear (**29**–**35**) (Figs. 6.3 and 6.4) are synthesized by the combination of $Re_2(CO)_{10}$, dihydroxyquinone-based chelating ligand and di- and tetra-topic phosphine (or) phosphine oxide donor under solvothermal reaction conditions (Schemes 6.4 and 6.5) [52,53].

The presence of oxygen and moisture in the solvent helps in the transformation of phosphine to phosphine oxide under thermal conditions. Direct use of phosphine oxide donor also results in the formation of similar complexes. Recently, complex **30** containing helicene as spacer with P=O anchors was reported. The complex serves as a chiral molecule, first example of this kind [53]. The typical helical arrangement of helicene moiety provides a boat-like conformation to the assembly. The presence of the spacer motifs; alkyl, aryl,

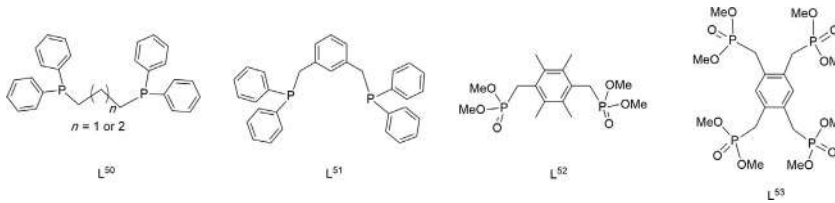

FIGURE 6.3 Chem draw representation of L^{50}–L^{53}.

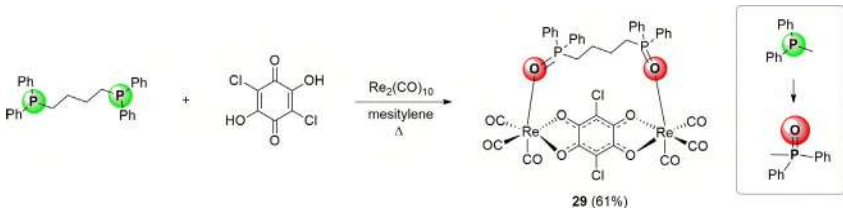

SCHEME 6.4 Synthetic approach for complex **29** [52].

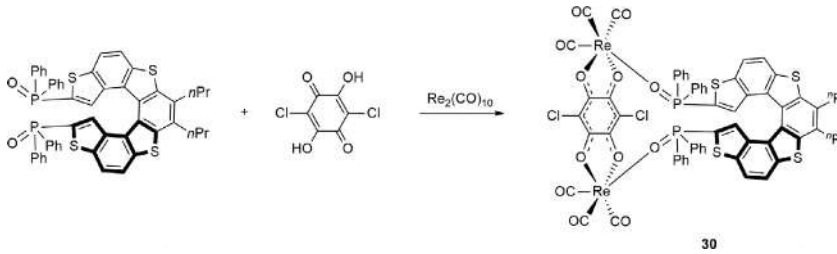

SCHEME 6.5 Synthetic approach for complex **30** [53].

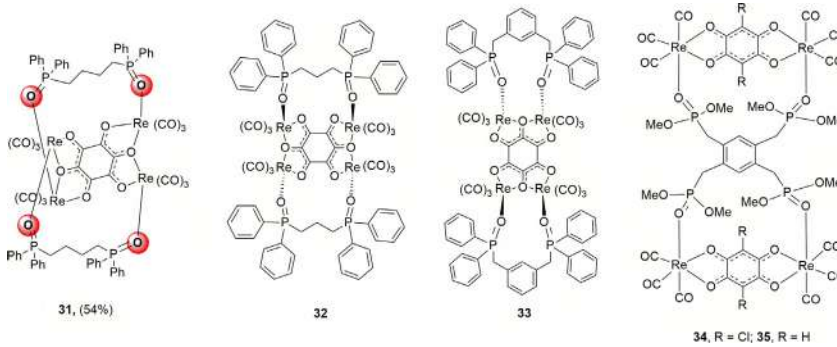

FIGURE 6.4 Chem draw representation of complexes **31**–**35**.

or fused aromatic motifs; and number of phosphine donors dictate the overall architecture and properties of the SCCs. In the above cases, the ancillary bis-chelating ligands are O,O-donors. By changing the bis-chelating donor to tris-/tetrakis-chelating donors, conjoined metallacycles can be obtained.

The absorption properties of the P=O donor-based SCCs are different from those of complexes obtained using benzimidazole-based nitrogen donors. These complexes display strong absorption in the visible region with significant red-shift as compared to the N-donors-based SCCs [34,52,53].

6.7 Neutral flexible tritopic N-donor ligands and its SCCs

The key factors in self-assembling SCCs are predesigning organic ligands and proper choice of metal precursors. Commonly, rigid ligands are more favorable for constructing SCCs; the coordination angle remains intact during the reaction, and in the final assembly. On contrary, the flexible ligands can have various conformations in solution depending upon the concentration, solvents, and reaction conditions. Although, the coordination angle of flexible organic ligands is less predictable, it provides SCCs with beneficial properties such as adaptability where cavity size can easily shrink or enlarge to have maximum noncovalent interactions. Recently, to control the flexibility of these ligands, rigid ancillary counterparts were used to assemble *fac*-$Re(CO)_3$ core-based SCCs [53–56].

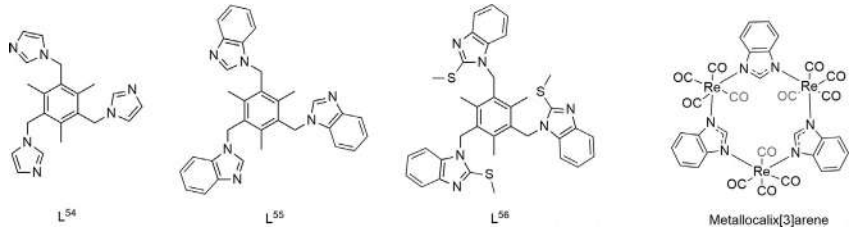

FIGURE 6.5 Chem draw representation of L^{54}-L^{56} and metallocalix[3]arene.

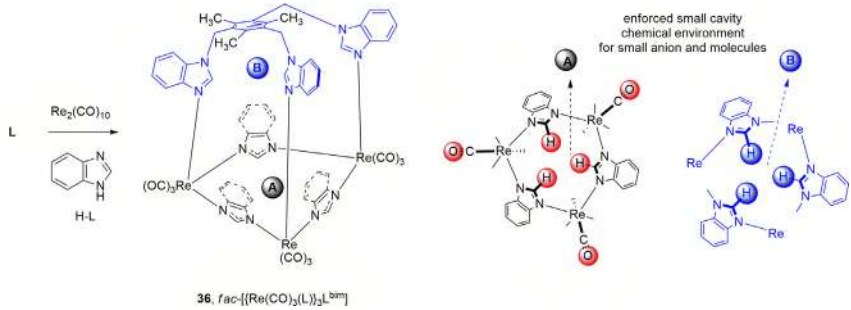

SCHEME 6.6 Synthetic approach for trinuclear cage **36** [12].

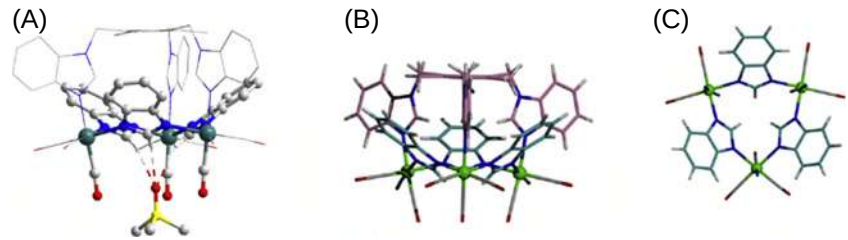

FIGURE 6.6 Molecular structure of (A) Cage **36** with DMSO guest molecule; (B) Cavity enforced.

The flexible tritopic- and poly-topic N-donors (Fig. 6.5) can be used to make SCCs with two or more molecular receptor units. For example, trinuclear cages similar to capped metallacalix[3]arene framework can be obtained by using benzimidazolyl-based tritopic ligand (L^{54}–L^{55}), benzimidazole/benzotriazole/imidazole/triazole and $Re_2(CO)_{10}$ via solvothermal one-pot approach (Scheme 6.6) [12]. The cages have two cavities, one endo- and one exocyclic, suitable to accommodate small anions and neutral guest molecules. The exocyclic cavity not only provides electron deficient three C–H donors but also provide electron rich oxygen from symmetrically arranged three carbonyl units. The molecular structure of the cage (**36**) with DMSO guest confirms that multiple noncovalent contacts stabilize the host:guest motif (Fig. 6.6). Both recognition units can be tuned by choosing desired heterocyclic units in tritopic ligands as well as rigid ligands.

6.8 Neutral flexible tetratopic N-donor ligands and its SCCs

The pyridyl, imidazolyl, or benzimidazolyl N-donor ligands are common class of organic building units for making flexible di-, tri-, tetra- or poly-topic ligands. The use of tetratopic ligands with a suitable rigid mono- or bi-dentate donor and Re(I) metal precursor may yield metallacycles having beautiful architecture and appropriate cavity. A vinyl benzene spacer-based tetratopic ligand with pyridyl coordinating units upon reaction with water/biimidazole ancillary ligand and $Re_2(CO)_{10}$ produced neutral π-stacked tetragonal prismatic metallacycles **37–38** (Scheme 6.7) [26]. The stacked arrangement of the two tetratopic ligands helps in stabilizing the metallacycles through various noncovalent interactions including $\pi\cdots\pi$ stacking, $CH\cdots\pi$, and H-bonding interactions.

On the other hand, a biphenylene spacer containing tetratopic ligand with benzimidazolyl pendants furnished a bridgeless biscalix[4]arene-shaped metallocavitand **39** upon reacting with quinone ligand unit and $Re_2(CO)_{10}$ (Scheme 6.8). The complex consists of two metallacalix[4]arene units lying

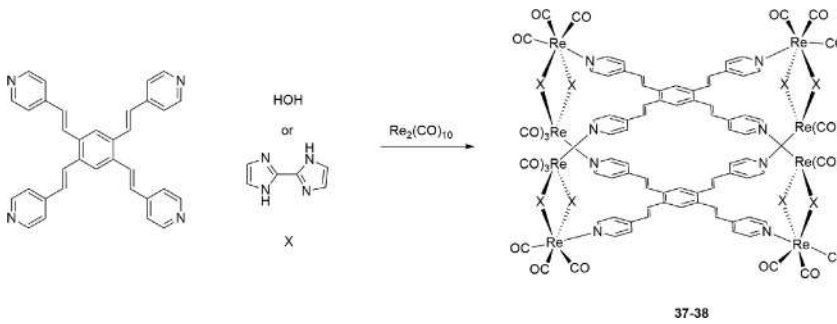

SCHEME 6.7 Synthetic approach for $\pi-\pi$ stacked metallacycles, **37–38** [26].

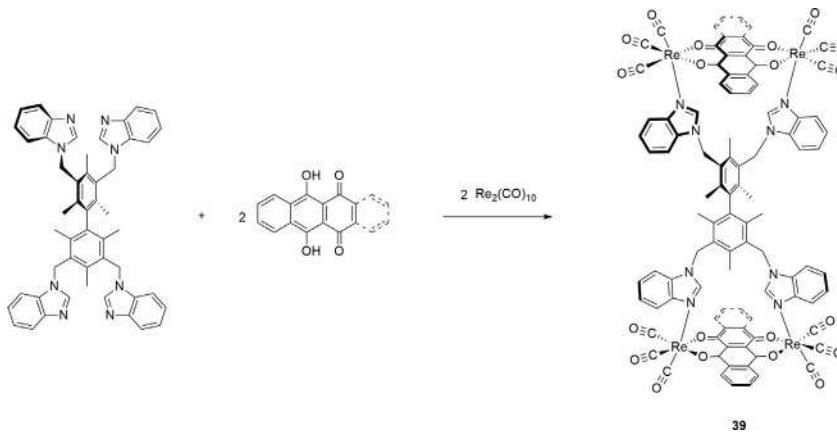

SCHEME 6.8 Synthetic approach for bridgeless biscalix[4]arene-shaped metallacavitand, **39** [15].

orthogonal to each other and connected through arene spacer units [15]. Upon changing the coordinating units, the shape and size of the metallacycles can be varied.

6.9 Neutral flexible hexatopic N-donor ligands and its SCCs

Hexatopic N-donor-based ligand motifs serve as a good class of ligands for constructing metallocavitands with larger cavity size (Chart 6.5). A series of neutral hexanuclear heteroleptic metallocavitands possessing multiple exocyclic cavities suitable to host guest molecules can be obtained by the combination of flexible hexatopic ligands, rigid bridging ligand, and $Re_2(CO)_{10}$ by using simple one-pot approach [28]. These SCCs adopt spheroid-shaped structure. Due to the arrangement of heterocyclic units in the spherical structure, the six calix[4]arene-shaped and two calix[3]arene-shaped exo-cavities are formed (Fig. 6.7). The solid-state structures of the SCCs clearly suggest that these SCCs have ability to act as multiple molecular receptors for small molecules. The overall size, cavity width, and solubility can be tuned by modulating the hexatopic ligands, in particular 5,6-positions of benzimidazolyl/imidazolyl cores.

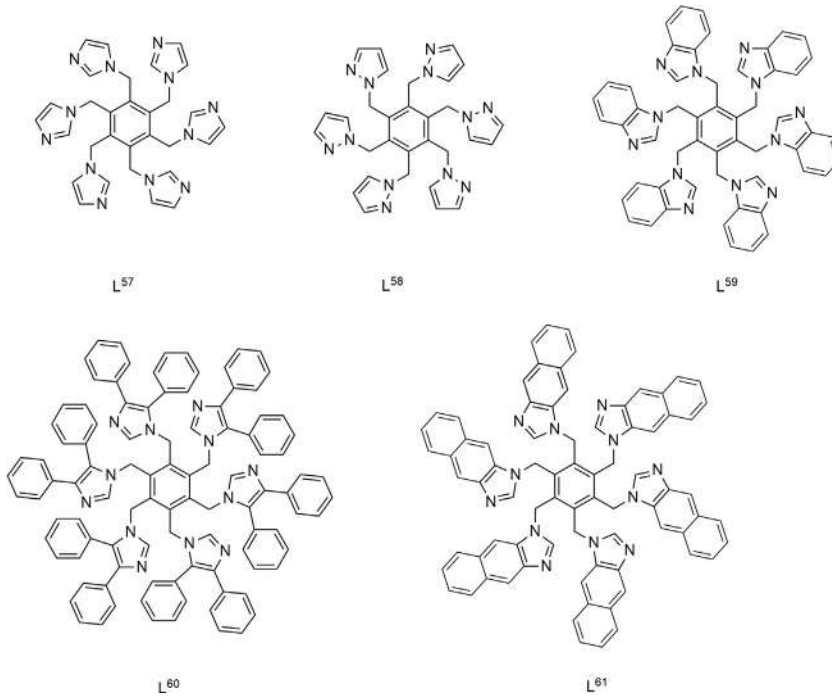

CHART 6.5 Flexible hexatopic N-donor ligands [28].

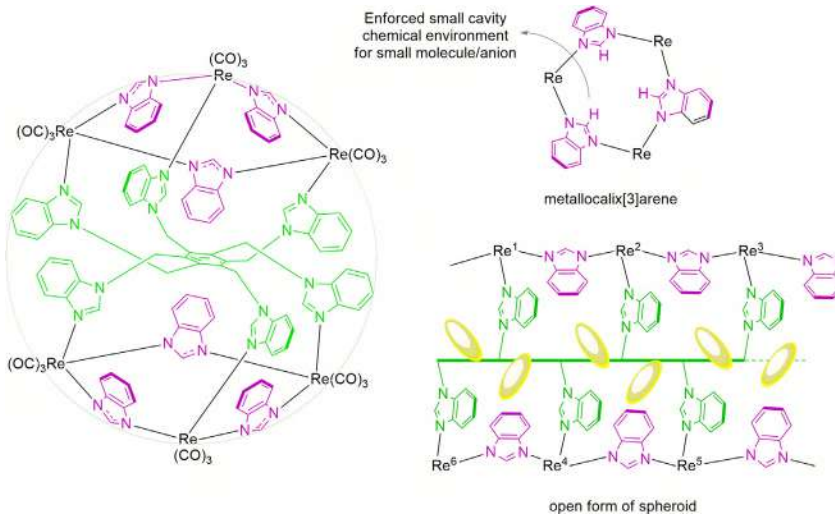

FIGURE 6.7 Spheroid cage **40**; metallacalix[3]arene and its open form [28].

6.10 Neutral flexible benzimidazole-based ditopic N-donor ligands and its SCCs

Benzimidazole and its derivatives-based neutral semiflexible ditopic N-donors with spacer motif, [–CH_2–$C_6H_3R_3$–CH_2–] where R = –H, –Me or –OMe, are excellent organic building units for making various SCCs such as helicates, mesocates, metallacalix[n]arenes, metallocavitands, and tetrahedrons [21,22,36,37,57–59]. The predominantly used flexible ditopic ligands are shown below (Chart 6.6). Several simple but elegant neutral heteroleptic dinuclear metallacalix[4]arenes can be obtained by treating $Re_2(CO)_{10}$, dihydroxyquinones, and ditopic N-donors by simple one-pot approach (Scheme 6.9) [22]. Constructing calixarene-shaped SCCs using this approach results in the cone-shaped conformation. Tuning the spacer or benzimidazolyl core by incorporating the substituents provides functional group decorated SCCs without any change in the cone-conformation (Scheme 6.10). The cavity in the calixarene-shaped SCCs can accommodate small molecules including toluene [22]. Further, the two benzimidazolyl framework arranged opposite to each other can swing back and forth to have maximum noncovalent interactions with the guest molecules.

The cavity size of metallacalix[4]arene can be enlarged by simply changing spacer unit to [–CH_2–C_6H_4–CH_2–C_6H_4–CH_2] motif in the above synthetic approach. Metallacalix[5]arenes (**46**) assembled using the similar self-assembly approach have enlarged hydrophobic cavity which can be modulated by proper choice of bis-chelating ligands (Scheme 6.11) [59]. Molecular recognition studies of these SCCs with various aromatic and nitroaromatic molecules clearly

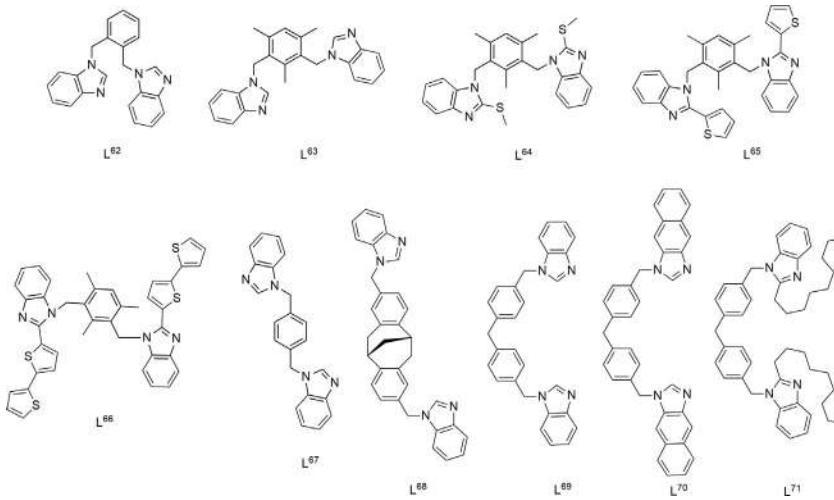

CHART 6.6 Flexible benzimidazole-based ditopic N-donor ligands [21,22,36,37,57–59].

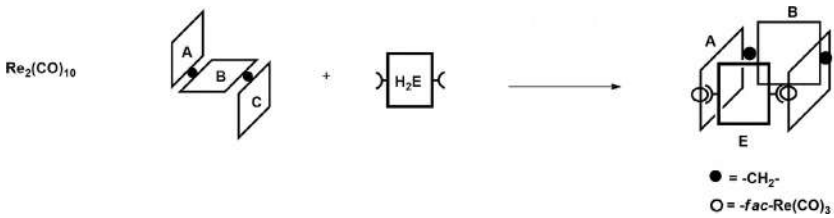

SCHEME 6.9 Schematic representation for self-assembly of metallacalix[4]arene-shaped SCCs.

suggest that the metallacalix[5]arene **46** acts as host for those molecules which can be stabilized by CH$\cdots\pi$ interactions within the host framework.

The above approach utilized for making metallacalix[n]arenes where $n = 4$ or 5 works with rigid dihydroxyquinone-based ligands, that is, bis-chelating ligands with length ~8 Å. Increasing the length of the rigid ligand provides entirely different molecular architecture. For example, the reaction of 1,4-phenylenebis(2-(2′-hydroxyphenyl)benzimidazolyl), and $Re_2(CO)_{10}$ in the presence of flexible ditopic ligands leads to the formation of tetranuclear pseudo tetrahedron-shaped SCCs (Scheme 6.12) [38]. The synthesis of molecular tetrahedrons using partially protected metal source via one-pot approach is rare. The face of the tetrahedrons acts as external cavity for accommodating guest molecules.

As mentioned earlier, flexible ligands offer various conformations in the solution and can have stable conformation after coordinating with metal ions.

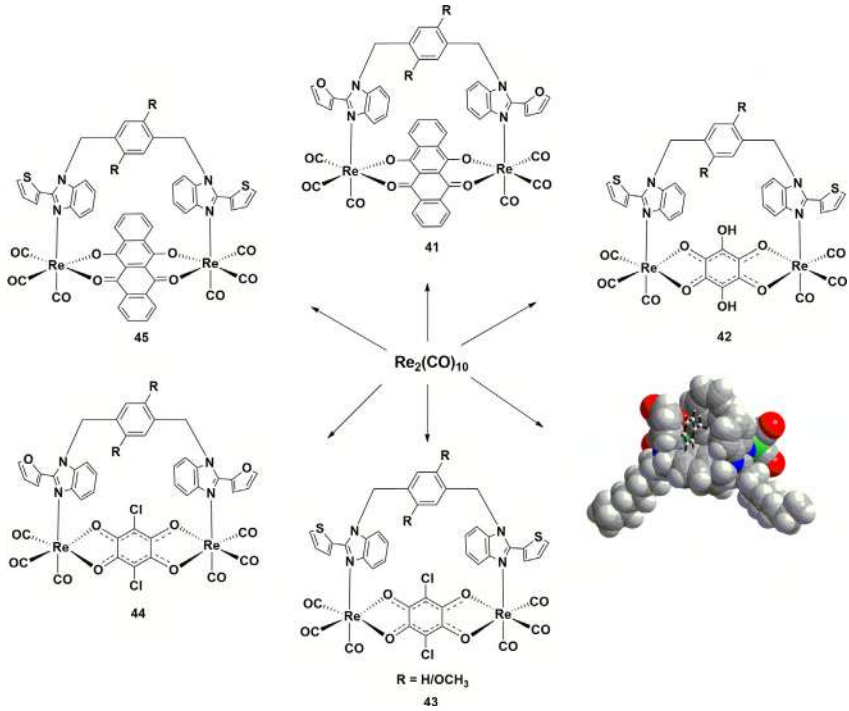

SCHEME 6.10 Self-assembly of metallacalix[4]arenes [21].

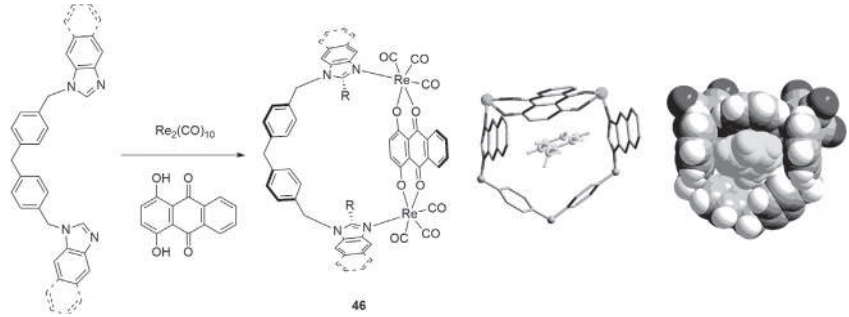

SCHEME 6.11 Synthetic approach for metallacalix[5]arene, **46** [59].

For example, simultaneous complexation of one flexible bis(monodentate) ligand, one flexible bis(bidentate) unit, and two *fac*-$Re(CO)_3$ cores forms dinuclear unsaturated double-heterostranded helicate and mesocate (**48–51**, Fig. 6.8) [37,58,60].

As the new design principles are emerging to modify the structural framework of these SCCs, the use of simple inorganic anions along with organic

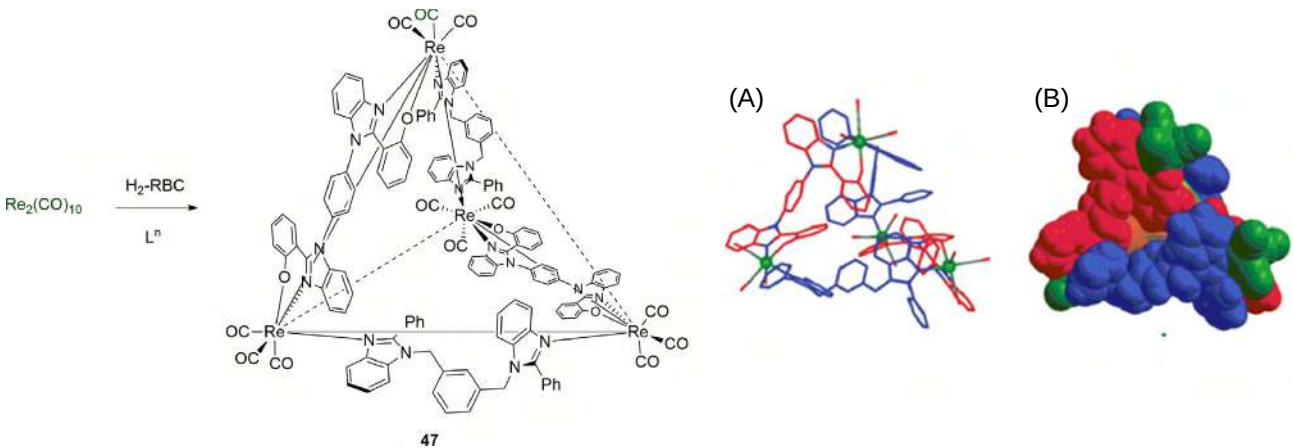

47

SCHEME 6.12 Synthetic approach for tetrahedron, **47** and molecular structures (A) capped-stick model and (B) space-fill model [38].

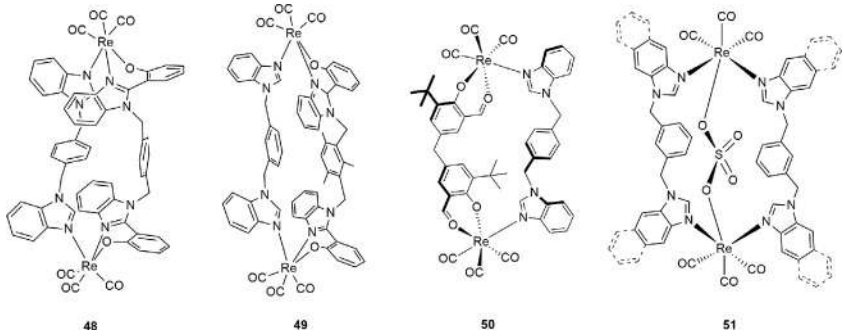

FIGURE 6.8 Dinuclear double- and triple-heterostranded helicate and mesocate, **48–51** [37,58,60].

building units is rare. The example includes a triple heterostranded helicate **51** obtained by the use of sodium bisulfite with benzimidazolyl-based N-donor and $Re_2(CO)_{10}$. The in situ transformation of SO_3^{2-} to SO_4^{2-} during the reaction provides an additional strand to the helical framework [58].

6.11 Heteroatom donor-based ligands and its SCCs

Functionalized chelating ligand such as pyridyl-triazole, pyridyl-N-heterocyclic carbene, and benzoylthiourea forms a different class of ligands apart from the usual benzimidazolyl-based systems. The planarity/rigidity of the ligands having flexible coordinating arm decides the shape of the complex. The preparation of such type of ligands requires multistep approach, however, new synthetic procedures are now being developed which makes them much easily accessible. The pyridine-triazole-based bifunctional chelating agent with $Re(CO)_5Cl$ and proper reaction conditions formed a dinuclear complex **52** (Fig. 6.9). The dimeric complex existed as isomers and the structure in which the ligand motifs are

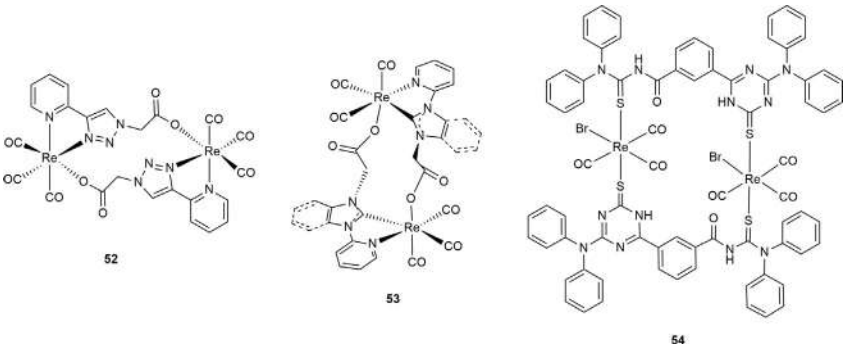

FIGURE 6.9 Chem draw representation of complexes **52–54**.

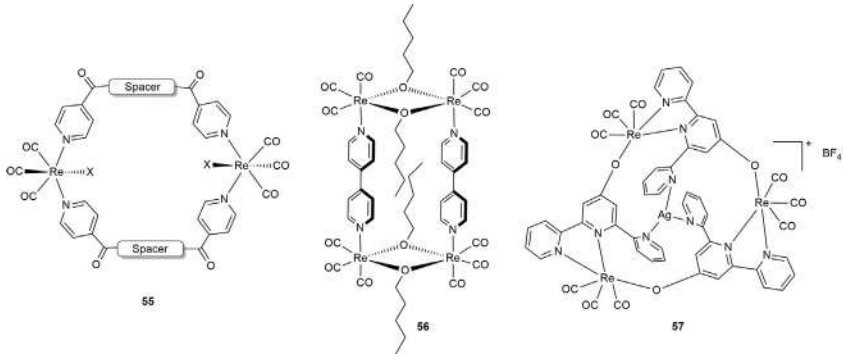

FIGURE 6.10 Chem draw representation for complexes **55**–**57**.

parallel contributed maximum to the isomeric ratio [45]. In a similar way, N-heterocyclic carbine-based bifunctional ligand with pyridine and carboxylic acid coordinating groups yielded complex **53** by Ag(I) transmetalation protocol using Ag_2O [46]. The strong σ-donating properties, high stability, and flexibility of such ligands make their study interesting. Recently, benzoylthiourea derivative with triazinethione moiety showed unusual binding with *fac*-$[Re(CO)_3]^+$ unit via thione sulfur atom of triazinethione unit, **54** [44]. The presence of various heteroatoms including –O, –N, –S in benzoylthiourea derivatives provides multitude bonding options with metal ions.

6.12 Applications of *fac*-$Re(CO)_3$ core-based SCCs

The *fac*-$Re(CO)_3$ core-based SCCs offer various interesting properties such as luminescence, kinetic inertness, lipophilicity, large Stokes shifts, membrane permeability, thermal stability, and low cytotoxicity [61,62]. Apart from the metal core, the ligand framework plays a crucial role in improving the properties of these discrete cyclic systems. These SCCs hold utility in various fields of material chemistry and biology including bioimaging, anticancer activity, host–guest chemistry, and as molecular devices [63]. A considerable amount of research has been focused on acyclic systems with *fac*-$Re(CO)_3$ core whereas only handful of examples are available for Re(I)-based cyclic systems that are utilized for biological studies [4]. Complexes **55** and **56** (Fig. 6.10) possessing lipophilic groups exhibited cytotoxicity toward various cancer cell lines including melanoma, cancer—lung, breast, and cervical [47,64]. The high stability and luminescent properties of such complexes provide motivation for their synthesis and utility in various bioactivities. Another fascinating example includes complex **57** in which a silver ion coordinates with the pyridyl pendants of metallcalix[3]arene vessel, thereby, acting as a stopper [65]. This ion further detaches from the system upon

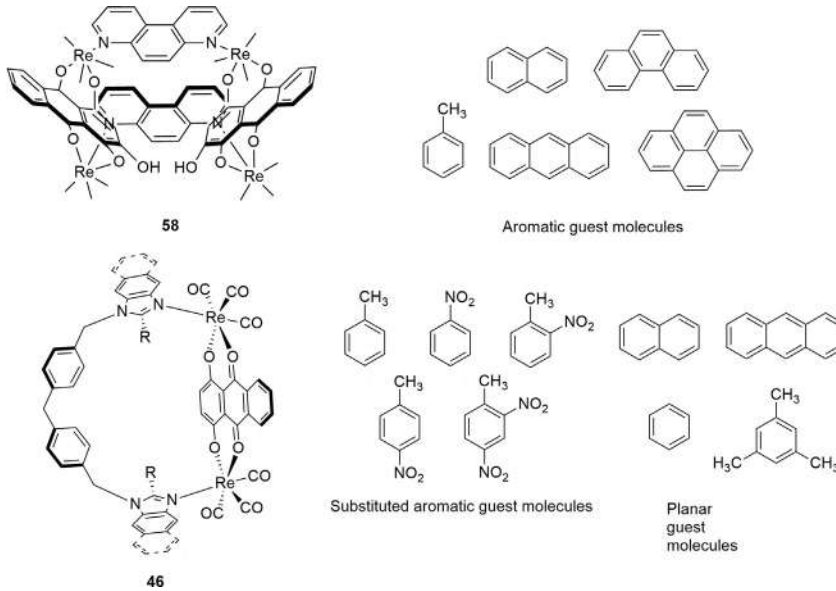

FIGURE 6.11 Chem draw representation of complexes **58**,**46** and their respective guest molecules.

irradiation at 405 nm, hence providing a neutral host-system, which can be useful for silver ions transport through cell membrane.

The presence of cavities in the complex provides scope for host–guest chemistry and molecular recognition studies. The complexes possessing an exo-/endocyclic cavity can serve as host for various guest molecules and stabilize them via noncovalent contacts. Examples include complex **58**, a sycee-like architecture that perfectly holds a toluene molecule in its bowl-shaped cavity Fig. 6.11 [23]. Further, a metallacalix[5]arene system **46** hosts planar aromatic and nitro aromatic guest molecules which interact to the host framework via CH$\cdots\pi$ interactions.

Now, in order to mimic the natural system, to perform a plethora of biological events or to construct functional materials, the *fac*-Re(CO)$_3$ core-based SCCs are being exploited. These SCCs also called as molecular devices such as molecular sensors, switches, rotors, trap, and valve are emerging due to their ease of synthesis, structural flexibility and sensitivity. For example complexes **60–63** are utilized as molecular sensors for selectively detecting volatile organic compounds or odorous amino compounds [20,66–68] Fig. 6.12. The proper shape, size, and properties of the SCCs play a deciding role for their use in various scientific fields. The flexible ligand motifs with arene spacer along with rigid ligand and Re(CO)$_3$ core provide rotor-shaped metallacycles [68]. The rotors consist of a stator part holding the rotating unit from two ends through

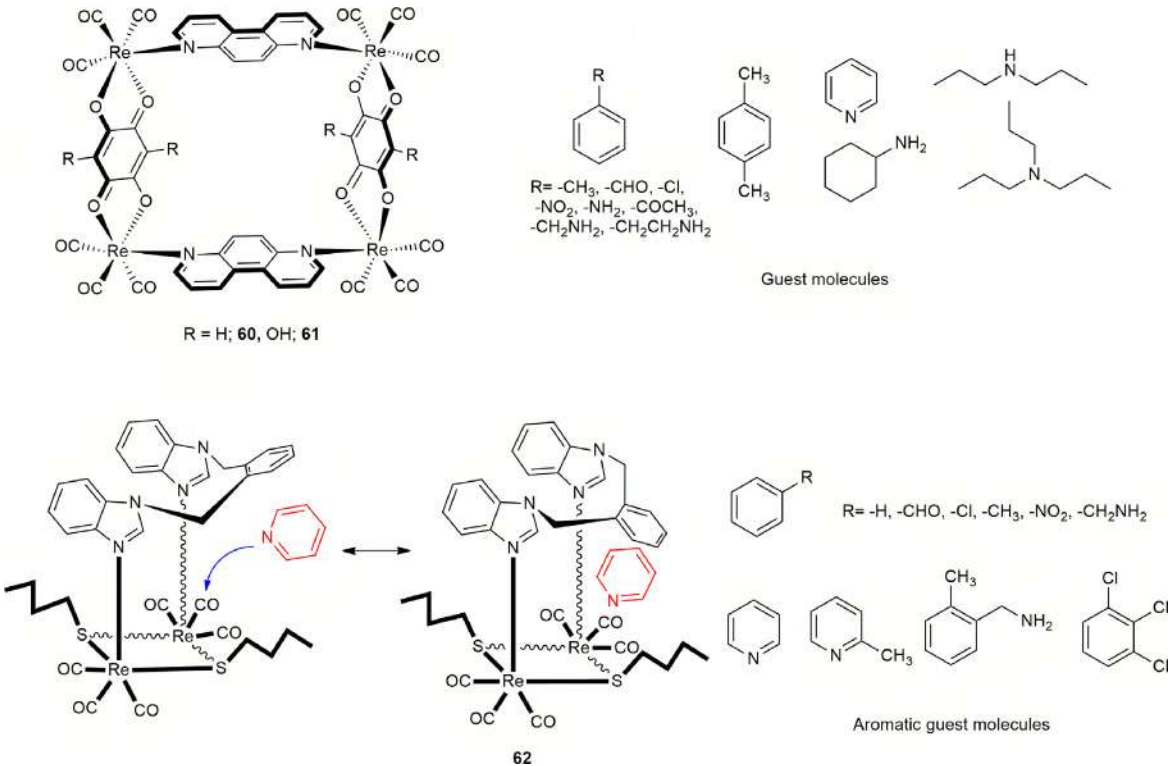

FIGURE 6.12 Chem draw representation of complexes **60–62** and their respective guest molecules.

an axle. Complex **64** is one such example of Re(I)-based molecular rotor having a phenylene rotor unit which rotates in the solution state and interacts to the underlying quinone unit through $CH\cdots\pi$ and $\pi\cdots\pi$ interactions. Such systems can be useful for making future functional material in information storage, electronics and mechanics.

References

[1] P. Thanasekaran, C. Lee, K. Lu, One-step orthogonal-bonding approach to the self-assembly of neutral rhenium-based metallacycles: synthesis, structures, photophysics, and sensing applications, Acc. Chem. Res. 45 (2012) 1403–1418.

[2] F. Würthner, C. You, C. R. Saha-Möller, Metallosupramolecular squares: from structure to function, Chem. Soc. Rev. 33 (2004) 133–146.

[3] D. Gupta, M. Sathiyendiran, Rhenium-carbonyl-based supramolecular coordination complexes: synthesis, structure and properties, ChemistrySelect 3 (2018) 7439–7458.

[4] K. K. Lo, M. Louie, K. Y. Zhang, Design of luminescent iridium(III) and rhenium(I) polypyridine complexes as in vitro and in vivo ion, molecular and biological probes, Coord. Chem. Rev. 254 (2010) 2603–2622.

[5] M. Panigati, M. Mauro, D. Donghi, P. Mercandellic, P. Mussini, L. De Cola, G. D′Alfonso, Luminescent dinuclear rhenium(I) complexes containing bridging 1,2-diazine ligands: photophysical properties and application, Coord. Chem. Rev. 256 (2012) 1621–1643.

[6] W. Gao, H. Zhang, G. Jin, Supramolecular catalysis based on discrete heterometallic coordination driven metallacycles and metallacages, Coord. Chem. Rev. 386 (2019) 69–84.

[7] A. A. Haase, E. B. Bauer, F. E. Kühn, D. C. Crans, Speciation and toxicity of rhenium salts, organometallics and coordination complexes, Coord. Chem. Rev. 394 (2019) 135–161.

[8] J. Rohacova, O. Ishitani, Photofunctional multinuclear rhenium(I) diimine carbonyl complexes, Dalton Trans. 46 (2017) 8899–8919.

[9] V. Sathish, A. Ramdass, M. Velayudham, K. L. Lu, P. Thanasekaran, S. Rajagopal, Development of luminescent sensors based on transition metal complexes for the detection of nitroexplosives, Dalton Trans. 46 (2017) 16738–16769.

[10] R. Govindarajan, R. Nagarajaprakash, V. Veena, N. Sakthivel, B. Manimaran, One-pot reaction of amide functionalized Re(I) based dinuclear metallacycles: synthesis, characterization and evaluation for anticancer potential, Polyhedron 139 (2018) 229–236.

[11] M. Saldías, J. Manzur, R. E. Palacios, M. L. Gómez, J. De La Fuente, G. Günther, N. Pizarroa, A. Vega, The binuclear dual emitter $[Br(CO)_3Re(P\cdots N)(N\cdots P)Re(CO)_3Br]$ (P···N): 3-chloro-6-(4-diphenylphosphinyl)butoxypyridazine, a new bridging P,N-bidentate ligand resulting from the ring opening of tetrahydrofuran, Dalton Trans. 46 (2017) 1567–1576.

[12] B. Shankar, P. Elumalai, R. Shanmugam, M. Sathiyendiran, Neutral heteroleptic rhenium-based M_3L_3L' type metallacycles: synthesis, structural characterization and DFT/TDDFT studies, J. Organomet. Chem. 749 (2014) 224–232.

[13] K. R. J. Thomas, J. T. Lin, Y. Lin, C. Tsai, S. Sun, Self-assembly molecular architectures incorporating fluorene- and carbazole-based bichromic oligopyridines. Novel photoactive materials, Organometallics 20 (2001) 2262–2269.

[14] S. Sun, A. J. Lees, Self-assembly triangular and square rhenium(I) tricarbonyl complexes: a comprehensive study of their preparation, electrochemistry, photophysics, photochemistry, and host-guest properties, J. Am. Chem. Soc. 122 (2000) 8956–8967.

[15] P. Elumalai, R. Kanagaraj, R. Marimuthu, B. Shankar, A. Ch. Kalita, M. Sathiyendiran, Rhenium(I)-based bridgeless double metallocalix[4]arenes, Dalton Trans. 44 (2015) 11274–11277.

[16] M. L. Merlau, M. P. Mejia, S. T. Nguyen, J. T. Hupp, Artificial enzymes formed through directed assembly of molecular square encapsulated epoxidation catalysts, Angew. Chem. Int. Ed. 40 (2001) 4239–4242.

[17] M. Boccalon, E. Iengo, P. Tecilla, New meso-substituted *trans*-A_2B_2 di(4-pyridyl)-porphyrins as building blocks for metal-mediated self-assembling of 4 + 4 Re(I)–porphyrin metallacycles, Org. Biomol. Chem. 11 (2013) 4056–4067.

[18] R. Govindarajan, R. Nagarajaprakash, B. Manimaran, Synthesis, structural characterization, and host−guest studies of aminoquinonato-bridged Re(I) supramolecular rectangles, Inorg. Chem. 54 (2015) 10686–10694.

[19] B. Manimaran, P. Thanasekaran, T. Rajendran, R. Lin, I. Chang, G. Lee, S. Peng, S. Rajagopal, K. Lu, Luminescence enhancement induced by aggregation of alkoxy-bridged rhenium(I) molecular rectangles, Inorg. Chem. 41 (2002) 5323–5325.

[20] M. Sathiyendiran, R. Liao, P. Thanasekaran, T. Luo, N.S. Venkataramanan, G. Lee, S. Peng, K. Lu, Gondola-shaped luminescent tetrarhenium metallacycles with crown-ether-like multiple recognition sites, Inorg. Chem. 45 (2006) 10052–10054.

[21] P. Rajakannu, S. M. Mobin, M. Sathiyendiran, Thiophene/furan units decorated unsymmetrical dinuclear metallocalix[4]arenes, J. Organomet. Chem. 771 (2014) 68–77.

[22] P. Rajakannu, P. Elumalai, B. Shankar, F. Hussain, M. Sathiyendiran, Rhenium(I) based metallocalix[4]arenes decorated with free functionalized benzimidazolyl units, Dalton Trans. 42 (2013) 11359–11362.

[23] M. Sathiyendiran, C. Tsai, P. Thanasekaran, T. Luo, C. Yang, G. Lee, S. Peng, K. Lu, Organometallic calixarenes: syceelike tetrarhenium(I) cavitands with tunable size, color, functionality, and coin–slot complexation, Chem. Eur. J. 17 (2011) 3343–3346.

[24] D. Gupta, P. Rajakannu, B. Shankar, R. Shanmugam, F. Hussain, B. Sarkar, M. Sathiyendiran, Furan-decorated neutral Re(I)-based 2D rectangle and 3D trigonal prism, Dalton Trans. 40 (2011) 5433–5435.

[25] D. Bhattacharya, C. Chang, Y. Cheng, L. Lai, H. Lu, C. Lin, K. Lu, Multielectron redox chemistry of a neutral, NIR-active, Indigo-Pillared Re^{I}-based triangular metalloprism, Chem. Eur. J. 18 (2012) 5275–5283.

[26] B. Shankar, P. Elumalai, F. Hussain, M. Sathiyendiran, Synthesis and characterization of tetragonal prismatic π-stacked metallacycles, J. Organomet. Chem. 732 (2013) 130−136.

[27] D. Gupta, P. Rajakannu, B. Shankar, F. Hussain, M. Sathiyendiran, Synthesis and crystal structure of a wheel-shaped supramolecular coordination complex, J. Chem. Sci. 126 (2014) 1501–1506.

[28] B. Shankar, R. Marimuthu, S. D. Sathiyashivan, M. Sathiyendiran, Spheroid metallacycles and metallocavitands with calixarene- and/or cleft-shaped receptors on the surface, Inorg. Chem. 55 (2016) 4537−4544.

[29] K. D. Benkstein, J. T. Hupp, C. L. Stern, Synthesis and characterization of molecular rectangles based upon rhenium thiolate dimers, Inorg. Chem. 37 (1998) 5404–5405.

[30] K. D. Benkstein, J. T. Hupp, C. L. Stern, Molecular rectangles based on rhenium(I) coordination chemistry, J. Am. Chem. Soc. 120 (1998) 12982.

[31] R. M. Spada, M. C. Plaza, M. L. Gomez, G. Gunther, P. Jaque, N. Pizarro, R. E. Palacios, A. Vega, Clean singlet oxygen production by a Re^{I} complex embedded in a flexible self-standing polymeric silsesquioxane film, J. Phys. Chem. C 18 (2015) 10148–10159.

[32] K. D. Benkstein, J. T. Hupp, Synthesis and characterization of hexametallic molecular hosts featuring large cavity volumes and constrained cavity port sizes, Mol. Cryst. Liq. Cryst. 342 (2000) 151–158.

[33] P. H. Dinolfo, M. E. Williams, C. L. Stern, J. T. Hupp, Rhenium-based molecular rectangles as frameworks for ligand-centered mixed valency and optical electron transfer, J. Am. Chem. Soc. 126 (2004) 12989–13001.

[34] B. Shankar, R. Arumugam, P. Elumalai, M. Sathiyendiran, Rhenium(I)-based monocyclic and bicyclic phosphine oxide-coordinated supramolecular complexes, ACS Omega 1 (2016) 507−517.

[35] B. Ramakrishna, C. A. Kumar, T. J. Logesh, B. Manimaran, Oxamidato pillared heteroligated dirhenium(I) metallacrown ethers: synthesis, spectroscopic and structural characterization, J. Organomet. Chem. 828 (2017) 116–121.

[36] P. Rajakannu, P. Eumalai, S. M. Mobin, K. L. Lu, M. Sathiyendiran, Hard and soft-donors decorated rhenium based metallocavitands, J. Organomet. Chem. 743 (2013) 17–23.

[37] B. Shankar, S. Sahu, N. Deibel, D. Schweinfurth, B. Sarkar, P. Elumalai, D. Gupta, F. Hussain, G. Krishnamoorthy, M. Sathiyendiran, Luminescent dirhenium(I)-double-heterostranded helicate and mesocate, Inorg. Chem. 53 (2014) 922−930.

[38] R. Arumugam, B. Shankar, K. R. Soumya, M. Sathiyendiran, *fac*-$Re(CO)_3$-based neutral heteroleptic tetrahedrons, Dalton Trans. 48 (2019) 7425–7431.

[39] Z. Z. Lu, C. C. Lee, M. Velayudham, L. W. Lee, J. Y. Wu, T. S. Kuo, K. L. Lu, Control of light-promoted [2+2] cycloaddition reactions by a remote ancillary regulatory group that is covalently attached to rhenium rectangles, Chem. Eur. J. 18 (2012) 15714–15721.

[40] H. Hartmann, S. Berger, R. Winter, J. Fielder, W. Kaim, Reversible and site-specific reduction of the ligand sides in a molecular rectangle with up to eight electrons, Inorg. Chem. 39 (2000) 4977–4980.

[41] Y. H. Tseng, D. Bhattacharya, S. M. Lin, P. Thanasekaran, J. Y. Wu, L. W. Lee, M. Sathiyendiran, M. W. Chung, K. C. Hsu, P. T. Chao, K. L. Lu, Highly emissive cyclometalated rhenium metallacycles: structure-luminescence relationship, Inorg. Chem. 49 (2010) 6805–6807.

[42] M. Karthikeyan, R. Govindarajan, C. A. Kumar, U. Kumar, B. Manimaran, Rectangular and hammock shaped ester functionalized chalcogenolato-bridged rhenium(I) tetranuclear metallacyclophanes, J. Organomet. Chem. 866 (2018) 27–34.

[43] B. Tzeng, A. Chao, M. Lin, G. Lee, T. Kuo, Molecular Re^{I} cages: structural and luminescent properties, Chem. Eur. J. 23 (2017) 18033–18040.

[44] J. Mukiza, H. Braband, R. Bolliger, O. Blacque, R. Alberto, J. B. Nkurunziza, A novel benzoylthiourea derivative with a triazinethione moiety: synthesis and coordination with the organometallic *fac*-$[Re(CO)_3]^+$ core, Inorg. Chim. Acta 516 (2021) 120116.

[45] A. Boulay, A. Seridi, C. Zedde, S. Laderia, C. Picard, L. Maron, E. Benoist, Tricarbonyl Re^{I} complexes from functionalised pyridine–triazole derivatives: from mononuclear to unexpected dimeric complexes, Eur. J. Inorg. Chem. (2010) 5058–5062.

[46] C. Y. Chan, P. A. Pellegrini, I. Greguric, P. J. Barnard, Rhenium and technetium tricarbonyl complexes of N-heterocyclic carbene ligands, Inorg. Chem. 53 (2014) 10862–10873.

[47] C. A. Kumar, B. Ramakrishna, U. Kumar, B. Manimaran, Synthesis and characterization of manganese(I) and rhenium(I) based M_2L_2- and $M_2(\mu\text{-}Br)_2$L-type diethyleneglycol decorated ester functionalized metallacycles, Inorg. Chim. Acta 471 (2018) 754–758.

[48] C. A. Kumar, D. Divya, R. Nagarajaprakash, V. Veena, P. Vidhyapriya, N. Sakthivel, B. Manimaran, Self-assembly of manganese(I) and rhenium(I) based semi-rigid ester functionalized M_2L_2-type metallacyclophanes: synthesis, characterization and cytotoxicity evaluation, J. Organomet. Chem. 846 (2017) 152–160.

[49] R. Govindarajan, D. Divya, R. Nagarajaprakash, B. Manimaran, Synthesis and characterization of aminoquinonato bridged Re(I)-based amide functionalized dinuclear metallastirrups and tetranuclear lemniscate metallacycles, ChemistrySelect 3 (2018) 3742–3750.

[50] R. Govindarajan, R. Nagarajaprakash, V. Veena, N. Sakthivel, B. Manimaran, One-pot reaction of amide functionalized Re(I) based dinuclear metallacycles: synthesis, characterization and evaluation for anticancer potential, Polyhedron 139 (2018) 229–236.

[51] G. Jin, T. Wang, Y. Sun, Y. Li, J. Ma, Photochromic rhenium-based molecular rectangles: syntheses, structures, photophysical properties, and electrochemistry, Inorg. Chem. 59 (2020) 15019–15027.

[52] B. Shankar, P. Elumalai, R. Shanmugam, V. Singh, D.T. Masram, M. Sathiyendiran, New class of phosphine oxide donor-based supramolecular coordination complexes from an in situ phosphine oxidation reaction or phosphine oxide ligands, Inorg. Chem. 52 (2013) 10217–10219.

[53] E. Q. Procopio, D. Dova, S. Cauteruccio, A. Forni, E. Licandro, M. Panigati, Dirhenium coordination complex endowed with an intrinsically chiral helical-shaped diphosphine oxide, ACS Omega 3 (2018) 11649–11654.

[54] J. P. Sauvage, Transition metal-containing rotaxanes and catenanes in motion: toward molecular machines and motors, Acc. Chem. Res. 31 (1998) 611–619.

[55] M. Fujita, K. Ogura, Supramolecular self-assembly of macrocycles, catenanes, and cages through coordination of pyridine-based ligands to transition metals, Bull. Chem. Soc. Jpn. 69 (1996) 1471–1482.

[56] L. Carlucci, G. Ciani, D.M. Proserpio, Borromean links and other non-conventional links in 'polycatenated' coordination polymers: re-examination of some puzzling networks, Cryst. Eng. Commun. 5 (2003) 269–279.

[57] B. F. Hoskin, R. Robson, D. A. Slizys, An infinite 2D polyrotaxane network in $Ag_2(bix)_3(NO_3)_2$ (bix = 1,4-Bis(imidazol-1-ylmethyl)benzene), J. Am. Chem. Soc. 119 (1997) 2952–2953.

[58] K. R. Soumya, R. Arumugam, B. Shankar, M. Sathiyendiran, Sulfate donor based dinuclear heteroleptic triple-stranded helicates from sulfite and ditopic nitrogen donor ligands and their transformation to dinuclear homoleptic double-stranded mesocates, Inorg. Chem. 57 (2018) 10718.

[59] M. Bhol, B. Shankar, M. Sathiyendiran, Rhenium(I) based irregular pentagonal-shaped metallacavitands, Dalton Trans. 47 (2018) 4494–4500.

[60] P. Saxena, B. Shankar, A. Sathyanarayana, G. Prabusankar, M. Sathiyendiran, Rhenium(I)-based double-heterostranded helicates, Chimia 69 (2015) 675–677.

[61] T. R. Cook, V. Vajpayee, M. H. Lee, P. J. Stang, K. W. Chi, Biomedical and biochemical applications of self-assembled metallacycles and metallacages, Acc. Chem. Res. 46 (2013) 2464–2474.

[62] V. Fernandez-Moreira, F. L. Thorp-Greenwood, M. P. Coogan, Application of d^6 transition metal complexes in fluorescence cell imaging, Chem. Commun. 46 (2010) 186–202.

[63] T. R. Cook, P. J. Stang, Recent developments in the preparation and chemistry of metallacycles and metallacages via coordination, Chem. Rev. 115 (2015) 7001–7045.

[64] D. K. Orsa, G. K. Haynes, S. K. Pramanik, M. O. Iwunze, G. E. Greco, J. A. Krause, D. M. Ho, A. L. Williams, D. A. Hill, S. K. Mandal, Synthesis, characterization, and fluorescence and cytotoxicity studies of a tetrarhenium molecular rectangle, Inorg. Chem. Commun. 10 (2007) 821–824.

[65] F. L. Thorp-Greenwood, V. Fernandez-Moreira, C. O. Millet, C. F. Williams, J. Cable, J. B. Court, A. J. Hayes, D. Lloyd, M. P. Coogan, A 'sleeping Trojan horse' which transports metal ions into cells, localises in nucleoli, and has potential for bimodal fluorescence/PET imaging, Chem. Commun. 47 (2011) 3096–3098.

[66] G. G. Huang, C. Lee, J. Yang, Z. Lu, M. Sathiyendiran, C. Huang, Y. Kao, G. Lee, K. Lu, Cavity-containing rhenium metallacycle treated evanescent wave infrared chemical sensors for the selective determination of odorous amines in the atmosphere, Sens. Actuators B 254 (2018) 424–430.

[67] G. G. Huang, C. J. Lee, J. Yang, C. H. Chang, M. Sathiyendiran, Z. Z. Lu, K. L. Lu, Rhenium-based molecular trap as an evanescent wave infrared chemical sensing medium for the selective determination of amines in air, ACS Appl. Mater. Interfaces 8 (2016) 35634–35640.

[68] P. Rajakannu, B. Shankar, A. Yadav, R. Shanmugam, D. Gupta, F. Hussain, C. H. Chang, M. Sathiyendiran, K.-L. Lu, Adaptation toward restricted conformational dynamics: from the series of neutral molecular rotors, Organometallics 30 (2011) 3168–3176.

Chapter 7

Photo switching self-assembled coordination macrocycles: Synthesis and functional applications

Aniket Chowdhury
Department of Industrial Chemistry, School of Physical Sciences, Mizoram University, Aizawl, Mizoram, India

7.1 Introduction

The supramolecular coordination complexes (SCC) or self-assembled metallacycles and metallacages (SAM) are a new class of compounds that were originally developed to achieve 2D and 3D discrete molecular architectures which were otherwise impossible to obtain using conventional methods [1]. The SCC are designed by joining metal acceptors with organic donor ligands by metal–ligand coordination covalent bond formation and this structural motif provide a unique advantage of self-error correction and self-repairing leading to the formation of quantitative product with a very high degree of purity. The metal-based acceptor and the organic donor exhibit orthogonal behavior, which prompted several research groups to incorporate various functionality in the final SCC by toying with the building blocks [2–4]. The modified SCC have found a wide array of application in fluorescence imaging, biomedical, explosive detection, catalysis, storage of unstable molecule, selective separation of the analyte, and many more [5–8]. But the current orientation of cutting-edge research is more driven toward multifunctional smart materials where mild stimuli such as light, heat, acoustics, pH can alter the physical and chemical properties of the target molecule [9]. In this regard, light-responsive photochromic materials are of particular interest due to several additional advantages such as noninvasive behavior, remote access, and reversibility. Several research groups have gradually developed photochromic macrocycles and investigated their photo reversibility [10–12]. Different molecular backbones such as diazo-aryl compounds, spiropyran, bisthienylethene, etc. have been used to produce multiple SCC but several

Supramolecular Coordination Complexes: Design, Synthesis, and Applications.
DOI: https://doi.org/10.1016/B978-0-323-90582-4.00008-7

issues have still eluded the researchers from achieving perfect photochromic macrocycles such as (i) photo fatigue, (ii) fast and uncontrolled switching, (iii) complicated synthesis, etc. Therefore a proper understanding of the currently developed photoswitching macrocycles will pave the way to produce an ideal SCC with a high degree of stability, photo reversibility, and fatigue resistance.

7.2 Bisthienylethene building block-based SCC

Bisthienylethene is a photochromic motif, well known for its photoswitching behavior, and ease of functionalization, and has been widely used as nonlinear optical materials, data storage, bioimaging, and more. It exhibits a reversible transformation between the ring-closed and ring-opened from under the influence of visible and UV photoirradiation.

Zhu et al. [13] reported the first example of bisthienylethene-based photochromic SCCs 1d and 1f. Both the SCCs contains dipyridyl donor 2,3-bis(2-methyl-5- (pyridine-4-yl)thiophene-3-yl)benzo[b]thiophene-1,1-dioxide (BTO) with the photochromic unit appended at the backbone. A combination of both linear and 120° acceptors with this donor in a 1:1 ratio gave rise to hexagons 1d and 1f, respectively (Fig. 7.1). Both the SCCs were thoroughly characterized by ^{1}H, ^{31}P NMR, and mass spectrometry analysis. Both the 1d and 1f exhibit ring-opened structures. For the photoswitching capacity analysis the dichloromethane (DCM) was chosen as the suitable solvent and both the samples were stimulated with a UV source of 365 nm at 298 K. Upon stimulation, the color of the DCM solution of macrocycle 1d changed from colorless to dark cyan. The change in coloration was associated with a change in the absorption spectra where two new peaks appeared at 420 and 622 nm. Two isosbestic points were found at 315 and 374 nm. On a similar note, UV exposure changed the color of the 1f solution from colorless to dark cyan with two new absorption peaks at 420 and 628 nm, respectively. The author proposed that the change in color and absorption spectra is due to the formation of ring-closed macrocycles. The authors established the reversibility of the macrocycles by forming the ring-opened form of 1d and 1f with the help of visible light irradiation at 510 nm. The macrocycles can be switched between the ring-opened and ring-closed form eve up to 10 cycles without any degradation. The authors also claimed that the macrocycle provides the first example of quantitative conversion between ring-opened and ring-closed states.

Although the bisthienylethene was used to demonstrate the structural switching in SCC Prof. Clever and coworkers [14] pushed the boundary even further by developing a 3D metallacage where the guest encapsulation and release were controlled by photoirradiation (Fig. 7.2). The group synthesized a new dipyridyl ligand 2a with bisthienylethene at the backbone and demonstrated that the ligand can reversibly transform between the ring-closed and ring-opened under the influence of UV and visible light, respectively. By carefully reacting the donor with

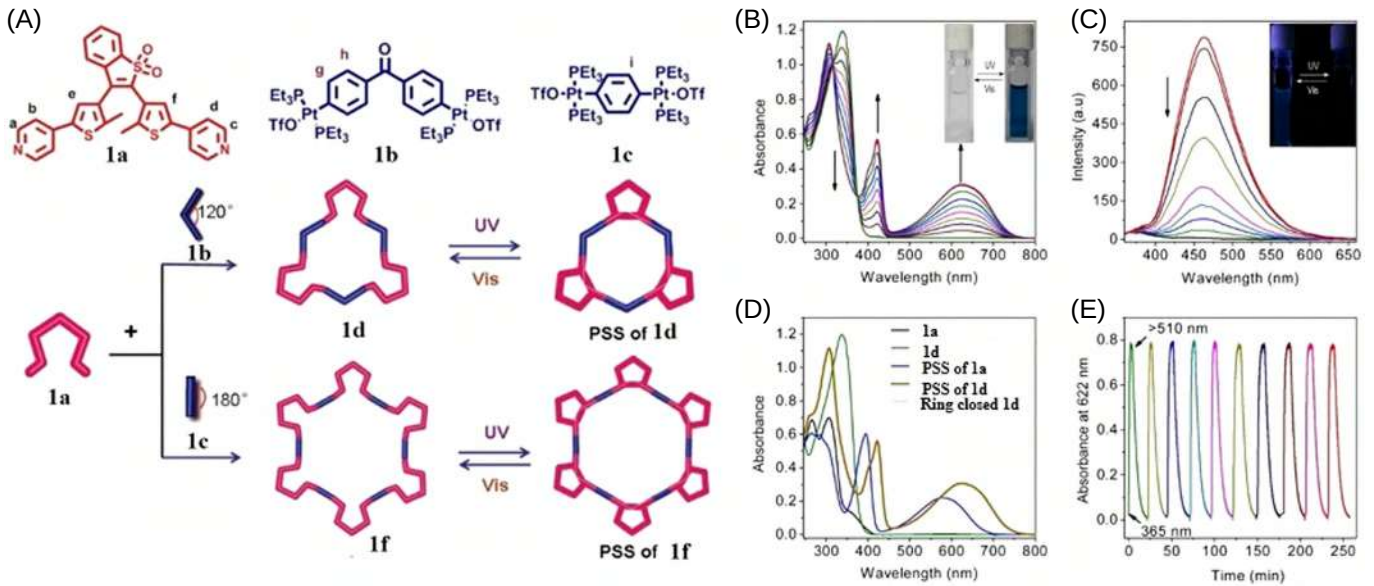

FIGURE 7.1 (A) Synthetic scheme of macrocycle 1d and 1f. (B) Photochromic behavior of 1d under UV exposure. (C) Loss of fluorescence intensity upon photoinduced ring cyclization for 1d. (D) Absorption spectra of 1d and its building block 1a. (E) Reversible photochromic behavior of 1d. (*Reprinted (adapted) with permission from Zhu* et al. (*2012*) © *2012 American Chemical Society.*)

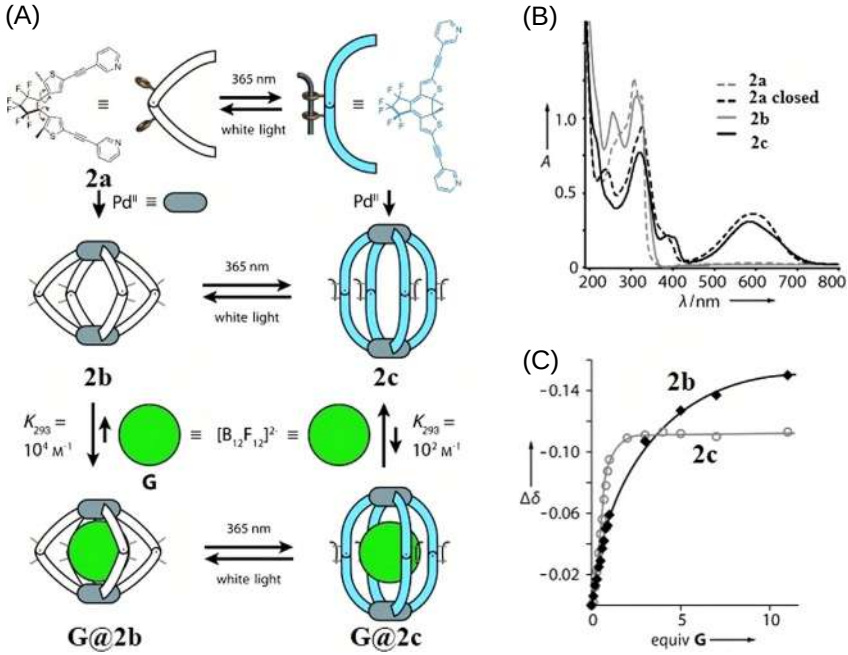

FIGURE 7.2 (A) Preparation of photochromic cage from building blocks. (B) Absorption spectra of the building block and the cage. (C) Binding isotherms at 293 K of the encapsulation of the guest molecule by the open cage and cyclized cage. (*Reprinted (adapted) with permission from Clever* et al. *(2013) © 2013 John Wiley and Sons.*)

$[Pd(CH_3CN)_4](BF_4)_2$ in acetonitrile a new metallacage 2b was formed. The existence of the cage was verified using NMR and mass spectrometry analysis. Upon exposure to UV irradiation, the ring-opened form of the cage 2b transformed into closed ring isomer 2c and diffusion ordered spectroscopy of both the open and closed ring cage revealed a large difference in the hydrodynamic radii of the two cages. The hydrodynamic radii of the 2b and 2c were found to be 7.04 Å and 8.67 Å. The small internal cavity of the 2b was attributed to the conformational flexibility. This photo-control over the internal cavity was exploited by encapsulating the anion dodecafluorododecaborate ($[B_{12}F_{12}]^{2-}$) and reversibly triggering the encapsulation and release of the guest by photoirradiation. The association constants between the open and closed forms of the cages 2b and 2c with the guest molecule were found to be 3.2×10^4 M^{-1} and 6.7×10^2 M^{-1}, respectively. The higher association constant for the ring-opened cage 2c with the guest molecule was attributed to the flexibility of the thiophene rings in the open form of the cage that allows induced fitting of the guest inside (Fig. 7.2).

The same group has reported a slightly modified ligand 3a where the bisthienylethene group is linked with the pyridyl moiety without any triple bond [15] and the conversion between the ring-opened donor 3a and ring-closed donor

3b were carried out using 313 and 617 nm respectively (Fig. 7.3). The treatment of the ligand 3a with $[Pd(CH_3CN)_4](BF_4)_2$ in acetonitrile with a 2:1 ratio produced a mixture of two–three and four-member metallacages 3c and 3d. The existence of such metallacages was established using 1H and 2D DOSY NMR. When the closed ring donor ligand 3b was treated with $[Pd(CH_3CN)_4](BF_4)_2$ in 2:1 ratio then, a monstrous supramolecular structure 3e was obtained which had 24 palladium atoms and 48 donor ligands. The existence of such a big structure was evident from 2D DOSY NMR where the hydrodynamic radii were found to be 3.5 nm and it closely matched with the predicted theoretical model with a size of 3.2 nm. Moreover, with the help of TEM, AFM, and grazing-incidence small-angle X-ray scattering (GISAXS) the formation of large-sized supramolecule was established. The interconversion experiments between the 3c and 3e using photoirradiation was carried out and it provided some surprising outcome. Unlike the previous report of the similar type ligand-based SCC, in this case, the conversion of ring-closed 3e from ring-opened 3c under 313 nm UV irradiation was found to be extremely slow and the complete cyclization took 15 h to complete. The authors attributed this slow behavior to the fact that the backbone of 3c is in a highly twisted conformation and is incapable to undergo photocyclization due to orbital mismatch. The authors also proposed that under photoirradiation the 3c disintegrated into palladium cation and ring-closed ligand and reassembled to form 3e. When the macrocycle was exposed to visible light of 617 nm it transformed into a ring-opened macrocycle 3f very fast which slowly broke down into more thermodynamically stable 3c (Fig. 7.3).

Although the bisthienylethene systems were utilized to create 2D and 3D macrocycles and metallacages where using photoirradiation, only their structural transformations were controlled but Yong Su et al. [16] first developed the application of such behavior in the creation of porous supramolecular gel (Fig. 7.4). The group reported the synthesis of a fluorinated bisthienylethene-based dipyridyl ligand 4a and created a ring-opened 3D metallacage 4c by combining the ligand with palladium in a 3:2 ratio. The free ligand 4a demonstrated light-induced reversible transformation from ring-opened ligand 4a to ring-closed ligand 4b and vice versa. A separate treatment of 4b with palladium resulted in a structurally similar 3D metallacage 4d. The light-induced transformation between the ring-opened cage 4c and ring-closed cage 4d was found to be reversible. Upon irradiation, with 254 nm light, the 4c transformed into 4d within 30 min and the opposite transformation took place under visible light. The UV–Vis maxima of the 4a were at 290 nm and upon UV irradiation, it transformed in the ring-closed cage 4d with two new maxima at 385 and 595 nm and two isosbestic points at 257 and 320 nm. The fluorinated backbone of the ligand imparted hydrophobic characteristics into the cage and this hydrophobic interaction was utilized in the formation of the supramolecular gel. When the DMSO solution of opened ring cage 4c was left for 10 h, it transformed into gel at ambient condition. It was speculated that the hydrophobic interaction of the ligand backbone generated supramolecular interaction among the neighboring

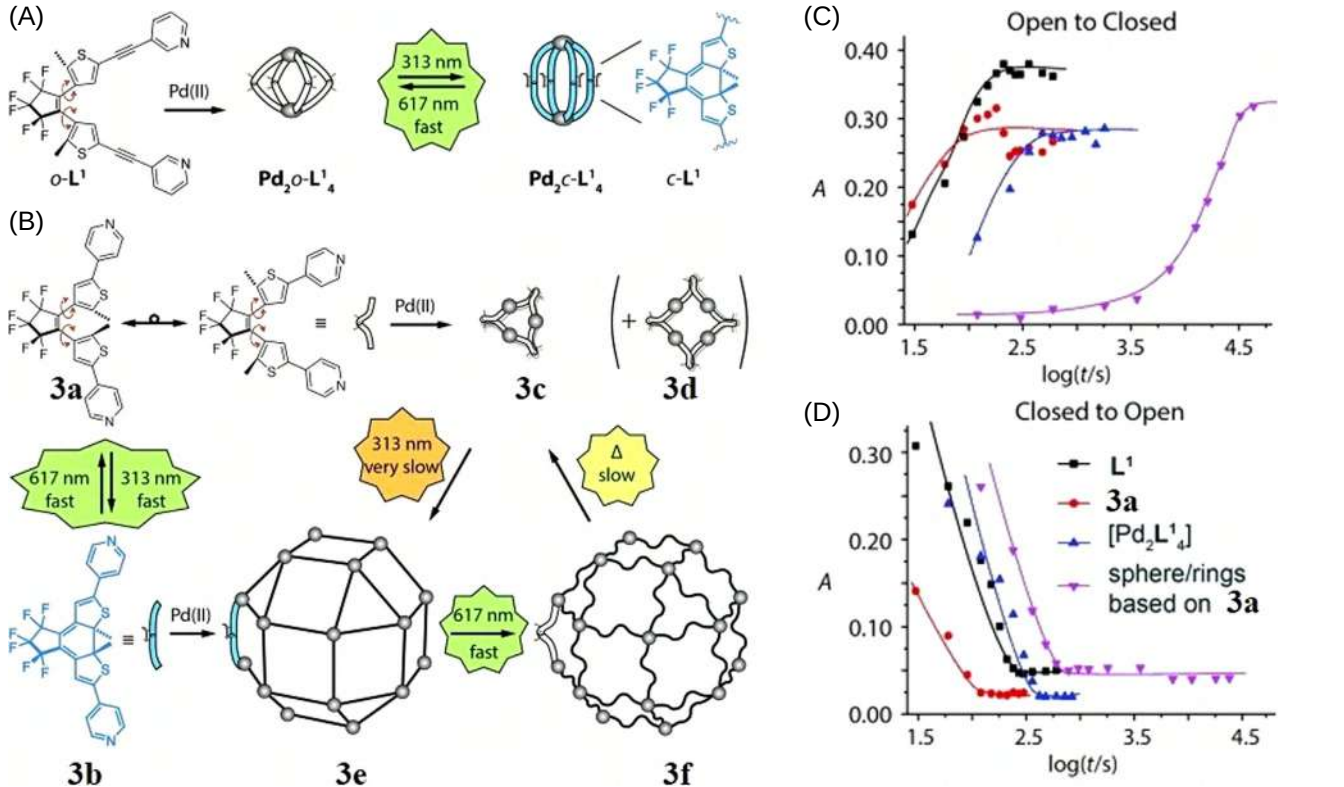

FIGURE 7.3 (A) Previous report on isostructural ligand and its cage formation. (B) The schematic representation of new ligand 3a and formation of various 3D cages from different building blocks. (C) Kinetics of photoconversion of 3a, 3c, and 3d upon exposure to 313 nm light. (D) Kinetics of photoconversion of 3b and 3e upon exposure to 617 nm light. (*Reprinted (adapted) with permission from Clever* et al. *(2016), © 2016 John Wiley and Sons.*)

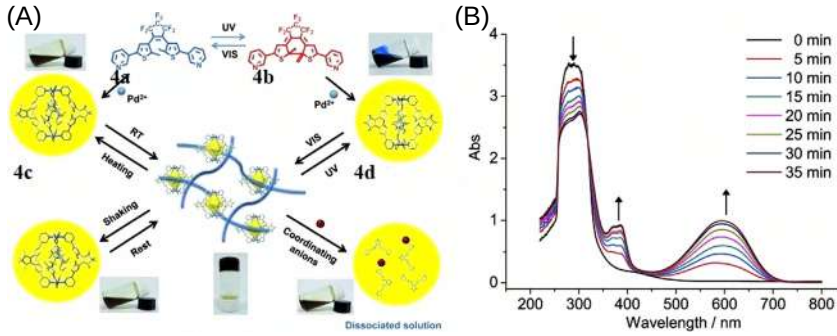

FIGURE 7.4 (A) Gelation properties of coordination cage-based gels derived from metalation of 4a and 4b, and their stimuli-responsive behavior and sol–gel transformation. (B) Absorption spectra of Pd:4a (1:2) solution in DMSO under 254 nm UV exposure indicating interconversion between 4c and 4d. (*Reprinted (adapted) with permission from Su* et al. *(2015) © 2015 John Wiley and Sons.*)

molecules leading to the formation of the supramolecular gel. Surprisingly, the DMSO solution of the ring-closed cage 4c, as well as free ligand 4a, did not produce any gelation even after a prolonged time. The authors proposed that the flexibility of the fluorinated functional groups on the periphery of the ring-opened cage allowed the hydrophobic interaction to take place leading to the formation of a network type structure, but in the case of the ring-closed cage 4d, the fluorinated backbone, due to its structural rigidity, failed to establish any type of supramolecular interaction between the cage molecules. This unique and selective gelation behavior of cage 4c was exploited to create a photo-responsive sol–gel type system. When the brown-colored DMSO gel of 4c was irradiated using 254 nm light, it transformed into a blue-colored solution of ring-closed cage 4d. The complete gel to sol transformation occurred with 12 h of UV exposure. When the blue-colored solution was exposed to visible light, the color faded within 20 min and complete gelation occurred after 10 h (Fig. 7.4).

One of the major drawbacks of using the bisthienylethene systems is the coexistence of photoactive antiparallel and photo inactive parallel forms of its derivatives. As a result of these equilibria, the total photo conversion efficiency from ring-closed to ring-opened form is always poor. Zhu and coworkers [17] have solved this issue by using a large bisbenzo(thiadiazole) substitution on the bisthienylethene backbone of a new pyridyl ligand 5a which completely restricted the rotation of the thiophene rings and hence disrupted the equilibria between the parallel and antiparallel form of the ligand (Fig. 7.5). The dipyridyl ligands were frozen in clockwise and anticlockwise orientation which generated a pair of stable enantiomers out of axial chirality and they were termed P-5a and M-5a. These enantiomers were not interconvertible and both of them formed during the ligand synthesis. Using chiral HPLC the enantiomer ligand was separated and both were subjected to metalation using the same protocol. When the racemic ligand 5a was treated with 120° Platinum acceptor 5b in a 1:1

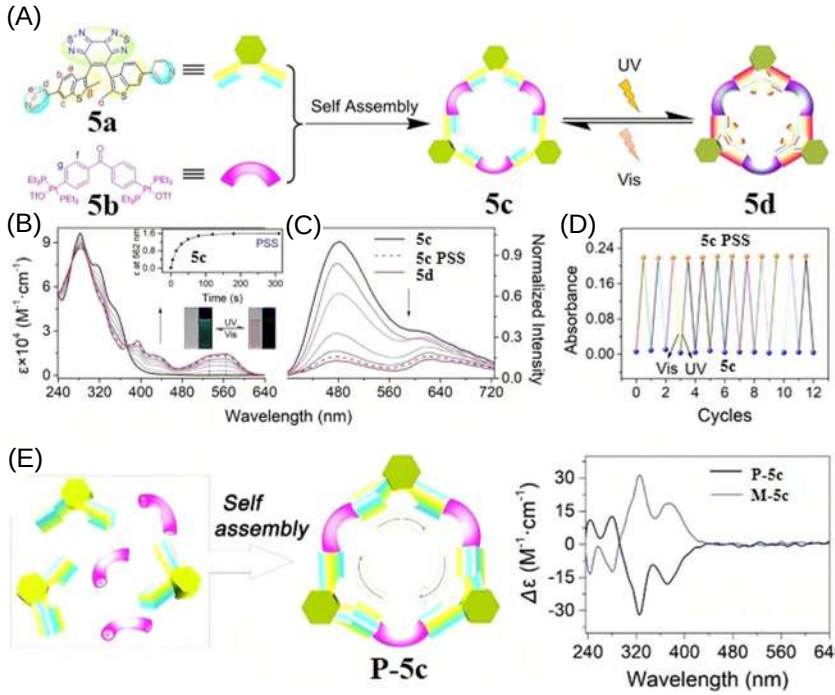

FIGURE 7.5 (A) Graphical representation of building blocks 5a, 5b and the light-induced interconversion of 5c and 5d. (B) Absorption spectra of metallacycle 5c. (C) Emission spectra of metallacycle under UV exposure of 302 nm. (D) Reversible transformation between 5c and 5d monitored by absorption spectra. (E) Self-assembly and CD spectra of the metallacycles. (*Reprinted (adapted) with permission from Zhu et al. (2019) © 2019 Elsevier.*)

ratio, it formed a racemic mixture of two platinum 3D metallacages P-5c and M-5c. The formation of the metallacages was verified by multinuclear NMR, mass spectrometry analysis, and 2D-DOSY experiments. When the photophysical behavior of 5c was investigated the cage showed two major absorption bands at 284 and 314 nm which, according to the authors, originated from the thiadiazole–ethene bridge and platinum acceptor 5b, respectively. Upon UV irradiation at 300 nm, the solution turned to red form colorless with the appearance of three new peaks at 562, 433, and 394 nm due to the formation of ring-closed metallacage 5d. To confirm the photoinduced reversible transformation, the ligand 5a was initially UV treated to form ring-closed ligand 5f and was subsequently treated with 5b in DCM to afford 5d. The multinuclear NMR and ESI-MS analysis confirmed the formation of ring-closed metallacage and it showed similar photophysical traits observed for the cage formed by UV exposure of 5c and the quantitative photo conversion yield was found to be 93%. The chirality of the 5c was explored using CD spectroscopy. For CD analysis pure P-5c cage was taken and it showed a negative Cotton effect at 287–350 nm. The M-5c cage showed the

same peaks but in the negative Cotton effect region. Upon UV exposure of the P-5c, two new peaks appeared for the ring-closed cage P-5d. 244–286 nm peak and 422–624 nm peaks were attributed to the negative and positive Cotton effect, respectively (Fig. 7.5).

Yang et al. [18] have utilized the photoswitching behavior of bisthienylethene to create a 2D platinum-based metallacycle with light-controlled singlet oxygen capability and utilized it for cancer treatment in mice models (Fig. 7.6). A new bisthienylethene-based 120° platinum acceptor 6a was coupled with a 120° porphyrin-based donor 6b with a 1:1 ratio to produce a molecular hexagon 6c containing three photochromic units and oxygen generation units. The orthogonal behavior of SCC was deliberately used in such a way that the two different behaviors did not interfere with each other. The formation of the macrocycle was established using multinuclear NMR, 2D DOSY, and NOESY NMR as well as ESI-MS analysis. The ring-opened metallacycle 6c furnished multiple peaks in the absorption spectra at 419, 514, 590, and 646 nm which were mainly attributed to the bisthienylethene and porphyrin units, respectively. UV stimulation at 315 nm leads to enhancement of peak intensity between 500 and 680 nm with a change in coloration from colorless to violet. Using the 19F NMR, the photoconversion efficiency was found to be 94%. Therefore, the formation of ring-closed metallacycle 6d was established using absorption spectroscopy and NMR analysis. As the photochromic unit and the singlet oxygen generation unit were nearby, the energy flow between them under external photostimulation was carried out using a singlet-oxygen sensor green. When 6c was excited with a 420 nm irradiation, the sample exhibited bright green fluorescence, indicating the generation of singlet oxygen by the porphyrin group. But the ring-closed cage 6d showed no such fluorescence indicating no formation of singlet oxygen. Hence metallacycle 6c which provides singlet oxygen at 420 nm UV exposure can easily be transformed into 6d by 315 nm irradiation and the singlet oxygen generation will cease effectively. Thus the UV and visible light can be utilized as triggers for singlet oxygen generation. The authors proposed that at the ring-opened cage the porphyrin donor absorbs UV irradiation and reaches the excited singlet state S1. The energy from the S1 state is then transferred to the triplet oxygen followed by the singlet oxygen level. But when the photochromic acceptor reorganized in the ring-closed form, it hijacked the energy from the triplet oxygen state thereby disrupting the singlet oxygen formation. Furthermore, the metallacycle 6c nanoparticles were prepared using amphiphilic polymer mPEG-DSPE and the nanoparticles were found to retain the photophysical behavior of the parent macrocycle. The nanoparticles were injected into immunocompromised mice infected with HeLa cells and the nanoparticles were used as photodynamic therapeutic agents. Using light as the trigger, the singlet oxygen was generated in the cancer-affected cells and the IC50 value was found to be 1.926 + 0.027 μM (Fig. 7.6).

The same group has reported Foster resonance energy transfer (Fig. 7.7) in a multicomponent bimetallic metallacycle 7c where the acceptor 7a was used in

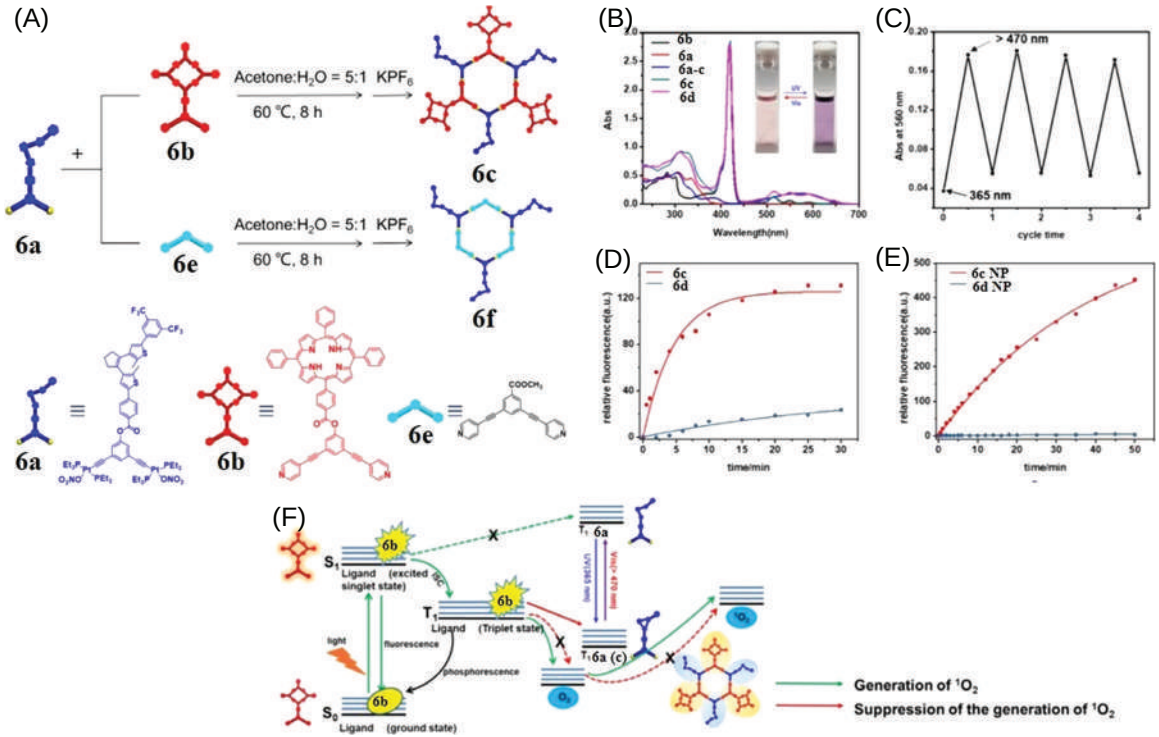

FIGURE 7.6 (A) Schematic representation of the building blocks and self-assembled metallacycle. (B) Absorption spectra of the donor 6b, acceptor 6a, and metallacycle 6c in open and ring-closed form. (C) Fatigue resistance of 6c after alternative exposure to UV irradiation of 365 and 470 nm. (B) Fluorescence response of singlet oxygen sensor green after treatment with 6c and 6d after 30 min. $\lambda_{ex} = 504$ nm and $\lambda_{em} = 560$ nm. (E) Fluorescence response of singlet oxygen sensor green after treatment with 6c and 6d in their nanoparticle form after 50 min. $\lambda_{ex} = 504$ nm and $\lambda_{em} = 529$ nm. (F) Proposed mechanism of energy transfer in the metallacycle. (*Reproduced (adapted) with permission from Yang et al. (2019) © 2019 American Chemical Society.*)

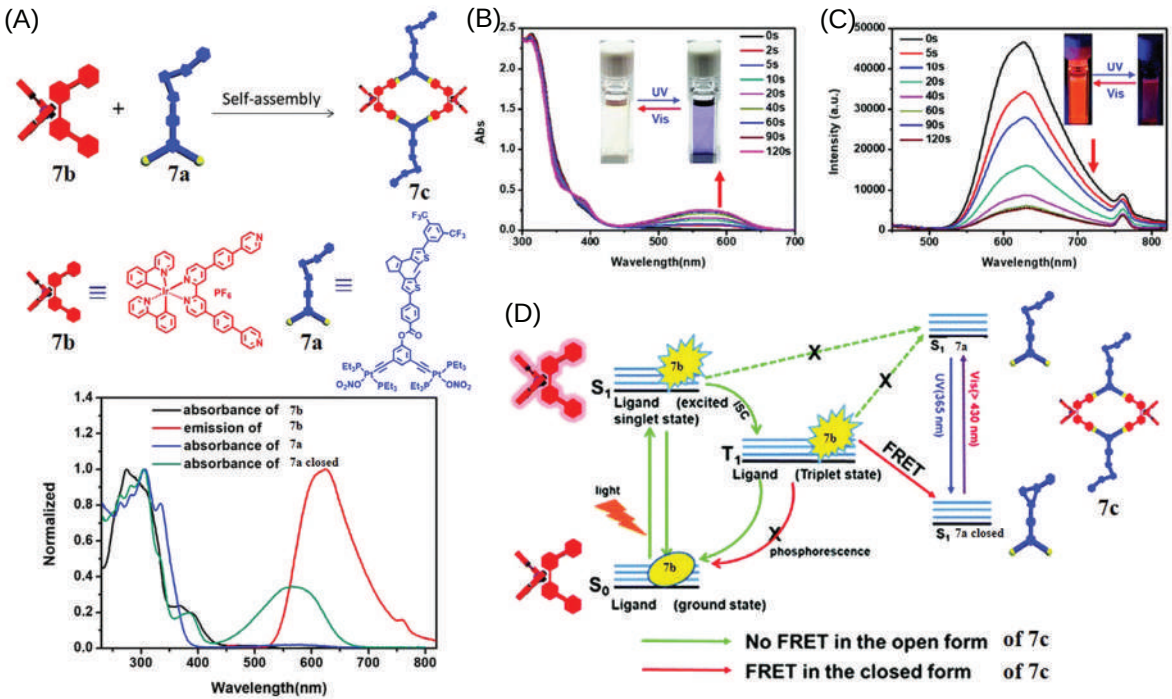

FIGURE 7.7 (A) Graphical representation of the building blocks and the final assembly, and their absorption spectra. (B) Change in the absorption spectra of 7c upon the exposure of 365 nm UV irradiation at inert atmosphere. (C) Emission spectra of the metallacycle 7c after excitation at 365 nm. (D) Proposed mechanism of the photoinduced Forster resonance energy transfer in the metallacycle 7c. (*Reproduced (adapted) with permission from Yang* et al. *(2019) © 2019 Royal Society of Chemistry.*)

combination with highly fluorescent donor 7b [19]. Although FRET was well known for multicomponent systems, light-triggered FRET was unheard of. The authors used the 7a and 7b in 1:1 ratio to afford rhombic metallacycle 7c. The authors proposed that the very close proximity of the Ir-based ligand 7b and photochromic acceptor 7a could lead to controllable FRET. The formation of the metallacycle was established using multinuclear NMR, 2D DOSY, NOESY NMR, and ESI-MS analysis where the appropriate molecular fragments were obtained. When the photophysical properties of the building blocks were examined the acceptor showed absorption peaks at 315 and 350 nm in the ring-opened form and 680 nm in ring-closed form, and the donor 7b displayed an absorption peak at 450 nm. Upon excitation at 380 nm, the donor displayed bright fluorescence at 630 nm. Thus the acceptor absorbance and the donor fluorescence matched perfectly to initiate FRET in the system. When the metallacycle 7c was exposed to 365 nm irradiation the color of the solution changed from light yellow to purple with the appearance of a new absorption peak at 560 nm. The formation of the ring-closed rhomboid 7d was responsible for this visual transformation. When the solution of 7d was kept under visible light, the system changed back to the ring-closed 7c within 180 s indicating fast reversible transformation. Along with that, the 365 nm UV irradiation on 7c led to quenching of the fluorescence peak at 630 nm indicating FRET from the Ir center the ring-closed acceptor. Using a DFT simulation the authors predicted that under normal circumstances the ligand absorbed external stimuli and got excited to S1 level. The excited-state energy was released to the triplet ligand state and thereby fluorescence originated from the triplet metal-centered ligand. But upon 365 nm UV irradiation, the closed acceptor triplet energy state became lower than the triplet donor state and the excited energy was siphoned off, leading to fluorescence quenching (Fig. 7.7).

Zhu and coworkers [20] used a similar approach of light-controlled FRET in photochromic metallacycle (Fig. 7.8). They synthesized a new bisthienylethene donor 8a combined it with a 120° platinum acceptor 8b with a napthalimide appended to its backbone. The treatment of the donor and the acceptor in a 1a:1 ratio at ambient condition generated the molecular 2D hexagon 8c in quantitative yield. The purity of the newly formed macrocycle was explored using multinuclear NMR and ESI-MS analysis. The transformation between the ring-opened SCC 8c and its ring-closed analog 8d was investigated using both NMR and UV–Vis spectroscopy. 8c displayed two absorption peaks at 306 and 416 nm which were assigned to the photochromic donor and the napthalimide acceptor respectively. When irradiated at 313 nm the color of the solution changed from colorless to light cyan along with the appearance of new absorption peaks at 615 nm. A 95% photoconversion efficiency was obtained when the formation of 8d was compared with a metallacycle obtained from a pure ring-closed ligand. Under visible light exposure of 480 nm, the ring-closed 8d transformed back to ring-opened 8c. To verify the fluorescence behavior of the macrocycle, 8c was exposed to a UV light of 313 nm, bright fluorescence emission was observed at

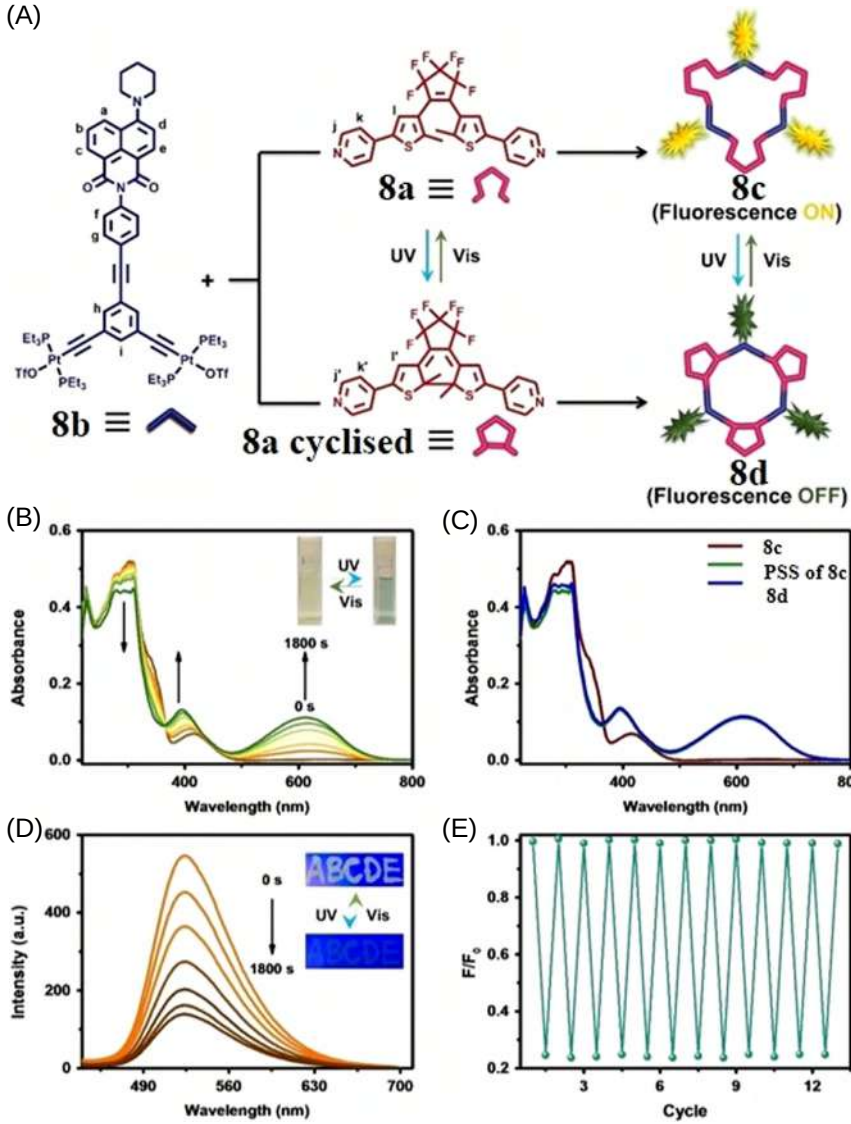

FIGURE 7.8 (A) Schematic representation of the donor, acceptor, and metallacycle. (B) Absorption spectra of 8c under UV exposure ($\lambda_{ex} = 313 \pm 20$ nm). (C) Absorption spectra of 8c, 8d, and the photostationary state of 8c. (D) Emission spectra of 8c after excitation ($\lambda_{ex} = 313 \pm 20$ nm). (E) Fatigue resistance of 8c after UV irradiation between 313 and 480 nm. (*Reproduced (adapted) with permission from Zhu* et al. *(2021) © 2021 John Wiley and Sons.*)

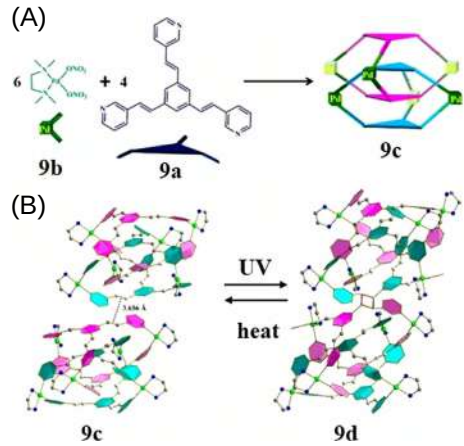

FIGURE 7.9 (A) Graphical illustration of the formation of metallacage 9c from the building blocks. (B) UV and thermal stimuli-induced reversible transformation of the metallacage 9c and 9d. (*Reproduced (adapted) with permission from Samanta and Mukherjee (2014) © 2014 American Chemical Society.*)

524 nm originated from the napthalimide unit. But with time the fluorescence emission gradually decreased. It took 30 min to completely quench the emission and the authors attributed the FRET from the napthalimide unit to the ring-closed acceptor for which formed after the UV exposure (Fig. 7.8).

7.3 Styryl building block-based SCC

The styryl group is well-known for its photocyclization behavior but to date, very few supramolecular systems are reported where the styryl building blocks are incorporated to display photoisomerization. The main reason for such rarity lies in the unpredictable geometry of the final assembly. The cyclization reaction only occurs when two styryl groups are properly oriented in close vicinity and such structural arrangements are merely serendipitous. Mukherjee and coworkers [21] have reported the sunlight-induced cyclization of 3D Palladium metallacages and their reversible ring-opening under thermal exposure (Fig. 7.9). The authors synthesized a tripyridyl donor 9a containing three double bonds. The donor was treated with cis-blocked palladium acceptor 9b in a 3:2 ratio in water at room temperature for 24 h and was kept for crystallization with slow acetone diffusion. The formation of the cage was first identified with a change in the proton NMR of the ligand where the sharp peaks split into multiple peaks indicating the possibility of interpenetrated cage formation. Finally from the crystal structure analysis, it was observed that the ligand formed a new type of 3D metallacage 9c containing 6 palladium atoms and four ligands and two such cages are interpenetrated. Moreover, the crystal structure also revealed that the double bond of two such interpenetrated cage molecules is just 3.65 Å away from each other. A prompt exposure of the crystals for 48 h revealed the

cyclization which lead to the formation of cyclobutane ring and a new type of interpenetrated metallacage 9d. The existence of the cyclized metallacage was established with the single-crystal X-ray analysis. A similar cyclization was also observed when the 9c crystals were exposed to UV irradiation at 0°C. Such cyclobutane formation by (2+2) cycloaddition reactions is known to transform back to original building blocks under thermal treatment. When the crystals of 9d were subjected to heat treatment at 90°C then the cyclized ring system slowly disintegrated into a double-bonded precursor within 2 h. The progress of the ring-opening reaction was monitored by using pure cyclized crystals in D_2O and the disappearance of the cyclobutane proton and the appearance of the styryl proton confirmed the reversibility of the system (Fig. 7.9).

7.4 Azo building block-based SCC

The diazo group is one of the most well-studied functional groups for its photochromic behavior. Therefore, several research groups have developed numerous SCC containing diazo moiety at various locations of the macromolecules.

Fujita and coworkers [22] have reported a new type of 3D large metallacage 10b by reacting a 120° azo dipyridyl donor 10a containing appended diazo group and by treating it with palladium nitrate in a 2:1 ratio (Fig. 7.10). The very large metallacage contained 12 Pd centers and 24 ligands. The azo groups were strategically located with an inward orientation. The formation of the 10b was characterized by a change in ^{1}H NMR of the ligand and was further established by CSI-MS analysis. Finally, suitable single-crystals of 10b were obtained and the single-crystal X-ray diffraction study established the structure of the macro cage. The azobenzene-based cage displayed two peaks at 365 and 436 nm in the absorption spectra which were assigned to the π–π^* and n–π^* transition in the ligand. When exposed to the 365 nm UV radiation a 17% conversion from trans to cis-azobenzene metallacage 10c was observed and after further irradiation at 436 nm 20% total conversion was observed. The cis-azobenzene is thermally unstable and as a result, when the cis-isomerized metallacage was heated at 50°C the cis isomer transformed into the more stable trans form. The trans azobenzene ligand is nonpolar but the cis-azobenzene is more polar due to high dipole moment, therefore the interior of the 10b is hydrophobic but the interior of 10c is hydrophilic. Therefore using light as external stimuli the interior of the metallacage can be changed between hydrophobic and hydrophilic. This unique behavior was exploited by the research group in the light-induced encapsulation and release of hydrophobic guest molecules inside the cage. The pyrenealdehyde is well known as a hydrophobic guest molecule and is well studied for encapsulation in macrocyclic systems. When the pyrenealdehyde was added to the acetonitrile: water solution of the cage 10b, an upfield shift in the guest ^{1}H NMR was observed indication encapsulation and more shielding, but when the guest encapsulated cage was irradiated with UV light, the cage interior transformed into more hydrophilic nature and the guest was released from the

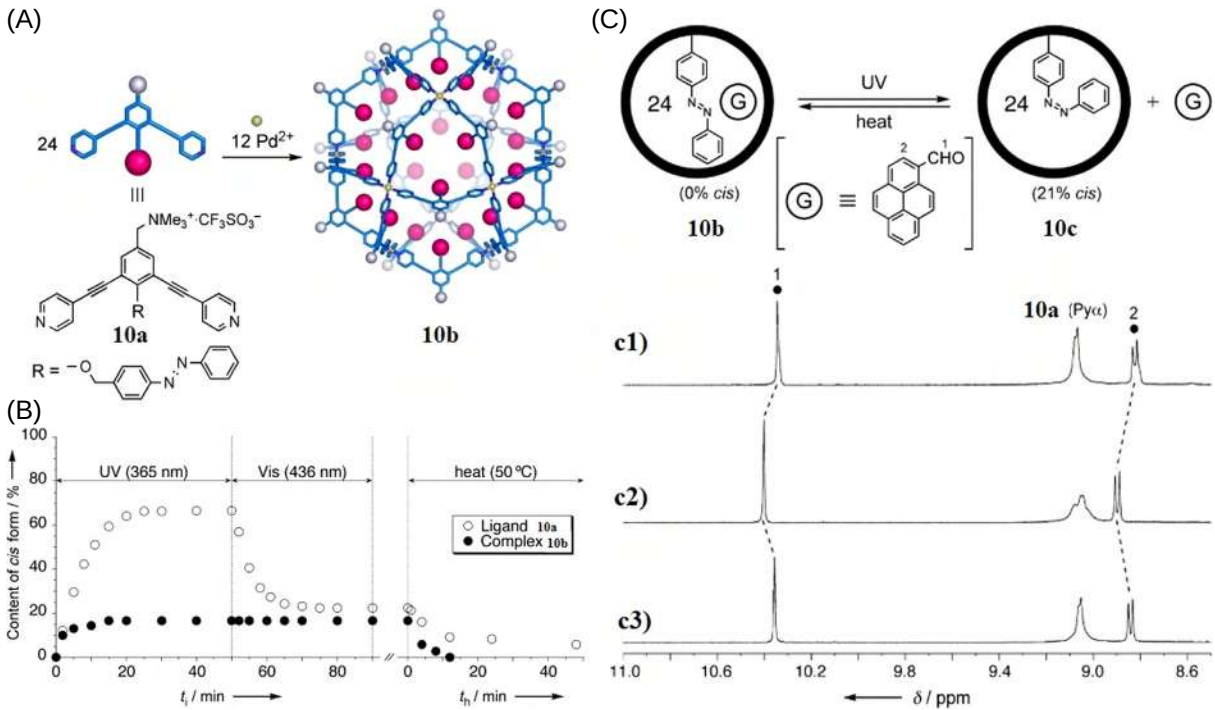

FIGURE 7.10 (A) Graphical illustration of the self-assembly of 10b from the building blocks. (B) Changes in the content of the cis form in 10a and 10b under UV irradiation (365 nm). (C) The proton NMR spectra of pyrene in the presence of (c1) no additive, (c2) 10b, (c3) 10a, (c3) 10c. (*Reproduced (adapted) with permission from Fujita et al. (2007) © 2007 John Wiley and Sons.*)

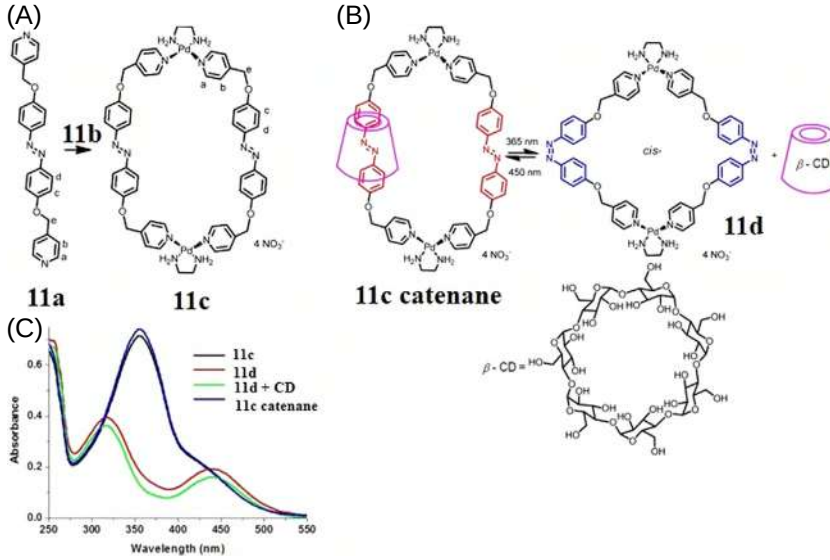

FIGURE 7.11 (A) Schematic presentation of the building blocks and the metallacycle. (B) Photoisomerization of 11d and 11c catenane. (C) Absorption spectra of 11c, 11d, 11d+CD, and 11c catenane in water. (*Reproduced (adapted) with permission from Stang* et al. *(2015) © 2015 American Chemical Society.*)

molecular capsule. When the isolated guest and cage were heated at 50°C the cage became hydrophobic due to cis to trans isomerization and an upfield shift in the guest proton was obtained (Fig. 7.10).

Stang and coworkers [23] have provided a new photochromic palladium metallacycle 11c containing azobenzene-based dipyridyl donor 11a and cis-blocked palladium acceptor 11b (Fig. 7.11). The nitrate salt of the acceptor 11b was treated with the donor 11a with 1:1 a ratio in a methanol–water mixture to afford the final macrocycle 11c. The formation of the macrocycle was established using multinuclear NMR and ESI-MS analysis. When the absorption spectra of the 11c were recorded a sharp peak at 356 nm was observed which was assigned to the trans azobenzene. But when the macrocycle was exposed to UV irradiation at 365 nm for 60 s, the main absorption peak decreased and a new peak at 442 nm appeared. The new peak was attributed to the formation of a new macrocycle 11d containing cis azobenzene ligand. When the 11d was exposed to visible light at 450 nm for 2 min then the absorption spectra reversed back to the original with the reappearance of the maxima at 356 nm. This cis–trans isomerization was further studied using photoirradiation and ^{1}H NMR. When the trans isomer was irradiated with 365 nm light the original proton peaks of the pyridyl moiety changed from 6.83, and 7.54 to 6.74 and 6.90 ppm, respectively. The radiation of the cis form at 450 nm changed the macrocycle in the original trans form. The 11c was further explored for the host–guest inclusion complex

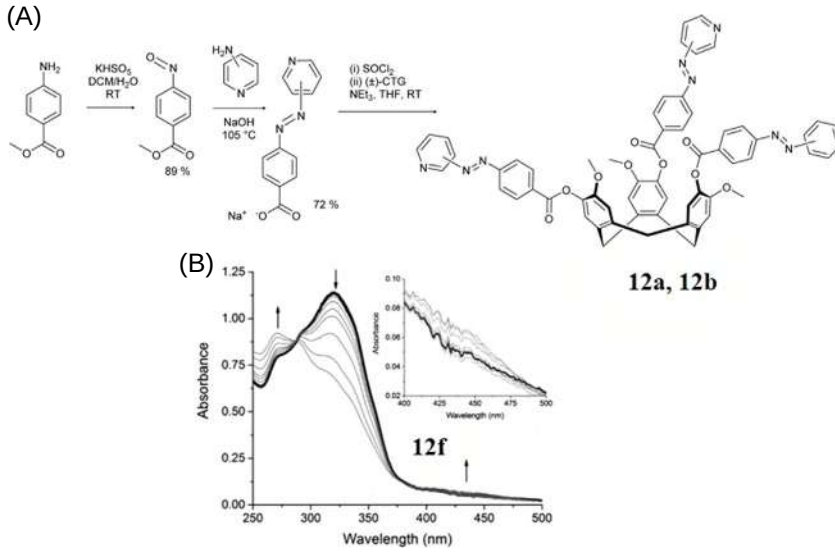

FIGURE 7.12 (A) Synthesis of the donor 12a, and 12b. (B) E–Z isomerization of cage 12f was studied utilizing absorption spectra. (*Reproduced (adapted) with permission from Hardie et al. (2018) © 2018 Royal Society of Chemistry.*)

formation with β-cyclodextrin (CD). When β-CD was added to a D_2O solution of 11c in a 1:1 ratio, some new peaks appeared in the proton NMR along with the reduced intensity of the previous pyridyl proton peaks. It was proposed that the β-CD formed inclusion complex with only one donor moiety and thus the two pyridyl donor ligands became magnetically nonequivalent which lead to the appearance of multiple proton peaks. The formation of the inclusion complex also enhanced the absorption peak intensity at 356 nm. When treated with β-CD, the cis isomeric macrocycle 11d was not found to display any change in the proton signal indicating the fact that the larger size of the cis linker hindered the host–guest complex formation. Therefore, by using light as the trigger the macrocycle was transformed between 11c and 11d which further controlled the host–guest complex formation capability (Fig. 7.11).

Hardie et al. [24] have reported a new set of chiral metallacages based on cyclotriguaiacylene (CTG) units (Fig. 7.12). The four new ligands 12a, 12b, 12c, and 12d contained azobenzene-based tripyridyl donors with para and meta coordination sites. The ligands were combined with a new iridium-based accurate ESI-MS analysis and multinuclear 1D and 2D NMR. Since all the cages exhibited similar photophysical behavior, the authors reported the absorbance, fluorescence, and photochromic behavior of cage 12f. The absorption of the cage was recorded in DC and two ligand-centered peaks were obtained at 274 and 293 nm. When irradiated with UV light of 355 nm, the cage transformed from E isomer to Z isomeric cage 12k. The UV irradiation also reduced the

peak associated with the ligand centered π–π^* transition. The cages gave very high conversion efficiency from E to Z isomer with a range between 39% and 40%. The transformation of the 12f and 12k was studied by utilizing proton NMR spectra. When the newly formed mixture of E and Z isomeric cages were subjected to an exposure of 450 nm light for 15 min, all the metallacages transformed back to the original E isomeric form, indicating photo-controlled reversible transformation (Fig. 7.12).

7.5 Spiropyran building blocks-based SCC

Apart from the previously discussed azobenzene, bisthienylethene, styrene, spiropyran is another well-known photochromic unit that has been molded in a variety of platforms for various applications. But the example of spiropyran-based metallacycles or metallacages is extremely rare.

Mukherjee et al. [25] have first reported a spiropyran-based molecular hexagon (Fig. 7.13). The authors developed two new platinum-based 120° acceptors 13a and 13b and combined them with spiropyran-based dipyridyl donor 13c to afford two new molecular hexagons 13d and 13e and aldehyde-based donor 13f to afford metallacycle 13g. The 13e molecular hexagon contained both aggregation-induced emission active triphenyl unit in the acceptor backbone and photochromic spiropyran on the donor building block making the system a unique multifunctional SCC. The hexagonal SCCs were thoroughly characterized using IR, multinuclear NMR, 2D NMR, and ESI-MS analysis. The photophysical experiments were carried out in DCM for the SCC. The hexagons 13d and 13e gave absorption maxima at 331 and 335 nm, respectively, which was attributed to the π–π^* transition originating from the photochromic donor. When the photochromic experiments were carried out the free donor ligand 13c did not exhibit any switching behavior, but when the hexagon 13f was exposed to UV light of 365 nm for 2 min, the color of the solution changed from yellow to intense green. A new absorption peak appeared at 625 nm indicating the formation of the ring-opened spiropyran ligand. The hexagon 13d also exhibited similar photochromic behavior. When the metallacycle solutions were kept under sunlight, the color of the solutions turned yellow within a minute indicating fast reversibility. The ring-opened form of the spiropyran or the so-called photo stationary state (PSS) was found thermodynamically unstable and switched back to the ring-closed form quickly. Literature preview showed that the metalation of the spiropyran ring can enhance the stability of the PSS state and that was the reason why the free donor ligand did not exhibit any photochromism but the same ligand upon metalation showed light-induced transformation (Fig. 7.13).

Mukherjee and coworkers [26] further elaborated the concept of metalation-induced photochromism by reporting three new metallacycles 14b, 14c, and 14d which were prepared using previously reported building blocks and a new photochromic spiropyran donor 14a (Fig. 7.14). The metallacycles were

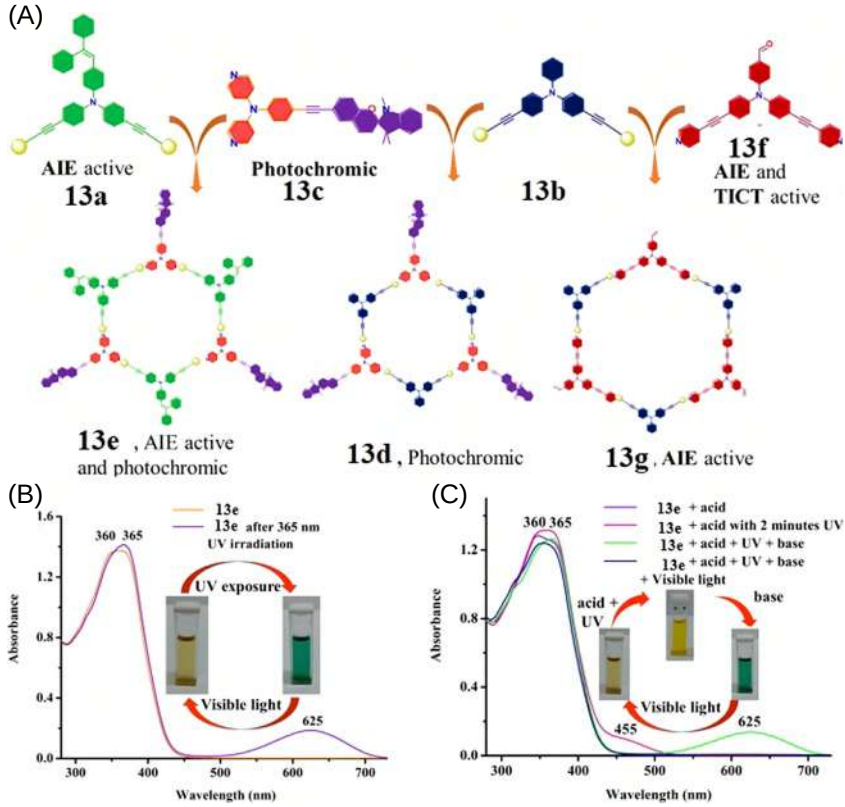

FIGURE 7.13 (A) Schematic presentation of the self-assembly of the metallacycles from the building blocks. (B) Photochromism of 13e was studied using absorption spectroscopy. (C) Acidochromism of 13e upon exposure to mild base and acid. (*Reproduced (adapted) with permission from Mukherjee et al. (2019) © 2019 American Chemical Society.*)

properly characterized using NMR, 2D NMR, and ESI-MS analysis. When the photochromic studies on the macrocycles were carried out they gave different results. Although the free ligands did not show any photochromism, the DMSO solution of 14b, displayed a change in coloration from colorless to a blue color with the vanishing of the absorption peak at 347 nm and the appearance of a new peak at 632 nm. The authors attributed the change in coloration due to the formation of PSS or the open merocyanine architecture of the ligand which was facilitated by metalation. When exposed to visible light for 5 min, the blue color of the solution faded to colorless leading to the formation of thermodynamically stable 14b. But for 14c and 14d, the stability of the PSS was low and only 2 min of visible light exposure reversibly transformed the ring-opened macrocycles. The authors proposed that the position of the spiropyran linker in the metallacycle 14c and 14d is at the periphery and hence the opening and the closing of the ring

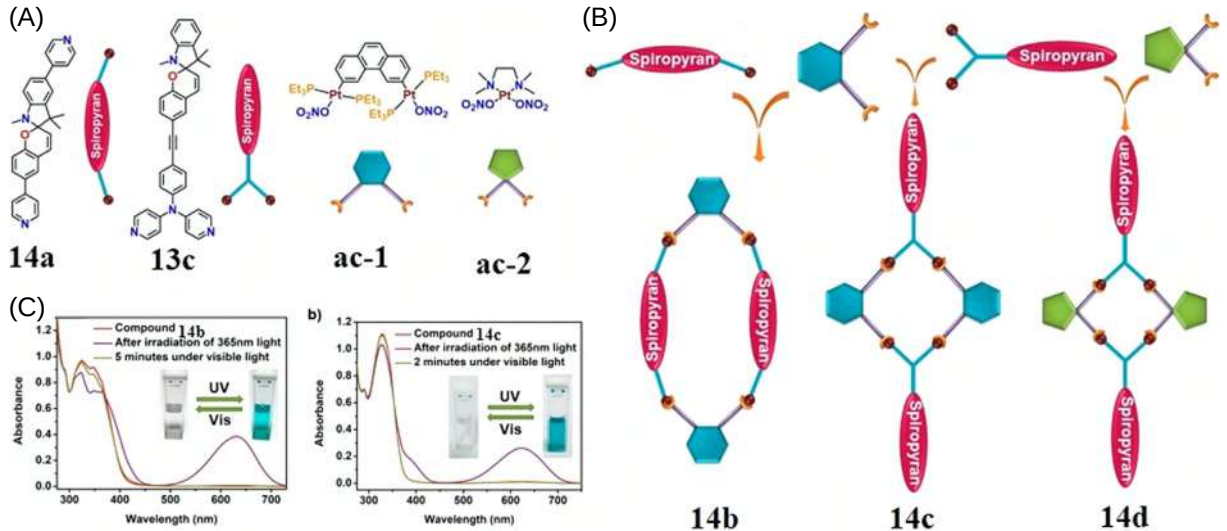

FIGURE 7.14 (A) Graphical presentation of the building blocks of the metallacycles. (B) Schematic representation of the synthesis of the metallacycles. (C) Reversible photochromic behavior of the metallacycles 14b and 14c upon exposure to UV and visible light. Reproduced (adapted) with permission from Mukherjee et al. (2020) © 2020 American Chemical Society.

did not influence the stability of the PSS. But in the case of 14b, which contained the spiropyran unit in the molecular skeleton, the ring-opening lead to structural change with the bite angle of the donor decreasing from 134° to 125°. Hence more electron density is whisked to the metal center as the bite angle reaches the ideal value of 120° and the stability of the PSS increased (Fig. 7.14).

7.6 Host–guest interaction driven photochromism in SCC

All the aforementioned systems consisted of photochromic units in their building blocks, but recently a new class of systems has emerged where the host–guest interaction of 3D metallacages is exploited to trap photochromic guest molecules inside the metallacages and the photochromic behavior of the host–guest inclusion systems was experimented on.

Klajn et al. [27] reported a set of 3D metallacages 15a and 15b and their encapsulation of three different spiropyran derivatives 15c, 15d, and 15f (Fig. 7.15). The cages were prepared following the previously reported protocol and cage 15a was structurally rigid whereas, 15b is highly flexible. This encapsulation study aimed to understand the effect of confinement on the photochromic behavior of the guests. Spiropyran is well known to display an equilibrium between a highly stable ring-closed spiropyran (SP) form and a transient ring-opened merocyanine (MC) form. The authors prepared the protonated MC form of the guest 15c and treated it with the cage solution of 15b and the appearance of an intense blue coloration with an absorption peak at 592 nm was observed indicating the formation of stable deprotonated MC form of 15c. It should be noted that although the MC form of spiropyran is highly unstable here the authors found the blue color to exist for a prolonged period. The formation of the MC form inside the confined cage 15b was further established by the single-crystal X-ray diffraction study where it was found that the MC form of the 15c is thoroughly packed inside the cage cavity due to strong π–π interaction. Moreover, after encapsulation, the flexible cage 15b underwent structural distortion where the distance between two opposite Pd ions increased from 16.9 Å to 18.3 Å. The rigid cage 15a did not exhibit any guest binding behavior. The other two guest molecules 15d and 15f were also found to be stabilized in their MC form after encapsulation. When the photochromic experiments of the encapsulated cage were carried out, some unusual responses appeared. Upon excitation at the absorption maxima of 580 nm of 15c encapsulated in 15b, no change in coloration was found which was surprising because the free guest 15c photoisomerized at this irradiation. Surprisingly excitation with more energetic 460 nm light changed the coloration of the host–guest system from blue to colorless. To explain this surprising phenomenon, the authors proposed that on the solution the cage encapsulated guest existed in an equilibrium of protonated and deprotonated form $15cMC@15b + H_2O = 15cMCH^+@15b + OH^-$. Upon photoirradiation, the protonated MCH^+ form underwent photoisomerization to the colorless ring-closed form and the equilibrium shifted to the right side leading

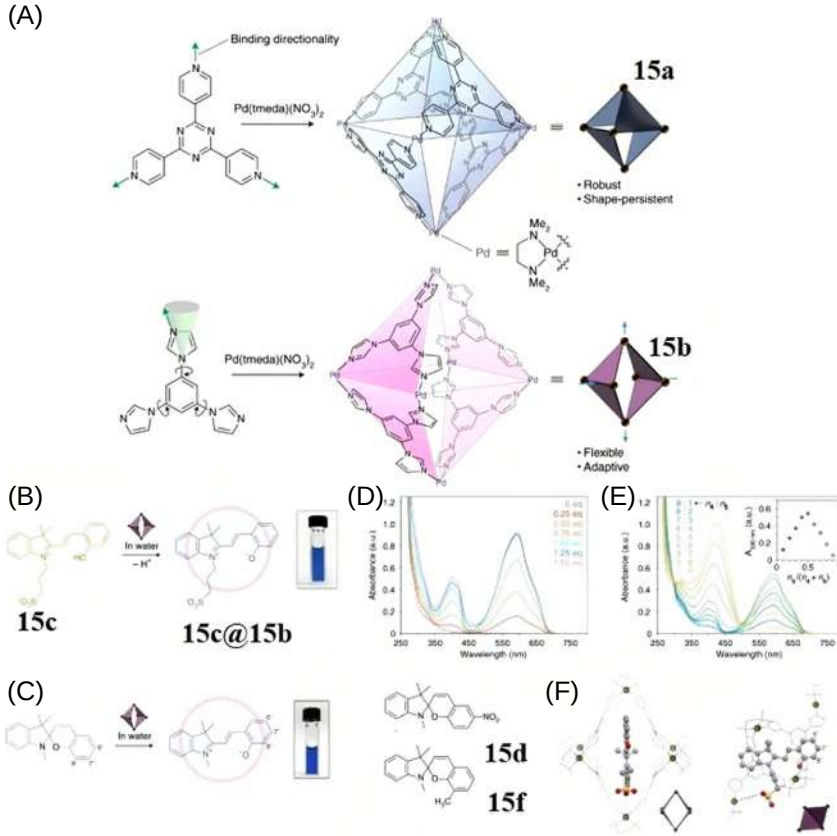

FIGURE 7.15 (A) Synthesis of octahedral cages 15a and 15b from their precursors. (B) Encapsulation-induced deprotonation of 15c. (C) Encapsulation-induced deprotonation of 15d, 15f. (D) Changes in the absorption spectra of 15b after the addition of 15c. (E) Stochiometry determination by Jobs plot from the absorption spectra of a mixture of 15b a, and 15c. (F) X-ray crystal structure of 15c@15b. (*Reproduced with permission from Klajn et al. (2018) © 2018 D. Samanta, D. Galaktionova, J. Gemen, L. Shimon, Y.D. Posner, l. Avram, P. Kral, R. Klajn.*)

to the disappearance of the blue coloration. This photoinduced transformation was found to be reversible. When the colorless host–guest complex was kept under visible light, the color immediately changed to the original intense blue indicating formation of MC form. Similar photochromic behavior was also observed for the guests 15d and 15f. The authors also experimented on the solid state photochromic behavior of the host–guest complex and created thin films of the inclusion complex on a glass plate and verified positive photochromic behavior which lead the author to propose the application of such systems for photochromic memory devices (Fig. 7.15).

A unique concept of the creation of photochromic SCC (Fig. 7.16) was first developed by Severin et al. [28]. The conventional SCC are well known

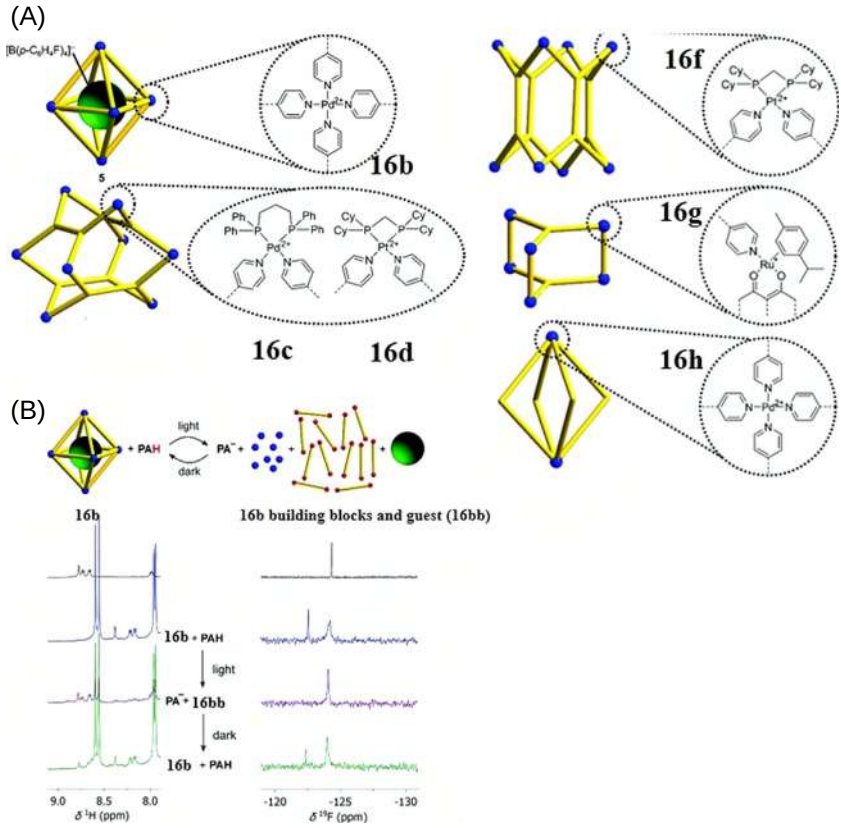

FIGURE 7.16 (A) Structure of various metallacages based on different metal centers. (B) Photoinduced dissociation of 16b upon addition of 16a monitored by proton NMR spectroscopy. (*Reproduced (adapted) with permission from Severin et al. (2018) © 2018 Royal Society of Chemistry.*)

for their sensitivity toward the change in pH of the system. A minute quantity of acid is known to deconstruct most of the SCC and removal of the excess protons reconstructs the SCC. Using this concept, instead of using photochromic building blocks of photochromic guests, the authors proposed the application of a photochromic acid or photoacid 16a where the molecule is a merocyanine molecule and under UV excitation of 425 nm, it released a proton and absorbs it back upon removal of the light source. The uniqueness of this concept lied in the fact that any self-assembled architecture which is sensitive to pH will undergo reversible deconstruction in presence of this photoacid. The authors prepared a series of SCC 16b, 16c, 16d, 16f, 16g, and 16h containing Pd, Pt, and Ru metal centers for the photo-responsive study. To prove the concept at first, 24 eq of trifluoroacetic acid (TFA) was added to an acetonitrile–water (4:1) solution of 16b and the proton NMR spectra were recorded. From the spectra, it was observed that the acid addition completely broke the metallacage in its building

blocks. A similar experiment was also carried out for 16b, where excess 16a was added to a solution of 16b in deuterated acetonitrile and water mixture. The mixture was exposed to violet light and the change was monitored using 1H and 19F NMR spectroscopy. The NMR analysis revealed that light stimulation prompted the disassembly of the metallacage. The metallacage contained a fluorinated guest molecule and before UV exposure two different ^{19}F signals were obtained indicating the existence of encapsulated and free guest molecule. But the UV exposure revealed the existence of only the free guest molecule indicating assembly collapse. When the system was kept under dark for 8 h, the multinuclear NMR analysis revealed the reformation of the original guest encapsulated cage indicating the reabsorption of the proton by the photoacid. Similar photoinduced deconstruction and reconstruction were observed for all the self-assemblies indicating the validity of this simple but effective concept (Fig. 7.16).

Mukherjee and coworkers [29] have reported a pair of metallacages 17a and 17b and experimented on their photochromic guest encapsulation behavior (Fig. 7.17). As reported earlier, spiropyran is a well-known photochromic molecule that is insoluble in water and mostly stays in the ring-closed spiropyran form. Under UV irradiation it transforms into unstable ring-opened merocyanine form which will revert immediately once the UV light source is removed. In this work the authors demonstrated two new unique behavior of the spiropyran encapsulated cage compounds, first the cage compounds enabled the spiropyran derivatives 17c, 17d to solubilize in water, and second, the cages stabilized the so-called transient MC state of the guest molecules for a prolonged period. The metallacage 17a was newly synthesized and was characterized by NMR, ESI-MS analysis, and single-crystal X-ray diffraction analysis. Cage 17b was previously reported by the same group and the crystal structure revealed large cavity and open pathways for both the cages. When insoluble bromo-spiropyran 17c was added to the deuterated water solution of cage 17a, the color of the solution gradually changed from yellow to greenish-blue within a period of 6 h and the color remained stable for several weeks indicating very high stability of the MC state of 17c. Moreover, the ^{1}H NMR spectra of the host–guest complex indicated the formation of ring-opened MC form in the cage. The other spiropyran derivative 17d also furnished similar photophysical behavior in the encapsulated form in cage 17a. The guest molecules 17c and 17d also showed similar photophysical behavior when encapsulated in cage 17b with a change in coloration from light yellow to blue after guest addition. When the thermal stability of the inclusion complex was analyzed, the color of the complex slowly changed from blue to colorless for both the guest molecules along with the formation of insoluble precipitate in the medium. The proton NMR study revealed that upon heating the cage released the guest molecules which were insoluble in water and thus the color changed with the formation of ppt. Moreover, when the heat source was removed the system returned to the original blue-colored inclusion complex indicating the reversibility of the system (Fig. 7.17).

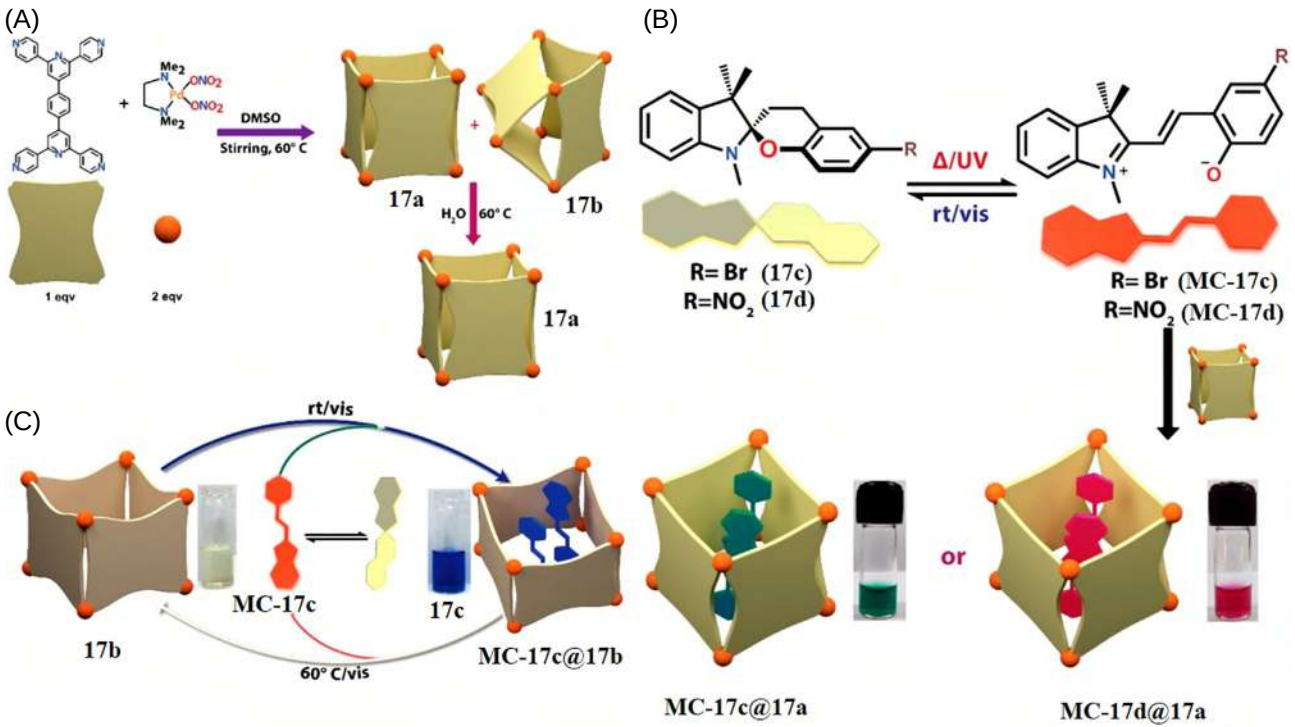

FIGURE 7.17 (A) Self-assembly of the molecular barrels from the tetrapyridyl donor and palladium acceptor. (B) Encapsulation of 17c and 17d in their merocyanine form in the nanobarrel 17a. (C) Reversible thermochromism of merocyanine form of 17c in nanobarrel 17b. (*Reproduced (adapted) with permission from Mukherjee et al. (2018) © 2018 American Chemical Society.*)

Klajn et al. [30] have first reported the encapsulation and photochromic behavior of a set of azobenzenes (Fig. 7.18) in a previously reported palladium-based 3D metallacage 15b. It was predicted that the trans-cis isomerization of azobenzene involves a substantial change in the geometry and therefore would require a highly flexible confined space, and cage 15b was well reported for its structural flexibility. Although the azobenzene derivatives were insoluble in water, the host–guest complex was prepared by simply adding the solid azobenzene in the aqueous solution of the cage. The color of the cage immediately changed from colorless to intense yellow indicating encapsulation of guest. For the guest 18a, the absorption spectra of the guest encapsulated cage revealed maxima at 325 nm indicating the existence of π–π^* transition in the guest. The UV/Vis spectroscopy also showed that the inclusion complex has a composition of 1:1.2 for cage and guest respectively leading to the clue that more than one guest was encapsulated in the cage. Finally, the single-crystal X-ray structure analysis revealed the orientation of two azobenzene inside each cage molecule. The coexistence of the two guests inside the cage was facilitated by π–π interaction and hydrophobic interaction. When the host–guest complex was subjected to UV irradiation of 365 nm, then the main absorption maxima slowly diminished and a new peak appeared at 420 nm with comparatively poor intensity. The authors assigned the peak to n–π^* transition of cis azobenzene. But the proton NMR analysis revealed the trans to cis conversion to only 60%. It was predicted by the author that the cis conformation occupied more space in the cage capsule thereby exerting more strain on the cage structure. The mixture of 40% trans and 60% cis azobenzene inside the cage capsule was established by an NMR spectroscopy study. To initiate the reverse reaction, the total system was irradiated with 420 nm radiation and the mixture composition changed to 89% trans and 11% cis respectively. The switching of the total cage complex was successfully repeated several times. The retention of the small quantity of the cis isomer was attributed to photo fatigue. The other azobenzene derivatives also displayed similar photophysical behavior indicating the universal guest encapsulation-induced photochromic behavior of the cage system (Fig. 7.18).

Mukherjee and coworkers [31] have reported a new guest-induced photochromic behavior of a new cage 19a in presence of new photochromic molecular systems known and donor–acceptor Stenhouse adducts (DADSA) (Fig. 7.19). Two different derivatives of DASA 19b, 19c were used for this study. The DASA is a recently developed photochromic system that provides some unique photophysical behavior. Under the influence of visible light, it transforms between a ring-closed form and a ring-opened form. The ring-closed form is found to be more stable in polar solvents like water, and methanol, whereas the ring-opened form is more stable in DCM and other halogenated solvents. The light-induced reversible behavior is most prominent in nonpolar organic solvents like toluene, and hexane. The formation of a new water-soluble host 19a provided a new opportunity to study the photophysical behavior of DASA derivatives in water. For guest encapsulation experiments, the DASA compound was added

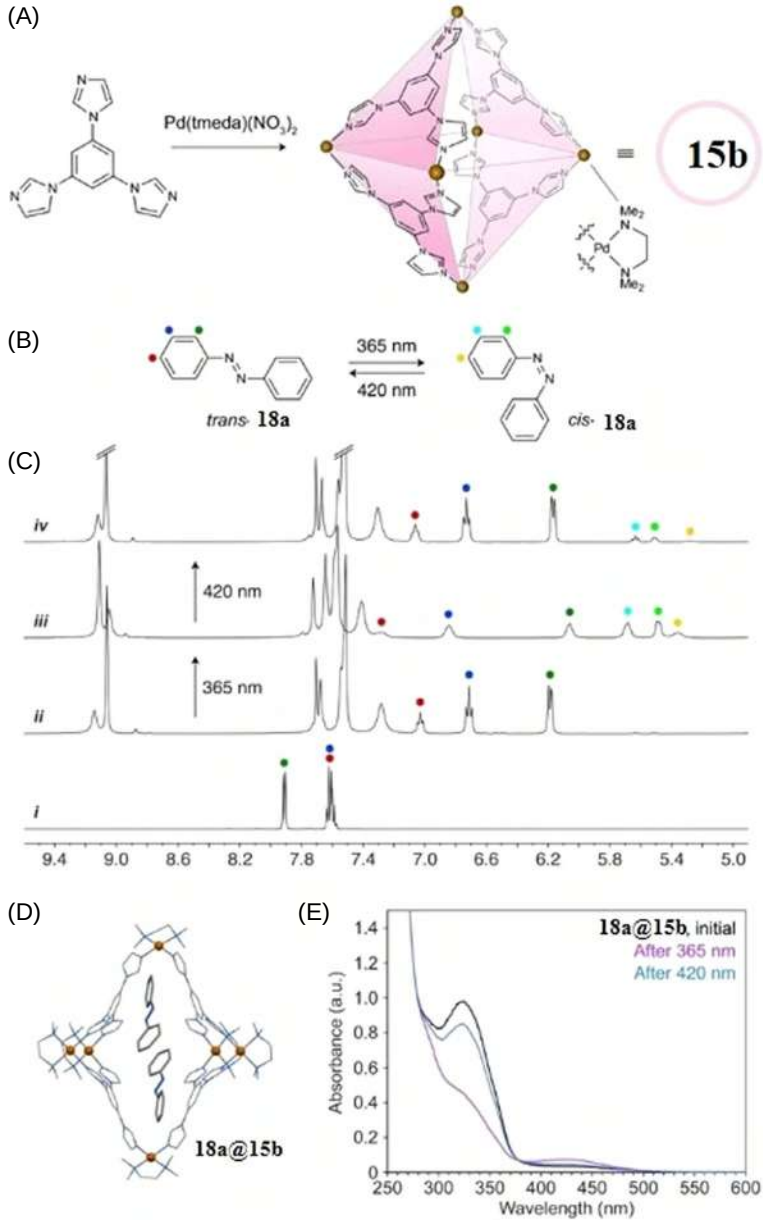

FIGURE 7.18 (A) Synthesis of the metallacage 15b from the precursors. (B) Light-induced isomerization of the guest 18a between cis and trans form. (C) Changes in the proton NMR spectrum of trans-18a (i) upon encapsulation within 15b (ii) and subsequent irradiation with UV light (iii) and blue light (iv). Spec spectrums recorded in DMSO-*d6* and spectra ii–iv in D_2O (400 MHz, 298 K). (D) Crystal structure of 18a encapsulated in 15b. (E) Change in the absorption spectra of 18a encapsulated in 15b after UV and blue light irradiation. (*Reproduced (adapted) with permission from Klajn* et al. *(2018) © 2018 National Academy of Sciences, USA.*)

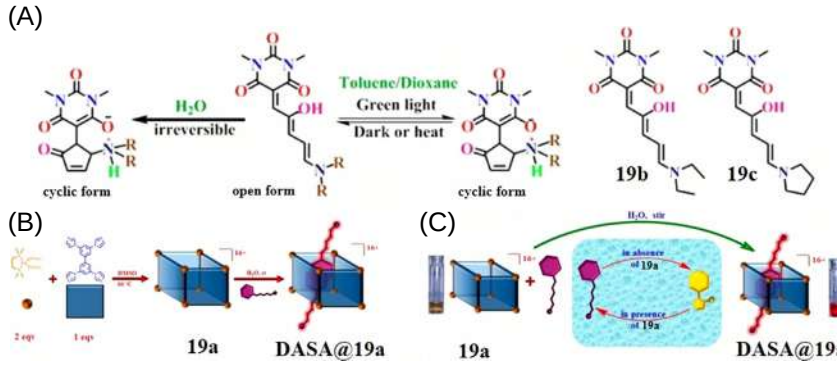

FIGURE 7.19 (A) General photoswitching behavior of DASA dye, and two new guest molecules 19b, 19c. (B) Self-assembly of the molecular vessel and stabilization of open form of DASA in the nanocontainer. (C) Reversible encapsulation of DASA guests inside the metallacage 19a. (*Reproduced (adapted) with permission from Mukherjee* et al. *(2019) © 2019 American Chemical Society.*)

directly to the aqueous solution of 19a and was stirred for 2 days before the recording of absorption spectra. Surprisingly in the absorption spectra, the host–guest complex showed absorption maxima at 509 and 512 nm for 19b and 19c, respectively. Although it is well known that in water the DASA compounds are more stable in the ring-opened form with absorption maxima around 264 nm, but here the reverse phenomenon was found. The encapsulation arrested the unstable ring-opened form in the cage. The host–guest complex formation was further elucidated with proton NMR spectroscopy. In the NMR analysis, the imidazole proton peak changed from 9.04 to 9.11 ppm indicating from the aromatic encapsulated guest. Although no photochromism behavior was observed for the inclusion complex this example was unique due to the role of the cage in encapsulation and stabilization of unusual forms of a photochromic system (Fig. 7.19).

Klajn et al. [32] reported the photochromic behavior of dihydropyrene (DHP) while encapsulating in the previously reported cage 15b (Fig. 7.20). The DHP is well known to photoisomerize between the dihydropyrene and cyclophanediene (CPD) state. But one of the major drawbacks of this photochromic system is very poor reversibility originating from the reactivity of the biradical intermediate formed during C–C bond cleavage. The authors predicted that if the photoisomerization is carried out in a confined space, then the intermediate will be more protected from outside influence and the fatigue resistance will be high. To synthesize the DHP host complex, solid DHP was added directly in excess to an aqueous solution of 15b and was stirred at room temperature for 24 h. The unconsumed DHP was removed by centrifugation and the clear solution was subjected to NMR and UV/Vis spectroscopy analysis. Upon encapsulation, the aromatic peaks of the free DHP were more shielded and the methyl protons

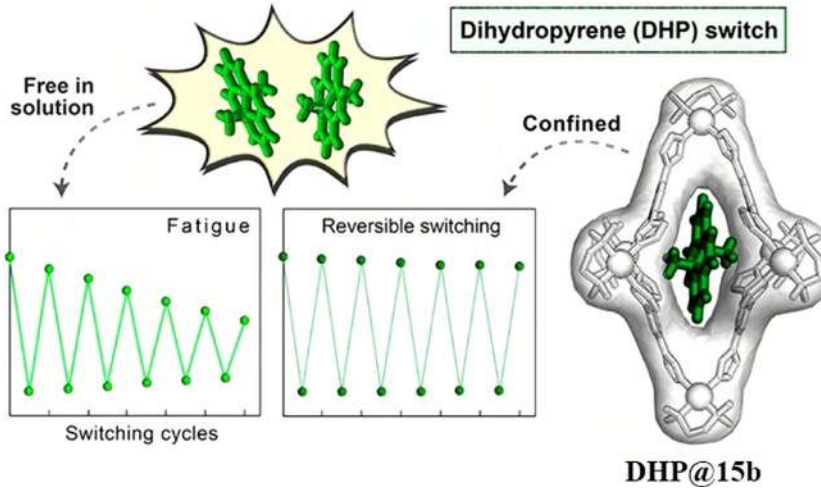

FIGURE 7.20 Reversible fatigue-resistant switching of dihydropyrene in the nano container 15b. (*Reproduced (adapted) with permission from Klajn et al. (2020) © 2020 American Chemical Society. http://pubs.acs.org/doi/10.1021/jacs.0c06146. Further permissions related to the materials excerpted should be directed to the ACS.*)

changed from −4.24 to −6.44 ppm. The shielding was due to the aromatic wall of the cage. The absorption spectra of DHP@cage showed two maxima at 346 and 383 nm and a minor peak at 460 nm. The photochromic behavior of the DHP@cage was carried out by illuminating the system with 460 nm light. The solution color changed from green to light brown upon photoirradiation indicating photoisomerization to CPD form inside the cage capsule. When the formation of the CPD@cage was studied with the help of UV/Vis and NMR analysis, a 94% conversion was observed under 1 h. The existence of the CPD@cage was established by NMR analysis where a large shift in the proton signals was observed when compared with free CPD. All the aromatic protons showed more shielding and the methyl protons changed from −1.52 ppm to −0.60 ppm indicating more upfield shifts. The UV and NMR study revealed a 1:1 inclusion complex formation for both DHP and CPD. To evaluate the reversible characteristics, the CPD@cage was exposed to 256 nm UV light and the color of the solution changed back to green indicating the reversible formation of DHP. The conversion yield was evaluated to be around 98% indicating a very good photochromic system with very high fatigue resistance (Fig. 7.20).

7.7 Conclusion

This chapter delivers an extensive overview of the recent progress in the field of photochromic metal-based self-assemblies including 2D metallacycles and 3D metallacages and their applications. Different types of photochromic units are utilized to afford the target systems. Although sufficient progress has been

accomplished, challenges still recreating more sophisticated systems that can be applied in cutting-edge science.

Acknowledgment

The author sincerely thanks Dr. Soumalya Bhattacharyya for his kind cooperation for the manuscript preparation. The author is also thankful to the University Grants Commission, India [UGC-FRPS Grant No: F. 30-554/2021(BSR)] for the financial support.

References

[1] R. Chakrabarty, P.S. Mukherjee, P.J. Stang, Supramolecular coordination: self-assembly of finite two- and three-dimensional ensembles, Chem. Rev. 111 (11) (2011) 6810–6918.

[2] M. Yoshizawa, J.K. Klosterman, M. Fujita, Functional molecular flasks: new properties and reactions within discrete, self-assembled hosts, Angew. Chem. Int. Ed. 48 (19) (2009) 3418–3438.

[3] P. Howlader, E. Zangrando, P.S. Mukherjee, Self-assembly of enantiopure Pd12 tetrahedral homochiral nanocages with tetrazole linkers and chiral recognition, J. Am. Chem. Soc. 142 (19) (2020) 9070–9078.

[4] X. Yan, T.R. Cook, P. Wang, F. Huang, P.J. Stang, Highly emissive platinum(II) metallacages, Nat. Chem. 7 (4) (2015) 342–348.

[5] J.B. Pollock, T.R. Cook, P.J. Stang, Photophysical and computational investigations of bis(phosphine) organoplatinum(II) metallacycles, J. Am. Chem. Soc. 134 (25) (2012) 10607–10620.

[6] A. Chowdhury, P. Howlader, P.S. Mukherjee, Aggregation-induced emission of platinum(II) metallacycles and their ability to detect nitroaromatics, Chem. Eur. J. 22 (22) (2016) 7468–7478.

[7] J. Jiao, Z. Li, Z. Qiao, X. Li, Y. Liu, J. Dong, J. Jiang, Y. Cui, Design and self-assembly of hexahedral coordination cages for cascade reactions, Nat. Commun. 9 (2018) 4423.

[8] E.G. Percastegui, T.K. Ronson, J.R. Nitschke, Design and applications of water-soluble coordination cages, Chem. Rev. 120 (24) (2020) 13480–13544.

[9] M. Stuart, W. Huck, J. Genzer, et al., Emerging applications of stimuli-responsive polymer materials, Nat. Mater. 9 (2010) 101–113.

[10] J. Yu, D. Qi, J. Li, Design, synthesis and applications of responsive macrocycles, Commun. Chem. 3 (189) (2020).

[11] J-X. Wang, C. Li, H. Tian, Energy manipulation and metal-assisted photochromism in a photochromic metal complex, Coord. Chem. Rev. 427 (2021) 213579.

[12] A.B. Grommet, L.M. Lee, R. Klajn, Molecular photoswitching in confined spaces. ACC photo-isomerizing, Chem. Res. 53 (11) (2020) 2600–2610.

[13] S. Chen, L-J. Chen, H-B. Yang, H. Tian, W. Zhu, Light-triggered reversible supramolecular transformations of multi- bisthienylethene hexagons, J. Am. Chem. Soc. 134 (33) (2012) 13596–13599.

[14] M. Han, R. Michel, H. Bice, Y-S. Chen, D. Stalke, M. John, G. Clever, Light-triggered guest uptake and release by a photochromic coordination cage, Angew. Chem. Int. Ed. 52 (2013) 1319–1323.

[15] M. Han, Y. Luo, B. Damaschke, L. Gomez, X. Ribas, A. Jose, P. Peretzki, M. Seibet, G. Clever, Light-controlled interconversion between a self-assembled triangle and a rhombicuboctahedral sphere, Angew. Chem. Int. Ed. 55 (2016) 445–449.

[16] S-C. Wei, M. Pan, Y-Z. Fan, H. Liu, J. Zhang, C-Y. Su, Creating coordination-based cavities in a multiresponsive supramolecular gel, Chem. Eur. J. 20 (21) (2015) 7418–7427.

[17] M. Li, L-J. Chen, Y. Cai, Q. Luo, W. Li, H-B. Yang, H. Tian, W-H. Zhu, Light-driven chiral switching of supramolecular metallacycles with photoreversibility, Chem. 5 (3) (2019) 634–648.

[18] Y. Qin, L-J. Chen, F. Dong, S-T. Jiang, G-Q. Yin, X. Li, Y. Tian, H-B. Yang, Light-controlled generation of singlet oxygen within a discrete dual-stage metallacycle for cancer therapy, J. Am. Chem. Soc. 141 (22) (2019) 8943–8950.

[19] Y. Qin, L-J. Chen, Y. Zhang, Y-X. Hu, W-L. Jiang, G-Q. Yin, H. Tan, X. Li, L. Xu, H-B. Yang, Photoswitchable Förster resonance energy transfer (FRET) within a heterometallic Ir–Pt macrocycle, Chem. Commun. 55 (2019) 11119–11122.

[20] S. Chen, L. Chen, Y. Cai, W.-H. Zhu, Photoswitchable fluorescent self-assembled metallacycles with high photostability, Chem. Eur. J. 27 (16) (2021) 5240–5245.

[21] D. Samanta, P.S. Mukherjee, Sunlight-induced covalent marriage of two triply interlocked Pd6 cages and their facile thermal separation, J. Am. Chem. Soc. 136 (49) (2014) 17006–17009.

[22] T. Murase, S. Sato, M. Fujita, Switching the interior hydrophobicity of a self-assembled spherical complex through the photoisomerization of confined azobenzene chromophores, Angew. Chem. Int. Ed. 46 (27) (2007) 5133–5136.

[23] D. Zhang, Y. Nie, M.L. Saha, Z. He, L. Jiang, Z. Zhou, P.J. Stang, Photoreversible [2]catenane via the host−guest interactions between a palladium metallacycle and β-cyclodextrin, Inorg. Chem. 54 (24) (2015) 11807–11812.

[24] S. Oldknow, D.R. Matir, V.E. Pritchard, M.A. Blitz, C. Fishwick, E. Colman, M. Hardie, Structure-switching M3L2 Ir(III) coordination cages with Bhattacharyya azo-aromatic linkers, Chem. Sci. 9 (2018) 8150–8159.

[25] S. Bhattachryya, A. Chowdhury, R. Saha, P.S. Mukherjee, Multifunctional self-assembled macrocycles with enhanced emission and reversible photochromic behavior, Inorg. Chem. 58 (6) (2019) 3968–3981.

[26] S. Bhattacharyya, M. Maity, A. Chowdhury, M.L. Saha, S.K. Panja, P.J. Stang, P.S. Mukherjee, Coordination-assisted reversible photoswitching of spiropyran-based platinum macrocycles, Inorg. Chem. 59 (3) (2020) 2083–2091.

[27] D. Samanta, D. Galaktionova, J. Gemen, L. Shimon, Y.D. Posner, l. Avram, P. Kral, R. Klajn, Reversible chromism of spiropyran in the cavity of a flexible coordination cage, Nat. Commun. 9 (2018) 641.

[28] S.M. Jansze, G. Cecot, K. Severin, Reversible disassembly of metallosupramolecular structures mediated by a metastable-state photoacid, Chem. Sci. 9 (2018) 4253–4257.

[29] P. Howlader, B. Mondal, P.C. Purba, E. Zangrando, P.S. Mukherjee, Self-assembled Pd(II) barrels as containers for transient merocyanine form and reverse thermochromism of spiropyran, J. Am. Chem. Soc. 140 (25) (2018) 7952–7960.

[30] D. Samanta, J. Gemen, Z. Chu, Y. Posner, L.J.W. Shimon, R. Klajn, Reversible photoswitching of encapsulated azobenzenes in water, Proc. Natl. Acad. Sci. 115 (38) (2018) 9379–9384.

[31] R. Saha, A. Devraj, S. Bhattacharyya, S. Das, E. Zangrando, P.S. Mukherjee, Unusual behaviour of donor-acceptor Stenhouse adducts (DASA) in confined space of a water-soluble PdII8 molecular vessel, J. Am. Chem. Soc. 141 (21) (2019) 8638–8645.

[32] M. Canton, A.B. Grommet, L. Pesce, J. Gemen, S. Li, Y. Posner, A. Credi, G.M. Pavan, J. Andreasson, R. Klajn, Improving fatigue resistance of dihydropyrene by encapsulation within a coordination cage, J. Am. Chem. Soc. 142 (34) (2020) 14557–14565.

Chapter 8

Photoactive finite supramolecular coordination cages for photodynamic therapy

Nidhi Tyagi and Prakash P. Neelakandan
Institute of Nano Science and Technology, Knowledge City, Mohali, Punjab, India

8.1 Introduction

Three-dimensional layouts of metal–organic materials (MOMs) have garnered tremendous attention over the years owning to their wide-spread practical applications [1–3]. Structurally, MOMs may be divided into metal organic frameworks (MOFs) (Fig. 8.1) and supramolecular coordination complexes (SCCs) (Fig. 8.1). While MOFs are infinite porous coordination polymers assembled from appropriate metal-containing nodes with organic linkers, SCCs are constructed by mixing metal ions (acceptors) and organic precursors (donors) in an appropriate ratio which results in a finite structure with coordination bonds through "Werner-type" coordination chemistry. By following this approach, a variety of two- and three-dimensional SCCs have been synthesized with different shapes, sizes, tunable cavities, and morphologies (triangles, rectangles, hexagons, prisms, helicates, and cages, etc.). Many of these simulated molecular assemblies were successful in mimicking the structure and functions of natural supramolecular biological/nonbiological assemblies [4–11].

The first example of a well-defined coordination macrocycle was reported by Verkade in 1983 [12]. A plethora of SCCs has since been prepared incorporating a variety of metal ions and organic ligands. Upon the formation SCCs, the physical and chemical properties of both the metal ions and organic ligands change significantly thereby imparting unique properties to the SCCs. The initial progress in the field of SCCs was driven mainly by the curiosity in preparing complex molecular architectures using simple subcomponents, SCCs are now considered as robust, next generation materials capable of solving challenging issues in energy, environment and healthcare sectors. Over the last decade, the utility of SCCs has grown beyond our imagination owing to the simple and

Supramolecular Coordination Complexes: Design, Synthesis, and Applications.
DOI: https://doi.org/10.1016/B978-0-323-90582-4.00007-5

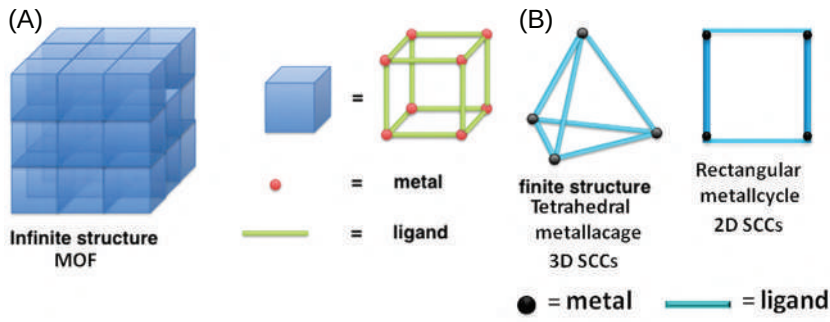

FIGURE 8.1 Different types of metal-containing assemblies. (A) Infinite metal–organic frameworks and (B) discreet supramolecular complexes formed by convergent combinations of metal nodes and organic linkers. (*Copyright Carolineneil, CC BY-SA 4.0.*)

efficient synthesis, and good adaptability and processability for applications in molecular recognition, biosensing, cell imaging, drug delivery, supramolecular host/guest interactions, catalysis and optoelectronics [13–15]. This chapter will summarize the recent developments pertaining to the preparation of SCCs incorporating common chromophores such as porphyrins, BODIPYs and ruthenium complexes and their application as photosensitizers for photodynamic therapy (PDT).

Several research groups have developed different design strategies for the construction of SCCs with intriguing properties [7,16–23]. The formation of metallacycles or cages not only depends on metal–ligand coordination but also on several other additional interactions such as hydrogen bonding, $\pi-\pi$ stacking, host–guest complexation, electrostatic, and hydrophobic or hydrophilic interactions. SCCs are a versatile class of compounds because (i) their dimensions can be tuned by changing the self-assembly conditions, (ii) the metal ions and ligands can be varied systematically to form SCCs of variable sizes, shapes and geometries for any desired application, and (iii) specific groups can be conjugated to SCCs through pre- or postsynthetic modifications.

The resourcefulness of SCCs is evidenced by the breakthroughs ushered by these materials in different fields [7,23–26]. In this section, we will discuss a few recent advances of SCCs for biological applications other than PDT. Schmidt and coworkers prepared the water soluble star-shaped octahedral Pd^{II}_6 $(TPT)_4$ cage **1** (Fig. 8.2) and showcased the mechanochemical release of pharmaceutically active compounds such as ibuprofen and progesterone from the hydrophobic nanocavity of the supramolecular cage through NMR spectroscopy and gel permeation chromatography [27]. The release of the noncovalently bound cargo (ibuprofen and progesterone) was triggered by the shear force produced by ultrasonication which ruptured the cage.

An interesting example of heterometallic (Cu^I/Pt^{II}) triangular necklace architecture **2** was reported with excellent nuclease and antibacterial activities (Fig. 8.3). The synergy of positive charges in **2** and the presence of two metal centers (Cu^I/Pt^{II}) were observed to disrupt the negatively charged DNA/cell

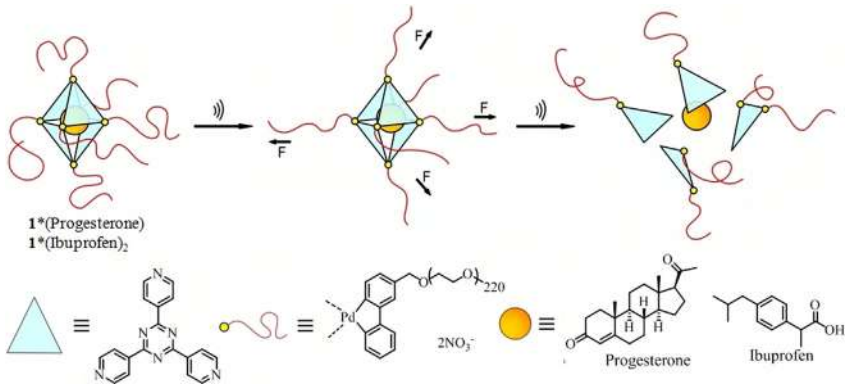

FIGURE 8.2 Schematic representation of PEG-functionalized star-shaped octahedral cage **1** with 220 repetitive ethylene glycol units at each vertex. The preloaded cargo is depicted as the orange sphere within the cavity of cage **1** representing one molecule of progesterone or two molecules of ibuprofen per supramolecular entity. (*Adapted with permission from Ref. [27].*)

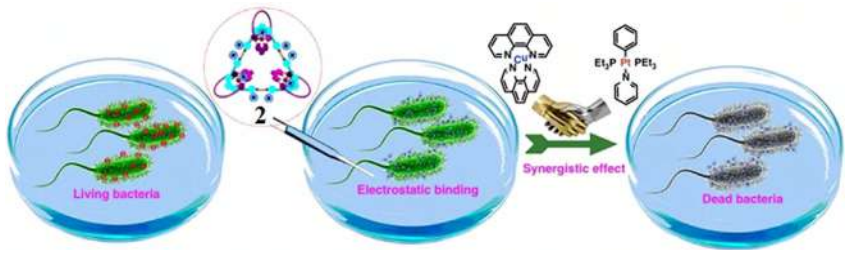

FIGURE 8.3 Schematic representation of triangular necklace **2** binding to bacteria and their synergetic bactericidal mechanism. (*Adapted with permission from Ref. [28]. Copyright ©2020Springer Nature Limited.*)

wall/plasma membrane. Additionally, the presence of Pt^{II} boosted the bacterium-binding capability of Cu^{I} and disrupted the negatively charged lipopolysaccharides or teichoic acid and phospholipids. A "threading-followed-by-ring-closing" approach for the supramolecular assemblies or necklace construction endowed promising biomedical applications [28].

A versatile Pt(II) metallacage **6** with dual-emissive and phosphorescence properties was reported by Wang, Huang, Stang, and coworkers and was used for *in vivo* hypoxia imaging and chemotherapy (Fig. 8.4) [29]. Heteroligation was crucial in the metallacage **6** as it endowed the dual-emissive property to the cage using the red phosphorescent ligand (Pt(II)-*meso*-tetra(4-carboxyphenyl)porphine) **3** and the blue fluorophore (anthracene) **4**. Under hypoxic conditions, a large enhancement (48 times) in the phosphorescence of **6** was observed, while the blue fluorescence nearly remained unchanged upon deaeration. Physiologically stable, metallacage-loaded spherical nanoparticles (MNPs, ~150 nm in diameter) functionalized with amphiphilic polymer methylpoly(ethyleneglycol)-*block*-poly(γ-benzyl-*L*-glutamate) (mPEG-*b*-PBLG) of **6** was also prepared and was observed to internalize in 4T1 cells

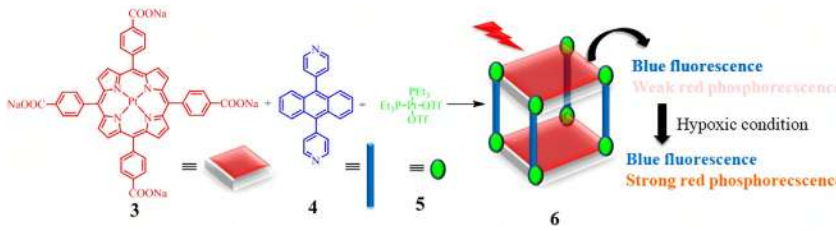

FIGURE 8.4 Cartoon representation of the metallacage **6** and its optical properties under hypoxic conditions. (*No permission required.*)

via endocytosis with an increase in the intracellular accumulation of platinum (182 ng per million cells in 8 h). The cytotoxicity of **6** ($IC_{50} = 8.58 \pm 1.36$ μM) was comparable to cisplatin under similar conditions (7.43 ± 1.34 μM). *In vivo* hypoxia imaging of MNPs showed intense emission in large tumor regions which was consistent with the enhanced phosphorescence of **6** under low oxygen conditions. Also, in cellular environment ~450% enhancement was observed in red phosphorescence under hypoxic conditions while the blue fluorescence remained constant. Furthermore, *in vivo* studies showed that the administration of MNPs resulted in apoptosis and necrosis in tumor with an inhibition rate of 79.6%. These results suggested that MNPs can be used for theranostics with both hypoxia imaging and antitumor capabilities.

These representative examples show that metallacages or coordination-driven self-assembled structures are well-suited for biomedical applications. There are several informative reviews on the structural and design perspectives and applications of SCCs [30]. As mentioned previously, the goal of this chapter is to spotlight the recent examples of photoactive SCCs for photodynamic therapy (PDT).

8.2 SCCs for PDT applications

PDT is an approved therapeutic practice for the treatment of malignant tissues. As compared to the traditional anticancer treatments, PDT has numerous advantages such as high selectivity and spatiotemporal accuracy, noninvasiveness, precise controllability as well as the possibility of repeated doses. PDT requires a photosensitizer (PS) with negligible dark toxicity capable of absorbing low energy light to produce cytotoxic reactive oxygen species (ROS) that can destroy cancer cells [31]. The energy given to PS is efficiently utilized to excite triplet oxygen ($^3O_2$) into its singlet state ($^1O_2$) which is the main cytotoxic agent to eradicate cancer cells through the "type II" mechanism [32]. The ideal PS should have strong absorbance in the long wavelength regions with high $^1O_2$ quantum yields. Investigation of metallacages as PDT agents is an emerging area and is still in its infancy. The common approach to assemble SCCs for PDT application is to incorporate PSs as bridging ligands and so far three families

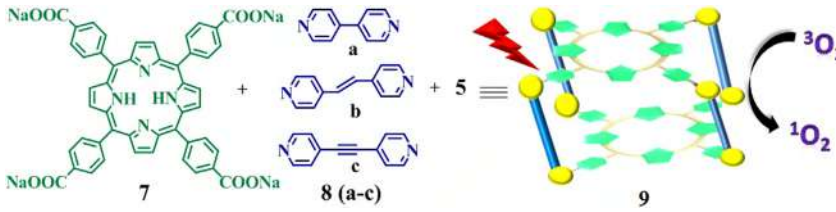

FIGURE 8.5 Cartoon representation of the self-assembly of metallacages **9** and their singlet oxygen generation ability. (*No permission required.*)

of PSs have been commonly used as bridging units. They include porphyrins, boron dipyrromethenes (BODIPY), and ruthenium complexes.

8.2.1 SCCs containing porphyrins

Porphyrins have attracted much attention for biomedical applications due to their planar structure and extended π-conjugation resulting in visible light absorption. Delocalization of the π-electron cloud imparts interesting and favorable photophysical properties as demanded for PS. However, owing to the large planar structure of porphyrins, they tend to undergo aggregation through π–π stacking resulting in reduced singlet oxygen generation efficiency and are thus rarely used for clinical applications [33]. Metallosupramolecular assemblies of porphryins overcome these drawbacks to a large extent due to directional coordination and the charges on SCCs, and therefore reduce the possibility of aggregation. Additionally, SCCs have better solubility which allows efficient transport to cancer cells.

Recently, a series of tetragonal prismatic cages (denoted as **9**) was synthesized in excellent yields by the self-assembly of a porphyrin derivative (**7**), $Pt(PEt_3)_2(OTf)_2$ (**5**), and the dipyridyl ligands (**8a–c**) (Fig. 8.5). Investigation of their photophysical properties disclosed the efficient photosensitizing ability of **9** with $\phi_\Delta = 0.62$–0.73 that is comparable to that of 5,10,15,20-tetraphenylporphyrin (TPP) ($\phi_\Delta = 0.64$). Incorporation of Pt(II) center to metallacages encouraged intersystem crossing for better $^1O_2$ generation efficiency and demonstrated their potential as photochemotherapy candidates [34].

Combination therapies open up a promising way to surmount drug resistance by incorporating different mechanisms of actions to achieve synergistic efficacy. With this consideration, Stang and coauthors are extensively working in this area to modify SCCs for combination therapies. For example, two component metalla-assemblies **10** consisting of 5,10,15,20-tetra(3-pyridyl)porphyrin ligand and a 120° di-Pt(II) acceptor was synthesized (Fig. 8.6) [35]. This system was observed to have improved stability along with structural simplicity as compared to multicomponent systems. Single crystal XRD structure of **10** revealed the presence of a large cavity due to the twisting of the porphyrin group thereby reducing the possibility of aggregation of the porphyrin core. This complex

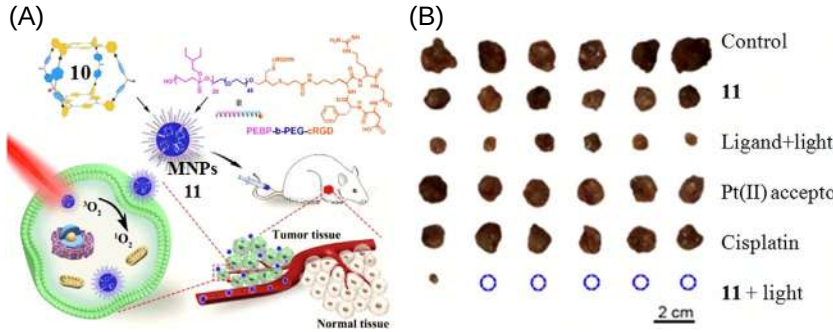

FIGURE 8.6 (A)Schematic representation of **10** and its metal nanoparticles (MNP) **11** for cancer treatment. (B) Photographs of 4T1 orthotopic tumors harvested from the mice that received different treatments. (*Adapted with permission from Ref. [35]. Copyright ©2020, American Chemical Society.*)

was observed to exhibit absorption at ~638 nm and showed efficient $^1O_2$ generation. *In vitro* and *in vivo* examination of nanoformulation or fabricated metal nanoparticles (MNPs) **11** demonstrated excellent cytotoxicity, with half-maximal inhibitory concentration (LD_{50}) value of 0.087 ± 0.009 μM upon irradiation against orthotopic breast cancer (4T1). In addition, *in vivo* PDT was examined on orthotopic breast cancer-bearing mice and it was observed the growth inhibition in the case of **11** was 98.4% upon light irradiation (Fig. 8.6B).

In an another report, the multifunctional Pt(II) metallacage **12** and their MNPs **13** with synergistic chemotherapy and PDT efficacy was reported (Fig. 8.7) [36]. The metallacage **12** was synthesized using 5,10,15,20-tetra(4-pyridyl)porphyrin (TPP) as the donor, disodium terephthalate (DSTP) as the bridging block and the Pt(II) complex **5** as the metal acceptor. Cage **12** showed suppressed intermolecular π–π stacking of porphyrin cores resulting in enhancement in fluorescence as well as $^1O_2$ generation thus displaying its potential as near infrared fluorescence imaging agent. Additionally, **12** functioned as an efficient magnetic resonance (MRI) and positron emission tomography (PET) imaging agent due to its guest encapsulation capability toward various metal ions (Mn and ^{64}Cu ion). The MNPs **13** was functionalized by two amphiphilic diblock polymers (mPEG-b-PEBP and RGD-PEG-b-PEBP) which showed effective internalization of **13** and were up taken by the U87MG cells with an intracellular platinum content of 1.05 ng/10^6 cells after 4 h of incubation. The MNPs **13** showed 110-fold higher $^1O_2$ generation efficiency ($\phi_\Delta = 0.44$) in water than TPP as Pt with high spin–orbit coupling constant of $\chi = 4481$ cm^{-1} enhanced the intersystem crossing process. The exceptionally high phototoxicity index of 246 for **13** proved their excellent phototherapeutic potential. *In vivo* tri-modality imaging displayed exceptionally intense signals in tumor area than other tissues. Fig. 8.7C and D shows quantitative radiolabeling of MNPs by isotope ^{64}Cu to track the delivery and biodistribution of ^{64}Cu@MNPs (PET) and Mn@MNPs

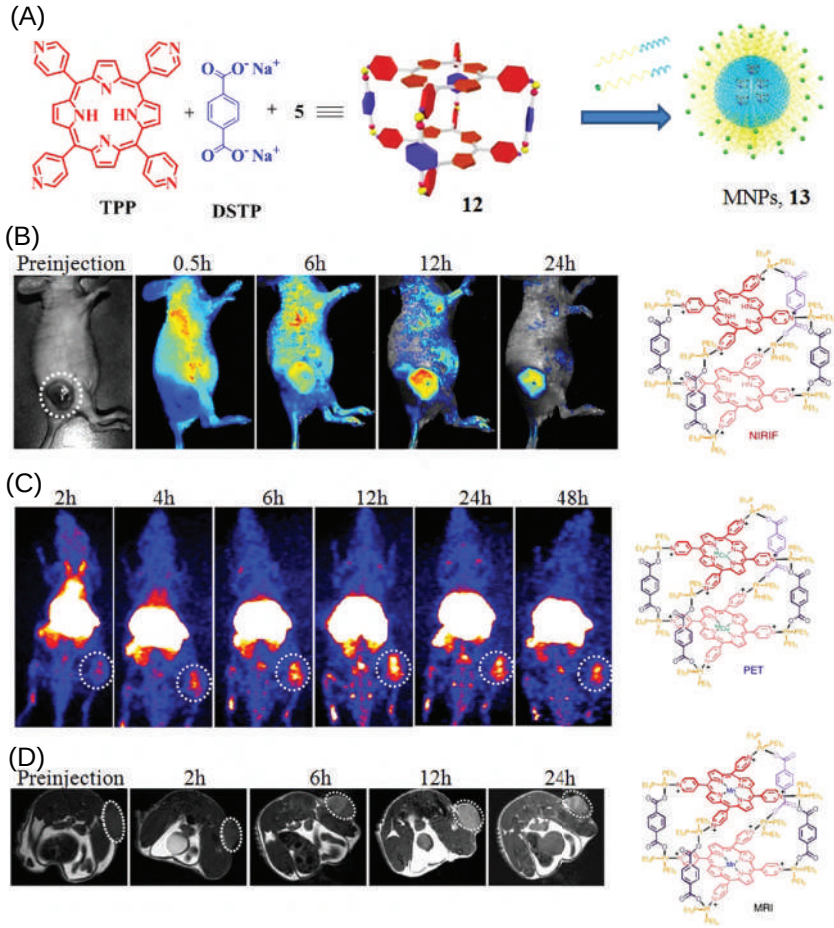

FIGURE 8.7 (A) Cartoon representation of SCC **12** and its MNPs **13**. (B) NIR fluorescence image of U87MG tumor-bearing nude mice following i.v. injection of MNPs. (C) PET image of tumor-bearing nude mice at 2, 4, 6, 12, 24, and 48 h postinjection of ^{64}Cu@MNPs. (d) In vivo T1-weighted axial MRI images (7T) of the mice before and after injection of Mn@MNPs. The white dotted circle denotes the tumor site. (*Adapted with permission from Ref. [36]. Copyright ©2018 Springer Nature Limited.*)

as T1 MRI contrast agents. Gene chip investigation further established the contribution of different therapeutic modalities to the tumor abrogation.

The first successful example of spatiotemporal controllable $^1O_2$ release in Pt-based hexagonal SCCs upon irradiation was reported by Qin et al. [4]. This Pt-based dual-stage metallacycle consisted of porphyrin and diarylethene building blocks and was synthesized by stirring a mixture of diarylethene-based diplatinum-(II) acceptor **14** and the 120° porphyrin donor ligand **15** in a 1:1 ratio in acetone and water (Fig. 8.8A). The light-responsive property

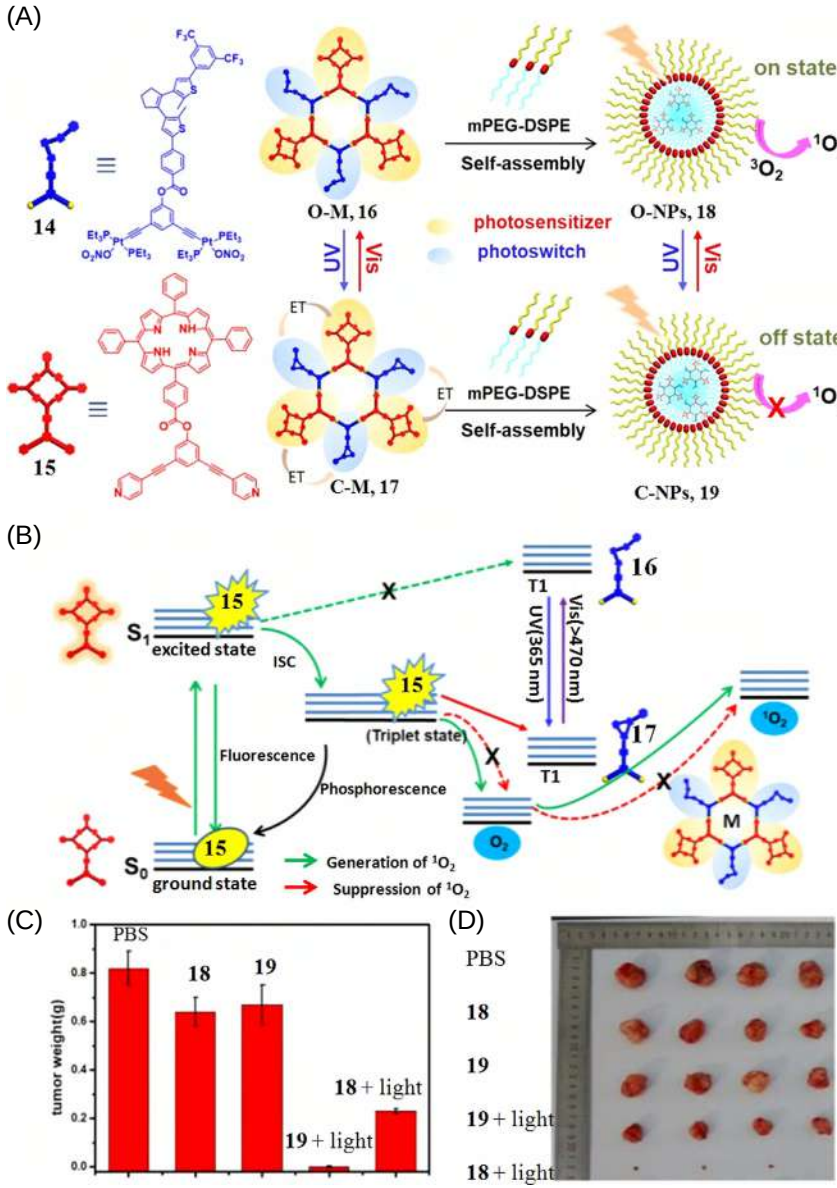

FIGURE 8.8 (A) Schematic representation of the controllable generation of $^1O_2$ by **16** and **17**. (B) The proposed mechanism of energy transfer (ET) in **16**. (C) Tumor weight curves with relevant treatments. (D) Photo of tumors treated with **18** and **19** in dark and 18 and 19 followed by light. One tumor in the 18 + light was completely eradicated at the end point. (*Adapted with permission from Ref. [4]. Copyright ©2019, American Chemical Society.*)

of metallacycle originated from the photochromic properties of diarylethene moiety which switched between the ring-closed (C–M, **17**) and ring-open (O–M, **16**) forms upon irradiation (Fig. 8.8A). Due to the proximal and well defined placement of the porphyrin and diarylethene in SCCs, an efficient generation of $^1O_2$ was observed and upon UV light irradiation, a photoinduced energy transfer occurred between **16** and **17** thereby quenching singlet oxygen generation in **17**. Additionally, the metallacycle was further encapsulated by 1,2-distearoylsn-glycero-3-phosphoethanolamine-N-methoxy(polyethylene glycol) (mPEG-DSPE) to give MNPs as spherical micelles (60 nm) preserving their light-responsive properties and *in vitro*/*in vivo* singlet oxygen generation abilities (Fig. 8.8A). The MNPs generated $^1O_2$ efficiently in "on state" (O-NPs, **18**) whereas it was quenched effectively in the "off state" (C-NPs, **19**). The singlet oxygen generation efficiency of **18** was about 155 times faster than that of **19** thus verifying the controllability on $^1O_2$ generation. The short distance between the photosensitizer and the photochromic-switch allowed sufficient energy transfer to control $^1O_2$ generation (Fig. 8.8B). The MNPs **18** allowed for efficient delivery to cancer cells through enhanced permeability and retention (EPR) effect and showed photocytotoxicity ($IC_{50} = 1.926 \pm 0.027$ μM). *In vivo* examination confirmed that **18** upon irradiation induced phototoxicity to the tumor, whereas only slight inhibition of the tumor growth was observed in the case of **19** (Fig. 8.8C and D). Thus, this switchable dual-stage nanomedicine was able to ablate the tumors through controllable light irradiation [4].

In an another example, a discrete organoplatinum(II) metallacage containing multiple therapeutic agents/diagnostic probes was described [37]. The well-defined cavity of organoplatinum(II) metallacage **20** was capable of encapsulating a photosensitizer (octaethylporphyrin, OEP) to give a host–guest complex **21** through noncovalent interactions (Fig. 8.9A). The MNPs **22** with a diameter of 109 ± 8.4 nm was formed by wrapping it into the hydrophobic core of an amphiphilic diblock copolymer (N3-PEG-b-PLBG) to increase solubility and stability under physiological environment. Confocal laser scanning microscopy (CLSM) images of **22** showed green fluorescence of DCF in the cytoplasm of A2780CIS cell thereby confirming efficient $^1O_2$ generation. Further, the cytotoxicity results showed that the IC_{50} values of cisplatin, **5** and **22** were 2.53 ± 0.16, 3.57 ± 0.28, 1.32 ± 0.10 μM, respectively, upon light irradiation. Moreover, a combination index (CI) of 0.67 was obtained for **22**, which being lower than 1, implied the synergy of PDT and chemotherapy. *In vivo* studies of **22** showed high tumor accumulation (Fig. 8.9B) and retention capabilities of OEP (an NIR fluorophore) thus exhibiting a superior antitumor performance by combining chemotherapy and PDT.

8.2.2 SCCs containing BODIPYs

Boron-dipyrromethenes (BODIPY) are an important class of fluorescent compounds with low dark toxicity, high extinction coefficients, low photobleaching

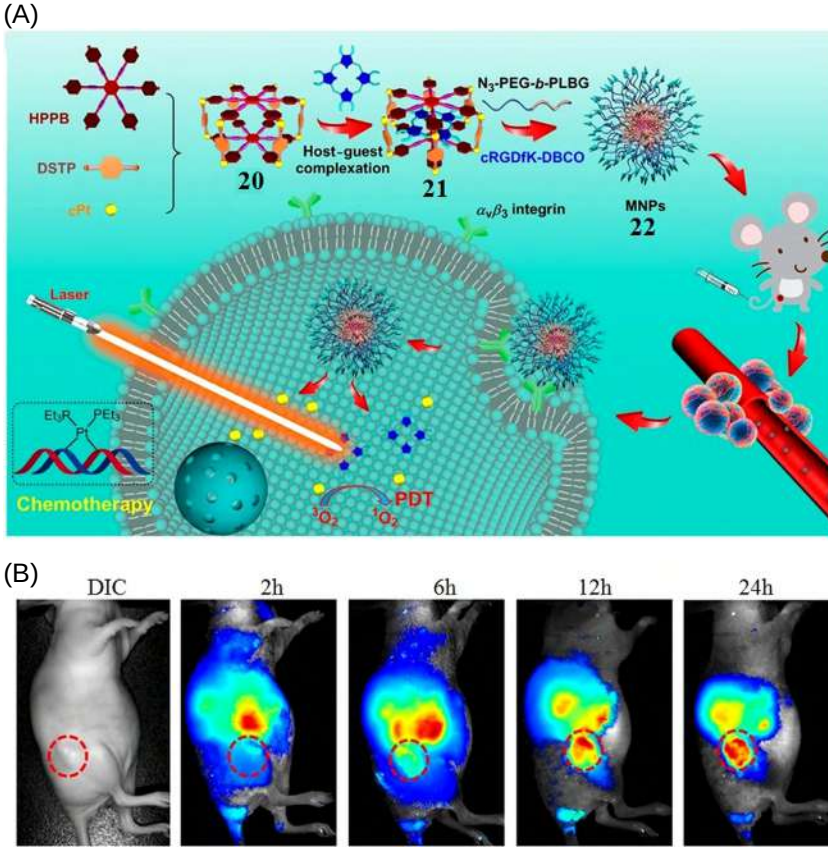

FIGURE 8.9 (A) Cartoon illustration of the photochemotherapy showing tumor accumulation through EPR effect and receptor-mediated internalization of MNPs prepared from the metallacage **20**. (B) Time-dependent fluorescence images of A2780CIS tumor-bearing mouse after i.v. injection of **22**. (*Adapted with permission from Ref. [37].*)

and good cellular uptake properties which make them suitable for PDT applications [23,30,38]. Although BODIPYs are extensively used for various applications including PDT, preparation and use of metallacages containing BODIPY for PDT application is a relatively less-explored area of research. This section summarizes the limited number of examples of SCCs featuring BODIPY ligands for PDT and related applications.

Cook and coworkers reported the first examples of Pt(II) supramolecular triangles containing a pyridyl-functionalized BODIPY ligand as theranostic agents [39]. The synergistic therapeutic effects of triangles were achieved by the incorporation of chemotherapeutic Pt(II) ion and BODIPY as photosensitizer. Self-assembled [3+3] triangular metallacycles **25** and **26** were synthesized by the treatment of Pt(II) acceptors (**5** and **23**) with the BODIPY linker **24** (Fig. 8.10A).

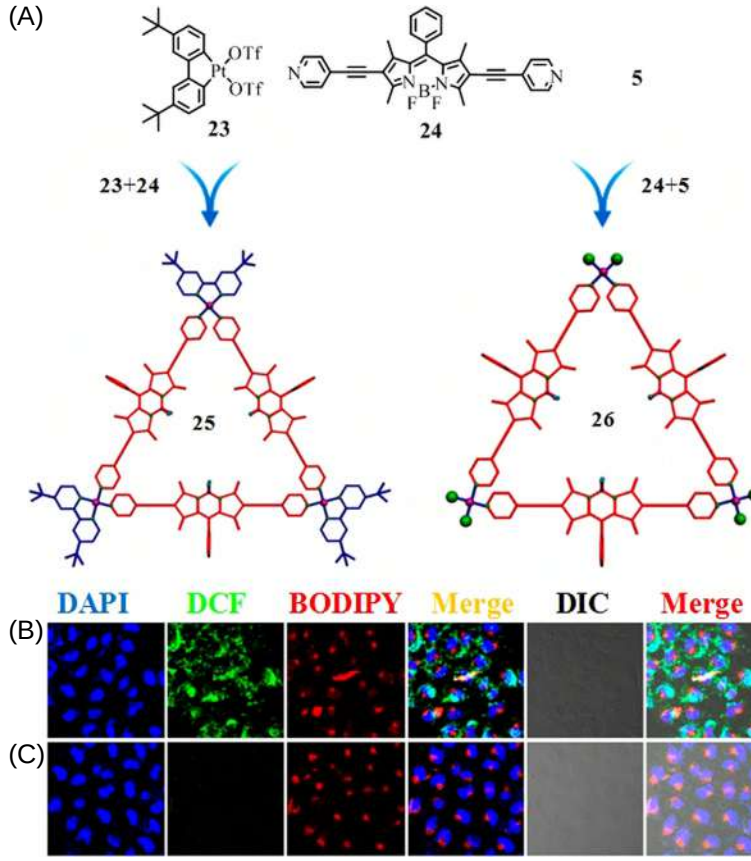

FIGURE 8.10 (A) Structures of self-assembled triangular metallacycles **25** and **26**. Confocal microscopy images of HeLa cells after incubation with **26** in the (B) absence and (C) presence of vitamin C. (*Adapted with permission from Ref. [39]. Copyright ©2018, American Chemical Society.*)

Triangular metallacycles **25** and **26** showed high florescence with emission maxima at ~577 nm (λ_{ex} = 365 nm) and confocal imaging demonstrated that the cationic NPs of these metallacycles exhibited favorable uptake and higher intracellular accumulation in *HeLa* cells as compared to the BODIPY ligand. The Pt(II) moieties acted as cytotoxic agents and *in vitro* studies of **25** and **26** showed efficient cytotoxicity (IC_{50} = 6.41 and 2.11 μM, respectively) against *HeLa* cells which is quite comparable to Pt(II) acceptors (IC_{50} = 3.60 and 1.76 μM for **23** and **5**, respectively). In addition, the cellular uptake of **25** and **26** (653 and 713 ng/10^6 cells) were observed to improve upon the formation of metallacycles as free Pt(II) acceptor **5** showed only a cellular uptake of 274 ng/10^6. BODIPY ligands were the key for PDT application and intracellular $^1O_2$ generation from **26** was confirmed from the strong green fluorescence signal from dichlorofluorescein (DCF) (Fig. 8.10B) which was significantly decreased

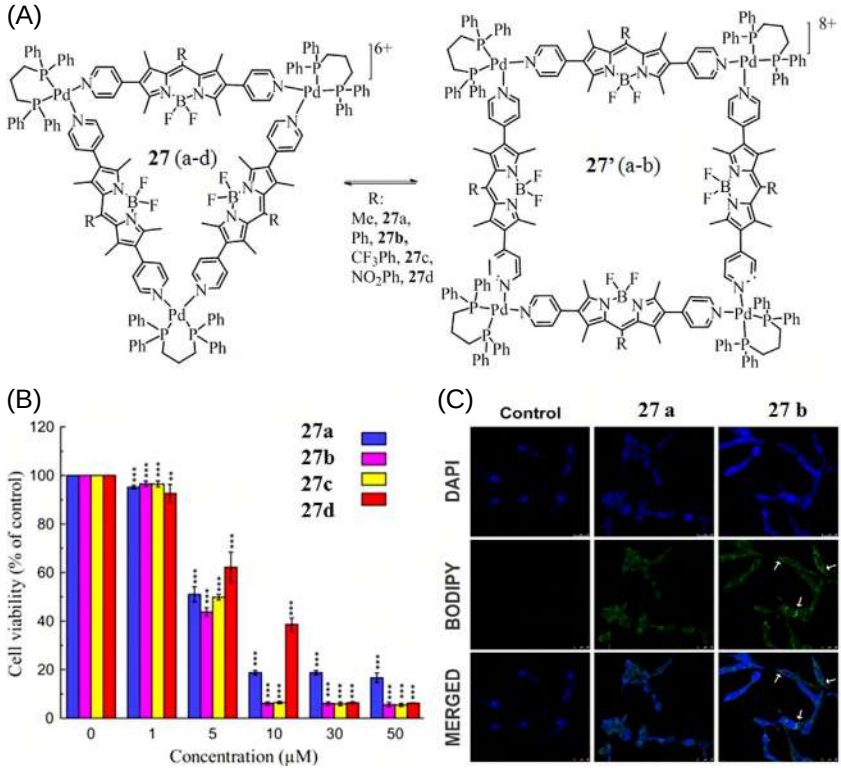

FIGURE 8.11 (A) Structures of triangular and square Pd(II) containing SCCs **27** and **27'**. (B) Cell proliferation and viability of cancer (U87) cells treated with increasing concentration of **27** for 48 h. (C) Intracellular localization of **27a** and **27b** in U87 cells and visualized by confocal images. (*Adapted with permission from Ref. [40]. Copyright ©2017, American Chemical Society.*)

in the presence of the ROS scavenger vitamin C (Fig. 8.10C). The obtained results showed that introduction of BODIPY into the Pt(II) SCCs introduced a fluorophore which facilitated fluorescence imaging-guided cancer therapy, combination of PDT and chemotherapy to promote anticancer efficacy.

Gupta, Lee, and coworkers reported the solvent dependent formation of triangular- and square-shaped palladium supramoleculclar architectures that exhibited high toxicity against brain cancer (glioblastoma) cells [40]. The self-assembled Pd(II) SCCs **27** and **27'** were synthesized by the reaction of Pd(dppp) triflate with BODIPY ligands in dichloromethane (Fig. 8.11A). NMR spectroscopy measurements revealed the equilibrium between triangular **27** and square **27'** molecular architectures in low-polarity solvents, whereas an increase in the solvent polarity shifted this equilibrium toward the triangular architecture **27**. Interestingly, these SCCs showed cytotoxicity against brain cancer (U87)

and normal lung fibroblast cell line (WI-38) with IC_{50} values of 3.43–6.39 and 8.01–16.71 μM, respectively (Fig. 8.11B) which were better than cisplatin (IC_{50} = 6.06 μM for U87 and 7.051 μM for WI-38). The triangular metallacage **27** permitted visualization of their intracellular localization in the cytoplasm and the plasma membrane. Triangular metallacage with phenyl rings (**27b–d**) showed enhanced green fluorescence arising because of an AIE phenomenon due to the formation of nanoaggregates (Fig. 8.11C). The bioactivity of **27** was explained using a cytoplasmic cell death mechanism as well as strong interaction with biomolecules such as protein and DNA.

The same group extends their work with the incorporation of iron-based heterometallic center to the supramolecular assemblies as potential drug candidates for anticancer therapy [41]. The novel octanuclear self-assembled square complexes **28–31** (Fig. 8.12) were synthesized by the reaction of heterometallic palladium/platinum iron triflate complex with dipyridyl BODIPY ligands in dichloromethane–nitromethane mixtures. BODIPY ligand was modified to incorporate the ethynyl moiety between the BODIPY and pyridyl groups to increase coplanarity and improve the π-conjugated network in the metallacycles **30** and **31**. These metallacycles **28–31** were found to be 7.0–15.2 times less toxic than cisplatin in normal cells (HEK-293) and induced cytotoxicity in cancer cells through apoptotic and necrotic pathways. BODIPY cores enabled their transport within cancer cells and enabled visualization by confocal laser scanning microscopy. In addition, ruthenium and iridium metalla-rectangles of a BODIPY linker with efficient antiproliferative activities were also reported by the same group [42,43]. These interesting triangular, square, and rectangular shapes are strong contenders as PDT agents but remains unexplored which needs to be investigated further.

8.2.3 SCCs containing ruthenium complexes

Ruthenium complexes are attractive for biological applications because of their favorable photophysical properties, water solubility, high ROS production, chemical- and photostability [44,45]. Stang and Chi have prepared various ruthenium-based SCCs and investigated their antiproliferative activities against various tumor models. Their results indicate that ruthenium-based SCCs exhibits inherent anticancer activity due to presence of ruthenium centers [46,47]. In another study, it was shown that a metallarectangle and a metallaprism of a bis-benzimidazole-bridged ruthenium acceptor with dipyridyl and tripyridyl donors showed high cytotoxicity as compared to cisplatin and the precursor dinuclear complex [48]. In spite of interesting photophysical properties and structural stability in cell culture media, ruthenium-based SCCs are not often used for PDT applications. However, recently Gasser, Gibson, and coworkers reported a (Ru–Pt) conjugate as combination therapy agents for chemotherapy and PDT which acts on multiple targets inside cancer cells [49,50]. The Ru–Pt bimetallic

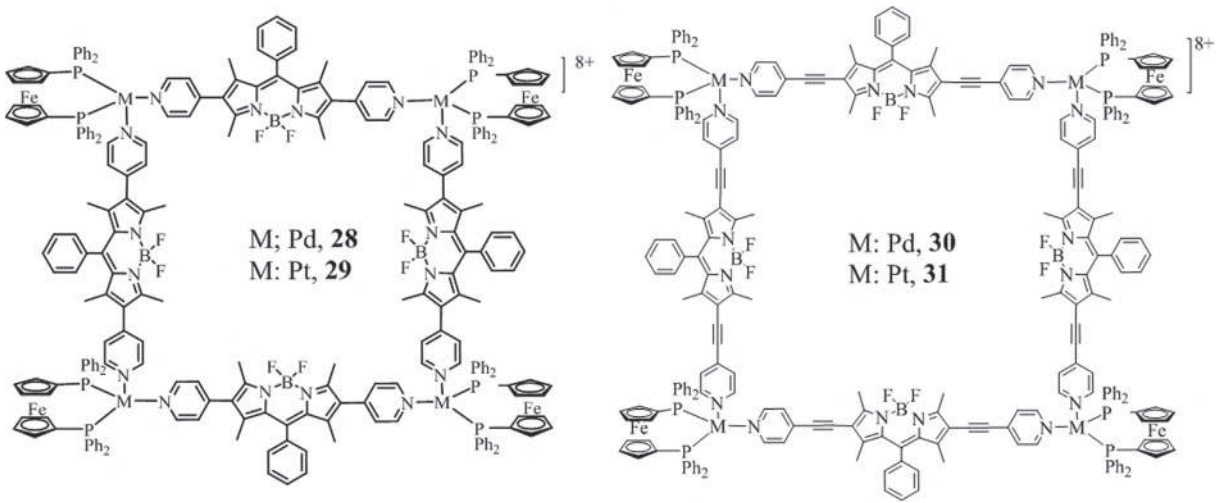

FIGURE 8.12 Structures of heterometallic SCCs **28–31**. (*No permission required.*)

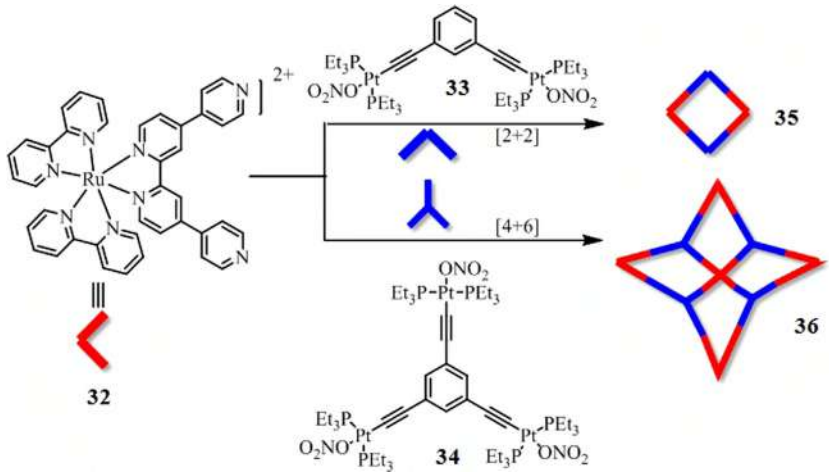

FIGURE 8.13 Self-assembly of [2+2] and [6+4] SCCs **35** and **36**, respectively. (*No permission required.*)

metallacage functioned as photosensitizers for PDT through two-photon absorption. The [2+2] rhomboidal metallacycle **35** or the [6+4] octahedral metallacage **36** was synthesized by combination of **32** with di-Pt(II) acceptor **33** or tri-Pt(II) acceptor **34** (Fig. 8.13) [51]. The MNPs of **36** using an amphiphilic polymer was formulated which showed selective accumulation in lysosomes. **35** and **36** exhibited red emission bands at 672 and 673 nm along with long fluorescence lifetimes (>400 ns) and high singlet oxygen generation quantum yields (Φ_Δ = 75.3% and 85.0% for **35** and **36**, respectively). Additionally, **35** and **36** displayed two-photon absorption efficiency at 820 nm with high values of two-photon absorption cross-section (σ_2) = 1969 and 5468 GM, respectively, which is the crucial parameter for the therapeutic efficiency of the photosensitizers. *In vitro* studies of MNPs showed high cytotoxicity (IC_{50} = 4.83 μM) and mitochondrial localization with a high intracellular accumulation of ruthenium (9.0 mg per million cells) and platinum (37.1 mg per million cells). Furthermore, *in vivo* studies on A549 tumor-bearing mice displayed significant antitumor efficacy of two-photon PDT using MNPs.

In an another recent example, Liu and coworkers constructed a multifunctional ruthenium-based SCC and its MNPs **39** via strong host–guest interaction of adamantane-functionalized transferrin (Ad-TRF) **37** and b-cyclodextrin(CD)-functionalized Ru(II) complex **38** in water at room temperature (Fig. 8.14). Incorporation of CD not only increased the physiological compatibility but also allowed noncovalent connection of transferrin to Ru(II)-based PDT sites. This hybrid assembly acted as a specific targeted site for tumor cells (A549) expressing the transferrin receptor, and the coordinated Ru(II) centers functioned as active sites for targeted PDT upon irradiation at 450 nm which produced sufficient ROS to damage lysosomes [52].

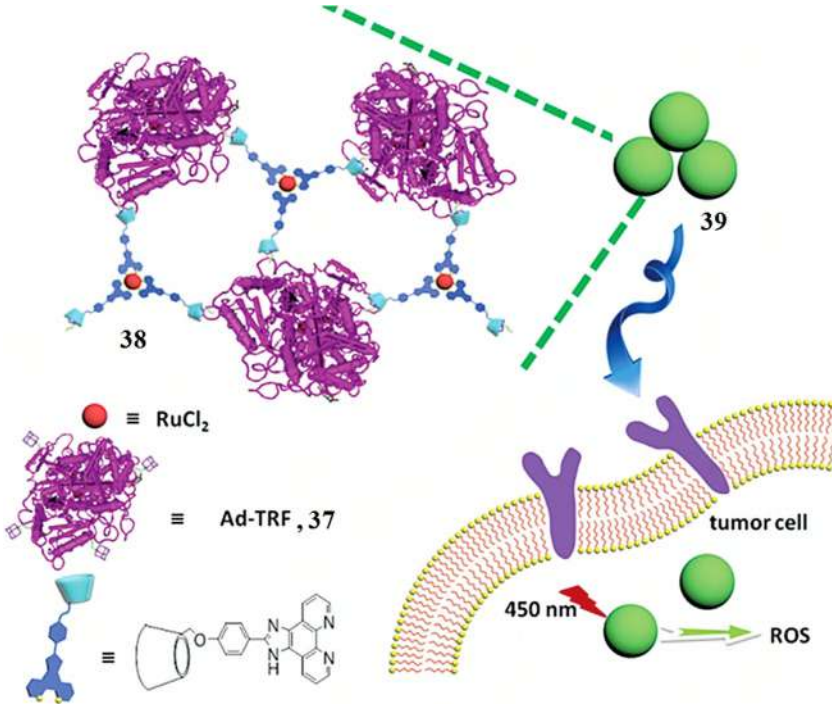

FIGURE 8.14 Schematic representation of phenanthroline-modified β-CD derivative Ad-TRF, **37**, Ad-TRF/Ru-CD supramolecular assembly **38**, MNPs **39** and its tumor-targeting PDT activity. (*Adapted with permission from Ref. [52].*)

8.2.4 Others SCCs

Apart from the above discussed SCCs, a few other photoactive moieties and their two- and three-dimensional architectures have recently been investigated for PDT applications. A self-assembled Pt(II) metallacycle containing a novel photosensitizer BTZPy **40** as bridging ligand was reported to exhibit photochemotherapeutic potential (Fig. 8.15A) [53]. This ligand showed thermally activated delayed fluorescence (TADF) due to the small energy gap of $\Delta E_{ST} = 0.085$ eV. Owing to the high emission along with sufficiently large triplet lifetime of 1.87 and 1.76 μs, respectively, **40** and the metallacycle BTZPy-Pt **41** showed superior $^1O_2$ generation capability ($\phi_\Delta = 95\%$ and 86% for **40** and **41**, respectively). Furthermore, spherical nanoparticles of **42** that are ~30 nm in diameter were prepared and were observed to be highly stable in the culture medium and exhibited excellent blood compatibility as assessed by the hemolysis test. Confocal microscopy images of HeLa cells showed excellent cell uptake of **42** in the cytoplasmic region due to its positive charge (2.8 ± 0.11 mV) in the culture medium interacting with negative potential of the cell membrane (Fig. 8.15D). Because of the synergistic effect between the antitumor Pt(II) center and the efficient photoinduced $^1O_2$ generation of **40**, supramolecular

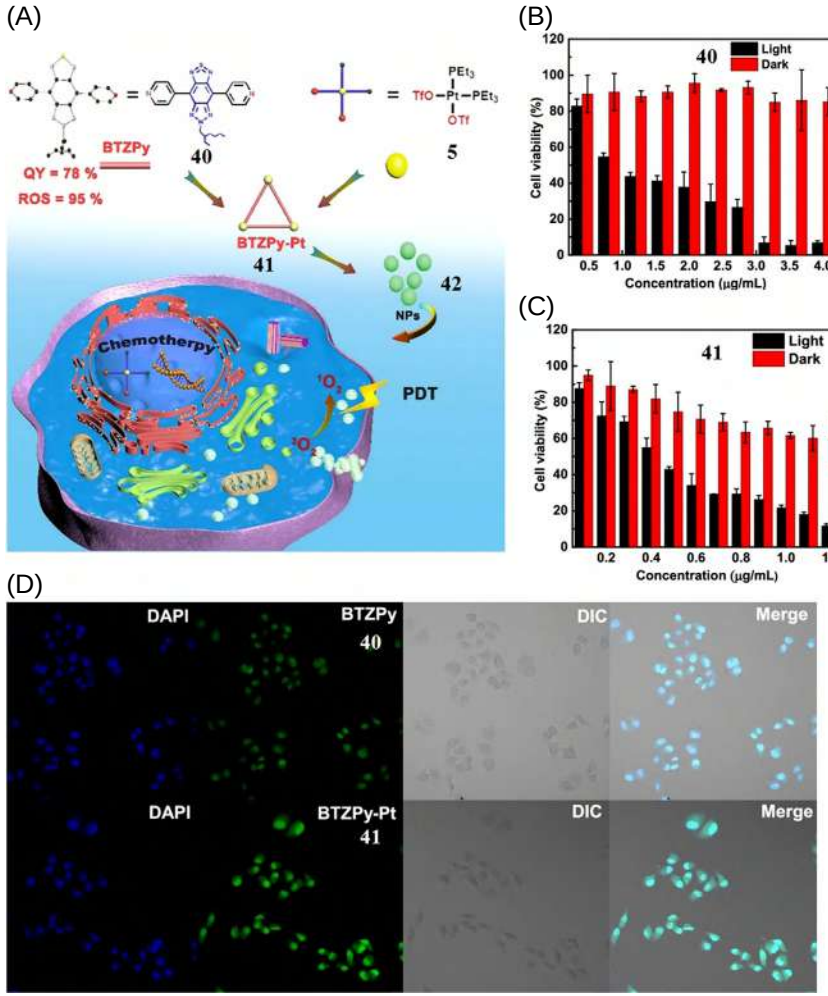

FIGURE 8.15 (A) Schematic representation and synthesis of **41** and its MNPs **42**. (B and C) MTT assay against HeLa cells of **40** and **41** with/without light irradiation. (D) Confocal microscopy images of HeLa cells after treatment with **40** and **41** followed by staining with DAPI. (*Adapted with permission from Ref. [53]. Copyright ©2021, American Chemical Society.*)

metallacycle **41** exhibited excellent photocytotoxicity under light irradiation with an IC_{50} value of 0.5 μg/mL which was much lower than that of **40** (Fig. 8.15B and C).

Chen, Lin, Sun, and coworkers employed highly stable luminescent organopalladium metallacycles (Pd_8L_4) for image-guided photodynamic cancer therapy [54]. The octanuclear metallacycle Pd_8L_4, **45** was quantitatively synthesized by stirring of the ligand **43** with $(bpy)_2Pd(NO_3)_2$ **44** (Fig. 8.16A). In addition, a dinuclear complex Pd_2L_2, **46** with monosubstituted PDI-pyrazole

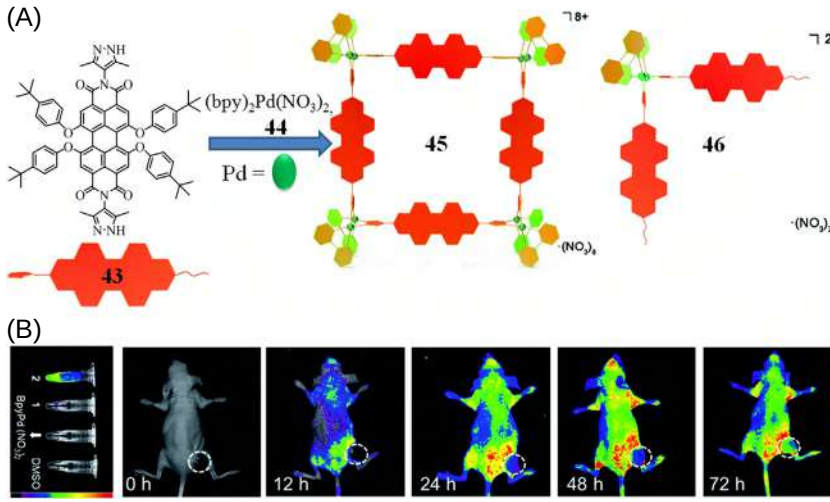

FIGURE 8.16 (A) Synthesis of **45** and **46** from a PDI-based ligand **43** via a spontaneous deprotonation self-assembly process. (B) In vivo fluorescence images showing the accumulation of **45** in HeLa xenograft nude mice at different time points. (*Adapted with permission from Ref. [54].*)

ligand was also prepared for various control studies (Fig. 8.16A). The metallacycle **45** showed characteristic PDI absorption bands (400–630 nm) with high extinction coefficients in DMSO along with a strong red emission that tailed to the NIR region ($\lambda_{em} = 617$ and 627 nm). The metallacycle **45** showed enhanced photoluminescence quantum yields of 0.51 in comparison to **46** (0.46) due to the rigidity of the PDI chromophores by the second pyrazole chelate. The rate constant of singlet oxygen generation by **45** was three times larger (0.0179 s^{-1}) than **43** (0.0069 s^{-1}) and was comparable to complex **46** (0.0191 s^{-1}) with monosubstituted PDI-pyrazole ligand. The IC_{50} values of **46** and **45** were 29.7 and 9.7 mM, respectively, against HeLa cells, whereas upon irradiation using 560 nm light for 2 min, the IC_{50} of **45** decreased significantly, indicating the enhancement of anticancer activities in combination with PDT. *In vitro* fluorescence imaging and intracellular translocation in HeLa cells of **45** showed that it binds to the cell membrane through the cytoplasmic path. Furthermore, *in vivo* fluorescence imaging and biodistribution in HeLa xenograft nude mice showed **45** gathered around the tumor sites after 48 h and the fluorescence intensity increased after 72 h (Fig. 8.16B). The metallacycle with expanded size and complicated structure exhibited better growth inhibitory effects on HeLa cervical cancer cells than the dinuclear complex, **46**.

Recently, an example of a water soluble tetragonal barrel type metallacage (M_8L_4) **49** was constructed with a new benzothiadiazole-based tetrapyridyl ligand **48** and *cis*-block 90° Pt(II) acceptor **47** (Fig. 8.17A) [55]. Cage **49** worked as a dual warhead with extraordinary photosensitizing ability in water ($\phi_\Delta = 26\%$) and with excellent photoinduced disinfection of pathogens at very low concentrations against Gram-positive bacteria such as *Staphylococcus aureus*,

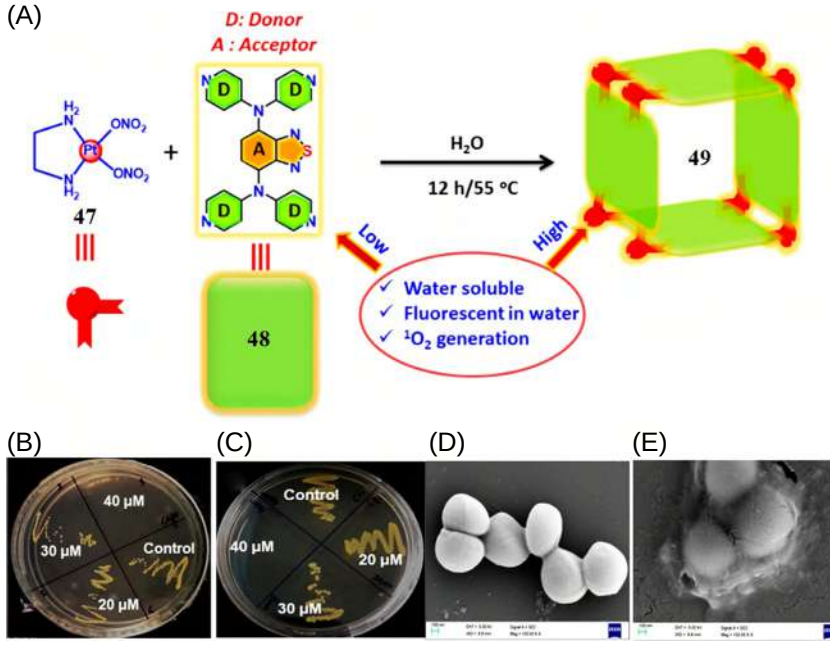

FIGURE 8.17 (A) Schematic representation of the synthesis of the tubular cage **49**. (B and C) Bactericidal concentration (MBC) estimation of MRSA and PA, respectively, after irradiation. SEM images of (D) untreated MRSA and (E) treated with **49** in the presence of light. (*Adapted with permission from Ref. [55]. Copyright © 2020, American Chemical Society.*)

MRSA and Gram-negative bacteria such as *Pseudomonas aeruginosa*, PA with higher inhibitory concentration in the presence and absence of light (Fig. 8.17B and C). The possible mechanisms for the antibacterial activity are the membrane depolarization or electrostatic interaction between negatively charged interior membrane of the bacterial cells with cationic **49** and the photoinduced singlet oxygen generation. SEM images confirmed that untreated MRSA retained their membrane integrity with spherical structure, however upon treatment with **49**, the cell membrane integrity was disrupted and resulted in the release of internal cell solutions (Fig. 8.17D and E). Efficient singlet oxygen efficiency in aqueous medium indicated its potential role as a PDT agent [55].

8.3 Conclusion and future prospects

We have summarized the latest examples of SCCs that were successfully implemented for PDT through various strategies for formulation and administration. These recent examples not only provide a blueprint for the development of new photosensitizers but also shed light on designing novel two- or three-dimensional SCCs for application in PDT. Despite the fact that the studies of these SCCs as PDT agents are still in their infancy, these reports demonstrate that Ru/Pd/Pt/heterometallic-based SCCs incorporating chromophores have great

potential as antitumor agents. Moreover, it is noteworthy that combination therapy and the postsynthetic modification of SCCs serve to induce unique properties such as stability and biocompatibility which would allow SCCs to be used as multifunctional nanomedicines. Future direction of SSCs is to overcome the challenges in designing strategy and transforming it to a drug for human therapy is the desired destination.

Acknowledgment

N.T. acknowledges support from DST, Government of India (SR/WOS-A/CS114/2017(G).

References

[1] T.R. Cook, Y.-R. Zheng, P.J. Stang, Metal–organic frameworks and self-assembled supramolecular coordination complexes: comparing and contrasting the design, synthesis, and functionality of metal–organic materials, Chem. Rev. 113 (1) (2013) 734–777.

[2] P.J. Lusby, Supramolecular coordination chemistry, Annu. Rep. Sect. Inorg. Chem. 109 (2013) 254–276.

[3] H.-C."J" Zhou, S. Kitagawa, Metal–organic frameworks (MOFs), Chem. Soc. Rev. 43 (16) (2014) 5415–5418.

[4] Y. Qin, L.-J. Chen, F. Dong, S.-T. Jiang, X.Li G.-Q.Yin, Y. Tian, H.-B. Yang, Light-controlled generation of singlet oxygen within a discrete dual-stage metallacycle for cancer therapy, J. Am. Chem. Soc. 141 (22) (2019) 8943–8950.

[5] W.-J. Chung, J.-W. Oh, K. Kwak, B.Y. Lee, J. Meyer, E. Wang, A. Hexemer, S.-W. Lee, Biomimetic self-templating supramolecular structures, Nature 478 (2011) 364–368.

[6] S. Mann, Molecular tectonics in biomineralization and biomimetic materials chemistry, Nature 365 (1993) 499–505.

[7] D. Fujita, Y. Ueda, S. Sato, N. Mizuno, T. Kumasaka, M. Fujita, Self-assembly of tetravalent Goldberg polyhedra from 144 small components, Nature 540 (2016) 563–566.

[8] B. Song, S. Kandapal, J. Gu, K. Zhang, A. Reese, Y. Ying, L. Wang, H. Wang, Y. Li, M. Wang, S. Lu, X.-Q. Hao, X. Li, B. Xu, X. Li, Self-assembly of polycyclic supramolecules using linear metal-organic ligands, Nat. Commun. 9 (2018) 4575–4584.

[9] H. Ube, K. Endo, H. Sato, M. Shionoya, Synthesis of hetero-multinuclear metal complexes by site-selective redox switching and transmetalation on a homo-multinuclear complex, J. Am. Chem. Soc. 141 (26) (2019) 10384–10389.

[10] B. Chen, J.J. Holstein, S. Horiuchi, W.G. Hiller, G.H. Clever, Pd(II) coordination sphere engineering: pyridine cages, quinoline bowls, and heteroleptic pills binding one or two fullerenes, J. Am. Chem. Soc. 141 (22) (2019) 8907–8913.

[11] D.A. Leigh, L. Pirvu, F. Schaufelberger, Stereoselective synthesis of molecular square and granny knots, J. Am. Chem. Soc. 141 (14) (2019) 6054–6059.

[12] P. Stricklen, J. Verkade, Novel homo and heterometallic coordination macrocycles, J. Am. Chem. Soc. 105 (8) (1983) 2494–2495.

[13] L.-J. Chen, S. Chen, Y. Qin, L. Xu, G.-Q. Yin, J.-L. Zhu, F.-F Zhu, W. Zheng, X. Li, H.-B. Yang, Construction of porphyrin-containing metallacycle with improved stability and activity within mesoporous carbon, J. Am. Chem. Soc. 140 (15) (2018) 5049–5052.

[14] C.-H. Leung, T.-S. Kang, C. Yang, K.-H. Leung, D.-L. Ma, Compr Supramol Chem II, second ed., Elsevier, 2017.

[15] N. Dey, C.J.E. Haynes, Supramolecular coordination complexes as optical biosensors, ChemPlusChem 86 (3) (2021) 418–433.
[16] M. Fujita, M. Tominaga, A. Hori, B. Therrien, Coordination assemblies from a Pd(II)-cornered square complex, Acc. Chem. Res. 38 (4) (2005) 369–378.
[17] S. Datta, M.L. Saha, P.J. Stang, Hierarchical assemblies of supramolecular coordination complexes, Acc. Chem. Res. 51 (9) (2018) 2047–2063.
[18] R. Chakrabarty, P.S. Mukherjee, P.J. Stang, Supramolecular coordination: self-assembly of finite two- and three-dimensional ensembles, Chem. Rev. 111 (11) (2011) 6810–6918.
[19] I.V. Grishagin, J.B. Pollock, S. Kushal, T.R. Cook, P.J. Stang, B.Z. Olenyuk, In vivo anticancer activity of rhomboidal Pt(II) metallacycles, Proc. Natl Acad. Sci. 111 (52) (2014) 18448–18453.
[20] G.R. Newkome, C.N. Moorefield, From 1 → 3 dendritic designs to fractal supramacromolecular constructs: understanding the pathway to the Sierpiński gasket, Chem. Soc. Rev. 44 (12) (2015) 3954–3967.
[21] J. Mendez-Arroyo, A.I. d'Aquino, A.B. Chinen, Y.D. Manraj, C.A. Mirkin, Reversible and selective encapsulation of dextromethorphan and β-estradiol using an asymmetric molecular capsule assembled via the weak-link approach, J. Am. Chem. Soc. 139 (4) (2017) 1368–1371.
[22] C.J. Hastings, R.G. Bergman, K.N. Raymond, Origins of large rate enhancements in the Nazarov cyclization catalyzed by supramolecular encapsulation, Chem. – Eur. J. 20 (14) (2014) 3966–3973.
[23] P.P. Neelakandan, A. Jiménez, J.R. Nitschke, Fluorophore incorporation allows nanomolar guest sensing and white-light emission in M_4 L_6 cage complexes, Chem. Sci. 5 (3) (2014) 908–915.
[24] M. Fujita, D. Oguro, M. Miyazawa, H. Oka, K. Yamaguchi, K. Ogura, Self-assembly of ten molecules into nanometre-sized organic host frameworks, Nature 378 (1995) 469–471.
[25] Y. Wang, Y. Zhang, Z. Zhou, R.T. Vanderlinden, B. Li, B. Song, X. Li, L. Cui, J. Li, X. Jia, J. Fang, C. Li, P.J. Stang, A cyclic bis[2]catenane metallacage, Nat. Commun. 11 (2020) 2727–2734.
[26] Z. Li, X. Liu, G. Wang, B. Li, H. Chen, H. Li, Y. Zhao, Photoresponsive supramolecular coordination polyelectrolyte as smart anticounterfeiting inks, Nat. Commun. 12 (2021) 1363–1371.
[27] R. Küng, T. Pausch, D. Rasch, R. Göstl, B.M. Schmidt, Mechanochemical release of non-covalently bound guests from a polymer-decorated supramolecular cage, Angew. Chem. Int. Ed. 60 (24) (2021) 13626–13630.
[28] G.-Y. Wu, X. Shi, H. Phan, H. Qu, Y.-X. Hu, G.-Q. Yin, X.-L. Zhao, X. Li, L. Xu, Q. Yu, H.-B. Yang, Efficient self-assembly of heterometallic triangular necklace with strong antibacterial activity, Nat. Commun. 11 (2020) 3178–3189.
[29] H. Zhu, Q. Li, B. Shi, F. Ge, Y. Liu, Z. Mao, H. Zhu, S. Wang, G. Yu, F. Huang, P.J. Stang, Dual-emissive platinum(II) metallacage with a sensitive oxygen response for imaging of hypoxia and imaging-guided chemotherapy, Angew. Chem. Int. Ed. 59 (45) (2020) 20208–20214.
[30] P.P.P. Kumar, P. Yadav, A. Shanavas, P.P. Neelakandan, Aggregation enhances luminescence and photosensitization properties of a hexaiodo-BODIPY, Mater. Chem. Front. 4 (3) (2020) 965–972.
[31] M. Tampa, M.-I. Sarbu, C. Matei, C.-I. Mitran, M.-I. Mitran, C. Caruntu, C. Constantin, M. Neagu, S.-R. Georgescu, Photodynamic therapy: a hot topic in dermato-oncology (Review), Oncol. Lett. 17 (5) (2019) 4085–4093.

[32] R.L. Yanovsky, D.W. Bartenstein, G.S. Rogers, S.J. Isakoff, S.T. Chen, Photodynamic therapy for solid tumors: a review of the literature, Photodermatol. Photoimmunol. Photomed. 35 (5) (2019) 295–303.

[33] L.B. Josefsen, R.W. Boyle, Photodynamic therapy and the development of metal-based photosensitisers, Met. Based Drugs 2008 (2008) 1–23.

[34] Z. Zhao, Z. Zhang, H. Wang, X. Li, M. Zhang, Multicomponent porphyrin-based tetragonal prismatic metallacages and their photophysical properties, Isr. J. Chem. 59 (3-4) (2019) 299–305.

[35] X. Jiang, Z. Zhou, H. Yang, C. Shan, H. Yu, L. Wojtas, M. Zhang, Z. Mao, M. Wang, P.J. Stang, Self-assembly of porphyrin-containing metalla-assemblies and cancer photodynamic therapy, Inorg. Chem. 59 (11) (2020) 7380–7388.

[36] G. Yu, S. Yu, M.L. Saha, J. Zhou, T.R. Cook, B.C. Yung, J. Chen, Z. Mao, F. Zhang, Z. Zhou, Y. Liu, L. Shao, S. Wang, C. Gao, F. Huang, P.J. Stang, X. Chen, A discrete organoplatinum(II) metallacage as a multimodality theranostic platform for cancer photochemotherapy, Nat. Commun. 9 (2018) 4335–4348.

[37] G. Yu, B. Zhu, L. Shao, J. Zhou, M.L. Saha, B. Shi, Z. Zhang, T. Hong, S. Li, X. Chen, P.J. Stang, Host−guest complexation-mediated codelivery of anticancer drug and photosensitizer for cancer photochemotherapy, Proc. Natl. Acad. Sci. 116 (14) (2019) 6618–6623.

[38] Y. Qin, X. Liu, P.-P. Jia, L. Xu, H.-B. Yang, BODIPY-based macrocycles, Chem. Soc. Rev. 49 (16) (2020) 5678–5703.

[39] J. Zhou, Y. Zhang, G. Yu, M.R. Crawley, C.R.P. Fulong, A.E. Friedman, S. Sengupta, J. Sun, Q. Li, F. Huang, T.R. Cook, Highly emissive self-assembled BODIPY-platinum supramolecular triangles, J. Am. Chem. Soc. 140 (24) (2018) 7730–7736.

[40] G. Gupta, A. Das, K.C. Park, A. Tron, H. Kim, J. Mun, N. Mandal, K.W. Chi, C.Y. Lee, Self-assembled novel BODIPY-based palladium supramolecules and their cellular localization, Inorg. Chem. 56 (8) (2017) 4615–4621.

[41] G. Gupta, Y. You, R. Hadiputra, J. Jung, D.-K. Kang, C.Y. Lee, Heterometallic BODIPY-based molecular squares obtained by self-assembly: synthesis and biological activities, ACS Omega 4 (8) (2019) 13200–13208.

[42] G. Gupta, A. Das, N.B. Ghate, T. Kim, J.Y. Ryu, J. Lee, N. Mandal, C.Y. Lee, Novel BODIPY-based Ru(II) and Ir(III) metalla-rectangles: cellular localization of compounds and their antiproliferative activities, Chem. Commun. 52 (23) (2016) 4274–4277.

[43] G. Gupta, A. Das, S. Panja, J.Y. Ryu, J. Lee, N. Mandal, C.Y. Lee, Selective cytotoxicity of self-assembled BODIPY metalla-rectangles: evidence of p53-Dependent apoptosis via both intrinsic and extrinsic pathways, Dyes Pigments 180 (2020) 108478–108488.

[44] J. Karges, M. Jakubaszek, C. Mari, K. Zarschler, B. Goud, H. Stephan, G. Gasser, Synthesis and characterization of an epidermal growth factor receptor-selective Ru^{II} polypyridyl–nanobody conjugate as a photosensitizer for photodynamic therapy, ChemBioChem 21 (4) (2020) 531–542.

[45] S. Monro, K.L. Colón, H. Yin, J. Roque, P. Konda, S. Gujar, R.P. Thummel, L. Lilge, C.G. Cameron, S.A. McFarland, Transition metal complexes and photodynamic therapy from a tumor-centered approach: challenges, opportunities, and highlights from the development of TLD1433, Chem. Rev. 119 (2) (2019) 797–828.

[46] T.R. Cook, P.J. Stang, Recent developments in the preparation and chemistry of metallacycles and metallacages via coordination, Chem. Rev. 115 (15) (2015) 7001–7045.

[47] T.R. Cook, V. Vajpayee, M.H. Lee, P.J. Stang, K.-W. Chi, Biomedical and biochemical applications of self-assembled metallacycles and metallacages, Acc. Chem. Res. 46 (11) (2013) 2464–2474.

[48] V. Vajpayee, S. mi Lee, J.W. Park, A. Dubey, H. Kim, T.R. Cook, P.J. Stang, K.W. Chi, Growth inhibitory activity of a bis-benzimidazole-bridged arene ruthenium metalla-rectangle and -prism, Organometallics 32 (6) (2013) 1563–1566.

[49] J. Karges, T. Yempala, M. Tharaud, D. Gibson, G. Gasser, A multi-action and multi-target Ru^{II}–Pt^{IV} conjugate combining cancer-activated chemotherapy and photodynamic therapy to overcome drug resistant cancers, Angew. Chem. Int. Ed. 59 (18) (2020) 7069–7075.

[50] Z. Zhou, J. Liu, T.W. Rees, H. Wang, X. Li, H. Chao, P.J. Stang, Heterometallic Ru–Pt metallacycle for two-photon photodynamic therapy, Proc. Natl Acad. Sci. 115 (22) (2018) 5664–5669.

[51] Z. Zhou, J. Liu, J. Huang, T.W. Rees, Y. Wang, H. Wang, X. Li, H. Chao, P.J. Stang, A self-assembled Ru–Pt metallacage as a lysosome-targeting photosensitizer for 2-photon photodynamic therapy, Proc. Natl Acad. Sci. 116 (41) (2019) 20296–20302.

[52] H.-G. Fu, Y. Chen, Q. Yu, Y. Liu, A tumor-targeting Ru/polysaccharide/protein supramolecular assembly with high photodynamic therapy ability, Chem. Commun. 55 (21) (2019) 3148–3151.

[53] S. Lv, Y. Miao, D. Zheng, X. Li, D. Liu, F. Song, Self-assembled platinum supramolecular metallacycles based on a novel TADF photosensitizer for efficient cancer photochemotherapy, Mol. Pharm. 18 (3) (2021) 1229–1237.

[54] L. He, L.-X. Cai, M.-H. Li, G.-L. Zhang, L.-P. Zhou, T. Chen, M.-J. Lin, Q.-F. Sun, Designing a highly stable coordination-driven metallacycle for imaging-guided photodynamic cancer theranostics, Chem. Sci. 11 (30) (2020) 7940–7949.

[55] S. Bhattacharyya, M. Venkateswarulu, J. Sahoo, E. Zangrando, M. De, P.S. Mukherjee, Self-assembled Pt^{II}_8 metallosupramolecular tubular cage as dual warhead antibacterial agent in water, Inorg. Chem. 59 (17) (2020) 12690–12999.

Chapter 9

Biosensing properties of supramolecular coordination complexes

Dipanjana Sarkar[a], **Pandurangan Nanjan**[b] **and Sankarasekaran Shanmugaraju**[a,1]

[a] *Department of Chemistry, Indian Institute of Technology Palakkad (IITPKD), Palakkad, Kerala, India,* [b] *School of Physical Sciences, Amrita Vishwa Vidyapeetham, Mysuru Campus, Karnataka, India*

9.1 Introduction

Supramolecular chemistry is an emerging field of science that provides a surplus of opportunities for the generation and exploration of different kinds of synthetic macrocyclic model systems which can be applied to mimic the structures and essential functions of various biological systems and biological processes [1]. The conventional multistep covalent synthesis of large macromolecules is tedious, time-consuming, and thus results in a low yield of the final product [2]. On the other hand, it is also difficult to isolate the desired products in high yield using weak noncovalent interactions such as hydrogen bonding, $\pi-\pi$ stacking, ion-dipole, van der Waals force, and lipophilic/hydrophilic attractions [3]. However, in recent years, metal–ligand coordination-directed self-assembly has evolved to be a powerful and alternative synthetic protocol for the synthesis of abiological macrocyclic structures [4]. Owing to the strong bond-enthalpy and high bonding directionality, the coordination-driven self-assembly has been successfully adopted for the generation of a plethora of finite supramolecular coordination complexes (SCCs) of different shapes, sizes, and functions [5]. The desired SCCs can easily be designed by the judicial selection of preprogrammed building units and their appropriate stoichiometry combination in a proper solvent system. The coordination-driven self-assembly is especially appealing because a variety of structurally diverse molecular building units can be designed through the functionalization of coordinatively unsaturated

[1] Sankarasekaran Shanmugaraju is a corresponding author of this chapter.

Supramolecular Coordination Complexes: Design, Synthesis, and Applications.
DOI: https://doi.org/10.1016/B978-0-323-90582-4.00016-6

transition metal cations [6]. In recent decades, a plethora of aesthetically elegant functionalized SCCs of different topologies starting from simple 2D molecular squares to intricate 3D dodecahedron cages, have been constructed via directional coordination self-assembly. Many of them have successfully been used for numerous applications like host-guest chemistry, cavity-controlled catalysis, chemosensors, optoelectronic devices, stimuli-responsive drug delivery, etc. [7]. Among the various SCCs, luminescent supramolecular assemblies have gained special attention because of their application as potential fluorescent sensors and imaging probes [8]. Especially, hollow 3D supramolecular cages have gained a special interest in recent years because their well-defined nanoscopic internal cavity can be used as a potential host for selective sensing and encapsulation of bio-related analytes stabilized by multiple weak noncovalent interactions [9]. Furthermore, the desired functional groups can easily be introduced within SCCs through post- or presynthetic functionalization using appropriately programmed building units [10]. SCCs are mostly soluble or well-disperse in the aqueous medium because of their highly charged cationic structures which makes them a suitable candidate for biosensing applications. In this chapter, we have discussed the biosensing properties of luminescent metallacycles and metallocages toward a wide range of bioanalytes such as nucleotides, proteins, amines, carbohydrates, lipids, and steroids. We have highlighted the effect of the structure of SCCs on the extent of biosensing in terms of their selectivity, sensitivity, and different sensing mechanism. This chapter will benefit the readers working on interdisciplinary areas of science.

9.2 Biosensing properties of supramolecular coordination complexes (SCCs)

9.2.1 Interaction of SCCs with nucleosides

Specific molecular recognition of nucleoside derivatives is necessary for different biological functions. Although many sensing strategies have been developed for the detection of nucleoside analogues, it is always challenging to achieve a selective and sensitive detection of the nucleoside. Duan et al. designed a truncated octahedral nanocage (**SCC-1**) for the detection of nucleosides [11]. The Pd(II)-based cage comprises quinoline and amide, functional groups. The quinoline unit acts as a donor to form a coordination bond with Pd(II) as well as acts as a signaling unit for detection. While the amide groups function as a receptor site for the recognition of nucleosides through hydrogen-bonding interactions (Fig. 9.1A).

The nanocage **SCC-1** showed a strong emission around $\lambda = 410$ nm and the emission was found to be drastically enhanced upon mixing of nucleosides which strongly binds with amide moiety through hydrogen-bonding interactions. The fluorescent enhancement of **SCC-1** upon binding with nucleosides is due to

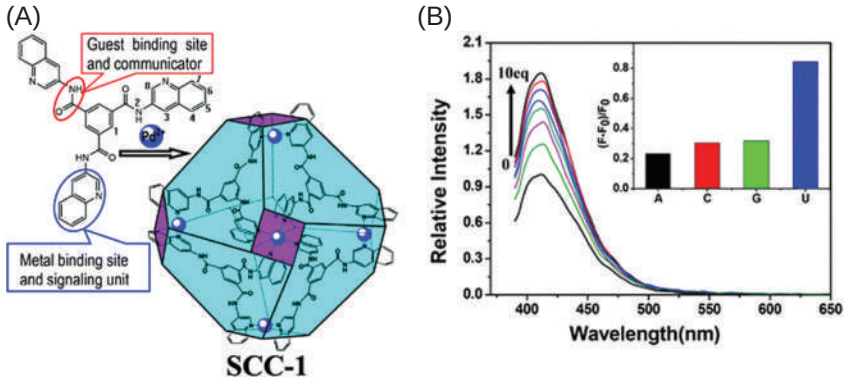

FIGURE 9.1 (A) Self-assembly formation of **SCC-1** from a tri-quinoline donor reacted with Pd(II)-based acceptor. (B) The changes in emission intensity of **SCC-1** upon the addition of uridine standard solution in DMF (Insert: the extend of fluorescence changes observed for four RNA-based nucleosides). (*Reprinted with permission from Ref. [10]. Copyright 2008 Royal Society of Chemistry.*)

the photoinduced electron transfer (PET) process. The highest fluorescence enhancement was observed for uridine and other RNA-based nucleotides displayed a poor to the moderate binding affinity for **SCC-1** (Fig. 9.1B).

Similarly, the molecular recognition of anions in an aqueous solution is one of the key challenges. Most of the reported anion receptors suffer from poor aqueous solubility, inadequate cavity space, and lack of selectivity. To surmount these issues, Nitschke and coworkers designed a water-soluble fluorescent metal-organic tetrahedron (**SCC-2**) to distinguish negatively charged nucleotides from their neutral analogs [12]. The self-assembled tetrahedron **SCC-2** is composed of fluorescent triazatriangulenium ($TATA^+$) panels chelated with Zn(II) in the vertices which are substituted with tris(2-aminoethyl) amine (TREN) (Fig. 9.2A). The vertex has been efficiently chelated through Zn(II) without the interference of fluorescence of the $TATA^+$ panels and TREN molecule. This provides good structural stability to the polyhedron by reducing the electrostatic repulsion between the $TATA^+$ panels. The $TATA^+$ panels are stable aromatic carbocations that engender the cationic charges on the cage and provide a large internal cavity for efficient anion encapsulation. **SCC-2** showed a greater binding affinity for the negatively charged nucleotides compared to the neutral nucleotides. The high selectivity toward phosphorylated nucleotides could be attributed to the cationic surrounding of the cavity by $TATA^+$ panels which offer an internal cavity that is perfectly matched with the size of nucleotides (Fig. 9.2C). Also, the electronic repulsion was observed between the $TATA^+$ panels on the addition of an anion. The UV–visible absorption spectrum exhibited several peaks at $\lambda = 347, 489$, and 532 nm signifying the $\pi \rightarrow \pi^*$ transitions of the $TATA^+$ moieties. Fluorescence quenching is observed upon the interaction of the negatively charged nucleotide with **SCC-2**. The tetrahedral cage exhibited an orange fluorescence, resulting in

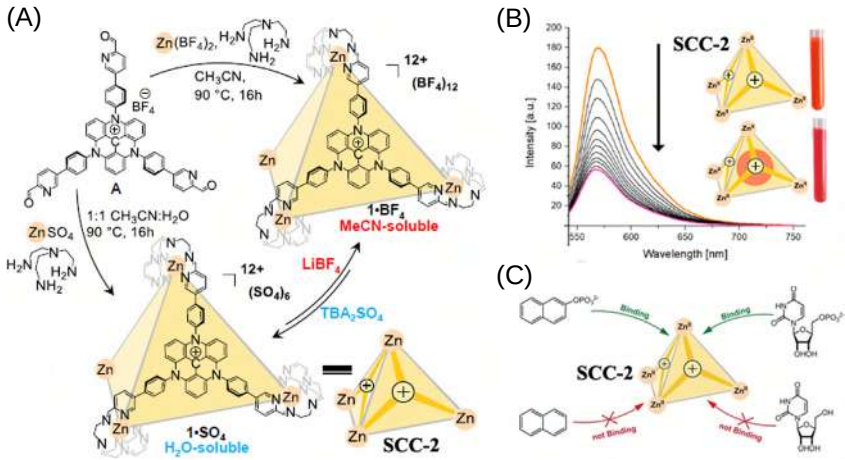

FIGURE 9.2 (A) Self-assembly formation of **SCC-2** along with their reversible anion exchange sequence. (B) Observed fluorescence quenching of **SCC-2** upon the addition of AMP and corresponding color changes solution of **SCC-2** before and after the addition of AMP. (C) The binding propensity of **SCC-2** for various analytes. (*Reprinted with permission from Ref. [11]. Copyright 2019 Wiley.*)

a pink fluorescence when bound to the anionic nucleotides (Fig. 9.2B). GMP showed the highest binding constant of $1.03 \pm 0.04 \times 10^3$ M^{-1} which is comparable to the biosensing properties of other tetrahedral coordination cages.

9.2.2 Interaction of SCCs with nucleic acids

In the context of the growing demand for anticancer drugs due to the worldwide outspread of cancer, there is a rising interest in the synthesis of finite supramolecular coordination complexes for targeting DNA to be utilized for therapeutic purposes [13]. These macrocyclic complexes primarily target the DNA and binding strongly with the G-quadruplex. Telomerase inhibition can be explored by targeting quadruplex DNA and the specified ligands. Targeting quadruplex DNA is the latest research interest in cancer treatment. With this perception, Chi and coworkers synthesized two heterometallic metallacycles (**SCC-3** and **SCC-4**) from the reaction of the H_2L ligand (H_2L = 2,6-bis(N-(4-pyridyl)carbamoyl)pyridine) mixed with cis-Pd[(dppf)$(OTf)_2$] or cis-Pt[(dppf)$(OTf)_2$] (dppf =1,1′-bis(diphenylphosphino)-ferrocene; OTf = trifluoromethane sulfonate) acceptors (Fig. 9.3A and B) [14]. Each Pt(II) and Pd(II) centers attain a distorted square planar geometry upon coordination with two phosphorous atoms of dppf containing ferrocenyl moieties and two nitrogen atoms from the pyridine moieties of H_2L. The photophysical and gel-electrophoresis studies are extremely useful for the specific interactions of discrete metallacycles with DNA. The absorption peaks of **SCC-3** and **SCC-4**

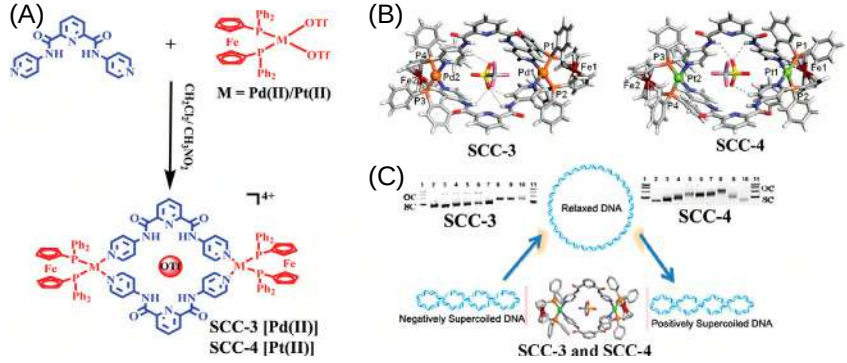

FIGURE 9.3 (A) [2+2] Self-assembly formation of **SCC-3** and **SCC-4**. (B) Single-crystal X-ray structure of **SCC-3** and **SCC4**. (C) Electrophoresis experiments reveal the DNA binding properties of **SCCs**. (*Reprinted with permission from Ref. [13]. Copyright 2011 American Chemical Society.*)

were observed in the range of $\lambda = 270$ nm due to the intra-ligand π–π^* transition. A hypochromic shift was observed when **SCC-3** and **SCC-4** bound with DNA, and it was further confirmed by the binding constant, that is, 2.58×10^5 M^{-1} for **SCC-3** and 1.23×10^5 M^{-1} for **SCC-4**. Spectroscopic techniques were utilized to investigate the complex's binding toward DNA using EtBr as the probe. Quenching of fluorescence emission was observed on the binding of the complex with DNA. The electrophoresis experiment confirmed that **SCCs** distort the DNA through unwinding rather than cleavage. CD experiments further verified conformational changes in DNA (Fig. 9.3C).

In 2017, Zhao et al. developed a metallohelix resembling an alpha-helix structure, which targets the human telomeric hybrid G-quadruplex and inhibits telomerase enzyme activity [15]. The G-quadruplexes are the guanine-like structure that is associated with the controlling of the telomerase enzyme activity. Alkylation of (R)-2-phenylglycinol with dibromo-xylene gave an optically pure diamine. The diamine reaction with 2-pyridine carboxaldehyde and $Fe(ClO_4)_2 \cdot 6H_2O$ yielded the desired metallohelix (**SCC-5**). The binding constant for G-quadruplexes DNA of the metallohelix was found to be 2.8×10^7 M^{-1}, which confirms the strong interaction of the metallohelix with the G-quadruplex. Further, metallohelix **SCC-5** showed a high propensity in telomerase enzyme inhibition with an IC_{50} value of 600 nM. In the same year, Sleiman et al. synthesized Pt(II)-based supramolecular complexes using ball milling mechanochemistry [16]. The cationic supramolecular complexes were found to be strongly bound with the guanine of DNA quadruplexes and inhibit the telomerase activity of cancer-specific enzymes. The supramolecular square complexes (**SCC-6 to SCC-9**) were generated in two-step reactions from the commercially available K_2PtCl_4 salt, combining 4,4′-bipyridine and related bridging ligands. Each Pt(II) center is tetra-coordinated with two different nitrogen coordination (Fig. 9.4). All the complexes exhibited varying binding

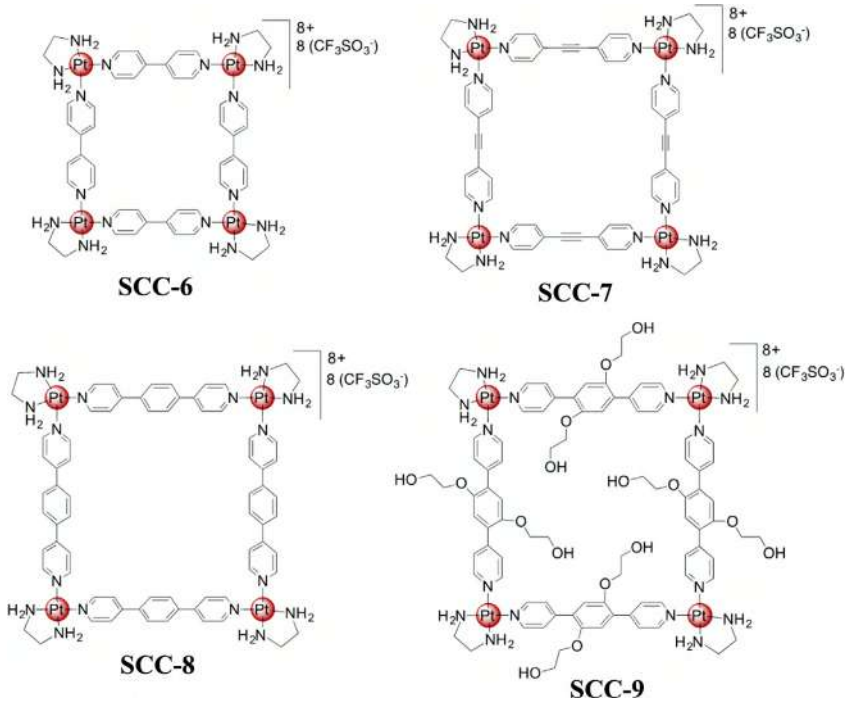

FIGURE 9.4 The structure of four different Pt(II)-molecular squares (**SCC-6** to **SCC-9**) was synthesized via mechanochemical synthesis. (*Reprinted with permission from Ref. [15]. Copyright 2011 American Chemical Society.*)

affinity toward DNA due to their varied bridging ligands. The presence of the phenyl groups strengthens the π–π interaction, and hydroxyl-ethoxy units involve hydrogen-bonding interactions to stabilize the quadruplex structure. Furthermore, the thiazole orange showed a high fluorescence upon binding with RNA, but the fluorescence intensity decreased on replacement with Pt-square complexes. This confirms that the thiazole orange has a binding affinity toward the RNA telomeric sequence. Further absorption studies provided evidence for π–π stacking interactions between the molecular squares and DNA structures through hypochromic and redshift at $\lambda = 300$ nm.

9.2.3 Interaction of SCCs with protein and amino acids

Proteins play a vital role in the proper functioning of various physiological processes like DNA replication, catalytic metabolism, etc. [17]. The protein's primary structure comprises amino acids that control the 3D protein folding. 3D protein folding plays a pivotal role in maintaining crucial biological processes [18]. Most therapeutic drugs were designed, considering DNA as the primary target. The current research aims the development of therapeutic drugs which

can selectively bind to specific proteins and amino acids for targeted therapy. Chi et al. synthesized a Ru(II)-based supramolecular coordination complex (**SCC-10**) with a dipyridyl ligand and was used to sense the green fluorescent protein [19]. The ditopic ligand comprises pyridyl-2,6-dicarboxamide moiety and ethynyl groups. The amide group interacts with protein kinases through hydrogen bonding, and ethynyl groups provide structural rigidity and enhance the photophysical properties. The **SCC-10** was designed by the [2+2] self-assembly of the dipyridyl ligand with the dinuclear arene Ru(II) oxalato bridged building block (Fig. 9.5A and B). The enhanced green fluorescent protein (EGFP) consists of a tripeptide chromophore with a p-hydroxy benzylidene imidazolidone moiety. This functional moiety renders them sensitive to agents inducing conformational changes. **SCC-10** metallacycle can change the conformational structure of EGFP protein by disrupting the secondary or tertiary structure. It leads to inhibit the chromophoric activity of the imidazolidone moiety. **SCC-10** showed a characteristic absorption at $\lambda = 380$ nm, but in combination with EGFP, a hypochromic shift at $\lambda = 350$ nm and a hyperchromic shift were observed at $\lambda = 500$ nm (Fig. 9.5C). The selectivity of the metallacycle toward EGFP was proved by comparing the binding studies with BSA and ovalbumin. The observed conformational changes were understood from the photophysical studies and the calculated binding constant was $7.394 \times 10^8\ M^{-1}$. The conformational changes lead to protein aggregation which was confirmed by gel electrophoresis, circular dichroism, and atomic force microscopy. The in vivo studies showed quenching of fluorescence upon the binding of GFP proteins with **SCC-10** inside the cells. It further proves the membrane permeability property of **SCC-10** (Fig. 9.5D). Thus, the metallacycles **SCC-10** can act as potential therapeutic agents by selectively targeting proteins.

Duan et al. designed a Ce(III)-based molecular tetrahedron (**SCC-11**) for the selective sensing of tryptophan (Trp) [20]. **SCC-11** was synthesized by combining ligand H_6TTS and $Ce(NO_3)_3 \bullet 6H_2O$. Ligand H_6TTS was synthesized from 4,4',4"-nitrilotribenzocarbohydrazide and salicylaldehyde (Fig. 9.6A). The amide linkages in the ligand act as hydrogen-bonding donors, triphenylamine moieties act as potential luminophores, and π stacking centers. The synergistic effect of hydrogen bonding, π–π stacking, and the cavity size promote the high sensitivity and selectivity of the tetrahedron toward Trp. **SCC-11** exhibited a strong emission around $\lambda = 470$ nm, and it further increased to 6.5-fold intensity with the addition of Trp (Fig. 9.6B). The emission intensity of Trp-induced luminescence remains unaffected even in the presence of aliphatic amines and other aromatic amines. The results indicated that the ligand H_6TTS endowed the macrocycle **SCC-11** to show specific selectivity toward Trp. The fluorescent emission on the interaction of Trp with **SCC-11** enables the bioimaging of Trp in living cells which can be utilized for the treatment of various diseases like chronic hepatitis, parkinsonism, aplastic anemia, and atrophic arthritis.

Therrien and coworkers developed protein targeting hexanuclear Ru(II)-based trigonal metalloprisms (**SCC-12** to **SCC-14**) using various Ru(II)-bridged

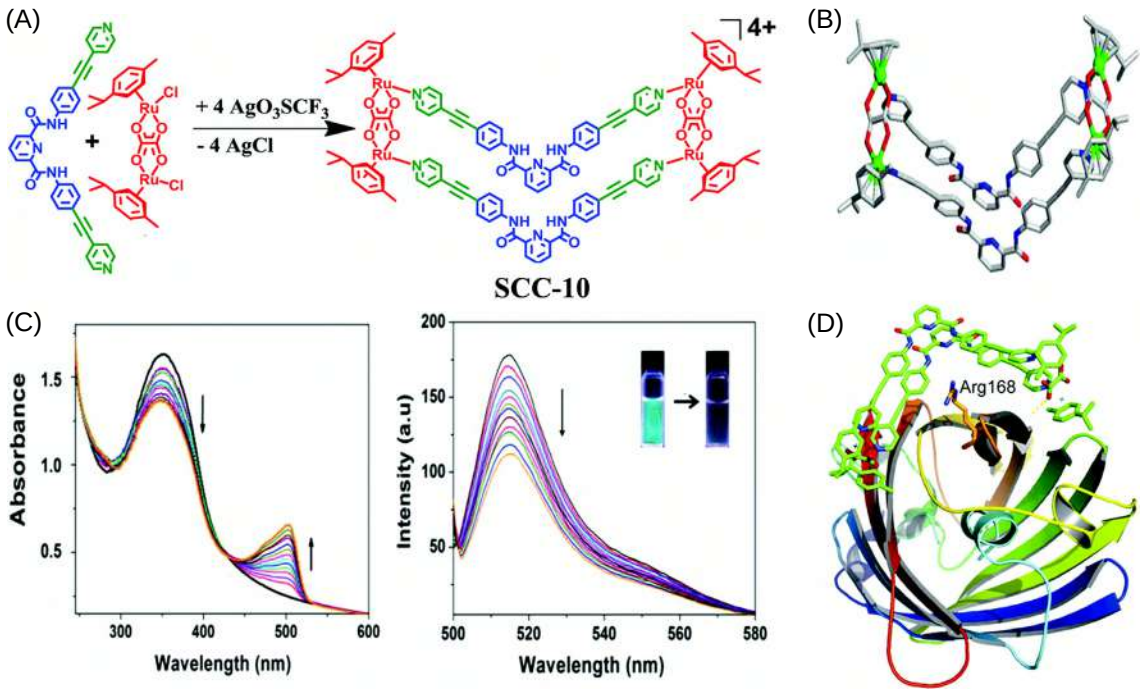

FIGURE 9.5 (A) [2+2] Self-assembly formation of **SCC-10** from a clip-type dipyridyl donor reacted with Ru(II) acceptor. (B) X-ray crystal structure of **SCC-10**. (C) UV–vis absorption spectra of **SCC-10** upon mixing of EGFP and changes in emission intensity of EGFP after the addition of **SCC-10** (Insert: observed visual color changes). (D) Docking model structure of binding of **SCC-10** with EGFP. (*Reprinted with permission from Ref. [18]. Copyright 2014 Royal Society of Chemistry.*)

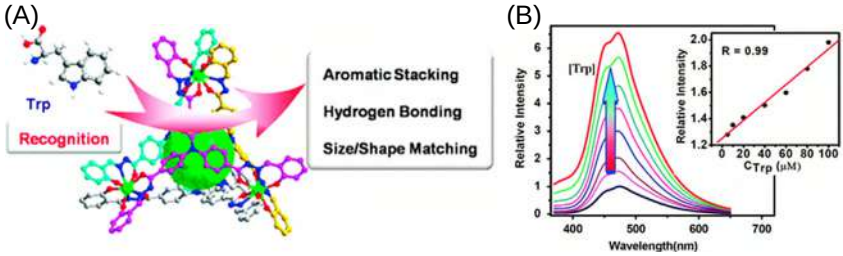

FIGURE 9.6 (A) The fluorescence recognition ability of **SCC-11** toward tryptophan. (B) The fluorescent emission enhancement of **SCC-11** upon the binding of tryptophan (Inset: the change in fluorescence emission of **SCC-11** as a function of tryptophan concentration). (*Reprinted with permission from Ref. [19]. Copyright 2012 Royal Society of Chemistry.*)

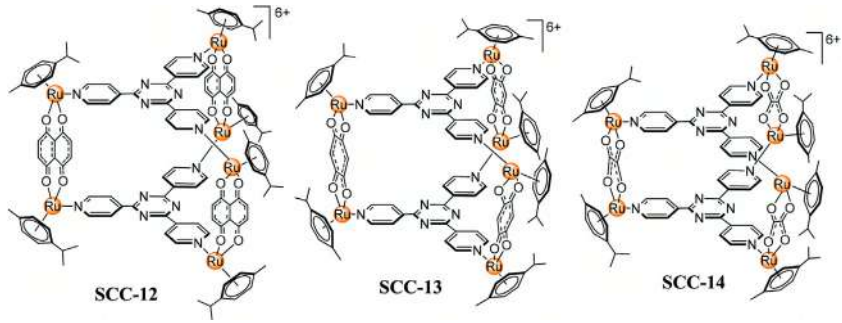

FIGURE 9.7 The structure of hexanuclear trigonal prismatic complexes **SCC-12, SCC-13**, and **SCC-14**. All these prisms were obtained via two-component self-assembly processes. (*Reprinted with permission from Ref. [20]. Copyright 2012 Royal Society of Chemistry.*)

acceptors with different bridging ligand and 2,4,6-tris-(pyridyl-4-yl)-1,3,5-triazine donor (Fig. 9.7) [21]. The unfolding of proteins by **SCCs** resulted from electrostatic interaction arising between the negatively charged surface of the protein and the cationic metalloprisms. Further studies with other proteins showed a similar structural modification in proteins like human serum albumin, transferrin, cytochrome-c, myoglobin, and ubiquitin. The existence of electrostatic interactions between protein and **SCCs** was supported by NMR, MS, and CD experiments. Thus, **SCC-12** to **SCC-14** can selectively target proteins and thus pave the way for designing metallacycles that target proteins that are overexpressed in cancer cells and act as an anticancer drug.

Fujita et al. designed a self-assembled coordinated nanocage (**SCC-15**) comprising Pd(II) ions capable of encapsulating small protein-like ubiquitin [22]. The $M_{12}L_{24}$ nanocage **SCC-15** was obtained by the self-assembly of 12 eq. of Pd(II) ions (M) and 24 eq. of bent ligands (L). Ubiquitin is a small globular protein that can fit into the cavity of the spherical framework and binds through the covalent interaction with the ligands on the interior edges. The ultracentrifugation experiments and the reduction in the diffusion coefficient

of ubiquitin signals observed in DOSY NMR analysis further confirmed the encapsulation of the protein within the coordination sphere, **SCC-15**. Ubiquitin plays an important role in proteasomal degradation, and thus, its encapsulation paves the way for various biological applications. In another study, the same group developed a hydrophobic cavity containing a self-assembled host molecule (**SCC-16**) self-assembled from zinc(II)-tetrakis-(3-pyridyl)porphyrin and [Pd((S, S)-1,2-diaminocyclohexane)$(NO_3)_2$] which can encapsulate short peptides (Fig. 9.8) [23]. The foldings generated in the short peptides due to hydrogen bonding between the carbonyl group of the N-terminal end and the amide N–H bonds lead to helical secondary structures. Thus, the study of short peptide folding inside these hydrophobic host molecules would provide us with a picture of the folding of oligopeptides in the hydrophobic protein pocket in the biological system. NMR and X-ray studies proved the inclusion of short peptides and their conformational changes within the complex cavity (Fig. 9.8).

Stang group designed a 3D supramolecular Pt(II) complex (**SCC-17**) by the hierarchical self-assembly of a positively charged tetraphenylethylene (TPE) with a selective negatively charged rod-shaped Tobacco Mosaic Virus (TMV) (Fig. 9.9) [24]. The biohybrid **SCC-17** was synthesized as a result of electrostatic interactions. The TPE-Pt metallacycle exhibited a sharp absorption band around $\lambda = 334$ nm with $\varepsilon = 1.48 \times 10^5$ per M/cm. The addition of TMV to the metallacycle shifted the absorption peak to $\lambda = 331$ nm with a decrease of $\varepsilon = 1.28 \times 10^5$ per M/cm. The spectral absorption studies confirm that the electrostatic interaction is a driving force for the aggregation of the **SCC-17** and the TMV virus; this was further verified through transmission electron microscopy (TEM) imaging. The free **SCC-17** exhibited a fluorescence emission at $\lambda = 490$ nm and with the addition of TMV, there was no noticeable shift in the emission band observed but only pronounced fluorescence enhancement around the same region of $\lambda = 490$ nm seen. The fluorescent enhancement effect observed on the binding of TMV with **SCC-17** is a result of the nanoconfinement effect and aggregation-induced effect (AIE) generated from the TPE units (Fig. 9.9). The metal–organic hybrid skeletal is reversible since the biohybrid can be disassembled in the presence of TBAB, thereby making it suitable for application in stimuli-responsive drug delivery.

9.2.4 Interaction of SCCs with carbohydrates

Carbohydrates are the most abundant biomolecules in the living system and are extensively studied for potential biomedical applications. This section highlights a few selected examples of SCCs interacting with various carbohydrates biomolecules. Two luminescent active Werner type cerium (Ce)-based tetrahedrons (**SCC-18** and **SCC-19**) were designed for the selective sensing of carbohydrates (Fig. 9.10) [25]. The complexes **SCC-18** and **SCC-19** were obtained from the reaction of salicylaldehyde with 2,6-dicarbohydrazide naphthalene and 1,10-dicarbohydrazide 4,4'-biphenyl, respectively. The tetrahedrons

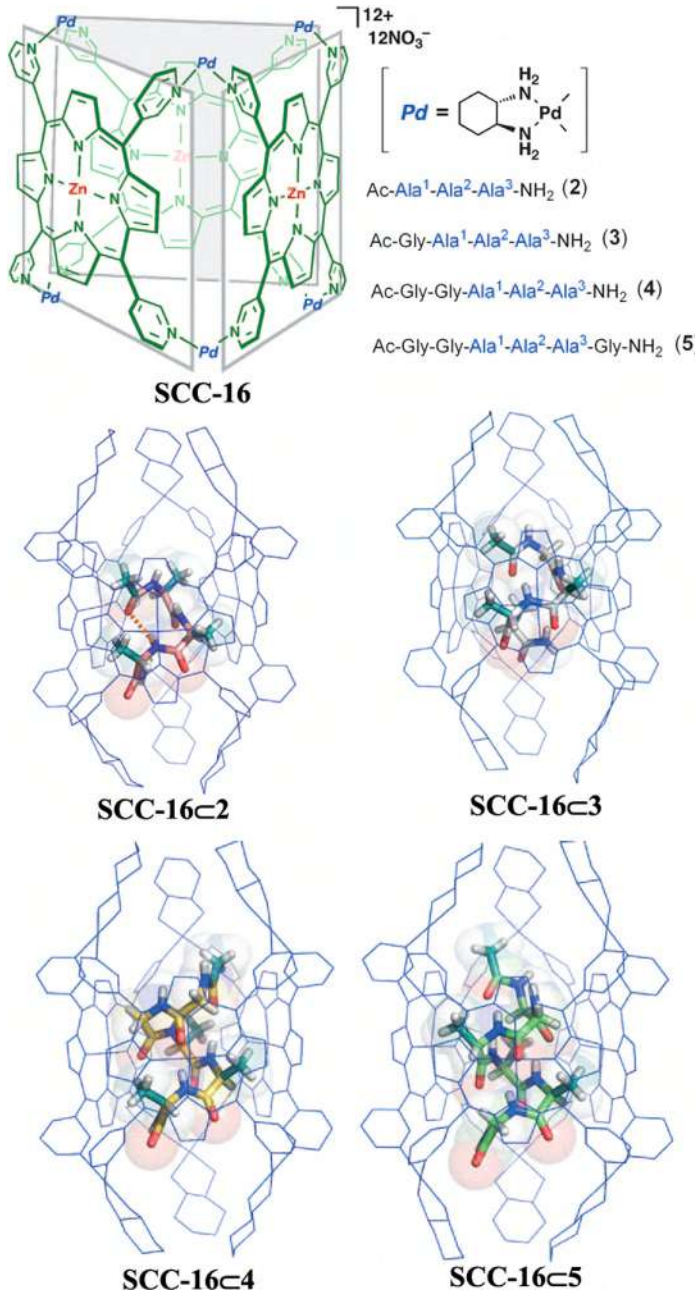

FIGURE 9.8 Self-assembly formation of molecular trigonal prims (**SCC-16**) and the host-guest complexes formation between **SCC-16** and four different short-peptide fragments. The peptide fragments are stabilized within the **SCC-16** cavity through multiple hydrogen-bonding interactions. (*Reprinted with permission from Ref. [22]. Copyright 2009 Willey.*)

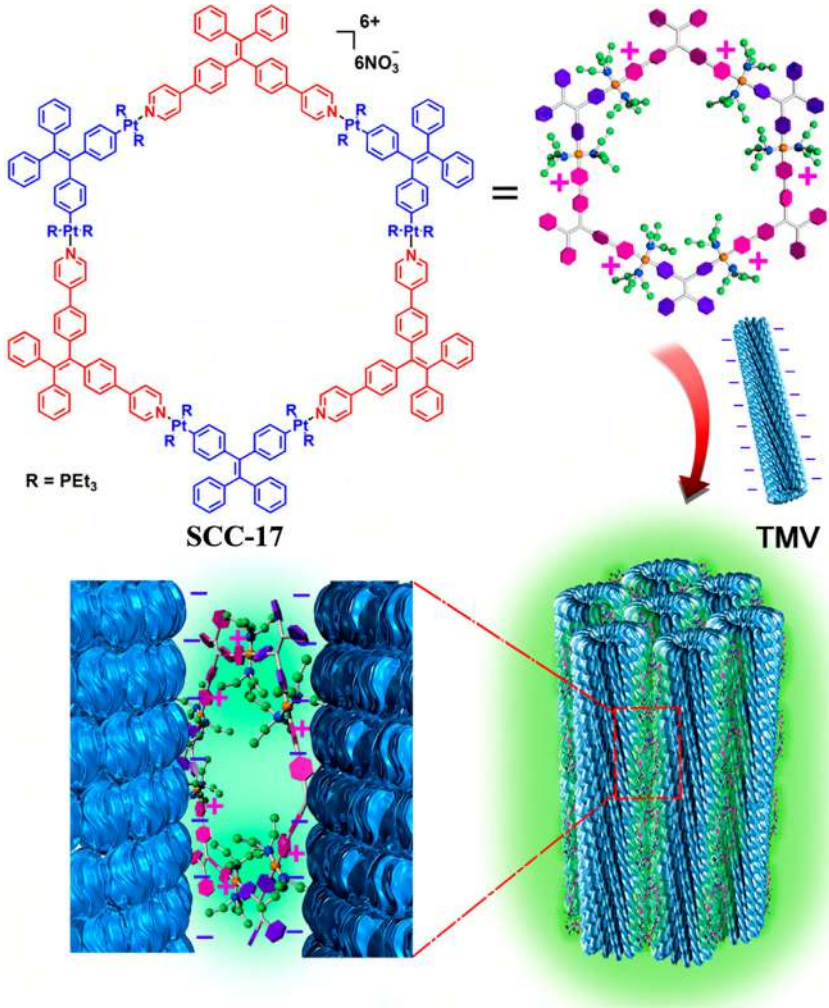

FIGURE 9.9 [3+3] Self-assembly formation of a 2D cationic molecular hexagon (**SCC-17**) and its hierarchical self-assembly with tobacco mosaic virus (TMV) resulting in a biohybrid assembly. (*Reprinted with permission from Ref. [23]. Copyright 2016 American Chemical Society.*)

comprise four metal centers placed at the vertices, and each metal center is coordinated to three tridentate ligands. The tetrahedron, **SCC-18**, exhibited broad emission spectra in the range of $\lambda = 450–600$ nm and an intense band around $\lambda = 525$ nm along with a weak band around $\lambda = 465$ nm which is overlapped with the broadband. Photophysical studies exhibited enhancing fluorescence emission intensity around $\lambda = 525$ nm only selectively for hexoses like glucose and mannose upon their interactions with **SCC-18** (Fig. 9.10).

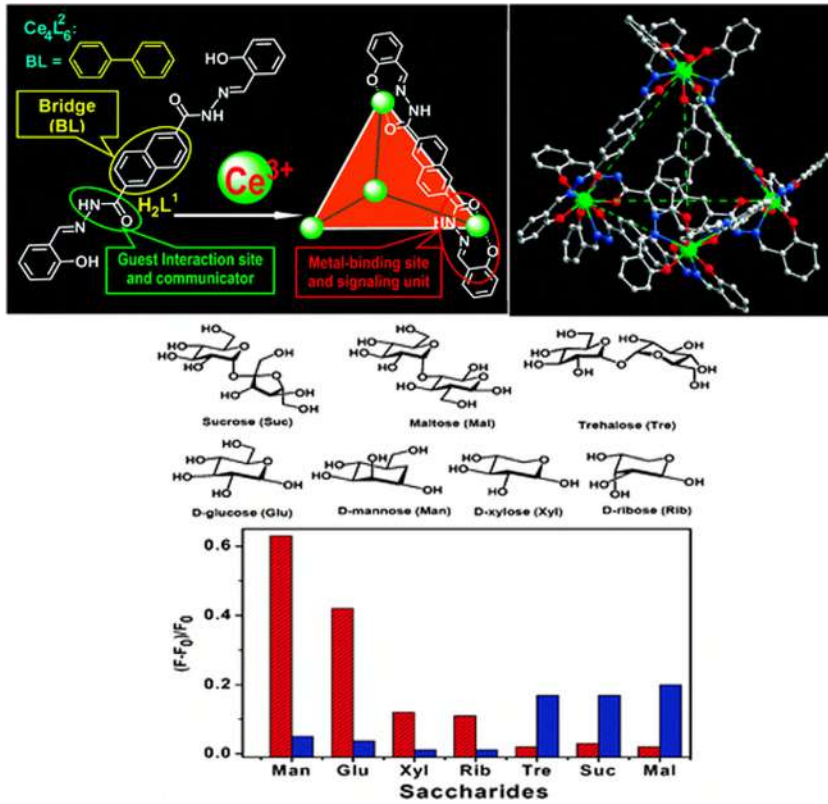

FIGURE 9.10 Self-assembly formation of Ce-based molecular tetrahedron **SCC-18** and **SCC-19** showing large internal cavity (top left) and X-ray crystal structure of **SCC-18** (top right). The fluorescence responses of **SCC-18** (red bars) and **SCC-19** (blue bar) for saccharides sensing. (*Reprinted with permission from Ref. [24]. Copyright 2009 Royal Society of Chemistry.*)

The cavity size of **SCC-19** was found to be comparatively larger than **SCC-18** and was found to exhibit fluorescence enhancement selectively for disaccharides around $\lambda = 480$ nm. The fluorescence enhancement is attributed to the formation of hydrogen bonding between the amide group of ligand and the carbohydrate guest molecule. These results confirm that the size of the internal cavity is crucial for discriminative complexation toward different carbohydrates. The size of the cavity is very important for this selectivity toward carbohydrates.

Yang and coworkers reported the polyanion-induced self-assembly formation of metallacycles for the first time [26]. The hierarchical self-assembled complex formed as a result of aggregation of organo-Pt metallacycle (**SCC-20**) with heparin can be utilized for the selective sensing of heparin. The tetraphenylethylene (TPE) units were introduced into the hexagonal Pt(II) metallacycle **SCC-20** through coordination-driven self-assembly (Fig. 9.11A). The self-assembled macrocycle **SCC-20** possesses a high positive charge. Heparin is a sulfated

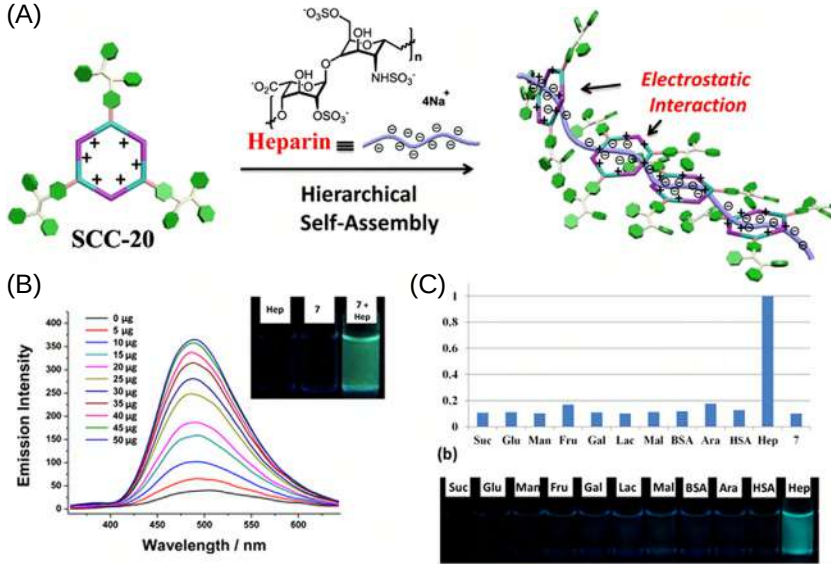

FIGURE 9.11 Hierarchical self-assembly of discrete organoplatinum(II) metallacycle (**SCC-20**) with polysaccharide via electrostatic interactions and their application for turn-on fluorescence sensing of heparin. (*Reprinted with permission from Ref. [25]. Copyright 2015 American Chemical Society.*)

polysaccharide commonly used as an anticoagulant. It contains sulfate and carboxylic groups in the polymeric chain, making highly negatively charged species. Therefore, the electrostatic interaction drives the hierarchical self-assembly of heparin with the hexagonal metallacycle **SCC-20** (Fig. 9.11B). The metallacycle **SCC-20** exhibited fluorescence emission at $\lambda = 486$ nm due to the aggregation-induced effect (AIE) active of the TPE unit. In general, heparin is nonemissive, but a fluorescent enhancement around $\lambda = 486$ nm was observed on adding heparin into the metallacycle. This effect is due to the AIE effect resulting from the aggregation of the TPE units (Fig. 9.11C). The fluorescence enhancement proved the electrostatic interaction between the positively charged **SCC-20** and the negatively charged heparin-induced hierarchical self-assembly by bringing them close. The photophysical studies provided evidence for the hierarchical self-assembly, and it was further identified by SEM, TEM, and LCMS analysis. Heparin detection plays a vital role in anticoagulant therapy and also during surgery since an overdose of heparin may lead to hemorrhages. This turn-on fluorescent probe can be utilized for the quantification of heparin.

9.2.5 Interaction of SCCs with steroids and fatty acids

Steroids and fatty acids act as biomarkers in the living system. Thus, their selective encapsulation within the supramolecular coordination cages can pave the way for detecting and treating several biological disorders. In this context,

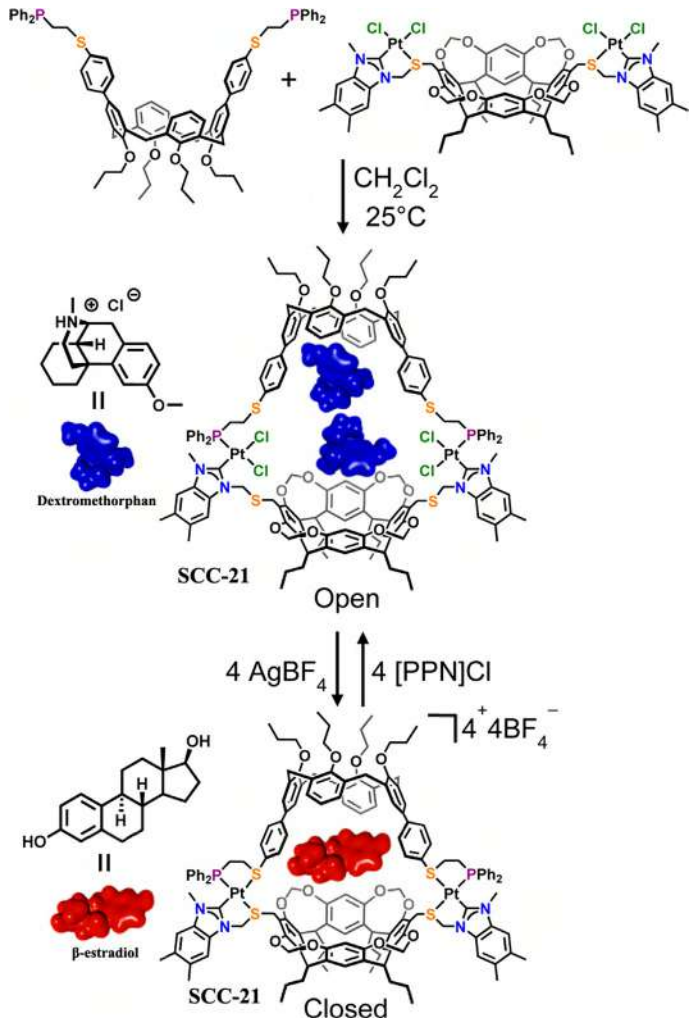

FIGURE 9.12 Self-assembly formation of the open dimeric capsule (**SCC-21**) from two-cavidant-based ligands and allosteric control between open and closed configurations of **SCC-21** that exhibit selectivity for dextromethorphan HCl and β-estradiol, respectively. (*Reprinted with permission from Ref. [26]. Copyright 2017 American Chemical Society.*)

Mirkin et al. synthesized an asymmetric molecular capsule (**SCC-21**) via the weak ligand approach (Fig. 9.12) [27]. The molecular capsule can switch between flexible and rigid architectures by controlling the coordination state of the Pt(II) metal center. The capsule contains two Pt(II) metal centers which are chelated with calyx[4]arene (made up of two phosphine alkyl thioether moieties) and a resorcin[4]arene (two N-heterocyclic carbene alkyl thioether moieties). The chloride ligand attached to the metal center plays a significant

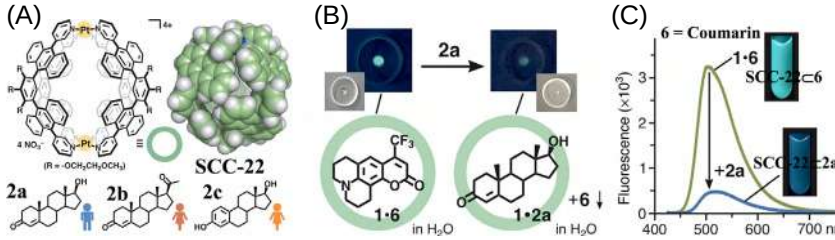

FIGURE 9.13 (A) Polyaromatic receptor **SCC-22** and space-filling representation of the core framework and representative male hormone, testosterone (**2a**); and female hormones, progesterone (**2b**) and β-estradiol (**2c**). (B) Representation of fluorescent detection of male hormone **2a** using an aqueous solution of **SCC-**coumarin and their photograph taken on a Petri dish. (C) Fluorescence emission spectra of **SCC-**coumarin before and after the addition of **2a**. (*Reprinted with permission from Ref. [27]. Copyright 2019 Science.*)

role in modulating the change in the size of the receptor cavity. The neutral receptor containing a Cl-coordinated Pt(II) center possessing a larger cavity size can accommodate dextromethorphan. The host–guest interaction is stabilized by the cation–π interaction between the guest molecule containing the electron-deficient ammonium group and the electron-rich cavity of the molecular receptor **SCC-21**. The abstraction of the chloride ligand from the Pt(II) center by silver reduces the cavity size of the receptor and makes it a rigid architecture. The rigid molecular receptor facilitates the binding of hydrophobic guest molecules like β-estradiol due to the C$-$H/π interactions. The designed supramolecular coordination capsule allows these large bioactive molecules' to form a reversible and selective host–guest complexation.

Yamashina et al. developed a polyaromatic receptor (**SCC-22**) that can bind with androgenic hormones such as progesterone and estrogen (Fig. 9.13A) [28]. The receptor comprises polyaromatic anthracene panels and a semirigid cavity with four bent polyaromatic ligands linked by two Pt(II) ions. The hydrophobic cavity provides multiple CH–π contacts and hydrogen-bonding interactions, resulting in the selective binding of androgenic hormones inside the polyaromatic cavity. The fluorescent detection of the androgenic hormone was performed in the presence of a fluorescent dye, hydrophobic coumarin, which exhibited bluish-green fluorescence around $\lambda = 509$ nm in the presence of the receptor (Fig. 9.13B). The decrease in fluorescent intensity was observed in the presence of the androgenic hormone since it was more hydrophobic and displaced the dye molecule. The displaced dye aggregated into sediments that were found to be nonemissive (Fig. 9.13C). In 2020, Yoshizawa and coworkers developed a polyaromatic receptor (**SCC-23**) for the selective binding of unsaturated fatty acids in water [29]. The Pt(II)-based receptor contains hydrophilic and hydrophobic faces, in which the Pt–nitrogen cavity acts as hydrophilic functionality and polyaromatic act as hydrophobic surfaces. The fatty acids get incorporated into the hydrophobic cavity through induced guest coiling. The selectivity of

the unsaturated fatty acid over the saturated is attributed to the conformational change adopted by the unsaturated fatty acid from a linear to a spiral structure. The encapsulation of the fatty acid into the receptor cavity and its conformational arrangement was promoted by the polar CO_2H group in the fatty acids. The polyaromatic anthracene panels that stabilize the fatty acid inside the cavity through CH–π/π–π interaction also play a significant role in the selectivity of the fatty acids. The receptor showed a higher binding affinity toward the polyunsaturated fatty acid than the monounsaturated fatty acid due to the more efficient π–π stacking interactions.

9.3 Conclusion

The diversity of supramolecular coordination complexes (**SCCs**) provides a fascinating platform for cavity-based applications. The selective guest binding property of the SCCs paves the way for its application in targeted therapy, and the luminescent property can be utilized for biosensing. The host–guest interactions in SCCs are governed mostly by the mode of interaction of the SCCs with analytes and the shape and size of the cavities. The negatively charged species prefer binding to cavities possessing cationic centers since they are stabilized through charge pairing interactions. Similarly, molecules containing multiple N–H or O–H units are stabilized through hydrogen-bonding interactions. Hydrophobic guest molecules fit well into cavities comprising hydrophobic moieties. These interactions are the driving force behind the selective encapsulation of the analytes to the **SCCs**. Thus, **SCCs** are designed with spacers containing prerequisite functional groups and metal centers to facilitate proper molecular interaction for efficient and selective binding of analytes. Hence SCCs prove to be a suitable candidate as selective sensors for biological analytes.

Acknowledgments

We gratefully acknowledge the Science and Engineering Research Board (EMEQ Award EEQ/2018/000799 to S.S.), India, and the Indian Institute of Technology Palakkad (IITPKD) for financial support.

References

[1] R. Chakrabarty, P.S. Mukherjee, P.J. Stang, Supramolecular coordination: self-assembly of finite two- and three-dimensional ensembles, Chem. Rev. 111 (2011) 6810–6918.

[2] J.R. Nitschke, Construction, substitution, and sorting of metallo-organic structures via subcomponent self-assembly, Acc. Chem. Res. 40 (2007) 103–112.

[3] P.J. Stang, From solvolysis to self-assembly, J. Org. Chem. 74 (2009) 2–20.

[4] P.J. Stang, B. Olenyuk, Self-assembly, symmetry, and molecular architecture: coordination as the motif in the rational design of supramolecular metallacyclic polygons and polyhedra, Acc. Chem. Res. 30 (1997) 502–518.

[5] B. Therrien, Arene ruthenium cages: boxes full of surprises, Eur. J. Inorg. Chem. 2009 (2009) 2445–2453.
[6] H.-B. Yang, Metallomacrocycles: From Structures to Applications, Royal Society of Chemistry, UK, 2018.
[7] D.L. Caulder, K.N. Raymond, Supermolecules by design, Acc. Chem. Res. 32 (1999) 975–982.
[8] P.J. Stang, B. Olenyuk, Self-assembly, symmetry, and molecular architecture: coordination as the motif in the rational design of supramolecular metallacyclic polygons and polyhedra, Acc. Chem. Res. 30 (1997) 502–518.
[9] N. Dey, C.J.E. Haynes, Supramolecular coordination complexes as optical biosensors, ChemPlusChem 86 (2021) 418–433.
[10] S. Leininger, B. Olenyuk, P.J. Stang, Self-assembly of discrete cyclic nanostructures mediated by transition metals, Chem. Rev. 100 (2000) 853.
[11] Y. Liu, X. Wu, C. He, R. Zhang, C.A. Duan, A truncated octahedral nanocage for fluorescent detection of nucleoside, Dalton Trans. 43 (2008) 5866–5868.
[12] A.J. Plajer, E.G. Percástegui, M. Santella, F.J. Rizzuto, Q. Gan, B.W. Laursen, J.R. Nitschke, Fluorometric recognition of nucleotides within a water-soluble tetrahedral capsule, Angew. Chem. Int. Ed. 131 (2019) 4244–4248.
[13] N.C. Gianneschi, M.S. Masar, C.A. Mirkin, Development of a coordination chemistry-based approach for functional supramolecular structures, Acc. Chem. Res. 38 (2005) 825–837.
[14] A. Mishra, S. Ravikumar, S.H. Hong, H. Kim, V. Vajpayee, H. Lee, B. Ahn, M. Wang, P.J. Stang, K.W. Chi, DNA binding and unwinding by self-assembled supramolecular heterobimetallacycles, Organometallics 30 (2011) 6343–6346.
[15] A. Zhao, S.E. Howson, C. Zhao, J. Ren, P. Scott, C. Wang, X. Qu, Chiral metallohelices enantioselectively target hybrid human telomeric G-quadruplex DNA, Nucleic. Acids. Res. 45 (2017) 5026–5035.
[16] A. Garci, K.J. Castor, J. Fakhoury, J.L. Do, D.J. Trani, P. Chidchob, R.S. Stein, A.K. Mittermaier, T. Friščić, H. Sleiman, Efficient and rapid mechanochemical assembly of platinum (II) squares for guanine quadruplex targeting, J. Am. Chem. Soc. 139 (2017) 16913–16922.
[17] R. Kramer, J.-M. Lehn, A. Marquis-Rigault, Self-recognition in helicate self-assembly: spontaneous formation of helical metal complexes from mixtures of ligands and metal ions, Proc. Natl. Acad. Sci. 90 (1993) 5394–5398.
[18] P. Thanasekaran, C.-H. Lee, K.-L. Lu, Neutral discrete metal-organic cyclic architectures: opportunities for structural features and properties in confined spaces, Coord. Chem. Rev. 280 (2014) 96–175.
[19] A. Mishra, S. Ravikumar, Y.H. Song, N.S. Prabhu, H. Kim, S.H. Hong, S. Cheon, J. Noh, K.W. Chi, A new arene–Ru based supramolecular coordination complex for efficient binding and selective sensing of green fluorescent protein, Dalton Trans. 43 (2014) 6032–6040.
[20] C. He, J. Wang, P. Wu, L. Jia, Y. Bai, Z. Zhang, C. Duan, Fluorescent differentiation and quantificational detection of free tryptophan in serum within a confined metal-organic tetrahedron, Chem. Commun. 48 (2012) 11880–11882.
[21] L.E. Paul, B. Therrien, J. Furrer, Interactions of arene ruthenium metallaprisms with human proteins, Org. Biomol. Chem. 13 (2015) 946–953.
[22] D. Fujita, K. Suzuki, S. Sato, M. Yagi-Utsumi, Y. Yamaguchi, N. Mizuno, T. Kumasaka, M. Takata, M. Noda, S. Uchiyama, K. Kato, Protein encapsulation within synthetic molecular hosts, Nat. Commun. 3 (2012) 1–7.

[23] Y. Hatakeyama, T. Sawada, M. Kawano, M. Fujita, Conformational preferences of short peptide fragments, Angew. Chem. Int. Ed. 121 (2009) 8851–8854.
[24] Y. Tian, X. Yan, M.L. Saha, Z. Niu, P.J. Stang, Hierarchical self-assembly of responsive organoplatinum (II) metallacycle–TMV complexes with turn-on fluorescence, J. Am. Chem. Soc. 138 (2016) 12033–12036.
[25] Y. Liu, X. Wu, C. He, Y. Jiao, C. Duan, Self-assembly of cerium-based metal-organic tetrahedrons for size-selectively luminescent sensing natural saccharides, Chem. Commun. 48 (2009) 7554–7556.
[26] L.J. Chen, Y.Y. Ren, N.W. Wu, B. Sun, J.Q. Ma, L. Zhang, H. Tan, M. Liu, X. Li, H.B. Yang, Hierarchical self-assembly of discrete organoplatinum (II) metallacycles with polysaccharides via electrostatic interactions and their application for heparin detection, J. Am. Chem. Soc. 137 (2015) 11725–11735.
[27] J. Mendez-Arroyo, A.I. d'Aquino, A.B. Chinen, Y.D. Manraj, C.A. Mirkin, Reversible and selective encapsulation of dextromethorphan and β-estradiol using an asymmetric molecular capsule assembled via the weak-link approach, J. Am. Chem. Soc. 139 (2017) 1368–1371.
[28] M. Yamashina, T. Tsutsui, Y. Sei, M. Akita, M.A. Yoshizawa, A polyaromatic receptor with high androgen affinity, Sci. Adv. 5 (2019) 3179.
[29] K. Niki, T. Tsutsui, M. Yamashina, M. Akita, M. Yoshizawa, Recognition, and stabilization of unsaturated fatty acids by a polyaromatic receptor, Angew. Chem. Int. Ed. 132 (2020) 10575–10578.

Chapter 10

Hierarchical molecular self-assemblies of coordination complexes

Krishnan Kartha Kalathil and Gustavo Fernández
Organisch Chemisches Institut, Universität Münster, Corrensstraße 36, 48149 Münster, Germany

10.1 Introduction

Molecular self-assembly is the spontaneous organization of molecules into nanoarchitectures of different size and shape through a number of noncovalent interactions including H-bonding, electrostatic interactions, dipole–dipole attraction, $\pi-\pi$ stacking, van der Waals forces, and solvophobic effects [1–3]. Self-assembly processes that involve a single aggregation step are well documented [4,5], whereas more intricate multistep self-assembly processes are still in its infancy stage. Most recently, hierarchical molecular self-assembly of discrete systems has emerged as a promising area to construct structurally complex architectures with distinct properties [6,7]. Typically, hierarchical molecular self-assembly can be a process that involves a single aggregation step that evolves into higher-order structures through multiple intermediate stages in a stepwise manner [8]. In other cases, more than one component participates in different stages of the hierarchical process to induce the formation of higher-order structures [9].

Supramolecular coordination complexes are often referred to as discrete systems containing organic ligands coordinated to a metal center [10]. Over the past few decades, a plethora of coordination complexes based on transition metals have been extensively studied [11]. Notably, these systems have drawn attention due to its importance in developing functional materials with tunable properties and wide-ranging applications in materials science and biology [12]. Incorporation of functional groups to induce the additional supramolecular interactions opened a new strategy to construct well-defined structures through hierarchical self-assembly processes with intriguing properties [13]. Notably, noncovalent interactions such as metal–metal interactions, $\pi-\pi$ stacking, H-bonding, host–guest and hydrophobic effects are the secondary driving force

Supramolecular Coordination Complexes: Design, Synthesis, and Applications.
DOI: https://doi.org/10.1016/B978-0-323-90582-4.00001-4

that has been used to induce hierarchical self-assembly of coordination complexes in solution [14]. Typically, introduction of more than one noncovalent interaction can also induce cooperative effects in the self-assembly processes if no significant steric effects occur [15]. Therefore, an orthogonal substitution of these noncovalent interactions is a prerequisite for hierarchical organization to form superstructures in solution. In this article, we attempt to review the advancement of the design of discrete coordination complexes focusing on their hierarchical self-assembly processes in solution.

10.2 Hierarchical self-assembly of metal complexes containing π-systems

Metal–metal interactions have become relevant in recent years due to their importance in the field of material chemistry [16,17]. Inclusion of aromatic π-conjugated systems as a ligand in metal complexes can induce additional π–π stacking interactions during the self-assembly . Normally, these interactions (metal–metal and π–π stacking) operate cooperatively and consequently metal complexes bearing π-conjugated systems as ligands have shown high cooperativity during self-assembly in solution. Notably, in many cases, solubilizing chains are also included in the design as this enables fabrication of self-assembled materials in solution. These chains can also provide additional van der Waals interactions, which can lead to a hierarchical organization to form highly ordered structures.

Our group demonstrated the cooperative supramolecular polymerization process—initiated with a nucleation followed by an elongation—of an oligophenyleneethynylene (OPE)-based bispyridyldichlorido Pd(II) complex bearing long alkyl chains (-$C_{12}H_{25}$, **1**, see Fig. 10.1A) in solution [18]. Cooling of a solution of **1** in in methylcyclohexane (MCH) from 313 K to 278 K resulted in the formation of fibrillar assemblies through π–π and interactions involving the Cl-Pd(II)-Cl metal fragment. No evidence of orthogonal self-assembly to form hierarchical superstructures via alkyl chain interdigitation was present in **1**, mostly due to the strong tendency of this complex to grow in a preferred direction. Subsequently, analogous Pt(II) complexes bearing OPE units were also investigated to probe the influence of the metal type on the self-assembly processes in solution [19]. In addition to the formation of one dimensional fibrous assemblies in nonpolar solvents like MCH, the analogous Pt(II) complex (**2**, Fig. 10.1A) showed a reversible sol-gel transition through multiple intermolecular interactions (π–π, Cl···H, Pt···π) with notable absence of Pt···Pt interactions. Importantly, shortening the peripheral alkyl chain length from C_{12} to C_2 resulted in the formation of crystalline assemblies with shorter Pt···Pt contacts (4.4 Å), indicating the contribution of the peripheral alkyl chains on the hierarchical self-assembly process of these systems. Upon mixing the structurally related π-conjugated Pd(II) and Pt(II) complexes (**1** and **2**, respectively) in nonpolar solutions, a narcissistic self-assembly into fibers for **1** and

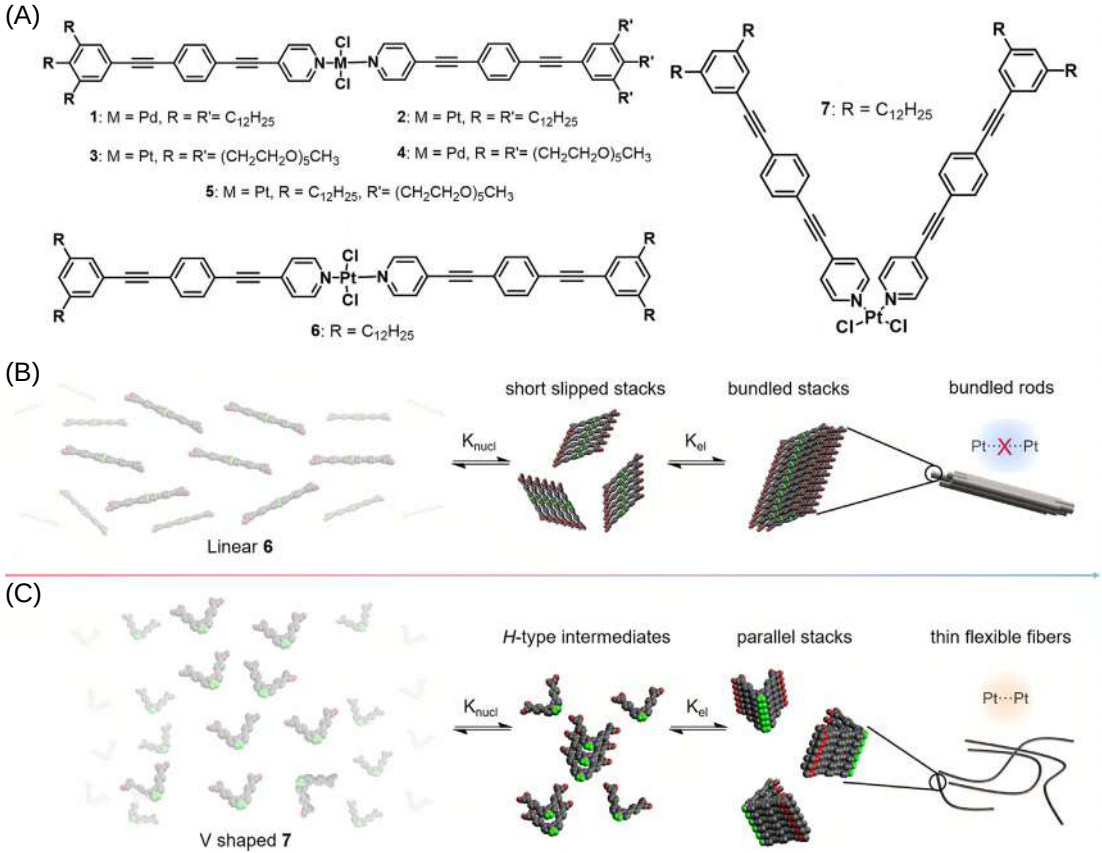

FIGURE 10.1 (A) Chemical structures of Pt(II) complexes **1–7** and cartoon representation of the hierarchical self-assembly process of **6** (B) and **7** (C) in solution leading to the formation of higher order nanostructures. Fig. 10.1B and 10.1C reproduced from Ref. 20 with permission from the Royal Society of Chemistry.

nanodisks for **2** was observed if any of the components is in excess [20]. On the other hand, social self-sorting dictated by **1** was observed upon monitoring the co-assembly process of an equimolar mixture of **1** and **2** in solution. In these co-assemblies, the molecules of **1** and **2** are randomly distributed along the fibers, therefore yielding statistical supramolecular co-polymers. In a different work, triethylene glycol (TEG) chains were introduced on the periphery of the OPE-based Pt(II) complex (**3**, Fig. 10.1A), enabling aggregation in polar solvents such as alcohols and aqueous mixtures mainly driven by solvophobic interactions [21]. Self-assembly process of **3** was driven by π–π and weak CH···X (X=O, Cl) hydrogen-bonding interactions resulting in long flexible nanofibers. The analogous Pd(II) complex (**4**, Fig. 10.1A) showed a similar aggregation behaviour in solution with CH···O, CH···Cl and π-stacking interactions [22]. This complex self-assembles into thin fibrous structures in alcohols with a stable gelation tendency. Systematic increase in the hydrophilic side-chain length on the OPE-based Pt(II) complex allowed the authors to control the molecular packing in the crystalline state [23]. In a different approach, our group has also reported the effect of unsymmetrical substitution of alkyl/glycol chains on the hierarchical self-assembly processes of Pt(II) complexes (**5**, Fig. 10.1A) with detailed mechanistic insights on the molecular packing [24]. This amphiphilic Pt(II) complex self-assembles in MCH into two different nanoscale morphologies, namely discs and fibers, with distinct molecular arrangement. The effect of coordination geometry on the hierarchical self-assembly process has been investigated [25] by comparing the step-wise aggregation behavior of Pt(II) complexes based on either monodentate bis-pyridine ligands (**6**) or a bidentate bipyridine ligand leading to a V-shaped Pt(II) complex (**7** Fig. 10.1A). Similar to the many other Pt(II) complexes, **6** followed a single cooperative step—nucleation and elongation—into bundled rods, whereas Pt(II) complex **7** with V-shaped geometry self-assembles in a two-step cooperative process into thin fibers in solution. Detailed spectroscopic and morphological studies of these complexes in solution revealed that the formation of short Pt···Pt interactions is hindered due to the out-of-plane arrangement of the Cl ligands at the Pt(II) center for **6** leading to the formation of short slipped stacks with an offset, which further bundle into rods as shown in Fig. 10.1B. On the other hand, V shaped geometry of **7** favors the formation of short Pt···Pt contacts, which transformed into a 1D parallel stacking to form thin and flexible fibers (Fig. 10.1C). Upon reducing the aromatic surface of these metal complexes, V-shaped (bidentate) Pt(II) complex showed a hierarchical growth into 2D plates, whereas the corresponding linear shaped Pt(II) complex self-assembled into bundled fibers with poor colloidal stability resulting in precipitation in solution [26].

Yang and co-workers have reported a multitude of discrete metallacycles, which can hierarchically self-assemble into highly ordered nanostructures through π–π stacking, CH–π interactions and hydrogen bonds [27]. Metal complexation of dipyridine donors (**D1**) with suitable functions and di-Pt(II)

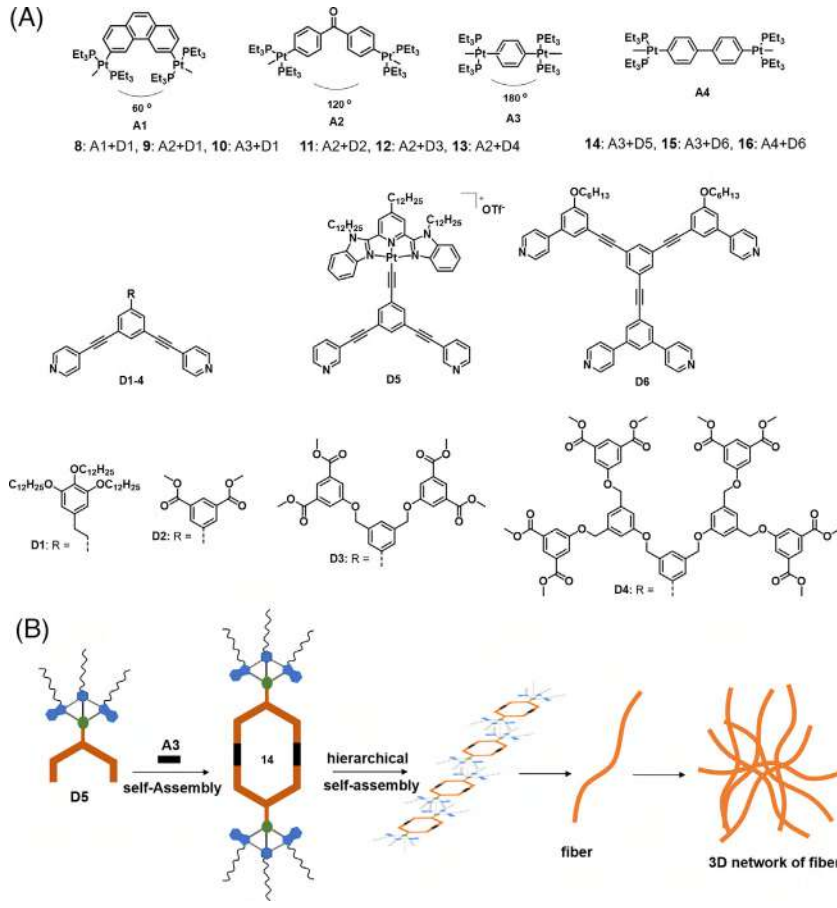

FIGURE 10.2 (A) Chemical structures of dipyridine (**D**) and di-Pt(II) (**A**) segments, which were used to synthesize complexes **8–16** and (B) a scheme showing the hierarchical self-assembly process of **14** in solution to form 3D network of fibers and gels.

acceptors (**A1–3**) with different binding angles were elegantly used to create metallacycles with various geometries (see Fig. 10.2A). These metallacycles (**8**–**10**) decorated with long alkyl chains hierarchically evolved into ordered nanostructures through multiple noncovalent interactions [28]. Notably, small nanospheres derived from a rhomboidal metallacycle could change to long fibers upon changing the experimental conditions. A series of hexagonal Pt(II) based metallacycles (**11**–**13**) were also prepared through coordination driven self-assembly of **D2–4** with **A2** (Fig. 10.2A), which further self-assembled into monodisperse vesicle-like structures mainly driven by multiple intermolecular interactions induced by the peripheral (Fréchet) dendritic structures [29]. These self-assembled metallacycles have been further used for encapsulation and

controlled release of small molecules, by exploiting the vesicle-like nanostructures in solution. By introducing alkynylplatinum(ll) 2,6-bis-(benzimidazole-2′-yl)-pyridine (bzimpy) moiety on discrete supramolecular Pt(II) [30,31] metallacages, additional intermolecular metal–metal and $\pi-\pi$ stacking interactions could be induced. In this way, an alkynylplatinum(II) bzimpy functionalized supramolecular metallacycle (**14**) self-assembled hierarchically into a three-dimensional (3D) network leading to the formation of a gel. This functionalized metallacycle was prepared by mixing the donor ligand (**D5**, Fig. 10.2A) and metal acceptor (**A3,** Fig. 10.2A) under suitable experimental conditions that favors the metal coordination. This metallacycle **14** showed a strong tendency to undergo Pt···Pt and $\pi-\pi$ stacking interactions, which eventually led to a hierarchical self-assembly process to form fibers and networks of fibers in a step-wise manner as shown in Fig. 10.2B. Scanning electron microscopy (SEM) images revealed a 3D network of fibrous structures in the xerogel state. A stable supramolecular metallogel formation of **14** in a mixture of cyclohexane and dichloromethane was monitored as these cross-linked fibrous networks can immobilize the solvent. Hierarchical self-assembly of discrete 2D macrocycles (**15–16**) based on Pt(II) acceptors (**A**3 and **A**4, Fig. 10.2A) with a novel ligand **D6** (Fig. 10.2A) into entangled fibrous networks with gelation in solution have also been demonstrated [32]. It is assumed that the fiber formation in solution might be driven by a combination of intermolecular interactions, such as $\pi-\pi$ stacking and hydrophobic interactions of the ligand appended to the metallacycles.

De Cola and co-workers reported a neutral Pt(II) complex (**17**, Fig. 10.3A) with a dianionic tridentate (N^N^N) ligand showing high tendency of aggregation and gelation [33]. Injection of monomeric solution of this Pt(II) complex in $CHCl_3$ to an excess of *n*-hexane resulted in self-assembled entangled networks of fibers with turn-on of the emission. Insertion of a polar ethylene glycol chain on the ancillary pyridine ligand enabled the aggregation and gelation of this complex in moderately polar solvents like DCM with the formation of bundles of fibers with micrometer length and 50–100 nm width [34]. More importantly, control over morphology [35] and length [36] of nanostructures of amphiphilic Pt(II) complexes (**18–21,** Fig. 10.3A) bearing different glycol chain lengths were demonstrated in solution. Spontaneous self-assembly of a neutral Pt(II) complex (**22**, Fig. 10.3A) in solution via Pt···Pt and $\pi-\pi$ interactions resulted in bright polarized-light emitting fibrous nanostructures comprised of thin nanofibrils [37]. Typically, monomers of these complexes in solution in the presence of an additional poor solvent or at low temperature self-assemble into aggregates through metal–metal and $\pi-\pi$ stacking interactions, leading to the formation of fibers (Fig. 10.3B). Many of these self-assembled nanostructures derived from the analogous square-planar Pt(II) complexes have been exploited for different applications [38,39]. Che and co-workers demonstrated the self-assembly processes of cationic Pd(II) (**23–25**) and Pt(II) (**26–28**) isocyanide complexes (Fig. 10.3C), where a kinetically trapped aggregate evolved into another aggregate over time [40]. Such a dynamic self-assembly process highly

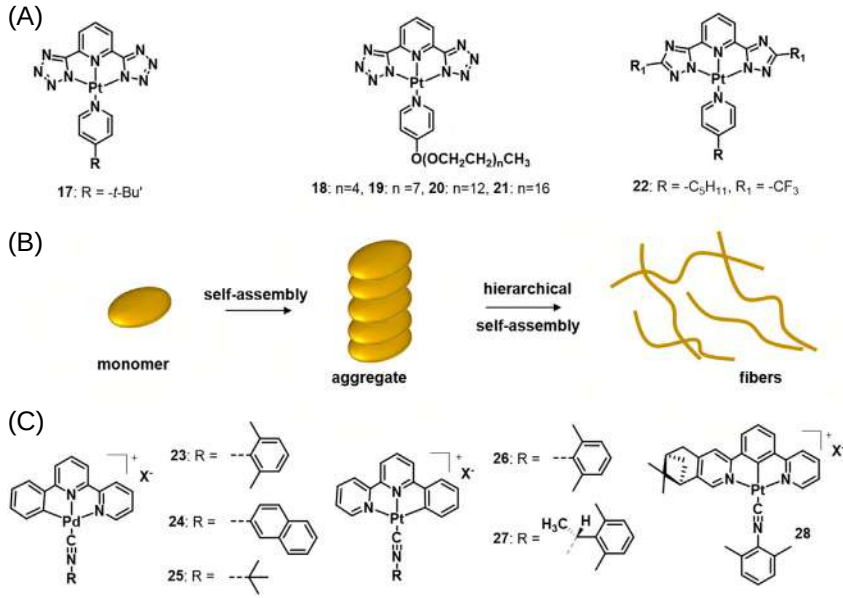

FIGURE 10.3 (A) Chemical structures of Pt(II) complexes **17–22** bearing tridentate ligands, (B) a scheme showing hierarchical self-assembly process of metal complex **17** leading to the formation of fibers in solution, and (C) chemical structures of cationic Pd(II)- (**23–25**) and Pt(II)- (**26–28**) isocyanide complexes.

depends on the counteranion and corresponding cation–anion electrostatic interactions. Analogous Pt(II) complexes containing chiral centers were used to fabricate chiral nanostructures with distinct supramolecular chirality, with a counteranion and solvent tunable self-assembly pathways, similar to the other complexes [41].

Metal complexes based on Pt(II) containing tridentate N^N^N ligands are known for their excellent spectroscopic and luminescent properties. Consequently, considerable efforts have been devoted to the fabrication of self-assemblies and gels through Pt$\cdots$Pt and $\pi-\pi$ interactions for a series of Pt(II) complexes [42–44]. Yam and co-workers reported dinuclear alkynylplatinum(II) terpyridine complexes (**29–31**, Fig. 10.4A) bridged by glycol chain appended binaphthol, where formation of single turn helices stabilized with intramolecular Pt$\cdots$Pt interaction has been observed, which in turn undergo further aggregation into hierarchical helices of helices in aqueous solution [45]. Later, a series of dinuclear platinum(II) complexes (**32–34**, Fig. 10.4A) with phenyleneethynylene (PE) repeating units that can engage in intra- or intermolecular metal−metal interactions depending on the PE chain length have been demonstrated by the same authors [46]. The self-assembly process of the molecule with shorter chain (**32**) proceeded via intermolecular Pt$\cdots$Pt and $\pi-\pi$ interactions to form one dimensional (1D) ribbon-like structures (Fig. 10.4B). Increasing the chain length

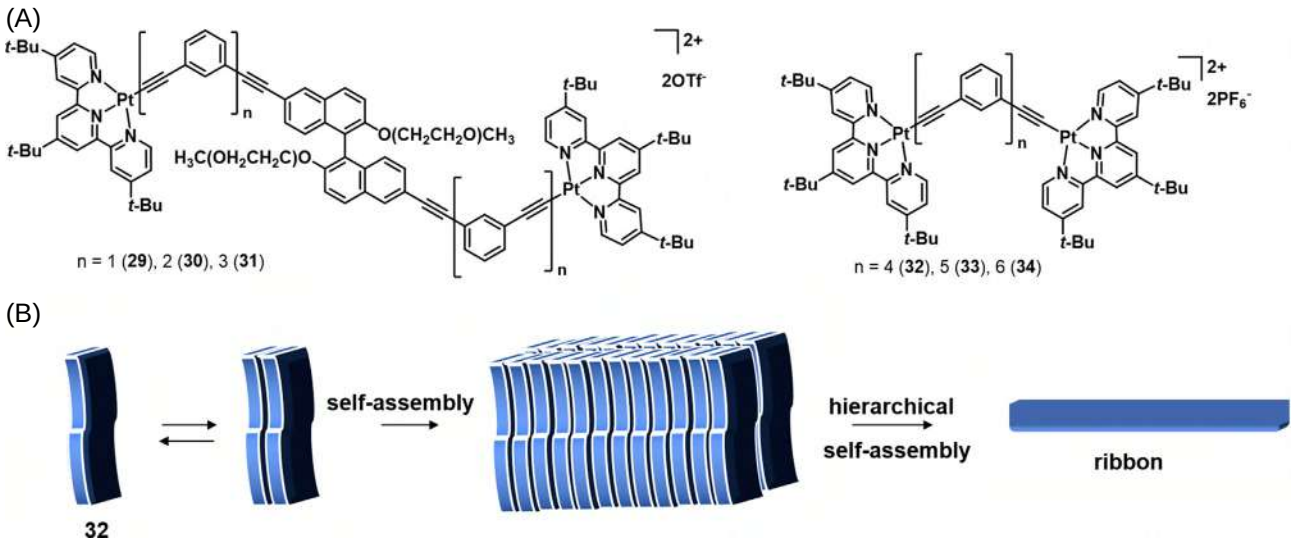

FIGURE 10.4 (A) Chemical structure of dinuclear platinum(II) complexes **29–34** and (B) cartoon representation of self-assembly process of **32** in solution leading to the formation of ribbons.

(**33**) resulted into the formation of a folded helix through intramolecular Pt···Pt and $\pi-\pi$ interactions, which further participate in intermolecular interactions hierarchically to form network of fibers and gels in solution. Further increasing the chain length (**34**) detrimentally affected the stability of the helices and therefore resulted in loosely formed nanofibers with no gel formation.

10.3 Effect of hydrogen bonding on the self-assembly of metal complexes in solution

Hydrogen bonding has been extensively used as an additional noncovalent interaction to induce the hierarchical organization of supramolecular metal complexes with complex self-assembly pathways. Stang and co-workers introduced a quadruple hydrogen bonding motif, 2-ureido-4-pyrimidinone (UPy) onto the dipyridine ligands (**D8** and **D9**, Fig. 10.5A) and synthesized Pt(II) metallacycles **35–37** by treating these donors with different di-Pt(II) segments (Fig. 10.5A). These metallacycles **35–37** facilitated a hierarchical self-assembly process mainly driven by hydrogen bonding interactions of UPy [47]. Upon changing the supramolecular coordination complex geometry from rhomboidal to hexagonal the authors were able to produce linear cross-linked self-assembled structures, respectively. Later, nanofibers with widths of 6.0−50 nm and lengths of several micrometers were fabricated in solution through amide hydrogen bonding of rhomboidal metallodendrimers bearing pendant UPy groups [48]. A hexagonal metallacycle with bisamide groups (**38**) showed hierarchical self-assembly behavior in solution to form highly ordered fibrous networks in solution and stable metallogels [49]. Cholesterol-containing rhomboidal metallacycles with rigid carbonate (**39**) and amide (**40**) linkers were prepared by treating **A1** with **D10** and **D11** (see Fig. 10.5A for the chemical structures), respectively. It was found that these molecules **39** and **40** undergo hierarchical self-assembly in solution through van der Waals forces and hydrogen bonding to form helical bundles and tadpole shaped structures, respectively [50].Upon self-assembly in solution, **39** and **40** initially turned into 1D helical fibers and bilayer structures, leading to the formation of helical bundles and hollow spheres respectively (Fig. 10.5B). The major driving force for the formation of these distinct nanostructures was the length and flexibility of the linking group of the cholesterol units. The preparation of these cholesterol-based metallacycles from corresponding ligand donors and acceptors and their hierarchical processes are shown graphically in Fig. 10.5B. The authors have also reported that the evolution of these hierarchical self-assembly process could be controlled by varying the solvent polarity. Li, Zhang and co-workers constructed supramolecular self-assemblies and gels from dichloro Pd(II) and Pt(II) complexes (**41–42**, Fig. 10.5C) with amide-containing pyridyne ligands through cooperative metal–metal and amide hydrogen bonding interactions [51]. The influence of amide hydrogen bonding on the hierarchical organization of these metal complexes (**43–44**, Fig. 10.5C) was further demonstrated by replacing the amide with an

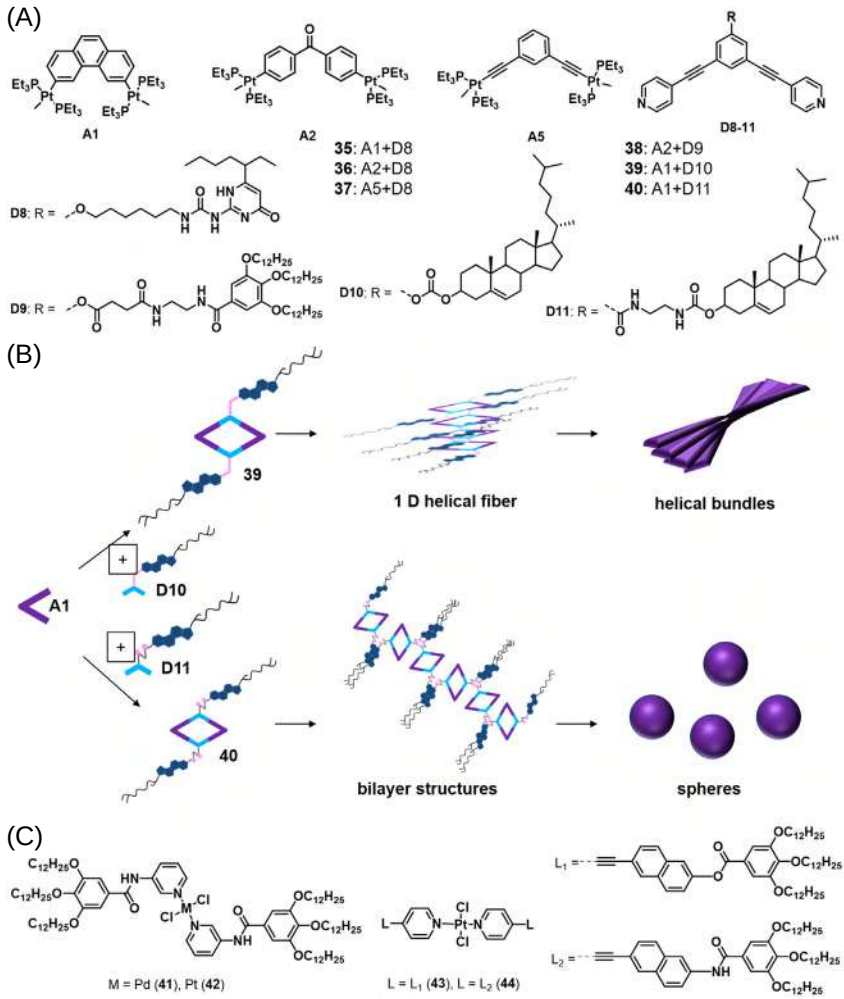

FIGURE 10.5 (A) Chemical structures of dipyridine (**D**) and di-Pt(II) (**A**) segments, which were used to synthesize complexes **35–40**, (B) schematic representation of hierarchical self-assembly processes of **39** and **40** leading to the formation of different nanoarchitectures, and (C) chemical structures of **41–44**.

ester linkage, where the latter packs into slipped stacks to form bundles of fibers and gels in cyclohexane [52].

Self-assembly of Pt(II) acetylide complexes has been extensively studied by Wang and co-workers mainly focusing on the metal complexes bearing amide groups that self-assemble into 1D supramolecular polymers in solution. Upon inclusion of amide hydrogen bonding units with peripheral achiral or chiral chains (**45–46**, Fig. 10.6A) these rod-like monomeric units self-assemble into

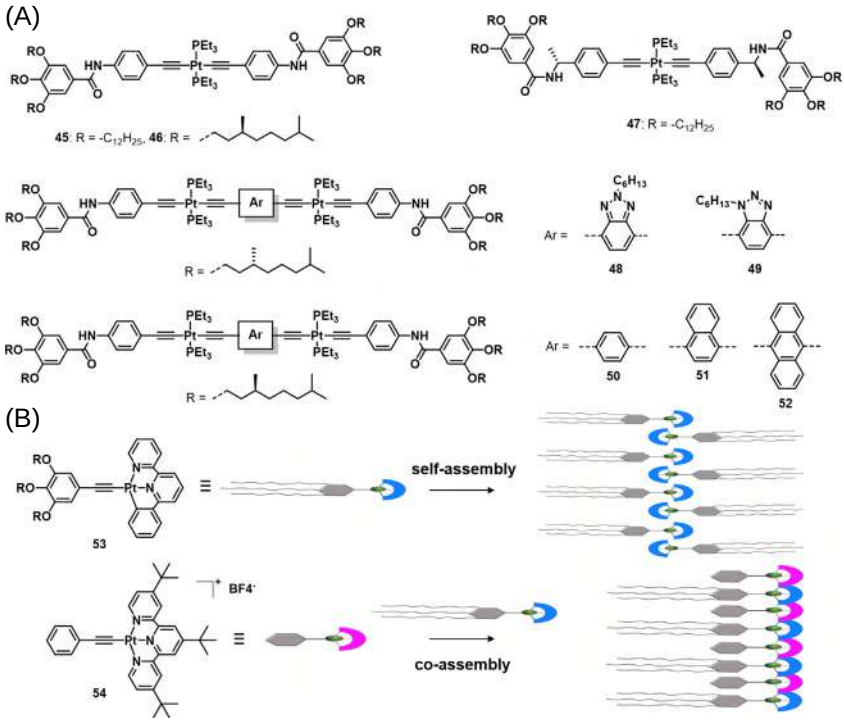

FIGURE 10.6 (A) Chemical structures of Pt(II) acetylide complexes **45–52** and (B) chemical structures of **53**–**54** with cartoon representation of self-assembly of **53** and co-assembly processes of **53**+**54** .

nonhelical or helical fibril structures, which bundle hierarchically into entangled networks to form gels [53]. This macroscopic morphologies and gelation capabilities of these Pt(II) acetylide complexes were tuned by modifying the steric hindrance on the metal center [54]. Less bulky PMe_3 substitution leads to the formation of nanofibers and gels, whereas PBu_3 substitution resulted in no aggregation in solution. Replacement of the N-phenylbenzamide linkages on these Pt(II) acetylide complexes with N-[(1S)-1-phenylethyl]benzamide linkages (**47**, Fig. 10.6A) resulted in intertwined nanofibers comprised of single-handed supramolecular polymers with gel formation [55]. 3D networks of fibers derived from 1D supramolecular polymers of Pt(II) acetylide complexes with different N-hexyl substitution positions on the benzotriazole core (**48–49**, Fig. 10.6A) were also reported [56]. Both derivatives exhibited a hierarchical self-assembly and gelation behavior in nonpolar solvents, however with a difference in the molecular packing. Systematic investigations on the effects of solvent and structural variation (**50–52**, Fig. 10.6A) on the self-assembly behavior of Pt(II) acetylide have been demonstrated by Wang and co-workers [57].

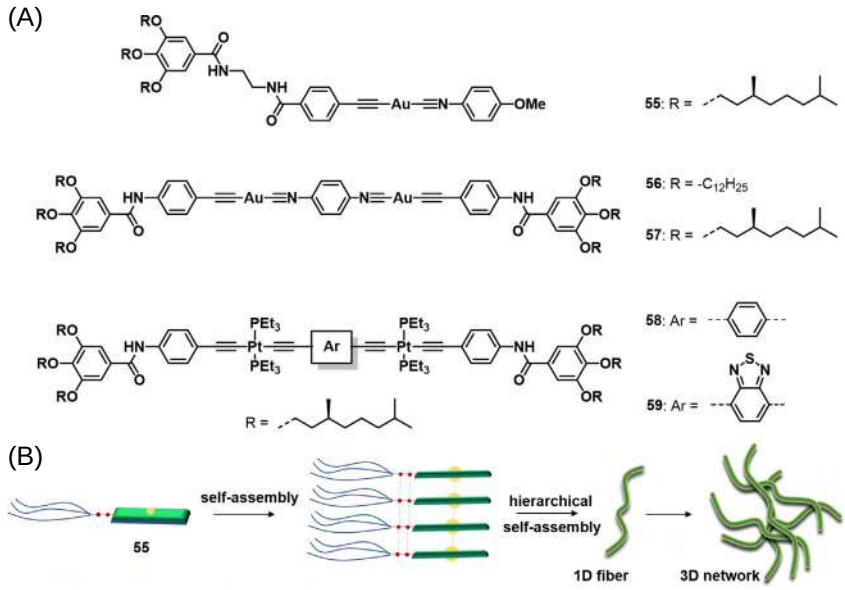

FIGURE 10.7 (A) Chemical structures of Au(I) **55–57** and Pt(II) **58–59** acetylide complexes and (B) cartoon representation of the formation of 3D networks from monomeric **55** through hierarchical self-assembly processes.

Higher-order acenes (anthracene in this case) bearing Pt(II) complexes showed a tendency to form 3D networks comprised of self-assembled nanofibers with a gel formation in linear alkanes (like *n*-decane). Hierarchically self-assembled nanofibers constructed from a fluorescent platinum acetylide has been used as an optical waveguiding material with high performance [58]. Apart from these one-component self-assembly processes, Wang and co-workers have also developed a two-component strategy, where two different Pt(II) complexes (**53–54**, Fig. 10.6B) were employed to fabricate higher-order structures and gels [59]. Typically, these square-planar d^8 Pt(II) complexes (**53** and **54**) are prone to form 1D assemblies through metal–metal and $\pi-\pi$ stacking interactions and due to the similarity of π-surfaces, co-assembly between geometrically similar complexes can facilitate co-assembly as shown in Fig. 10.6B, especially through additional donor–acceptor interactions.

Self-assembled fibers and gel formation through intermolecular Au···Au, $\pi-\pi$ stacking and H-bonding interactions of a rod-coil alkynyl–gold(I)–isocyanide monomer (**55**, Fig. 10.7A) with peripheral alkyl chains and two amide units were also demonstrated [60]. The lower steric hindrance due to the linear coordination geometry of Au(I) in combination with acetylide isocyanide units and amide hydrogen units allowed the complex **55** to self-assemble in a 1D fashion to form fibers in solution (Fig. 10.7B). As observed in many other cases, interlinking of fibers to form 3D networks and gels were also observed

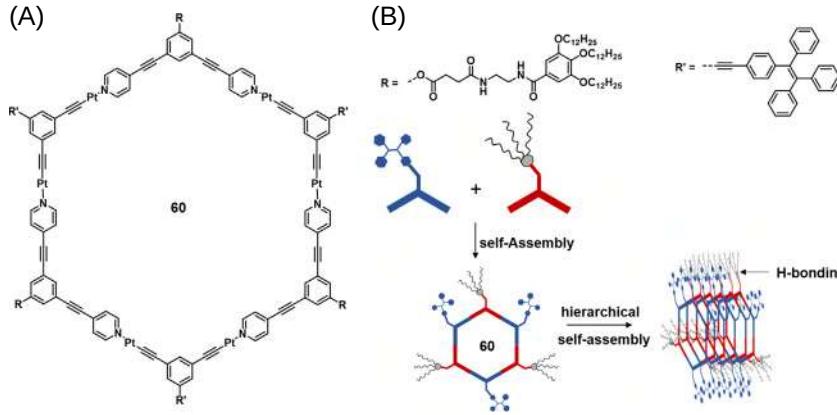

FIGURE 10.8 (A) Chemical structure of the hexagonal metallacycle **60** and (B) schematic representation of self-assembly processes of **60**.

for **55** in nonpolar solvents. A stronger aggregation tendency was shown by alkynyl-gold(I) complexes (**56–57**, Fig. 10.7A) when compared to analogous organoplatinum(II)-based systems (**58–59**, Fig. 10.7A) due to the lower steric hindrance of Au(I) over Pt(II) [61]. Chiral self-assembled interconnected fibers with well-defined helicity were fabricated from enantiomerically pure Pt(II) complexes through amide hydrogen bonding and Pt···Pt interactions [62]. Yam and co-workers reported Pt(II) terpyridyl complexes with l-valine-modified alkynyl ligands, which form networks of fibers and gels in solution through hydrogen bonding, Pt···Pt and $\pi-\pi$ stacking interactions [63]. A hexagonal metallacycle **60** with tetraphenylethylene, amide groups and hydrophobic long alkyl chains (Fig. 10.8A) was used to construct fluorescent organogels through hierarchical self-assembly in acetone/water [64]. Initial coordination-driven self-assembly of pyridine donor and acceptor resulted in the formation of an hexagonal metallacycle **60** (Fig. 10.8B). Later, hydrogen bonding between amide groups appended on the donor ligand facilitate the hierarchical self-assembly (Fig. 10.8B) and gelation process of **60**.

Fernández and co-workers exploited cooperative $\pi-\pi$ interactions and amide H-bonding to control the molecular packing, which ultimately determines the morphology of higher-order structures. Self-assembly of a hydrophobic bispyridyldichlorido Pd(II) complex (**61**, Fig. 10.9A) with an extended π-surface and polarizable amide functional groups yields highly stable aggregates with a strong tendency to bundle into fibrillar structures [65]. Notably, the formation of slipped stacks stabilized by unconventional interactions (N-H···Cl-Pd(II) noncovalent bonds) were observed. Consequently, the authors have reported that upon rapid cooling of a hot monomer solution of **61**, a kinetic and consecutive (hierarchical) pathway could be achieved, which overrules the thermodynamic pathway leading to the formation of different aggregates [66]. Replacing the central Pd(II)

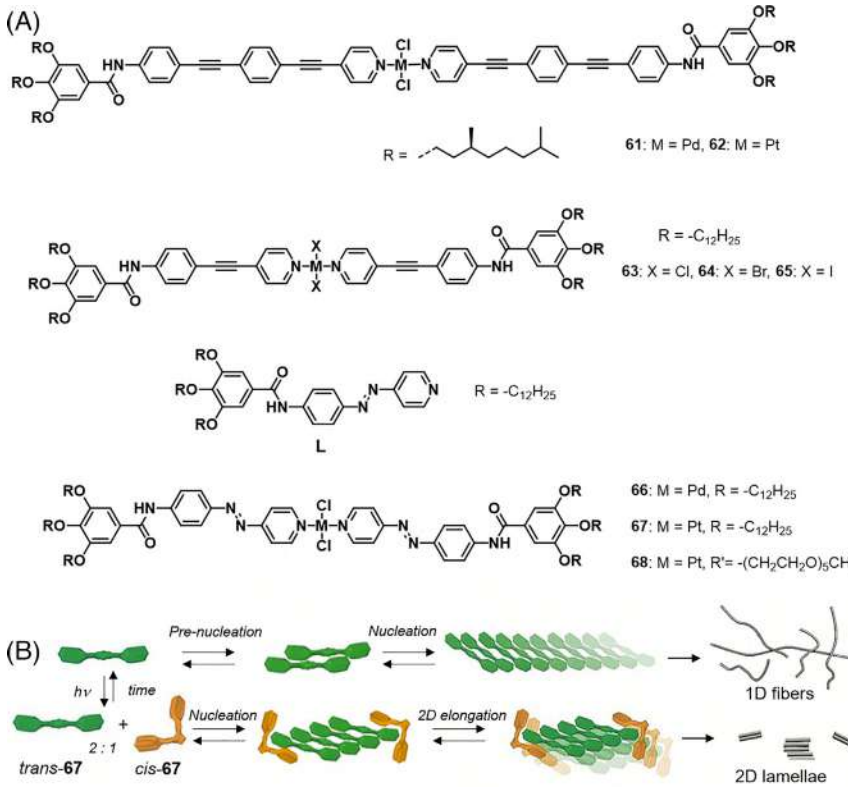

FIGURE 10.9 (A) Chemical structures of bispyridyldichlorido metal complexes **61–68** and ligand **L** with (B) a cartoon representation showing the geometry-controlled self-assembly process of **67**. Fig. 10.9B reproduced from with permission from Ref. 63. Copyright 2019 John Wiley and Sons.

ion with Pt(II) (**62**, Fig. 10.9A) induced a totally different phenomenon, which was termed supramolecular packing polymorphism [67]. A careful selection of temperature, solvent, concentration and cooling rate allowed the authors to identify two different supramolecular polymers with distinct molecular packing (slipped vs pseudoparallel) and high stability. Importantly, precise control of experimental conditions, particularly the cooling rate, enabled the formation of two polymorphs that could be isolated concomitantly in the same solution without interconversion. The role of the halogen nature on the self-assembly behavior of this type of Pt(II) complexes in solution has been demonstrated with a detailed investigation by using -Cl, -Br and -I bearing derivatives (**63–65**, Fig. 10.9A) [68]. A kinetically-driven slipped stacking which is stabilized by NH-Cl hydrogen bonding interactions resulted in the formation of rings with a height and width of 1 nm and 25 nm, respectively. Thermodynamically stable aggregates were fabricated by tuning the experimental conditions, which allows the formation of cooperative π-stacking and NH···O=C interactions leading to

the formation of flexible fibers of several micrometers in length and a height of approximately 5 nm. Bundling of these fibers, possibly through van der Waals interaction was also monitored for these fibrillar structures through atomic force microscopy.

The impact of light and metal complexation on the hierarchical self-assembly processes of a small π-conjugated azo-containing pyridyl ligand (**L**, Fig. 10.9A) has been reported [69]. The ligand (L) self-assembles hierarchically into long twisted fibers with antiparallel molecular arrangement, which dissociates upon photoisomerization of the azobenzene groups, resulting in shorter rigid rods with a different packing. On the other hand, complexation of Pd(II) to yield complex (**66** Fig. 10.9A) led to enhanced cooperativity in the aggregation behavior and a concomitant molecular rearrangement into slipped stacks. The obtained long thin fibers of the pristine complex were converted into thinner, shorter rods upon light irradiation. Interestingly, an inherent geometrical isomerism of the corresponding Pt(II) complex (**67**, Fig. 10.9A) was observed, which was used as a new tool to control the self-assembly processes [70]. Interestingly, the pure *trans* form of **67** forms defined 1D fibers, whereas the formation of the distorted *cis* form leads to an attenuated growth into small 2D lamellae (Fig. 10.9B). Short rods of *trans*-**67** with a height of 2–3 nm and a length of 40–70 nm were observed at the elongation temperature of the supramolecular polymerization process. Upon decreasing the temperature further down, a longitudinal growth of these rods to 1D fibers with lengths between 60 nm and 700 nm also occurred. On the other hand, self-assembly of the mixture of *trans*- and *cis*-**67** exhibited short rod formation initially, which further transformed into 2D lamellar structures in solution. Analogous glycol-appended Pt(II) complex (**68**, Fig. 10.9A) was investigated to examine the impact of solvent polarity on the self-assembly behavior in solution [71]. In aqueous media, this complex self-assembled into spherical particles, whereas in nonpolar media a hierarchical self-assembly to form 2D-nanosheets was observed.

10.4 Hierarchical self-assembly of metal complexes in solution driven by hydrophobic interactions

The hydrophobic nature of aromatic systems has been utilized to fabricate aqua materials with intriguing properties [72]. Solvent-induced aggregation of amphiphilic metal complexes (**69–71**, Fig. 10.10A) has also been used to construct various nanoarchitectures in water [73]. Inclusion of hydrophilic chains, such as ethylene glycol, onto the aromatic ligand has been extensively used to prepare amphiphilic coordination complexes (**72–73**, Fig. 10.10A) that can form self-assemblies in water with excellent properties [74]. Moreover, hydrogels derived from the self-assembly of coordination complexes are also studied intensively due to their wide applications [75,76]. Stang and co-workers prepared diverse architectures in water from Pt(II) based rhomboids (**74–75**) by tuning the hydrophilic segments of the rhombic building blocks (**D12** and

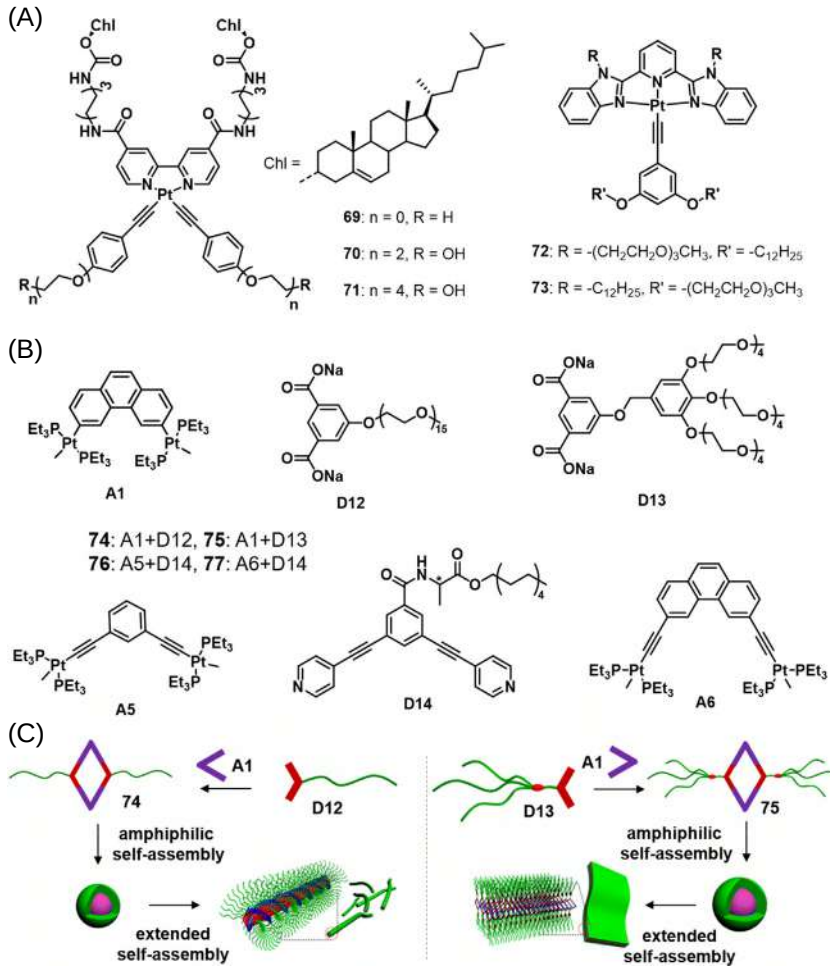

FIGURE 10.10 Chemical structures of (A) amphiphilic coordination complexes **69–73** and (B) dipyridine and di-Pt(II) segments, which were used to synthesize complexes **74–77**. (C) Cartoon representation of the step-wise self-assembly process of **74** and **75** leading to the formation of 1D fibers and two-dimensional (2D) tapes, respectively. Fig. 10.10B is adapted with permission from Ref. 69. Copyright 2013 American Chemical Society.

D13, Fig. 10.10A) as well as by changing the experimental conditions [77]. These amphiphilic supramolecular coordination complexes initially organized into micelles which further rearrange to 1D fibers or 2D ribbons and later to 3D networks of fibers in water (Fig. 10.10B). Apart from this hierarchical nanostructure formation in water, these metallacycles were able to immobilize water to form metallohydrogels, as revealed by scanning electron microscopy (SEM) experiments. In a different work, a series of alanine-based chiral metallacycles (**76–77**), namely, rhomboids and hexagons, were prepared by introducing

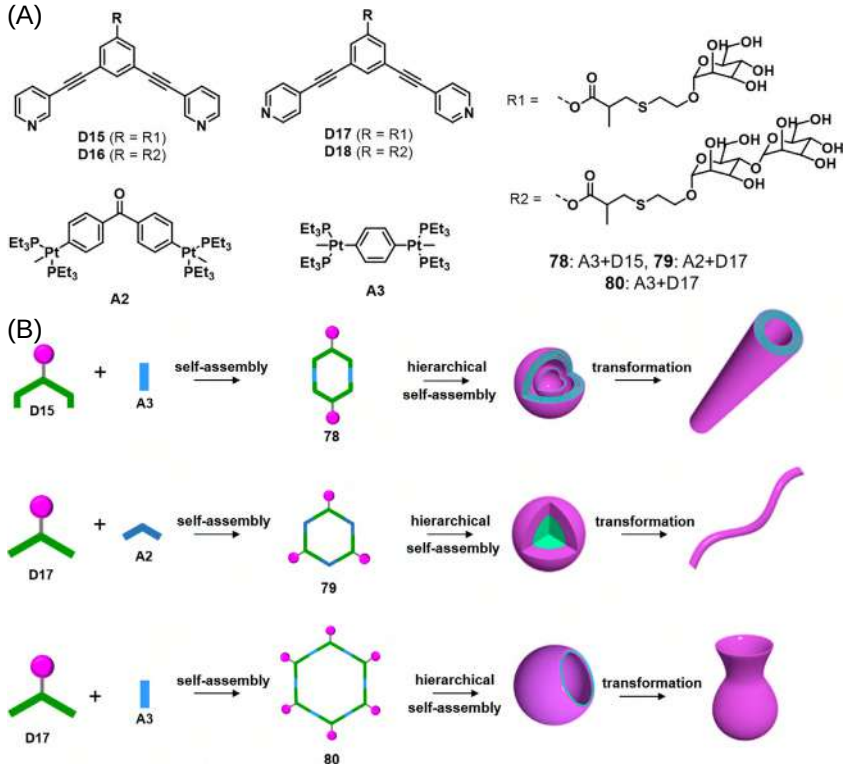

FIGURE 10.11 (A) Chemical structure of dipyridine (**D15**–**D18**) and di-Pt(II) (**A2** and **A3**) segments, which were used to synthesize complexes **78–80** and (B) scheme showing their hierarchical self-assembly processes and corresponding morphological transformation. Fig. 10.11B is adapted with permission from Ref. 71 Copyright © 2019, American Chemical Society.

chiral centers on the dipyridine donor (**D14**, Fig. 10.10A) to fabricate chiral self-assemblies [78]. These complexes formed metallogels in methanol and ethanol at higher concentration with formation of interconnected fibers with well-defined helicity. Saccharide-containing dipyridine building blocks (**D15–D18**, Fig. 10.11A) and di-Pt(II) segments (**A2** and **A3**, Fig. 10.11A) were used to synthesize a series of amphiphilic metallocarbohydrates (**78–80**). In this work, the authors have demonstrated the hierarchical self-assembly of **78–80** through hydrophobic and $\pi-\pi$ interactions with tunable structures in aqueous solution [79]. These metallostructures self-assemble into programmable vesicles (including multilayered and open vesicles), micelles, and fibers, etc., in water, by varying the metallacycles and saccharides (Fig. 10.11B). The different tendency showed by **78–80** in their hierarchical self-assembly process has been attributed to a kinetically driven structural transformation and subsequent reshaping over time.

Amphiphilic alkynylplatinum(II) terpyridine complexes (**81–85**, Fig. 10.12A) showed a strong tendency towards the formation of nanotubes or helical ribbons in solution through metal−metal interactions that can be controlled by modulating the steric effects [80]. Strong hydrophobic−hydrophobic interactions between aliphatic tails in solution enabled the interdigitation of complex **82** to form dimers as shown in Fig. 10.12B. X-ray diffraction experiments were used to confirm the formation of a dimer of **82** and subsequent formation of lamellar structures. Microscopic experiments revealed the formation of nanotubes in solution, where the wall of these nanotubes is comprised of interdigitated hydrocarbon chains. De Cola and co-workers reported the self-assembly of luminescent Pt(II) complex with different aggregation pathways leading to the formation of two kinetic assemblies and the thermodynamic assembly in water [81].

A series of polynuclear alkynylgold(I) complexes (**86–89**, Fig. 10.13A) with different alkyl chains were reported for tunable morphologies such as spherical and sheet-like aggregates in THF-water mixtures [82]. Self-assembly through hydrophobic-hydrophobic interactions has been reported as the reason for the formation of spherical assemblies of **86** in aqueous solution (Fig. 10.13B). However, increase in chain length (**87**) induced the formation of ordered staircase-like structures, which transform into layered sheet-like structures in order to minimize the contact with the aqueous medium (Fig. 10.13B).

10.5 Hierarchical self-assembly of metal complexes through host–guest interactions

Host–guest complexation of Pt(II)-based hexakis-pillar[5]arene metallacycles with neutral ditopic halide guests has also been reported [83]. In this work, a series of discrete metallacycles **90–91** with different sizes were synthesized through the reaction of Pillar[5]arene dipyridyl donor **D19** (Fig. 10.14A) with two linear di-Pt(II) acceptors **A3** and **A4** of different length (Fig. 10.14A) under suitable experimental conditions. Cross-linked assemblies were formed upon mixing these host-appended metallacycles with a ditopic guest in solution due to the strong affinity of pillar[5]arenes towards neutral guests in organic solvents. These initially formed assemblies further transformed into fibers and networks of fibers through a hierarchical self-assembly process, as shown in Fig. 10.14B. Positively charged organoplatinum(II) metallacycle (**92**) was fabricated by combining di-Pt(II) **A2** and tetraphenylethylene (TPE) appended dipyridine donor **D20** (Fig. 10.14A). Addition of heparin (negatively charged polysaccharide) to a solution of **92** induced the host–guest interaction leading to the formation of entangled pearl-necklace type self-assembled materials [84]. Stang and co-workers studied the stepwise interaction of a multicationic organoplatinum(II) hexagon (**93**), which was prepared from a positively charged di-Pt(II) **A7** (Fig. 10.14A) and dipyridine segment bearing methyl viologen (MV) units (Fig. 10.14A). Addition of Cucurbit[*n*]urils and galactose-functionalized

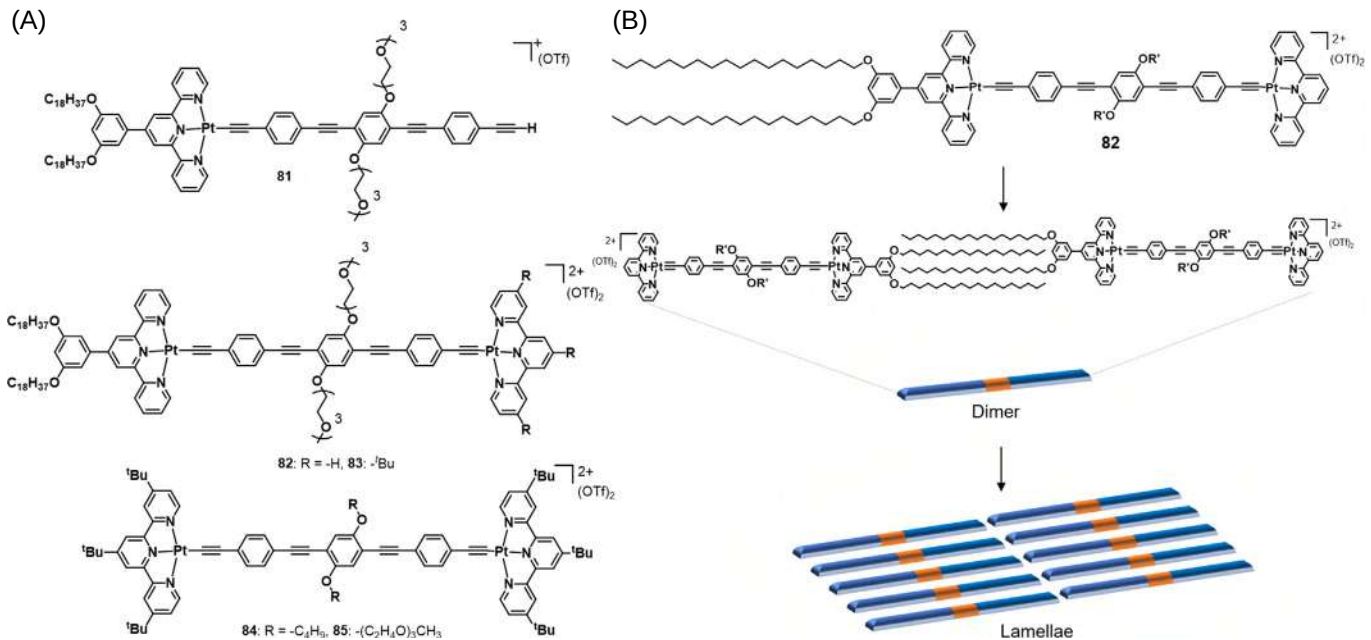

FIGURE 10.12 (A) Chemical structure of **81–85** and (B) cartoon representation of step-wise self-assembly of **82**.

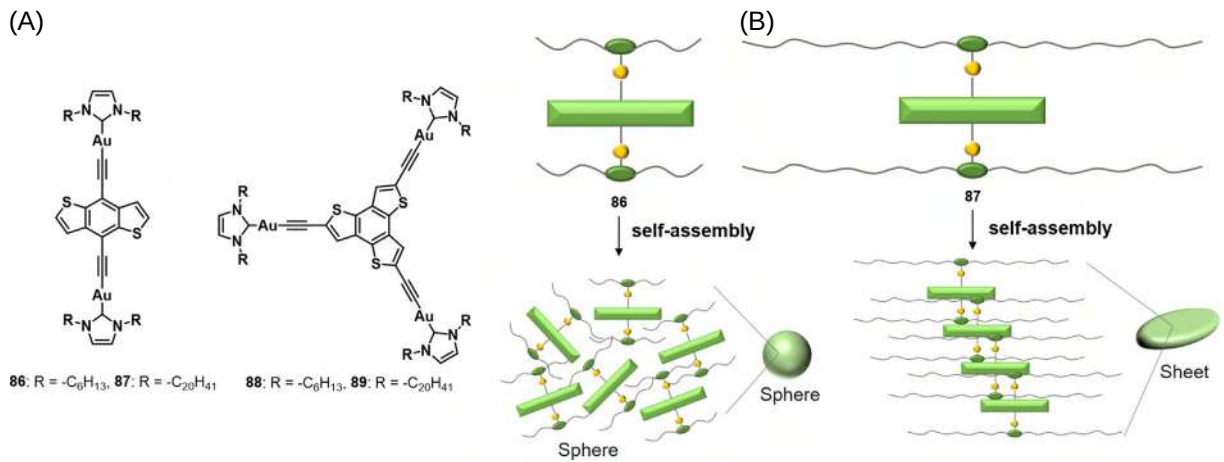

FIGURE 10.13 (A) Chemical structure of dinuclear Au(I) complexes **86–89** and (B) a scheme showing the self-assembly of **86** and **87** to form spheres and sheets, respectively.

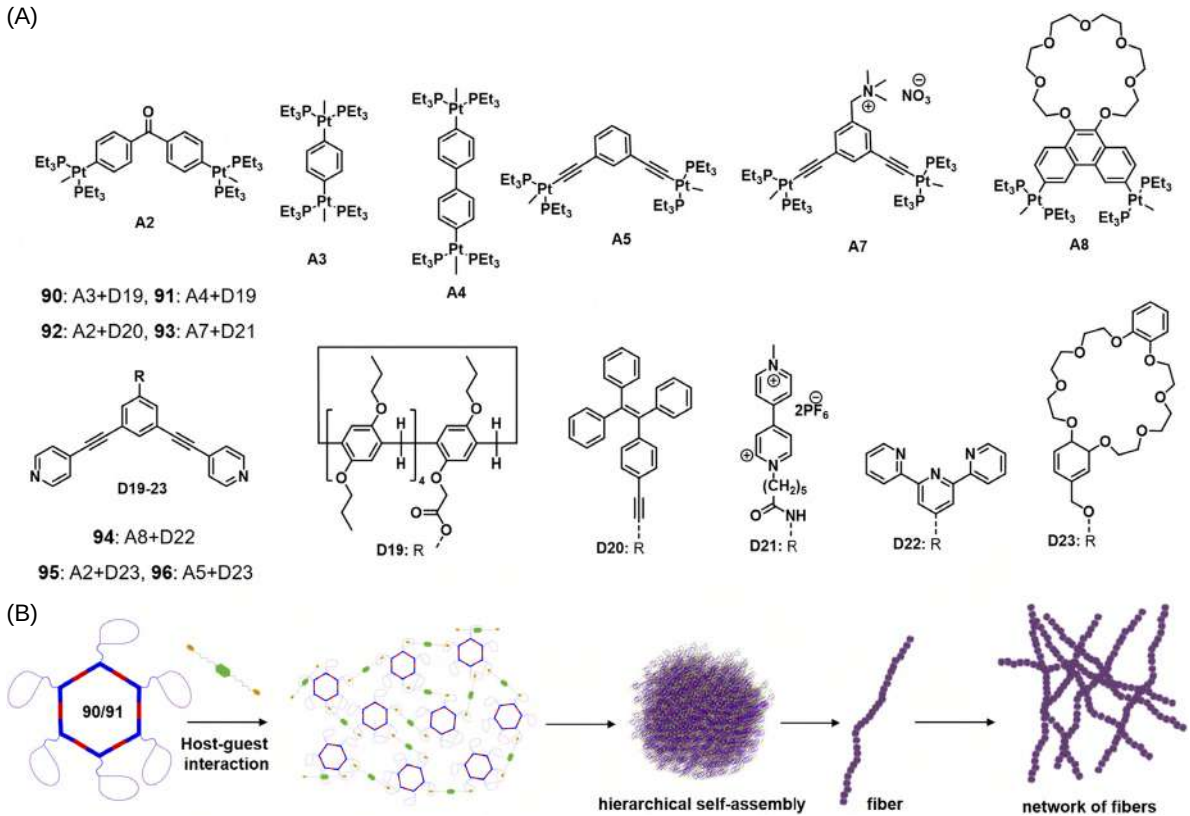

FIGURE 10.14 (A) Chemical structure dipyridine (**D19**–**D23**) and di-Pt(II) (**A2**–**A5** and **A7**–**A8**) segments, which were used to synthesize complexes **90–96** and (B) a scheme showing host–guest interaction-driven hierarchical self-assembly process of **90/91** leading to the formation of supramolecular polymer networks.

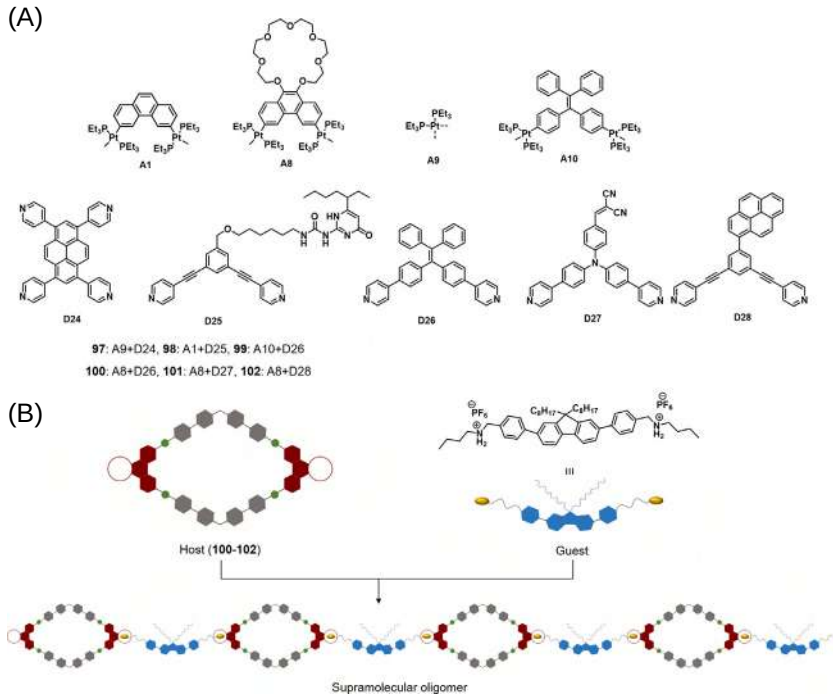

FIGURE 10.15 (A) Chemical structure of dipyridine (**D24**–**D28**) and di-Pt(II) (**A1** and **A8**–**A10**) segments, which were used to synthesize complexes **97–102** and (B) cartoon representation of supramolecular oligomer formation of **100–102** in the presence of a bisammonium linker via host–guest interactions.

naphthalene derivative into a solution of **93** resulted in self-assembled nanospheres and tape-like morphologies upon varying the concentration [85]. Heterometallic bicyclic supramolecular polymers comprised of Pt(II) and Zn(II) were fabricated through a hierarchical metal coordination of **94** through host–guest interactions [86], where the complex was prepared by mixing crown ether bearing di-Pt(II) segment (**A8**, Fig. 10.14A) with a terpyridine ligand (**D22**, Fig. 10.14A). Crown ether-based metallacyclic Pt(II) complexes (**95–96**) were also prepared by treating di-Pt(II) (**A2** and **A5**, Fig. 10.14A) with crown ether-appended dipyridine (**D23**, Fig. 10.14A) segment [87]. These complexes **95–96** were extensively used for the construction of hierarchically self-assembled nanostructures in solution.

Hierarchical self-assembly of a pyrene-based discrete organoplatinum(II) double-metallacycle **97** was demonstrated [88], where the double-metallacycle was synthesized by mixing phosphine-capped di-Pt(II) **A9**, tetrapyridine **D24** units (Fig. 10.15A) and a dicarboxylate ligand in one pot. Hierarchically self-assembled metallosupramolecular polymers and copolymers have been

fabricated using a crown ether-based [2]rotaxane and a discrete organoplatinum(II) metallacycle (**98**) through hydrogen bonding and host–guest interactions [89]. The metallacycle **98** was prepared by reacting di-Pt(II) **A1** with dipyridine **D25** bearing the UPy units (Fig. 10.15A). Formation of supramolecular polymers via hydrogen bonding of UPys was monitored for **98** alone in solution, whereas a combination of host–guest interactions and hydrogen bonding allowed the authors to fabricate metallosupramolecular copolymers from a mixture of **98** and crown ether-based [2]rotaxane. Dipyridine and di-Pt(II) segments bearing TPE units (**D26** and **A10**, respectively, see Fig. 10.15A) were used to prepare a discrete organoplatinum(II) metallacycle (**99**). Interaction of tobacco mosaic virus (TMV) with this complex **99** resulted in a hierarchical self-assembly process to form a metal−organic biohybrid complex [90]. Three Pt(II) rhomboidal metallacycles (**100–102**) exhibiting different emission properties were prepared by metal-coordination-driven self-assembly of di-Pt(II) acceptor (**A8**) with a crown ether-based guest and dipyridyl donors (**D26–28**, Fig. 10.15A) [91]. Subsequent hierarchical process led to the formation of supramolecular oligomers via host–guest interactions between the host (**100–102)** and guest (fluorene based ammonium salts), as shown graphically in Fig. 10.15B. Stimuli-responsive higher order self-assemblies and gels were prepared by engineering the host and guest functionalities [92–94]. Stimuli-responsive metallogels were prepared hierarchically by exploiting the metal coordination and host–guest interaction of a crown ether-based [3]pseudorotaxane and a di-Pt(II) complex [95]. The thus formed gel with 3D supramolecular polymeric network exhibited response to stimuli resulting in the transformation of gel to sol. Subsequently, pillararene-based stimuli-responsive gels were also prepared using host–guest and metal–ligand interactions [96]. Sequential addition of Pt(II) acceptor with a linear and tri-armed Pt(II) complexes resulted in the formation of 1D and 2D self-assembled architectures, respectively.

10.6 Conclusion

In conclusion, the present literature reveals that molecular self-assembly of coordination complexes is a powerful tool to fabricate diverse nanoarchitectures with intriguing properties. In this chapter, we have summarized the recent developments on the molecular design of different metal complexes with their hierarchical self-assembly behavior in solution. Appropriate design of the molecular building blocks has immense scope in controlling the stepwise self-assembly processes of supramolecular coordination complexes. This understanding, in turn, should represent a sound basis for the construction of programmable functional nanoarchitectures of coordination complexes in solution. Particularly, controlling the kinetic versus thermodynamic pathways of these systems is a prerequisite to obtain supramolecularly pure aggregates with specific properties. However, these efforts are still in their infancy stage and developing novel methods to engineer the hierarchical self-assemblies of supramolecular coordination

complexes is necessary for every potential application. We anticipate that the current understanding in controlling the different aggregation pathways of metal complexes will lead to unprecedented materials with intriguing properties in the coming years.

References

[1] T. Aida, E.W. Meijer, S.I. Stupp, Functional supramolecular polymers, Science 335 (2012) 813–817.

[2] S.S. Babu, V.K. Praveen, A. Ajayaghosh, Functional π-gelators and their applications, Chem. Rev. 114 (2014) 1973–2129.

[3] C. Rest, R. Kandanelli, G. Fernández, Strategies to create hierarchical self-assembled structures via cooperative non-covalent interactions, Chem. Soc. Rev. 44 (2015) 2543–2572.

[4] P.A. Korevaar, T.F.A. de Greef, E.W. Meijer, Pathway complexity in π-conjugated materials, Chem. Mater. 26 (2014) 576–586.

[5] J. Matern, Y. Dorca, L. Sánchez, G. Fernández, Revising complex supramolecular polymerization under kinetic and thermodynamic control, Angew. Chem. Int. Ed. 58 (2019) 16730–16740.

[6] J.A.A.W. Elemans, A.E. Rowan, R.J.M. Nolte, Mastering molecular matter: Supramolecular architectures by hierarchical self-assembly, J. Mater. Chem. 13 (2003) 2661–2670.

[7] H.M. Keizer, R.P. Sijbesma, Hierarchical self-assembly of columnar aggregates, Chem. Soc. Rev. 34 (2005) 226–234.

[8] K. Tashiro, T. Saito, H. Arima, N. Suda, B. Vedhanarayanan, S. Yagai, Scissor-shaped photochromic dyads: Hierarchical self-assembly and photoresponsive property, Chem. Rec. 22 (2021) e202100252, doi:10.1002/tcr.202100252.

[9] B. Li, T. He, Y. Fan, X. Yuan, H. Qiu, S. Yin, Recent developments in the construction of metallacycle/metallacage-cored supramolecular polymers via hierarchical self-assembly, Chem. Commun. 55 (2019) 8036–8059.

[10] T.R. Cook, P.J. Stang, Recent developments in the preparation and chemistry of metallacycles and metallacages via coordination, Chem. Rev. 115 (2015) 7001–7045.

[11] V.W.-W. Yam, V.K.-M. Au, S.Y.-L. Leung, Light-emitting self-assembled materials based on d^8 and d^{10} transition metal complexes, Chem. Rev. 115 (2015) 7589−7728.

[12] M. Mauro, A. Aliprandi, D. Septiadi, N.S. Kehra, L. De Cola, When self-assembly meets biology: Luminescent platinum complexes for imaging applications, Chem. Soc. Rev. 43 (2014) 4144–4166.

[13] L.-J. Chen, H.-B. Yang, Construction of stimuli-responsive functional materials via hierarchical self-assembly involving coordination interactions, Acc. Chem. Res. 51 (2018) 2699−2710.

[14] S. Datta, M.L. Saha, P.J. Stang, Hierarchical assemblies of supramolecular coordination complexes, Acc. Chem. Res. 51 (2018) 2047−2063.

[15] Y. Han, Z. Gao, C. Wang, R. Zhong, F. Wang, Recent progress on supramolecular assembly of organoplatinum(II) complexes into long-range ordered nanostructures, Coord. Chem. Rev. 414 (2020) 213300.

[16] V. Vreshch, W. Shen, B. Nohra, S.-K. Yip, V.W.-W. Yam, C. Lescop, R. Réau, Aurophilicity versus mercurophilicity: Impact of d10–d10 metallophilic interactions on the structure of metal-rich supramolecular assemblies, Chem. Eur. J. 18 (2012) 466–477.

[17] A. Aliprandi, D. Genovese, M. Mauro, L. De Cola, Recent advances in phosphorescent Pt(II) complexes featuring metallophilic interactions: Properties and applications, Chem. Lett. 44 (2015) 1152–1169.
[18] M.J. Mayoral, C. Rest, V. Stepanenko, J. Schellheimer, R.Q. Albuquerque, G. Fernández, Cooperative supramolecular polymerization driven by metallophilic Pd···Pd interactions, J. Am. Chem. Soc. 135 (2013) 2148−2151.
[19] N.K. Allampally, M.J. Mayoral, S. Chansai, M.C. Lagunas, C. Hardacre, V. Stepanenko, R.Q. Albuquerque, G. Fernández, Control over the self-assembly modes of PtII complexes by alkyl chain variation: From slipped to parallel π-stacks, Chem. Eur. J. 22 (2016) 7810–7816.
[20] J.P. Coelho, J. Matern, R.Q. Albuquerque, G. Fernández, Mechanistic insights into statistical co-assembly of metal complexes, Chem. Eur. J. 25 (2019) 8960–8964.
[21] C. Rest, M.J. Mayoral, K. Fucke, J. Schellheimer, V. Stepanenko, G. Fernández, Self-assembly and (hydro)gelation triggered by cooperative π–π and unconventional CH···X hydrogen bonding interactions, Angew. Chem. Int. Ed. 53 (2014) 700–705.
[22] C. Rest, A. Martin, V. Stepanenko, N.K. Allampally, D. Schmidt, G. Fernández, Multiple CH-O interactions involving glycol chains as driving force for the self-assembly of amphiphilic Pd(II) complexes, Chem. Commun. 50 (2014) 13366–13369.
[23] L. Herkert, P. Selter, C.G. Daniliuc, N. Bäumer, J.P. Palakkal, G. Fernández, M.R. Hansen, Tuning the molecular packing of self-assembled amphiphilic PtII complexes by varying the hydrophilic side-chain length, Chem. Eur. J. 27 (2021) 4617–4626.
[24] L. Herkert, J. Droste, K.K. Kartha, P.A. Korevaar, T.F.A. de Greef, M.R. Hansen, G. Fernández, Pathway control in cooperative vs. anti-cooperative supramolecular polymers, Angew. Chem. Int. Ed. 58 (2019) 11344–11349.
[25] N. Bäumer, K.K. Kartha, S. Buss, I. Maisuls, J.P. Palakkal, C.A. Strassert, G. Fernández, Tuning energy landscapes and metal–metal interactions in supramolecular polymers regulated by coordination geometry, Chem. Sci. 12 (2021) 5236–5245.
[26] N. Bäumer, K.K. Kartha, S. Buss, J.P. Palakkal, C.A. Strassert, G. Fernández, Exploiting coordination geometry to tune the dimensions and processability of metallosupramolecular polymers, Org. Chem. Front. 8 (2021) 4138–4143.
[27] L.-J. Chen, H.-B. Yang, Construction of stimuli-responsive functional materials via hierarchical self-assembly involving coordination interactions, Acc. Chem. Res. 51 (2018) 2699−2710.
[28] J. Zhang, R. Marega, L.-J. Chen, N.-W. Wu, X.-D. Xu, D.C. Muddiman, D. Bonifazi, H.-B. Yang, Hierarchical self-assembly of supramolecular hydrophobic metallacycles into ordered nanostructures, Chem. Asian J. 9 (2014) 2928–2936.
[29] L.-J. Chen, G.-Z. Zhao, B. Jiang, B. Sun, M. Wang, L. Xu, J. He, Z. Abliz, H. Tan, X. Li, H.-B. Yang, Smart stimuli-responsive spherical nanostructures constructed from supramolecular metallodendrimers via hierarchical self-assembly, J. Am. Chem. Soc. 136 (2014) 5993−6001.
[30] Y. Zhang, Q.-F. Zhou, G.-F. Huo, G.-Q. Yin, X.-L. Zhao, B. Jiang, H. Tan, X. Li, H.-B. Yang, Hierarchical self-assembly of an alkynylplatinum(ll) bzimpy-functionalized metallacage via Pt···Pt and π-π interactions, Inorg. Chem. 57 (2018) 3516−3520.
[31] B. Jiang, J. Zhang, W. Zheng, L.-J. Chen, G.-Q. Yin, Y.-X. Wang, B. Sun, X. Li, H.-B. Yang, Construction of alkynylplatinum(II) bzimpy-functionalized metallacycles and their hierarchical self-assembly behavior in solution promoted by Pt···Pt and π–π interactions, Chem. Eur. J. 22 (2016) 14664–14671.
[32] B. Sun, M. Wang, Z. Lou, M. Huang, C. Xu, X. Li, L.-J. Chen, Y. Yu, G.L. Davis, B. Xu,

H.-B. Yang, X. Li, From ring-in-ring to sphere-in-sphere: Self-assembly of discrete 2D and 3D architectures with increasing stability, J. Am. Chem. Soc. 137 (2015) 1556−1564.

[33] C.A. Strassert, C.-H. Chien, M.D.G. Lopez, D. Kourkoulos, D. Hertel, K. Meerholz, L. De Cola, Switching on luminescence by the self-assembly of a platinum(II) complex into gelating nanofibers and electroluminescent films, Angew. Chem. Int. Ed. 50 (2011) 946–950.

[34] N.K. Allampally, C.A. Strassert, L. De Cola, Luminescent gels by self-assembling platinum complexes, Dalton Trans. 41 (2012) 13132–13137.

[35] M.E. Robinson, A. Nazemi, D.J. Lunn, D.W. Hayward, C.E. Boott, M.-S. Hsiao, R.L. Harniman, S.A. Davis, G.R. Whittell, R.M. Richardson, L. De Cola, I. Manners, Dimensional control and morphological transformations of supramolecular polymeric nanofibers based on cofacially-stacked planar amphiphilic platinum(II) complexes, ACS Nano 11 (2017) 9162−9175.

[36] M.E. Robinson, D.J. Lunn, A. Nazemi, G.R. Whittell, L. De Cola, I. Manners, Length control of supramolecular polymeric nanofibers based on stacked planar platinum(II) complexes by seeded-growth, Chem. Commun. 51 (2015) 15921–15924.

[37] M. Mauro, A. Aliprandi, C. Cebrián, D. Wang, C. Kübel, L. De Cola, Self-assembly of a neutral platinum(II) complex into highly emitting microcrystalline fibers through metallophilic interactions, Chem. Commun. 50 (2014) 7269−7272.

[38] S. Carrara, A. Aliprandi, C.F. Hogan, L. De Cola, Aggregation-induced electrochemiluminescence of platinum(II) complexes, J. Am. Chem. Soc. 139 (2017) 14605–14610.

[39] D. Septiadi, A. Aliprandi, M. Mauro, L. De Cola, Bio-imaging with neutral luminescent Pt(II) complexes showing metal/metal interactions, RSC Adv. 4 (2014) 25709–25718.

[40] Q. Wan, W.-P. To, C. Yang, C.-M. Che, The metal–metal-to-ligand charge transfer excited state and supramolecular polymerization of luminescent pincer PdII–isocyanide complexes, Angew. Chem. Int. Ed. 57 (2018) 3089–3093.

[41] Q. Wan, X.-S. Xiao, W.-P. To, W. Lu, Y. Chen, K.-H. Low, C.-M. Che, Counteranion- and solvent-mediated chirality transfer in the supramolecular polymerization of luminescent platinum(II) complexes, Angew. Chem. Int. Ed. 57 (2018) 17189–17193.

[42] A.Y.-Y. Tam, K.M.-C. Wong, V.W.-W. Yam, Unusual luminescence enhancement of metallogels of alkynylplatinum(II) 2,6-bis(N-alkylbenzimidazol-2′-yl)pyridine complexes upon a gel-to-sol phase transition at elevated temperatures, J. Am. Chem. Soc. 131 (2009) 6253–6260.

[43] F. Camerel, R. Ziessel, B. Donnio, C. Bourgogne, D. Guillon, M. Schmutz, C. Iacovita, J.-P. Bucher, Formation of gels and liquid crystals induced by Pt···Pt and π-π interactions in luminescent s-alkynyl platinum(II) terpyridine complexes, Angew. Chem. Int. Ed. 46 (2007) 2659–2662.

[44] A.Y.-Y. Tam, K.M.-C. Wong, G. Wang, V.W.-W. Yam, Luminescent metallogels of platinum(ii) terpyridyl complexes: Interplay of metal···metal, π–π and hydrophobic–hydrophobic interactions on gel formation, Chem. Commun. 20 (2007) 2028–2030.

[45] S.Y.-L. Leung, V.W.-W. Yam, Hierarchical helices of helices directed by Pt/Pt and p–p stacking interactions: reciprocal association of multiple helices of dinuclear alkynylplatinum(II) complex with luminescence enhancement behavior, Chem. Sci. 4 (2013) 4228–4234.

[46] M.H.-Y. Chan, M. Ng, S.Y.-L. Leung, W.H. Lam, V.W.-W. Yam, Synthesis of luminescent platinum(II) 2,6-bis(ndodecylbenzimidazol-2′-yl)pyridine foldamers and their supramolecular assembly and metallogel formation, J. Am. Chem. Soc. 139 (2017) 8639−8645.

[47] X. Yan, S. Li, J.B. Pollock, T.R. Cook, J. Chen, Y. Zhang, X. Ji, Y. Yu, F. Huang, P.J. Stang, Supramolecular polymers with tunable topologies via hierarchical coordination-driven self-assembly and hydrogen bonding interfaces, Proc. Natl. Acad. Sci. U.S.A. 110 (2013) 15585–15590.

[48] X. Yan, B. Jiang, T.R. Cook, Y. Zhang, J. Li, Y. Yu, F. Huang, H.-B. Yang, P.J. Stang, Dendronized organoplatinum(II) metallacyclic polymers constructed by hierarchical coordination-driven self-assembly and hydrogen-bonding interfaces, J. Am. Chem. Soc. 135 (2013) 16813–16816.

[49] N.-W. Wu, L.-J. Chen, C. Wang, Y.-Y. Ren, X. Li, L. Xu, H.-B. Yang, Hierarchical self-assembly of a discrete hexagonal metallacycle into the ordered nanofibers and stimuli-responsive supramolecular gels, Chem. Commun. 50 (2014) 4231−4233.

[50] L.-J. Chen, B. Jiang, H.-B. Yang, Transformable nanostructures of cholesteryl containing rhomboidal metallacycles through hierarchical self-assembly, Org. Chem. Front. 3 (2016) 579–587.

[51] M. Chen, C. Wei, J. Tao, X. Wu, N. Huang, G. Zhang, L. Li, Supramolecular polymers self-assembled from trans-bis(pyridine) dichloropalladium(II) and platinum(II) complexes, Chem. Eur. J. 20 (2014) 2812–2818.

[52] M. Chen, C. Wei, X. Wu, M. Khan, N. Huang, G. Zhang, L. Li, Metallogels self-assembled from linear rod-like platinum complexes: Influence of the linkage, Chem. Eur. J. 21 (2015) 4213–4217.

[53] Y.-J. Tian, E.W. Meijer, F. Wang, Cooperative self-assembly of platinum(II) acetylide complexes, Chem. Commun. 49 (2013) 9197–9199.

[54] Z. Gao, J. Zhu, Y. Han, X. Lv, X. Zhang, F. Wang, Ligand effects on cooperative supramolecular polymerization of platinum(II) acetylide complexes, Polym. Chem. 7 (2016) 5763–5767.

[55] M. Gui, Y. Han, H. Zhong, R. Liao, F. Wang, Investigation of the amide linkages on cooperative supramolecular polymerization of organoplatinum(II) complexes, Molecules 26 (2021) 2832.

[56] Z. Chen, Y. Xue, M. Gui, C. Wang, F. Wang, Structural isomerism effect in platinum(II) acetylide-based supramolecular polymers, Inorg. Chem. 59 (2020) 6481−6488.

[57] D. Zhong, Y. Ying, M. Gui, C. Wang, H. Zhong, H. Zhao, F. Wang, Structure and solvent effects on the stability of platinum(II) acetylide-based supramolecular polymers, J. Organomet. Chem. 933 (2021) 121632.

[58] X. Wang, Y. Han, Y. Liu, G. Zou, Z. Gao, F. Wang, Cooperative supramolecular polymerization of fluorescent platinum acetylides for optical waveguide applications, Angew. Chem. Int. Ed. 56 (2017) 12466–12470.

[59] Z. Gao, P.A. Korevaar, R. Zhong, Z. Wu, F. Wang, Two-component supramolecular metallogels with the presence of Pt–Pt metal–metal interactions, Chem. Commun. 54 (2018) 9857–9860.

[60] J. Chen, Z. Zhang, C. Wang, Z. Gao, Z. Gao, F. Wang, Cooperative self-assembly and gelation of organogold(I) complexes via hydrogen bonding and aurophilic Au-Au interactions, Chem. Commun. 53 (2017) 11552–11555.

[61] C. Wang, Z. Chen, M. Liu, H. Zhong, F. Wang, Cooperative supramolecular polymerization of phosphorescent alkynyl-gold(I)–isocyanide complexes, Polym. Chem. 10 (2019) 3210–3216.

[62] A. Aliprandi, C.M. Croisetu, M. Mauro, L. De Cola, Chiral amplification by self-assembly of neutral luminescent platinum(II) complexes, Chem. Eur. J. 23 (2017) 5957–5961.

[63] C. Po, Z. Ke, A.Y.-Y. Tam, H.-F. Chow, V.W.-W. Yam, Platinum(II) terpyridine metallogel with an l-valine-modified alkynyl ligand: Interplay of Pt···Pt, π–π and hydrogen-bonding interactions, Chem. Eur. J. 19 (2013) 15735–15744.

[64] Y.-Y. Ren, Z. Xu, G. Li, J. Huang, X. Fand, L. Xu, Hierarchical self-assembly of a fluorescence emission-enhanced organogelator and its multiple stimuli-responsive behaviors, Dalton Trans. 46 (2017) 333–337.

[65] A. Langenstroer, Y. Dorca, K.K. Kartha, M.J. Mayoral, V. Stepanenko, G. Fernández, L. Sánchez, Exploiting N-H···Cl hydrogen bonding interactions in cooperative metallo-supramolecular polymerization, Macromol. Rapid Commun. 39 (2018) 1800191.

[66] J. Matern, K.K. Kartha, L. Sanchez, G. Fernández, Consequences of hidden kinetic pathways on supramolecular polymerization, Chem. Sci. 11 (2020) 6780–6788.

[67] A. Langenstroer, K.K. Kartha, Y. Dorca, J. Dröste, V. Stepanenko, R.Q. Albuquerque, M.R. Hansen, L. Sánchez, G. Fernández, Unraveling concomitant packing polymorphism in supramolecular polymer, J. Am. Chem. Soc. 141 (2019) 5192–5200.

[68] J. Matern, N. Bäumer, G. Fernández, Unraveling halogen effects in supramolecular polymerization, J. Am. Chem. Soc. 143 (2021) 7164–7175.

[69] K.K. Kartha, N.K. Allampally, A.T. Politi, D.D. Prabhu, H. Ouchi, R.Q. Albuquerque, S. Yagai, G. Fernández, Influence of metal coordination and light irradiation on hierarchical self-assembly processes, Chem. Sci. 10 (2019) 752–760.

[70] N. Bäumer, K.K. Kartha, N.K. Allampally, S. Yagai, R.Q. Albuquerque, G. Fernández, Exploiting coordination isomerism for controlled self-assembly, Angew. Chem. Int. Ed. 58 (2019) 15626–15630.

[71] N. Bäumer, K.K. Kartha, J.P. Palakkal, G. Fernández, Morphology control in metallo-supramolecular assemblies through solvent-induced steric demand, Soft Matter 16 (2020) 6834–6840.

[72] E. Krieg, A. Niazov-Elkan, E. Cohen, Y. Tsarfati, B. Rybtchinski, Noncovalent aqua materials based on perylene diimides, Acc. Chem. Res. 52 (2019) 2634–2646.

[73] Y. Mao, K. Liu, L. Meng, L. Chen, L. Chen, T. Yi, Solvent induced helical aggregation in the self-assembly of cholesterol tailed platinum complexes, Soft Matter 10 (2014) 7615–7622.

[74] C. Po, V.W.-W. Yam, A metallo-amphiphile with unusual memory behaviour: Effect of temperature and structure on the self-assembly of triethylene glycol (TEG)-pendant platinum(II) bzimpy complexes, Chem. Sci. 5 (2014) 4868–4872.

[75] N.K. Allampally, M. Bredol, C.A. Strassert, L. De Cola, Highly phosphorescent supramolecular hydrogels based on platinum emitters, Chem. Eur. J. 20 (2014) 16863–16868.

[76] J.L.-L. Tsai, T. Zou, J. Liu, T. Chen, A.O.-Y. Chan, C. Yang, C.-N. Lok, C.-M. Che, Luminescent platinum(II) complexes with self-assembly and anti-cancer properties: hydrogel, pH dependent emission color and sustained-release properties under physiological conditions, Chem. Sci. 6 (2015) 3823–3830.

[77] X. Yan, S. Li, T.R. Cook, X. Ji, Y. Yao, J.B. Pollock, Y. Shi, G. Yu, J. Li, F. Huang, P.J. Stang, Hierarchical self-assembly: Well-defined supramolecular nanostructures and metallohydrogels via amphiphilic discrete organoplatinum(II) metallacycles, J. Am. Chem. Soc. 135 (2013) 14036–14039.

[78] Y. Sun, S. Li, Z. Zhou, M.L. Saha, S. Datta, M. Zhang, X. Yan, D. Tian, H. Wang, L. Wang, X. Li, M. Liu, H. Li, P.J. Stang, Alanine-based chiral metallogels via supramolecular coordination complex platforms: Metallogelation induced chirality transfer, J. Am. Chem. Soc. 140 (2018) 3257−3263.

[79] G. Yang, W. Zheng, G. Tao, L. Wu, Q.-F. Zhou, Z. Kochovski, T. Ji, H. Chen, X. Li, Y. Lu, H.-M. Ding, H.-B. Yang, G. Chen, M. Jiang, Diversiform and transformable glyco-nanostructures constructed from amphiphilic supramolecular metallocarbohydrates through hierarchical self-assembly: The balance between metallacycles and saccharides, ACS Nano 13 (2019) 13474–13485.

[80] S.Y.-L. Leung, K.M.-C. Wong, V.W.-W. Yam, Self-assembly of alkynylplatinum(II) terpyridine amphiphiles into nanostructures via steric control and metal–metal interactions, Proc. Natl. Acad. Sci. U. S. A. 113 (2016) 2845−2850.

[81] A. Aliprandi, M. Mauro, L. De Cola, Controlling and imaging biomimetic self-assembly, Nat. Chem. 8 (2016) 10–15.

[82] E.Y.-H. Hong, H.-L. Wong, V.W.-W. Yam, From spherical to leaf-like morphologies: Tunable supramolecular assembly of alkynylgold(I) complexes through variations of the alkyl chain length, Chem. Eur. J. 21 (2015) 5732–5735.

[83] Z.-Y. Li, Y. Zhang, C.-W. Zhang, L.-J. Chen, C. Wang, H. Tan, Y. Yu, X. Li, H.-B. Yang, Cross-linked supramolecular polymer gels constructed from discrete multi-pillar[5]arene metallacycles and their multiple stimuli-responsive behavior, J. Am. Chem. Soc. 136 (2014) 8577–8589.

[84] L.-J. Chen, Y.-Y. Ren, N.-W. Wu, B. Sun, J.-Q. Ma, L. Zhang, H. Tan, M. Liu, X. Li, H.-B. Yang, Hierarchical self-assembly of discrete organoplatinum(II) metallacycles with polysaccharide via electrostatic interactions and their application for heparin detection, J. Am. Chem. Soc. 137 (2015) 11725–11735.

[85] S. Datta, M.L. Saha, N. Lahiri, G. Yu, J. Louie, P.J. Stang, Hierarchical self-assembly of a water-soluble organoplatinum(II) metallacycle into well-defined nanostructures, Org. Lett. 20 (2018) 7020–7023.

[86] Q. Zhang, D. Tang, J. Zhang, R. Ni, L. Xu, T. He, X. Lin, X. Li, H. Qiu, S. Yin, P.J. Stang, Self-healing heterometallic supramolecular polymers constructed by hierarchical assembly of triply orthogonal interactions with tunable photophysical properties, J. Am. Chem. Soc. 141 (2019) 17909–17917.

[87] H.-B. Yang, K. Ghosh, B.H. Northrop, Y.-R. Zheng, M.M. Lyndon, D.C. Muddiman, P.J. Stang, A highly efficient approach to the self-assembly of hexagonal cavity-cored tris[2]pseudorotaxanes from several components via multiple noncovalent interactions, J. Am. Chem. Soc. 129 (2007) 14187–14189.

[88] Z. Yang, Y. Wang, X. Liu, R.T. Vanderlinden, R. Ni, X. Li, P.J. Stang, Hierarchical self-assembly of a pyrene-based discrete organoplatinum(II) double-metallacycle with triflate anions via hydrogen bonding and its tunable fluorescence emission, J. Am. Chem. Soc. 142 (2020) 13689–13694.

[89] P. Wei, X. Yan, T.R. Cook, X. Ji, P.J. Stang, F. Huang, Supramolecular copolymer constructed by hierarchical self-assembly of orthogonal host−guest, H–bonding, and coordination interactions, ACS Macro Lett. 5 (2016) 671−675.

[90] Y. Tian, X. Yan, M.L. Saha, Z. Niu, P.J. Stang, Hierarchical self-assembly of responsive organoplatinum(II) metallacycle−TMV complexes with turn-on fluorescence, J. Am. Chem. Soc. 138 (2016) 12033–12036.

[91] M. Zhang, S. Yin, J. Zhang, Z. Zhou, M.L. Saha, C. Lu, P.J. Stang, Metallacycle-cored supramolecular assemblies with tunable fluorescence including white-light emission, Proc. Natl. Acad. Sci. U. S. A. 114 (2017) 3044–3049.

[92] X. Yan, T.R. Cook, J.B. Pollock, P. Wei, Y. Zhang, Y. Yu, F. Huang, P.J. Stang, Responsive supramolecular polymer metallogel constructed by orthogonal coordination-driven self-assembly and host/guest interactions, J. Am. Chem. Soc. 136 (2014) 4460–4463.

[93] Z. Zhou, X. Yan, T.R. Cook, M.L. Saha, P.J. Stang, Engineering functionalization in a supramolecular polymer: Hierarchical self-organization of triply orthogonal non-covalent interactions on a supramolecular coordination complex platform, J. Am. Chem. Soc. 138 (2016) 806–809.

[94] C. Lu, M. Zhang, D. Tang, X. Yan, Z. Zhang, Z. Zhou, B. Song, H. Wang, X. Li, S. Yin, H. Sepehrpour, P.J. Stang, Fluorescent metallacage-core supramolecular polymer gel formed by orthogonal metal coordination and host–guest interactions, J. Am. Chem. Soc. 140 (2018) 7674–7680.

[95] H. Xing, H. Wang, X. Yan, X. Ji, A responsive supramolecular metallogel constructed by coordination-driven self-assembly of a crown ether-based [3]pseudorotaxane and a diplatinum(II) acceptor, Dalton Trans. 44 (2015) 11264–11268.

[96] Z. Li, H. Xing, B. Shi, Two novel supramolecular metallogels constructed by platinum(II) coordination and pillar [5]arene-based host–guest interactions, Polym. Chem. 8 (2017) 2747–2751.

Chapter 11

Biomimetic supramolecular coordination chemistry and molecular machines

Renitta Benny, Diptiprava Sahoo, Nithish Kumar KS and Soumen De
School of Chemistry, Indian Institute of Science Education and Research Thiruvananthapuram (IISER-TVM), Thiruvananthapuram, India

11.1 Introduction

Nature often acts as a basis of stimulation for many supramolecular chemists to take inspiration from it and aspire to mimic the functions accessible by intricate biotic machinery [1,2]. They are not only mimicking but also pushing beyond what they can offer. Thus, it is not astonishing to see that significant development has been made in molecular switches and machines in the past decades [3,4]. This area was enormously contributed by the pioneering and seminal contributions of the Nobel Prize winners Fraser Stoddart, Jean-Pierre Sauvage and Ben Feringa [5].

Among various synthetic tools, coordination-driven self-assembly [6,7,104] has been a productive approach for planning and manufacturing many coordination architectures with diverse applications. This approach exploits preprogrammed information of ligand donor building blocks and the directionality of metal acceptors. A careful design of building blocks and appropriate metal ions enabled various molecular switches and machines to design. The use of transition metal complexes in switches and machines has the extra benefit over other stimuli such as: (1) the metal centers are often redox-active, and thus permitting them to activate motion via a metal-centered redox reaction, thus circumventing any possible difficulty accompanying with the formation of organic radicals, (2) the strength and dynamics of a metal complex can be accurately moderated and fine-tuned by choice of metal, ligand(s), and medium, and thus the assembly can be altered according to our will, (3) the high directionality of the metal–ligand interaction lets consistent design, and finally (4) the emergence of novel self-sorting procedures permit manifold of these interactions to be employed in parallel. In addition, intermolecular metal–ion translocation is a well-known

Supramolecular Coordination Complexes: Design, Synthesis, and Applications.
DOI: https://doi.org/10.1016/B978-0-323-90582-4.00005-1

factor in biotic signaling [8]. The reversible nature of the bond also offers an extra benefit as it offers a way for an inherent self-correction mechanism. Another notable facet of dynamic metal–ligand coordination is its ability for ligand interchange or metal interchange. An ideal machine should execute continuously without fatigue, whereas synthetic and natural machines show fatigue due to inevitable damages during their operation, thus requires service and maintenance. Replacement of ligand or metal is an easy way for repair, but the swapping of metal or ligand may also improve the machine as it may emerge with novel properties. When bound through weak, mostly noncovalent interactions on the molecular level, one can readily interchange the components, but it is not easy in a fully covalent device. As a result, there is much interest in the design, synthesis and operation of intricate molecular devices based on dynamic metal–ligand interaction.

11.2 Redox-triggered molecular motion

Among various stimuli, redox has been an attractive option for chemists to manipulate molecular level motions as it minimizes the accumulation of waste. One essential criterion for the successful outline of a redox activated switching process is that the products should be stable on the shuttling time scale after the redox process, and rapid charge recombination must be prohibited. Another necessary condition to make a redox-switchable system is that they should show a substantial thermodynamic bias in both states, easily accessible through metal–ligand interaction. In the context of mechanically interlocked devices and machines, redox controlled molecular motion has been pioneered and mastered by Jean-Pierre Sauvage [9–11,106,107] for almost three decades. The fundamental principle behind his redox-activated switches is the alteration in preference for coordination number and geometry of metal ions upon oxidation-reduction. Cu(I), for example, inclines to form tetrahedral four-coordinate complexes, whereas Cu(II) prefers five- and six-coordinate geometries.

The operation of the first redox-activated mechanically interlocked molecules (MIM) is shown in Fig. 11.1A [12]. The Cu^{+} was tetrahedrally coordinated with the two bidentate phenanthroline ligands in the catenane's initial state $[Cu(\mathbf{1})]^{+}$. However, one-electron oxidation of the central Cu^{+} ion produced the tetracoordinated $[Cu(\mathbf{1})]^{2+}$ that contained the Cu^{2+} ion in a thermodynamically less favorable tetra-coordination environment. Therefore, the short-lived intermediate $[Cu(\mathbf{1})]^{2+}$ experienced a complete reorganization to yield the more stable pentacoordinate complex $[Cu(\mathbf{2})]^{2+}$. Again, after reduction of $[Cu(\mathbf{2})]^{2+}$, the unstable pentacoordinated $[Cu(\mathbf{2})]^{+}$ was formed since the Cu^{+} atom was then present in a thermodynamically less favorable penta-coordination environment. Consequently, $[Cu(\mathbf{2})]^{+}$ again underwent a pirouetting motion of the macrocycle to restore the initial state $[Cu(\mathbf{1})]^{+}$. It was important to note that the rate constant for the forward motion was far less than that for the backward process, as ligand interchange reactions around Cu^{+} was more manageable than

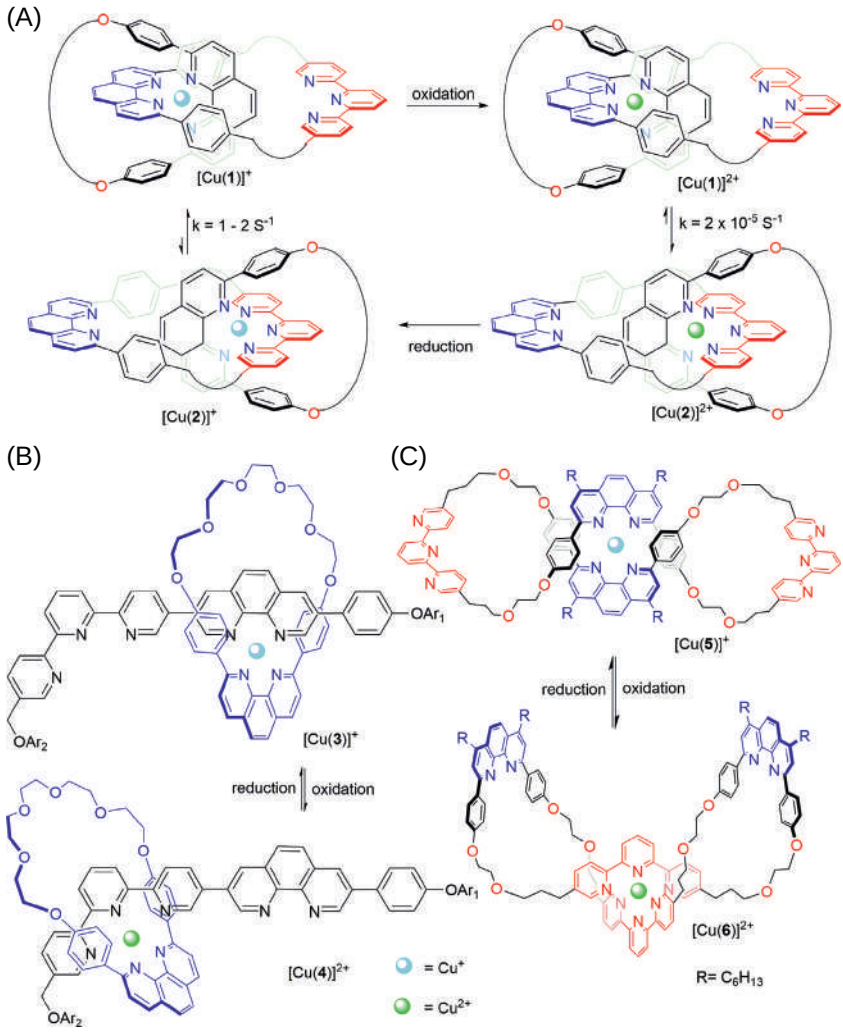

FIGURE 11.1 (A) Control of pirouetting motion in catenate **1** upon oxidation and reduction of central Cu(I) ion; (B) increase of shuttling speed with sterically less crowded phenanthroline in the thread of a rotaxane; (C) electrochemical switching between figure ∞ and 8.

those around Cu^{2+}. His group also exploited the diverse coordination preferences of Cu^{+} and Cu^{2+} to control both the spinning and translation motions in rotaxanes [13,14,111].

Typically, the spinning movement of the macrocycle about its axle is quicker than the gliding motion of the macrocycle along a molecular thread. In both cases, the rate-determining step is the cleavage of the copper–ligand coordination. The rate of the movement can be augmented with a solvent having

better donor properties as both shuttling and pirouetting motion requires dissociation of the copper–nitrogen bond. Gavina and Tatay [15] have shown that the shuttling speed can be faster by decreasing the steric crowding about the central copper ion, which will increase the size and flexibility of the ring's cavity near the chelating site. Thus, the thread of the present rotaxane is based on a 3,8-diarylphenanthroline (Fig. 11.1B) [16] instead of 2,9- diarylphenanthroline system, initially explored by Sauvage [17].

Based on the coordination favoritism of metal ions, Sauvage et al. also demonstrated the electrochemical toggling between figure "8" and figure "∞" of a macrocycle (Fig. 11.1C) [18]. Macrocycle **5** contained two phenanthrolines and two terpyridines alternately. When Cu^{+} was supplied to the macrocycle, two phenanthroline units formed an "8" shaped intramolecular complex $[Cu(\mathbf{5})]^{+}$. However, upon oxidation of $[Cu(\mathbf{5})]^{+}$, the resultant less stable tetracoordinated intermediate underwent a rearrangement such that Cu^{2+} was then coordinated to two terpyridine units to generate more stable $[Cu(\mathbf{6})]^{2+}$ that looked like "∞". Similar interconversion between two states was also validated by removing Cu^{+} and adding Fe^{2+}.

Crowley et al. explored ferrocene as a hinge [19–21,113] to demonstrate various electrochemical switching between the anti and syn conformation of 1,1'-disubstituted ferrocene. Bipyridine-appended ferrocene initially adopted a folded syn conformation due to electronic preference and π–π stacking interaction between 2,2′-bipyridine and the aryl group, as shown in Fig. 11.2A [22]. Adding $[Cu(\mathbf{8})]^{+}$ led to the formation of two heteroleptic complexes with the bipyridine units of **7**. Consequently, the scaffold adopted an extended conformation to minimize the steric repulsion and electrostatic repulsion between the cationic substituents of the ferrocene rotors. Oxidation of Cu^{+} to Cu^{2+} in the presence of **9** led to the discharge of the bipyridine moiety from $[Cu_2(\mathbf{7})(\mathbf{8})_2]^{4+}$. The thus generated $[Cu(\mathbf{8})(\mathbf{9})]^{2+}$ was more stable compared to $[Cu_2(\mathbf{7})(\mathbf{8})_2]^{4+}$ as the former was a pentacoordinate complex and **7** adopted its original contracted form.

Besides using Cu^{+}/Cu^{2+} as a redox couple, oxidation-reduction between Ni^{2+} and Ni^{3+} has also been used to control mechanochemical motion in interlocked molecules [23]. In the initial state, the rotaxane preferentially existed as a folded di-nickel complex **10** due to the π-π stacking, as shown in Fig. 11.2B [24]. Selective oxidation of one Ni^{2+} to Ni^{3+} increased the Coulomb repulsion between two nickel centers, leading to the unfolded state **11**. The system returned to the initial state after reducing to Ni^{2+} due to experiencing cohesive π–π interactions. The driving force for this reversible switching between folding and unfolding state arose from the interplay between electrostatic repulsion and cohesive π–π interaction. The electrostatic interaction outweighs the cohesive π–π interaction when $E > 1.31$ V, and the cohesive π–π interaction predominates when $E < 1.31$ V. In a similar example, the author demonstrated potential controlled switching between three states in a bimetallic rotaxane [25].

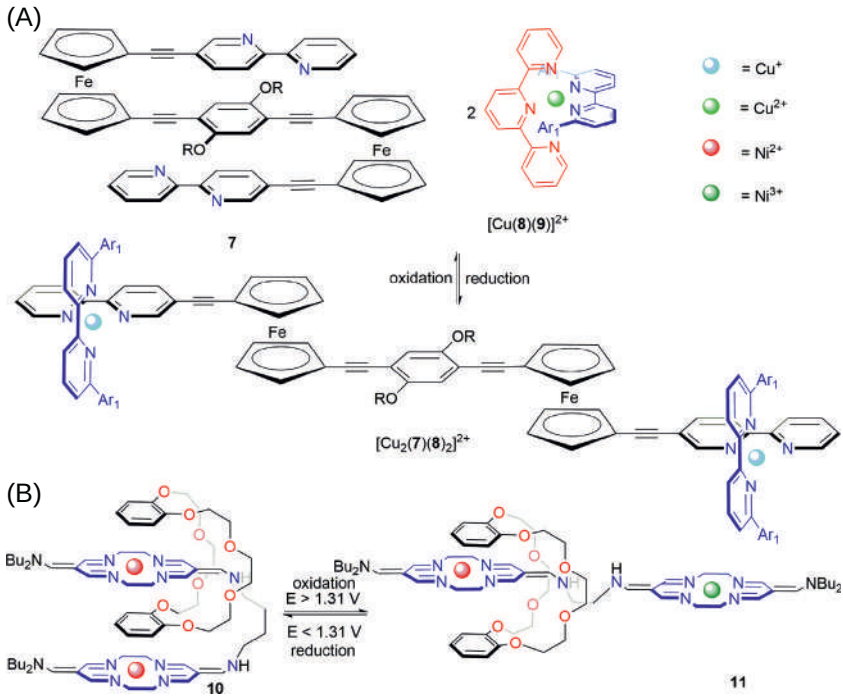

FIGURE 11.2 (A) Redox-triggered expansion/contraction motion; (B) reversible folding/unfolding of a rotaxane by electrochemical stimuli.

Until now, the selected examples deal with redox reactions at a metal center. Flood et al. validated that controlling the redox state of a redox-active ligand can drive reversible switching between [2]pseudorotaxane and [3]pseudorotaxane (Fig. 11.3A) [26]. Thus, the mixing of Cu^+, the macrocycle **12**, redox-inactive ligand **13** and redox-active ligand **14** in an appropriate ratio (1:2:1:2) led to the selective formation of [2]pseudorotaxane $[Cu(\mathbf{12})(\mathbf{13})]^+$. Due to the higher binding affinity of **13,** redox-active ligand **14** acted as a spectator ligand in the above self-sorting. However, after the reduction of **14**, the binding affinity was reversed due to an increase in electron-richness of the ligand **14**. Thus, the formation of [3]pseudorotaxane $[Cu_2(\mathbf{12})_2(\mathbf{14})]^+$ was observed by ligand exchange. The reverse switching was realized by oxidizing the thread of the [3]pseudorotaxane $[Cu_2(\mathbf{12})_2(\mathbf{14})]^+$. The conversion of [2]pseudorotaxane to [3]pseudorotaxane proceeded via a bimolecular associative ($k_f = 12000\ M^{-1}S^{-1}$) path, whereas the backward process followed a first-order dissociative path ($k_b = 50\ S^{-1}$).

Similarly, Schmittel and co-workers demonstrated that regulating the redox state of a ligand can reversibly switch the two-state nanoswitch $[Cu(\mathbf{15})(\mathbf{16})]^+$(Fig. 11.3B) [27]. When the nanoswitch **15** and the ligand **16**

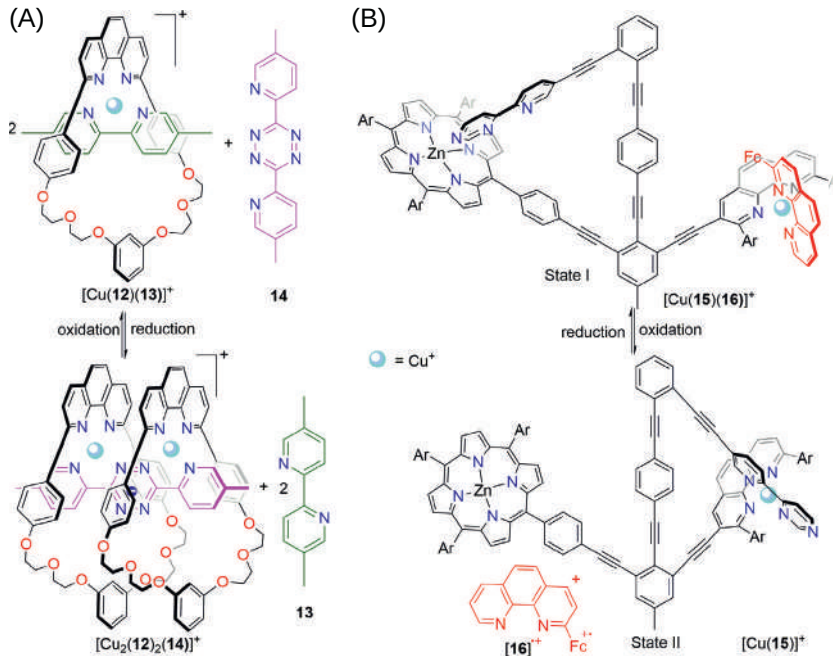

FIGURE 11.3 (A) Switching between two states of pseudorotaxane by oxidation/reduction of the redox-active thread; (B) switching between two states of a nanoswitch by controlling the redox state of a ligand.

were treated with one equivalent Cu^+, the state I was afforded. In this state, the zinc porphyrin was intramolecularly coordinated with the nitrogen of the azabipyridine unit and Cu^+ was complexed with **16** and phenanthroline unit of nanoswitch **15**. After oxidation of **16**, the oxidized ligand was detached from the phenanthroline station because of its decreased binding affinity. The azabipyridyl rotary arm occupied the thus generated vacant Cu^+ site by dissociating from the remote zinc porphyrin station. Thus, the rotary arm toggled over a 2 nm distance from porphyrin to the phenanthroline station.

11.3 Exchange of metal ions

The exchange of metal ions can alter coordination geometry preference leading to a conformation change. This approach is theoretically analogous to that of redox-activated switching in MIMs. Here, the transition metal itself is swapped instead of altering the oxidation state of the metal. Sauvage [28] presented this idea in a seminal paper on "molecular muscles." This principle has also been utilized to generate a "flapping" motion in a [3]rotaxane [29]. Leigh and co-workers also applied the exchange of metal ion protocols to fabricate a three-state switch [30]. Goldup and his co-workers also employed metal exchange

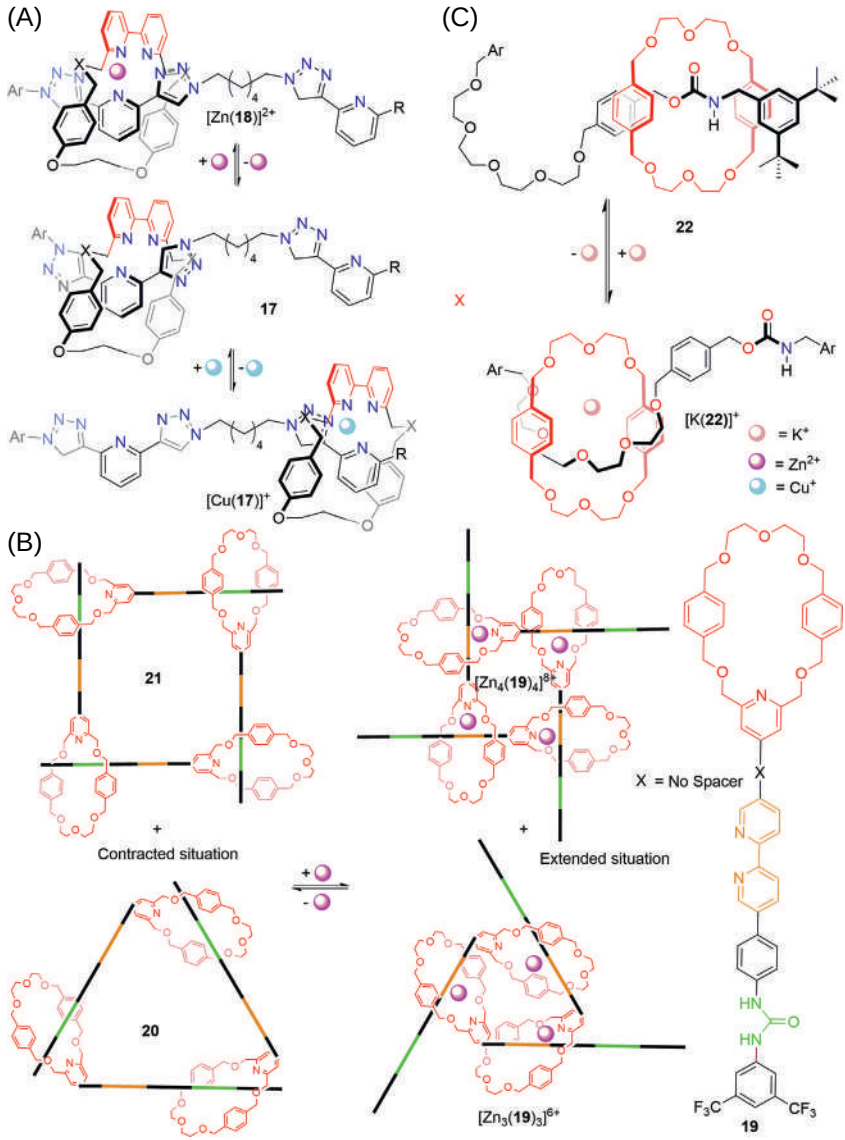

FIGURE 11.4 (A) Exchange of metal ions triggered shuttling of the macrocycle in the rotaxane; (B) control of 2 dimensional contraction−extension motion by exchanging metal ion.; (C) K^+ - triggered switching between two stations in a [2] rotaxane.

protocol to control Sauvage-type molecular shuttles in a [3] rotaxane. Initially, the macrocycle was predominantly situated on the bistriazolylpyridine (btp) station through two C−H…N hydrogen bonding interactions (Fig. 11.4A) [32]. However, the addition of Cu^+ shifted the macrocycle's position from btp station

to monotriazolylpyridine (mtp) station to afford tetrahedral complex [Cu(**17**)]$^{+}$. If the Cu^{+} was exchanged with Zn^{2+}, the macrocycle moved to the btp station where Zn is pentacoordinated.

11.3.1 Addition and removal of metal ions

An equally feasible technique to regulate molecular motion is to do metalation and demetalation of appropriate metal ions. Although redox-triggered switching is a waste-free process, metalation-demetalation techniques clearly benefit metal−ligand interaction's excellent predictability and directionality. One of the states is confirmed by coordination, whereas the other states are achieved using another noncovalent interaction such as π–π stacking, hydrogen bonding etc. Thus, this section will be subdivided by depending on the 2nd type of interaction other than metal–ligand interaction.

11.3.1.1 Hydrogen bonding vs metal ion

Incorporating metal–ligand coordination with hydrogen bonding interaction is one of the most frequently used procedures to control molecular level motion. This section will discuss selected examples that simultaneously apply metal–ligand coordination and hydrogen bonding interaction to control molecular motion. Chiu et al. extended the concept of extension/contraction of Sauvage's daisy chain [28] to the 2D space using a ligand (**19**) composed of three binding motifs. The ligand **19** assumed a contracted triangle **20** or square **21** architecture without any stimuli through hydrogen bonding between urea and the macrocycle's ethylene glycol units (Fig. 11.4B) [33]. Adding Zn^{2+} drove the rupturing of hydrogen bonding and the formation of extended 2D daisy-chain by chelating with bipyridine and pyridine units. The system could be reversed back by the removal of Zn^{2+}.

In another example, Chiu et al. reported shuttling of 26-crown-6 based macrocycle in rotaxane **22**. Initially, the macrocycle occupied the carbamate station through hydrogen bonding interaction (Fig. 11.4C) [34]. Upon adding one equivalent of K^{+}, the macrocycle relocated to the oligo ethylene glycol unit, where the K^{+} was stabilized by electrostatic attraction. Adding one equivalent of [2.2.2] cryptand removed the K^{+} leading to the regeneration of the initial state.

11.3.1.2 π–π interaction versus metal ion

An amalgamation of metal–ligand coordination with π–π interactions is also a successful strategy to regulate molecular level motion. Sauvage et al. exploited π–π interaction and metal–ligand interactions to control coconformation in catenates and rotaxanes [35]. In a recent example, Bardelang et al. used metal–ligand interaction and cation–π interaction to switch between two conformations of a rotaxane in an aqueous medium. In the initial state, the cucurbit[7]uril (**23** = CB[7]) unit was on the viologen station of the rigid molecular axle **22**

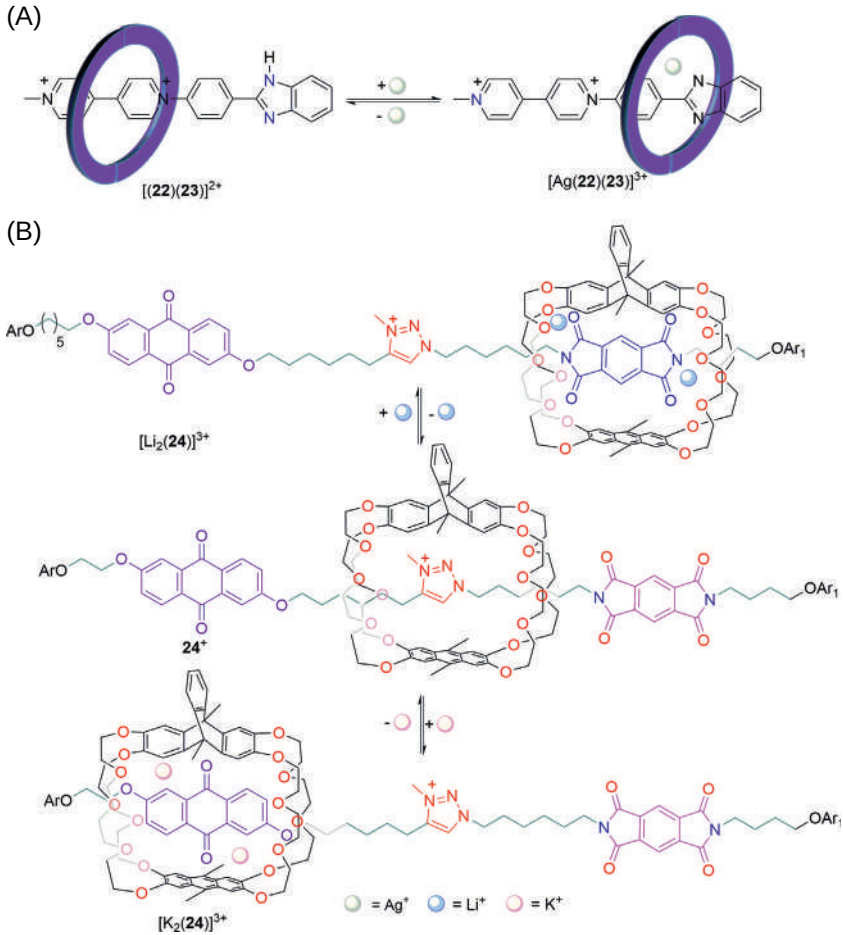

FIGURE 11.5 (A) Silver(I)-mediated translocation of cucurbit[7] uril (CB [7]) between two stations of a rigid molecular axle.; (B) K^+ ion triggered shuttling of triptycene-based macrocycle among three stations in the rotaxane.

through cation-π interaction (Fig. 11.5A). (H. [36]) After adding Ag^+, **23** was transported from the viologen station to the benzimidazole unit. The system can be reversed back to the initial state by the removal of Ag^+. It was observed that the ions such as Na^+, Mg^{2+}, Cs^+, Ca^{2+}, Co^{2+}, Ni^{2+}, Zn^{2+}, Mn^{2+}, and Ga^{3+} did not induce this repositioning of CB unit, whereas Cr^{3+}, Al^{3+}, and Fe^{2+} metal ions stimulated metal-actuated protonation leading to precipitation.

In another example, Chen et al. designed and synthesized a rotaxane using K^+ ion as a template. The center of the axle of rotaxane contained N-methyltriazolium (MtA) unit. In contrast, the two terminals of the axle were functionalized with a pyromellitic diimide (PmI) unit and an anthraquinone

(AQ) unit (Fig. 11.5B) [37]. The triptycene-based macrocycle was initially situated on the MtA station due to intercomponent hydrogen bonding and $\pi-\pi$ stacking interaction between methyltriazolium and anthracene units. However, after adding four equivalents of K^+, the macrocycle toggled to the AQ station due to $\pi-\pi$ interactions between the aromatic rings and ion−dipole stabilization. When K^+ was removed by adding six equivalents of 18-crown-6, the macrocycle relocated to the MtA station. Again, the addition of three equivalents of Li^+ triggered the repositioning of the triptycene-based macrocycle from MtA station to the PmI station due to attractive interactions between the PmI and the lithium-ion bound anthracene. 12-crown-4 could remove the Li^+ ions and drive the macrocycle back to the MtA station. The same group also demonstrated a metal–ion triggered cable car type motion in tristable [n]rotaxane [38].

11.3.1.3 Electrostatic repulsion vs metal ion

Yashima et al. developed a series reversible springlike extension−contraction motion of double-stranded spiroborate helicate triggered by alkali metal ions [39–41]. In a recent example, the author synthesized a double-stranded spiroborate with terminal pyrene residues as a fluorophore. In the presence of Na^+ ion, the spiroborate **25** adopted a contracted racemic rac-[Na(**25**)]$^-$ (Fig. 11.6A) [42] in which pyrene units were tilted away from each other, consequently showing a monomer emission at 440 nm. The addition of cryptand [2.2.1] removed the Na^+ from the mixture, thereby forming an extended racemic form to minimize the electrostatic repulsion between two boronate units. In this extended state, the terminal pyrene residues in each strand were in close spatial vicinity, thereby displaying the green excimer emission around 500 nm. The contraction was less when the size of the cation increased, as revealed by the thermodynamic analysis. Thus, the fluorescence color change from the green excimer emission to the blue monomer emission due to the contracted form was most significant for Na^+ and negligible for Cs^+.

Bipyridine unit prefers to exist in the trans conformation due to electrostatic repulsion between two lone pairs on nitrogen. However, in the presence of a metal ion, bipyridine changes to syn conformation. Rebek recognized this concept in a seminal paper on metallo regulated allosteric switches [43,44,112]. Later, many other research groups have utilized this concept to design several other metallo regulated switches [45]. In a recent example, Che and co-workers utilized the conformational change of a triptycene derived polypyridiyl unit to make a molecular gear. Thus, molecule **26** existed in all anti conformation due to electrostatic repulsion among lone pairs on nitrogen (Fig. 11.6B) [46]. In this state, the closeness of the triptycene units prevented their movement and thus formed an intermeshed state. The addition of Ag^+ switched to all syn conformation due to the formation of metal pyridyl complex. Consequently, the triptycenes moved apart to form the demeshed gear state. The demeshed state was reversed to the initial intermeshed state simply by adding Cl^-, which

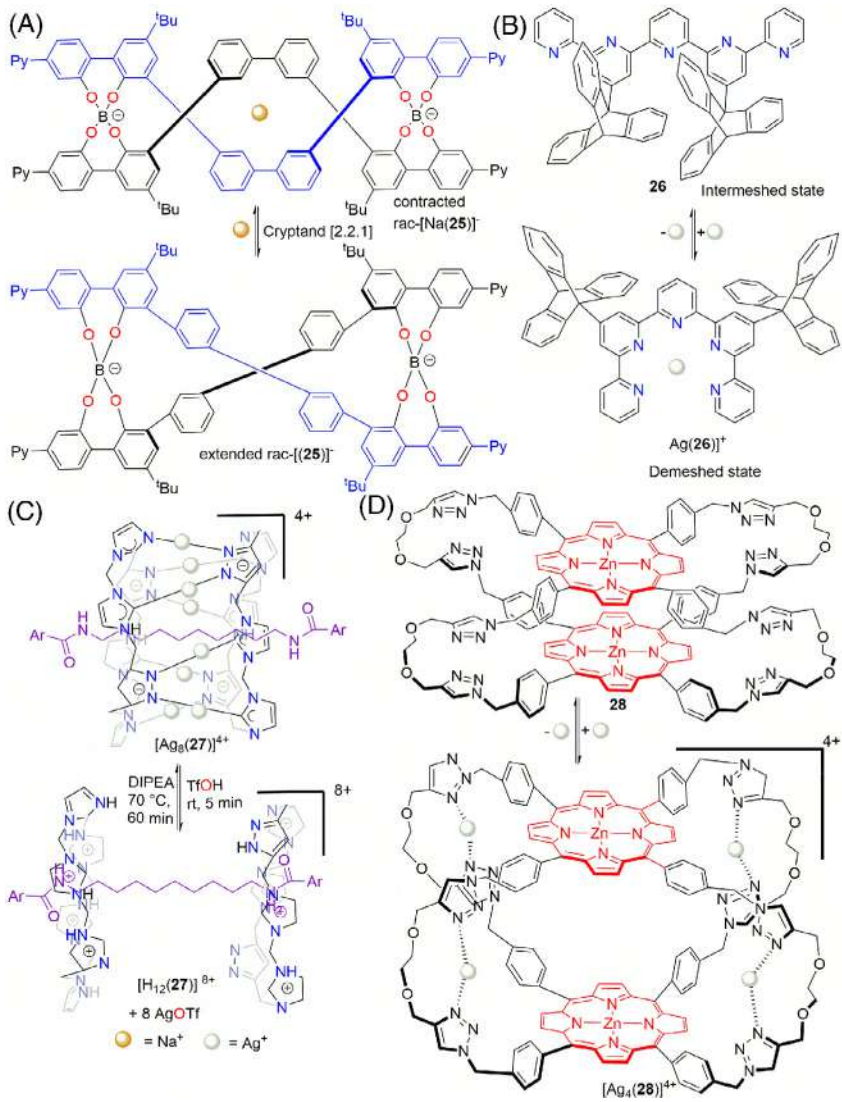

FIGURE 11.6 (A) Sodium-ion triggered reversible extension-contraction of a helicate; (B) coordination-driven interconversion of intermeshed−demeshed state of a triptycene-based gear; (C) reversible interconversion between [2]rotaxane and [3]rotaxane by metalation and demtallation; (D) metal ion driven cavity size change of a bisporphyrin host.

removed the Ag^+ as AgCl precipitate. Electrostatic repulsion and metal–ligand interaction have also been used for folding-unfolding or extension-contraction motion [47–49].

Metalation and demetallation technique has also been used for reversible interconversion between a [2]rotaxane and [3]rotaxane. In the presence of an

Ag^+ ion and a thread, the NHC-based organometallic scaffold pillarplex quantitatively formed the [2]rotaxane $[Ag_8(\mathbf{27})]^{4+}$ (Fig. 11.6C) [50]. The addition of triflic acid removed the Ag^+ from the [2]rotaxane. Due to the electrostatic repulsion of the positively charged imidazolium centers, cyclophane moieties gets separated. Thus the [2]rotaxane was converted to [3]rotaxane $[H_{12}(\mathbf{27})]^{8+}$. When diisopropylamine was added to the mixture and heated at 70°C for 1 h, the initial [2]rotaxane was regenerated. Several interconversions cycles were performed without causing any decomposition.

Electrostatic repulsion and metal–ligand interactions have been used together to control the internal cavity size of several hosts. Thus, Heitz and co-workers [51] synthesized bisporphyrin hosts connected with flexible linkers via triazole units. The hosts adopted a compact structure without any metal ion due to π–π stacking interaction between two porphyrin units. The addition of Ag^+ increased the cavity size due to the complex formation between two triazole units, as shown in Fig. 11.6D [52]. The cavity size could be brought back to its initial size by adding chloride ions to remove Ag^+. It was important to note that the addition of protons increased the cavity size of the hosts from 3.81 Å to 20 Å (maximum) due to electrostatic repulsion among protonated triazole.

The addition and removal of metal ions have also been used to control a linear strand's contraction–extension motion [53]. The ligand was made up of hydrazone-connected 2,5 and 2,6-disubstituted pyrazine units, as shown in Fig. 11.7. The ligand adopted a linear anti conformation to minimize the electrostatic repulsion among nitrogen lone pairs. Adding metal ions such as Ca^{2+}/ Mg^{2+}/ Zn^{2+} drove complex formation, leading to the contracted Z-shaped state. It was important to note that this reversible metal–ion-induced contraction of a linear strand to a Z-shaped structure was accompanied by an average change in length of about 17 Å.

11.4 Application of molecular motion

Over the last two and a half decades, chemists have utilized the progress in artificial molecular machines to perform sophisticated tasks such as controlled directional transport [54,55], synthesis of small molecules [56], ON/OFF regulation of catalysis [57,58,108], etc. The present chapter demonstrates how various functions may be controlled and switched due to the metal–ligand coordination-driven toggling between states. Although other stimuli often switch optical, electrical, and magnetic effects, coordination-driven molecular motion is an emerging substitute that opens future possibilities [59].

11.4.1 Chirality inversion

Metal coordination has been used to switch the absolute chirality of molecules, thus providing a way to make a chiral switch. Recently, we have summarized the fascinating developments in this crucial arena in a review [60]. This section

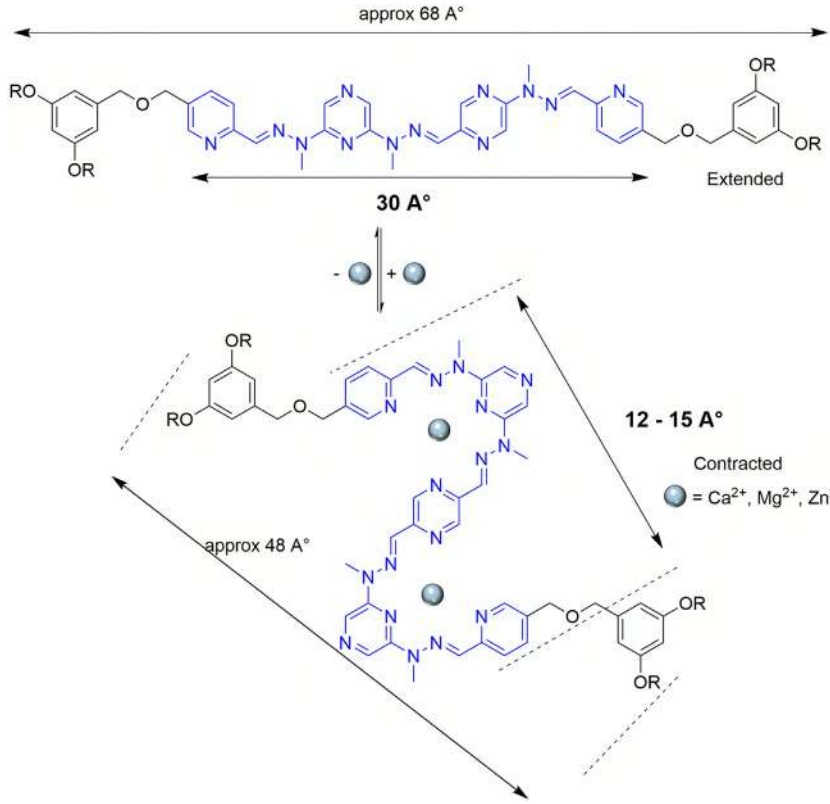

FIGURE 11.7 Schematic representation of metal ion-driven extension-contraction type motion.

will highlight some selected examples of coordination-driven nanomechanical motion to switch chirality.

Nabeshima and co-workers demonstrated manifold helicity reversals in a chiral switch by multiple metal exchanges [61]. Another example established novel molecular leverage for helicity control and helix inversion by changing the guest [31,62]. Albrecht and co-workers have extensively studied metal ion driven contraction-extension motion of catechol derived helicates [63,64,105]. In a recent example, they also demonstrated reversible helicity switching of a catechol derived helix [65]. The enantiopure ester-bridged dicatecholate ligand **29** formed an extended left-handed helix in the presence of two Ti^{4+} ions (Fig. 11.8A). The addition of Li^+ triggered the switching of helicate from the left-handed expanded state to the left-handed compressed state $[Ti_2Li_3(\mathbf{29})_3]^{4-}$ because of the coordination of oxygens to lithium. In contrast, the addition of K^+ drove the switching of helicity from the left-handed expanded to the right-handed expanded helix. The initial left-handed expanded state could be regenerated by removing Li^+ and K^+ with [2.1.1] cryptand and 18-crown-6, respectively. The

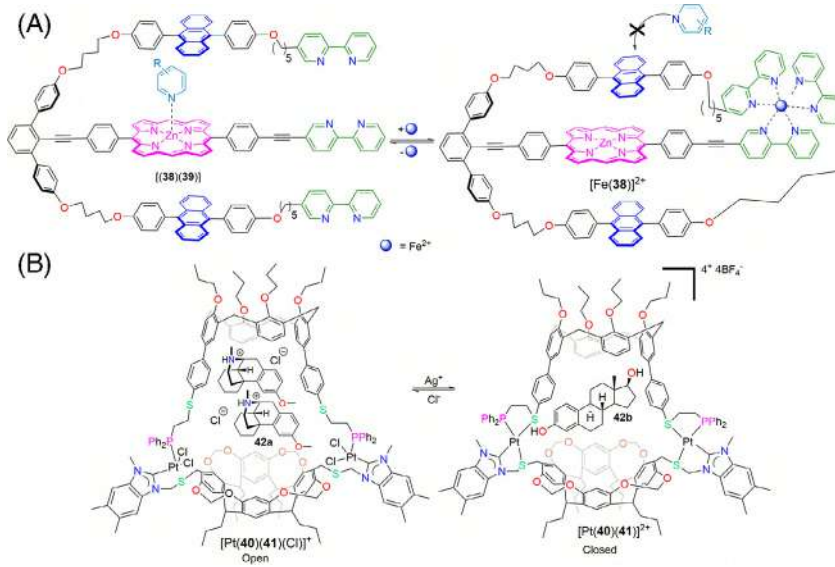

FIGURE 11.8 (A) Alkali metal triggered a helicity inversion; (B) inversion of pillar[5]arene derivatives by addition and removal of mercury ion; (C) redox triggered inversion of planar chirality switching of pillar[6]arene **34**.

direct metal exchange also activated the switching from right-handed extended $[Ti_2K_2(\mathbf{29})_3]^{2-}$ to left-handed contracted $[Ti_2Li_3(\mathbf{29})_3]^{-}$ because of the higher binding affinity of Li^+.

Lee and co-workers presented (E. [66]) metal ion-driven inversion of planar chirality of a pillar[5]thiacrown based pseudo [1]catenane. Due to the presence of alkoxy substituents and the hindered rotation of aromatic units, pillar[5]thiacrown based pseudo [1]catenane can exist in two stable enantiomers (*pS* and *pR*). Additionally, switch **30** has a possibility of *in*-and *out*-equilibrium of the fused thiacrown moiety. In the absence of any ion, the pseudo [1]catenane **30** existed in a conformation in which the fused thiacrown ring was included inside the pillar[5]arene cavity via stabilizing CH● ● ●π interactions (Fig. 11.8B). However, when Hg^{2+} was added to the system, the thiacrown cavity afforded a complex (log K = 4.1) in an endo mode through weaker coordination of ClO_4^- anion. Thus, the thiacrown expanded (0.70 nm Å$\sim$ 0.71 nm) and came outside the pillar[5]arene as the complex was too large to fit inside the pillar[5]arene. Consequently, the inversion of planar chirality from in-*pS*-**30** to *out-pR*-**31** occurs. The addition of excess S^{2-} (as Na_2S) removed the Hg^{2+}, thereby switching back to the initial state. In contrast, if HgI_2 was used instead of $Hg(ClO_4)_2$, the thiacrown moiety formed an exo complex *in-pS*–**32** due to the strongly coordinated iodo ligands without significant conformational changes, resulting in no chiral inversion.

The planar chirality of a bicyclic pillar[6]arene derivative has also been switched by controlling the redox state of a metal [67]. The pillar[6]arene scaffold was integrated with a ferrocene-based side ring. In a polar solvent such as acetonitrile, P[6] core **34** adopted an *out*-(*pS*) configuration. The ferrocenyl side-chain was situated outside the P[6] cavity, possibly due to better solvation of ferrocene moiety (Fig. 11.8C) and solvent-induced disruption of the intramolecular hydrogen bond between ferrocene unit and P[6] core. When the ferrocene unit was oxidized to ferrocenium ion with $Fe(ClO_4)_3$, a self-inclusion (*in* conformer) complex was obtained due to the higher binding affinity of the ferrocenium unit towards the host P[6]. Simultaneously, the chirality of the system was also inverted from *out-pS* to *in-pR*. The system can be reversed back to its original *out-pS* states by reducing ferrocenium ions with sodium ascorbate. The reversible interconversion between "*in*" and "*out*" states could be iterated for at least five cycles without noticeably decreasing the signals' intensity.

11.4.2 Guest release and uptake

As the large amplitude motions between different states are often accompanied by significant changes in electronic and steric environments at binding centers, the binding constants for guest molecules may be significantly modified. This change in the guest binding affinity between different states is advantageous for selective encapsulation and separation of guests, cargo delivery, toxin sequestration, etc. [68].

In this regard, 2,2′-bipyridine derivatives have been used to regulate guest uptake and release by controlling the conformations between syn and anti. In a recent example, Lützen and co-workers demonstrated the allosteric encapsulation of nonpolar guests by the coordination-driven conformational switching of bipyridine derivatives (Fig. 11.9) [69]. Thus, the cyclodextrin appended bipyridine switch **35** adopted an anticonformation without any metal ion. In this state, two β-cyclodextrin units were far apart and thus were ineffective for encapsulating guests such as capsaicin (**37**). In contrast, when $[Zn(\mathbf{36})]^{2+}$ was added to **35**, the conformation of bipyridine was changed from anti to syn due to the formation of complex $[Zn(\mathbf{35})(\mathbf{36})]^{2+}$. The two β-cyclodextrin units were then in a perfect position to encapsulate capsaicin. The syn form had a five times higher binding constant toward capsaicin than the antiform, and thus release was possible by removing Zn^{2+} with EDTA. Several allosteric binding events were moderated based on the similar conformational control in bipyridines [70,71]. Like bipyridine, the bis-indole [72] unit has also been utilized as a hinge to regulate selective uptake and release of guest molecules.

The conformational control of a trisbipyridine unit has also been used to modulate guest binding affinity. In the metal-free state, pyridine derivatives coordinated to the central zinc porphyrin of **38** due to higher affinity (Fig. 11.10A) [73]. However, when one equivalent of Fe^{2+} was added to the system, the three bipyridine terminals of the **38** engaged themselves to form

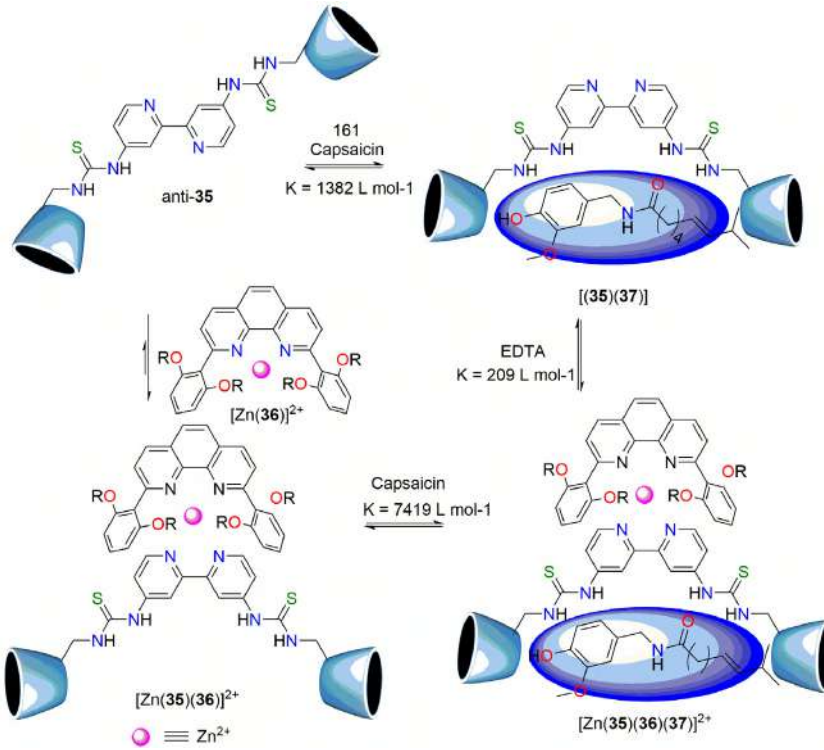

FIGURE 11.9 Control of guest uptake and release by controlling anti- and syn-conformation of a bipyridine derivative.

an octahedral complex. The thus formed complex forced middle anthracene groups to block the zinc porphyrin from both the upper and lower face resulting in a decrease in the binding constant of pyridine by a factor of 10. Based on the similar porphyrin pyridine axial coordination, the cavity size of several bisporphyrin based tweezers [74,75] have been modulated for guest uptake and release.

Based on the weak-link approach, Mirkin demonstrated several examples of regulation of guest encapsulations. In a recent example, the author synthesized an open asymmetric capsule composed of a calix[4]arene derivative and a resorcin[4]arene derivative [76]. Fig. 11.10B shows that each Pt^{2+} center is coordinated to a thioether unit, an N-heterocyclic carbine and two chlorides. The open state can encapsulate guest molecules such as **42a** (Ka11 $= 70 \pm 5$ M^{-1}, Ka12 is 6 ± 2 M^{-1}) due to favorable cation-π interactions between the electron-rich aromatic moieties of the host and the electron-deficient cationic ammonium moiety of the guest molecule. The addition of Ag^{+} removed the chloride, thereby forming a closed, contracted host which selectively encapsulated β-estradiol (Ka11 $= 44 \pm 6$ M^{-1}), probably because of hydrophobic

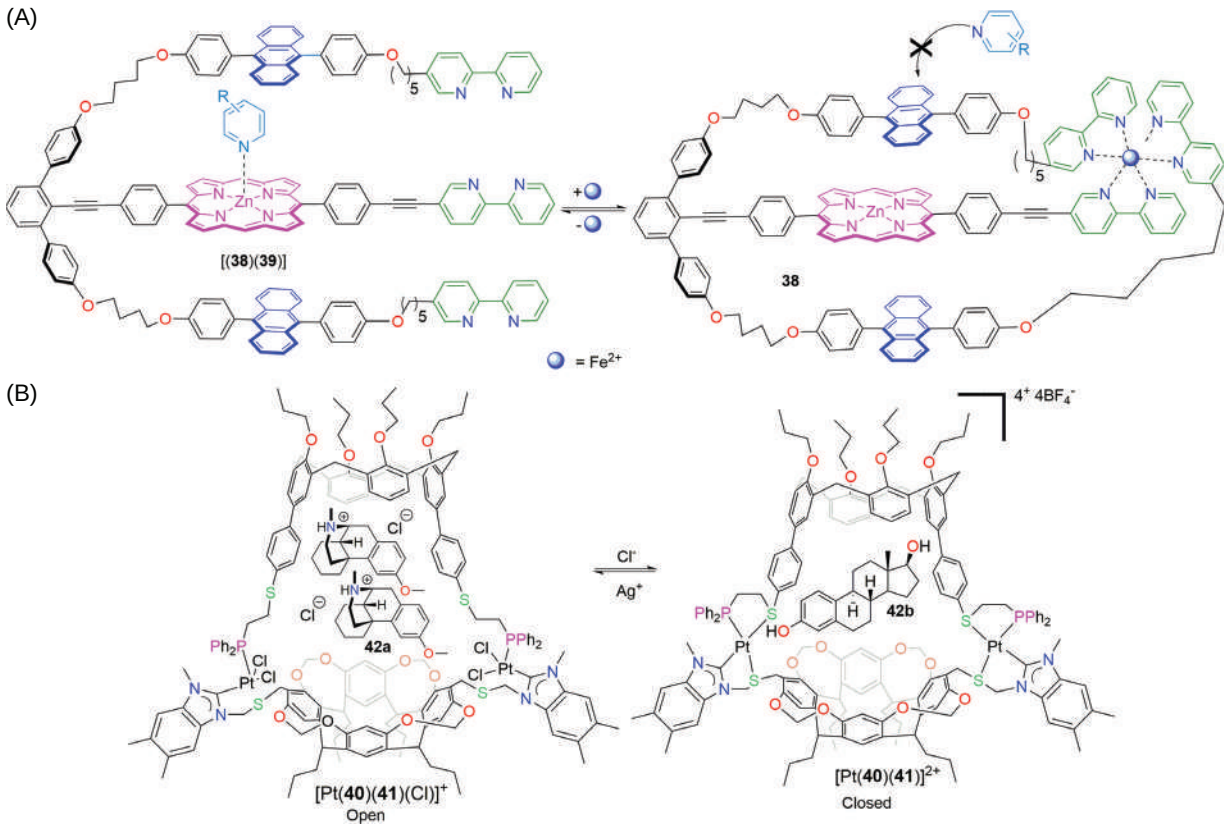

FIGURE 11.10 (A) Coordination-driven control of guest binding; (B) regulation of guest encapsulation via weak-link approach.

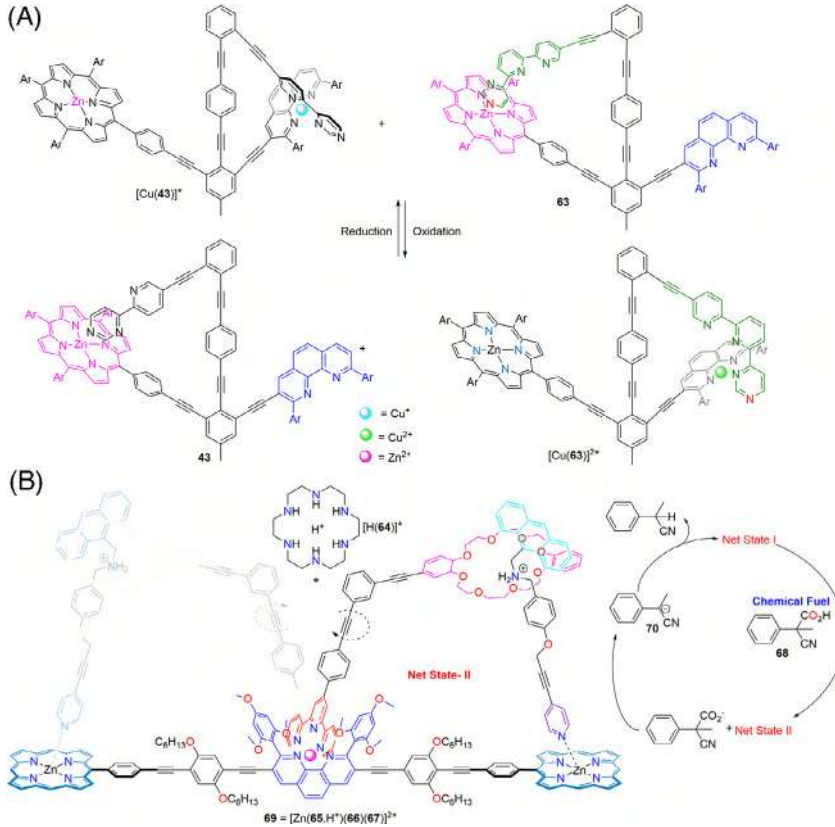

FIGURE 11.11 Schematic representation of metal ion-driven cavity size changes of a capsule that leads to conformational change of a guest.

interactions and C−H/π interactions between the rigid hydrophobic binding cavity of host and the guest **6**. In another example, phosphine alkyl thioether substituted calix[4]arene was used to control the uptake of charged and neutral guest molecules by modulating the charge- and size of the inside cavity [77]. Stoddart et al. also reported on metal–ion-driven allosteric regulation of guest binding affinities of a host [78].

The addition and removal of metal ions have also been utilized to modulate the cavity size of cages that eventually control the folding unfolding of a guest molecule. Thus, the author synthesized a resorcinarene-based dimeric capsule with a bipyridine unit in between, as shown in Fig. 11.11 [79]. In the absence of any metal, the capsule existed as an extended conformation (**43a**) that weakly encapsulated acetoxy group-terminated alkanes. When Cu^+ was added to the capsule, the bipyridine units engaged themselves in making complex, thereby leading to the contraction of the cavity size of the capsule (**43b**). It was important

to note that the contracted capsule encapsulated the acetoxy group-terminated alkanes strongly and changed their conformation from unfolded state to folded state.

11.4.3 Switchable catalysis

In recent years, switchable catalysis has gained enormous interest among the scientific community [80] where natural systems frequently act as a source of inspiration. In the following, we will highlight systems that utilize coordination-induced motion(s) for switchable catalysis.

Over the decades, the Schmittel group has mastered coordination-driven self-assembly and their application in designing switches that regulate ON/OFF catalysis. Thus, they prepared several two-state nanoswitches that can be used for ON/OFF control of Knovenagel reaction [81], isomerization of azastilbene [82], cyclopropanation reaction [84], etc. In a relatively recent example, the authors demonstrated that two different states of a nanoswitch could control two different reactions [83]. In this case, the two-state nanoswitch **15** was a self-locked system by intramolecular coordination of the azabipyridine arm to the ZnPor unit. When one equivalent Cu^+ was added, the azabipyridine arm moved from the porphyrin station to the shielded-[1,10]-phenanthroline station to yield a HETPHEN complex. The nanoswitch can be reversed back to its initial state by removing the Cu^+ with cyclam. The nanoswitch can also be reversibly toggled between the three states (states I → II → III → I) in the presence of piperidine. When appropriate ratio of **15, 44**, $[Cu(\mathbf{45})]^+$ and Cu^+ (1:1:1:2) were mixed, the nanoswitch existed in State 1 (Fig. 11.12). In this state, azabipyridine was coordinated to phenanthroline via a HETPHEN type complex, and piperidine was coordinated to the zinc porphyrin. Thus, piperidine was unavailable in solution to catalyze a Knoevenagel reaction between diethyl malonate (**46**) and 4-nitrobenzaldehyde (**47**). However, as $[Cu(\mathbf{45})]^+$ was present in the solution, it can promote a click reaction between alkyne **48** and azide **49**. If one equivalent of **45** was added to State 1, nanoswitch did not change its conformation. However, Cu^+ was then masked as bishomoleptic complex, and the click reaction was shut down. When one equivalent of **45** was added to State 2, the nanoswitch's shielded [1,10]- phenanthroline formed a HETPHEN complex with the **45**. Subsequently, the bipyridine unit detached from the phenanthroline station and coordinated to the Zn porphyrin. The released piperidine can promote Knovenagel reaction between **46** and **47**. The system can be reset to its initial state by the addition of one equivalent of Cu^+. Sequential catalysis [85] has also been reported by the same group employing coordination-driven molecular motion of a four-state nanoswitch.

Schmittel et al. have also developed a family of multi-component nanorotors [86] (S. [87]) [88,89,109] where the speed of the blades can be modulated. The same group also had utilized these multi-component machineries for controlling catalysis. Thus, the state I was fabricated when the tetrahedral circular track

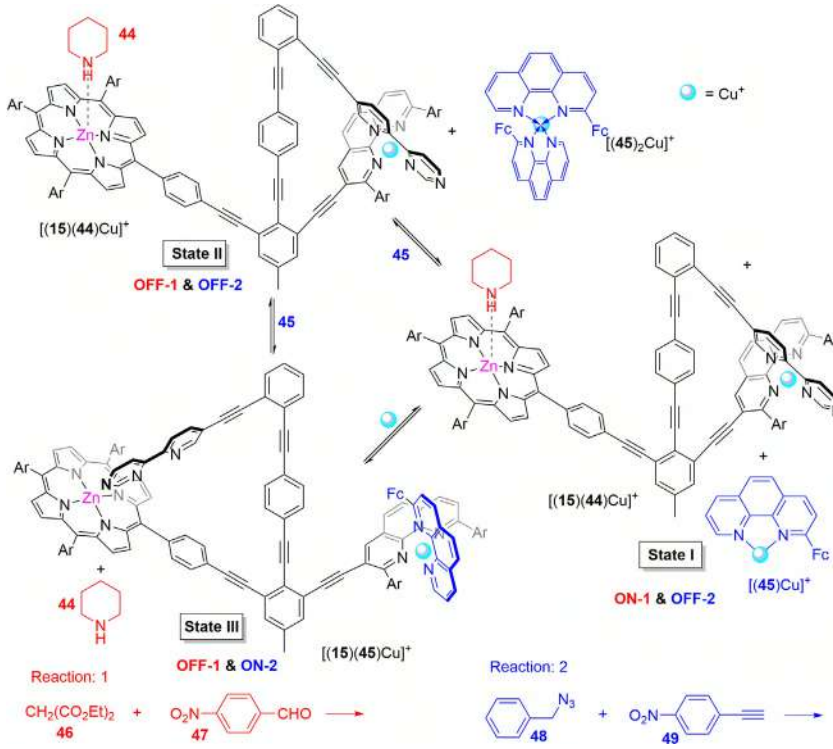

FIGURE 11.12 Metal ion triggered regulation of two catalytic reactions from two different states.

50, biped **51**, and N-methyl pyrrolidine were mixed [90]. In this state, the two picoline terminals of **51** were coordinated to Zn porphyrin forcing the N-methyl pyrrolidine (cat) to be free in solution (Fig. 11.13). Thus, the exposed catalyst can catalyze the conjugate addition of thiophenol (**52**) to cyclopentenone (**53**). The addition of 1 equivalent of Cu^+ to State I generated [Cu(**50**)(**51**)]$^+$ which forced the biped to detach one picoline foot from the zinc porphyrin and to attach it to the Cu^+ loaded phenanthroline station. In this state, half of N-methyl pyrrolidine was bound to the zinc porphyrin, while the other half was still accessible in a solution that would give a catalytic reaction. When another equivalent Cu^+ was supplied, state III was generated. In this state, two picoline terminals of **51** were coordinated to two Cu^+ loaded phenanthroline stations. N-methyl pyrrolidines were coordinated to two zinc porphyrin stations, and thus catalysis was switched off.

Chiu et al. demonstrated that the coordination-driven pirouetting motion of a [2]rotaxane could regulate the outcome of a Michael addition reaction of diethyl malonate to β-nitrostyrene (Fig. 11.14A). (Y. J. [91]) An amide group was present in the middle of the thread of the rotaxane. In contrast, the macrocycle comprised triethylene glycol and tertiary-amine as binding sites for the thread.

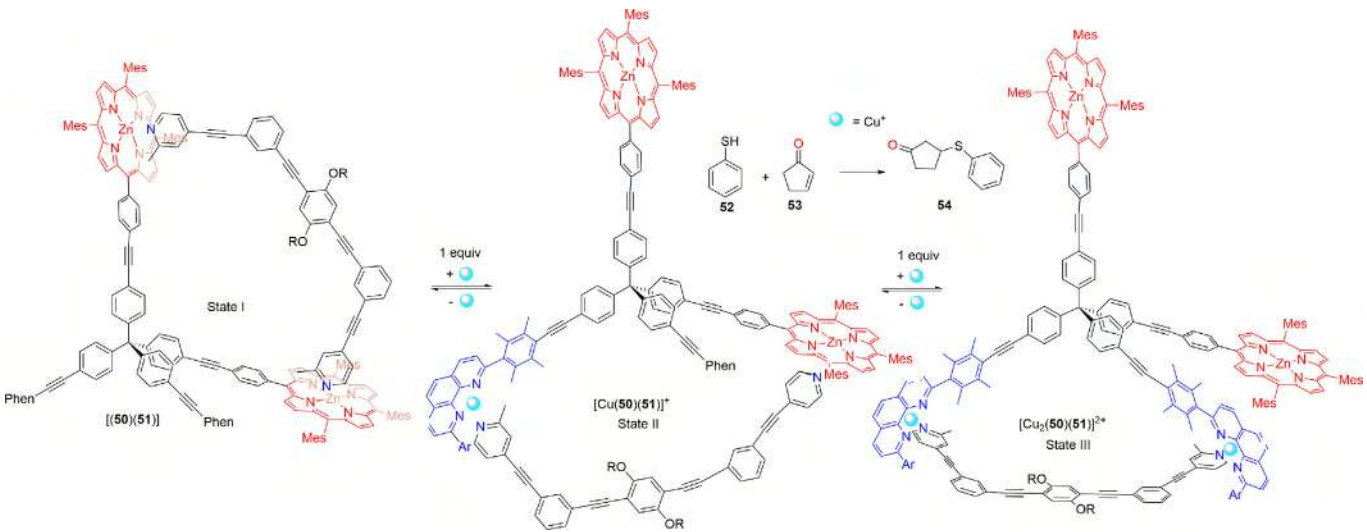

FIGURE 11.13 A multi-component supramolecular machine for controlling catalysis.

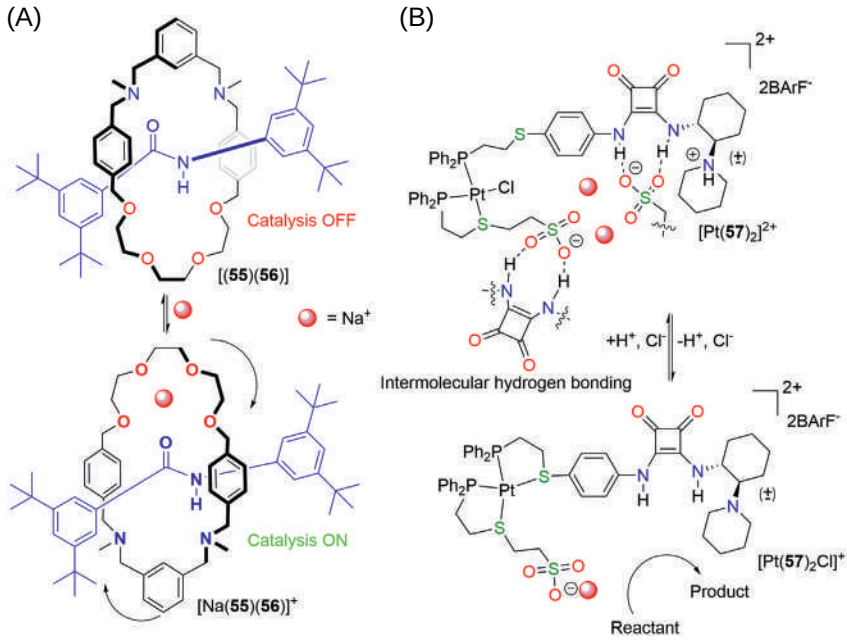

FIGURE 11.14 (A) Switchable catalysis triggered by coordination-driven pirouetting motion of a [2]rotaxane; (B) allosteric control of the Diels–Alder reaction by exploiting weak-link approach.

In the initial state of the rotaxane, the triethylene glycol unit remained close to the central amide unit's −NH− due to weak hydrogen bonding. This state was catalytically inactive for Michael addition reaction of diethyl malonate to β-nitrostyrene. However, when Na^+ was added, the macrocycle underwent a pirouetting motion to bring the ethylene glycol motifs close to Na^+. In this state, Na^+ was complexed with ethylene glycol's oxygen and the thread's carbonyl oxygen and can promote the Michael addition of diethyl malonate to β-nitrostyrene. A redox responsive nanoswitch altered the enantioselectivity of the same Michael addition reaction [92].

Mirkin and co-workers developed and exploited the weak-link approach (WLA) to control a metal center's coordination environment to regulate several diverse catalytic reactions allosterically [93,94]. Thus, the author synthesized a heteroligated Pt^{2+} tweezer functionalized with sodium sulfonate and a squaramide–tertiary amine unit in a recent example [95]. In the absence of any auxiliary ligands, the tweezer adopted a fully closed state $[Pt(\mathbf{57})_2]^{2+}$ (Fig. 11.14B). Because of the rigidity, steric bulk, and geometry of the fully chelated metal center, the sulfonate unit cannot establish hydrogen bonding with squaramide unit, thus allowing the squaramide to increase the electrophilicity of cyclic ester through hydrogen bonding. So, the closed state can catalyze the ring-opening polymerization between alcohol and cyclic ester. The addition of

auxiliary ligand such as Cl^- (as pyridinium chloride) led to substituting weakly the weakly coordinated sulfur donor sites, allowing a switch from a rigid-closed to a flexible semi-open form $[Pt(\mathbf{57})_2Cl]^+$. This state allowed the sulfonate unit to establish intermolecular hydrogen bonding with squaramide, thus switching of the polymerization reaction. Several in-situ ON-OFF cycles were performed by adding pyridinium chloride and NaHDMS consecutively.

11.4.4 Signal transduction and networking of several switches

Recently, the focus of this field has been changing beyond stand-alone molecular devices to complex networks as observed in biological systems. Thus, we expect emerging functions from these networked machineries that are not possible from stand-alone molecular switches. To realize these networked machineries, we need high fidelity communications between individual molecular switches via orthogonal stimuli. In this regard, metal coordination offers a reliable protocol to control multiple devices. The following section will portray recent examples of the operation of multiple switches in solution to obtain some emerging functions.

Aprahamian and co-workers first established a metal ion-induced cascade of signal transduction between two architecturally diverse hydrazone-based rotary nanoswitches. The same group also utilized a hydrazone based-switch to demonstrate a negative feedback loop. (S. [96]) The switch **58** preferentially existed in the *E* configuration through an intramolecular hydrogen bond, as shown in Fig. 11.15A. When Zn(II) ions were added to a mixture of **58** and **59**, nanoswitch **58** selectively bound to the Zn^{2+} with quinolinyl nitrogen, amide nitrogen, and ester oxygen. The switch then underwent *E* to *Z* isomerization with a simultaneous shifting of the N–H proton from amide nitrogen to pyridine nitrogen. The protonated pyridine can catalyze the deprotection of **59** to **60,** which reacted with pyridine aldehyde (**61**) to form the tridentate imine ligand **62**. Zn(II) was then transferred from $[Zn(\mathbf{58})]^{2+}$ to the ligand **62** because of its higher binding affinity towards Zn^{2+} than the initial switch **58**. As a result, the initial state was regenerated. It was important to note that if the concentration of the Zn^{2+} was above a particular threshold concentration of 20 mol%, then only the protonated pyridine can catalyze the deprotection of **59**, leading to a cascade of reactions to regenerate the initial state. This example established an advanced negative feedback loop to regulate the active concentration of available protons in solution.

Similar to proton translocation, metal ion translocation triggered by another metal ion has been extensively used by Schmittel et al. to demonstrate the networking of molecular switches and communication catalysis. Thus, the two triangular nanoswitches **43** and **59** constituted state 1 (Fig. 11.15B) [97] in the presence of Cu^+, where the nanoswitch **59** was intramolecularly coordinated with Cu^+. Formation of $[Cu(\mathbf{43})]^+$ should be less favorable as it would require the intramolecular axial Npy → ZnPor coordination cleavage. When Fe^{2+} was

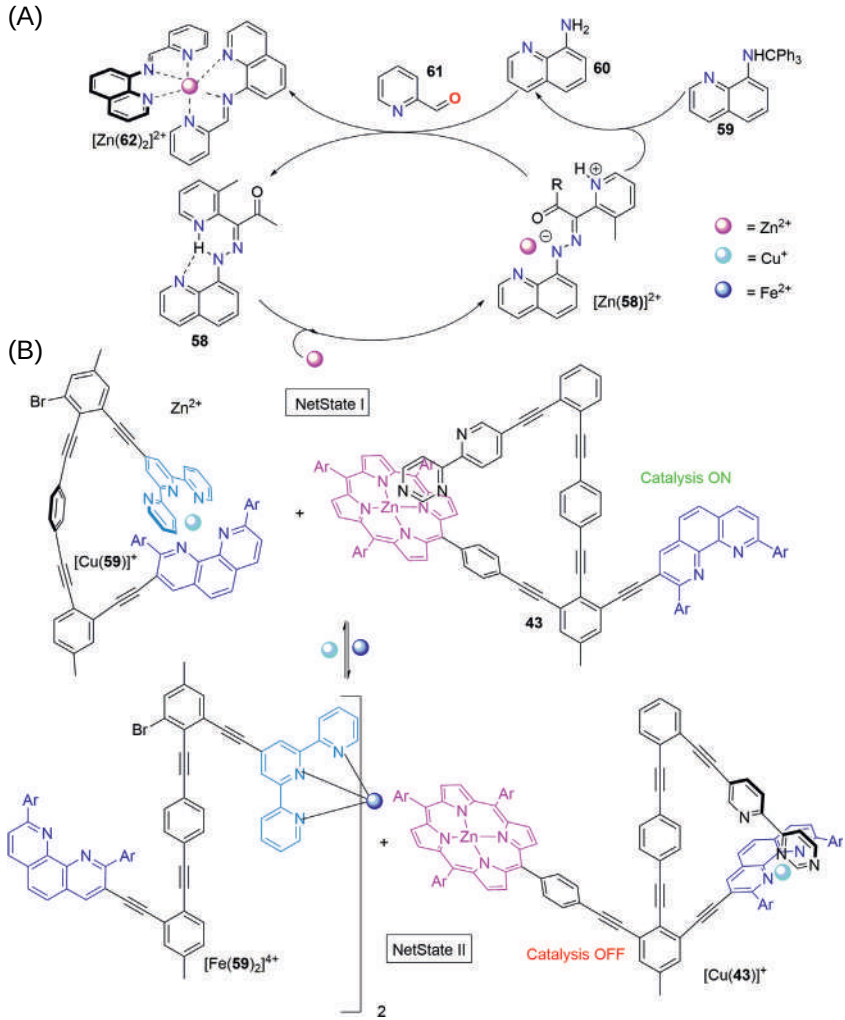

FIGURE 11.15 (A) A metal ion triggered negative feedback loop; (B) metal ion assisted networked catalytic machinery.

added to state 1, Cu^+ of the $[Cu(\mathbf{59})]^+$ was replaced by iron to form $[Fe(\mathbf{59})_2]^{4+}$ due to the higher binding affinity of terpyridine towards Fe^{2+}. The released Cu^+ triggered a nanomechanical reorganization of the rotary arm of nanoswitch **43** to form $[Cu(\mathbf{43})]^+$. In this state, azaterpyridine unit of **43** made the HETPHEN type complex with phenanthroline. The system can be reversed back by selective removal of Fe^{2+} from the mixture. The switching process was additionally used to control an ON/OFF Michael addition reaction. Due to the stronger intramolecular coordination of the azabipyridine arm in nanoswitch **43**, the

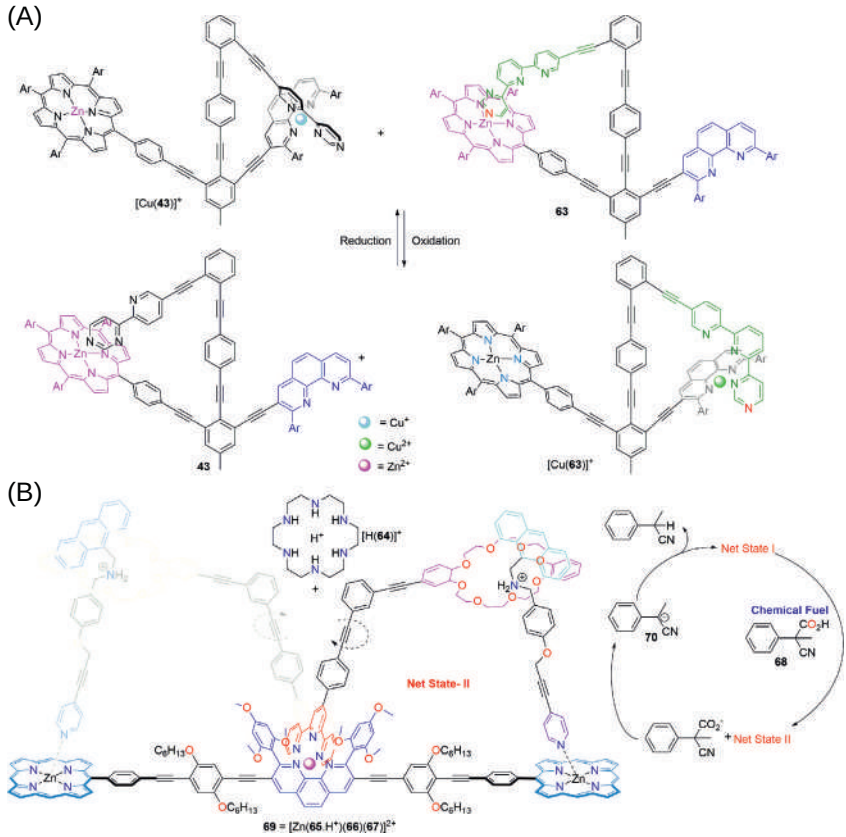

FIGURE 11.16 (A) Electrochemical stimuli induced bidirectional chemical communication between two nanoswitches; (B) fuel-driven three-component nanorotor.

N-methyl pyrrolidine was exposed in solution in NetState I. Thus, this state catalyzed a 1,4-conjugate addition. In NetState II, the catalyst was shielded due to its coordination with zinc porphyrin of switch [Cu(**43**)]$^+$, leading to the shut down of catalysis.

The change in the oxidation state of metal ions has also been used for communication between nanoswiches (S. [98]). Thus, when switches **43** and **63** were treated with one equivalent of Cu^+ ion, a 97:3 mixture of complexes [Cu(**43**)]$^+$ and [Cu(**63**)]$^+$ was afforded (Fig. 11.16A). The selectivities of nanoswtich **43** towards Cu^+ over **63** were due to Cu^+'s preferred tetrahedral coordination environment of Cu^+ in [Cu(**43**)]$^+$. However, when Cu^+ was oxidized to Cu^{2+}, the produced [Cu(**43**)]$^{2+}$ became unstable as Cu^{2+} preferred pentacoordination. As a result, the complex dissociated and intermolecular translocation of Cu^{2+} led to the quantitative formation of [Cu(**63**)]$^{2+}$. Dissociation of Cu^+ from **43** was also accompanied by toggling of the azabipyridine arm from phenanthroline station

to porphyrin station. At the same time formation of complex $[Cu(\mathbf{63})]^{2+}$ was associated with the toggling of azaterpyridine arm of **63** from porphyrin station to phenanthroline station. The original state was restored within two minutes of adding one equivalent of decamethylferrocene, reducing the Cu^{2+} to Cu^{+}. The same group extended the above concept to design a two-step communication process between three nanoswitches [99]. In another example, the same group also demonstrated redox control for triggering communication between the nanoswitches, which turned ON/OFF catalysis of a Knoevenagel addition [100]. Schmittel et al. have also demonstrated communication between multiple multicomponent nanorotors that ultimately controls catalytic reaction [101].

In a recent example, Schmittel et al. demonstrated coordination-driven molecular switches to work away from equilibrium [102]. When compounds **65, 66, 67, 68** and Zn^{2+} were mixed in an appropriate ratio, clean self-sorting led to the formation of NetState 1 where Zn^{2+} existed as $[Zn(\mathbf{64})]^{2+}$and pyridine unit of **65** was coordinated to zinc porphyrin of **67**. If two equivalents of acid **68** (fuel) were added to NetState 1, one equivalent would protonate the complex $[Zn(\mathbf{64})]^{2+}$. The free Zn^{2+} formed a HETTAP complex with the terpyridine unit of **66** and phenanthroline unit of **67**. The other equivalent of acid protonated the amine of ligand **65** to create a pseudorotaxane linkage with ligand **66**. Eventually, the combination of both these complexes furnished the NetState-II (Fig. 11.16B) composed of $[H(\mathbf{64})]^{+}$ and rotor $[Zn(\mathbf{65} \bullet H^{+})(\mathbf{66})(\mathbf{67})]^{2+}$. However, after decarboxylation, the strong base **70** reclaimed the protons, enforcing the disassembly of **69**. The fluorescence spectroscopy revealed the rotor's rapid formation, and after 6 min, the rotor amount decreased. After 60 min, the rotor had fully decomposed into the prerotor that over 300 min converted to Net state 1.

11.5 Conclusion and outlook

Several molecular switches and machines have been designed and tailored to respond to a dozen different kinds of stimuli— light, pH, redox, cations, anions, solvents, temperature, pressure, hydrogen bonding, etc., that have been summarized in a recent review [103]. Nevertheless, the examples touched upon in this chapter leave us in no doubt that coordination driven self-assembly offers a remarkably versatile platform for designing and making molecular switches and machines. Coordination-driven molecular motion has high fidelity and can be used to set up novel functions (intermolecular communication, catalytic machinery, and cybernetic systems) that make this approach unique. It is also clear that in situ ON−OFF regulation of catalytic activity by metal−ligand association is more robust than using other stimuli due to the significant differential binding constants. Most of the research efforts have been directed towards operating individual switches that require multistep synthesis. Artificial molecular switches and machines produced by self-assembly of different components through high fidelity self-sorting is a way forward to circumvent the synthetic issue and

mimic many natural systems. Instead of individual switches, multiple switches are now being used in a mixture in an interference-free manner to get new emergent properties at our will. Thus, the next generation autonomous machines should operate away from equilibrium that may show emergent properties like a feedback loop, autocatalysis etc.

References

[1] K. Kinbara, T. Aida, G. Saper, H. Hess, Chem. Rev. 105 (2005) 288–309.

[2] G. Saper, H. Hess, Synthetic systems powered by biological molecular motors, Chem. Rev. 120 (1) (2020) 288–309, doi:10.1021/acs.chemrev.9b00249.

[3] S.E. Cakmak, D.A. Leigh, C.T. McTernan, A.L. Nussbaumer, Artificial molecular machines, Chem. Rev. 115 (2015) 125–199.

[4] A. Goswami, S. Saha, P.K. Biswas, M. Schmittel, (Nano)mechanical motion triggered by metal coordination: From functional devices to networked multicomponent catalytic machinery, Chem. Rev. 120 (1) (2020) 125–199, doi:10.1021/acs.chemrev.9b00159.

[5] D.A. Leigh, Genesis of the nanomachines: The 2016 Nobel prize in chemistry, Angew. Chem. Int. Ed. 55 (47) (2016) 14506–14508, doi:10.1002/anie.201609841.

[6] S. De, K. Mahata, M. Schmittel, Metal-coordination-driven dynamic heteroleptic architectures. Chem. Soc. Rev. 39 (2010) 1555–1575.

[7] M.L. Saha, S. De, S. Pramanik, M. Schmittel, Orthogonality in discrete self-assembly: Survey of current concepts, Chem. Soc. Rev. 42 (16) (2013) 6860–6909, doi:10.1039/c3cs60098j.

[8] K. Krzywoszyńska, D. Witkowska, J.Ś. Kozłowska, A. Szebesczyk, H. Kozłowski, General Aspects of Metal Ions as Signaling Agents in Health and Disease, Biomolecules 10 (10) (2020) 1417.

[9] N. Armaroli, V. Balzani, J.P. Collin, P. Gaviña, J.P. Sauvage, B. Ventura, Rotaxanes incorporating two different coordinating units in their thread: Synthesis and electrochemically and photochemically induced molecular motions, J. Am. Chem. Soc. 121 (18) (1999) 4397–4408, doi:10.1021/ja984051w.

[10] U. Létinois-Halbes, D. Hanss, J.M. Beierle, J.P. Collin, J.P. Sauvage, A fast-moving [2]rotaxane whose stoppers are remote from the copper complex core, Org. Lett. 7 (26) (2005) 5753–5756, doi:10.1021/ol052051c.

[11] M. Weck, B. Mohr, J.P. Sauvage, R.H. Grubbs, Synthesis of catenane structures via ring-closing metathesis, J. Org. Chem. 64 (15) (1999) 5463–5471, doi:10.1021/jo990268c.

[12] A. Livoreil, C.O. Dietrich-Buchecker, J.P. Sauvage, Electrochemically triggerred swinging of a [2]-catenate, J. Am. Chem. Soc. 116 (20) (1994) 9399–9400, doi:10.1021/ja00099a095.

[13] J.M. Kern, L. Raehm, J.P. Sauvage, B. Divisia-Blohorn, P.L. Vidal, Controlled molecular motions in copper-complexed rotaxanes: An XAS study, Inorg. Chem. 39 (7) (2000) 1555–1560, doi:10.1021/ic991163v.

[14] N. Weber, C. Hamann, J.M. Kern, J.P. Sauvage, Synthesis of a copper [3]rotaxane able to function as an electrochemically driven oscillatory machine in solution, and to form SAMs on a metal surface, Inorg. Chem. 42 (21) (2003) 6780–6792, doi:10.1021/ic0347034.

[15] E. Coronado, P. Gaviña, J. Ponce, S. Tatay, Fast pirouetting motion in a pyridine bisamine-containing copper-complexed rotaxane, Chem. Eur. J. 20 (23) (2014) 6939–6950, doi:10.1002/chem.201304434.

[16] E. Coronado, P. Gaviña, J. Ponce, S. Tatay, Fast redox-triggered shuttling motions in a copper rotaxane based on a phenanthroline-terpyridine conjugate, Org. Biomol. Chem. 12 (38) (2014) 7572–7580, doi:10.1039/c4ob01206b.

[17] A. Goswami, M. Schmittel, Heteroleptic copper phenanthroline complexes in motion: From stand-alone devices to multi-component machinery, Coord. Chem. Rev. 376 (2018) 478–505, doi:10.1016/j.ccr.2018.08.011.

[18] F. Niess, V. Duplan, J.P. Sauvage, Interconversion between a vertically oriented transition metal-complexed figure-of-eight and a horizontally disposed one, J. Am. Chem. Soc. 136 (16) (2014) 5876–5879, doi:10.1021/ja501765y.

[19] J.D. Crowley, I.M. Steele, B. Bosnich, Protonmotive Force: Development of Electrostatic Drivers for Synthetic Molecular, Chem. Eur. J. 12 (2006) 8935–8951.

[20] S.O. Scottwell, A.B.S. Elliott, K.J. Shaffer, A. Nafady, C.J. McAdam, K.C. Gordon, J.D. Crowley, Chemically and electrochemically induced expansion and contraction of a ferrocene rotor, Chem. Commun. 51 (38) (2015) 8161–8164, doi:10.1039/c5cc01973g.

[21] B. Sivaev, Ferrocene and Transition Metal Bis(Dicarbollides) as Platform for Design of Rotatory Molecular Switches, Molecules 22 (12) (2017) 2201.

[22] S.O. Scottwell, J.E. Barnsley, C.J. McAdam, K.C. Gordon, J.D. Crowley, A ferrocene based switchable molecular folding ruler, Chem. Commun. 53 (54) (2017) 7628–7631, doi:10.1039/c7cc03358c.

[23] B. Korybut-Daszkiewicz, A. Wi??ckowska, R. Bilewicz, S. Domagała, K. Woźniak, An electrochemically controlled molecular shuttle, Angew. Chem. Int. Ed. 43 (13) (2004) 1668–1672, doi:10.1002/anie.200352528.

[24] M. Wozny, J.P. łowska, A. Osior, P. wider, R. Bilewicz, B. Korybut-Daszkiewicz, An electrochemically switchable foldamer – a surprising feature of a rotaxane with equivalent stations, Chem. Sci. 5 (2014) 2836–2842.

[25] M. Woźny, J. Pawłowska, K.M. Tomczyk, R. Bilewicz, B. Korybut-Daszkiewicz, Potential-controlled rotaxane molecular shuttles based on electron-deficient macrocyclic complexes, Chem. Commun. (2014) 13718–13721, doi:10.1039/C4CC06718E.

[26] C.R. Benson, A.I. Share, M.G. Marzo, A.H. Flood, Double switching of two rings in palindromic [3]pseudorotaxanes: Cooperativity and mechanism of motion, Inorg. Chem. 55 (8) (2016) 3767–3776, doi:10.1021/acs.inorgchem.5b02554.

[27] M. Schmittel, S. De, S. Pramanik, Redox-dependent self-sorting toggles a rotary nanoswitch, Organ. Biomol. Chem. 13 (33) (2015) 8937–8944, doi:10.1039/c5ob01041a.

[28] M.C. Jiménez, C. Dietrich-Buchecker, J.P. Sauvage, Towards synthetic molecular muscles: Contraction and stretching of a linear rotaxane dimer, Angew. Chem. Int. Ed. 39 (18) (2000) 3284–3287, doi:10.1002/1521-3773(20000915)39:18<3284::AID-ANIE3284>3.0.CO;2-7.

[29] A. Joosten, Y. Trolez, J.P. Collin, V. Heitz, J.P. Sauvage, Copper(I)-assembled [3]rotaxane whose two rings Act as flapping wings, J. Am. Chem. Soc. 134 (3) (2012) 1802–1809, doi:10.1021/ja210113y.

[30] D.A. Leigh, P.J.,M.Z. Lusby, A. Slawin, D.B. Walker, Half-rotation in a kinetically locked [2]catenane induced by transition metal ion substitution, Chem. Commun. 48 (44) (2012) 5826–5828, doi:10.1039/c2cc32418k.

[31] S. Akine, T. Taniguchi, T. Nabeshima, Helical metallohost-guest complexes via site-selective transmetalation of homotrinuclear complexes, J. Am. Chem. Soc. 128 (49) (2006) 15765–15774, doi:10.1021/ja0646702.

[32] J.E.M. Lewis, R.J. Bordoli, M. Denis, C.J. Fletcher, M. Galli, E.A. Neal, E.M. Rochette, S.M. Goldup, High yielding synthesis of 2,2′-bipyridine macrocycles, versatile intermediates in the synthesis of rotaxanes, Chem. Sci. 7 (5) (2016) 3154–3161, doi:10.1039/c6sc00011h.

[33] J.C. Chang, S.H. Tseng, C.C. Lai, Y.H. Liu, S.M. Peng, S.H. Chiu, Mechanically interlocked daisy-chain-like structures as multidimensional molecular muscles, Nat. Chem. 9 (2) (2017) 128–134, doi:10.1038/NCHEM.2608.

[34] K.D. Wu, Y.H. Lin, C.C. Lai, S.H. Chiu, Na+ ion templated threading of oligo(ethylene glycol) chains through BPX26C6 Allows synthesis of [2]rotaxanes under solvent-free conditions, Org. Lett. 16 (4) (2014) 1068–1071, doi:10.1021/ol403602j.

[35] D.B. Amabilino, C.O. Dietrich-Buchecker, A. Livoreil, L. Pérez-García, J.P. Sauvage, J.F. Stoddart, A switchable hybrid [2]-catenane based on transition metal complexation and π-electron donor-acceptor interactions, J. Am. Chem. Soc. 118 (16) (1996) 3905–3913, doi:10.1021/ja954329+.

[36] H. Yin, R. Rosas, D. Gigmes, O. Ouari, R. Wang, A. Kermagoret, D. Bardelang, Metal actuated ring translocation switches in water, Org. Lett. 20 (11) (2018) 3187–3191, doi:10.1021/acs.orglett.8b01019.

[37] Z. Meng, C.F. Chen, Highly efficient synthesis of a tristable molecular shuttle and its controlled motion under chemical stimuli, Organ. Biomol. Chem. 12 (35) (2014) 6937–6943, doi:10.1039/c4ob01283f.

[38] Z. Meng, J.F. Xiang, C.F. Chen, Tristable [n]rotaxanes: From molecular shuttle to molecular cable car, Chem. Sci. 5 (4) (2014) 1520–1525, doi:10.1039/c3sc53295j.

[39] N. Ousaka, E. Yashima, Stimuli-responsive molecular springs based on single- and multi-stranded helical structures, Chem. Lett. 50 (2) (2021) 320–330, doi:10.1246/cl.200737.

[40] N. Ousaka, K. Shimizu, Y. Suzuki, T. Iwata, M. Itakura, D. Taura, H. Iida, Y. Furusho, T. Mori, E. Yashima, Spiroborate-based double-stranded helicates: Meso-to-racemo isomerization and ion-triggered springlike motion of the racemo-helicate, J. Am. Chem. Soc. 140 (49) (2018) 17027–17039, doi:10.1021/jacs.8b08268.

[41] Y. Suzuki, T. Nakamura, H. Iida, N. Ousaka, E. Yashima, Allosteric regulation of unidirectional spring-like motion of double-stranded helicates, J. Am. Chem. Soc. 138 (14) (2016) 4852–4859, doi:10.1021/jacs.6b00787.

[42] D. Taura, K. Shimizu, C. Yokota, R. Ikeda, Y. Suzuki, H. Iida, N. Ousaka, E. Yashima, Fluorescent molecular spring that visualizes the extension and contraction motions of a double-stranded helicate bearing terminal pyrene units triggered by release and binding of alkali metal ions, Chem. Commun. 55 (2019) 12084–12087.

[43] J. Rebek, J.E. Trend, R.V. Wattley, S.C.,J.A. Rebek, R.V.W.J. Rebek, T. Costello, L. Marshall, R. Wattley, R.C. Gadwood, K. Onan, J. Am. Chem. Soc. 101 (1979) 7481–7487.

[44] J. Rebek, R.V. Wattley, Allosteric effects. remote control of ion transport selectivity, J. Am. Chem. Soc. 102 (14) (1980) 4853–4854, doi:10.1021/ja00534a058.

[45] P. Yin, T. Li, R.S. Forgan, C. Lydon, X. Zuo, Z.N. Zheng, B. Lee, D. Long, L. Cronin, T. Liu, Exploring the programmable assembly of a polyoxometalate-organic hybrid via metal ion coordination, J. Am. Chem. Soc. 135 (36) (2013) 13425–13432, doi:10.1021/ja404777g.

[46] F. Huang, G. Wang, L. Ma, Y. Wang, X. Chen, Y. Che, H. Jiang, Molecular spur gears based on a switchable quinquepyridine foldamer acting as a stator, J. Org. Chem. 82 (23) (2017) 12106–12111, doi:10.1021/acs.joc.7b01864.

[47] A. Petitjean, N. Kyritsakas, J.M. Lehn, Ion-Triggered Multistate Molecular Switching Device Based on Regioselective Coordination-Controlled Ion Binding, Chem. Eur. J. 11 (2005) 1618–1628.

[48] A.M. Stadler, J.M.P. Lehn, Coupled nanomechanical motions: Metal-ion-effected, pH-modulated, simultaneous extension/contraction motions of double-domain helical/linear molecular strands, J. Am. Chem. Soc. 136 (9) (2014) 3400–3409, doi:10.1021/ja408752m.

[49] A.M. Stadler, L. Karmazin, C. Bailly, A Ca2+-, Mg2+-, and Zn2+-based dendritic contractile nanodevice with two pH-dependent motional functions, Angew. Chem. Int. Ed. 54 (48) (2015) 14570–14574, doi:10.1002/anie.201506474.

[50] P.J. Altmann, A. Pöthig, A pH-dependent, mechanically interlocked switch: Organometallic [2]rotaxane vs. organic [3]rotaxane, Angew. Chem. Int. Ed. 56 (49) (2017) 15733–15736, doi:10.1002/anie.201709921.

[51] L. Kocher, S. Durot, V. Heitz, Control of the cavity size of flexible covalent cages by silver coordination to the peripheral binding sites, Chem. Commun. 51 (67) (2015) 13181–13184, doi:10.1039/c5cc04972e.

[52] L. Schoepff, L. Kocher, S. Durot, V. Heitz, Chemically Induced Breathing of Flexible Porphyrinic Covalent Cages, J. Org. Chem. 82 (2017) 5845–5851.

[53] F. Ge, X. Tao, C.G. Daniliuc, G. Kehr, G. Erker, Angew. Chem. Int. Ed. 54 (2015) 14570–14574.

[54] S. Kassem, A.T.L. Lee, D.A. Leigh, A. Markevicius, J. Solà, Pick-up, transport and release of a molecular cargo using a small-molecule robotic arm, Nat. Chem. 8 (2) (2016) 138–143, doi:10.1038/nchem.2410.

[55] S. Kassem, A.T.L. Lee, D.A. Leigh, A. Markevicius, D.J. Tetlow, N. Toriumi, Site-to-site peptide transport on a molecular platform using a small-molecule robotic arm, Chem. Sci. 12 (6) (2021) 2065–2070, doi:10.1039/d0sc05906d.

[56] B. Lewandowski, G. De Bo, J.W. Ward, M. Papmeyer, S. Kuschel, M.J. Aldegunde, P.M.E. Gramlich, D. Heckmann, S.M. Goldup, D.M. D'Souza, A.E. Fernandes, D.A. Leigh, Sequence-specific peptide synthesis by an artificial small-molecule machine, Science 339 (6116) (2013) 189–193, doi:10.1126/science.1229753.

[57] D.A. Blanco, V. Leigh, Marcos, Artificial switchable catalysts, Chem. Soc. Rev. 44 (2015) 5341–5370.

[58] J. Choudhury, Recent developments on artificial switchable catalysis, Tetrahedr. Lett. 59 (6) (2018) 487–495, doi:10.1016/j.tetlet.2017.12.070.

[59] M. Barboiu, L. Prodi, M. Montalti, N. Zaccheroni, N. Kyritsakas, J.M. Lehn, Dynamic chemical devices: Modulation of photophysical properties by reversible, ion-triggered, and proton-fuelled nanomechanical shape-flipping molecular motions, Chem. Eur. J. 10 (12) (2004) 2953–2959, doi:10.1002/chem.200306045.

[60] S. De, D. Sahoo, R. Benny, N.K. K S, Stimuli-responsive chiroptical switching, ChemPlusChem 87 (2022) e202100322, doi:10.1002/cplu.202100322.

[61] S. Akine, S. Sairenji, T. Taniguchi, T. Nabeshima, Stepwise helicity inversions by multisequential metal exchange, J. Am. Chem. Soc. 135 (35) (2013) 12948–12951, doi:10.1021/ja405979v.

[62] S. Akine, S. Hotate, T. Nabeshima, A molecular leverage for helicity control and helix inversion, J. Am. Chem. Soc. 133 (35) (2011) 13868–13871, doi:10.1021/ja205570z.

[63] C. Mevissen, A.C.N. Kwamen, L. Himmel, X. Chen, M. Brückner, S. Huda, C. Göb, J. Jenniches, I. Oppel, J.S. Ward, K. Rissanen, M. Albrecht, Helicates with ether-substituted catechol esters as ligands, Eur. J. Org. Chem. 2020 (32) (2020) 5161–5172, doi:10.1002/ejoc.202000843.

[64] C. Mevissen, D. Sommer, S. Vasanthakumar, K.N. Truong, K. Rissanen, M. Albrecht, Cation-translocation based isomerism offers a tool for the expansion of compressed helicates, Dalton Trans. 50 (27) (2021) 9372–9375, doi:10.1039/d1dt01707a.

[65] X. Chen, T.M. Gerger, C. Räuber, G. Raabe, C. Göb, I.M. Oppel, M. Albrecht, A helicate-based three-state molecular switch, Angew. Chem. Int. Ed. 57 (36) (2018) 11817–11820, doi:10.1002/anie.201806607.

[66] E. Lee, H. Ju, I.H. Park, J.H. Jung, M. Ikeda, S. Kuwahara, Y. Habata, S.S. Lee, Pseudo[1]catenane-type pillar[5]thiacrown whose planar chiral inversion is triggered by metal cation and controlled by anion, J. Am. Chem. Soc. 140 (30) (2018) 9669–9677, doi:10.1021/jacs.8b05751.

[67] C. Xiao, W. Wu, W. Liang, D. Zhou, K. Kanagaraj, G. Cheng, D. Su, Z. Zhong, J.J. Chruma, C. Yang, Redox-triggered chirality switching and guest-capture/release with a pillar[6]arene-based molecular universal joint, Angew. Chem. Int. Ed. 59 (21) (2020) 8094–8098, doi:10.1002/anie.201916285.

[68] A. Blanco-Gómez, P. Cortón, L. Barravecchia, I. Neira, E. Pazos, C. Peinador, M.D. García, Controlled binding of organic guests by stimuli-responsive macrocycles, Chem. Soc. Rev. 49 (12) (2020) 3834–3862, doi:10.1039/d0cs00109k.

[69] C. Kremer, A. Lützen, Allosteric binding of capsaicin by a bis(β-cyclodextrin)-2,2'- bipyridine receptor, Chem. Eur. J. 20 (29) (2014) 8852–8855, doi:10.1002/chem.201403503.

[70] H. Staats, F. Eggers, O. Haß, F. Fahrenkrug, J. Matthey, U. Lüning, A. Lützen, Towards allosteric receptors: Synthesis of resorcinarene-functionalized 2,2′-bipyridines and their metal complexes, Eur. J. Org. Chem. 28 (2009) 4777–4792, doi:10.1002/ejoc.200900642.

[71] H. Staats, A. Lützen, Size selective recognition of small esters by a negative allosteric hemicarcerand, Beilstein J. Org. Chem. 6 (10) (2010). https://doi.org/10.3762/bjoc.6.10.

[72] C.H. Lee, H. Yoon, W.D. Jang, Biindole-bridged porphyrin dimer as allosteric molecular tweezers, Chem. Eur. J. 15 (39) (2009) 9972–9976, doi:10.1002/chem.200901988.

[73] Y. Ninomiya, M. Kozaki, S. Suzuki, K. Okada, Allosteric regulation of the ligand-binding ability of zinc porphyrins with sterically bulky shielding units by metal complexation, Bull. Chem. Soc. Japan 87 (11) (2014) 1195–1201, doi:10.1246/bcsj.20140197.

[74] J. Frey, C. Tock, J.P. Collin, V. Heitz, J.P. Sauvage, A [3]Rotaxane with Two Porphyrinic Plates Acting as an Adaptable Receptor, J. Am. Chem. Soc. 130 (2008) 4592–4593.

[75] J.P. Collin, J. Frey, V. Heitz, J.P. Sauvage, C. Tock, L. Allouche, J. Am. Chem. Soc. (2009) 131.

[76] J.M. Arroyo, A.I. Aquino, A.B. Chinen, Y.D. Manraj, C.A. Mirkin, J. Am. Chem. Soc. 139 (2017) 1368–1371.

[77] J. Mendez-Arroyo, J. Barroso-Flores, A.M. Lifschitz, A.A. Sarjeant, C.L. Stern, C.A. Mirkin, A multi-state, allosterically-regulated molecular receptor with switchable selectivity, J. Am. Chem. Soc. 136 (29) (2014) 10340–10348, doi:10.1021/ja503506a.

[78] J.J. Henkelis, A.K. Blackburn, E.J. Dale, N.A. Vermeulen, M.S. Nassar, J.F. Stoddart, Allosteric modulation of substrate binding within a tetracationic molecular receptor, J. Am. Chem. Soc. 137 (41) (2015) 13252–13255, doi:10.1021/jacs.5b08656.

[79] K. Harada, R. Sekiya, T. Haino, Folding and unfolding of acetoxy group-terminated alkyl chains inside a size-regulable hemicarcerand, J. Org. Chem. 86 (6) (2021) 4440–4447, doi:10.1021/acs.joc.0c02833.

[80] G. Olivo, G. Capocasa, D. Del Giudice, O. Lanzalunga, S. Di Stefano, New horizons for catalysis disclosed by supramolecular chemistry, Chem. Soc. Rev. 50 (13) (2021) 7681–7724, doi:10.1039/d1cs00175b.

[81] M. Schmittel, S. De, S. Pramanik, Reversible ON/OFF nanoswitch for organocatalysis: Mimicking the locking and unlocking operation of CaMKII, Angew. Chem. Int. Ed. 51 (16) (2012) 3832–3836, doi:10.1002/anie.201108089.

[82] M. Schmittel, S. Pramanik, S. De, A reversible nanoswitch as an ON–OFF photocatalyst, Chem. Commun. 48 (96) (2012) 11730–11732, doi:10.1039/c2cc36408e.

[83] S. De, S. Pramanik, M. Schmittel, A toggle nanoswitch alternately controlling two catalytic reactions, Angew. Chem. Int. Ed. 53 (51) (2014) 14255–14259, doi:10.1002/anie.201408457.

[84] S. De, S. Pramanik, M. Schmittel, A monomer–dimer nanoswitch that mimics the working principle of the SARS-CoV 3CLpro enzyme controls copper-catalysed cyclopropanation, Dalton Trans. 43 (28) (2014) 10977–10982, doi:10.1039/C4DT01508H.

[85] S. Gaikwad, A. Goswami, S. De, M. Schmittel, A metalloregulated four-state nanoswitch controls two-step sequential catalysis in an eleven-component system, Angew. Chem. Int. Ed. 55 (35) (2016) 10512–10517, doi:10.1002/anie.201604658.

[86] P.K. Biswas, S. Saha, Y. Nanaji, A. Rana, M. Schmittel, Influence of Rotator Design on the Speed of Self-Assembled Four-Component Nanorotors: Coordinative Versus Dispersive Interactions, Inorg. Chem. 56 (2017) 6662–6670.

[87] S. Saha, P.K. Biswas, M. Schmittel, Reversible Interconversion of a Static Metallosupramolecular Cage Assembly into a High-Speed Rotor: Stepless Adjustment of Rotational Exchange by Nucleophile Addition, Inorg. Chem. 58 (2019) 3466–3472.

[88] M.S. Özer, A. Rana, P.K. Biswas, M. Schmittel, Four-component zinc-porphyrin/zinc-salphen nanorotor, Dalton Trans. 46 (29) (2017) 9491–9497, doi:10.1039/c7dt01323j.

[89] S.K. Samanta, J.W. Bats, M. Schmittel, A five-component nanorotor with speed regulation, Chem. Commun. 50 (18) (2014) 2364–2366, doi:10.1039/c3cc49476d.

[90] N. Mittal, M.S. Özer, M. Schmittel, Four-component catalytic machinery: Reversible three-state control of organocatalysis by walking back and forth on a track, Inorg. Chem. 57 (7) (2018) 3579–3586, doi:10.1021/acs.inorgchem.7b02703.

[91] Y.J. Lee, K.S. Liu, C.C. Lai, Y.H. Liu, S.M. Peng, R.P. Cheng, S.H. Chiu, Na+ ions induce the pirouetting motion and catalytic activity of [2]rotaxanes, Chem. Eur. J. 23 (41) (2017) 9756–9760, doi:10.1002/chem.201702525.

[92] S. Mortezaei, N.R. Catarineu, J.W. Canary, A redox-reconfigurable, ambidextrous asymmetric catalyst, J. Am. Chem. Soc. 134 (19) (2012) 8054–8057, doi:10.1021/ja302283s.

[93] A.M. Lifschitz, M.S. Rosen, C.M. McGuirk, C.A. Mirkin, Allosteric Supramolecular Coordination Constructs, J. Am. Chem. Soc. 137 (2015) 7252–7261.

[94] C.M. McGuirk, C.L. Stern, C.A. Mirkin, Small molecule regulation of self-association and catalytic activity in a supramolecular coordination complex, J. Am. Chem. Soc. 136 (12) (2014) 4689–4696, doi:10.1021/ja500214r.

[95] C.M. McGuirk, J. Mendez-Arroyo, A.I. D'Aquino, C.L. Stern, Y. Liu, C.A. Mirkin, A concerted two-prong approach to the: In situ allosteric regulation of bifunctional catalysis, Chem. Sci. 7 (11) (2016) 6674–6683, doi:10.1039/c6sc01454b.

[96] S. Pramanik, I. Aprahamian, Hydrazone switch-based negative feedback loop, J. Am. Chem. Soc. 138 (46) (2016) 15142–15145, doi:10.1021/jacs.6b10542.

[97] N. Mittal, S. Pramanik, I. Paul, S. De, M. Schmittel, Networking nanoswitches for ON/OFF control of catalysis, J. Am. Chem. Soc. 139 (12) (2017) 4270–4273, doi:10.1021/jacs.6b12951.

[98] S. Pramanik, S. De, M. Schmittel, Bidirectional chemical communication between nanomechanical switches, Angew. Chem. Int. Ed. 53 (18) (2014) 4709–4713, doi:10.1002/anie.201400804.

[99] Pramanik, Susnata, S. De, M. Schmittel, A trio of nanoswitches in redox-potential controlled communication, Chem. Commun. 50 (87) (2014) 13254–13257, doi:10.1039/C4CC05773B.

[100] S. Gaikwad, S. Pramanik, S. De, M. Schmittel, A high-speed network of nanoswitches for on/off control of catalysis, Dalton Trans. 47 (6) (2018) 1786–1790, doi:10.1039/c7dt04695b.

[101] A. Goswami, S. Pramanik, M. Schmittel, Catalytically active nanorotor reversibly self-assembled by chemical signaling within an eight-component network, Chem. Commun. 54 (32) (2018) 3955–3958, doi:10.1039/c8cc01496e.
[102] A. Ghosh, I. Paul, M. Schmittel, Multitasking with chemical fuel: Dissipative formation of a pseudorotaxane rotor from five distinct components, J. Am. Chem. Soc. 143 (14) (2021) 5319–5323, doi:10.1021/jacs.1c01948.
[103] S. Kassem, T. Van Leeuwen, A.S. Lubbe, M.R. Wilson, B.L. Feringa, D.A. Leigh, Artificial molecular motors, Chem. Soc. Rev. 46 (9) (2017) 2592–2621, doi:10.1039/c7cs00245a.
[104] R. Chakrabarty, P.S. Mukherjee, P.J. Stang, Supramolecular coordination: Self-assembly of finite two- and three-dimensional ensembles, Chem. Rev. 111 (11) (2011) 6810–6918, doi:10.1021/cr200077m.
[105] X. Chen, M. Baumert, R. Fröhlich, M. Albrecht, Cation triggered spring-like helicates based on ketone-substituted bis-catechol ligands, J. Incl. Phenom. Macrocycl. Chem. 94 (3–4) (2019) 133–140, doi:10.1007/s10847-019-00888-9.
[106] J.P. Collin, F. Durola, J. Lux, J.P. Sauvage, A copper-based shuttling [2]rotaxane with two bidentate chelates in the axis: Steric control of the motion, New J. Chem. 34 (1) (2010) 34–43, doi:10.1039/b9nj00296k.
[107] J.P. Collin, F. Durola, J. Lux, J.P. Sauvage, A rapidly shuttling copper-complexed [2]rotaxane with three different chelating groups in its axis, Angew. Chem. Int. Ed. 48 (45) (2009) 8532–8535, doi:10.1002/anie.200903311.
[108] L.V. Dijk, M.J. Tilby, R. Szpera, O.A. Smith, H.A.P. Bunce, S.P. Fletcher, Molecular machines for catalysis, Nat. Rev. Chem. 2 (2018) 117.
[109] A. Goswami, I. Paul, M. Schmittel, Three-component nanorotors generated from fusion of complexes and post-fusion metal metal exchange, Chem. Commun. 53 (2017) 5186–5189.
[110] C. Mevissen, A.C.N. Kwamen, L. Himmel, X. Chen, M. Brückner, s. Huda, C. Göb, J. Jenniches, I. Oppel, J.S. Ward, K. Rissanen, M. Albrecht, X. Chen, M. Baumert, R. Fröhlich, M. Albrecht, J. Incl. Phenom. Macrocycl. Chem. 50 (2019) 133–140.
[111] L. Raehm, J.M. Kern, J.P. Sauvage, A transition metal containing rotaxane in motion: Electrochemically induced pirouetting of the ring on the threaded dumbbell, Chem. Eur. J. 5 (11) (1999) 3310–3317, doi:10.1002/(SICI)1521-3765(19991105)5:11<3310::AID-CHEM3310>3.0.CO;2-R.
[112] J. Rebek, J.E. Trend, R.V. Wattley, S. Chakravorti, Allosteric effects in organic chemistry. Site-specific binding, J. Am. Chem. Soc. 101 (1979) 4333–4337.
[113] S. Scottwell, J.D. Crowley, Ferrocene-containing non-interlocked molecular machines, Chem. Commun. 52 (12) (2016) 2451–2464, doi:10.1039/c5cc09569g.

Chapter 12

Biomedical application of supramolecular coordination complexes

Sushobhan Ghosh
Department of Chemistry, Alipurduar University, Alipurduar, India

12.1 Introduction

Natural molecules, such as proteins, oligonucleotides, lipids, and their multimolecular complexes, have been the major source of inspiration to supramolecular chemists. Supramolecular synthesis of multinuclear architectures with diverse shapes, compositions, and functionalities is now possible in a wide range of conditions in solution and solid-state. Most of the supramolecular complexes display their specific properties in the solid or gel state or in organic solvents. Gaining control over the supramolecular interactions is the key to understanding and targeting (off-regulated) biological processes in diseases. The most successful approach to obtaining control over these biological processes is the modulation of specific biomolecules with small molecules. So-called target-based drug discovery is essentially supramolecular chemistry. Drugs bind to proteins via supramolecular host–guest interactions and therewith influence the functioning or conformation of the protein. Apart from individual host–guest interactions, applied in medicinal chemistry, biological systems also feature more complex supramolecular interactions, for example, when cells interact. Several transition metals are important to the chemistry of living systems, the most familiar examples being Fe, Co, Cu, Pt, Pd, Mo, etc. Transition metals show different oxidation states and can interact with negatively charged molecules. This activity of transition metals has led to the recent development of drugs that are based on metals and are considered to be potential candidates for pharmacological and therapeutic applications. Here we focus on the works carried out over the past few decades that have sought to possess preclinical pharmacological screenings like antimicrobial, anti-inflammatory, and anticancer action of synthetic transition metal supramolecular complexes.

Supramolecular Coordination Complexes: Design, Synthesis, and Applications.
DOI: https://doi.org/10.1016/B978-0-323-90582-4.00002-6

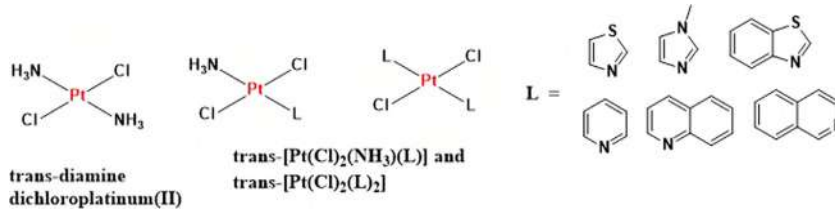

FIGURE 12.1 Chemical structures of biologically active heteroaromatic ligands-based trans-Pt (II) complexes.

12.2 Platinum complexes as anticancer agent

The most notable examples of metal-based drugs are Pt anticancer agents which are very effective anticancer drugs and are used in 50% of all chemotherapeutic regimens administered in the clinic. Currently, there are three Pt-based anticancer drugs that are used worldwide: cisplatin, carboplatin, and oxaliplatin. In addition to the three Pt anticancer agents that are being used today worldwide, there are many other Pt complexes that have been under work for approval for use in humans. Substitution of the ammine ligand(s) in transdiamminedichloroplatinum(II) with bulky, planar N-donor ligands affords trans-Pt (II) complexes with high in vitro cytotoxicity. Some analogs, such as trans-[PtCl2(NH3)- L] and trans-[PtCl2L2] where L = pyridine, quinoline, isoquinoline, thiazole, or benzothiazole (Fig. 12.1), display therapeutically significant activities in cisplatin- and oxaliplatin resistant cell lines [1,2]. Their unique cytotoxicity profiles are attributed to their structural and DNA-binding properties. The presence of bulky planar ligands increases the propensity for monofunctional adduct formation and subsequent interstrand cross-linking. In vitro studies in cultured breast cancer cells showed that these complexes formed DNA-topoisomerase I cross-links that are capable of triggering DNA strand breaks and apoptosis [3]. Such ternary DNA−protein cross-links are not observed following treatment with cisplatin [3] and could explain, in part, the distinctive cellular response evoked by trans-Pt (II) complexes with bulky planar ligands.

Polynuclear Pt complexes which have similarities with trans-Pt (II) complexes are another class of pharmacologically active Pt-based anticancer agents [4–7]. Such compounds contain trans-{Pt(NH3)2Cl} units with bridging alkanediamine linkers of variable length, designed to facilitate long-distance, flexible intrastrand, and interstrand cross-links (Fig. 12.2). The di-Pt complex trans-[(PtCl(NH3)2)2μ-(H2N(CH2)4NH2)]Cl2 forms 1,2-, 1,3-, and 1,4-interstrand cross-links between guanines on opposite strands [8,9]. To improve the DNA binding ability of the di-Pt(II) complex, tri-nuclear Pt(II) complexes were prepared by incorporating a third Pt center within the alkanediamine linker [10] bis[trans-diamminechloroplatinum(II)][μ-transdiamminebis(hexanediamine)platinum(II)] nitrate (BBR3464) is taken up in large amounts by cancer cells and forms characteristic DNA cross-links, which mediate its cytotoxic effects [11,12]. Other studies claim that BBR3464

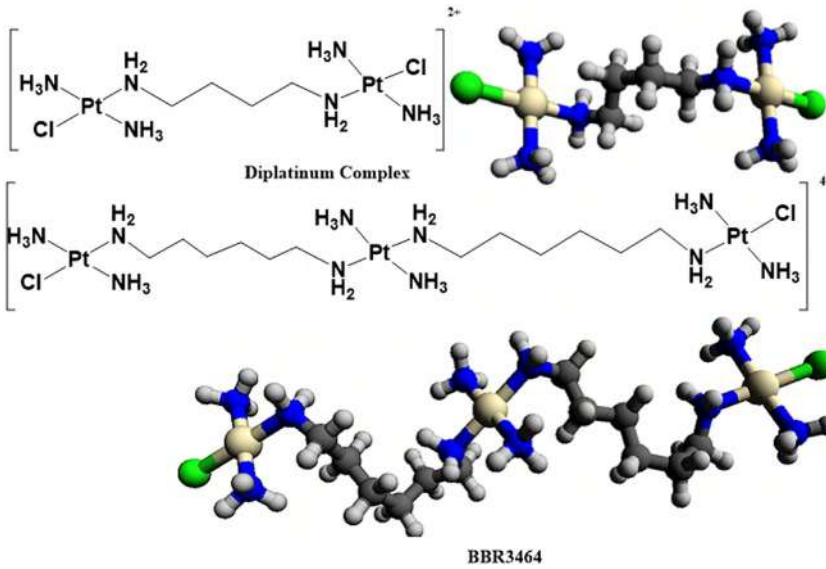

FIGURE 12.2 Chemical structures of di- and tri-nuclear Pt complexes.

induces DNA damage by triggering B-to-Z and B-to-A transitions in DNA conformation [13,14]. The major drawback of BBR3464 is its inherent systemic toxicity. Although BBR3464 displayed a distinct lack of activity in gastric and small cell lung cancers, it showed better activity in non-small cell lung cancer patients and advanced ovarian cancer patients failing Pt-taxane regimens.

Mitochondria are potential therapeutic targets for anticancer drugs. Xiaoyong Wang and his group [15] designed and studied a series of mitochondrion-targeted monofunctional Pt complexes, [Pt(ortho-PPh3CH2Py)(NH3)2Cl](NO3)2 (OPT), [Pt(meta-PPh3CH2Py)(NH3)2Cl](NO3)2 (MPT), and [Pt(paraPPh3 CH2Py)(NH3)2Cl](NO3)2 (PPT) (PPh3 = triphenylphosphonium, Py = pyridine) by modifying pyriplatin with –CH2Ph3P+ (Fig. 12.3) for antitumor activity. The antitumor activity and mechanism of action have been investigated in vitro as well as in vivo and also on molecular levels. The complex OPT exhibits higher efficacy than cisplatin against A549 lung cancer cells; moreover, it exhibits a strong inhibition toward the growth of nonsmall-cell lung cancer in nude mice. The DNA binding ability of these complexes follows an order of PPT>OPT>MPT. Cellular uptake and distribution studies show that OPT accumulates mainly in mitochondria, while MPT and PPT accumulate more preferentially in nuclei than in mitochondria. As a result, OPT induces remarkable changes in the ultrastructure and membrane of mitochondria, leading to more radical mitochondrial dysfunctions than cisplatin. The release of cytochrome c from mitochondria is more evident for cells treated by OPT than by cisplatin, though the apoptosis of A549 cells induced by OPT is similar to that induced by cisplatin. Disruption of mitochondrial oxidative phosphorylation

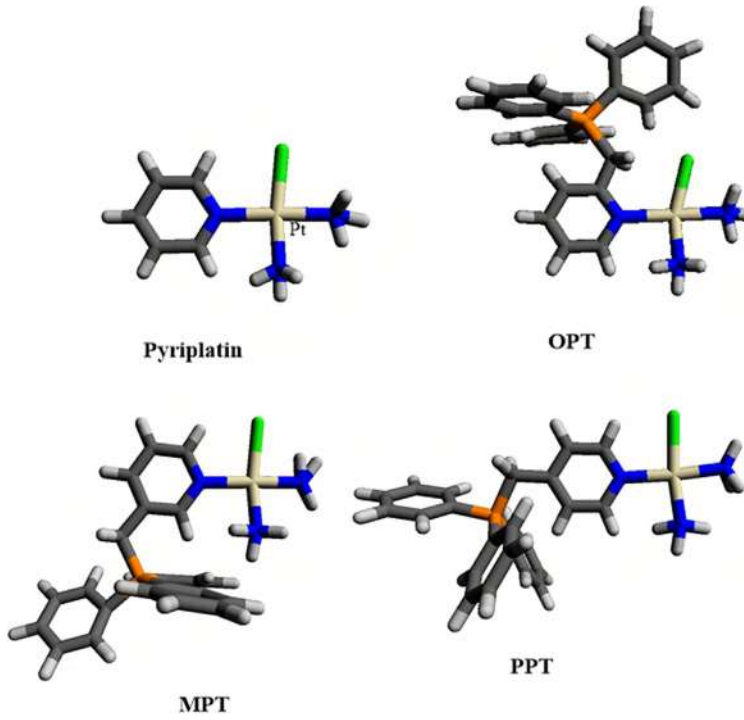

FIGURE 12.3 Chemical structure of pyriplatin, OPT, MPT, and PPT.

and glycolysis is involved in the antitumor mechanism of these compounds. The results indicate that in addition to DNA binding, bioenergetic pathways also play crucial roles in the antitumor activity of mitochondrion-targeted monofunctional Pt complexes.

Carlson Alexander and his group [16] synthesized and characterized the dinucleating ligands 1,2-bis(2-(1H-imidazo[4,5-f][1,10]phenanthrolin-2-yl)phenoxy)ethane (L1) and 1,2- bis(2-(1H-imidazo[4,5-f][1, 10]phenanthrolin-2-yl)phenoxy)hexane (L2) and their dinuclear complexes [Pt2(L1)Cl4] and [Pt2(L2)Cl4] where these imidazophenanthroline-based ligands are present as bridging ligands (Fig. 12.4) and the in vitro cytotoxicity of the complexes against HeLa, HepG2, and MCF-7 cell lines were reported. The complexes undergo aquation following first-order kinetics. The MTT and trypan blue assays show higher cytotoxicity of the complexes toward the HepG2 and MCF-7 cell lines compared to cisplatin. The AO/EB assay and flow cytometry by Annexin V alexa fuor488/PI double staining assay demonstrate distinct morphological changes of apoptosis in a dose-dependent manner. The cell cycle analysis indicates a marked decrease in the DNA content in the G0/G1 phase with an increase in the G2/M phase on increasing the concentration of the complexes. The potential of the complexes for use as anticancer agents was demonstrated by

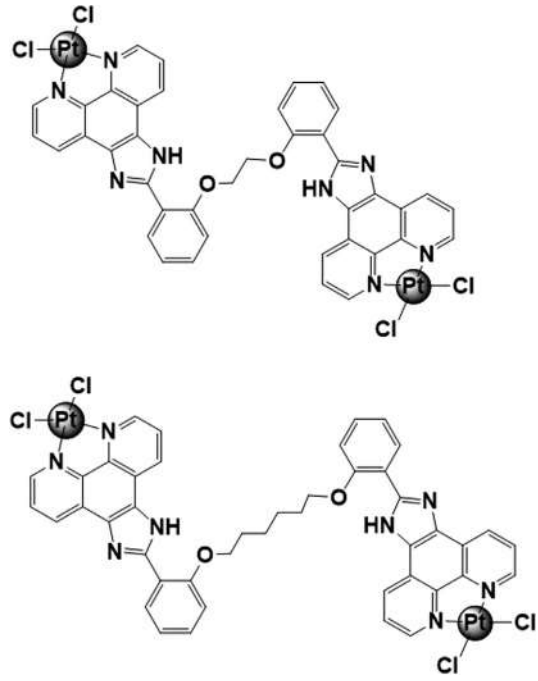

FIGURE 12.4 Chemical structure of complexes [Pt2(L1)Cl4] and [Pt2(L2)Cl4].

their antiproliferative activity on the cell lines. The complexes interact with the major groove of DNA through H-bonding between the imidazole N–H protons and the nucleotide residues DC‘21/N4 (cytosine) for complex [Pt2(L1)Cl4] and DT‘7/O2 (thymine) and DT‘19/O2 (thymine) for complex [Pt2(L2)Cl4], with the binding energy of −1.98 and −4.45 kcal/mol, respectively.

Michael J. Hannon and his group [17] investigated the DNA binding properties, the ability to affect DNA transactions, and the cytotoxicity of 2,7-diazapyrenium- based ligand(L3) and its Pt (II) complex (Fig. 12.5). They have shown that the metallosupramolecular complex and its ligand L3 are effective DNA binding agents. The complex prevents DNA processing in PCR experiments whereas the ligand does not. The supramolecular Pt (II) complex is active against a panel of cancer cell lines whereas the ligand is not. The supramolecular Pt (II) complex has activities at concentration ranges comparable to those for the anticancer agent cisplatin though, as expected given its different mode of DNA binding, its spectrum of activity is different. This provides further demonstration of the excitement and the potential of much metallosupramolecular architecture as DNA-binding anticancer metallodrugs.

Sourav Bhowmick, Achintya Jana, Khushwant Singh, Prerak Gupta, Ankit Gangrade, Biman B. Mandal* and Neeladri Das* *Inorg. Chem.* 2018, 57, 7, 3615–3625}. Copyright {2018} American Chemical Society.”

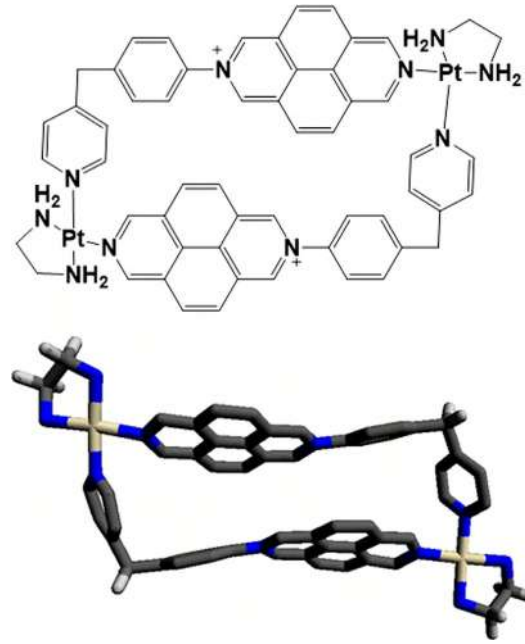

FIGURE 12.5 2,7-diazapyrenium-based Pt (II) complex.

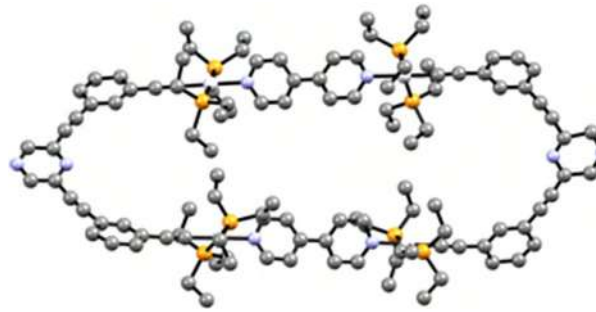

FIGURE 12.6 Organometallic clip and irregular hexagonal Pt macrocycle "Reprinted (adapted) with permission from "Coordination-driven self-assembly of ionic irregular hexagonal metallamacrocycles via an organometallic clip and their cytotoxicity potency."

Sourav Bhowmick and his group [18] synthesized two new irregular hexagons (Fig. 12.6) from a pyrazine motif containing an organometallic acceptor clip [bearing Pt (II) centers] and two neutral donor ligands separately (4,4′-bipyridine or pyrazine) using a coordination-driven self-assembly protocol. The cytotoxicity of Pt (II)-based supramolecules was studied using different cell lines such as A549 (human lung carcinoma), KB (human oral cancer), HaCaT (human skin keratinocyte) and MCF7 (human breast cancer) cell lines, and the results were compared with those of cisplatin. The smaller macrocycle exhibited

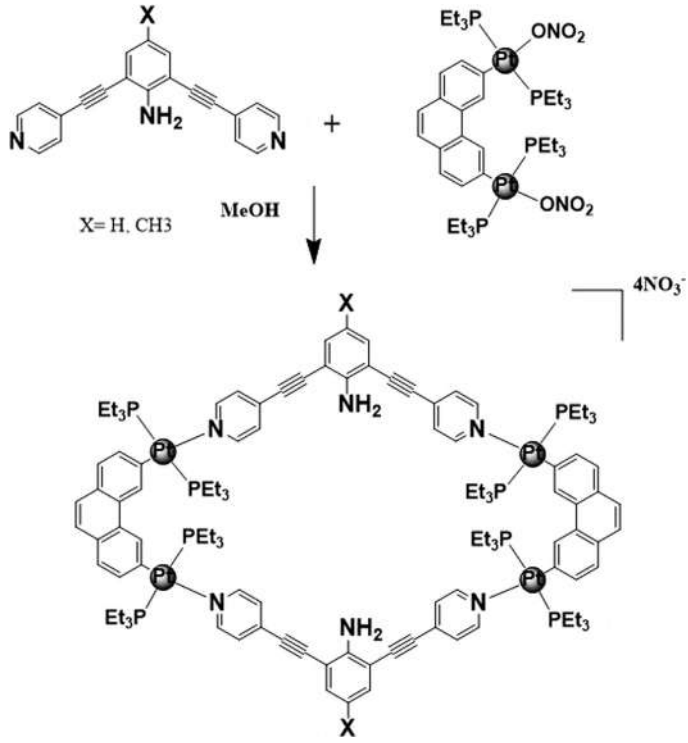

FIGURE 12.7 Rhomboidal Pt (II) supramolecular complexes.

a higher cytotoxic effect against all cell types, and its sensitivity was found to be comparable with that of cisplatin for A549 and MCF7 cells.

Ivan V. Grishagin and his group [19] investigated the uptake, intracellular localization, and antitumor activity of two rhomboidal Pt (II)-based supramolecular complexes (Fig. 12.7). Laser-scanning confocal microscopy in A549 and HeLa cell lines was performed to determine the uptake and localization of the assemblies within cells and their effect on tumor growth was studied in mouse s.c. tumor xenograft models. The supramolecular complexes are soluble in cell culture media within the entire range of studied concentrations (1-5 μM), are nontoxic, and showed efficacy in reducing the rate of tumor growth in s.c. mouse tumor xenografts. These properties reveal the potential of Pt (II)-based supramolecular complexes for future biomedical applications as therapeutic agents.

Mishra et al., [36] synthesized tetracationic heterobimetallic complexes (Fig. 12.8) obtained from an N, N′-bis(4-(pyridin-4-ylethynyl)phenyl) pyridine-2,6-dicarboxamide ligand and cis-blocked Pt(II) 1,1′-bis(diphenylphosphino)ferrocene triflates. Its structure and composition have been characterized by NMR spectroscopy, HR-ESMS, and elemental analysis and further modeled by molecular mechanics calculations. The stability of the

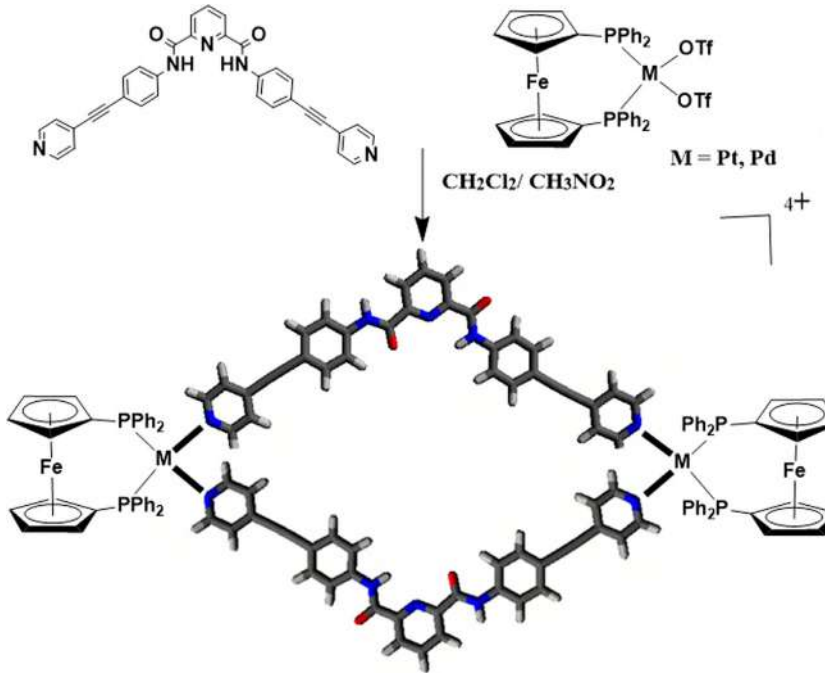

FIGURE 12.8 Hetracationic heterobimetallic supramolecular complexes (M=Pt, Pd).

metallacycle has been tested either by monitoring the cytotoxicity effect after different periods of pre-incubation in cell culture medium (Dulbecco's modified eagle medium—DMEM) or in DMSO (for 0, 10, 25, and 50 hours at 37°C) or by fluorescence spectroscopy measurements in physiological buffer solution at pH 7.4 and in presence of redox-active compounds (H_2O_2 or dithiothreitol). This complex exhibits cytotoxicity higher than cisplatin against the tested human cancer cell lines (T98G, KB, and SNU-80), it is twice less toxic to the normal human embryonic kidney cells (HEK-293) than cisplatin, which indicates much better cancer cell selectivity. The stability studies indicated that under physiological conditions and even in presence of redox-active compounds the supramolecule 67 remain intact for at least 50 h, whereas in presence of DMSO a significant loss of cytotoxicity was observed for pre-incubation periods of $>$ 25 h. These observations could suggest that the metallosupramolecular structure is crucial for the observed cytotoxicity profiles since the DMSO-induced disassembly is proposed as the main reason for the decrease in cytotoxicity. The mode of action, which leads to the observed cytotoxicity, has been associated with apoptosis and it is evidenced by the caspase-3/7 activity assays.

Zheng et al. [20] presented a novel approach for developing a delivery system for cisplatin-based on the use of Pt (IV) prodrugs and a self-assembled

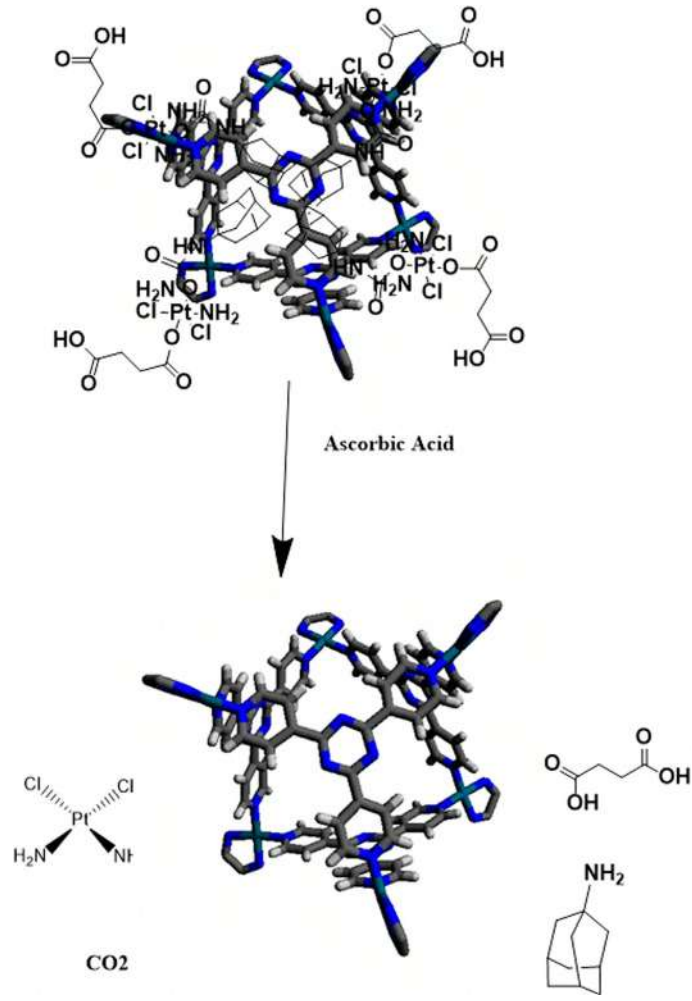

FIGURE 12.9 Self-assembled Pt complex for encapsulation of platinum prodrug and its delivery.

metal-based complex (Fig. 12.9). The delivery system consists of a hexanuclear Pt(II) cage that can host four Pt (IV) prodrug guest molecules. This host–guest complex, exhibiting a diameter of about 3 nm, has been characterized by detailed NMR analysis. The biological properties of the system were evaluated by the MTT assay, cellular uptake studies, flow cytometry, and fluorescence microscopy. Because of the high positive charge, this nanostructure exhibits high cellular uptake. The improved anticancer activity is caused by biological reductions of the Pt (IV)- prodrug, as evidenced by adding ascorbic acid, and release of the cytotoxic cisplatin which leads to cell cycle arrest and apoptosis. The detailed study on the mechanism of action of this supramolecular cage

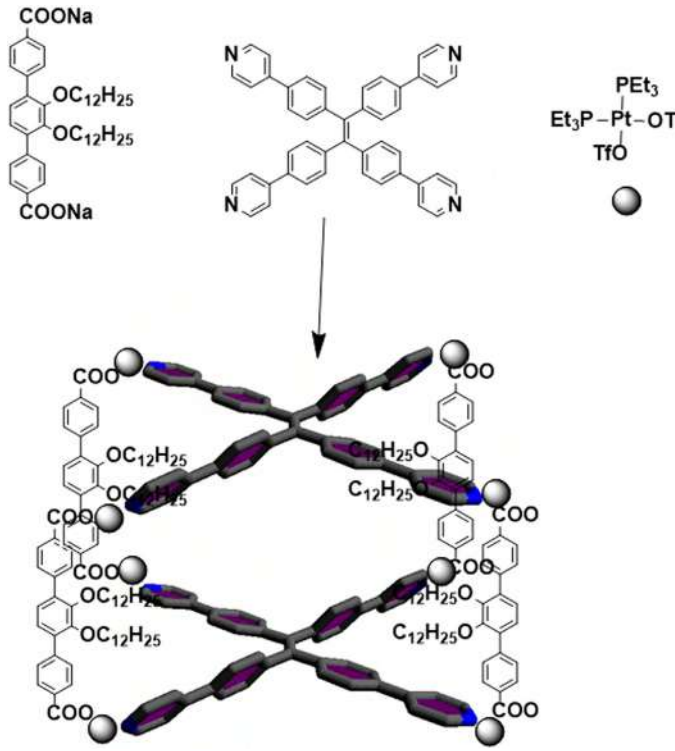

FIGURE 12.10 Tetraphenylethene-based Pt metallacage theranostic system.

showed that it interacts with DNA in a non-covalent intercalative way leading to DNA damage, and inducing apoptosis through up-regulation of p53 and p21 proteins.

Peter J. Stang and coworkers [21] prepared a highly emissive tetraphenylethene-based metallocage theranostic system (Fig. 12.10) with the capability to perform dual functions (i.e., imaging and therapy) by unifying self-assembly, coordination chemistry, and supramolecular chemistry. When the assembly is treated with two variants of a 1,2-distearoyl-phosphatidylethanolamine (DSPE)/polyethylene glycol (PEG) conjugate, mPEGDSPE, and biotin-PEG-DSPE metallocages are formed. Upon the formation of self-assembled polymeric aggregates with sizes of about 37 nm (as determined by TEM and DLS techniques) selective delivery to cancer cells has been achieved employing the EPR effect additionally to the biotin-mediated internalization in cancer cells. Confocal laser scanning microscopy and flow cytometry confirmed the selective targeting of the biotin functionalized nanoparticles to cancer cells overexpressing the corresponding receptor (HeLa and HepG2 cells) in contrast to normal cells (CHO and HEK-293). This is corroborated with their higher and selective cytotoxicity and high Pt-content in

the cancer cells nuclei. The theranostic functions of the biotin-functionalized nanoparticles have been reported also in vivo in HeLa tumor-bearing female nude mice confirming their superiority than the clinical formulations of oxaliplatin, carboplatin, or cisplatin used as control. Accumulation of Pt from the nanoparticles was observed in the tumor in comparison with the control Pt-drugs, but administration of nanoparticles resulted in a lower Pt uptake by the liver, spleen, lung, and kidneys, which suggested that the use of PEGylated nanoparticles also provides way to decrease the systemic toxicity of Pt-drugs. highly emissive Pt (II) supramolecular triangles (Fig. 12.11) containing boron dipyrromethene (BODIPY) based bridging ligands. The formation of two triangular metallocycles was fully characterized by multinuclear NMR (1H and 31P), ESI-MS, 2D DOSY, UV–Vis, and fluorescence spectroscopy. The metallocycles exhibited favorable anticancer activities against HeLa cell lines (IC50 of 6.41 μM and 2.11 μM). The BODIPY fluorophore was found to be an excellent photodynamic agent, making the metallocycles as ideal therapeutics for photodynamic therapy (PDT) and chemotherapy. In vitro studies demonstrated that the combination indexes against HeLa cells are 0.56 and 0.48 for 70a and 70b, respectively, confirming their synergistic anticancer effect. These supramolecular triangles also showed superior anticancer efficacy toward cisplatin-resistant A2780cis cell by combining PDT and chemotherapy, indicating promise in overcoming drug resistance and for fluorescence imaging-guided cancer therapy.

Eskandari and group [23] have recently synthesized platinum-based molecular triangle (Fig. 12.12) based on benzotriazole ligands which showed selective cytotoxicity toward breast cancer stem cells and were found more efficient as compared to cisplatin. The cytotoxicity is found to be dependent on the supramolecular structure with the dinuclear complex showing less potency as compared to trinuclear supramolecule. Platinum trinuclear supramolecule exhibits impressive potency and selectivity toward breast CSCs in vitro. Strikingly the trinuclear platinum complex exhibits significantly greater breast CSC potency than salinomycin, cisplatin, and carboplatin in monolayer and three-dimensional cell cultures. It induces breast CSC apoptosis by entering breast CSCs in relatively large quantities, bypassing the nuclear membrane, and inducing genomic DNA damage.

Sleiman et al. [24] reported that the self-assembled Pt molecular square [Pt(en)(4,4′-dipyridyl)]4 (Fig. 12.13) was an efficient G-quadruplex binder and telomerase inhibitor. Molecular modeling studies revealed the square arrangement of the four bipyridyl ligands, the highly electropositive nature of the overall complex, and also the H-bonding interactions between the ethylenediamine ligands and phosphates of the DNA backbone contribute to the observed strong binding affinity to the G-quadruplex.

“Reprinted (adapted) with permission from {A platinum supramolecular square as an effective G-quadruplex binder and telomerase inhibitor by roxanne kieltyka †, Pablo Englebienne †, Johans Fakhoury, Chantal Autexier, Nicolas

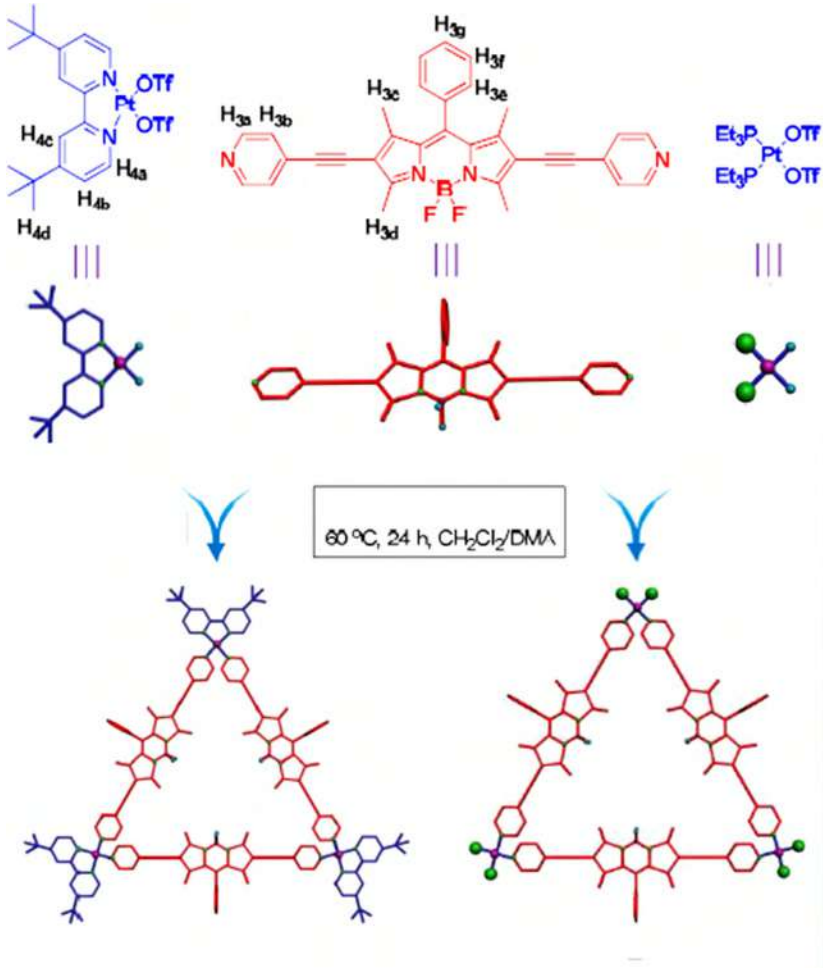

FIGURE 12.11 Pt (II) supramolecular triangles from BODIPY ligand. Reprinted (adapted) with permission from {Highly emissive self-assembled BODIPY-platinum supramolecular triangles Jiong Zhou, Yuzhen Zhang, Guocan Yu*, Matthew R. Crawley, Cressa Ria P. Fulong, Alan E. Friedman, Sanghamitra Sengupta, Jifu Sun, Qing Li, Feihe Huang* and Timothy R. Cook* J. Am. Chem. Soc. 2018, 140, 24, 7730–7736}. Copyright {2018} American Chemical Society." Timothy R. Cook and co-worker [22] reported the coordination-driven self-assembly of two.

Moitessier †and Hanadi F. Sleiman † *J. Am. Chem. Soc.* 2008, 130, 31, 10040–10041}. Copyright {2008} American Chemical Society." A. Terenzi and his group [25] presented the evaluation as DNA binders of three Pt (II) dinuclear squares of different sizes and their constituent L-shaped 4,4′- bipyridine ligands (Fig. 12.14). These three di-nuclear Pt (II) molecular squares of distinct size (ranging between 110 and 220 Å) inhibited cancer cells' growth and heavily influenced the expression of genes known to form G-quadruplexes in their

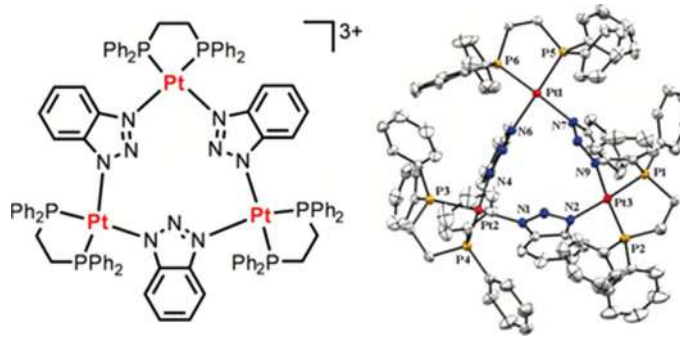

FIGURE 12.12 Pt (II) supramolecular triangle based on benzotriazole. Reprinted (adapted) with permission from {A triangular platinum(II) multinuclear complex with cytotoxicity toward breast cancer stem cells by Arvin Eskandari, Arunangshu Kundu, Dr. Sushobhan Ghosh, Dr. Kogularamanan Suntharalingam *Angew. Chemie*. 131 (2019) 12187–12192}. Copyright {2019} Wiley.

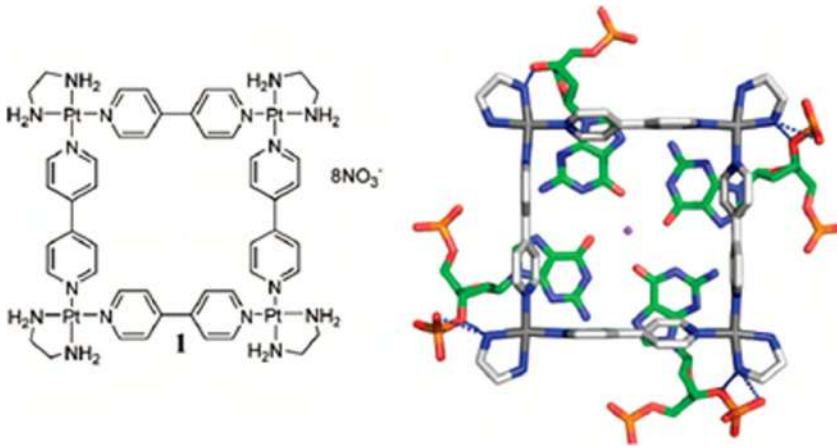

FIGURE 12.13 Self-assembled Pt molecular square.

promoter regions. Interestingly, the smallest Pt-box displayed less activity, but enhanced selectivity for the G4 promoter c-Kit, as shown by FRET (Fluorescence Resonance Energy Transfer) DNA melting assays.

Stang and co-workers [26] developed a Pt (II) metallocage (Fig. 12.15) using therapeutic cis-(PEt3)2Pt(OTf)2 (cPt), 5,10,15,20-tetra(4-pyridyl)porphyrin (TPP) and disodium terephthalate (DSTP) as the building blocks, acting as a theranostic platform to fabricate metal nanoparticles (MNPs) with the idea of achieving synergistic anticancer efficacy. The MNPs exhibited long blood circulation time and high tumor accumulation benefiting from the EPR effect and active targeting ability. Indeed, superior tumor suppression compared to separate cisplatin treatment and light irradiation were observed without recurrence after

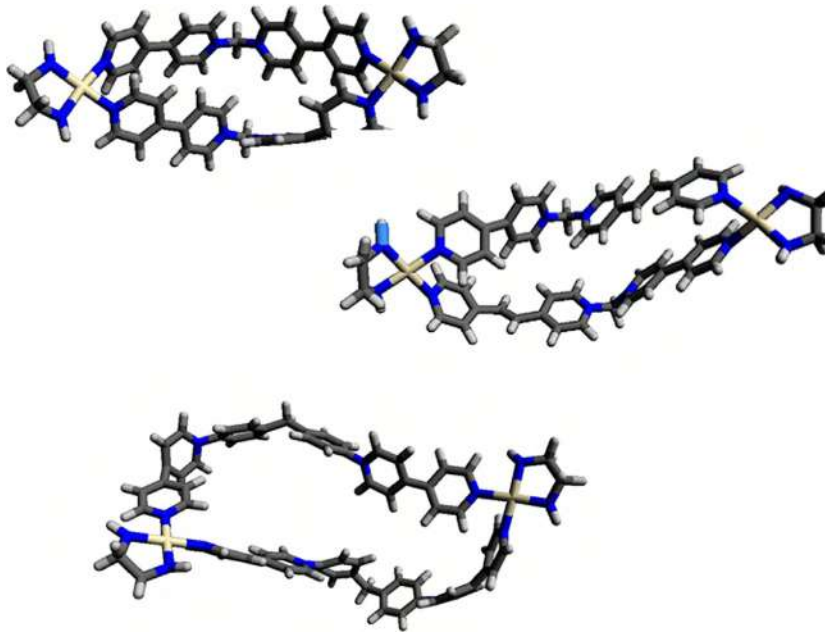

FIGURE 12.14 Schematic representation of the PT-boxes with bypyridine based ligands.

single-dose injection of the targeted MNPs in xenograft models of tumors from $\alpha v\beta 3$ integrin overexpressing U87MG cells and cisplatin-resistant human ovarian cancer A2780cisR cells. Furthermore, in order to check the in vivo antitumor performance and antimetastasis effect of photochemotherapy, as is done in experimental animal model for stage IV human breast cancer, 4T1 (breast cancer) tumors were orthotopically inoculated in the mammary fat pads to generate spontaneous metastases in the lung.

Tubular Cage "Reprinted (adapted) with permission from {Self-assembled PtII8 metallosupramolecular tubular cage as dual warhead antibacterial agent in water."

By Soumalya Bhattacharyya, Mangili Venkateswarulu, Jagabandhu Sahoo, Ennio Zangrando, Mrinmoy De* and Partha Sarathi Mukherjee* *Inorg. Chem.* 2020, 59, 17, 12690–12699}. Copyright {2020} American Chemical Society." Partha Sarathi Mukherjee and his group [27] assembled a new benzothiadiazole-based tetrapyridyl ligand (L) with cis-[(en)Pt(NO3)2] and constructed a highly water-soluble metallosupramolecular photoactive tubular cage (Fig. 12.16). This cage could bring an extraordinary photosensitizer, benzothiadiazole, into the water which is otherwise insoluble and it could photogenerate singlet oxygen. The cage has been successfully applied for the disinfection of pathogens in water using both MRSA and PA as model pathogens as representatives for gram (+ve) and gram (-ve) bacteria, respectively. The results suggest two possible mechanisms for the antibacterial activity: generation of singlet oxygen in the

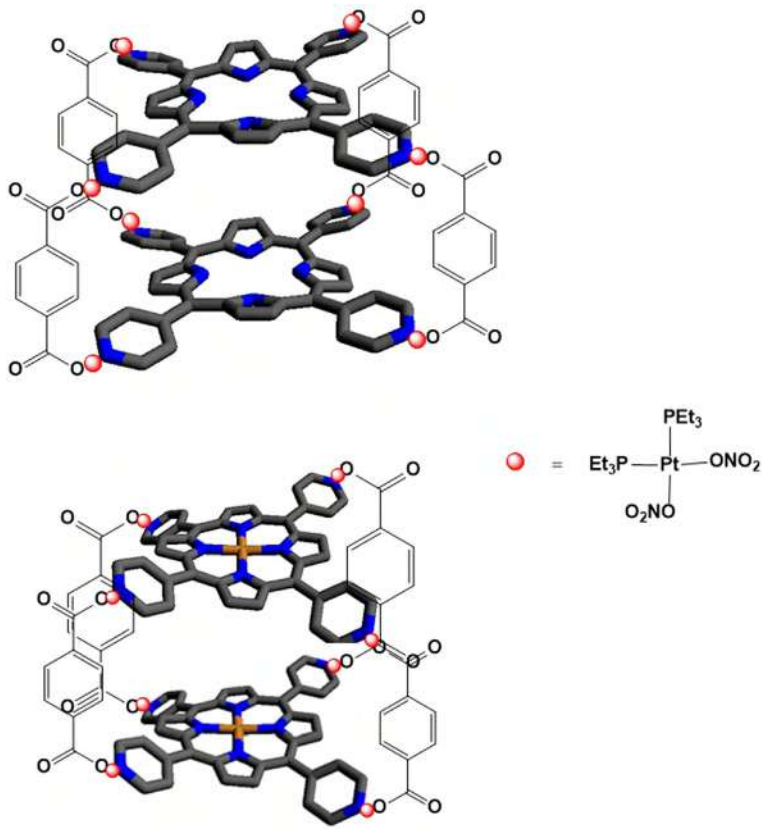

FIGURE 12.15 Schematic representation of Pt (II) porphyrin-based metallocages.

FIGURE 12.16 Benzothiadiazole-based tetrapyridyl ligand and Pt metallosupramolecular.

presence of light and electrostatic interaction with the membrane which can cause death by hydrolyzing the bacteria cell wall. Furthermore, ligand (L) and Pt-acceptor are unable to inhibit bacterial growth. The net positive charge and hydrophobic aromatic walls of the cage are contributing toward antibacterial activity which is evident from the low MIC values in the absence of light. The cell toxicity was measured by considering both HeLa and HEK 293 cell lines. The IC50 value confirms the lower toxicity of the cage toward both cancer and normal cell lines. The ability of such a supramolecular architecture to inactivate bacteria in the water is noteworthy and may lead to the generation of new antimicrobial supramolecular systems.

12.3 Palladium complexes as anticancer agent

Globally, the demand for Pt-based drugs has been growing steadily, although several side effects ranging from nephrotoxicity to drug resistance of the tumor cells have posed real challenges to researchers [28–31]. Side effects associated with cisplatin administration, along with limited applicability arising from specificity shown toward certain cancer cell lines have prompted researchers to look for alternatives. Pd-based complexes are closely related to their Pt analogs, due to their structural similarities and significant overlap of coordination chemistry for the two metals. A recent trend observed in Pd-based anticancer drugs is to focus on the development of Pd complexes with slower rates of hydrolysis brought about by the judicious choice of the ligands. Naturally occurring compounds such as alkaloid harmine display significant biological activity including antitumor activity. In an attempt to explore the possible enhancement in the antitumor properties of the metal coordinated analog of harmine, Al-Allaf and coworkers reported the synthesis of trans-[Pd(harmine)(DMSO)Cl2] complex (Fig. 12.17) [32]. Cytostatic studies performed on P388, L1210, and K562 cell lines revealed the superior activity of the metal-coordinated version of harmine than cisplatin or the uncoordinated harmine itself.

Navarro-Ranninger and co-workers [33] synthesized dimeric Pd complexes 40 and 41 (Fig. 12.18) and investigated their cytotoxic activity. The dimeric Pd complexes were tested against MDA-MB 468 and HL-60 human cancer cell lines for in vitro-antiproliferative activity. The antitumor activity was comparable to that observed with cisplatin. These results reiterate the potential of dimeric Pd complexes toward enhancing the cytotoxic activity.

Navarro-Ranninger and co-workers recently disclosed the synthesis of a novel tetrameric Pd complex (Fig. 12.19) [34]. This complex was tested for antitumor properties against several tumor and normal cell lines like PAM-RAS, GLIOMA-108, GLIOMA-112, JURKAT, HeLa, 3T3, and PAM with cisplatin, etoposide, and adriamycin as reference standards. The IC50 values exhibited by the complex suggest that it has potential anticancer activities as the one shown by cisplatin. However, in certain cases, the values exceeded those of

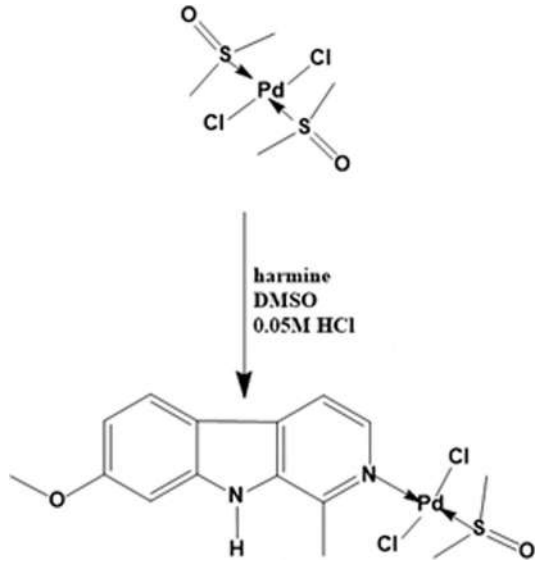

FIGURE 12.17 Palladium harmine complex.

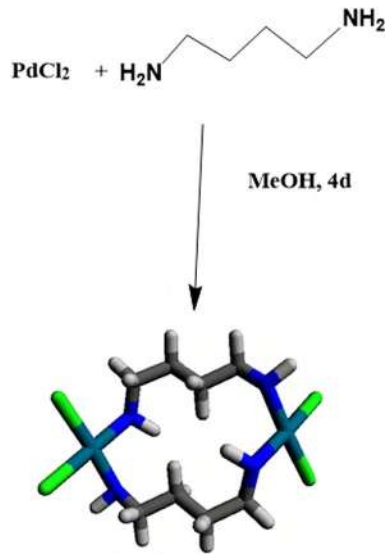

FIGURE 12.18 Dimeric Pd complexes.

cisplatin too, and resulted in DNA interhelical cross-links upon their interaction with DNA.

Gupta et al. [35] synthesized four new Pd metal supramolecules (Fig. 12.20) using square/triangular architectures which were derived from boron dipyrromethane (BODIPY) ligands by self-assembly; they fully characterized

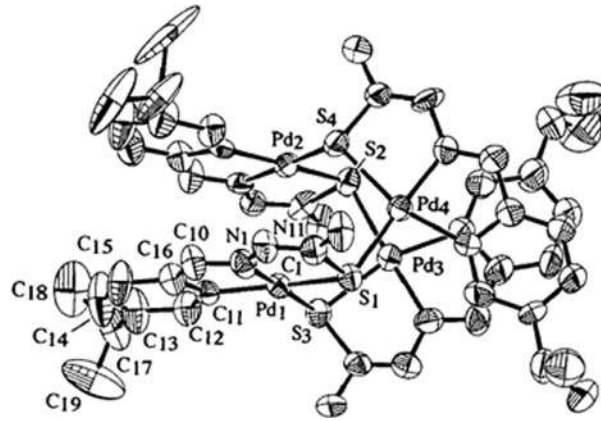

FIGURE 12.19 Tetrameric Pd complex.

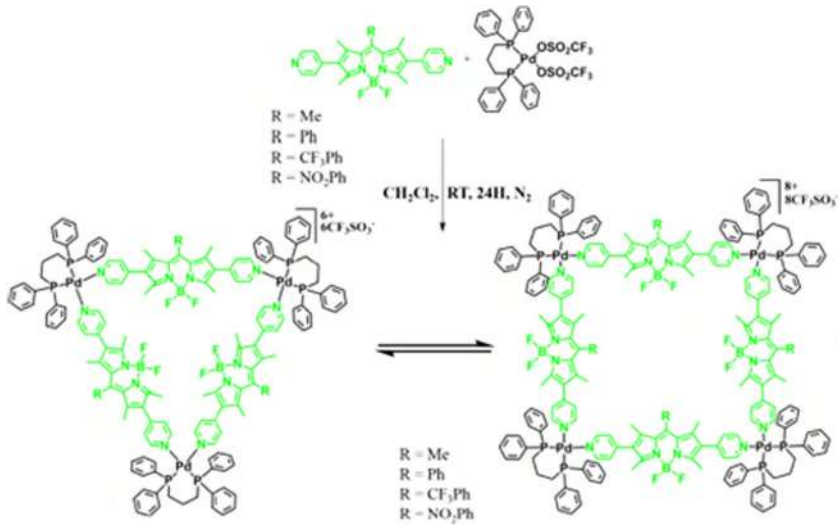

FIGURE 12.20 Self-assembled supramolecular Pd complexes with triangular/square.

all the supramolecules by 1H and 31P NMR, ESI-MS, and single-crystal X-ray diffraction. These complexes exhibited selective cytotoxicity against brain cancer (glioblastoma) cells U87 in comparison to that against normal brain cells WI-38. Their cytotoxicity to the glioblastoma cells was higher than cisplatin. The supramolecular triangles showed appreciable interaction, compared to the smaller precursors.

Architectures from BODIPY ligand. "Reprinted (adapted) with permission from {Self-Assembled Novel BODIPY-Based Palladium Supramolecules and Their Cellular Localization By Gajendra Gupta *†, Abhishek Das, Kyoung Chul Park, Artur Tron, Hyunuk Kim §, Junyoung Mun, Nripendranath Mandal, Ki-Whan Chi ‖ and Chang Yeon Lee *†¶ Inorg. Chem. 2017, 56, 8, 4615–4621}.

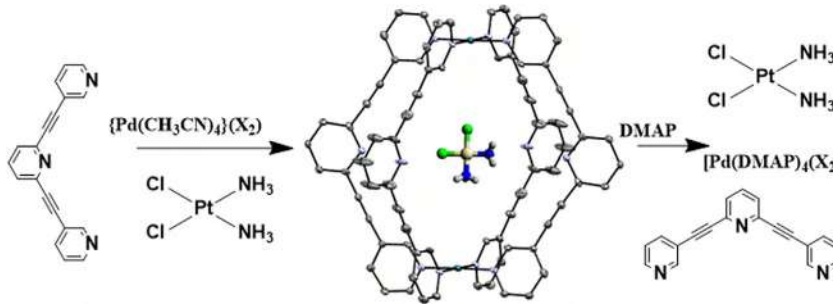

FIGURE 12.21 Self-assembled di-Pd(II) molecular cage for delivery of cisplatin.

Copyright {2020} American Chemical Society." Mishra et al. [36] synthesized tetracationic heterobimetallic complex (Fig. 12.8) from N, N′-bis(4-(pyridin-4-ylethynyl)phenyl)pyridine-2,6-dicarboxamide ligand and cis-blocked Pd(II) 1,1′-bis(diphenylphosphino)ferrocene triflates. Its structure and composition have been characterized by NMR spectroscopy, elemental analysis, and HR-ESMS and further modeled by molecular mechanics calculations. The stability of the metallocycle has been tested either by monitoring the cytotoxicity effect after different periods of pre-incubation in cell culture medium (Dulbecco's modified eagle medium—DMEM) or in DMSO (for 0, 10, 25, and 50 h at 37°C) or by fluorescence spectroscopy measurements in physiological buffer solution at pH 7.4 and in presence of redox-active compounds (H_2O_2 or dithiothreitol). While the complex exhibited cytotoxicity higher than cisplatin against the tested human cancer cell lines (T98G, KB, and SNU-80), it is twice less toxic to the normal human embryonic kidney cells (HEK-293) than cisplatin indicating the complex has much better cancer cell selectivity. The stability studies indicated that under physiological conditions and even in presence of redox-active compounds the Pd-supramolecule remains intact for at least 50 h, whereas in presence of DMSO a significant loss of cytotoxicity was observed for pre-incubation periods of more than 25 h. These observations could suggest that the metallosupramolecular structure is crucial for the observed cytotoxicity profiles since the DMSO-induced disassembly is proposed as the main reason for the decrease in cytotoxicity. The mode of action, which leads to the observed cytotoxicity, has been associated with apoptosis and it is evidenced by the caspase-3/7 activity assays.

Lewis et al. [37] showed that di-Pd(II) molecular cages of the formula [Pd2L4](X)4 (Fig. 12.21) can be quantitatively self-assembled from a simple tripyridyl ligand (2,6-bis(pyridin-3-ylethynyl)pyridine) and [Pd(CH3CN)4](X)2 (X = BF4 or SbF6). The cages have been fully characterized using 1H, 13C, and DOSY NMR spectroscopy, elemental analysis, IR spectroscopy, and HR-ESMS. The reported encapsulation of the anticancer drug cisplatin by this supramolecular cage has created interest for developing controlled release by external stimuli. The cage formation and cisplatin encapsulation proceed virtually quantitatively

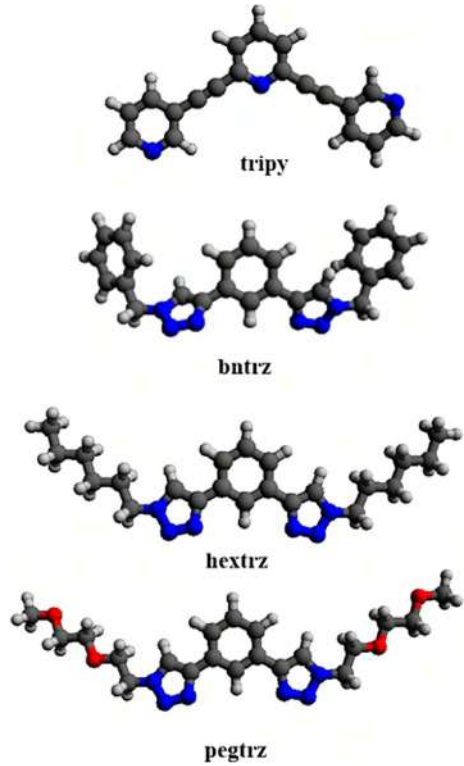

FIGURE 12.22 Chemical structures of the pyridine- (tripy) and triazole-(bntrz, hextrz and pegtrz) based ligands which form four supramolecular complexes [Pd$_2$ (tripy)$_4$](BF$_4$)$_4$, [Pd$_2$ (bntrz)$_4$](BF$_4$)$_4$, [Pd$_2$(hextrz)$_4$](BF$_4$)$_4$, [Pd$_2$(pegtrz)$_4$](BF$_4$)$_4$.

and the supramolecular cage and its host–guest complex with encapsulated two molecules of cisplatin have been characterized by single-crystal X-ray diffraction studies. While the cage and the host–guest complex are stable in organic solvents, the cage readily disassembles in presence of competing amine ligands or chlorides, and thus the encapsulated cisplatin molecules can be released. The authors studied in detail the encapsulation phenomenon and highlighted the importance of the H-bonding interactions between the cage and the amine ligands of the cisplatin guest. This host–guest chemistry could open the way to relatively unexplored methods of drug delivery, which circumvent the malicious side effects and drug resistance associated with cisplatin and other anticancer therapeutics.

James D. Crowley [38] screened a small series of [Pd2(L)4](BF4)4 quadruply-stranded, di- Pd(II) architectures (Fig. 12.22) for their cytotoxic effects against three cancer cell lines and one nonmalignant line. The helicates exhibited a range of cytotoxic properties, with the most cytotoxic complex [Pd2 (hextrz)4](BF4)4 possessing low micromolar IC50 values against all of the cell

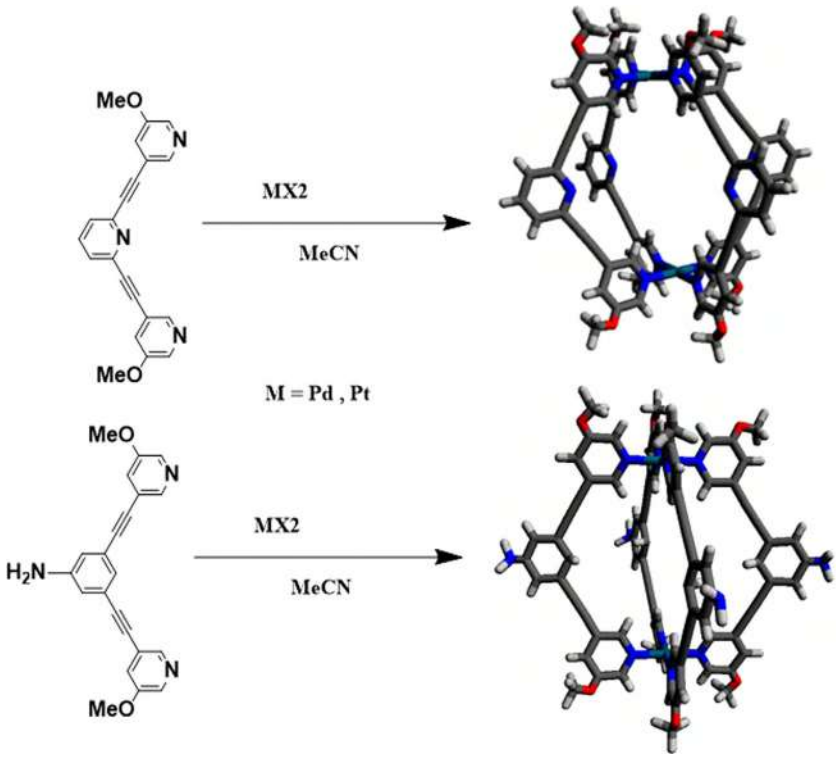

FIGURE 12.23 Schematic representation of self-assembled coordination cages for encapsulation of cisplatin and increased cytotoxicity toward human lung adenocarcinoma A549 cells.

lines tested, while the other helicates displayed moderate or no cytotoxicity. [Pd2 (hextrz)4](BF4)4 was found to be 7-fold more active than cisplatin against the MDAMB- 231 cell line. Additionally, preliminary mechanistic studies indicate that the [Pd2 (hextrz)4](BF4)4 helicate does not induce cell death in the same way as clinically used metal complexes such as cisplatin. In this case, the helicate appears to disrupt the cell membrane rather than interacting with DNA, Fritz E. Kühn and his group [39] reported the synthesis of new Pd2L4 molecular cages (Fig. 12.23), derived from highly fluorescent, rigid polyaromatic ligands. The host–guest chemistry of the Pd cages with cisplatin has been investigated confirming the encapsulation. The Cisplatin encapsulated cages exhibit a significantly enhanced cytotoxicity toward A549 (human lung adenocarcinoma) cells as compared to bare cisplatin. This appears to be promising delivery vectors for the anticancer drug cisplatin. Ghosh et al. have synthesized Pd and Pt-based supramolecular rectangular complexes [40] (Fig. 12.24) with a new guanosine-terpyridine ligand system which were fully characterized by 1H NMR, ESI MS as well as single crystal X-ray diffraction. Both the complexes showed in vitro

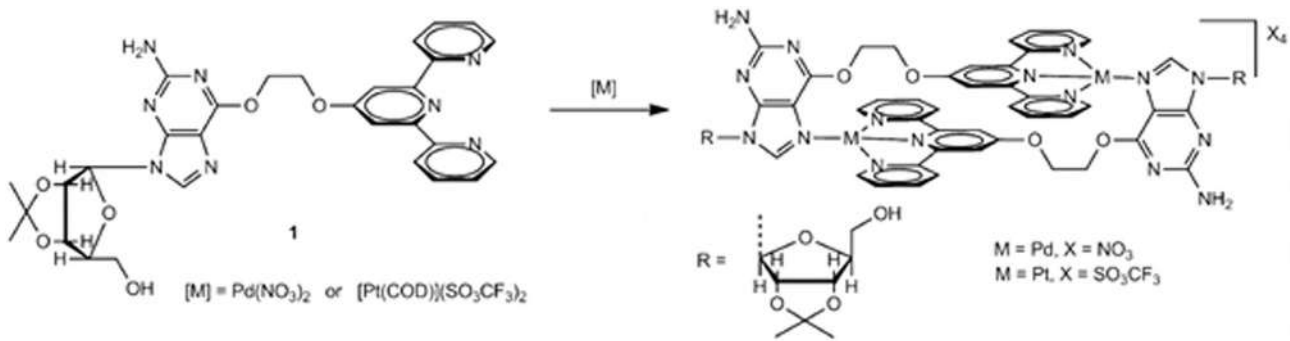

FIGURE 12.24 Self-assembled rectangular coordination cages from novel guanosine-terpyridine ligand showing invitro binding with G-quadruplex DNA. "Reprinted (adapted) with permission from {Assembly of palladium(II) and platinum(II) metallorectangles with a guanosine-substituted terpyridine and study of their interactions with quadruplex DNA by Sushobhan Ghosh [1], Oscar Mendoza, Leticia Cubo, Frédéric Rosu, Valérie Gabelica, Andrew J P White, Ramon Vilar Chem. - *A Eur. J*. 20 (2014) 4772–4779}. Copyright {2014} Wiley."

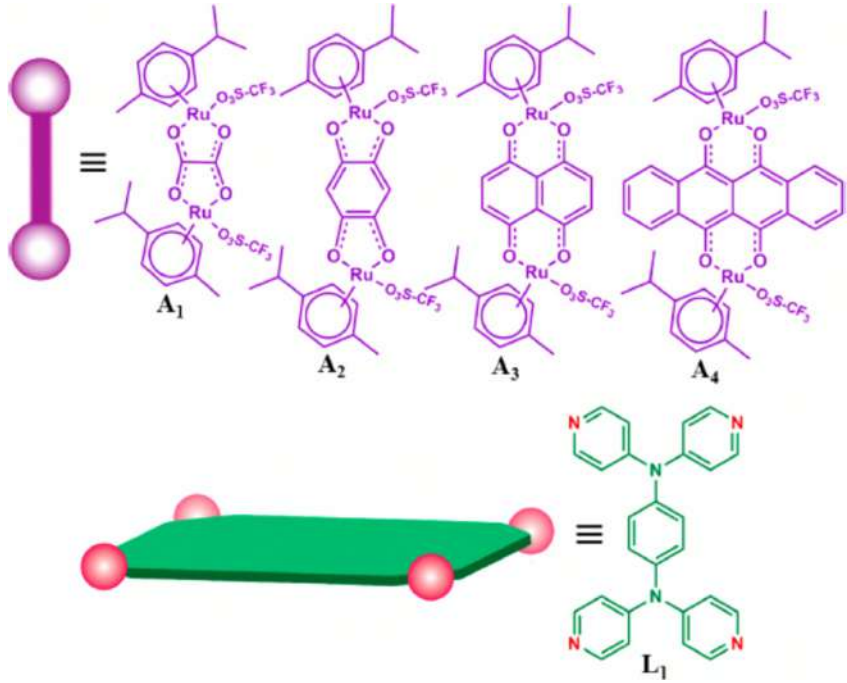

FIGURE 12.25 Self-assembled rectangular Ru based coordination cages for anticancer studies.

binding studies with H-telo and c-myc G-quadruplex DNA sequences making them potential candidates for G-quadruplex targeted antitumor agents.

Eskandari et al. have recently shown [41] the selective breast cancer cell potency of a novel supramolecular triangular palladium complex based on benzotriazole and cisblocked bisphosphinoethane palladium corner units. The triangular complex displayed equal toxicity toward bulk cancer cells and CSCs in the micromolar range. Therefore it has the potential to remove heterogeneous cancer populations in vitro with a single micromolar dose. Remarkably the supramolecular palladium complex exhibited a greater CSC spheroid inhibitory effect than the analogous tri-platinum(II) complex previously reported [23] and salinomycin. In terms of mechanism of action, the palladium(II) complex triggered DNA damage and apoptosis in CSCs.

12.4 Ruthenium and other metallosupramolecular complexes as anticancer agent

Platinum (Pt)-based anticancer drugs like cisplatin and carboplatin have been widely used to treat various cancers. However, poor selectivity and toxicity toward normal cells and increasing chemoresistance remain as major limitations for platinum-based chemotherapeutics. Since the initial introduction of

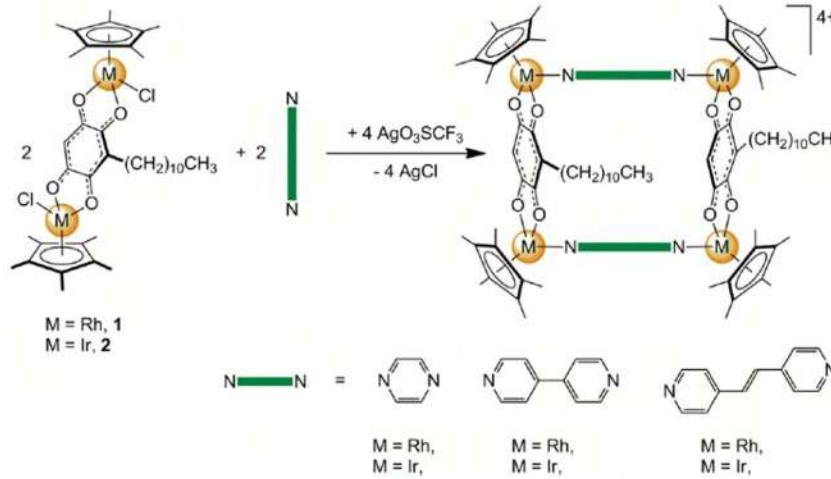

FIGURE 12.26 Self-assembled rectangular Rh(III)/Ir(III) coordination cages.

ruthenium (Ru) polypyridyl complex as anticancer agents, a number of attempts at structural evolution have been conducted to improve efficacy. Among them, half-sandwich Ru-arene complexes have been the most prominent anticancer platform. These complexes have clearly shown superior anticancer profiles like increased selectivity toward cancer cells and ameliorating toxicity against normal cells compared to existing Pt-based anticancers. Currently, several Ru complexes are under human clinical trials. For improvement in selectivity and toxicity associated with chemotherapy, Ru complexes as PDT, and photoactivated chemotherapy, which can selectively activate prodrug moieties in a specific region, have also been investigated.

Recently Mukherjee et al. [42] have shown octanuclear Ru(II) cages (Fig. 12.25) synthesized from dinuclear p-cymene ruthenium(II) acceptors separately with a tetradentate pyridyl ligand The self-assembled cages show strong in vitro anticancer activity against human lung adenocarcinoma A549 and human cervical cancer HeLa cell lines as observed from the 3-(4,5-dimethylthiazol-2-yl)-2,5.

Reprinted (adapted) with permission from { Self-Assembly of Discrete RuII8 Molecular Cages and Their in Vitro Anticancer Activity by Aderonke Ajibola Adeyemo, Abhijith Shettar †#, Imtiyaz Ahmad Bhat ‡, Paturu Kondaiah *† and Partha Sarathi Mukherjee * Inorg. Chem. 2017, 56, 1, 608–617}. Copyright {2017} American Chemical Society." diphenyltetrazolium bromide assay. The excellent anticancer activity of OC-3 and OC-4 highlights the importance of the synergistic effects of the spacer component of the dinuclear p cymene Ru(II) acceptor clips.

Gupta et al. have recently reported [43] Rh (III) and Ir(III) based metallarectangles (Fig. 12.26) based on embelin-derived metallaclips. The antiproliferative

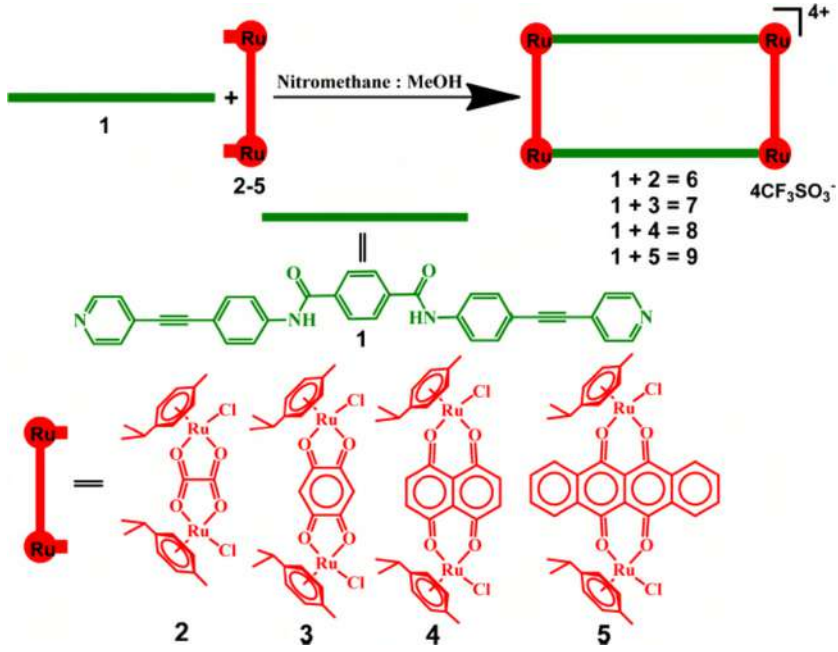

FIGURE 12.27 Self-assembled Ru-coordination cages with fluorescent based terepthalamide linear ligand. "Reprinted (adapted) with permission from {Coordination-Driven Self-Assembly and Anticancer Potency Studies of Arene–Ruthenium-Based Molecular Metallarectangles By Anurag Mishra †, Yong Joon Jeong ‡, Jae-Ho Jo †, Se Chan Kang *‡, Hyunuk Kim § and Ki-Whan Chi *† Organometallics 2014, 33, 5, 1144–1151}. Copyright {YEAR} American Chemical Society."

activity of these tetranuclear complexes was evaluated *in vitro* on cancerous (DU-145, A-549, HeLa) and noncancerous (HEK-293) cell lines. The biological study has shown a better activity for the rhodium derivatives over the iridium analogs and for all complexes a very good selectivity for cancerous over noncancerous cells.

Mishra et al. [44] have shown the two new large molecular metallarectangles (Fig. 12.27) obtained by the reaction of the two different arene-ruthenium acceptors with a symmetrical N,N′-bis(4-(pyridin-4-ylethynyl)phenyl)-Terephthalamide donor ligand. The cytotoxicities of metallarectangles were established in SK-hep-1 (liver cancer), AGS (gastric cancer), and HCT-15 (colorectal cancer) human cancer cell lines. The cytotoxicity of metallarectangle 8 was found to be considerably stronger against a than the well-known anticancer drugs doxorubicin and cisplatin.

Stang et al. [45] have reported six tetranuclear rectangular metallacycles (Fig. 12.28) were synthesized via the [2+2] coordination-driven self-assembly of imidazole-based ditopic donor 1,4-bis(imidazole-1-yl)benzene and 1,3-bis(imidazol-1-yl)benzene, with dinuclear half-sandwich p-cymene ruthenium (II) acceptors. The self-assembled macrocycles and cage containing the

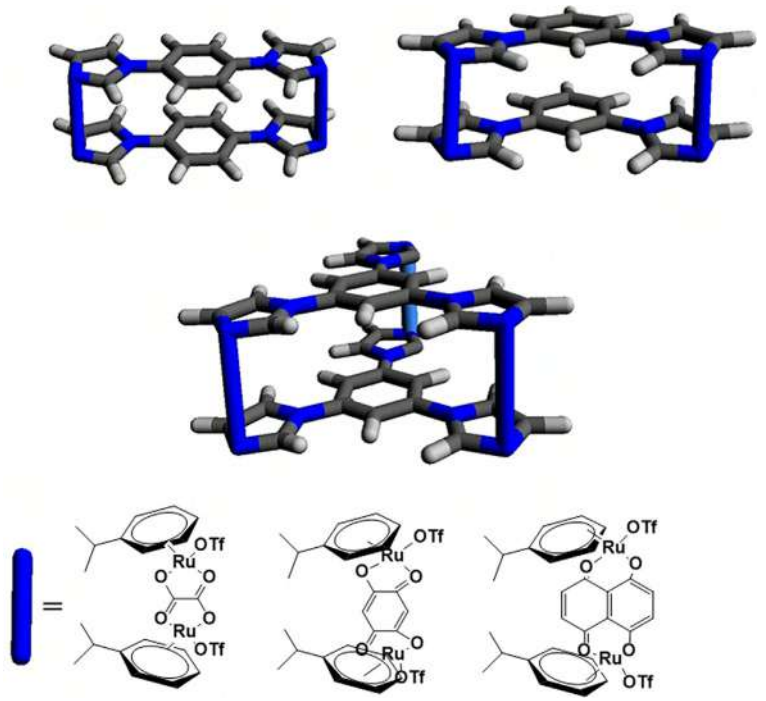

FIGURE 12.28 Schematic representation of self-assembled Ru-coordination cages from imidazole-based ditopic donors.

5,8-dioxido-1,4-naphtoquinonato (donq) spacer exhibited good anticancer activity on all tested cancer cell lines (HCT-116, MDA-MB-231, MCF-7, HeLa, A549, and HepG-2), and showed decreased cytotoxicities in HBE and THLE-2 normal cells.

References

[1] C.F.J. Barnard, B.A. Murrer, M. Jones, P.M. Goddard, M. Valenti, A. Bryant, K.R. Harrap, A novel trans-platinum coordination complex possessing in vitro and in vivo antitumor activity, Cancer Res. 54 (1994) 5618–5622.

[2] R.F. Murphy, N. Farrell, A. Aguila, M. Okada, F.M. Balis, T. Fojo, Accumulation of novel transplatinum complexes in cisplatin and oxaliplatin resistant cell lines overcomes resistance, Cancer Res. 65 (2005) 969 LP-969.

[3] N. Farrell, L.F. Povirk, Y. Dange, G. Demasters, M.S. Gupta, G. Kohlhagen, Q.A. Khan, Y. Pommier, D.A. Gewirtz, Cytotoxicity, DNA strand breakage and DNA-protein crosslinking by a novel transplatinum compound in human A2780 ovarian and MCF-7 breast carcinoma cells, Biochem. Pharmacol. 68 (2004) 857–866.

[4] C. Billecke, S. Finniss, L. Tahash, C. Miller, T. Mikkelsen, N.P. Farrell, O. Bögler, Polynuclear platinum anticancer drugs are more potent than cisplatin and induce cell cycle arrest in glioma, Neuro. Oncol. 8 (2006) 215–226. https://doi.org/10.1215/15228517-2006-004.

[5] N. Farrell, Y. Qu, U. Bierbach, M. Valsecchi, E. Mentab, Structure-activity relationships within di- and trinuclear platinum phase-i clinical anticancer agents, Cisplatin Chem. Biochem. a Lead. Anticancer Drug (2006) 477–496.
[6] M.P. Hacker, Cytotoxicity and antitumor activity of bis(p1atinum) complexes, A novel class, J. Med. Chem. 12 (1990) 2179–2184.
[7] N. Farrell, Nonclassical platinum antitumor agents: perspectives for design and development of new drugs complementary to cisplatin, Cancer Invest. 11 (1993) 578–589.
[8] Y. Zou, N. Farrell, B. Van Houten, Sequence specificity of DNA-DNA interstrand cross-link formation by cisplatin and dinuclear platinum complexes, Biochemistry 33 (1994) 5404–5410.
[9] R. Sauer, Nature Structural Biology, Nature 2 (1995) 1115–1122. http://www.nature.com/nsmb.
[10] V. Brabec, J. Kašpárková, O. Vrána, O. Nováková, J.W. Cox, Y. Qu, N. Farrell, DNA modifications by a novel bifunctional trinuclear platinum Phase I anticancer agent, Biochemistry 38 (1999) 6781–6790.
[11] P. Perego, C. Caserini, L. Gatti, N. Carenini, S. Romanelli, R. Supino, D. Colangelo, I. Viano, R. Leone, S. Spinelli, G. Pezzoni, C. Manzotti, N. Farrell, F. Zunino, A novel trinuclear platinum complex overcomes cisplatin resistance in an osteosarcoma cell system, Mol. Pharmacol. 55 (1999) 528 LP-534.
[12] J.D. Roberts, J. Peroutka, G. Beggiolin, C. Manzotti, L. Piazzoni, N. Farrell, Comparison of cytotoxicity and cellular accumulation of polynuclear platinum complexes in L1210 murine leukemia cell lines, J. Inorg. Biochem. 77 (1999) 47–50.
[13] T.D. McGregor, Z. Balcarová, Y. Qu, M.C. Tran, R. Zaludová, V. Brabec, N. Farrell, Sequence-dependent conformational changes in DNA induced by polynuclear platinum complexes, J. Inorg. Biochem. 77 (1999) 43–46.
[14] A.L. Harris, J.J. Ryan, N. Farrell, Biological consequences of trinuclear platinum complexes: comparison of [[trans-PtCl(NH_3)2]2mu-(trans-Pt(NH_3)2($H_2N(CH_2)6$-NH_2)2)]$^{4+}$ (BBR 3464) with its noncovalent congeners, Molecular Pharmacology 69 (n.d.) 666–672.
[15] Z. Zhu, Z. Wang, C. Zhang, Y. Wang, H. Zhang, Z. Gan, Z. Guo, X. Wang, Mitochondrion-targeted platinum complexes suppressing lung cancer through multiple pathways involving energy metabolism, Chem. Sci. 10 (2019) 3089–3095.
[16] C. Alexander, N.U. Prajith, P.V. Priyanka, A. Nithyakumar, N. Arockia Samy, Dinuclear platinum(II) complexes of imidazophenanthroline-based bridging ligands as potential anticancer agents: synthesis, characterization, and in vitro cytotoxicity studies, J. Biol. Inorg. Chem. 24 (3) (2019) 405–418.
[17] A. Terenzi, C. Ducani, V. Blanco, L. Zerzankova, A.F. Westendorf, C. Peinador, J.M. Quintela, P.J. Bednarski, G. Barone, M.J. Hannon, DNA binding studies and cytotoxicity of a dinuclear PtII diazapyrenium-based metallo-supramolecular rectangular box, Chem. - A Eur. J. 18 (2012) 10983–10990.
[18] S. Bhowmick, A. Jana, K. Singh, P. Gupta, A. Gangrade, B.B. Mandal, N. Das, Coordination-driven self-assembly of ionic irregular hexagonal metallamacrocycles via an organometallic clip and their cytotoxicity potency, Inorg. Chem. 57 (2017) 3615–3625.
[19] I.V. Grishagin, J.B. Pollock, S. Kushal, T.R. Cook, P.J. Stang, B.Z. Olenyuk, In vivo anticancer activity of rhomboidal Pt(II) metallacycles, Proc. Natl. Acad. Sci. U. S. A. 111 (2014) 18448–18453.
[20] Y.R. Zheng, K. Suntharalingam, T.C. Johnstone, S.J. Lippard, Encapsulation of Pt(IV) prodrugs within a Pt(II) cage for drug delivery, Chem. Sci. 6 (2015) 1189–1193.

[21] G. Yu, T.R. Cook, Y. Li, X. Yan, D. Wu, L. Shao, J. Shen, G. Tang, F. Huang, X. Chen, P.J. Stang, Tetraphenylethene-based highly emissive metallacage as a component of theranostic supramolecular nanoparticles, Proc. Natl. Acad. Sci. U.S.A. 113 (2016) 13720–13725.

[22] J. Zhou, Y. Zhang, G. Yu, M.R. Crawley, C.R.P. Fulong, A.E. Friedman, S. Sengupta, J. Sun, Q. Li, F. Huang, T.R. Cook, Highly emissive self-assembled BODIPY-platinum supramolecular triangles, J. Am. Chem. Soc. 140 (2018) 7730–7736.

[23] A. Eskandari, A. Kundu, S. Ghosh, K. Suntharalingam, A triangular platinum(II) multinuclear complex with cytotoxicity towards breast cancer stem cells, Angew. Chemie. 131 (2019) 12187–12192. https://doi.org/10.1002/ange.201905389.

[24] R. Kieltyka, P. Englebienne, J. Fakhoury, C. Autexier, N. Moitessier, H.F. Sleiman, A platinum supramolecular square as an effective G-quadruplex binder and telomerase inhibitor, J. Am. Chem. Soc. 130 (2008) 10040–10041.

[25] O. Domarco, D. Lötsch, J. Schreiber, C. Dinhof, S. Van Schoonhoven, M.D. García, C. Peinador, B.K. Keppler, W. Berger, A. Terenzi, Self-assembled Pt2L2 boxes strongly bind G-quadruplex DNA and influence gene expression in cancer cells, Dalt. Trans. 46 (2017) 329–332.

[26] G. Yu, S. Yu, M.L. Saha, J. Zhou, T.R. Cook, B.C. Yung, J. Chen, Z. Mao, F. Zhang, Z. Zhou, Y. Liu, L. Shao, S. Wang, C. Gao, F. Huang, P.J. Stang, X. Chen, A discrete organoplatinum(II) metallacage as a multimodality theranostic platform for cancer photochemotherapy, Nat. Commun. 9 (2018) 1–18.

[27] S. Bhattacharyya, M. Venkateswarulu, J. Sahoo, E. Zangrando, M. De, P.S. Mukherjee, Self-assembled PtII8Metallosupramolecular tubular cage as dual warhead antibacterial agent in water, Inorg. Chem. 59 (2020) 12690–12699.

[28] A. Gautier, F. Cisnetti, Advances in metal-carbene complexes as potent anti-cancer agents, Metallomics 4 (2012) 23–32.

[29] R.C. Todd, S.J. Lippard, Inhibition of transcription by platinum antitumor compounds, Metallomics 1 (2009) 280–291.

[30] F. Arnesano, G. Natile, "Platinum on the road": interactions of antitumoral cisplatin with proteins, Pure Appl. Chem. 80 (2008) 2715–2725.

[31] R.D. Graham, D.R. Williams, The synthesis and screening for anti-bacterial, -cancer, -fungicidal and -viral activities of some complexes of palladium and nickel, J. Inorg. Nucl. Chem. 41 (1979) 1245–1249.

[32] T.A.K. Al-Allaf, L.J. Rashan, Synthesis and cytotoxic evaluation of the first trans-palladium(II) complex with naturally occurring alkaloid harmine, Eur. J. Med. Chem. 33 (1998) 817–820.

[33] C. Navarro-Ranninger, F. Zamora, J.R. Masaguer, J.M. Pérez, V.M. González, C. Alonso, Palladium(II) compounds of putrescine and spermine. Synthesis, characterization, and DNA-binding and antitumor properties, J. Inorg. Biochem. 52 (1993) 37–49.

[34] A.G. Quiroga, J.M. Pérez, I. López-Solera, J.R. Masaguer, A. Luque, P. Román, A. Edwards, C. Alonso, C. Navarro-Ranninger, Novel tetranuclear orthometalated complexes of Pd(II) and Pt(II) derived from p-isopropylbenzaldehyde thiosemicarbazone with cytotoxic activity in cis-DDP resistant tumor cell lines. Interaction of these complexes with DNA, J. Med. Chem. 41 (1998) 1399–1408.

[35] G. Gupta, A. Das, K.C. Park, A. Tron, H. Kim, J. Mun, N. Mandal, K.W. Chi, C.Y. Lee, Self-assembled novel BODIPY-based palladium supramolecules and their cellular localization, Inorg. Chem. 56 (2017) 4615–4621.

[36] A. Mishra, S.C. Lee, N. Kaushik, T.R. Cook, E.H. Choi, N.K. Kaushik, P.J. Stang, K.W. Chi, Self-assembled supramolecular hetero-bimetallacycles for anticancer potency by intracellular release, Chem. - A Eur. J. 20 (2014) 14410–14420.

[37] J.E.M. Lewis, E.L. Gavey, S.A. Cameron, J.D. Crowley, Stimuli-responsive Pd 2L 4 metallo-supramolecular cages: towards targeted cisplatin drug delivery, Chem. Sci. 3 (2012) 778–784.

[38] S.M. McNeill, D. Preston, J.E.M. Lewis, A. Robert, K. Knerr-Rupp, D.O. Graham, J.R. Wright, G.I. Giles, J.D. Crowley, Biologically active [Pd2L4]4+ quadruply-stranded helicates: stability and cytotoxicity, Dalt. Trans. 44 (2015) 11129–11136.

[39] D. Benvenuto, M. Giovannetti, A. Ciccozzi, S. Spoto, S. Angeletti, M. Ciccozzi, J. Med. Virol. (2020) 1–3.

[40] S. Ghosh, O. Mendoza, L. Cubo, F. Rosu, V. Gabelica, A.J.P. White, R. Vilar, Assembly of palladium(II) and platinum(II) metallo-rectangles with a guanosine-substituted terpyridine and study of their interactions with quadruplex DNA, Chem. - A Eur. J. 20 (2014) 4772–4779.

[41] A. Eskandari, A. Kundu, A. Johnson, S. Karmakar, S. Ghosh, K. Suntharalingam, A tri-metallic palladium complex with breast cancer stem cell potency, Dalt. Trans. 49 (2020) 4211–4215.

[42] A. Ajibola Adeyemo, A. Shettar, I.A. Bhat, P. Kondaiah, P.S. Mukherjee, Self-assembly of discrete RuII8 molecular cages and their in vitro anticancer activity, Inorg. Chem. 56 (2017) 608–617.

[43] G. Gupta, J.M. Kumar, A. Garci, N. Nagesh, B. Therrien, Exploiting natural products to build metalla-assemblies: the anticancer activity of embelin-derived Rh(III) and Ir(III) metalla-rectangles, Molecules 19 (2014) 6031–6046.

[44] A. Mishra, Y.J. Jeong, J.H. Jo, S.C. Kang, H. Kim, K.W. Chi, Coordination-driven self-assembly and anticancer potency studies of arene-ruthenium-based molecular metalla-rectangles, Organometallics 33 (2014) 1144–1151.

[45] Y. Zhao, L. Zhang, X. Li, Y. Shi, R. Ding, M. Teng, P. Zhang, C. Cao, P.J. Stang, Self-assembled ruthenium (II) metallacycles and metallacages with imidazole-based ligands and their in vitro anticancer activity, Proc. Natl. Acad. Sci. U.S.A. 116 (2019) 4090–4098.

Chapter 13

Rise of supramolecular nanozymes: Next-generation peroxidase enzyme-mimetic materials

Huidrom Mangalsana [a,b], Abhijeet Mohanty [a,b] and Amit A. Vernekar [a,b]
[a] *Inorganic and Physical Chemistry Laboratory (IPCL), Council of Scientific and Industrial Research (CSIR)-Central Leather Research Institute (CLRI), Adyar, Chennai, India,* [b] *Academy of Scientific and Innovative Research (AcSIR), Ghaziabad, Uttar Pradesh, India*

13.1 Introduction

13.1.1 What are nanozymes?

Catalysts, often described in simple terms as substances that alter the rate 1‘of a chemical reaction without themselves getting consumed, play a crucial role in carrying out diverse reactions effectively and efficiently. They are often employed in the least quantities and are reusable. Catalysts that take part in biochemical reactions occurring inside a living organism are known as enzymes. Proteins are the main compositions of enzymes although some of them are catalytic RNA molecules [1]. Enzymes have an edge over the conventional catalysts used in chemical and industrial reactions in their usage conditions. The conventional catalysts usually require either one of or some of the following conditions: extreme pH environment, organic and inorganic solvents, high temperature, high pressure, etc. [2,3]. Enzymes, on the other hand, carry out the conversion of biomolecules in relatively milder conditions [4,5].

Enzymes, or biocatalysts, have high substrate specificities and high catalytic activities [6]. These salient features of enzymes are often exploited for their use in biological, industrial, and medical fields [7–9]. Enzymes, thus, are often used to replace conventional catalysts. However, they also suffer from various drawbacks such as difficulties in reusing and recycling, high cost of preparation and purification, sensitivity to environmental conditions in their catalytic activities, low operational stability, etc. [10]. These shortcomings paved the way for scientists to explore artificial enzymes [11,12]. It has also been already reported

Supramolecular Coordination Complexes: Design, Synthesis, and Applications.
DOI: https://doi.org/10.1016/B978-0-323-90582-4.00010-5

that certain materials like fullerenes, cyclodextrins, dendrimers, polymers, metal complexes, porphyrins, and some biomolecules could serve as artificial enzymes [13–19].

A breakthrough in catalytic discovery came in 2007 when Fe_3O_4 nanoparticles (NPs), having a solid inorganic core, were shown to act as a peroxidase mimic [20]. Ever since then, a lot of studies on "nanozymes" [10,21–23] or nanomaterial-based artificial enzymes have been on the rise [24–32]. Nanozymes are a kind of nanomaterials within the size range of 1–100 nm that possess enzymatic activities [33]. Nanozymes can be broadly classified into two categories [34]: nanomaterial hybrid enzymes which are enzymes modified on nanomaterials and nanomaterials which possess inherent enzymatic properties. Nanozymes offer some advantages over natural enzymes in terms of the low cost of preparation, high stability, and durability [10,21,33]. Nanozymes, thus find place for use in biosensing [35,36], antibacterial agents [37,38], environmental treatment [39,40], and cytoprotection among biomolecules in the cell [41,42] among other uses. Of the many discovered nanomaterials exhibiting enzyme-like activities, mention may be made of Fe_3O_4 NPs [20,43], Au NPs [44,45], graphene oxide (GO) nanosheets [30] possessing peroxidase like activities, Pt NPs [46,47], Pd nanomaterials [48], MnO_2 [31], and CeO_2 [49,50] possessing catalase and superoxide dismutase like activities, Au NPs [51] possessing glucose oxidase like activity, V_2O_5 nanowires [29] possessing Glutathione peroxidase like activity, etc.

13.1.2 What is supramolecular chemistry?

Supramolecular chemistry is an emerging field in chemistry that deals with a discrete number of molecules wherein weak chemical forces like electrostatic charge, hydrogen bonding, and Van Der Waals forces operate instead of strong covalent forces [52]. Other forces that operate in a supramolecular system include metal coordination, hydrophobic forces, and pi–pi interactions [53]. Emil Fischer in 1894 discovered the enzyme-substrate mechanism similar to the key and lock system [54]. The discovery of two main components of the mechanism-molecular recognition and supramolecular function initiated the transition to the discovery of supramolecular chemistry [55].

Coming out of the box, supramolecular chemistry aims at using the noncovalent interactions to build complex chemical systems [56]. Molecular self-assembly and recognition, host–guest interactions, and molecular folding are some of the important salient features covered in supramolecular chemistry [57]. Three nonmutually exclusive salient features very important in the formation of a supramolecular system as pointed out by Jean-Marie Lehn are stated as follows: molecular recognition and its derivatives such as catalysis and reactivity; self-assembly; and adaptation and evolution [58]. Self-assembly of the constituents is a very important criteria as it is seen that self-organization or self-assembly is the driving force for the evolution of all life forms on Earth [59].

13.1.3 Supramolecular nanozymes

Natural enzymatic systems possess inherent supramolecular catalysis which has been stalked for years to develop their artificial mimics [60,61]. As a solution for the mimicry of this supramolecular catalysis, supramolecular coordination chemistry serve as a plausible medium [62–67], with its ability to exhibit host–guest interactions. In designing artificial enzyme mimics, noncovalent interactions directed the mimetic system to resemble the natural catalysts [68]. The first supramolecular catalysts were developed using the properties of host–guest chemistry in the 1970s [12,69–71]. The principle of lock and the key enzymatic mechanism that a substrate fits inside a host molecule for its catalytic activity was the key factor in the development of these supramolecular catalysts.

Porous coordination solids are a front runner in the development of supramolecular catalysis. The inherent property that these solids possess well-defined coordination nanospace and functional sites make them best suited for catalytic activities [72]. Various metal-organic materials (MOMs) can be self-assembled from the metal and the ligands resulting from the good bond directionality, self-correcting kinetic reversibility, and moderate bond energy of the coordination assembly [73–75].

Certain MOMs fit to supramolecular catalysis based on their ability to recognize substrate specifically and to provide coordination space for stereochemical confinement [62–67]. A particular class of MOM, metal-organic frameworks (MOFs) are zeolites like porous crystalline solids that provide a maximum surface area from minimum organic ligands and metal ions [76]. In MOFs, the cavities formed are predictable, tailorable, controllable, and postmodifiable and this provides a lead to explore MOFs as a heterogenous supramolecular catalyst. MOFs are capable to act as hosts to encapsulate guest substrates inside their cavities [77,78,80,81].

Although ligands are bonded to metal centers by covalent bonds in MOFs, they are linked to supramolecular chemistry from the angle that these are formed by self-assembly *via* coordination. They possess pores with tunable sizes, large surface area, and pore volumes and the formed cavities are versatile in the sense that they can mimic the catalytic microenvironment by tuning the properties like polarity, charge, hydrophobicity, and hydrophilicity, etc. Thus, the use of MOFs as a supramolecular nanozyme is discussed in this chapter, with further extension to similar framework macromolecules such as covalent organic frameworks (COFs) and nanocages (NCs). While there is a vast diversity of enzymes present in nature and a lot of their mimics being developed so far by various research groups, this chapter focuses on peroxidase-based supramolecular enzyme mimics.

13.2 Peroxidases

Peroxidase is a heme-containing enzyme that oxidizes various chemical compounds in the presence of hydrogen peroxide. Horseradish (*Armoracia*

Rusticana) is a perennial herb grown in temperate regions and cultivated specifically for its roots. It is also a host to peroxidase. Peroxidase extracted from horseradish is generally termed as horseradish peroxidase (HRP). However, HRP has many isozymes of which the HRP isozyme C is commonly used. According to reports by Welinder, HRP C has a single polypeptide chain that contains 308 amino acid residues wherein pyroglutamate blocks the N-terminus. The C-terminus, however, is unique in the sense that some molecules are devoid of Ser308 which is the general C-terminal residue. Disulfide bonds are also bridged between cysteine residues 11 and 91, 44 and 49, 97 and 301, 177 and 209 [82].

However, the carbohydrate constituent of HRP C is not uniform. A lot of other minor glycans are present besides a major heptasachharide that accounts for 75%–80% of all the glycans [83]. HRP C possesses an iron (III) protoporphyrin, known as the heme group. Also located at a proximal and distal position with respect to the plane of the heme group are two calcium atoms. The calcium constituent is equally important for the normal functioning of the enzyme as loss in calcium results in the decline of thermal stability and enzymatic functions [84]. The general oxidation reactions catalyzed by HRP C and its analogs involve the conversion of hydrogen peroxide to water as shown below:

$$H_2O_2 + 2AH_2 \overset{HRP}{\rightarrow} H_2O + 2AH$$

Here, AH_2 is the reducing substrate and $AH^{\cdot}$ is its oxidized radical product.

HRP is used as an oxidizing agent in various reactions like organic synthesis, enzyme assays, biotransformation, immunoassays, chemiluminescent assays, treatment of wastewater, etc., [85]. Some other uses of HRP C have also been reported [86–88].

Herein, the use of MOFs, COFs, and NCs as HRP mimics is discussed.

13.2.1 MOFs As Peroxidase mimics

Common peroxidase substrates like TMB (3,3′,5,5′-Tetramethylbenzidine), ABTS {2,2′-azino-bis(3-ethylbenzothiazoline-6-sulfonic acid)}, OPD (o-Phenylenediamine), pyrogallol, etc., are oxidized by HRP to their corresponding oxidized colored products with the aid of H_2O_2. These common substrates can also be oxidized by the molecular frameworks (MOFs, COFs, NCs) as shown in Fig. 13.1.

13.2.1.1 Detection of biothiols

Thiol compounds like Cysteine (Cys), Homocysteine (Hcy), and Glutathione (GSH) present inside the body not only are an integral part of amino acids and proteins but play a very important role in human metabolism [89–91]. GSH, an antioxidant, maintains oxidative stress, redox dynamic balance, and cell growth. It also is related to various diseases like cancer [92–94]. Changes at the molecular levels in the GSH antioxidant system and disturbances in the

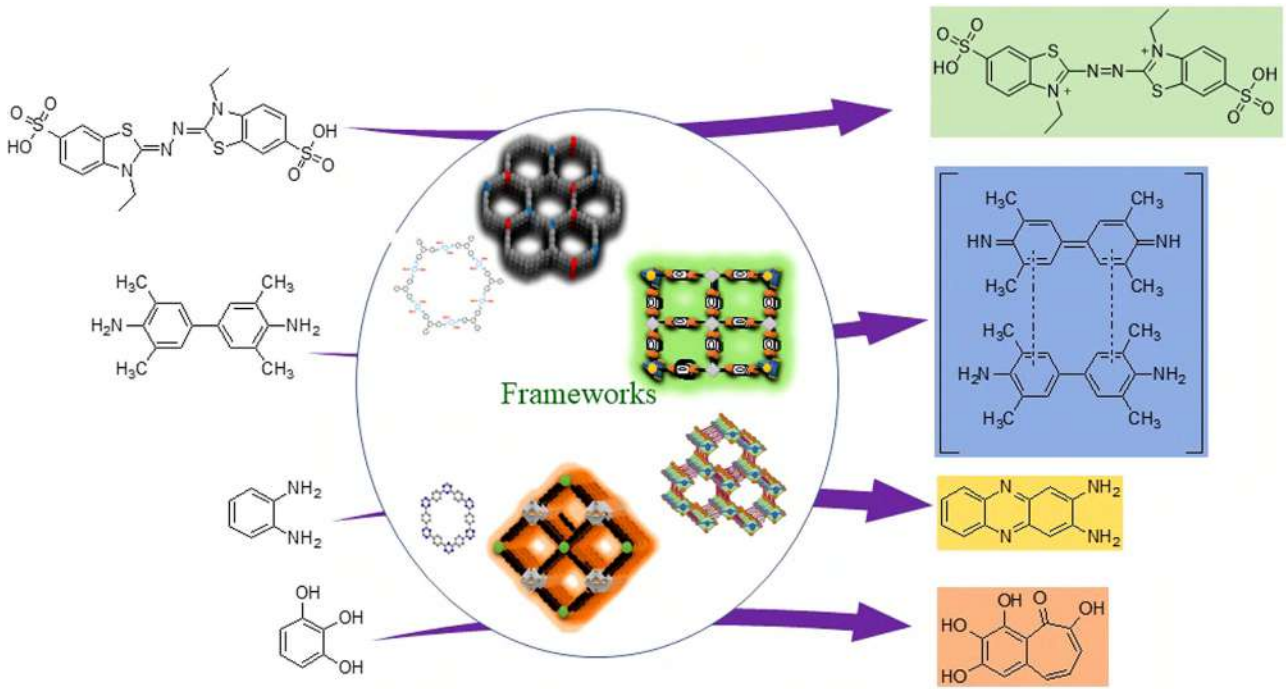

FIGURE 13.1 Peroxidase like activity of framework molecules on common peroxidase substrates.

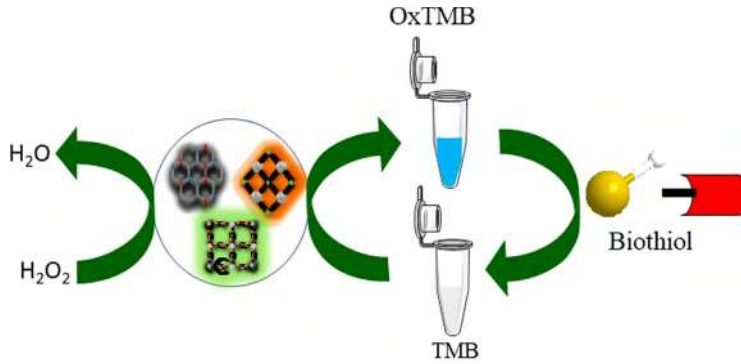

FIGURE 13.2 Detection of biothiols by framework molecules using TMB.

GSH homeostasis have been embroiled in the initiation and progression of tumor. GSH, although crucial for the removal and detoxification of carcinogens in normal healthy cells, present in elevated levels in tumor cells are associated with the progression of tumor and resistance to drugs. Cysteine deficiency in the body often can lead to problems like depigmentation of hair, liver cell damage, edema, somnolence, dermatosis, and obesity [95]. The presence of homocysteine in high levels is often a high-risk factor for the development of cardiovascular diseases, Alzheimer's diseases, and atherosclerosis [96]. Thus, the presence of biothiols in required quantity in the human biological system is of utmost importance for the normal functioning of the individual. This gives rise to the need for the detection of biothiols in our serum to check the increased levels.

In this regard, various MOFs have been developed for the detection of thiol compounds; some of which are, Fe-containing Fe-MIL-88-NH_2 [97], Ce-containing MVCM [98], Zr-containing UiO-66(NH_2) [99], and Eu-containing Eu-pydc [100]. The MOFs, due to their intrinsic peroxidase properties, were able to oxidize the colorless peroxidase substrate, TMB into OxTMB with the help of H_2O_2 thereby exhibiting a final blue color. However, in the presence of thiols, which are reducing in nature, the thus formed blue OxTMB starts to slowly fade its color away due to the competitive reaction between the thiols and TMB for H_2O_2 [97]. Thus, a chromogenic 'turn-off' method that could help detect the presence of biothiols like Cysteine (Cys), Homocysteine (Hcy) and Glutathione(GSH) present in the human serum was provided as shown in Fig. 13.2 (Table 13.1).

13.2.1.2 Detection of glucose

Glucose, the end product of starch hydrolysis, is a source of energy in human beings. However, the presence of glucose in excess amount in the human blood leads to diabetes [101] which may further lead to disability or death [102,103]. Thus, to alarm the presence of the excess amount of glucose in the blood, the

TABLE 13.1 Peroxidase mimicking MOFs for the detection of biothiols.

Sr. no.	MOF	Ligand	Optimum pH	Optimum temperature (°C)	Detection limit (μM)		References
1	Fe-MIL-88-NH_2	2-Aminoterephthalic acid	4.0	40	GSH	0.45	[97]
					HCy	0.40	
					Cys	0.39	
2	MVCM	1,3,5-benzenetricarboxylic acid	<7.0	-	GSH	0.135	[98]
					HCy	0.129	
					Cys	0.143	
3	Ui-O-66-(NH_2)	2-Aminoterephthalic acid	4.0	40	GSH	306×10^{-3}	[99]
					HCy	310×10^{-3}	
					Cys	330×10^{-3}	
4	Eu-pydc	2,5-Pyridinedicarboxylic acid (H_2pydc)	4.0	35	Cys	0.28	[100]

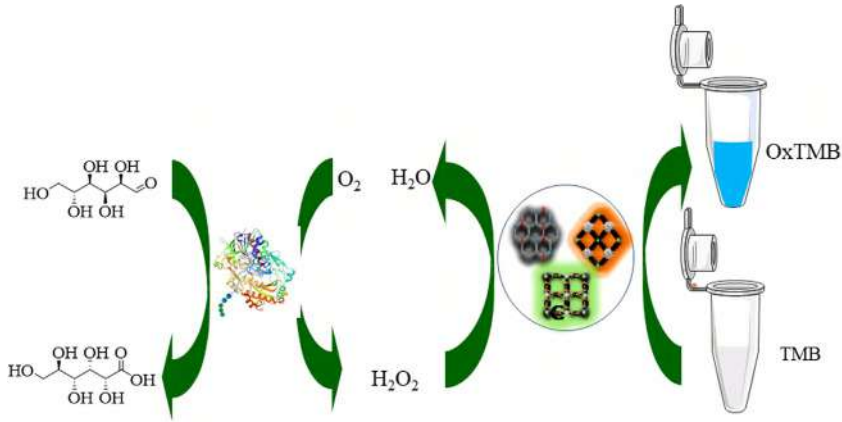

FIGURE 13.3 Oxidation of TMB by framework molecules using GOx for the sensing of glucose.

detection of the same is a necessity for monitoring various health issues and combating diabetes.

Rather than employing H_2O_2 externally, in-situ generated H_2O_2 can be used for the oxidation of the substrates by the peroxidase MOFs. With the aid of O_2, Glucose Oxidase (GOx) or a GOx mimic could oxidize Glucose to Gluconic acid with the liberation of H_2O_2. This released H_2O_2 can then be taken up by the MOFs for the oxidation of the substrates (Fig. 13.3).

Herein, we shall discuss various MOFs used for the detection of glucose based on the constituent atoms. MOFs constructed using Zirconium metal ion are a front runner in the detection of glucose (Table 13.2). In a hierarchically porous HP-PCN-224(Fe), GOx was encapsulated as GOx@HP-PCN-224(Fe) and ABTS was used as the sensing substrate [104]. In PCN-222(Fe), GOx was immobilized on the surface via electrostatic interaction. The resulting GOx/PCN-222(Fe) system used ABTS and pyrogallol for glucose sensing [105]. Park and his group developed a method to fabricate PCN-224 using benzoic acid as a competing agent [106]. This method was used by Li and his team to incorporate Fe into the Zr MOF to yield Fe@PCN-224 [107]. This fabricated MOF detected glucose using TMB.

MOF-808 was shown to display peroxidase activity within a wide range of pH encompassing all acidic, neutral, and alkaline pHs [108]. A Zr-MOF, $Zr_6O_8(H2O)_8(FeCl\text{-}tcpp)_2$ or simply PCN-222(Fe), was synthesized using a solvothermal method and was then further modified using sodium dodecyl sulfate (SDS) micelles to yield SDS/PCN-222(Fe). The SDS/PCN-222(Fe) with a much-lowered K_M value toward both ABTS and H_2O_2 showed better peroxidase activity than its precursor PCN-222(Fe). The plausible reason for this could be that the SDS initiates a strong electrostatic attraction between the MOF and ABTS *via* micelle formation. The micellar MOF was also used for the detection of glucose by a cascade reaction involving GOx [109]

TABLE 13.2 Zr MOFs used for glucose detection.

Sr. No.	MOF	Ligand	Optimum pH	Optimum temperature (°C)	Detection limit (μM)	References
1	HP-PCN-224(Fe)	Fe-TCPP(TCPP=tetrakis(4-carboxyphenyl)porphyrin)	5.5–6.5	60	0.87	[104]
2	PCN-222	Fe-TCPP(TCPP=tetrakis(4-carboxyphenyl)porphyrin)	–	35	–	[105]
3	Fe@PCN-224	Tetrakis(4-carboxyphenyl)porphyrin (H2TCPP)	3.5	45	22	[107]
4	MOF-808	1,3,5-benzenetricarboxylic acid (H3BTC)	3–10	40	5.7	[108]
5	SDS/PCN-222(Fe)	Fe-TCPP(TCPP=tetrakis(4-carboxyphenyl)porphyrin)	–	–	3	[109]

Another important class of MOF employed for peroxidase activity is Cu-based MOFs (Table 13.3). Zhang and coworkers synthesized a 2-D Cu-containing nanosheet, Cu-TCPP(Fe) [110]. With the knowledge that Au NPs possess activity similar to GOx [51], they grew Au NPs on the surface of Cu-TCPP(Fe). The MOF composite that was obtained, Au NPS/Cu-TCPP(Fe), was employed for a cascade reaction for the detection of glucose using TMB substrate [111]. Haifeng Yang and his coworkers introduced a tandem reaction system using highly selective and sensitive surface-enhanced Raman scattering (SERS). In the presence of H_2O_2, the Raman inactive leumachite green (LMG) was oxidized by Au NPs/Cu-TCPP(Fe) to the Raman active malachite green (MG) [112]. Instead of Au NPS, Pt NPs were incorporated into the Cu-TCPP(Fe). This hybrid nanosheet was shown to possess even a better peroxidase activity, and thereby a better detection ability of glucose than the one reported earlier using AuNPs [113].

A Cu MOF with 4,4'-bipyridine as ligand self-assembled with α-Glucosidase(GAA) and GOx was prepared [114]. The researchers started with maltose as the starting substrate which eventually got oxidized in the presence of GOx and gives out two molecules of H_2O_2. This was taken up by the MOF to help oxidize TMB giving the blue-colored OxTMB. However, they showed that if a GAA inhibitor is introduced, the final colored product is not formed, thereby providing easy colorimetric sensing of GAA inhibitors. Besides the use of the peroxidase activities of the MOF for the detection of GAA inhibitors, the whole assembly, GAA@GOx@MOF, was used to screen oleanolic acid as a potential antidiabetic drug.

A 2D MOF nanosheet, $Cu(bpy)_2(OTf)_2$ [115,116], already developed was employed for the fluorometric detection of glucose using GOx [117]. Unlike using other common peroxidase substrates, $Cu(bpy)_2(OTf)_2$ was shown to be able to convert thiamine, a non-fluorescent molecule, to thiochrome, an intense fluorescent product, in the presence of H_2O_2. Li Wang and coworkers synthesized a Cu-hemin MOF for the detection of glucose [118]. The group improved on this work when they fabricated Glucose Oxidase (GOx) into the Cu-hemin MOF and integrated it with an agarose-based hydrogel film to yield a composite Aga/GOx@Cu-hemin MOF/TMB [119]. The detection of the color change due to the oxidation of the employed substrate TMB was enhanced by the hydrogel film.

A compartmentalized nanozyme prepared from the fabrication of GOx into the Cu-BDC MOF *via* a one-step mineralization process was introduced by Quang and his group. The GOx@Cu-BDC encapsulated nanozyme exhibited a 12.5-fold enhanced activity as compared to the free GOx and Cu-BDC tandem reaction [120]. Other Cu-based MOFs used for the detection of glucose reported are a nanocomposite g-C_3N_4@CuMOF [121] prepared by introducing graphite C_3N_4 nanosheets (g-C_3N_4) into a copper-based flake like MOF, Cu@500-MOF [122] prepared by pyrolyzing HKUST-1 and Cu-MOF [123].

TABLE 13.3 Cu MOFs for glucose detection.

Sr. No.	MOF	Ligand	Optimum pH	Optimum temperature (°C)	Detection limit (μM)	References
1	Au NPS/Cu-TCPP(Fe)	TCPP{tetrakis(4-carboxyphenyl)porphyrin	–	–	8.5	[111]
2	AuNPs/Cu-TCPP(Fe)	TCPP{tetrakis(4-carboxyphenyl)porphyrin	7.0	37	3.9	[112]
3	Pt NPs/Cu-(TCPP(Fe)	TCPP{tetrakis(4-carboxyphenyl)porphyrin	4.0	40	0.0994	[113]
4	GAA@GOx@Cu-MOF	4,4′-bipyridine	7.0	–	–	[114]
5	$Cu(bpy)_2(OTf)_2$	4,4′-bipyridine	10.0	55	0.41	[115]
6	Cu-hemin	Hemin	7.0	–	2.73	[116]
7	Aga/GOx@Cu-hemin MOF/TMB	Hemin	–	45	2.8	[119]
8	GOx@Cu-BDC	Copper 1,4-benzenedicarboxylic acid	5.2	37	4.1	[120]
9	g-C_3N_4@CuMOF	Terephthalic acid	4.4	37	59×10^{-3}	[121]
10	Cu@500-MOF	Benzene-1,3,5-tricarboxylic acid	–	–	3.2×10^{-3}	[122]
11	Cu-MOF	Dithiodibenzoic Acid (DTDBA)	4.0	–	25	[123]

Quite a few MOFs prepared from Fe have been reported for the detection of glucose (Table 13.4). A 2D MOF, Fe-BTC was prepared from a Cu-based Cu(HTBC)-1 MOF by multivalent cation substitution strategy [124]. The Fe-BTC showed better peroxidase activity than its precursor Cu(HBTC)-1 77 times and a 3D MIL-100(Fe) 2.2 times. The K_M values for the oxidation of TMB and H_2O_2 by Fe-BTC were 0.2610 mM and 0.0332 mM, respectively which was 1.6 and 1.9 times lower than the corresponding values of the 3D-MIL-100(Fe) [125]. Based on the peroxidase properties, GOx was embedded on the surface of the 2D MOF for colorimetric sensing of glucose [126]. Fe-MIL-88-NH_2 (Fe-MOF) with intrinsic peroxidase activity was already reported [127]. Loaded with GOx *via* covalent bonding with the free amino groups of Fe-MOF, the Fe-MOF-GOx assemble was used for the detection of glucose [128]. The Fe-MOF-GOx system showed better temperature and acid-base resistance as well as higher reusability than the Fe-MOF/GOx system.

Shulin Zhao and his group integrated GOx into a peroxidase mimicking Fe-BTC MOF to form an integrated system, GOx@Fe-BTC. The MOF Fe-BTC, which could oxidize TMB, acts here as a support system for GOx, and thus the GOx@Fe-BTC was developed to detect the oxidation of glucose colorimetrically [129]. Another MOF, MIL-88B was prepared using 2-aminoterephthalic acid as the ligand. MIL-88B was further improvised to hierarchically porous HP-MIL-88B and was further functionalized with boronic acid as HP-MIL-88B-BA. This improvised MOF was then loaded with glucose oxidase (GOx). The GOx@HP-MIL-88B-BA system was used for a cascade reaction for the detection of glucose [130]. The ligand meso-tetra(4-carboxyphenyl)porphyrin (H4TCPP) was used as a support for integrating GOx in the MOF-545(Fe) to give the multi-enzyme system GOx@MOF-545(Fe) for the detection of glucose. The naked MOF-545(Fe) was shown to oxidize ABTS into a green solution in the presence of H_2O_2 [131].

Some other metals employed for the synthesis of MOFs for the detection of glucose include Eu, Al, and Co (Table 13.5). MIL-101(Al)-NH_2, prepared from Al and 2-aminoterephthalic acid, was anchored with hemin to form Hemin@MIL-101(Al)-NH_2 [132]. Hemin@MIL-101(Al)-NH_2 and Eu-pydc [100], prepared using Eu and 2,5-pyridinedicarboxylic acid (H_2pydc), use a "turn-on" mechanism for the detection of glucose in the presence of GOx and TMB.

A Co-containing MOF, Co-TCPP(Fe), was synthesized using TCPP(Fe) {TCPP=tetrakis(4-carboxyphenyl)-porphyrin)}. On incorporating GOx, the H_2O_2 released from the oxidation of glucose was taken up by Co-TCPP(Fe) to further oxidize luminol into the luminescent 3-aminophthalate, thereby detecting glucose [133]. $[Co(L)(H_2O)_2]_n$ or Co-MOF was synthesized using 4-(3-carboxy-1,2,4-1H-triazole)benzoic acid denoted as "L." The Co-MOF, besides its peroxidase activities, was shown to be able to catalyze the chemiluminescence (CL) reaction of luminol with H_2O_2(Fig. 13.4). A plausible mechanism of the CL reaction of luminol with H_2O_2 in the presence of Co-MOF was given as follows:

TABLE 13.4 Fe MOFs for glucose detection.

Sr. No.	MOF	Ligand	Optimum pH	Optimum temperature (°C)	Detection limit (μM)	References
1	Fe-BTC	H3BTC (1,3,5-benzenetricarboxylic acid)	3.5	45	39×10^{-3}	[126]
2	Fe-MOF-GOx	Terephthalic acid	4.0	37	0.487	[128]
3	GOx@Fe-BTC	1,3,5-Benzenetricarboxylic acid (BTC)	4.0	37	2.4	[129]
4	GOx@HP-MIL-88B-BA	2-aminoterephthalic acid	4.0	37	0.98	[130]
5	GOx@MOF-545(Fe)	Meso-tetra(4-carboxyphenyl)porphine (H4TCPP)	5.0	35	0.28	[131]

TABLE 13.5 Other metal MOFs for glucose detection.

Sr. No.	MOF	Ligand	Optimum pH	Optimum temperature (°C)	Detection limit (μM)	References
1	Hemin@MIL-101(Al)-NH_2	2-Aminoterephthalic acid	5.0	50	–	[132]
2	Eu-pydc	2,5-Pyridinedicarboxylic acid (H_2pydc)	4.0	35	6.9	[100]
3	Co-TCPP(Fe)	TCPP(Fe) {TCPP=tetrakis(4-carboxyphenyl)-porphyrin)}	7.0	37	30.5	[133]
4	$[Co(L)(H_2O)_2]_n$	4-(3-carboxy-1,2,4-1H-triazole)benzoic acid	11.3	–	0.10	[137]
5	GOx/FeNi-MOF	2,6-naphthalenedicarboxylic acid	4.5	37	1.3	[138]

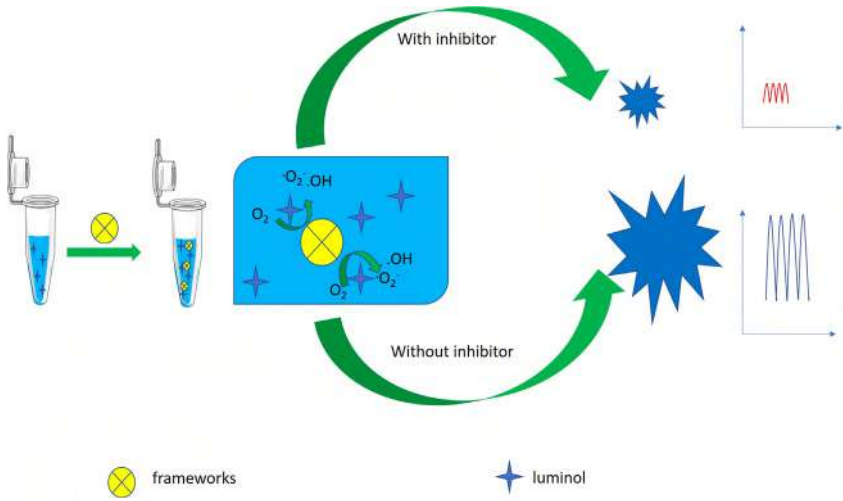

FIGURE 13.4 A general scheme of the chemiluminescence reaction of luminol in the presence of peroxidase mimicking framework molecules in the presence and absence of inhibitors.

In the alkaline medium, H_2O_2 is oxidized to hydrogen peroxide ions (HO_2^-) [134].

$$H_2O_2 \overset{HO^-}{\rightarrow} HO_2^-$$

H_2O_2 decomposes into hydroxyl radical ($^{\cdot}OH$) in the presence of Co-MOF. $^{\cdot}OH$ reacts with HO_2^- to produce $^{\cdot}O_2^-$.

$$H_2O_2 \overset{Co-MOF}{\rightarrow} 2 \cdot OH$$

$$\cdot OH + HO_2^- \rightarrow \cdot O_2^- + H_2O$$

Thus, Co-MOF catalyzes the decomposition of H_2O_2 to O_2- via O_2.

$$H_2O_2 \overset{Co-MOF}{\rightarrow} O_2 + H_2O$$

$$O_2 \overset{Co-MOF}{\rightarrow} \cdot O_2^-$$

Luminol molecules get transformed into luminol anions which then react with $^{\cdot}O_2^-$ and $^{\cdot}OH$ to obtain the excited 3-Aminophthalate (3-APA*) [135,136].

$$L + 2OH^- \rightarrow L^- + 2H_2O$$

$$L^- + \cdot O_2^- \rightarrow \text{3-APA*}$$

Based on this finding, the group thereby established a method for the determination of glucose from the H_2O_2 released from the oxidation of glucose by glucose oxidase [137].

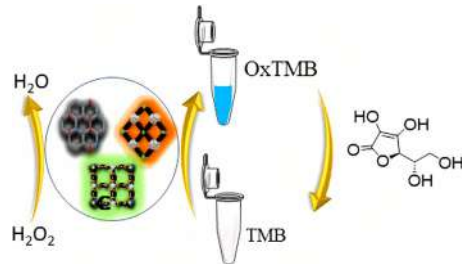

FIGURE 13.5 Oxidation of TMB by framework molecules for the detection of ascorbic acid.

A bimetallic MOF containing Fe and Ni, FeNi-MOF, was prepared using 2,6-naphthalenedicarboxylic acid as the linker. The FeNi-MOF possesses intrinsic peroxidase-like activity. GOx was immobilized on the FeNi-MOF to form GOx/FeNi-MOF which was then employed for the colorimetric detection of glucose in the presence of TMB [138].

13.2.1.3 Detection of ascorbic acid

The oxidation of the peroxidase substrate TMB to OxTMB in the presence of H_2O_2 is hindered in the presence of ascorbic acid. Thus, the blue-colored OxTMB can be reduced to TMB in the presence of ascorbic acid. Using this principle, many "turn off" methods for the colorimetric sensing of ascorbic acid were developed (Fig. 13.5). MIL-53(Fe) synthesized using terephthalic acid was shown to exhibit peroxidase-like activity to detect ascorbic acid colorimetrically [139]. Jian et al. demonstrated that two iron-based MOFs, MIL-68 [140] and MIL-100 [125] showed peroxidase-like activities and developed a colorimetric biosensing system for ascorbic acid [141]. Also, a Ce-containing MOF, Ce-BPyDC, having both oxidase and peroxidase properties was prepared using the linker 2,2′-bipyridine-5,5′-dicarboxylic acid (H_2BPyDC). Ce-BPyDC was shown to be able to oxidize TMB, OPD, and ABTS in the presence as well as in the absence of H_2O_2. Ce-BPyDC was used for the detection of ascorbic acid [142]. Also, a Zr-based MOF, MOF-808, was shown to exhibit peroxidase activity in a wide pH range encompassing all acidic, neutral, and alkaline pHs. Based on a colorimetric sensing method using TMB, MOF-808 was used to detect ascorbic acid and glucose. The detection limit of H_2O_2, glucose, and ascorbic acid was found to be respectively 4.5 μM, 5.7 μM, 15 μM, and the linear range in the same order are 10 μM to 15 mM, 5.7−1700 μM and 30−1030 μM, respectively [108]. The various MOFs used for the detection of ascorbic acid are summed up in Table 13.6.

13.2.1.4 Detection of H_2O_2

A Cu-hemin MOF/chitosan (CS)-reduced graphene oxide (CS-rGO) nanocomposite was synthesized. GO was reduced using chitosan (CS) leading to the

TABLE 13.6 MOFs for ascorbic acid detection.

Sr. No.	MOF	Ligand	Optimum pH	Optimum temperature (°C)	Detection limit (μM)	References
1	MIL-53(Fe)	terephthalic acid	4.0	40	15	[139]
2	MIL-68	1,4-benzenedicarboxylic acid (BDC)	4.0	45	6	[141]
3	MIL-100	1,3,5-benzenetricarboxylic acid (BTC)	3.0	45	6	[141]
4	Ce-BPyDC	2,2′-bipyridine-5,5′-dicarboxylicacid (H_2BPyDC)	4.0	25	0.28	[142]
5	MOF-808	1,3,5-benzenetricarboxylic acid (BTC)	3.0–10.0	40	15	[108]

formation of CS-rGO moiety. Then, Cu^{2+} and hemin were subsequently added to the CS-rGO moiety to finally give the Cu-hemin MOF/CS-rGO nanocomposite. On forming the nanocomposite, the crystalline structure of the Cu-MOFs was retained while the size of the Cu-hemin MOFs was decreased. The Cu-hemin MOF/CS-rGO nanocomposite was then fabricated on the glassy carbon electrode (GCE) to form the modified electrode. The peroxidase property of the modified electrode was able to utilize H_2O_2 for the conversion of hemin red to the oxidized hemin while the electrical conductivity of the modified electrode provides a positive electrocatalytic potential for the reduction of H_2O_2 Thus, an electrochemical sensing for the detection of H_2O_2 with a low detection limit of 0.019 μM was developed [143].

The Zr and 2-aminoterephthalic acid MOF, UiO-66-NH_2 was modified by anchoring ferrocene (Fc) using ferrocenecarboxylic acid (Fc-COOH) to obtain the hybrid amido UiO-66-Fc hybrid which possessed remarkable peroxidase activity in the oxidation of TMB and ABTS in the presence of H_2O_2. It was used for the detection of H_2O_2 with a detection limit of 0.23 μM [144].

A Zr and Mn-TCPP based MOF, PCN-222(Mn), having intrinsic peroxidase activities was prepared and then later activated before it was casted on the surface of the GCE resulting in the formation of PCN-222(Mn)/GCE. Glutamic acid monomer was electropolymerised on the casted MOF surface to form the Poly Glutamic Acid (PGA) hybrid, (PGA/PCN-222(Mn)/GCE). Taking advantage of the peroxidase property of the PCN-222(Mn) and the conductivity of PGA film on GCE, an amperometric biosensor for the detection of H_2O_2, with a low detection limit of 3.1×10^{-8} mol/L was developed [145].

Thakur et al. investigated a new and reliable MOFs/conducting polymer composites that find applications in biosensing. They investigated the peroxidase activities of five MOFs and MOF derivatives for the detection of H_2O_2 electrochemically as well as colorimetrically using the substrate TMB. Out of Fe-BTC, NH_2-MIL-101(Fe), composites of Fe-BTC with polymers polydopamine (PDA), poly *p*-phenylenediamine (PpPDA), and poly(3,4-ethylenedioxythiophene), at pH=7, the Fe-BTC/PEDOT composite shows the best activity and sensitivity toward the detection of H_2O_2. The reliable activity of the Fe-BTC/PEDOT composite can be attributed to the peroxidase property of the Fe-BTC and the conducting property of the polymer PEDOT [146].

Xie et.al. synthesized a 3D MOF, $[Zn_3(MoO_4)_2(trz)_2(H_2O)_2]$ by a surfactant method. The prepared compound possesses intrinsic peroxidase activity. It was able to oxidize TMB to OxTMB in the presence of H_2O_2. The MOF has a K_M value of 0.46 mM and a V_{max} of 9.47×10^{-8} M/s. Thus, it was used a system for the colorimetric sensing of H_2O_2 with a detection limit of 0.25 μM and a detection linear range of 1–80 μM [147]. Xiaoya Hu and his group synthesized a 2-D Ni-based MOF using the linker *p*-benzenedicarboxylic acid (PTA). Named as Ni-MOF, the MOF showed peroxidase activities as it can oxidize TMB in the presence of H_2O_2 to give the blue-colored OxTMB. This property was used as a biosensor to detect the presence of H_2O_2 [148].

Prussian Blue Fe-MIL-101 prepared from Fe-MIL-101 [149] was demonstrated to be capable of showing peroxidase-like activities for the detection of H_2O_2 [150]. A bimetallic 2D MOF containing Co and Mn, Co/Mn-MOF, was synthesized using phthalic acid *via* a one-step hydrothermal method. The Co/Mn-MOF showed peroxidase-like activity and was able to oxidize TMB to OxTMB in the presence of H_2O_2. The K_M for TMB and H_2O_2 were reported to be 0.27 mM and 0.24 mM, respectively. Thus, based on the peroxidase activity to catalyze TMB, a colorimetric method for the sensing of H_2O_2 in living cells and water samples was developed with a detection limit of 0.85 μM and a detection range of 1 to 100 μM [151].

Qi et al. synthesized a bimetallic and bifunctional MOF, PA-Tb-Cu MOF, using the luminescent Tb^{3+}, catalytic Cu^{2+}, and *m*-phthalic acid (PA) as the linker. This peroxidase mimetic MOF was shown to be able to detect the presence of H_2O_2 in the presence of ascorbic acid. Ascorbic acid was oxidized to diketohexanoic acid which forms an adduct with the Tb^{3+} to give a luminescent product [152]. A Co-based MOF, $[Co(pbda)(4,4\text{-bpy}).2H_2O]_n$ or simply Co-MOF, was synthesized using the linkers H_2pbdaa 3-{pyridine-3-yloxy}benzene-1,2-dicarboxylic acid} and 4.4'-bipyridine. Co-MOF was used to detect H_2O_2 electrochemically. The Co-MOF possesses intrinsic peroxidase property and was shown to be able to catalyze the oxidation of terephthalic acid to give a colored product [153]. Table 13.7 shows a list of MOFs employed for $H_2O_{2\ \text{detection}}$.

13.2.1.5 Detection of other biomolecules

Various other biomolecules are also detected using MOFs (Table 13.8). Jun et al. synthesized a Cu-based MOF, [Cu(PDA)-(DMF)], using the linker 1,10-phenanthroline-2,9-dicarboxylic acid (H2PDA). In the presence of H_2O_2, it can oxidize TMB to a blue-colored OxTMB. However, when dopamine is present, it inhibits the catalytic oxidation, thereby restricting the appearance of the blue color. Thus, a colorimetric sensing of dopamine was developed [154]. Similar to the detection of glucose using GOx, uric acid was also shown to be able to be detected in the presence of uricase enzyme [104,155]. The uricase immobilized Uricase@HP-PCN-224(Fe) was shown to detect uric acid by using the peroxidase substrate 4-aminophenazone and 2,4-dichlorophenol sulfonate (DCPS) which gets oxidized in the presence of H_2O_2 to quinoneimine which is kind of a red dye.

Reza et al., prepared the Fe-based MOF, NEQC-340, using tris(p-aminophenyl)amine (TAPA) as the linker. NEQC showed peroxidase activities and was used to detect the presence of glutathione. In the presence of H_2O_2, NEQC was shown to be able to oxidize 3,3′-diaminobenzidine (DAB) to a stable brown indamine polymer. However, the presence of glutathione on the surface of the MOF inhibits the catalytic activity of the MOF and thus the brown-colored indamine polymer was not formed. Thus, glutathione was shown to be detected by a colorimetric method [156].

TABLE 13.7 MOFs for H_2O_2 detection.

Sr. No.	MOF	Linker	Optimum pH	Optimum temperature (°C)	Detection limit (μM)	References
1	Cu-hemin MOF/CS-rGO	Hemin	7.0	–	0.019	[143]
2	UiO-66-Fc	2-aminoterephthalic acid	4.0	70	0.23	[144]
3	PGA/PCN-222(Mn)/GCE	Mn-tetra(4-carboxphenyl)-porphyrin chloride (Mn-TCPP)	6.0	–	0.031	[145]
4	Fe-BTC/PEDOT	1,3,5-benzenetricarboxylic acid	7.4	–	0.46×10^3	[146]
5	$[Zn_3(MoO_4)_2(trz)_2(H_2O)_2]$	Trz =1,2,4-triazole	3.5	40	0.25	[147]
6	Ni-MOF	*p*-benzenedicarboxylic acid (PTA)	3.5	50	0.008	[148]
7	Fe-MIL-101	terephthalic acid (1,4-BDC)	5.0	37	0.15	[150]
8	Co/Mn-MOF	Phthalic acid (BDC)	4.0	35	0.85	[151]
9	PA-Tb-Cu-MOF	*m*-phthalic acid	5.05	–	0.2	[152]
10	Co/Mn-MOF	Phthalic acid (BDC)	4.0	35	0.85	[151]

TABLE 13.8 MOFs for biomolecules detection.

Sr. No.	MOFs	Linker	Biomolecule capable of detecting	Optimum pH	Optimum temperature (°C)	Detection limit	References
1	[Cu(PDA)-(DMF)]	1,10-phenanthroline-2,9-dicarboxylic acid (H2PDA)	Dopamine	–	–	–	[154]
2	Th-MOF	2,6-pyridine dicarboxylic acid	Uric acid	5.5	40	1.15 μM	[155]
3	Uricase@HP-PCN-224(Fe)	Fe-TCPP(TCPP=tetrakis(4-carboxyphenyl)porphyrin)	Uric acid	5.5–6.5	60	1.8 μM	[94]
4	NEQC-340	tris(p-aminophenyl)amine (TAPA)	Glutathione	7.0	30	3.25×10^{-3} μM	[156]
5	Cu-MOF	polyvinylpyrrolidone (PVP)	Carbohydrate antigen 15-3 (CA15-3)	–	–	5.06 μU/mL	[157]
6	MIL-53	Terephthalic acid	Deoxyribonuclease I (DNase I) endonuclease,	4.0	37	0.09 U/mL	[158]
7	Tb-OBBA-Hemin	4,4′-oxybisbenzoic acid (OBBA)	endocrine-disrupting chemicals (EDCs)	5–7	–	50×10^{-6} μM	[159]

(*continued on next page*)

8	Zn-TCPP(Fe), Co-TCPP(Fe) and Cu-TCPP(Fe)	TCPP(Fe)	Heparin	–	–	–	[160]
9	ZnCo MOF	Imidazole	Atropine	–	–	27 pg/mL	[161]
10	Zr-MOF	Bipyridyl-4,40-dicarboxylic acid (BPDCA),	Phosphorylated proteins	4.0	–	0.16 μg/mL	[162]
11	Ni-TCPP(Fe)	TCPP(Fe)	Heart-type fatty acid-binding protein (h-FABP	8.5	–	44.5 fg/mL	[163]
12	MIL-100(Fe)	Trimesic acid (H_3BTC)	α-fetoprotein	–	–	7.7×10^{-11} g/L	[164]
13	Fe-MIL-53	Trimesic acid (H_3BTC)	Chloramphenicol	7.4	–	8.1 mg/L	[165]
14	$Cu_3(BTC)_2$ or HKUST-1	1,3,5-benzene tricarboxylate	Thiamine	–	–	–	[166]
15	Fe-MIL-101	1,4-Dicarboxylic acid (H_2BDC)	Cancer cells	–	–	–	[167]
16	Tα MOF	2,6-pyridine dicarboxylic acid	Ferulic acid	–	–	0.19 μM	[186]
			Tannic acid			0.06 μM	
			Chlorogenic acid			0.11 μM	
17	Fe-MIL-88A	Fumaric acid	Thrombin	–	–		[169]

A polyvinylpyrrolidone (PVP) based, peroxidase mimicking Cu-MOF was integrated with GOx and then with the antibody for the carbohydrate antigen 15-3 (CA15-3), Ab_2, yielding the immunoprobe Ab_2-GOx-Cu-MOF. AuNPs were doped on the GCE and were fabricated with CA15-3 antibody, Ab_1. The resultant Ab_1-Au-GCE was used as the immunosensor. Both the immunosensor and the immunoprobe were introduced with BSA to avoid binding at non-specific sites. When CA15-3, the target antigen, was introduced, the immunoprobes were immobilized on the immunosensor due to the reaction between the antibody and the antigen, BSA-Ab_2-GO_x-Cu-MOF/CA15-3/Ab_1-BSA/Au/GCE. When glucose, acetylacetone (ACAC), N-isopropylacrylamide (NIPAM), and N,N-methylene-bis-acrylamide (MBA) were introduced into the solution, GOx present was able to oxidize the glucose into gluconic acid, thereby releasing H_2O_2 which could facilitate the peroxidase mimicking Cu-MOF to act on the ACAC to produce ACAC radicals. The radicals produced would then initiate the polymerization of NIPAM to PNIPAM. PNIPAM possessed a poor conductivity and thus could restrict the charge transfer of $[Fe(CN)_6]^{3-}$ or $[Fe(CN)_6]^{4-}$and thereby the resistance difference was elevated prominently. Thus, a cascade reaction for the detection of carbohydrate antigen 15-3 with a very low detection limit of 5.06 μU/mL was developed as demonstrated in Fig. 13.6 [157].

Jing Jiang and his coworkers synthesized a terephthalic acid-containing Fe-MOF, MIL-53. MIL-53 was anchored with single-stranded DNAs, ssDNA's, having different base lengths. Short ssDNA's with up to 6 bases were shown not to affect the peroxidase activity of the peroxidase mimetic MIL-53(Fe) [139]. A 24 bases-containing ssDNA, M24, was used for the colorimetric detection of the endonuclease, deoxyribonuclease I (DNase I). When DNase I was introduced in the M24-anchored MIL-53(Fe)-H_2O_2-TMB system, the DNase I was able to cleave the M24 into smaller di, tri, and tetra nucleotides, and thus, the peroxidase activity of MIL-53(Fe) was unaffected (Fig. 13.7). However, in the absence of DNase I, the presence of long-chain M24 enhanced the oxidation of TMB by about 2.4 times [158].

Wang and Chen prepared a lanthanide-based luminescent MOF for the detection and disintegration of endocrine-disrupting chemicals (EDCs) such as natural 17β-estradiol (E2), estrone (E1), and synthetic 17α-ethinylestradiol (EE2). The fluorescent Tb^{3+}, bridging linker 4,4'-oxybisbenzoic acid (OBBA), and catalytic hemin was used for the synthesis of the MOF Tb-OBBA-Hemin which possessed intrinsic peroxidase properties. The Tb-OBBA-Hemin was able to oxidize TMB to OxTMB in the presence of H_2O_2. Also, the MOF could degrade E2 in the presence of H_2O_2. The weakly fluorescent Tb-OBBA-Hemin showed a 6.4-fold increase in the fluorescent intensity on the addition of E2 and H_2O_2. Thus, a fluorometric method for the detection of EDCs was developed with a low sensibility of 50pM [159].

TCPP(Fe) containing 2D MOFs, Zn-TCPP(Fe), Co-TCPP(Fe), and Cu-TCPP(Fe) nanosheets were synthesized by Hui Wei and his group by using a surfactant-assisted procedure. The MOFs were able to oxidize TMB to OxTMB

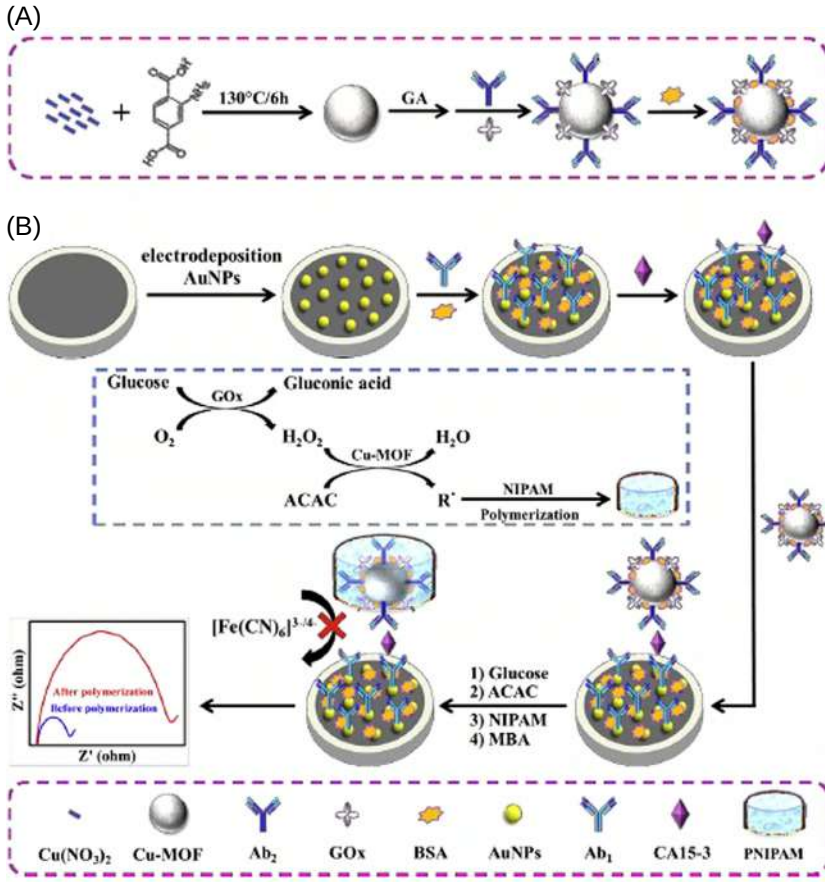

FIGURE 13.6 (A) Preparation of the immunoprobes, (B) schematic representation of the signal amplification for electrochemical detection of CA15-3 triggered by the catalysis-initiated radical polymerization. *Reprinted with permission from Reference* [157]. *Copyright @ 2019 Elsevier.*

and hence were shown to possess peroxidase properties. They were also able to oxidize ampliflu red to the fluorescent resorufin in the presence of H_2O_2. The porphyrin-containing MOFs were used for the detection of Heparin. Heparin-specific AG73 peptides were adsorbed on the nanosheets and were able to block the active sites of the peroxide mimicking nanozymes. Thus, in the presence of AG73 peptides, the MOFs were unable to oxidize TMB or ampliflu red. However, in the presence of Heparin in the system, the AG73 peptide strongly binds to Heparin, thereby leaving the active sites open and the nanosheets were able to oxidize ampliflu red to the fluorescent resorufin as shown in Fig. 13.8. However, this strategy was shown not to work with Heparin analogs like chondroitin sulfate, hyaluronic acid, and other endogenous bioactive molecules like

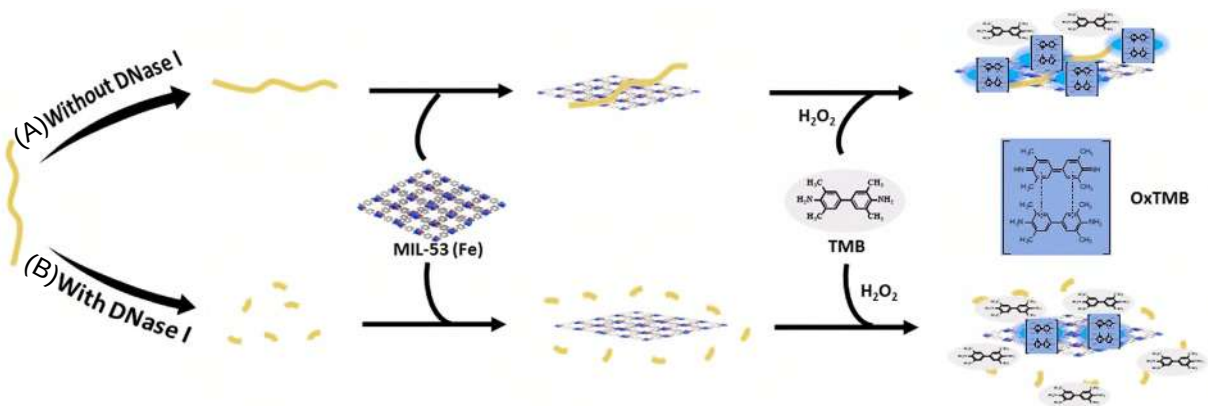

FIGURE 13.7 DNase I activity assay on the DNA-enhanced peroxidase-like activity of MIL-53(Fe).

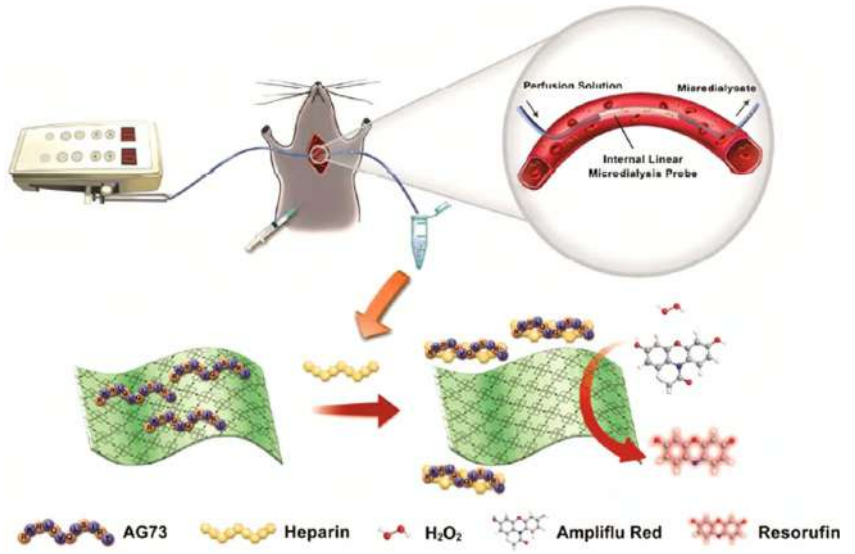

FIGURE 13.8 Monitoring of Hep elimination in live rats using 2-D nanozymes. *Reprinted with permission from Reference* [160]. *Copyright @ 2017 American Chemical Society.*

glucose, lactate, ascorbic acid, uric acid, ATP, ADP, AMP, and other ions like PO_4^{3-}, SO_4^{2-}, NO^{3-}, K^+, Mg^{2+}, and Ca^{2+} [160].

A bimetallic MOF containing the linker imidazole, ZnCo MOF, having peroxidase activity was used to detect atropine by using the molecular imprinted polymer (MIP). ZnCo MOF was able to oxidize OPD and terephthalic acid in the presence of H_2O_2 to give their respective colored products. The peroxidase activity was even higher than the individual Zn MOF and Cu MOF. The presence of atropine in the system inhibits the oxidation process. But due to low selectivity, the usage of the MIP system for the extraction of atropine was considered. Fe_3O_4@SiO_2 NPs were used as the MIP. A magnetic Fe_3O_4@SiO_2 NPs modified GO was used to extract atropine which was then detected by its effect on lowering the intensity of the oxidized peroxidase substrates. A limit of detection of 27pg/mL and a wide range of detection of 0.1–45 ng/mL was reported [161].

A Zr-based MOF prepared from the linker Bipyridyl-4,4-dicarboxylic acid (BPDCA), denoted as Zr-MOF, was used to identify phosphorylated proteins colorimetrically. In the presence of H_2O_2, Zr-MOF was shown to oxidize TMB to give a blue-colored product. Studied with a model protein, α-casein (α-CS), the phosphate groups present, which are negatively charged, are easily anchored into the metal center which carry a positive charge(s). This results in the inhibition of the chromogenic reaction of the MOF [162].

Ni-based MOF, Ni-TCPP(Fe), with intrinsic peroxidase properties, was synthesized and wrapped with polyethyleneimine (PEI) in order to introduce

amino groups on the MOF and finally was cross-linked with luminol to yield a self-enhanced Eletrochemiluminescent emitter in Ni-TCPP(Fe)-PEI-Lum. Secondary antibodies were immobilized to obtain Ni-TCPP (Fe)-PEI-luminol-Ab2. In the presence of Heart-type fatty acid-binding protein (h-FABP), a strong ECL signal was exhibited as is depicted in Fig. 13.9. This was attributed to the peroxidase properties already present in Ni-TCPP(Fe) [163].

An iron-containing MOF with intrinsic peroxidase activity, MIL-100(Fe) was adsorbed electrostatically with a negatively charged aptamer with an attempt to detect α-fetoprotein. When H_2O_2 is present along with luminol, the luminol anion or HO_2^- can combine with the peroxidase mimetic MIL-100(Fe) which catalyzes the CL system. More the number of aptamers adsorbed, weaker is the signal as the negatively charged aptamers shield the negative luminol anion and HO_2^- from interacting with the MOF. However, in the presence of α-fetoprotein (AFP), it gets bonded to the aptamers and the interaction between the MOF and the anions are influenced, thereby causing a difference in the CL signal [164].

Li et al. developed a MOF-aptamer-TMB-H_2O_2 system for the colorimetric sensing of antibiotics. The aptamers were adsorbed on the MOF *via* AuNPs. In the presence of H_2O_2, the MOF-AuNP-aptamer aggregate could oxidize TMB to the blue-colored OxTMB. However, when an antibiotic was introduced into the system, no OxTMB was formed. Fe-MIL-53 was shown to provide the best catalytic activity followed by Fe-MIL-88A and Fe-MIL-100. The system showed high sensitivity toward chloramphenicol with a detection level of 8.1 ng/mL [165].

A copper-containing MOF, $Cu_3(BTC)_2$ or HKUST-1, prepared using the linker 1,3,5-benzene tricarboxylate was synthesized by Li Wang and his group. HKUST-1 was shown to catalyze the oxidation of thiamine (TH) into thiochrome in the presence of H_2O_2. TH (or Vitamin B_1) is a nonfluorescent molecule. But the ability to oxidize it into the fluorescent thiochrome compound shows the peroxidase activity of HKUST-1, and thus a simple and effective method for the detection of thiamine was developed [166]. Fe-MIL-101 synthesized using 1,4-Dicarboxylic acid (H_2BDC) [149] was shown to exhibit excellent peroxidase-like activity over a broad range of pH. Fe-MIL-101 on conjugation with folic acid was used to detect cancer cells colorimetrically. [167]. Other MOFs such as Tα MOF [168] for the detection of antioxidants, Fe-MIL-88A [169] for the detection of biomolecules are also known.

13.2.1.6 Detection of metal ions

A 1,4-Benzenedioic acid (H_2BDC) containing Ni-MOF was etched with iron nitrate to yield the bimetallic Fe-Ni-MOF. The Fe-Ni-MOF was shown to exhibit peroxidase activity and thus was able to oxidize TMB to OxTMB in the presence of H_2O_2 with a K_M value of 0.09 mM and V_{max} of 4.63×10^{-8} M/s toward TMB. The peroxidase property of the Fe-Ni-MOF was used to colorimetrically detect the presence of Sn^{2+}, which is one of the leading toxic metals present in

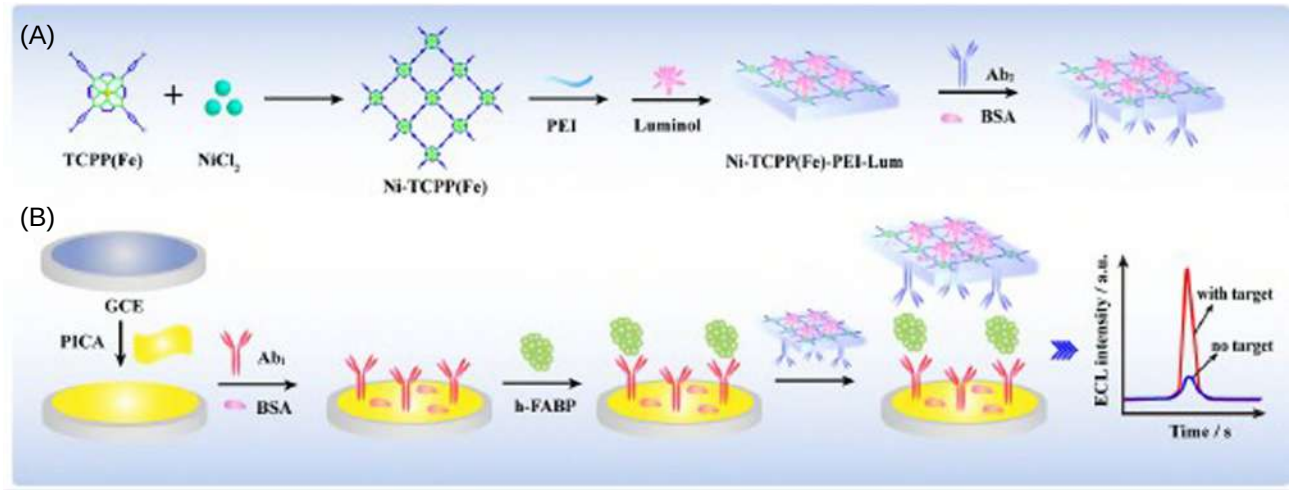

FIGURE 13.9 ECL immunosensor for detection of h-FABP. *Reprinted with permission from Reference [163]. Copyright@2021 Elsevier.*

water bodies. When Sn^{2+} was brought into the system, the blue color of OxTMB slowly faded away and the observed absorbance at 652 nm also decreased. This was due to the reducing capability of Sn^{2+} resulting in the inhibition of the catalytic activity of the Fe-Ni-MOF. The presence of other interfering reductive ions like Co^{2+}, Cr^{3+}, Cu^{+}, Fe^{2+}, Hg^{+}, Mn^{2+}, and Pb^{2+} tend not to show much of an effect because of the poorer reducing capability as compared to Sn^{2+}. Thus, a colorimetric and quantitative method to detect Sn^{2+} ions was developed [170].

Using TCPP linker, an Fe-based MOF, $(Fe\text{-}P)_n$-MOF was synthesized and DNA fragment GR-5 was anchored on it with the aid of AuNPS, leading to the formation of GR-5/$(Fe\text{-}P)_n$-MOF. A hairpin (HP) DNA probe was immobilized on the screen-printed carbon electrode (SPCE) via AuNPs and was used as the electrochemical sensor. The peroxidase mimetic $(Fe\text{-}P)_n$-MOF was able to oxidize TMB to OxTMB in the presence of H_2O_2 to yield a blue-colored solution with a K_M value of 1.27 mM toward H_2O_2 and 0.63 mM with TMB. When Pb^{2+} was introduced, the GR-5 from the $(Fe\text{-}P)_n$-MOF was splintered and a short oligonucleotide fragment linked to the $(Fe\text{-}P)_n$-MOF remained. The oligonucleotide was then ligated with the HP DNA and in the presence of H_2O_2 and TMB, an amplified electrochemical signal was recorded. However, in the presence of other cations like Ca^{2+}, Fe^{3+}, Cd^{2+}, Co^{2+}, Zn^{2+}, Mn^{2+}, Ni^{2+}, Cu^{2+}, Hg^{2+}, Mg^{2+}, and Ag^{+}, a negligible response was shown. Thus, an electrochemical method for the detection of Pb^{2+} with a low detection limit of 0.034 nM was developed [171].

From an already synthesized Cu-based MOF, HKUST-1, Iron (III) meso-5,10,15,20-tetrakis (4-carboxyphenyl) porphyrin chloride (FeTCPP) linker was incorporated to yield the porph@MOF with peroxidase properties for the colorimetric sensing of Pb^{2+} present in vegetables. The porph@MOF was grown with AuNPs and was then attached with thiolated DNA1. Another thiolated DNA2 attached to AuNPs on a GCE was used for sensing. When Pb^{2+} is present, the DNA2 was cleaved by Pb^{2+} at the ribonucleotide (rA) site and thus gets attached to the DNA1. This leads to the DNA1 detaching from the surface of the MOF, thereby making the MOF available for catalytic conversion of TMB to oxTMB at the expense of an H_2O_2 molecule. Thus, a CL method was developed for the determination of Pb^{2+} in ppt (parts per trillion) for assessing the quality of vegetables [172].

Detection of phosphate ion (Pi) is necessary because it is a significant indicator for monitoring the quality of water [173]. Li et al. designed a bimetallic MOF, UiO-66(Fe/Zr)-NH_2, from the linker 2-aminoterephthalic acid (1,4-BDC-NH_2), possessing threefold functions for the detection of Pi. The presence of the fluorescence linker allows for the MOF to show a strong intrinsic fluorescence at 453nm. The occurrence of Fe^{3+}/Fe^{2+} nodes is responsible for the peroxidase catalytic activity to oxidize OPD to OxOPD or DAP (2,3-diaminophenazine) with a peak at 555 nm. The fluorescence of DAP allows the fluorescence peak of the MOF to be shifted to 435 nm. Due to the inner filter effect, the signal of OxOPD quenches the intrinsic fluorescence of the MOF and consequently, the

fluorescence of the MOF was eliminated during the catalytic oxidation of OPD to OxOPD. Zr^{4+} nodes serve as the site for Pi recognition. When Pi is adsorbed into the MOF, the peroxidase activity is blocked and thus the production of the fluorescent OxOPD is minimized and as a result, the intrinsic fluorescence of the MOF at 435 nm is restored [174]. These metal ions detecting MOFs are collectively displayed in Table 13.9.

13.2.1.7 Detection of bacteria

MOFs are also used for detecting bacteria Table 13.10. A mixed metal MOF containing Co^{2+} and Fe^{3+} and the linkers pyrazine and terephthalic acid (BDC), Co_3Fe-MMOF, was shown to possess peroxidase activity and capable of oxidizing TMB to the blue and further to the yellow-colored OxTMB in the presence of H_2O_2. Dopamine hydrochloride was added to the Co_3Fe-MMOF along with the antibody (Ab) of the bacterium *Aeromonas hydrophila* to obtain the Co_3Fe-MMOF@PDA@Ab. Polydopamine (PDA) here could easily graft the Ab on the surface of the MMOF while it itself could outwit the MMOF NPs. Similarly, the magnetic Fe_3O_4@PDA@Ab was prepared. When Fe_3O_4@PDA@Ab NPs were added to the solution containing the bacterium, a specific interaction between the bacterium (antigen) and its antibody was created. When the Co_3Fe-MMOF@PDA@Ab was introduced into the solution, the presence of any other nontarget bacteria and free Co_3Fe-MMOF2PDA@Ab were removed with the help of a magnet. The presence of the target bacteria was detected by measuring the chromogenic oxidation reaction of TMB by the remainder Co_3Fe-MMOF@PDA@Ab and its corresponding absorption at 450 nm. Thus, a new ELISA method for the detection of *Aeromonas hydrophila* using MOF was developed with a low limit of detection (expressed in terms of colony-forming unit or CFU) corresponding to 17 CFU/mL [175]. Wang et al. synthesized a Cu^{2+} and 2-aminoterephthalic acid-containing Cu-MOF. The Cu-MOF showed peroxidase activities and was able to oxidize TMB to the yellow-colored OxTMB in the presence of H_2O_2. The amine groups present on the MOF made it easier for the attachment of *Staphylococcus aureus* aptamer on the MOF NPs. In the presence of *Staphylococcus aureus*, the aptamer will be bound to the bacteria and the availability of free Cu-MOF for the oxidation of TMB in the presence of H_2O_2 was reduced thereby leading to the formation of faint colored yellow product. Thus, a simple colorimetric method for the detection of *Staphylococcus aureus* with a low detection limit of 20 CFU/mL was developed [176].

Using 2-aminoterephthalic acid, a Cu-based MOF, Cu-MOF NPs were synthesized. It showed the ability to oxidize TMB to the blue-colored OxTMB in the presence of H_2O_2. This peroxidase property of Cu-MOF NPs was used to detect the presence of *Escherichia coli*. The Cu-MOF NPs were then attached with streptavidin *via* a glutaraldehyde reaction. To this, the *E. coli* modified with biotin was attached as the aptamer (apt-2). This Cu-MOF NPs-apt-1 was able

TABLE 13.9 MOFs for metal ions detection.

Sl. No.	MOF	Linker	Optimum pH	Optimum temperature (°C)	Metal ion	Detection limit (μM)	References
1	Fe-Ni-MOF	1,4-Benzenedioic acid (H_2BDC)	4.0	–	Sn^{2+}	0.36	[170]
2	GR-5/$(Fe\text{-}P)_n$-MOF	TCPP	7.0	37	Pb^{2+}	3.4×10^{-5}	[171]
3	porph@MOF	1,3,5-benzene tricarboxylate	–	–	Pb^{2+}	5×10^{-6}	[172]
4	UiO-66(Fe/Zr)-NH_2	2-aminoterephthalic acid (1,4-BDC-NH_2)	4.0	–	Pi	8.5×10^{-2}	[180]

TABLE 13.10 MOFs for bacteria detection.

Sr. No.	MOF	Linker	Optimum pH	Optimum temperature (°C)	Bacterium	Detection limit (CFU/mL)	References
1	Co_3Fe-MMOF	pyrazine and terephthalic acid (BDC)	–	–	*Aeromonas hydrophila*	17	[175]
2	Cu-MOF	2-Aminoterephthalic acid	7.4	37	*Staphylococcus aureus*	20	[176]
3	Cu-MOF NPs	2-Aminoterephthalic acid,	4.0	35	*Escherichia coli*	2	[177]

to oxidize TMB in the presence of H_2O_2. On a parallel side, another biotin-modified *E. coli* aptamer (apt1) was linked on a microplate already coated with streptavidin. When *E. coli* was introduced, it got sandwiched between the two aptamers. This sandwiched system was able to intensify the color of OxTMB formed. Based on the intensity of the OxTMB formed, a quantitative deduction of the amount of *E. coli* present could be estimated. The detection limit was found to be 2 CFU/mL while the linear detection range was 16–1.6 $\times$ 10^6 CFU/mL [177].

13.2.1.8 Detection and degradation of toxic chemicals

Detection and elimination of explosives is one important subject for national security as well as for environmental pollution (Table 13.11). A visual detection of perilous peroxide explosives like Triacetone triperoxide (3,3,6,6,9,9-hexamethyl-1,4,7-cyclononatriperoxane, TATP) was studied by Habibi and his coworkers. A flake like Zn-based MOF was prepared using terephthalic acid. Quoted as Zn-MOF, Ag NPs were grown on the MOF giving Ag@ZnMOF. Under acidic conditions, TATP is decomposed to release H_2O_2. This H_2O_2 is taken up by the Ag@ZnMOF to oxidize TMB to the blue-colored OxTMB [178]. Zheng et al. studied four Zr-based MOFs for their abilities to catalyze oxidative desulfurization (ODS) so as to combat increasing sulfur levels in the environment. UiO-66, UiO-67, NU-1000, and MOF-808, were shown to possess peroxidase like activity and thus analyzed for their catalytic ODS. Both $\cdot O^{2-}$ and $\cdot OH$ radicals from the decomposition of H_2O_2 by the peroxidase activity are responsible for the oxidation of dibenzothiophene (DBT). Among these four MOFs, MOF-808 has the best catalytic activity in desulfurizing DBT. MOF-808 was able to completely desulfurize DBT in a model gasoline which has a 1000ppm concentration within 5 minutes and requires a low Arrhenius activation energy (E_a) of 22.0 kJ/mol. The presence of maximum number of Zr-$(OH)(H_2O)$ catalytic sites make it the best fit for the catalytic activity [179].

13.2.1.9 Detection of miscellaneous chemicals

Xuan et al. group developed a sensitive detection method for determination of the presence of thiabendazole (TBZ) with a low detection limit of 50 ppb. An Fe and terephthalic acid (PTA) based MOF, MIL-101, was modified with inositol hexaphosphate (IP_6). Ag-Au-NPs were then grafted on the surface of the redesigned MOF yielding Ag-Au-IP_6-MIL-101. The resulting MOF was stable as the IP_6 molecules could behave as a bridging agent between the NPs and the MOF. Rhodamine 6G (R6G) was chosen to be used as a Raman probe for the estimation of the SERS properties TBZ containing substrates. Samples containing thiabendazole and Ag-Au-IP_6-MIL-101 were mixed in a 1:1 ratio for SERS measurement [180].

Using Zr and TCPP, an Fe-loaded MOF-545(Fe) having peroxidase properties was synthesized. The Fe-loaded MOF-545(Fe) was shown to oxidize TMB

TABLE 13.11 MOFs for toxic chemical detection and degradation.

Sr. No.	MOF	Linker	Optimum pH	Optimum temperature (°C)	Toxic Chemical	Detection limit	References
1	Ag@ZnMOF	Terephthalic acid	4.0	25	Triacetone triperoxide (3,3,6,6,9,9-hexamethyl-1,4,7-cyclononatriperoxane, TATP)	0.04 mg/L	[178]
2	MOF-808	1,3,5-benzenetricarboxylic acid (BTC)	–	40	dibenzothiophene (DBT)	–	[179]

to the blue-colored OxTMB in the presence of H_2O_2. Due to the peroxidase property, the Fe-loaded MOF-545(Fe) was shown to degrade the anionic (acidic) dye methyl orange (MO) and the cationic (basic) dye methylene blue (MB) without any adsorption. Due to the presence of Fe load, the degradation of the acidic dye MO was faster than that of MB. This method finds place in the removal of dye pollutants in wastewater [181].

A dual functional NH_2-MIL-101(Fe) having luminescent and peroxidase properties were synthesized and employed for the detection of pesticide residues. The presence of the 2-aminoterephthalic acid linker takes care of the photoluminescence property of the MOF, giving a peak at 428 nm while the Fe metal center is responsible for the peroxidase like activity. Exercising the peroxidase activity, in the presence of H_2O_2, NH_2-MIL-101(Fe) was shown to oxidize OPD to DAP which gave a fluorescence signal at 556nm and suppressed the peak at 428nm. When acetylcholinesterase enzyme (AChE) was introduced in a system containing NH_2-MIL-101(Fe), H_2O_2, OPD and acetylthiocholine, the latter got hydrolyzed to thiocholine. The thiol group present was able to block the catalytic sites of the MOF and thereby inhibited the oxidation of OPD to DAP. This resulted in the photoluminescence peak at 428 nm to escape the suppression. Pesticides are able to target the AChE enzymes. Thus, in the presence of any pesticide residues, they could inhibit the activity of AChE which could lead to an increase formation of DAP from OPD with a dominant peak at 556 nm and a suppressed peak at 428 nm [182].

Synthesized using the linker 2-aminoterephthalic acid by a bottom-up approach, the Cu-based MOF (NH_2-Cu-MOF) showed intrinsic peroxidase activity as well as fluorescence property with $\lambda_{em} = 425$ nm. The NH_2-Cu-MOF was used to detect hypoxanthine (Hx), which is a measure of the freshness of fish. In the presence of xanthine oxidase, Hx gets oxidized to uric acid at the expense of O_2 which generates H_2O_2. This H_2O_2 released oxidizes the peroxidase substrate OPD to the fluorescence active DAP. Thus, a fluorometric detection method of Hx was established with a detection limit of 3.96 μM and a linear detection range of 10–2000 μM [183]. An Fe-based MOF with Ni wires and Ag NPs, Ni@MIL-100(Fe)@Ag, was shown to exhibit peroxidase-like activities. The presence of dyes like MB, crystal violet (CV), MG, sunset yellow, methyl orange, erythrosine and amaranth red adsorbed on the surface of the MOF results in a SERS signal. However, on the addition of H_2O_2, the peroxidase activity of the MOF results in the release of $^{\cdot}OH^{-}$ which degrades the contaminants into a cleaner product. The removal of the dyes result in the disappearance of the SERS signal [184]. A multifunctional MOF, Fe_3O_4@Au@MIL-100(Fe) was synthesized to detect and degrade cationic dyes. The presence of large pores in the MOF structure allows for the organic dyes to be easily adsorbed on it and the unique structure of the MOF shell possesses a remarkable SERS capability. The magnetic Fe_3O_4 can enhance the Raman signal of the cationic dyes. In addition of H_2O_2, the MOF composite activates it peroxidase activity and consumes it to degrade the cationic

dyes [185]. The detection of these miscellaneous chemicals are collectively shown in Table 13.12.

13.2.1.10 Other applications of MOFs as peroxidase

Besides the above-mentioned MOFs used in various applications, many other MOFs have also been reported that exhibit peroxidase activities. A Co-based MOF, ZIF-67 was shown to exhibit peroxidase activity and oxidize TMB in the presence as well as absence of H_2O_2. At low concentrations of ZIF-67, the oxidation of TMB was checked at 450 nm rather than the usual 652 nm. At higher concentrations of H_2O_2, however, no oxidized compound showing yellow color was seen. This could be probably due to the excess H_2O_2 that might react with the MOF, poisoning its catalytic capacity [186]. A MOF containing two metals, MOF(Co/2Fe), reported already by Guohua Zhao and his coworkers [187] was shown to be able to catalyze the oxidation of TMB, OPD, ABTS in the presence as well as the absence of H_2O_2 [188]. MOF(Co/2Fe) was thus shown to act as both a peroxidase as well as an oxidase mimic.

A dark red Zirconium MOF, MMPF-6, was prepared using the ligand Fe-TCPP-Cl {Iron(III) meso-tetrakis(4-carboxyphenyl)porphyrin chloride}. MMPF-6 was shown to oxidize TMB and ABTS in the presence of H_2O_2, thereby showing its peroxidase properties [189]. A mesoporous Zirconium MOF, PCN-222, containing Fe-TCP {TCPP= tetrakis(4-carboxyphenyl)porphyrin} as the ligand has all the criteria required to act as a biomimetic system. PCN-222 has an exceptionally high water stability, ultra-large pore size, and thus potential catalytically active centers. PCN-222 was shown to oxidize pyrogallol, TMB, and OPD in the presence of H_2O_2 thereby showing its peroxidase activities [190]. A 2D ultrathin MOF nanosheet, Cu-TCPP(Fe) adsorbed with GOx was prepared to combat bacterial activities [191]. The adsorbed GOx converts glucose into gluconic acid and H_2O_2. The gluconic acid formed helps in reducing the pH of the system necessary enough for the peroxidase activity of Cu-TCPP(Fe) MOF to convert H_2O_2 to toxic $^{\cdot}OH$ which has antibacterial properties.

13.2.2 COFs as peroxidase mimics

An Fe-porphyrin-based COF, Fe-COF, was prepared by incorporating Fe^{2+} ions into COF-366 [192]. The Fe-COF was shown to oxidize TMB to OxTMB in the presence of H_2O_2. This peroxidase activity of the Fe-COF was used to detect the presence of Glucose by implementing GOx through a cascade reaction. The H_2O_2 liberated from the oxidation of glucose by GOx was taken up by the Fe-COF to give the blue-colored OxTMB. The limit of detection for glucose was found to be 1.0 μM. Fe-COF showed excellent peroxidase activity with K_M values of 0.02 mM and 0.143 mM toward TMB and H_2O_2, respectively [193].

A crystalline imine-based PTAzo COF, prepared from 1,3,5-tris-(4-formylphenyl) triazine (PT) and 4,4′-azodianiline (Azo), was coated with AuNPs to give

TABLE 13.12 MOFs for detection of other chemicals.

Sr. No.	MOF	Linker	Optimum pH	Optimum temperature (°C)	Chemicals	Detection limit	References
1	Ag-Au-IP_6-MIL-101	terephthalic acid (PTA)	–	–	thiabendazole	50 ppb	[180]
2	MOF-545(Fe)	TCPP	–	37°C	methyl orange	–	[181]
3	NH_2-MIL-101(Fe	2-aminoterephthalic acid	–	–	pesticide residues	–	[182]
4	NH_2-Cu-MOF	2-aminoterephthalic acid	–	–	Hypoxanthine (Hx)	3.96 μM	[183]
5	Ni@MIL-100(Fe)@Ag	trimesic acid (BTC)	3.6	–	Dyes	–	[184]
6	Fe_3O_4@Au@MIL-100(Fe)	benzenetricarboxylic acid	–	–	Cationic dyes	–	[185]

a COFAuNPs hybrid. The COFAuNPs showed excellent peroxidase activities and its ability to oxidize TMB to OxTMB in the presence of H_2O_2 was used for the colorimetric detection of Hg^{2+}. The presence of Hg^{2+} intensified the absorbance peak at 652 nm, characteristic of the formation of OxTMB. However, the COFAuNPs could not detect the presence of other cations such as Ca^{2+}, Mn^{2+}, Cr^{3+}, Pb^{2+}, Ba^{2+}, K^{+}, Na^{+}, Fe^{3+}, Mg^{2+}, and Cu^{2+}, thereby showing its high selectivity [194].

Zhang et al. constructed a MOF@COF nanozyme which possesses peroxidase like activity because of the MOF moiety while the porous architecture from the COF moiety enabled the capture of bacteria and subsequently inhibit its bacterial activities. Represented as $NMC_{TP\text{-}TTA}$, the nanozyme was prepared from the 2-NH_2-BDC ligand containing MOF NH_2-MIL-88B(Fe), written as NM-88. To this NM-88, 1,3,5-triformylphloroglucinol (Tp) and 4,4',4''-(1,3,5-triazine-2,4,6-triyl)trianiline (TTA) were sequentially grown to yield $NMC_{TP\text{-}TTA}$. Both NM-88 as well as $NMC_{TP\text{-}TTA}$ were shown to oxidize TMB to OxTMB in the presence of H_2O_2. $NMC_{TP\text{-}TTA}$ however shows a lower K_M value and a higher V_{max} value than NM-88, thereby proving to be a better peroxidase mimetic. The nanocavities and morphology of the COF were positioned in a way good enough to capture bacteria which could be easily terminated by the ROS generated from the peroxidase activity of the MOF component [195].

Using Au-COFs and Au@ZIF-8(NiPd) as matrix for conduction and nanocarriers respectively for the detection of Thrombin (TB), a sandwich aptasensor was constructed. 2-methylimidazole and Zr-based MOF, ZIF-8, was collaborated with NiPdNPs to form the hybrid ZIF-8(NiPd) and was further functionalized with AuNPs to finally yield the tracer label Au@ZIF-8(NiPd) rhombic dodecahedron nanocomposite. A Thrombin-binding aptamer (TBA-2) was attached to the nanocomposite *via* the interaction between the -NH_2 group and AuNPs. 1,4-benzenediboronic acid (BDBA) was organized to prepare a COF nanosheet and then was dried on the GCE. Au was then electrodeposited on the COFs/GCE thereby giving Au-COFs/GCE. This was then further dropped with the capture probe TBA-1 to finally form TBA-1/Au-COFs/GCE. Bovine Serum Albumin (BSA) was finally incorporated and BSA/TBA-1/Au-COFs/GCE was thus prepared. Au@ZIF-8(NiPd) were shown to oxidize TMB, ABTS, and OPD in the presence of H_2O_2 to give the blue colored OxTMB, green colored Ox-ABTS and orange-yellow DAP, respectively. Due to their high conductivity and high amount of TBA1 adsorbed, TBA-1/Au-COFs/GCE could achieve signal amplification while due to the excellent peroxidase activity of the Au@ZIF-8(NiPd), it was able to promote the sensing ability [196].

13.2.3 NCs as peroxidase mimics

Dopamine (3,4-dihydroxyphenethylamine) is known to inhibit the oxidation of TMB [197]. Thus, NCs with peroxidase properties capable of detecting dopamine were developed. The MOF ZIF-67 [186] was calcined and a Co_3O_4

hollow NC (Co_3O_4 HNCs) was obtained. Co_3O_4 HNCs show intrinsic peroxidase (and oxidase) properties by being able to oxidize TMB in the presence (as well as absence) of H_2O_2. Co_3O_4 HNCs showed better peroxidase catalytic activities than its precursor ZIF-67 as well as the analog Co_3O_4 NPs [198]. Co_3O_4 HNCs showed a K_M value of 0.13 mM and a high V_{max} value of 31.96×10^{-8} M/s which was higher than Co_3O_4 NPs and HRP[20]. This may be attributed to the larger specific surface area and porosity of the cage like structure, which could expose more catalytic surfaces. The peroxidase activity of Co_3O_4 HNCs to oxidize TMB to the blue-colored OxTMB with the help of H_2O_2 was hindered in the presence of dopamine. Thus, a colorimetric sensing of dopamine was developed with a detection limit of 0.015 μM and a detection linear range of 0.02 to 3.5 μM [199].

Gajendar et al. synthesized a $[Cu_3(OH)_2MoO_4)_2]$, copper molybdate cuboidal nanostructures (CMCNs) and its nanocomposite with reduced graphene oxide (rGO) to form rGO/CMCNs nanocomposites. The rGO/CMCNs nanocomposites showed excellent peroxidase activity with the ability to oxidize TMB to the blue-colored OxTMB in the presence of H_2O_2. The rGO nanosheets serve as a mechanical support as well as a platform for easier electron transport. The peroxidase activity of rGO/CMCNs nanocomposites to oxidize TMB to the blue-colored oxTMB with the help of H_2O_2 was hindered in the presence of dopamine. The detection limit of dopamine was found to be 1–10 μM with a detection limit of 0.17 μM [200]. A ZnO-Co_3O_4 NC was synthesized *via* the calcination of a ZnO-ZIF precursor MOF. The ZnO-Co_3O_4 NC was shown to oxidize TMB to the blue-colored OxTMB in the presence as well as absence of H_2O_2. However, the peroxidase activity was much larger than the oxidase behavior. The ZnO-Co_3O_4 NC has a K_M value of 0.164 mM and a V_{max} of 4.85×10^{-8} M/s toward TMB, which were close enough to that of HRP [20]. The addition of cysteine to the ZnO-Co_3O_4 NC-H_2O_2-TMB system inhibits the formation of OxTMB due to the oxidation of cysteine *via* the formation of a disulfide bond. However, on the addition of Cu^{2+} to this system, the Cu^{2+} strongly binds to Cysteine and the formation of disulfide bond was inhibited, thereby restoring the blue color of OxTMB. Thus, a "turn on" system for the detection of Cu^{2+} was developed with a detection limit of 1.09 nM and a linear range of 2 to 100 nM [201].

ZIF-67 was used as a precursor to generate Co_3O_4@Co-Fe oxide double-shelled nanocages (DSNCs) via an anion exchange reaction followed by pyrolysis at low-temperature. The Co_3O_4@Co-Fe oxide DSNCs showed peroxidase activity in oxidizing TMB to OxTMB in the presence of H_2O_2. Co_3O_4@Co-Fe oxide DSNCs have a K_M value much lower than its single-shelled NC and NP counterparts, thereby making the DSNC a better peroxidase mimic. It showed a linear H_2O_2 detection in the range of 0.02 to 600 μM and a detection limit of 20 nM. A colorimetric sensing method for the detection of Acetylcholinesterase enzyme (AChE) activity was developed. The thiol group present in acetylthiocholine (ATCh) was able to reduce OxTMB to TMB [202] and block the catalytic

active sites. But in the presence of AChE, ATCh gets hydrolyzed into Thiocholine (TCh), thereby the oxidation of TMB was not inhibited. This sensing method was further extended to the detection of AChE inhibitor huperzine A (HA). In the presence of HA, the activity of AChE would be suppressed and hence oxidation of TMB would be restricted. Also, the Co_3O_4@Co-Fe oxide DSNCs was used for the degradation of organic contaminants like Acid fuchsin (AF) by the activation of peroxymonosulfate (PMS). Since PMS has similar O-O structure like in H_2O_2, in the presence of the Co_3O_4@Co-Fe oxide DSNCs, PMS could generate reactive $SO_4^{\cdot -}$ and $^{\cdot}OH$ which were then involved in the degradation of AF [202].

Dong et al. developed an FeNPs@Co_3O_4 Hollow NCs, HNCs, *via* the pyrolysis of the ZIF-67 precursor and then immobilizing Fe NPs on the surface of the HNCs. The FeNPs@Co_3O_4 HNCs showed peroxidase activity and were able to oxidize TMB in the presence of H_2O_2. The K_M value for H_2O_2 was found to be 0.019 mM which was comparatively very low than that of HRP. This HNCs was used for the colorimetric sensing of glucose. In the presence of glucose oxidase, glucose gets converted into gluconic acid and release H_2O_2 which was further taken up by the HNCs to oxidize TMB [203].

Xiao Li et al. synthesized two Keggin Polyoxometalates Based Hybrid NCs $[Cu^{I}_2Cu^{II}_2(fkz)_2(H_2O)_7(SiW_{12}O_{40})]$ (compound 1) and $[(Hfkz)_3(H_4SiW_{12}O_{40})]$ (compound 2) using the bioactive Hfkz molecules, (fluconazole, 1-(2,4-difluorophenyl)-1,1-bis[(1H-1,2,4-triazol-1-yl)methyl]methanol, Keggin-type $H_4SiW_{12}O_{40}$. Both compounds 1 and 2 showed peroxidase like activities and were able to oxidize TMB to OxTMB in the presence of H_2O_2 and thus were used for the colorimetric sensing of H_2O_2. Compound 1 showed a detection limit of 0.13 μM with a linear range of 1–90 μM while compound 2 shows 0.20 μM and 1–80 μM, correspondingly. Toward H_2O_2, compound 1 exhibits a Keggin value of 0.160 mM while it was 0.207 mM for compound 2 [204].

An Ag-Au NC with nanoceria was developed as a high-performance catalyst for a cascade reaction for the colorimetric sensing of glucose. By galvanic replacement reaction, hollow structured Ag-Au NCs were prepared to which CeO_2 NPs were surface coated by hydrothermal self-assembly method. The Ag-Au NC@CeO_2 was able to show both oxidase as well as peroxidase properties. In the presence of glucose, the Ag-Au NC@CeO_2 would oxidize it to gluconic acid and H_2O_2 which would then be used up to oxidize TMB to the blue-colored OxTMB [205].

Zhou et al. prepared a bimetallic ZnO-Co_3O_4 NC [208] by using Zno-Co_3O_4 as a precursor. The ZnO-Co_3O_4 NC exhibited peroxidase activity and was able to oxidize TMB to OxTMB. Amyloid-β peptide (Aβ) has excellent adsorption ability to metal ions including Zn^{2+} and Co^{3+} [206]. Thus, when Aβ was introduced into a ZnO-Co_3O_4 NC-H_2O_2-TMB system, it got adsorbed onto the metallic surfaces of the NC, thereby blocking the catalytic sites, and hence the oxidation of TMB was inhibited. Thus, a colorimetric sensing for the detection of Aβ was developed. The detection limit for the Aβ monomer was reported

to be 3.5 nM with a linear detection range of 5–150 nM. Detection of Aβ is necessary as Alzheimer's disease often start with the aggregation of Aβ into oligomers, fibrils and plaques [207]. However, on addition of Aβ like curcumin and β-cyclodextrin, the oxidation of TMB to OxTMB resumes but with lesser intensity in the color change [208].

A $PtCu_3$ NCs was prepared via a solvothermal method. The $PtCu_3$ NCs were then modified using a poly(maleic anhydride-alt-1-octadecene)-polyethylene glycol (C_{18}PMH-PEG) through hydrophobic interaction to obtain the $PtCu_3$-PEG. $PtCu_3$-PEG NCs were shown to exhibit peroxidase like activities in catalyzing H_2O_2 to the reactive oxygen species (ROS) $^{\cdot}OH$ which could kill cells. The peroxidase activity was studied by the oxidation of TMB in the presence of H_2O_2 using $PtCu_3$-PEG NCs, wherein the blue-colored OxTMB was formed. Also, the $PtCu_3$-PEG NCs possessed glutathione-peroxidase (GPx) like property that was able to convert glutathione (GSH) to its oxidized form (GSSG) at the expense of a H_2O_2 molecule. The GPx activity was checked by incubating the $PtCu_3$-PEG NCs with excess GSH and by 5,5 ′-dithiobis(2-nitrobenzoic acid) (DTNB) popularly known as Ellman's reagent. Besides the GSH oxidized by $PtCu_3$-PEG NCs, the remaining GSH were determined by the Ellman's reagent. The dual enzymatic property of the $PtCu_3$-PEG NCs helped in the generation of ROS and also suppressed GSH-induced ROS scavenging. This property of the nanozyme finds applications in sonotoxicity enhanced by chemodynamic therapy (CDT) and delaying of tumor growth [209].

Halloysite $\{Al_2Si_2O_5(OH)_{4.n}H_2O\}$ with a large surface area and a tubular nanostructure are often used as a support for catalysts. Siyu li et al., fabricated Ag on halloysite nanotubes, Ag@HNT, *via* a modified silver mirror reaction. Then, by galvanic exchange, Au-Ag and Pt-Ag NCs were generated on the HNT. The two bimetallic Au-Ag@HNT and Pt-Ag@HNT were shown to possess peroxidase like activity. The NCs were able to oxidize OPD to DAP in the presence of H_2O_2 [210]. Xiaoqiang Wang et al. prepared a peroxidase mimic by the noncovalent attachment of hemin into the hydrophobic central cavities of the bacterial chaperonin GroEl, a cylindrical NC for natural protein folding by a detergent dialysis procedure [211]. GroEl is accompanied with an edge over other protein cages in that the chaperonin possesses with multiple hydrophobic grooves facing the central cavity attracting a wide range of hydrophobic residues [212]. The hemin-GroEl NC was checked for the oxidation of Orange II, with an absorbance at 484 nm, in the presence of H_2O_2. The absorbance of the azo dye, Orange II, showed a decrease in the presence of both the hemin-GroEl NC and H_2O_2 which confirmed the peroxidase activity of the NC degrading the substrate. A chromogenic method for the detection of H_2O_2 was carried out in the presence of TMB, wherein TMB got oxidized to the blue-colored OxTMB. The detection limit of H_2O_2 was found to be 10μM. Moving further, the same group studied the peroxidase activity of the GroEl-hemin for the chromogenic detection of H_2O_2, glucose, and catechol using OPD. In the presence of H_2O_2,

the GroEl-hemin NC was able to oxidize OPD to the yellow-colored DAP. The detection limit of H_2O_2 was found to be 7 mM. Using glucose oxidase for the oxidation of glucose to release H_2O_2, a cascade reaction was developed for the detection of glucose. The detection limit was reported to be 11 mM for glucose. With a hemin to GroEl proportion of 40:1, the NC displayed the maximum catalytic performance. Catechol, a dihydroxy group with a maximum absorbance at 275 nm, displayed a decrease peak at this wavelength and the emergence of a new peak at 257nm in the presence of the GroEl-hemin NC and H_2O_2 which was attributed to the formation of the pink-colored oxidation product, quinone. Thus, this method was developed for the detection of catechol and also paved a way for the oxidative removal of the same [213]. The colorimetric detection of glucose and catechol was also carried out using the substrate TMB [214]. The detection limit for glucose and catechol was reported to be 12 μM and 17 μM, respectively.

Peroxidase mimetic $Cu(OH)_2$ NC and G-quadruplex/hemin DNAzyme were coupled to form a double-integrated mimic enzyme. The double-integrated mimic enzyme, $Cu(OH)_2$NC@DNAzyme, showed excellent peroxidase activity in the chromogenic reaction of ABTS in the presence of H_2O_2 having a K_M value of 0.71 mM with ABTS. An immunosensor was developed based on the peroxidase activity of $Cu(OH)_2$NC@DNAzyme to detect microcystin-LR (MC-LR), a toxin produced by cyanobacteria. SiO_2@Ni silicate modified microplates were used as the substrate to immobilize the MC-LR antigens. Ab_2-$Cu(OH)_2$NC-S_0 (Ab_2= secondary goat antibody, S_0= initiator strand) were used as the label. The Ab_2-$Cu(OH)_2$NC-S_0 in the presence of ABTS and H_2O_2 showed a color change due to the oxidation of ABTS. But when MC-LR antigens are present, it acts on the antibodies, causing a lower association ability of the double-integrated enzyme, thereby further resulting in a faint color change. Thus, a colorimetric immunosensor, with a detection limit of 6 ng/L, was developed [215].

Liu et al. synthesized a magnetic bimetallic Ni-introduced CuAu NCs from the Cu_2O precursor by a coreduction process. By a galvanic displacement reaction, Cu_2O was converted to Cu_2O/Au nano-octahedra which was then introduced with Ni and Cu simultaneously to give the Ni-introduced CuAu NCs. This magnetic bimetallic NC was able to exhibit peroxidase activity by the oxidation of TMB to OxTMB in the presence of H_2O_2 with a low K_M value (0.489 mM) and a high V_{max} value (1.04×10^{-7} M/s) [216]. A molybdenum polysulfide deposited nickel-iron bimetal Prussian blue analog-based hollow NCs having peroxidase, catalase and laccase activities were synthesized by wang and his group. The HNCs were able to oxidize TMB, OPD, ABTS, and NADH in the presence of H_2O_2 to give their respective oxidized products, thereby proving its peroxidase activity. Also, measured using a dissolved oxygen meter, the catalase activity of converting H_2O_2 to O_2 was detected. These peroxidase and catalase like activities were used in the application for the elimination of ROS in cells [217]. Peroxidase mimetic $Cu(OH)_2$ NC and G-quadruplex/hemin DNAzyme

were coupled to form a double-integrated mimic enzyme. The double-integrated mimic enzyme, $Cu(OH)_2NC@DNAzyme$, showed excellent peroxidase activity in the chromogenic reaction of ABTS in the presence of H_2O_2 having a K_M value of 0.71 mM with ABTS. An immunosensor was developed based on the peroxidase activity of $Cu(OH)_2NC@DNAzyme$ to detect microcystin-LR (MC-LR), a toxin produced by cyanobacteria. $SiO_2@Ni$ silicate modified microplates were used as the substrate to immobilize the MC-LR antigens. Ab_2-$Cu(OH)_2NC$-S_0 (Ab_2= secondary goat antibody, S_0= initiator strand) were used as the label. The Ab_2-$Cu(OH)_2NC$-S_0 in the presence of ABTS and H_2O_2 showed a color change due to the oxidation of ABTS. But when MC-LR antigens are present, it acts on the antibodies, causing a lower association ability of the double-integrated enzyme, thereby further resulting in a faint color change. Thus, a colorimetric immunosensor, with a detection limit of 6 ng/L, was developed [215] The various nanocages used as peroxidase mimics are shown in Table 13.13.

13.3 Conclusion

In this chapter, we have showcasted various MOFs, COFs, and NCs used as peroxidase mimics. Work on artificial enzyme mimetics has been on the rise since the discovery of Fe_3O_4 as peroxidase mimics. Artificial enzyme mimics have wide use in fields like environment treatment, biosensing, antibacterial, and anticancer treatment, antioxidation, detection of biomolecules like glucose, uric acid, ascorbic acid, etc. Their low cost of preparation and excellent stability gives them this advantage. However, not everything is perfect. Nanozymes have a drawback side too. Although, some nanozymes exhibit excellent enzymatic activities, many of them, however, show inferior enzymatic properties. Some of them require to work in non-physiological pHs, while some require thermal environments and some of them show multiple activities. So, a thorough investigation into this matter for realizing a definite working environment with proper selectivity for the enzyme mimetics need to be proceeded.

Nanozymes used in cancer therapy and treatment of other disease-related issues should not be satisfied with their remarkable results with in vitro experiments. Their cytotoxicity, stability, and biocompatibility with in vivo experiments need to be examined. Unlike natural enzymes, proper reaction mechanisms have not been developed for many nanozymes, failing which the enzymatic property of the nanozymes may be due to sheer luck with a particular substrate and may not work with similar substrates. Also, less studies have been conducted, and more need to be performed on the fate of these nanozymes inside the cells after degradation.

In this chapter, we have primarily focused on MOFs, COFs and NCs used as peroxidase mimics. Considering MOFs and COFs, not all can be termed as nanozymes, unless their pore size lies within the range of 1nm to 100nm, as per the definition of NP. Also, nanozymes that focus on other enzymatic functions

TABLE 13.13 NCs used as peroxidase mimics.

Sr. No.	NC	Biomolecule capable of detecting	Detection limit	References
1	Co_3O_4 HNCs	Dopamine	0.015 μM	[199]
2	$[Cu_3(OH)_2MoO_4)_2]$	Dopamine	0.17 μM	[200]
3	ZnO-Co_3O_4 NC	Cu^{2+}	1.09 nM	[201]
4	Co_3O_4@Co-Fe oxide (DSNCs)	Acetylcholinesterase	–	[202]
5	FeNPs@Co_3O_4 HNCs	Glucose	–	[203]
6	$[Cu^{I}_2Cu^{II}_2(fkz)_2(H_2O)_7(SiW_{12}O_{40})]$	H_2O_2	0.13	[204]
7	$[(Hfkz)_3(H_4SiW_{12}O_{40})]$	H_2O_2	0.20	[204]
8	Ag-Au NC@CeO_2	Glucose	–	[205]
9	ZnO-Co_3O_4 NC	Amyloid-β peptide (Aβ)	3.5 nM	[208]

such as hydrolases, transferases, lyases, isomerases, ligases, and antioxidants, such as Glutathione peroxidase, catalases, superoxide dismutases, etc., are not explored in depth till date. This issue also opens a huge scope for future studies. Thus, developing more types of nanozymes with different functions and exploring their cascade reactions will give us an idea about how natural enzymes function and about the complex life processes.

Herein, we have tried to fit the nanozyme concept into the supramolecular chemistry realm considering the basic aspects of supramolecular chemistry such as substrate recognition and host–guest chemistry. The idea of the nanozymes to capture the substrates and hold them into their active sites give them the room to slide into the supramolecular world.

Although the field of nanozymes is still in its infancy, it has so far accomplished a lot, as is seen from the various number of nanozymes developed so far. As of this emerging trend, more discoveries and further breakthroughs in enzyme mimetics will pave the way for novel biocatalysts which may find use in various applications. Thus, it is of utmost importance that deeper research on the development of nanozymes with various other enzymatic functions that work in similar conditions with their natural enzyme counterparts be focused on.

Acknowledgement

A.A.V. thanks the Department of Science and Technology (DST), New Delhi, India, for the DST INSPIRE faculty award. H.M. thanks DST for the DST INSPIRE fellowship and AM thanks University Grants Commission (UGC), New Delhi, India, for a research fellowship. CSIR-CLRI communication number: 1562

Conflict of Interest

The authors declare no conflict of interest.

References

[1] U.T. Bornscheuer, G.W. Huisman, R.J. Kazlauskas, S. Lutz, J.C. Moore, K. Robins, Engineering the third wave of biocatalysis, Nature 485 (7397) (2012) 185–194.

[2] J.P. Genet, Asymmetric catalytic hydrogenatio. Design of new Ru catalysts and chiral ligands : from laboratory to industrial applications, Acc. Chem. Res. 36 (12) (2003) 908–918.

[3] M. Behrens, F. Studt, I. Kasatkin, S. Kühl, M. Hävecker, S.Z F.Abild-Pedersen, P.K F.Girgsdies, B.L. Kniep, M. Tovar, R.W. Fischer, J.K. Nørskov, R. Schlögl, The active site of methanol synthesis over $Cu/ZnO/Al_2O_3$ industrial catalysts, Science 336 (2012) 893–898 May.

[4] A.J. Kirby, Efficiency of proton transfer catalysis in models and enzymes, Acc. Chem. Res. 30 (7) (1997) 290–296.

[5] B. Meunier, S.P. Visser, S. Shaik, Mechanism of oxidation reactions catalyzed by cytochrome P450 enzymes, Chem. Rev. 104 (2004) 3947–3980.

[6] I. Hubatsch, M. Ridderstrom, B. Mannervik, Human glutathione transferase A4-4: an alpha class enzyme with high catalytic efficiency in the conjugation of 4-hydroxynonenal and other genotoxic products of lipid peroxidation, Biochem. J. 330 (1998) 175–179.

[7] L.H. Posorske, Industrial-scale application of enzymes to the fats and oil industry, J. Am. Oil Chem. Soc. 61 (11) (1984) 1758–1760.
[8] M. Choct, Enzymes for the feed industry : past, present and future, Worlds Poult. Sci. J. 62 (1) (2006) 5–16.
[9] N. Gurung, S. Ray, S. Bose, V. Rai, Broader view : microbial enzymes and their relevance in industries, medicine, and beyond, Biomed. Res. Int. (2013) 329121.
[10] H. Wei, E. Wang, Nanomaterials with enzyme-like characteristics (nanozymes): next-generation artificial enzymes, Chem. Soc. Rev. 42 (2012) 6060–6093.
[11] A.J. Kirby, Enzyme mimics, Angew. Chem. Int. Ed. 33 (5) (1994) 551–553.
[12] R. Breslow, Biomimetic chemistry and artificial enzymes: catalysis by design, Acc. Chem. Res. 28 (3) (1995) 146–153.
[13] B.V. Romanovsky, Transition metal complexes in inorganic polymers as enzyme, Macromol. Symp. 80 (1994) 185–192.
[14] H.L. Anderson, J.K.M. Sanders, Enzyme mimics based on cyclic porphyrin oligomers: strategy, design and exploratory synthesis, Perkin Trans. 1 (1995) 2223–2229.
[15] R. Kataky, E. Morgan, Potential of enzyme mimics in biomimetic sensors : a modified-cyclodextrin as a dehydrogenase enzyme mimic, Biosens. Bioelectron. 18 (2003) 1407–1417.
[16] S.S. Ali, J.I. Hardt, K.L. Quick, J.S. Kim-Han, B.F. Erlanger, T. Huang, C.J. Epstein, L.L. Dugan, Abiologically effective Fullerene (C60) derivative with superoxide dismutase mimetic properties, Free Radic, Biol. Med. 37 (8) (2004) 1191–1202.
[17] D. Astruc, L. Liang, A. Rapakousiou, J. Ruiz, Click dendrimers and triazole-related aspects: catalysts, mechanism, synthesis, and functions. A bridge between dendritic architectures and nanomaterials, Acc. Chem. Res. 45 (4) (2012) 630–640.
[18] K. Kirkorian, A. Ellis, L.J. Twyman, Catalytic hyperbranched polymers as enzyme mimics ; exploiting the principles of encapsulation and supramolecular chemistry, Chem. Soc. Rev. 41 (2012) 6138–6159.
[19] L. Gong, Z. Zhao, Y.F. Lv, S.Y. Huan, T. Fu, X.B. Zhang, G.L. Shen, R.Q. Yu, DNAzyme-based biosensors and nanodevices, Chem. Commun. 51 (2015) 979–995.
[20] L. Gao, J. Zhuang, L. Nie, J. Zhang, Y. Zhang, N. Gu, T. Wang, J. Feng, D. Yang, S. Perrett, X. Yan, Intrinsic peroxidase-like activity of ferromagnetic nanoparticles, Nat. Nanotechnol. (2007) 577–583.
[21] Y. Lin, J. Ren, X. Qu, Catalytically active nanomaterials : a promising candidate for artificial enzymes, Acc. Chem. Res. 47 (4) (2014) 1097–1105.
[22] R. Ragg, M.N. Tahir, W. Tremel, Solids go bio: inorganic nanoparticles as enzyme mimics, Eur. J. Inorg. Chem. (2016) 1906–1915.
[23] H. Wang, K. Wan, X. Shi, Recent advances in nanozyme research, Adv. Mater. 1805368 (2019) 1–10.
[24] A. Asati, S. Santra, C. Kaittanis, S. Nath, J.M. Perez, Oxidase-like activity of polymer-coated cerium oxide, Angew. Chem. Int. Ed. 48 (13) (2009) 2308–2312.
[25] X. Zheng, Q. Liu, C. Jing, Y. Li, D. Li, W. Luo, Y. Wen, Y. He, Q. Huang, Y.T. Long, C. Fan, Catalytic gold nanoparticles for nanoplasmonic detection of DNA, Angew. Chem. Int. Ed. 50 (50) (2011) 11994–11998.
[26] F. Natalio, R. André, A.F. Hartog, B. Stoll, K.P. Jochum, R. Wever, W. Tremel, Vanadium pentoxide nanoparticles mimic vanadium haloperoxidases and thwart biofilm formation, Nat. Nanotechnol. 7 (2012) 3–8.
[27] R. Ragg, F. Natalio, M.N. Tahir, H. Janssen, A. Kashyap, D. Strand, S. Strand, W. Tremel, Molybdenum trioxide nanoparticles with intrinsic Sulfite oxidase activity, ACS Nano 5 (2014) 5182–5189.

[28] H. Sun, N. Gao, K. Dong, J. Ren, X. Qu, Graphene quantum dots-band-aids used for wound disinfection, ACS Nano 6 (2014) 6202–6210.

[29] A.A. Vernekar, D. Sinha, S. Srivastava, P.U. Paramasivam, P. D'Silva, G. Mugesh, An antioxidant nanozyme that uncovers the cytoprotective potential of vanadia nanowires, Nat. Commun. 5 (2014) 5301.

[30] F. Pogacean, C. Socaci, S. Pruneanu, A.R. Biris, M. Coros, L. Magerusan, G. Katona, R. Turcu, G. Borodi, Chemical graphene based nanomaterials as chemical sensors for hydrogen peroxide—a comparison study of their intrinsic peroxidase catalytic behavior, Sens. Actuators B Chem. 213 (2015) 474–483.

[31] W. Zhang, S. Hu, J.J. Yin, W. He, W. Lu, M. Ma, N. Gu, Y. Zhang, Prussian blue nanoparticles as multienzyme mimetics and reactive oxygen species scavengers, J. Am. Chem. Soc. 138 (2016) 5860−5865.

[32] B. Liu, J. Liu, Surface modification of nanozymes, Nano Res. 10 (4) (2017) 1125–1148.

[33] E.A.J. Bleeker, W.H. de Jong, R.E. Geertsma, M. Groenewold, E.H.W. Heugens, M. Koers-Jacquemijns, D. Meent, J.R. Popma, A.G. Rietveld, S.W.P. Wijnhoven, F.R. Cassee, A.G. Oomen, Considerations on the EU definition of a nanomaterial: science to support policy making, Regul. Toxicol. Pharmacol. 65 (2013) 119–125.

[34] Y. Zhou, B. Liu, R. Yang, J. Liu, Filling in the gaps between nanozymes and enzymes: challenges and opportunities, Bioconjugate Chem. 28 (2017) 2903−2909.

[35] H. Qiu, F. Pu, X. Ran, C. Liu, J. Ren, X. Qu, Nanozyme as artificial receptor with multiple readouts for pattern recognition, Anal. Chem. 90 (20) (2018) 11775–11779.

[36] L. Tian, J. Qi, O. Oderinde, C. Yao, W. Song, Y. Wang, Planar intercalated Copper (II) complex molecule as small molecule enzyme mimic combined with Fe3O4 nanozyme for bienzyme synergistic catalysis applied to the microRNA biosensor, Biosens. Bioelectron. 110 (2018) 110–117.

[37] Z. Chen, Z. Wang, J. Ren, X. Qu, Enzyme mimicry for combating bacteria and biofilms, Acc. Chem. Res. 51 (3) (2018) 789–799.

[38] J. Niu, Y. Sun, F. Wang, C. Zhao, J. Ren, X. Qu, Photo-modulated nanozyme used for gram-selective antimicrobial, Chem. Mater. 30 (20) (2018) 7027–7033.

[39] Y. Huang, X. Ran, Y. Lin, J. Ren, X. Qu, Self-assembly of an organic–inorganic hybrid nanoflower as an efficient biomimetic catalyst for self-activated tandem reactions, Chem. Commun. 51 (2015) 4386–4389.

[40] L. Gao, X. Yan, Nanozymes: an emerging field bridging nanotechnology and biology, Acc. Chem. Res. 51 (2018) 789−799.

[41] E.V. Batrakova, S. Li, A.D. Reynolds, R.L. Mosley, T.K. Bronich, A.V. Kabanov, H.E. Gendelman, A macrophage - nanozyme delivery system for Parkinson's disease, Bioconjugate Chem. 18 (2007) 1498–1506.

[42] A.L. Popov, N.R. Popova, N.V. Tarakina, O.S. Ivanova, A.M. Ermakov, V.K. Ivanov, G.B. Sukhorukov, Intracellular delivery of antioxidant CeO2 nanoparticles via polyelectrolyte microcapsules, ACS Biomater. Sci. Eng. 4 (2018) 2453–2462.

[43] M. Liang, K. Fan, Y. Pan, H. Jiang, F. Wang, D. Yang, D. Lu, J. Feng, J. Zhao, L. Yang, X. Yan, Fe_3O_4 magnetic nanoparticle peroxidase mimetic-based colorimetric assay for the rapid detection of organophosphorus pesticide and nerve agent, Anal. Chem. 85 (1) (2013) 308–312.

[44] Y. Hu, H. Cheng, X. Zhao, J. Wu, F. Muhammad, S. Lin, J. He, L. Zhou, C. Zhang, Y. Deng, P. Wang, Z. Zhou, S. Nie, H. Wei, Surface-enhanced raman scattering active gold nanoparticles with enzyme-mimicking activities for measuring glucose and lactate in living tissues, ACS Nano 11 (6) (2017) 5558–5566.

[45] W. Luo, C. Zhu, S. Su, D. Li, Y. He, Q. Huang, C. Fan, Self-catalyzed, self-limiting growth of glucose oxidase-mimicking gold nanoparticles, ACS Nano 4 (12) (2010) 7451–7458.
[46] Y. Zhang, F. Wang, C. Liu, Z. Wang, L. Kang, Y. Huang, K. Dong, J. Ren, X. Qu, Nanozymes decorated metal-organic frameworks for enhanced photodynamic therapy, ACS Nano 12 (1) (2018) 651–661.
[47] J. Fan, J.J. Yin, B. Ning, X. Wu, Y. Hu, M. Ferrari, G.J. Anderson, J. Wei, Y. Zhao, G. Nie, Direct evidence for catalase and peroxidase activities of ferritin platinum nanoparticles, Biomaterials 32 (2011) 1611–1618.
[48] C. Ge, G. Fang, X. Shen, Y. Chong, W.G. Wamer, X. Gao, Z. Chai, C. Chen, J.J. Yin, Facet energy versus enzyme-like activities: the unexpected protection of palladium nanocrystals against oxidative damage, ACS Nano 10 (11) (2016) 10436–10445.
[49] C.K. Kim, T. Kim, I.Y. Choi, M. Soh, D. Kim, Y.J. Kim, H. Jang, H.S. Yang, J.Y. Kim, H.K. Park, S.P. Park, S. Park, T. Yu, B.W. Yoon, S.H. Lee, T. Hyeon, Ceria nanoparticles that can protect against ischemic stroke, Angew. Chem. Int. Ed. 51 (44) (2012) 11039–11043.
[50] Y. Li, X. He, J.J. Yin, Y. Ma, P. Zhang, J. Li, Y. Ding, J. Zhang, Y. Zhao, Z. Chai, Z. Zhang, Acquired superoxide-scavenging ability of ceria nanoparticles, Angew. Chem. Int. Ed. 54 (6) (2015) 1832–1835.
[51] Y. Lin, Z. Li, Z. Chen, J. Ren, X. Qu, Mesoporous silica-encapsulated gold nanoparticles as artificial enzymes for self-activated cascade catalysis, Biomaterials 34 (11) (2013) 2600–2610.
[52] A.J. Wilson, Supramolecular chemistry, Annu. Rep. Prog. Chem., Sect. B: Org. Chem. 104 (2008) 164–183.
[53] F. Biedermann, H.J. Schneider, Experimental binding energies in supramolecular complexes, Chem. Rev. 116 (9) (2016) 5216–5300.
[54] E. Fischer, Influence of configuration on the action of enzymes, J. Am. Chem. Soc. 3 (1894) 2985–2993.
[55] G.R. Desiraju, The all-chemist Linus Pauling set the agenda for a century of chemical research, Nature 408 (2000) 2000.
[56] J.M. Lehn, From supramolecular chemistry towards constitutional dynamic chemistry and adaptive chemistry, Chem. Soc. Rev. 36 (2) (2007) 151–160.
[57] G.V. Oshovsky, D.N. Reinhoudt, W. Verboom, Supramolecular chemistry in water, Angew Chem. Int. Ed. 46 (14) (2007) 2366–2393.
[58] J.M. Lehn, Towards complex matter: supramolecular chemistry and self-organization, Eur. Rev. 17 (2) (2009) 263–280.
[59] M. Eigen, Selforganization of matter and the evolution of biological macromolecules, Naturwissenschaften 58 (10) (1971) 465–523.
[60] Z.J. Wang, K.N. Clary, R.G. Bergman, K.N. Raymond, F.D. Toste, A supramolecular approach to combining enzymatic and transition metal catalysis, Nat. Chem. 5 (2) (2013) 100–103.
[61] J. Meeuwissen, J.N.H. Reek, Supramolecular catalysis beyond enzyme mimics, Nat. Chem. 2 (8) (2010) 615–621.
[62] S. Leininger, B. Olenyuk, P.J. Stang, Self-assembly of discrete cyclic nanostructures mediated by transition metals, Chem. Rev. 100 (3) (2000) 853–907.
[63] S.R. Seidel, P.J. Stang, High-symmetry coordination cages via self-assembly, Acc. Chem. Res. 35 (11) (2002) 972–983.

[64] C.L. Chen, J.Y. Zhang, C.Y. Su, Coordination assemblies of metallacyclic, prismatic and tubular molecular architectures based on the non-rigid ligands, Eur. J. Inorg. Chem. 19 (2007) 2997–3010.
[65] R.W. Saalfrank, H. Maid, A. Scheurer, Supramolecular coordination chemistry: the synergistic effect of serendipity and rational design, Angew Chem. Int. Ed. 47 (46) (2008) 8794–8824.
[66] M. Yoshizawa, J.K. Klosterman, M. Fujita M, Functional molecular flasks: new properties and reactions within discrete, self-assembled hosts, Angew Chem. Int. Ed. 48 (19) (2009) 3418–3438.
[67] M.J. Wiester, P.A. Ulmann, C.A. Mirkin, Enzyme mimics based upon supramolecular coordination chemistry, Angew. Chem. Int. Ed. 50 (1) (2011) 114–137.
[68] L. Pauling, Nature of forces between large molecules of biological interest, Nature 161 (4097) (1948) 707–709.
[69] I. Tabushi, N. Shimizu, T. Sugimoto, M. Shiozuka, K. Yamamura, Cyclodextrin flexibly capped with metal ion, J. Am. Chem. Soc. 99 (21) (1977) 7100–7102.
[70] I. Tabushi, Cyclodextrin catalysis as a model for enzyme action, Acc. Chem. Res. 15 (3) (1982) 66–72.
[71] I. Tabushi, Design and synthesis of artificial enzymes, Tetrahedron 40 (2) (1984) 269–292.
[72] M. Ranocchiari, J.A.V. Bokhoven, Catalysis by metal-organic frameworks: fundamentals and opportunities, Phys. Chem. Chem. Phys. 13 (14) (2011) 6388–6396.
[73] Z. Wang, G. Chen, K. Ding, Self-supported catalysts, Chem. Rev. 109 (2) (2009) 322–359.
[74] J.J. Perry, J.A. Perman, M.J. Zaworotko, Design and synthesis of metal–organic frameworks using metal–organic polyhedra as supermolecular building blocks, Chem. Soc. Rev. 38 (5) (2009) 1400–1417.
[75] Q. Zhang, J. Zhang, Q.Y. Yu, M. Pan, C.Y. Su, Ring-opening isomerization based on the 3-connecting node: Formation of a 0-D M2L3 cage, 1-D loop-and-chain, and 2-D (6, 3) network, Cryst. Growth Des. 10 (9) (2010) 4076–4084.
[76] J. Liu, L. Chen, H. Cui, J. Zhang, L. Zhang, C.Y. Su, Applications of metal-organic frameworks in heterogeneous supramolecular catalysis, Chem. Soc. Rev. 43 (16) (2014) 6011–6061.
[77] L. Ma, C. Abney, W. Lin, Enantioselective catalysis with homochiral metal-organic frameworks, Chem. Soc. Rev. 38 (5) (2009) 1248–1256.
[78] J. Lee, O.K. Farha, J. Roberts, K.A. Scheidt, S.T. Nguyen, J.T. Hupp, Metal-organic framework materials as catalysts, Chem. Soc. Rev. 38 (5) (2009) 1450–1459.
[80] M. Yoon, R. Srirambalaji R, K. Kim, Homochiral metal-organic frameworks for asymmetric heterogeneous catalysis, Chem. Rev. 112 (2012) 1196–1231.
[81] T.R. Cook, Y.R. Zheng, P.J. Stang, Metal-organic frameworks and self-assembled supramolecular coordination complexes: Comparing and contrasting the design, synthesis, and functionality of metal-organic materials, Chem. Rev. 113 (1) (2013) 734–777.
[82] K.G. Welinder, Covalent structure of the glycoprotein horseradish peroxidase (EC 1.11.1.7), FEBS Lett. 72 (1) (1976) 19–23.
[83] B.Y. Yang, J.S.S. Gray, R. Montgomery, The glycans of horseradish peroxidase, Carbohydr. Res. 287 (2) (1996) 203–212.
[84] R.H. Haschke, J.M. Friedhoff, Calcium-related properties of horseradish peroxidase, Biochem. Biophys. Res. Commun. 80 (4) (1978) 1039–1042.
[85] N.C. Veitch, A.T. Smith, Horseradish peroxidase C, Adv. Inorg. Chem. 51 (2000) 107–162.

[86] H. Setälä, A. Pajunen, P. Rummakko, J. Sipilä, G. Brunow, A novel type of spiro compound formed by oxifiative cross coupling of methyl sinapate with a syringyl lignin model compound. A model system for the β-1 pathway in lignin biosynthesis, J. Chem. Soc. - Perkin Trans. 1. (1999) 461–464.

[87] M. Sottomayor, M.L. Serrano, F. Dicosmo, A.R. Barceló, Purification and characterization of α-3',4'-anhydrovinblastine synthase (peroxidase-like) from Catharanthus roseus (L.) G. Don, FEBS Lett. 42 (3) (1998) 299–303.

[88] M. Sottomayor, F. Dicosmo, A.R. Barceló, On the fate of catharanthine and vindoline during the peroxidase-mediated enzymatic synthesis of α-3',4'-anhydrovinblastine, Enzyme Microb. Technol. 21 (7) (1997) 543–549.

[89] K. Kuśmierek, G. Chwatko, R. Głowacki, P. Kubalczyk, E. Bald, Ultraviolet derivatization of low-molecular-mass thiols for high performance liquid chromatography and capillary electrophoresis analysis, J. Chromatogr. B 879 (17–18) (2011) 1290–1307.

[90] K. Kuśmierek, G. Chwatko, R. Głowacki, E. Bald, Determination of endogenous thiols and thiol drugs in urine by HPLC with ultraviolet detection, J. Chromatogr. B 877 (28) (2009) 3300–3308.

[91] A. Zinellu, A. Lepedda, S. Sotgia, E. Zinellu, G. Marongiu, M.F. Usai, L. Gaspa, P.D. Muro, M. Formato, L. Deiana, C. Carru, Albumin-bound low molecular weight thiols analysis in plasma and carotid plaques by CE, J. Sep. Sci. 33 (1) (2010) 126–131.

[92] Y. Chen, H. Dong, D.C. Thompson, H.G. Shertzer, D.W. Nebert, V. Vasiliou, Glutathione defense mechanism in liver injury: insights from animal models, Food Chem. Toxicol. 60 (2013) 38–44.

[93] D.M. Townsend, K.D. Tew, H. Tapiero, Sulfur containing amino acids and human disease, Biomed. Pharmacother. 58 (1) (2004) 47–55.

[94] L. Kennedy, J.K. Sandhu, M.E. Harper, M. Cuperlovic-Culf, Role of glutathione in cancer: from mechanisms to therapies, Biomolecules 10 (10) (2020) 1429.

[95] S. Shahrokhian, Lead phthalocyanine as a selective carrier for preparation of a cysteine-selective electrode, Anal. Chem. 73 (24) (2001) 5972–5978.

[96] S. Seshadri, A. Beiser, P.F.J J.Selhub, I.H. Rosenberg, R.B.D. Agostino, P.W.F. Wilson, P.A. Wolf, Plasma homocysteine as a risk factor for dementia and Alzheimer's disease, N. Eng. J. Med. 346 (7) (2002) 476–483.

[97] Z. Jiang, Y. Liu, X. Hu, Y. Li, Colorimetric determination of thiol compounds in serum based on Fe-MIL-88NH2 metal-organic framework as peroxidase mimetics, Anal. Methods 6 (15) (2014) 5647–5651.

[98] Y. Xiong, S. Chen, F. Ye, L. Su, C. Zhang, S. Shen, S. Zhao, Synthesis of a mixed valence state Ce-MOF as an oxidase mimetic for the colorimetric detection of biothiols, Chem. Commun. 51 (2015) 4635–4638.

[99] Z. Hu, X. Jiang, F. Xu, J. Jia, Z. LongX, X. Hou, Colorimetric sensing of bithiols using photocatalytic UiO-66(NH_2) as H_2O_2-free peroxidase mimics, Talanta 158 (2016) 276–282.

[100] L. Wang, Y. Ling, L. Han, J. Zhou, Z. Sun, N. Bing, L. Hong, Q. Luo, Catalase active metal-organic framework synthesized by ligand regulation for the dual detection of glucose and cysteine, Anal. Chim. Acta 1131 (2020) 118–125.

[101] C. Probes, W. Wu, T. Zhou, A. Berliner, P. Banerjee, S. Zhou, Glucose-mediated assembly of phenylboronic acid modified CdTe /ZnTe / ZnS quantum dots for intracellular glucose probing, Angew. Chem. Int. Ed. 49 (2010) 6554–6558.

[102] A. Pandey, P. Tripathi, R. Pandey, R. Srivatava, Alternative therapies useful in the management of diabetes : a systematic review, J. Pharm. BioAllied Sci. 3 (4) (2011) 504–513.

[103] P. Zimmet, K.G.M.M. Alberti, J. Shaw, Global and societal implications of the diabetes epidemic, Nature 414 (2010) 782–787.

[104] X. Liu, W. Qi, Y. Wang, D. Lin, X. Yang, R. Su, Z. He, Rational design of mimic multi-enzyme systems in hierarchically porous biomimetic metal- organic frameworks, ACS Appl. Mater. Interfaces 10 (39) (2018) 33407–33415.

[105] W. Tan, T. Wei, J. Huo, M. Loubidi, T. Liu, Y. Liang, L. Deng, Electrostatic interaction-induced formation of enzyme-on-MOF as chemo-biocatalyst for cascade reaction with unexpectedly acid-stable catalytic performance, ACS Appl. Mater. Interfaces 11 (40) (2019) 36782–36788.

[106] J. Park, Q. Jiang, D. Feng, L. Mao, H.C. Zhou, Size-controlled synthesis of porphyrinic metal-organic framework and functionalization for targeted photodynamic therapy, J. Am. Chem. Soc. 138 (10) (2016) 3518–35125.

[107] T. Li, P. Hu, J. Li, P. Huang, W. Tong, C. Gao, Enhanced peroxidase-like activity of Fe@PCN-224 nanoparticles and their applications for detection of H_2O_2 and glucose, Colloids Surf. A Physicochem. Eng. Asp. 577 (2019) 456–463.

[108] H. Zheng, C. Liu, X. Zeng, J. Chen, J. Lu, R.G. Lin, R. Cao, Z.J. Lin, J.W. Su, MOF-808: a metal—organic framework with intrinsic peroxidase- like catalytic activity at neutral ph for colorimetric biosensing, Inorg. Chem. 57 (2018) 9096–9104.

[109] M. Aghayan, A. Mahmoudi, S. Sohrabi, S. Dehghanpour, K. Nazari, N.M. Tabrizi, Micellar catalysis of an iron(III)-MOF: enhanced biosensing characteristic, Anal. Methods 11 (2019) 3175–3187.

[110] Y. Wang, M. Zhao, J. Ping, B. Chen, X. Cao, Y. Huang, C. Tan, Q. Ma, S. Wu, Y. Yu, Q. Lu, J. Chen, W. Zhao, Y. Ying, H. Zhang, Bioinspired design of ultrathin 2D bimetallic metal—organic-framework nanosheets used as biomimetic enzymes, J. Adv. Mater. 28 (2016) 4149–4155.

[111] Y. Huang, M. Zhao, S. Han, Z. Lai, J. Yang, C. Tan, Q. Ma, Q. Lu, J. Chen, X. Zhang, Z. Zhang, B. Li, B. Chen, Y. Zong, H. Zhang, Growth of Au nanoparticles on 2D metallo-porphyrinic metal-organic framework nanosheets used as biomimetic catalysts for cascade reactions, J. Adv. Mater. 29 (32) (2017) 1–5.

[112] S. Hu, Y. Jiang, Y. Wu, X. Guo, Y. Ying, Y. Wen, H. Yang, Enzyme-free tandem reaction strategy for surface-enhanced raman scattering detection of glucose by using the composite of Au nanoparticles and porphyrin-based metal-organic framework, ACS Appl. Mater. Interfaces 12 (49) (2020) 55324–55330.

[113] H. Chen, Q. Qiu, S. Sharif, S. Ying, Y. Wang, Y. Ying, Solution-phase synthesis of platinum nanoparticle-decorated metal-organic framework hybrid nanomaterials as biomimetic nanoenzymes for biosensing applications, ACS Appl. Mater. Interfaces 10 (28) (2018) 24108–24115.

[114] Y. Zhong, L. Yu, Q. He, Q. Zhu, C. Zhang, X. Cui, J. Zheng, S. Zhao, Bifunctional hybrid enzyme-catalytic metal organic framework reactors for α-glucosidase inhibitor screening, ACS Appl. Mater. Interfaces 11 (2019) 32769–32777.

[115] A. Kondo, H. Kajiro, H. Noguchi, L. Carlucci, D.M. Proserpio, G. Ciani, K. Kato, M. Takata, H. Seki, M. Sakamoto, Y. Hattori, F. Okino, K. Maeda, T. Ohba, K. Kaneko, H. Kanoh, Super flexibility of a 2D Cu-based porous coordination framework on gas adsorption in comparison with a 3D framework of identical composition : framework dimensionality-dependent gas adsorptivities, J. Am. Chem. Soc. 133 (2011) 10512–10522.

[116] M. Xu, S. Yuan, X.Y. Chen, Y.J. Chang, G. Day, Z.Y. Gu, H.C. Zhou, Two-dimensional metal−organic framework nanosheets as an enzyme inhibitor: modulation of the α–chymotrypsin activity, J. Am. Chem. Soc. 139 (2017) 8312–8319.

[117] M. Shi, M. Xu, Z. Gu, Copper-based two-dimensional metal-organic framework nanosheets as horseradish peroxidase mimics for glucose fluorescence sensing, Anal. Chim. Acta 1079 (2019) 164–170.

[118] J. He, H. Yang, Y. Zhang, J. Yu, L. Miao, Y. Song, L. Wang, Smart nanocomposites of Cu-hemin metal-organic frameworks for electrochemical glucose biosensing, Sci. Rep. 6 (2016) 36637.

[119] C. Lin, Y. Du, S. Wang, L. Wang, Y. Song, Glucose oxidase@Cu-hemin metal-organic framework for colorimetric analysis of glucose, Mater. Sci. Eng. C 118 (2021) 111511.

[120] X. Cheng, Z. Zheng, X. Zhou, Q. Kuang, Metal−organic framework as a compartmentalized integrated nanozyme reactor to enable high-performance cascade reactions for glucose detection, ACS Sustain. Chem. Eng. 8 (48) (2020) 17783–17790.

[121] N. Bagheri, M. Dastborhan, A. Khataee, J. Hassanzadeh, M. Kobya, Synthesis of g-C3N4 @ CuMOFs nanocomposite with superior peroxidase mimetic activity for the fluorometric measurement of glucose, Spectrochim. Acta Part A Mol. Biomol. Spectrosc. 213 (2019) 28–36.

[122] Y. Song, D. Cho, S. Venkateswarlu, M. Yoon, Systematic study on preparation of copper nanoparticle embedded porous carbon by carbonization of metal – organic framework for enzymatic glucose sensor, RSC Adv. 7 (2017) 10592–10600.

[123] S.S. Menon, S.V. Chandran, A. Koyappayil, S. Berchmans, Copper-based metal-organic frameworks as peroxidase mimics leading to sensitive H_2O_2 and glucose detection, ChemistrySelect 3 (2018) 8319–83124.

[124] W. Li, Y. Zhang, C. Zhang, Q. Meng, Z. Xu, P. Su, Q. Li, C. Shen, Z. Fan, L. Qin, G. Zhang, Transformation of metal-organic frameworks for molecular sieving membranes, Nat. Commun. 7 (2016) 1–9.

[125] P. Horcajada, S. Surble, C. Serre, D.Y. Hong, Y.K. Seo, J.S. Chang, J.M. Greneche, I. Margiolaki, G. Ferey, Synthesis and catalytic properties of MIL-100 (Fe), an iron (III) carboxylate with large pores, J. Am. Chem. Soc. 100 (2007) 2820–2822.

[126] A. Yuan, Y. Lu, X. Zhang, Q. Chen, Y. Huang, Two-dimensional iron MOF nanosheet as a highly efficient nanozyme for glucose biosensing, J. Mater. Chem. B 8 (40) (2020) 9295–9303.

127 Y.L. Liu, X.J. Zhao, X.X. Yang, Y.F. Li, A nanosized metal–organic framework of Fe-MIL-88NH2 as a novel peroxidase mimic used for colorimetric detection of glucose, Analyst 138 (2013) 4526–4531.

[128] W. Xu, L. Jiao, H. Yan, Y. Wu, L. Chen, W. Gu, D. Du, Y. Lin, C. Zhu, Glucose oxidase-integrated metal—organic framework hybrids as biomimetic cascade nanozymes for ultrasensitive glucose biosensing, ACS Appl. Mater. Interfaces 11 (2019) 22096–22101.

[129] Z. Zhao, J. Pang, W. Liu, T. Lin, F. Ye, A bifunctional metal organic framework of type Fe (III) -BTC for cascade (enzymatic and enzyme-mimicking) colorimetric determination of glucose, Microchim. Acta 186 (2019) 295.

[130] Z. Zhao, Y. Huang, W. Liu, F. Ye, S. Zhao, Immobilized glucose oxidase on boronic acid-functionalized hierarchically porous MOF as an integrated nanozyme for one-step glucose detection, ACS Sustain. Chem. Eng. 8 (11) (2020) 4481−4488.

[131] X. Zhong, H. Xia, W. Huang, Z. Li, Y. Jiang, Biomimetic metal-organic frameworks mediated hybrid multi-enzyme mimic for tandem catalysis, Chem. Eng. J. 381 (2020) 122758.

[132] F.X. Qin, S.Y. Jia, F.F. Wang, S.H. Wu, J. Song, Y. Liu, Hemin@metal-organic framework with peroxidase-like activity and its application to glucose detection, Catal. Sci .Technol. 3 (2013) 2761–2768.

[133] N. Zhu, L. Gu, J. Wang, X. Li, G. Liang, J. Zhou, Z. Zhang, Novel and sensitive chemiluminescence sensors based on 2D-MOF nanosheets for one-step detection of glucose in human urine, J. Phys. Chem. C 123 (14) (2019) 9388–9393.

[134] Z. Lin, J. Lin, Peroxide induced ultra-weak chemiluminescence and its application in analytical chemistry, Analyst 138 (5) (2013) 182–5193.

[135] C. Zhao, H. Cui, J. Duan, S. Zhang, J. Lv J, Self-catalyzing chemiluminescence of luminol-diazonium ion and its application for catalyst-free hydrogen peroxide detection and rat arthritis imaging, Anal. Chem. 90 (3) (2018) 2201–2209.

[136] I.F. Hodgson, The role of O_2 - in the chemiluminescence of luminol, Photochem. Photobiol. 18 (1973) 451–455.

[137] D. Li, S. Zhang, X. Feng, H. Yang, F. Nie, W. Zhang, A novel peroxidase mimetic Co-MOF enhanced luminol chemiluminescence and its application in glucose sensing, Sens. Actuators B Chem. 296 (2019) 126631.

[138] J. Wang, M. Bao, T. Wei, Z. Wang, Z. Dai, Bimetallic metal–organic framework for enzyme immobilization by biomimetic mineralization: constructing a mimic enzyme and simultaneously immobilizing natural enzymes, Anal. Chim. Acta 1098 (2020) 148–154.

[139] L. Ai, L. Li, C. Zhang, J. Fu, J. Jiang, MIL-53 (Fe): a metal – organic framework with intrinsic peroxidase-like catalytic activity for colorimetric biosensing, Chem. Eur. J. 19 (2013) 15105–15108.

[140] A. Fateeva, P. Horcajada, T. Devic, C. Serre, J. Marrot, J.M. Grenèche, M. Morcrette, J.M. Tarascon, G. Maurin, G. Férey, Synthesis, structure, characterization, and redox properties of the porous MIL-68(Fe) solid, Eur. J. Inorg. Chem. 2010 (2010) 3789–3794.

[141] J.W. Zhang, H.T. Zhang, Z.Y. Du, X. Wang, S.H. Yu, H.L. Jiang, Water-stable metal–organic frameworks with intrinsic peroxidase-like catalytic activity as a colorimetric biosensing platform, Chem. Commun. 50 (2014) 1092–1094.

[142] L. Luo, L. Huang, X. Liu, W. Zhang, X. Yao, L. Dou, X. Zhang, Y. Nian, J. Sun, J. Wang, Mixed-valence Ce-BPyDC metal-organic framework with dual enzyme-like activities for colorimetric biosensing, Inorg. Chem. 58 (17) (2019) 11382–11388.

[143] L. Wang, H. Yang, J. He, Y. Zhang, J. Yu, Y. Song, Cu-hemin metal-organic-frameworks/chitosan-reduced graphene oxide nanocomposites with peroxidase-like bioactivity for electrochemical sensing, Electrochim. Acta 213 (2016) 691–697.

[144] P. Gao, Y. Feng, M. Wang, N. Jiang, W. Qi, R. Su, Z. He, Ferrocene—modified metal—organic frameworks as a peroxidase—mimicking catalyst, Catal. Lett. 151 (2021) 478–486.

[145] Y. Chen, W. Huang, C. Wang, X. Zhai, T. Zhang, Y. Wang, X. Hu, Direct growth of polyglutamic acid film on peroxidase mimicking PCN-222(Mn) for constructing a novel sensitive nonenzymatic electrochemical hydrogen peroxide biosensor, ACS Sustain. Chem. Eng. 8 (35) (2020) 13226–13235.

[146] B. Thakur, V.V. Karve, D.T. Sun, A.L. Semrau, L.J.K. Weiß, L. Grob, R.A. Fischer, W.L. Queen, B. Wolfrum, An investigation into the intrinsic peroxidase-like activity of Fe-MOFs and Fe-MOFs/polymer composites, Adv. Mater. Technol. 6 (2021) 2001048.

[147] F. Xie, X. Ma, W. Liu, Y. Wang, H. Dong, T. Mi, An unprecedented molybdenum oxide based helical MOF with peroxidase-like activity synthesized by surfactant-thermal method, Inorg. Chem. Commun. 97 (2018) 93–97.

[148] J. Chen, Y. Shu, H. Li, Q. Xu, X. Hu, Nickel metal-organic framework 2D nanosheets with enhanced peroxidase nanozyme activity for colorimetric detection of H_2O_2, Talanta 189 (2018) 254–261.

[149] K.M.L. Taylor-Pashow, J.D. Rocca, Z. Xie, S. Tran, W. Lin, Postsynthetic modifications of iron-carboxylate nanoscale metal - organic frameworks for imaging and drug delivery, J. Am. Chem. Soc. 131 (40) (2009) 14261–14263.

[150] F. Cui, Q. Deng, L. Sun, Prussian blue modified metal–organic framework MIL-101(Fe) with intrinsic peroxidase-like catalytic activity as a colorimetric biosensing platform, RSC Adv. 5 (2015) 98215–98221.

[151] X. Qi, H. Tian, X. Dang, Y. Fan, Y. Zhang, H. Zhao, A bimetallic Co/Mn metal-organic-framework with a synergistic catalytic effect as peroxidase for the colorimetric detection of H_2O_2, Anal. Methods 11 (2019) 1111–1124.

[152] Z. Qi, L. Wang, Q. You, Y. Chen, PA-Tb-Cu MOF as luminescent nanoenzyme for catalytic assay of hydrogen peroxide, Biosens. Bioelectron. 96 (2017) 227–232.

[153] L. Yang, C. Xu, W. Ye, W. Liu, An electrochemical sensor for H_2O_2 based on a new Co-metal-organic framework modified electrode, Sen. Actuators B Chem. 215 (2015) 489–496.

[154] J. Wang, Y. Hu, Q. Zhou, L. Hu, W. Fu, Y. Wang, Peroxidase-like activity of metal−organic framework [Cu(PDA)(DMF)] and its application for colorimetric detection of dopamine, ACS Appl. Mater. Interfaces 11 (2019) 44466–44473.

[155] A. Badoei-dalfard, N. Sohrabi, Z. Karami, G. Sargazi, Fabrication of an efficient and sensitive colorimetric biosensor based on Uricase /Th-MOF for uric acid sensing in biological samples, Biosens. Bioelectron. 141 (2019) 111420.

[156] S. Reza, H. Jangi, M. Akhond, Synthesis and characterization of a novel metal-organic framework called nanosized electroactive quasi-coral-340 (NEQC-340) and its application for constructing a reusable nanozyme-based sensor for selective and sensitive glutathione quantification, Microchem. J. 158 (1) (2020) 105328.

[157] C. Zhang, D. Zhang, Z. Ma, H. Han, Cascade catalysis-initiated radical polymerization amplified impedimetric immunosensor for ultrasensitive detection of carbohydrate antigen 15-3, Biosens. Bioelectron. 137 (2019) 1–7.

[158] C. Song, W. Ding, H. Liu, W. Zhao, Y. Yao, C. Yao, Label-free colorimetric detection of deoxyribonuclease I activity based on DNA-enhanced peroxidase-like activity of MIL-53(Fe), New J. Chem. 43 (2019) 12776–12784.

[159] L. Wang, Y. Chen, Luminescence-sensing Tb-MOF nanozyme for the detection and degradation of estrogen endocrine disruptors, ACS Appl. Mater. Interfaces 12 (7) (2020) 8351–8358.

[160] H. Cheng, Y. Liu, Y. Hu, Y. Ding, S. Lin, W. Cao, Q. Wang, J. Wu, F. Muhammad, X. Zhao, D. Zhao, Z. Li, H. Xing, H. Wei, Monitoring of heparin activity in live rats using metal-organic framework nanosheets as peroxidase mimics monitoring of heparin activity in live rats using metal-organic framework nanosheets as peroxidase mimics, Anal. Chem. 89 (21) (2017) 11552–11559.

[161] N. Bagheri, B. Habibi, A. Khataee, J. Hassanzadeh, Application of surface molecular imprinted magnetic graphene oxide and high performance mimetic behavior of bi-metal ZnCo MOF for determination of atropine in human serum, Talanta 201 (2019) 286–294.

[162] L. Wang, Z. Hu, S. Wu, J. Pan, X. Xu, X. Niu, A peroxidase-mimicking Zr-based MOF colorimetric sensing array to quantify and discriminate phosphorylated proteins, Anal. Chim. Acta 1121 (2020) 26–34.

[163] X. Gan, D. Han, J. Wang, P. Liu, X. Li, Q. Zheng, Y. Yan, A highly sensitive electrochemiluminescence immunosensor for h-FABP determination based on self-enhanced luminophore coupled with ultrathin 2D nickel metal-organic framework nanosheets, Biosens. Bioelectron. 171 (2021) 112735.

[164] R. Han, Y. Sun, Y. Lin, H. Liu, Y. Dai, X. Zhu, D.X. Gao, C.L. Wang, A simple chemiluminesce aptasensor 1 for detection of 2 α-fetoprotein based on iron-based metal organic frameworks, New J. Chem. 44 (2020) 4099–4107.

[165] J. Li, C. Yu, Y. Wu, Y. Zhu, J. Xu, Y. Wang, Novel sensing platform based on gold nanoparticle-aptamer and Fe-metal- organic framework for multiple antibiotic detection and signal amplification, Environ. Int. 125 (2019) 135–141.

[166] H. Tan, Q. Li, Z. Zhou, C. Ma, Y. Song, F. Xu, L. Wang, A sensitive fluorescent assay for thiamine based on metal-organic frameworks with intrinsic peroxidase-like activity, Anal. Chim. Acta 856 (2015) 90–95.

[167] D. Chen, B. Li, L. Jiang, D. Duan, Y. Li, J.J.H. Wang, Y. Zeng, Highly efficient colorimetric detection of cancer cells utilizing Fe- MIL-101 with intrinsic peroxidase-like catalytic activity over broad pH range, RSC Adv. 5 (2015) 97910-97917.

[168] Z. Karami, A. Jeibar, N. Sohrabi, A. Badoei–dalfard, A porous tantalum–based metal–organic framework (Tα–MOF) as a novel and highly efficient peroxidase mimic for colorimetric evaluation of the antioxidant capacity, Catal. Lett. 150 (8) (2020) 2167–2179.

[169] Y. Wang, Y. Zhu, A. Binyam, M. Liu, Y. Wu, F. Li, Discovering the enzyme mimetic activity of metal-organic framework (MOF) for label-free and colorimetric sensing of biomolecules, Biosens. Bioelectron. 86 (2016) 432–438.

[170] Y. Hu, C. Yue, J. Wang, Y. Zhang, W. Fang, J. Dang, Y. Wu, H. Zhao, Z. Li, Fe-Ni metal-organic frameworks with prominent peroxidase-like activity for the colorimetric detection of Sn^{2+} ions, Analyst 145 (2020) 6349–6356.

[171] L. Cui, J. Wu, J. Li, H. Ju, Electrochemical sensor for lead cation sensitized with a DNA functionalized porphyrinic metal−organic framework, Anal. Chem. 87 (20) (2015) 10635–10641.

[172] X. Zhang, X. Huang, Y. Xu, X. Wang, Z. Guo, X. Huang, Z. Li, J. Shi, X. Zou, Single-step electrochemical sensing of ppt-level lead in leaf vegetables based on peroxidase-mimicking metal-organic framework, Biosens. Bioelectron. 168 (2020) 112544.

[173] S.R. Carpenter, Phosphorus control is critical to mitigating eutrophication, Proc. Natl. Acad. Sci. U.S.A. 105 (32) (2008) 11039–11040.

[174] X. Li, P. Liu, X. Niu, K. Ye, L. Ni, D. Du, J. Pan, Y. Lin, Tri-functional Fe-Zr bi-metal-organic frameworks enable high-performance phosphate ion ratiometric fluorescent detection, Nanoscale 12 (37) (2020) 19383–19389.

[175] D. Xu, K. Ge, Y. Chen, S. Qi, Y. Tian, S. Wang, J. Qiu, X. Wang, Q. Dong, Q. Liu, Cobalt-Iron mixed-metal-organic framework (Co3Fe-MMOF) as peroxidase mimic for highly sensitive enzyme-linked immunosorbent assay (ELISA) detection of Aeromonas hydrophila, Microchem. J. 154 (2020) 104591.

[176] S. Wang, W. Deng, L. Yang, Y. Tan, Q. Xie, S. Yao, Copper-based metal-organic framework nanoparticles with peroxidase-like activity for sensitive colorimetric detection of Staphylococcus aureus, ACS Appl. Mater. Interfaces 9 (29) (2017) 24440–24445.

[177] N. Duan, W. Yang, S. Wu, Y. Zou, Z. Wang, A Visual and sensitive detection of Escherichia coli based on aptamer and peroxidase-like mimics of copper-metal organic framework nanoparticles, Food Anal. Methods 13 (7) (2020) 1433–1441.

[178] N. Bagheri, A. Khataee, J. Hassanzadeh, B. Habibi, Visual detection of peroxide-based explosives using novel mimetic Ag nanoparticle/ZnMOF nanocomposite, J. Hazard Mater. 360 (2018) 233–242.

[179] H.Q. Zheng, Y.N. Zeng, J. Chen, R.G. Lin, W.E. Zhuang, R. Cao, Z.J. Lin, Zr-based metal-organic frameworks with intrinsic peroxidase-like activity for ultradeep oxidative desulfurization: mechanism of H_2O_2 decomposition, Inorg. Chem. 58 (10) (2019) 6983–6992.

[180] T. Xuan, Y. Gao, Y. Cai, X. Guo, Y. Wen, H. Yang, Fabrication and characterization of the stable Ag-Au-metal-organic-frameworks: an application for sensitive detection of thiabendazole, Sens. Actuators B Chem. 293 (2019) 289–295.

[181] C. Zhang, H. Li, C. Li, Z. Li, Fe-Loaded MOF-545(Fe): peroxidase-like activity for dye degradation dyes and high adsorption for the removal of dyes from wastewater, Molecules 25 (1) (2020) 168.

[182] P. Liu, X. Li, X. Xu, K. Ye, L. Wang, H. Zhu, M. Wang, X. Niu, Integrating peroxidase-mimicking activity with photoluminescence into one framework structure for high-performance ratiometric fluorescent pesticide sensing, Sens. Actuators B Chem. 328 (2021) 129024.

[183] S. Hu, J. Yan, X. Huang, L. Guo, Z. Lin, F. Luo, B. Qiu, K.Y. Wong, G. Chen, A sensing platform for hypoxanthine detection based on amino-functionalized metal organic framework nanosheet with peroxidase mimic and fluorescence properties, Sens. Actuators B Chem. 267 (2018) 312–319.

[184] G. Jiang, Z. Wang, S. Zong, K. Yang, K. Zhu, Y. Cui, Peroxidase-like recyclable SERS probe for the detection and elimination of cationic dyes in pond water, J. Hazard Mater. 408 (2021) 124426.

[185] D. Fantanas, A. Brunton, S.J. Henley, R. Dorey, Ultra-sensitive SERS detection, rapid selective adsorption and degradation of cationic dyes on multifunctional magnetic metal-organic framework-based composite, Nanotechnology 31 (31) (2020) 315501.

[186] S. Wang, D. Xu, L. Ma, J. Qiu, X. Wang, Q. Dong, Q. Zhang, J. Pan, Q. Liu, Ultrathin ZIF-67 nanosheets as a colorimetric biosensing platform for peroxidase-like catalysis, Anal. Bioanal. Chem. 410 (27) (2018) 7145–7152.

[187] W.G. Zhao, Catalytic activity of MOF (2Fe /Co)/ carbon aerogel for improving H_2O_2 and • OH generation in solar photo – electro – Fenton process, Appl. Catal. B Environ. 203 (2017) 127–137.

[188] H. Yang, Y. R, P. Zhang, Y. Qin, T. Chen, F. Ye, A bimetallic (Co /2Fe) metal-organic framework with oxidase and peroxidase mimicking activity for colorimetric detection of hydrogen peroxide, Microchim. Acta 184 (2017) 4629–4635.

[189] Y. Chen Y, T. Hoang, S. Ma, Biomimetic catalysis of a porous iron-based metal-metalloporphyrin framework, Inorg. Chem. 51 (2012) 12600–12602.

[190] D. Feng, Z.Y. Gu, J.R. Li, H.L. Jiang, Z. Wei, H.C. Zhou, Zirconium-metalloporphyrin PCN-222: mesoporous metal-organic frameworks with ultrahigh stability as biomimetic catalysts, Angew. Chem. Int. Ed. 51 (41) (2012) 10307–10310.

[191] X. Liu, Z. Yan, Y. Zhang, Z. Liu, Y. Sun, J. Ren, X. Qu, Two-Dimensional Metal−Organic Framework enzyme hybrid nanocatalyst as a benign and self activated cascade reagent for in vivo wound healing, ACS Nano 13 (2019) 5222−5230.

[192] S. Wan, F. Gándara, A. Asano, H. Furukawa, A. Saeki, S.K. Dey, L. Liao, M.W. Ambrogio, Y.Y. Botros, X. Duan, S. Seki, J.F. Stoddart, O.M. Yaghi, Covalent organic frameworks with high charge carrier mobility, Chem. Mater. 23 (18) (2011) 4094–4097.

[193] J. Wang, X. Yang, T. Wei, J. Bao, Q. Zhu, Z. Dai, Fe-porphyrin-based covalent organic framework as a novel peroxidase mimic for a one-pot glucose colorimetric assay, ACS Appl. Bio. Mater. 1 (2) (2018) 382–388.

[194] W. Li, Y. Li, H.L. Qian, X. Zhao, C.X. Yang, X.P. Yan, Fabrication of a covalent organic framework and its gold nanoparticle hybrids as stable mimetic peroxidase for sensitive and selective colorimetric detection of mercury in water samples, Talanta 204 (2019) 224–228.

[195] L. Zhang, Z. Liu, Q. Deng, Y. Sang, K. Dong, J.A. Ren, X. Qu, Nature-inspired construction of MOF@COF nanozyme with active sites in tailored microenvironment and pseudopodia-like surface for enhanced bacterial inhibition, Angew. Chem. Int. Ed. 60 (2021) 3469–3474.

[196] T. Zhang, Y. Song, Y. Xing, Y. Gu, X. Yan, H. Liu, N. Lu, H. Xu, Z. Xu, Z. Zhang, M. Yang, The synergistic effect of Au-COF nanosheets and artificial peroxidase Au@ZIF-8(NiPd) rhombic dodecahedra for signal amplification for biomarker detection, Nanoscale 11 (2019) 20221–20227.

[197] M. Bisaglia, S. Mammi, L. Bubacco, Kinetic and structural analysis of the early oxidation products of dopamine: analysis of the interactions with α-synuclein, J. Biol. Chem. 282 (2007) 15597–15605.

[198] H. Jia, D. Yang, X. Han, J. Cai, H. Liu, W. He, Peroxidase-like activity of the Co3O4 nanoparticles used for biodetection and evaluation of antioxidant behavior, Nanoscale 8 (2016) 5938–5945.

[199] H. Wang, W. Fu, Y. Chen, F. Xue, G. Shan, ZIF-67-derived Co3O4 hollow nanocage with efficient peroxidase mimicking characteristic for sensitive colorimetric biosensing of dopamine, Spectrochim. Acta Part A Mol. Biomol. Spectrosc. 246 (2020) 119006.

[200] S. Gajendar, K. Amisha, S. Manu, Mildly acidic pH and room temperature triggered peroxidase - mimics of rGOCu3(OH)2(MoO4)2 cuboidal nanostructures: An effective colorimetric detection of neurotransmitter dopamine in blood serum and urine samples, Cryst. Eng. Commun. 23 (2021) 599–616.

[201] J. Lv, C. Zhangb, S. Wang, M. Li, W. Guo, MOF-derived porous ZnO-Co3O4 nanocages as peroxidase mimics for colorimetric detection of copper(II) ions in serum, Analyst 146 (2020) 605–611.

[202] Q. Chen, X. Zhang, S. Li, J. Tan, C. Xu, Y. Huang, MOF-derived Co3O4 @ Co-Fe oxide double-shelled nanocages as multi- functional specific peroxidase-like nanozyme catalysts for chemo /biosensing and dye degradation, Chem. Eng. J. 395 (2020) 125130.

[203] J. Zhao, W. Dong, X. Zhang, H. Chai, Y. Huang, FeNPs@Co3O4 hollow nanocages hybrids as effective peroxidase mimics for glucose biosensing, Sens. Actuators B Chem. 263 (2018) 575–584.

[204] X. Li, K. Zhou, Z. Tong, J. Yang, N. Sheng, J. Li, J. Sha, Keggin polyoxometalates based hybrid compounds containing helix/nanocages for colorimetric biosensing, J. Solid State Chem. 265 (2018) 372–380.

[205] L. Zhang, J. Pan, Y. Long, J. Li, W. Li, S. Song, Z. Shi, H. Zhang, CeO_2-encapsulated hollow Ag–Au nanocage hybrid nanostructures as high-performance catalysts for cascade reactions, Small (2019) 1903182.

[206] S. Asthana, Z. Hazarika, P.S. Nayak, J. Roy, A.N. Jha, B. Mallick, S. Jha, Insulin adsorption onto zinc oxide nanoparticle mediates conformational rearrangement into amyloid-prone structure with enhanced cytotoxic propensity, Biochim. Biophys. Acta 1863 (1) (2019) 153–166.

[207] F. Panza, M. Lozupone, G. Logroscino, B.P. Imbimbo, A critical appraisal of amyloid-β-targeting therapies for Alzheimer disease, Nat. Rev. Neurol. 15 (2019) 73–88.

[208] X. Zhou, S. Wang, C. Zhang, Y. Lin, J. Lv, S. Hu, S. Zhang, M. Li, Colorimetric determination of amyloid-β peptide using MOF-derived nanozyme based on porous ZnO-Co3O4 nanocages, Microchim. Acta 188 (2021) 56.

[209] X. Zhong, X. Wang, L. Cheng, Y. Tang, G. Zhan, F. Gong, R. Zhang, J. Hu, Z. Liu, Z. Yang, GSH-depleted PtCu3 nanocages for chemodynamic- enhanced sonodynamic cancer therapy, Adv. Funct. Mater. 30 (2020) 1907954.

[210] S. Li, F. Tang, H. Wang, J. Feng, Z. Jin, Au-Ag and Pt-Ag bimetallic nanoparticles@halloysite nanotubes: morphological modulation, improvement of thermal stability and catalytic performance, RSC Adv. 8 (19) (2018) 10237–10245.

[211] X. Wang, C. Wang, M. Pan, J. Wei, F. Jiang, R. Lu, X. Liu, Y. Huang, F. Huang, Chaperonin-nanocaged hemin as an artificial metalloenzyme for oxidation catalysis, ACS Appl. Mater. Interfaces 9 (30) (2017) 25387–25396.

[212] J.E. Coyle, J. Jaeger, M. Gro, C.V. Robinson, S.E. Radford, Structural and mechanistic consequences of polypeptide binding by GroEL, Fold. Des. 2 (6) (1997) 93–104.

[213] X. Wang, H. Sun, C. Liu, C. Wang, A hemin-functionalized GroEL nanocage as an artificial peroxidase and its application in chromogenic detection, Anal. Methods 11 (16) (2019) 2197–2203.

[214] X. Wang, H. Sun, C. Wang, Functionalization of GroEL nanocages with hemin for label-free colorimetric assays, Anal. Bioanal. Chem. 411 (17) (2019) 3819–3827.

[215] W. Liua, C. Gana, W. Changa, A. Qilenga, H. Lei, Y. Liu, Double-integrated mimic enzymes for the visual screening of microcystin-LR: copper hydroxide nanozyme and G-quadruplex/hemin DNAzyme, Anal. Chim. Acta 1054 (2019) 128–136.

[216] C. Liu, L. Li, Q. Su, F. Wu, J. Dong, W. Qian, Ni-introduced CuAu nanocages: facile co-reduction synthesis of a novel magnetic multi- metallic nanostructure with high peroxidase mimetic activity, Cryst. Eng. Commun. 20 (2018) 1978–1984.

[217] C. Wang, G. Ren, B. Yuan, W. Zhang, M. Lu, J. Liu, K. Li, Y. Lin, Enhancing enzyme-like activities of prussian blue analog nanocages by molybdenum doping: toward cytoprotecting and online optical hydrogen sulfide monitoring, Anal. Chem. 92 (11) (2020) 7822–7830.

Chapter 14

Cavity-controlled supramolecular catalysis

Bijnaneswar Mondal
Department of Chemistry, Guru Ghasidas Vishwavidyalaya, Bilaspur, Chhattisgarh, India

14.1 Introduction

Mother nature continuously overwhelmed scientists with its beauty to demonstrate plentiful biological processes with such specific mechanistic pathways and sophistication by the support of proteins, vesicles, enzymes, DNA, etc. [1–5]. In this respect, innumerable biological processes are catalyzed by natural enzymes with high selectivity and prime accuracy [6,7]. Moreover, biological enzymes are very powerful catalysts in the natural process (Fig. 14.1) owing to the synergistic combination of specific active sites, porous microenvironment, and suitable substrate affinity [8,9]. Notably, the presence of active sites in enzymes enhances the binding affinity of substrate–enzyme complex and the nanocavity on the enzyme surface further enhances the high substrate adsorption [10]. The unique molecular pocket of enzymes preorganizes the incoming substrates in a specific orientation and alignment which could further improve catalytic transformations [11]. Furthermore, the presence of various auxiliary functional moieties around the internal porous cavity of enzyme could stabilize many transition states or reactive intermediates during the catalytic process and accelerate the reaction [12]. As a result, these essential facts distinguish enzymes from any bulk catalysts and increase the probability of fruitful catalytic reaction occurrence.

Stimulated by the true characteristics of biological enzymes, scientists are attracted to the design and synthesis of various artificial catalytic hosts which could mimic the functions like enzymes with high precision and intricacy [13,14]. After elaborated research and intensive analysis, supramolecular hosts appeared as the most promising choice for catalysis [15,16]. These host molecules are comprised of hydrophobic guest accessible cavities and robust structural backbones which portray the beneficial properties as like natural enzymes [17,18]. Moreover, several weak noncovalent interactions enhance the incoming guest binding which further endorses the chances of catalytic transformation [19,20].

Supramolecular Coordination Complexes: Design, Synthesis, and Applications.
DOI: https://doi.org/10.1016/B978-0-323-90582-4.00015-4

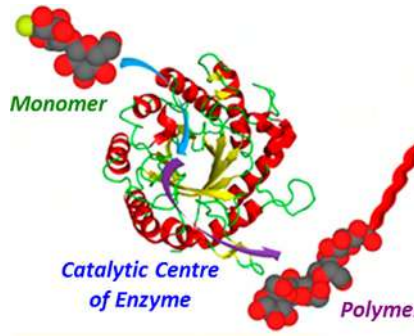

FIGURE 14.1 Schematic representation of enzyme catalyzed polymerization. Reproduced with permission from Ref. [12]. © 2015 American Chemical Society.

Therefore, numerous novel molecular architectures with different shapes and sizes are developed by exploiting simple and suitable building block units [21,22]. In this regard, numerous discrete and porous cage compounds are designed and developed via metal-ligand coordination-driven self-assembly approach [23–26]. Later on, coordination-driven metal-organic cage (**MOC**) compounds are extensively employed in several applied disciplines such as host–guest chemistry, molecular sensing and separation, catalysis, and biological fields [27–30].

In this present book chapter, the recent advancements in the field of cavity-directed catalysis employing self-assembled **MOCs** are primarily conferred. Several important and influencing parameters regarding catalysis in discrete confined cavities have been explained. Also, the unique ability of coordination molecular cage compounds to function as mechanistic probes to deconvolute microenvironment catalysis is intricately highlighted. Moreover, this book chapter has culminated with the discussion on the existing challenges and further conceivable signs of progress in supramolecular coordination cages in the forthcoming future.

14.2 Catalysis in confined cavity

To acquire an insight into enzymatic working functions and mechanisms, researchers always choose to perform chemical reactions by employing various porous materials [31,32]. In this regard, several advantages are observed using confined space as nanoreactors, which usually rely on the nature of molecular pockets (Fig. 14.2). Therefore, many transition states or intermediates of a reaction, can be stabilized by various weak noncovalent interactions inside the molecular cage. Such stabilization diminishes the activation energy barrier of the reaction leading to higher catalytic efficiency compared to the bulk medium reaction. Also, owing to the small space in the confined molecular pocket, the

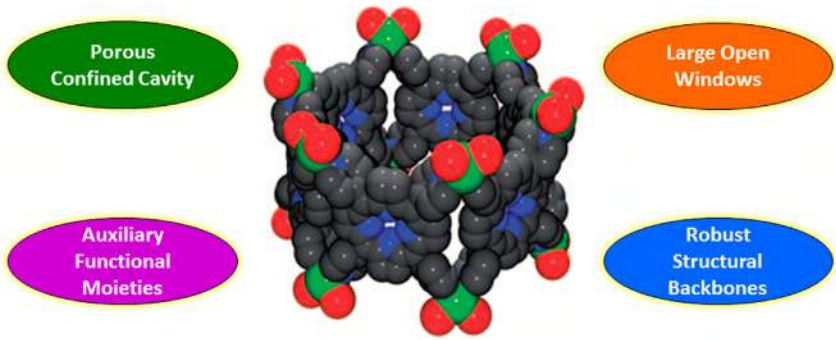

FIGURE 14.2 Schematic representation of a self-assembled metal-organic cage (**MOC**) and its various characteristic features for catalysis. Reproduced with permission from Ref. [25]. © 2008 John Wiley & Sons, Ltd.

effective concentration of the incoming substrates is much higher compared to the bulk medium. As a result, the catalysis inside the porous cages enhances the reaction rate significantly with respect to the uncatalyzed bulk reaction [33]. Furthermore, the reaction mechanism followed in the confined space can differ from the conventional bulk reaction which leads to unique and alternate product formation. Furthermore, robust structural backbones and multiple open windows of molecular vessels ease the entry and exit of incoming substrates and outgoing products respectively.

It can be expected that the nature of encapsulated substrates within confined molecular space will be different from the bulk medium owing to the restricted degrees of freedom. Such restrictions in rotational and vibrational motions may be beneficial to stabilize unusual orientations of substrates or products inside the molecular vessel. Hence, the preorganization of the accumulated substrate molecules in the nanospace may allow the generation of a particular isomeric product with higher stereoselectivity [34,35]. Additionally, the presence of auxiliary functional groups or moieties incorporated in the building blocks favors the multiple substrates accumulation owing to the weak intermolecular interactions (Fig. 14.2). Moreover, water-soluble coordination cage compounds can be smoothly employed to perform catalytic reactions of hydrophobic guests without using toxic organic solvents. In this distinction, the stoichiometric usage of molecular nanoreactor for organic transformations is one of the key disadvantages. Therefore, for the higher catalytic efficiency, the interactions between product and molecular vessel are the governing factor. Here we have intricately discussed many **MOCs** which are involved in various catalytic organic transformations.

14.2.1 Metal-organic cage (MOC) with transition metal ions

The construction of self-assembled molecular cages is mainly governed by the kinetically labile metal-ligand coordination bonds [36,39]. Two predominant

factors associated in the synthesis of **MOC** compounds are (1) the highly directional nature of building blocks and (2) strong coordination bonds between metal counterparts and organic ligands [40–43]. Notably, nature of such metal-ligand coordination bonds plays crucial part in the transformation of initially formed kinetic stable products to most stable thermodynamic products in higher yield [44–47]. Usually, treating multidentate organic ligands with suitable metal ions such as Fe(III), Ga(III), Pd(II), Pt(II), etc., **MOCs** are designed and synthesized. In his regard, the building blocks are modified by incorporating functional moieties for the envisioned applications such as guest encapsulation, analyte sensing and catalysis. Also, the apertures of the molecular vessel can be tuned by the choice of starting materials.

Water soluble **MOCs** are always received superior attention because they can be employed for various catalysis in water which is the solvent of nature. For this purpose, use of square planar metal ions provides benefits on the shape and size control of the premeditated molecular cage structures. Also, the strong advantage of square planar metal ions is that they can offer 90° building units by blocking two adjacent sites. This feature is not possible to achieve in organic compounds owing to the hybridization of carbon atom which does not deliver such bond angles. Therefore, Fujita et al. prepared many highly water-soluble **MOC**s (**MOC1-MOC4**) by the self-assembly of *cis*-Pd(II) 90° acceptors (**B1-B4**) with 2,4,6-tri(pyridin-4-yl)-1,3,5-triazine (**B6**) donor in stoichiometric ratio [48]. These reported cages are having octahedral architectures where four alternate faces are occupied by organic donors and six corners are connected by metal counterparts (Fig. 14.3). Later, an unusual bowl-shaped cage structure (**MOC6**) was synthesized with high yield by the same research group [49]. The porous cage **MOC6** was prepared by treating 2,4,6-tri(pyridin-3-yl)-1,3,5-triazine donor (**B7**) with ethylenediamine blocked *cis*-Pd(II) 90° acceptor (**B3**) in stoichiometric manner in aqueous medium (Fig. 14.4). Both of these molecular cages further exhibited excellent catalytic activity for various organic reactions.

The [2+2] photodimerization reaction of acenaphthylene (**B8**) employing **MOC3** as homogenous catalyst, resulted exclusive formation of the syn-isomeric product (**B9**) in water. In distinction, the same chemical reaction demonstrated a mixture formation of *syn*- and *anti*-isomers (**B9** and **B10**) without cage **MOC3** in common organic solvents (Fig. 14.5A). These results clearly advocated the decisive role of confined cavity of cage **MOC3** which not only enhances the reaction rate but also regulate the stereochemistry of final catalytic products. Likewise, the substantial *syn*-dimer (**B12**) product formation (> 98% yield) was observed in the [2+2] photodimerization of naphthaquinone (**B11**) in presence of cage **MOC6.** Although from ^{1}H NMR analysis, *anti*-dimer (**B13**) was detected as the major product (21%) and *syn*-dimer as the minor product (2%) in the same uncatalyzed photodimerization reaction (Fig. 14.5B). Further, the porous cage **MOC3** exhibited regio-selective formation of [2+2] addition product (**B15**) of asymmetric 1-methylacenaphthylene (**B14**) in an aqueous medium which is hard to achieve owing to the steric hindrance of attached methyl

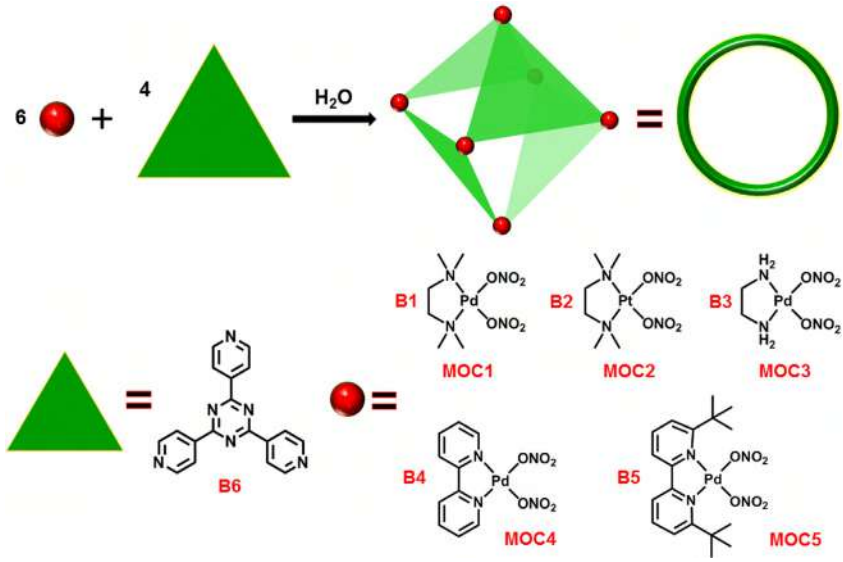

FIGURE 14.3 Schematic representation for the preparation of various octahedral supramolecular hosts (**MOC1–MOC5**).

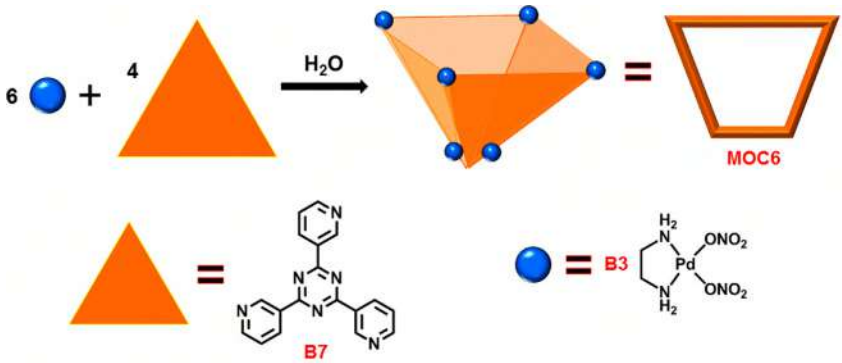

FIGURE 14.4 Schematic representation for the preparation of bowl-shaped supramolecular host (**MOC6**).

group (Fig. 14.5C). Thus, it can be strongly accredited that the microenvironment inside the **MOCs** ease the substrate reactivity and control the stereo- and regio-selective nature of catalytic products.

Fujita and co-workers reported that many organic transformations are possible in the confined cavity of cage compounds, which are not feasible in bulk medium. Like, polyaromatic hydrocarbons (PAHs) which are generally reluctant toward intermolecular [2+2] photo-addition reaction with N-cyclohexylmaleimide (**B19**) in common organic solvents. But in presence of

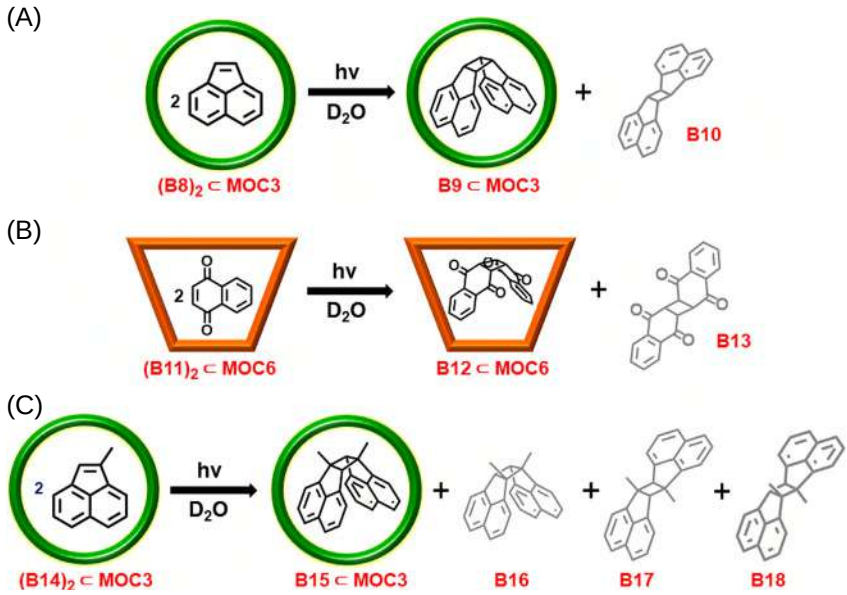

FIGURE 14.5 Schematic representation of [2+2] photodimerization reactions inside coordination cages **MOC3** and **MOC6**.

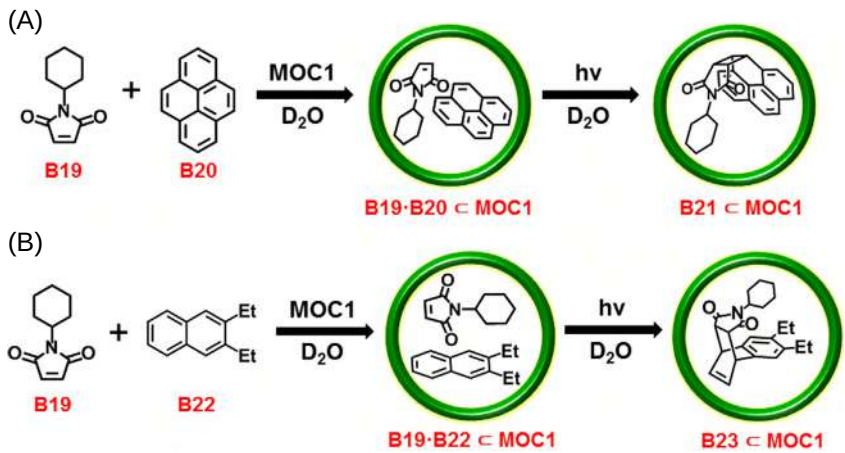

FIGURE 14.6 Diels–Alder reaction of (A) pyrene and (B) naphthalene derivative inside **MOC1.**

cage **MOC1** the same organic reaction was carried out in water with good product yield (Fig. 14.6A). Usually, these reactions are entropically unfavorable and can only be endorsed by such porous molecular cages. The presence of hydrophobic binding pocket inside **MOC1** in aqueous medium, organizes the incoming substrates to embrace a suitable orientation which resulted in desired

product formation. For example, Diels–Alder reaction of pyrene molecule (**B20**) provides product in low yield and the final product gets oxidized in air. However, upon employing cage **MOC1** in the same reactions, it not only promoted the catalysis but also shield the final product from oxidation [50]. These experimental outcomes clearly recommended that confined cage cavity could mimics the functions like reaction pocket of natural enzymes.

Afterward, Murase et al. explored several Diels–Alder reactions of inert aromatic compounds exploiting the cavity of cage **MOC1** [51]. [2+4] cycloaddition reaction of naphthalene derivatives (**B22**) and N-cyclohexylmaleimide (**B19**) was performed in water in presence of molecular host **MOC1** at room temperature (Fig. 14.6B). ^{1}H NMR study showed the effective formation of 1:1:1 host–guests complex and followed by indicating 60% conversion of the reactant to product. Later the final catalytic product (**B23**) was extracted from the porous host and further characterizations were carried out to examine its stereochemistry. Remarkably, in absence of host **MOC1**, no chemical transformation was detected in ^{1}H NMR analysis. X-ray crystal structure of the product-captured cage molecule displayed the *syn* stereochemistry which evidently emphasized the compact packing of the product inside the confined cavity. However, the catalytic reaction not only presented stereoselectivity but also it exhibited regioselective nature because the [2+4] cycloaddition reaction predominantly ensued at the unsubstituted aromatic ring.

Later, Murase and co-workers described the selective cycloaddition reaction in both thermal and photochemical conditions employing cage **MOC1** as an efficient homogenous catalyst [52]. The reaction between aceanthrylene (**B24**) and N-cyclohexylmaleimide (**B19**) produces [4+2] cycloaddition product (**B27**) in good yield under thermal conditions. In distinction, the same encapsulated substrates deliver [2+2] cycloaddition product (**B26**) under photolytic condition (Fig. 14.7B). Similar experimental facts were also perceived in case of using 1H-cyclopenta[l]phenanthrene (**B25**) as diene and N-cyclohexylmaleimide (**B19**) as dienophile (Fig. 14.7C). ^{1}H NMR study on the catalytic reaction progress further revealed that the porous host distinctively recognize the encapsulated substrates in close contiguity. As a results, two different reaction pathways were followed to generate two different cycloaddition products under thermal and photochemical conditions. These observations clearly highlighted the fact of restricted environment inside the molecular cavity which favors the substrate to adopt a selective conformation.

Subsequently, the self-assembled porous cage **MOC1** was exploited to endorse Diels–Alder reactions of various inert PAHs in aqueous medium [53]. Typical [4+2] cycloaddition reactions of anthracene in bulk medium generate adduct formation at the middle benzene ring positions (C9 and C10). But in presence molecular host **MOC1**, the same substrates yielded unprecedented and compact *syn*-adduct at terminal ring positions (C1 and C4). These experimental facts strongly highlighted the crucial role of preorganization of the encapsulated substrates for the enhanced reactivity. Owing to such benefits in structural

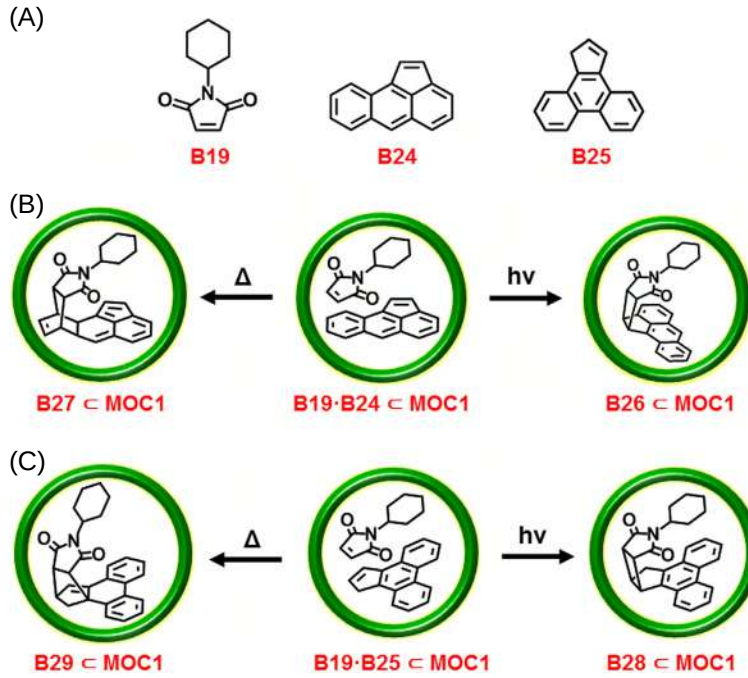

FIGURE 14.7 (A) Various examples of dienes and dienophiles. (B and C) [2+2] and [4+2] cycloadditions of stable aromatic compound under thermal and photolytic conditions.

orientation inside supramolecular hosts, many unreactive aromatic hydrocarbons such as triphenylene (**B30**) and perylene (**B32**) undergo Diels–Alder reactions and exhibited catalytic products with *regio*- and *stereo*-selective nature (Fig. 14.8). In this regard, authors provided the x-ray crystal structure of host–guest complex which evidently displayed the favored alignment of two different substrates inside the confined cavity.

Afterward, Fang and co-workers developed an exceptional coordination cage **MOC5** by following previously reported self-assembly process employing a sterically hindered Pd(II) metal acceptor [54]. X-ray crystal structure of cage **MOC5** revealed that the inner cavity volume was 380 $Å^3$ which substantially less compare to volume of cage **MOC1** (462 $Å^3$). Further, several Diels–Alder reactions were carried out by means of cage **MOC5** as homogenous catalyst and compare the experimental outcomes with cage **MOC1** to recognize the significant role of inner cavity space. Although the encapsulation of large organic substrates was futile due to the steric hindrance of bulky t-butyl groups, but small aromatic molecules exhibited enhanced catalytic reactivity. For example, [4+2] cycloaddition reaction between naphthalene (**B34**) molecule with *N-tert*-butylmaleimide (**B35**) in presence of cage **MOC5** engender catalytic product (**B36**) with high yield and *syn*-selectivity (Fig. 14.9). In contrast, the cage **MOC1**

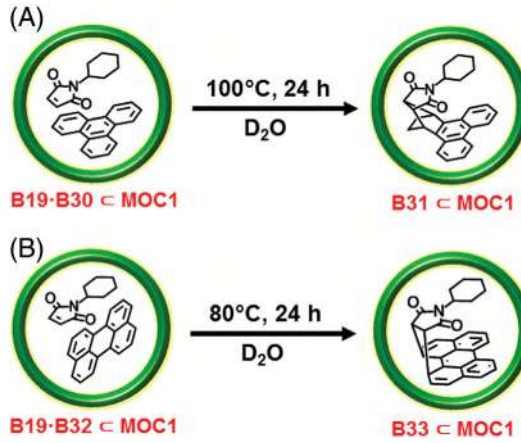

FIGURE 14.8 (A, B) Diels–Alder reaction of inert polyaromatic hydrocarbons employing cage **MOC1** as catalyst.

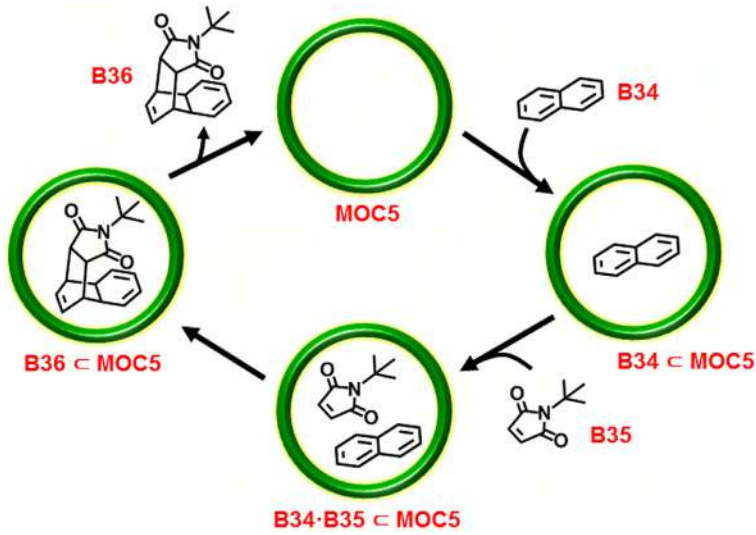

FIGURE 14.9 Proposed reaction pathway of Diels–Alder reaction of naphthalene using cage **MOC5** as catalyst.

encompassed with large cavity size, could not demonstrated such catalytic competence under identical reaction conditions. Authors also conveyed that upon employing cage **MOC5**, Diels–Alder reaction of inert triphenylene with *N-tert*-butylmaleimide offers much improved catalytic conversion than cage **MOC1**.

Apart from high *regio*- and *stereo*-selectivity, a distinguished feature of supramolecular cage catalysis is the unusual products formation. Earlier, we

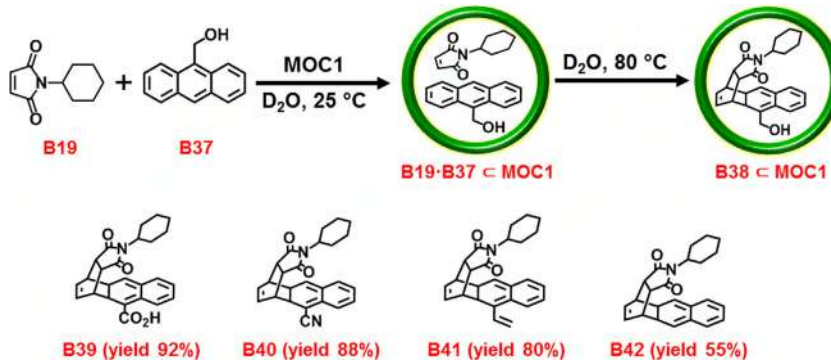

FIGURE 14.10 Unusual 1,4-Diels–Alder adduct formation of anthracene derivatives in presence of cage **MOC1.**

have already discussed about several Diels–Alder reactions which delivers usual catalytic product with high yield and selectivity in the aqueous medium. Nevertheless, the [4+2] cycloaddition reaction between several anthracene derivatives and N-maleimide in presence of catalyst **MOC1** displayed the rare regioselective products formation at C1-C4 positions of anthracene rather than C9-C10 positions (Fig. 14.10). Further, detailed computational study revealed the accessibility of terminal benzene ring close to the dienophile due to the steric hindrance of N-cyclohexyl group which block the central benzene ring [55]. Moreover, the molecular modeling of host molecule **MOC1** displayed that the catalytic reaction profile was altered from bimolecular to pseudo-unimolecular owing to local concentration and preorganization of the substrates. In this regard, previously conferred [2+2] and [2+4] cycloaddition reactions comprised with the key disadvantage of product inhibition. Notably, the present catalytic Diels–Alder reaction of 9-hydroxymethylanthrancene (**B37**) and N-cyclohexylmaleimide (**B19**), yielded the *syn*-isomer of the 1,4-adduct and the product (**B38**) smoothly released from the confined cavity of cage **MOC1**.

Besides, above discussed Diels–Alder reactions of various organic compounds, these self-assembled **MOCs** can also be applied for hydration reaction under certain reaction conditions. In this regard, Murase et al. demonstrated the anti-Markovnikov hydration of internal aromatic alkynes (**B43**) inside the confined cavity of cage **MOC1** [56]. The catalysis was performed under UV light irradiation at room temperature which produce the photodegradable benzyl ketones (**B44**). Further characterizations and analyses recommended that molecular cage **MOC1** acted as photosensitizer by which electron transfer occurred from host to guest (Fig. 14.11A). This report established a unique example of cage-mediated reactivity as well as selectivity toward encapsulated guest molecules.

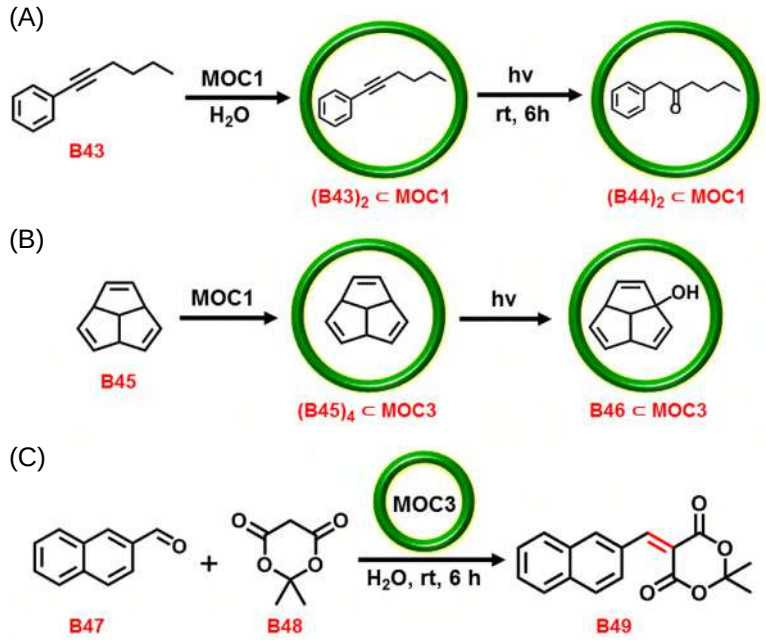

FIGURE 14.11 (A) Anti-Markovnikov hydration of internal aromatic alkynes inside cage **MOC1**. (B) Electron transfer in photo-oxidation of triquinacene employing cage **MOC3**. (C) Knoevenagel condensation reaction within cage **MOC3**.

Another fascinating catalysis was reported by Murase and co-workers which demonstrated guest to host electron transfer inside the cage cavity. The photo-oxidation of triquinacene to 1-hydroxytriquinacene was performed in water employing porous cage **MOC3** as catalyst [57]. ^{1}H NMR analysis portrayed that molecular host accumulated four units of triquinacene (**B45**) which generate radical upon UV irradiation (Fig. 14.11B). Next, this radical readily reacted with dissolved molecular oxygen which resulted into 1-hydroxytriquinacene (**B46**) as catalytic product. Further NMR analysis depicted the catalytic conversion was around 35% whereas the maximum theoretical product yield should be around 25% because of the 1:4 host–guest ratio. These experimental outcomes strongly designated that supramolecular host **MOC3** acts as redox media which accepts a second electron partially to yield overall 35% product formation. Analogous results were also perceived using bowl-shaped molecular cage **MOC6**, where product conversion was around 60%, measured from the ^{1}H NMR analysis.

From the viewpoint of a synthetic organic chemist, Knoevenagel condensation has key significance as it forms C=C bond by the treatment of aldehyde with active methylene group containing organic compound. In this context, same research group demonstrated the Knoevenagel condensation of various aromatic

aldehydes using the self-assembled cage **MOC3** in water [58]. Upon employing 1 mol% of cage **MOC3**, the homogenous catalysis was performed by treating Meldrum's acid (**B48**) and diverse aromatic aldehydes under neutral conditions (Fig. 14.11C). Further, spectroscopic analysis advocated that reaction rate of the catalysis substantially depends on aromatic unit attached to the aldehyde group. It is also observed that anionic intermediate generated during the catalysis, gets stabilized inside the cage cavity owing to its cationic nature. Eventually, in the final catalytic step, the product (**B49**) evicted from the cage cavity and another incoming substrate occupy the slot for the next catalytic cycle. Thus, upon utilizing catalytic amount of supramolecular host **MOC3**, the reaction rate of the Knoevenagel condensation was improved.

However, all the earlier discussed catalytic reactions performed in the self-assembled molecular vessels (**MOC1**-**MOC6**) demonstrated exceptional product selectivity and reactivity. But the product inhibition in such porous cages becomes the major challenge in catalysis. In this context, Mukherjee and co-workers developed several barrel-shaped **MOCs** and they displayed their potential applications in various disciplines [59–62]. Barrel-shaped molecular architectures comprised with two large open windows which can easily favors catalytic substrates or products for their smooth entry and exit from the confined cavity. Apart from this advantage, these molecular barrels are highly water soluble which ease the product release from the cavity owing to the less engrossment in product inhibition. The first example Mukherjee and co-workers reported was a semicylindrical hollow cage **MOC7** which exhibited outstanding catalytic activity for both the Diels–Alder and Knoevenagel reactions in water [63]. Discrete cage **MOC7** was synthesized via two-component reaction of a tri-topic imidazole donor (**B50**) with *cis*-block Pd(II) acceptor (**B1**) in 4:6 stochiometric manner (Fig. 14.12). Moreover, X-ray crystal structures of cage **MOC7** were obtained separately using both hydrophilic and hydrophobic guest molecule. Remarkably, it was observed that hydrophobic guest was inside the molecular cage whereas the hydrophilic guest was outside cage walls. These outcomes further justified that the confined cavity of cage **MOC7** was hydrophobic where exterior portion was hydrophilic.

Subsequently, the Knoevenagel condensation of various aromatic aldehydes were performed using 10 mol% of cage **MOC7** as homogeneous catalyst. Two active methylene compounds such as Meldrum's acid (**B48**) and 1,3-dimethyl-barbituric acid (**B53**) were employed in the catalysis. For instance, 1-pyrenecarboxaldehyde (**B51**) displayed good yield (43%–54%) of catalytic products (**B52** and **B54**) in aqueous medium at room temperature (Fig. 14.13A). In distinction, absence of any catalyst 1-pyrenecarboxaldehyde presented negligible (1%–2%) condensation product formation owing to its inert aromatic nature. Conventionally, Knoevenagel condensations were performed in water-free organic solvents. Water can lead the reaction in backward direction which is also generated in the medium as the side product. Therefore, it is quite difficult to achieve the Knoevenagel condensation in water, but it is accomplished efficiently

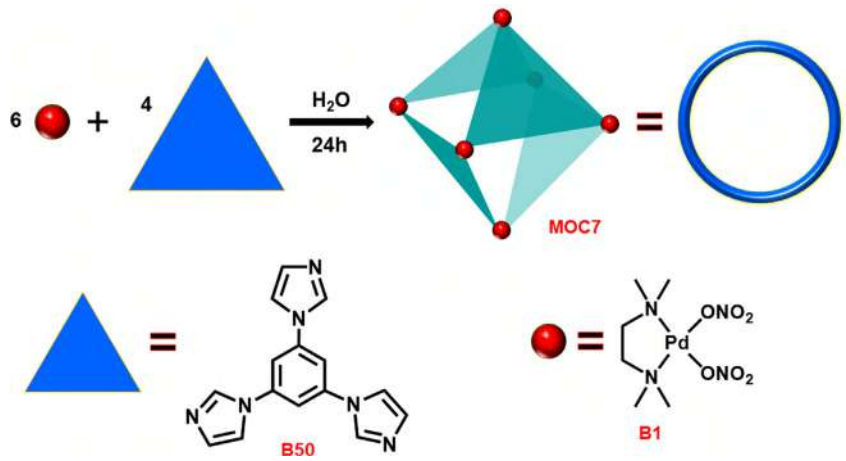

FIGURE 14.12 Schematic representation for preparation of octahedral molecular cage **MOC7**.

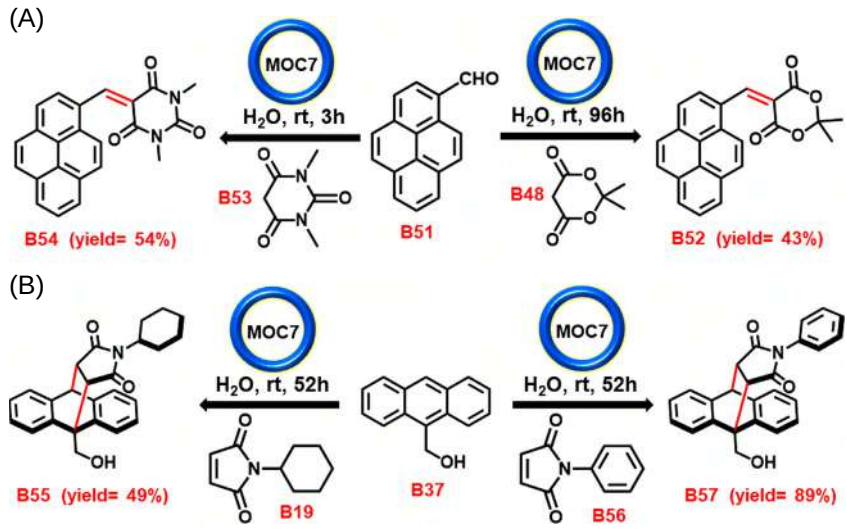

FIGURE 14.13 (A) Knoevenagel condensation and (B) Diels–Alder reactions within cage **MOC7**.

with the support of water-soluble cage **MOC7**. The hydrophobic nature of internal cage cavity helps to carry out the forward reaction by the quick removal products (Fig. 14.13A). Also, the bulky nature and weak interactions of product in the confined cavity, further favors the exit from cage **MOC7**.

Similarly, [4+2] Diels–Alder reaction was carried out choosing 9-hydroxymethylanthracene (**B37**) as diene and N-phenylmaleimide (**B56**) as dienophile in water under ambient conditions. Using 10 mol% of the cage **MOC7** as catalyst leads to generate 89% yield of corresponding product (**B57**)

whereas only 11% product yield was observed in absence of cage (Fig. 14.13B). Similar results were also noticed when N-cyclohexylmaleimide (**B19**) was used as dienophile and 49% yield was detected for the respective product (**B55**). While a drastic change in product yield (9%) was observed in absence of cage **MOC7**. However, catalytic product yield of **B57** perceived was greater compared to **B55** in identical conditions. The reason was the weak interactions of cyclohexyl ring inside the cage cavity which was not suitable for π–π stacking with aromatic walls of cage **MOC7**. Therefore, the less stabilization of transition state inside cage **MOC7** was presumed due to the poor π overlap which resulted in lower product yield.

Supramolecular chemists have broadly explored the two-component self-assembly reactions owing to the advantages of easy control and predictable directionality of substrate toward product formation. However, multicomponent self-assembly between donors and acceptors makes it more complex and challenging for single discrete product formation as well as structure predictability [64–66]. Yet both the two-component and multi-component reactions are entropically not favorable but the later one is more. In this regard, Samanta et al. reported a water-soluble molecular nanocage **MOC8** via one-pot multi-component reaction using both tri- and tetra-topic donors with Pd(II) metal acceptor [67]. Cage **MOC8** was synthesized by the treatment of cis-block Pd(II) acceptor (**B1**) along with tri-topic donor (**B50**) and tetra-topic donor (**B58**) in a 7:2:2 stochiometric ratio (Fig. 14.14A). Further, several spectroscopic analyses and X-ray crystal structure revealed that the self-shorted nanocage **MOC8** has a boat-shaped architecture. The four faces were covered by the tri-topic and tetra-topic imidazole donors in alternate fashion whereas the seven corners were linked by the Pd(II) metal acceptors.

The porous pocket of cage **MOC8** surrounded by large aromatic walls of multiple imidazole donors makes the confined nanospace suitable for polyaromatic guest encapsulation. Hence, the molecular boat **MOC8** was explored as homogeneous catalyst for the Knoevenagel condensation of several aromatic aldehydes with active methylene compound such as 1,3-dimethyl-barbituric acid (**B53**) in water media (Fig. 14.14B). For example, catalytic reactions of anthracene (**B60**) and pyrene aldehydes (**B51**) using 10 mol% of cage **MOC8** displayed 35% and 33% the product formation, respectively. While product yields were drastically dropped to 2%–5% in absence of porous cage **MOC8** under equal reactions. Other smaller aromatic aldehydes employed in this homogeneous catalysis also displayed excellent product yield at room temperature. Moreover, aliphatic aldehydes did not exhibit any reaction rate improvement experimentally in this catalytic system. This observation suggests that cage cavity of **MOC8** was quite selective toward aromatic aldehydes which are typically less responsive in water.

Xanthenes are a distinct class of heterocyclic organic compounds that are mainly used as important building blocks in natural product synthesis and medicinal chemistry [68]. In addition, tetraketones are extensively applied to prepare

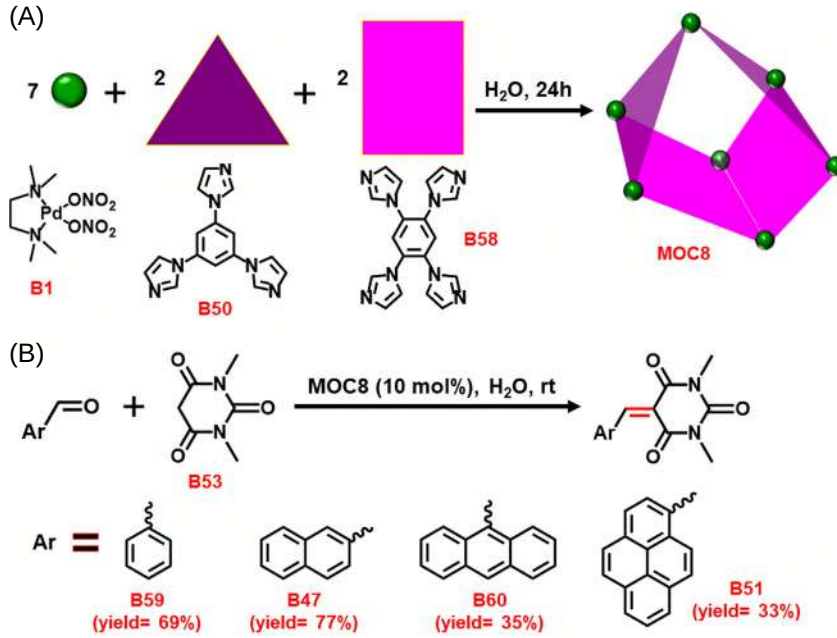

FIGURE 14.14 (A) Schematic representation for preparation of molecular boat **MOC8**. (B) Knoevenagel condensation of various aromatic aldehydes within molecular boat **MOC8.**

unusual heterocyclic compounds which are primary employed in biological systems and laser dyes [69]. Hence, the development of various functionalized xanthene and corresponding tetraketones compounds is extremely demanded in recent times. Therefore, Das et al. explored a tri-facial molecular barrel **MOC9** as homogenous catalyst to prepare xanthenes and its derivatives in aqueous medium [70]. The self-assembled molecular barrel **MOC9** was synthesized upon treatment of tetra-topic donor (**B61**) with cis-block Pd(II) acceptor (**B1**) in 1:2 stoichiometric ratio at 50°C temperature in water (Fig. 14.15A). X-ray crystal structure further confirmed that tri-facial molecular barrel **MOC9** embraces with confined space surrounded by large aromatic π walls and two open windows for substrate entry/exits. These structural features make the molecular barrel **MOC9** as a suitable contender for catalytically active nanovessel.

Subsequently, the dehydration reaction was performed using 2-naphthaldehyde (**B47**) and dimedone (**B62**) applying 5 mol% of trifacial barrel **MOC9** as homogeneous catalyst (Fig. 14.15B). However, a profound effect was noticed on product yields of cyclic xanthene (**B64**) and noncyclic tetraketone (**B63**) derivatives by slightly altering reaction conditions. Interestingly, higher temperature (60°C) in the catalytic reaction favored the xanthene product (**B64**) whereas at room temperature (25°C) tetraketone (**B63**) obtained as major product (Fig. 14.15B). The plausible reaction mechanism demonstrated that

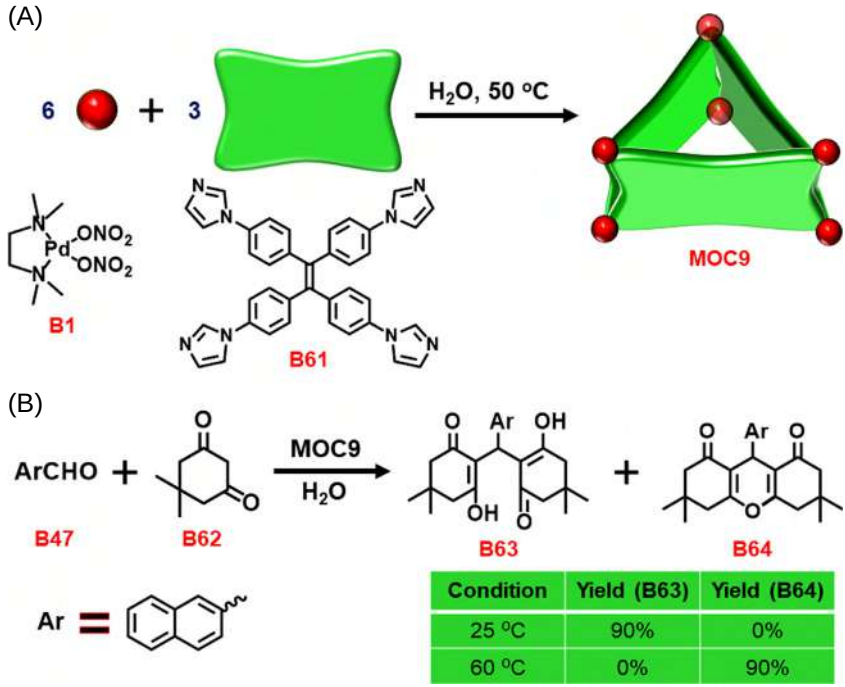

FIGURE 14.15 (A) Schematic representation for the preparation of trifacial barrel **MOC9**. (B) Catalytic dehydration reaction within molecular barrel **MOC9**.

water elimination was more facile at higher temperature from the hydrophobic cavity of trifacial barrel **MOC9** which leads to generate dehydrated cyclic xanthene product. Moreover, at both higher and room temperature, no products were detected without cage **MOC9** which indicate the importance of the hydrophobic confined cavity. The versatility of the present catalysis was the formation of xanthene and tetraketone derivatives at two different conditions for electron-donating substrates which were extremely difficult to accomplish in conventional methods. The present catalytic methodology was further applied for several other aromatic aldehyde derivatives which delivered corresponding catalytic products in good to excellent yield.

Amidst of numerous coordination-driven self-assembled architectures, a handful of molecular barrel structures were reported and their applications in various fields were till now unexplored [71]. In this context, Mukherjee and co-workers reported a tetra-facial molecular barrel **MOC10** which unveiled exceptional homogeneous catalysis for intra-molecular hetero Diels–Alder (IMHDA) reactions [72]. The self-assembly reaction of carbazole-based tetradentate donor (**B66**) with *cis*-Pd(II) metal acceptor (**B65**) in 1:2 stoichiometric ratio leads to produce molecular barrel **MOC10** (Fig. 14.16A). Finally, single crystal XRD analysis confirmed that cage **MOC10** has a two-face opened tetrafacial tube

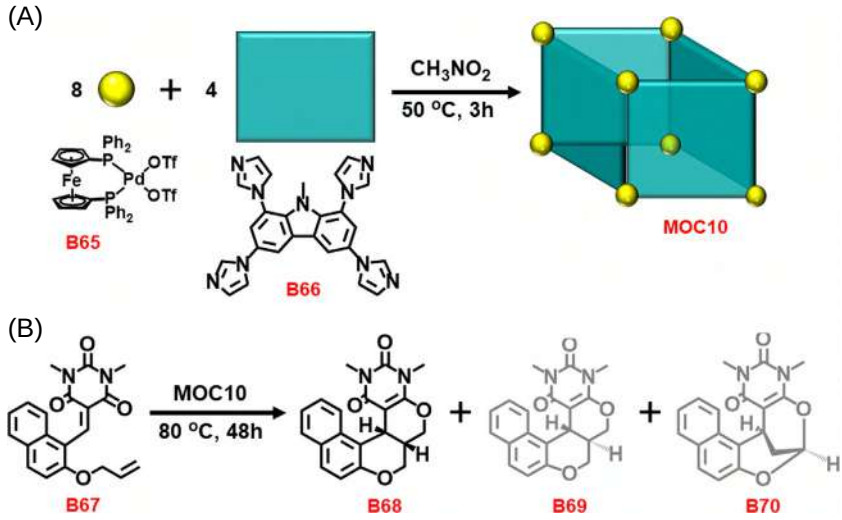

FIGURE 14.16 (A) Schematic representation for the synthesis of tetra-facial barrel **MOC10**. (B) Intramolecular Diels–Alder reaction employing molecular barrel **MOC10**.

architecture where four faces were covered by tetraimidazole donor (**B66**) and the eight corners linked by Pd(II) metal acceptors (**B65**). In, addition, [4+8] tetra-facial barrel **MOC10** comprised with the highly symmetric porous nature (12.4×12.4 Å^2).

Intramolecular hetero Diels–Alder (IMHDA) reactions played as a prime synthetic approach for the development of fused hetero-cyclic compounds. Such reactions were conventionally carried out (1) at elevated temperature or (2) in carcinogenic solvent medium or (3) using solid-state melt reaction techniques [73]. The previous literature reports exhibited severe drawback on regio- and stereo-selective control over final product formation. Therefore, tetra-facial barrel **MOC10** was exploited as supramolecular catalyst to perform IMHDA reactions under mild conditions. For instance, naphthylidene-barbituric acid derivative (**B67**) chosen as the model substrate which comprised with 1-oxa-1,3-butadiene as hetero-diene and a terminal alkene group as dienophile (Fig. 14.16B). Upon applying 10 mol% of molecular barrel **MOC10** in homogeneous condition, the *cis*-fused [4+2] cyclo-addition product (**B68**) achieved 78% product yield. Although in absence of barrel **MOC10**, a minor amount (11%) of *cis*-fused product was detected along with mixture of trans-fused (**B69**) and bridged heterocyclic (**B70**) derivatives. The present supramolecular catalysis strongly validated the benefit of the confined cavity in the cycloaddition reaction which resulted exclusive formation of the cis-product.

Afterward, Saha et al. reported another example of water-soluble tetra-facial barrel **MOC11** which demonstrated exceptional catalytic reactivity in Michael addition reaction [74]. The self-assembly reaction between a symmetrical

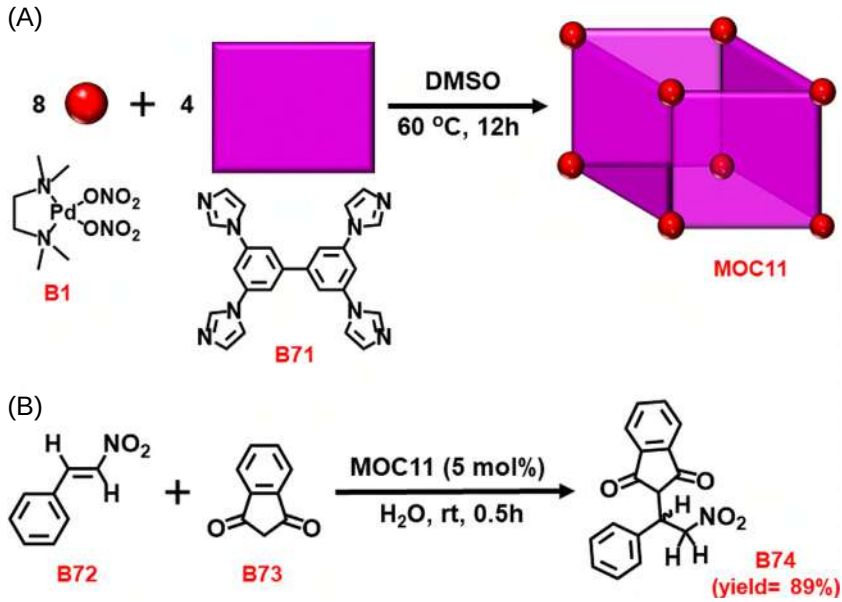

FIGURE 14.17 (A) Schematic representation for the synthesis of tetra-facial barrel **MOC11**. (B) Michael addition reaction employing molecular barrel **MOC11**.

tetra-imidazole donor (**B71**) with *cis*-Pd(II) metal acceptor (**B1**) in dimethylsulfoxide (DMSO) solvent leads to produce molecular barrel **MOC10** (Fig. 14.17A). Further, several spectroscopic analyses and X-ray crystal structure revealed that the [4+8] molecular container **MOC11** has a two face opened tetra-facial barrel architecture. The four faces were covered by the tetra-dentate imidazole donors (**B71**) whereas the eight corners were connected by the Pd(II) metal acceptors (**B1**). Next, the encapsulation of various nitrostyrene derivatives inside molecular barrel **MOC11** was perceived in aqueous medium which encouraged authors to perform Michael addition reaction. In conventional organic synthesis, excessive acid catalysts are used in Michael addition reaction in presence of organic solvents which generate unwanted and toxic side products due to the probable condensation [75,76]. In the present catalysis, nitrostyrene (**B72**) employed as Michael acceptor whereas 1,3-indandione (**B73**) acted as a nucleophile in aqueous medium (Fig. 14.17B). Using 5 mol% of barrel **MOC11**, 89% yield of Michael adduct (**B74**) was observed at room temperature in just 0.5 h. Although without any cage catalyst, 25% yield of Michael adduct (**B74**) was noticed which clearly emphasized the catalytic involvement of molecular vessel. Besides, several nitrostyrene derivatives were exploited in the present homogeneous catalysis and corresponding Michael adducts were obtained in good to excellent yields.

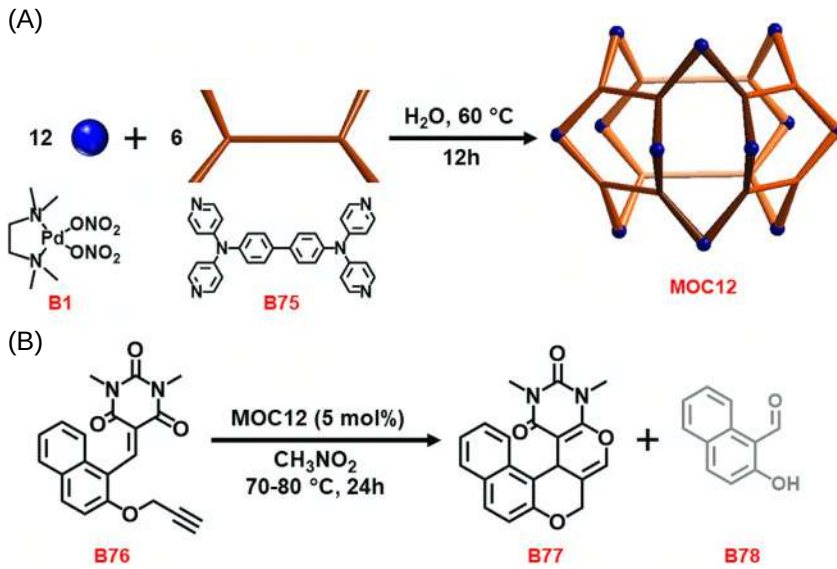

FIGURE 14.18 (A) Schematic representation for the synthesis of hexa-facial barrel **MOC12**. (B) Intramolecular Diels–Alder reaction employing molecular barrel **MOC12**.

Till now the reported molecular barrels were mostly $M_{2n}L_n$ types structures such as M_6L_3 and M_8L_4 which were embraces with trigonal and square prismatic architectures, respectively [70,72,74,77]. In this discrepancy, very few molecular barrels are prepared where eight or higher numbers of metal centers were directly involved in the $M_{2n}L_n$ assembly which includes a unique hexagonal $Pt_{12}L_6$ and $Pt_{16}L_8$ system reports by Mukherjee and Severin group [25, 78]. In this regard, Bhat et al. first reported a two side open hexa-facial molecular barrel **MOC11** which exhibited superior catalytic performance for intramolecular [4+2] cycloaddition reactions [79]. The [6+12] self-assembled molecular barrel **MOC11** was synthesized by treating a symmetrical tetra-pyridyl donor (**B75**) with usual *cis*-Pd(II) acceptor (**B1**) in water medium at 60°C for 12 h under open atmosphere (Fig. 14.18A). Several spectroscopic analyses and X-ray crystal structure revealed that cage **MOC11** possess an unusual distorted triangular orthobicupola-like geometry. Typically, $M_{12}L_6$ type assembly expected to display hexagonal faced open barrel or simple cubic architectures. But in the present state, the cage **MOC11** demonstrated two triangular face cupolas jointly share the same hexagonal base which makes it very rare molecular structure. Moreover, the dimension of the inner hydrophobic cavity was around $\sim 23.74 \times 22.66 \times 22.66$ Å^3, which makes it appropriate to host large organic guest molecules.

Further, the intramolecular hetero Diels–Alder reactions were performed on various polyaromatic barbituric acid derivatives using 5 mol% of cage catalyst **MOC12**. In the present case, the model substrate (**B76**) resulted 98% product (**B77**) formation in nitromethane at 70–80°C under homogeneous condition (Fig. 14.18B). In distinction, absence of hexa-facial barrel **MOC12** for the same [4+2] cyclo-addition reaction displayed severe change in desired product formation (25%) which undoubtedly established the crucial function of 3D confined space. Although, the hexa-facial barrel **MOC12** was water soluble but the catalysis was performed in nitromethane solvent. The reason was only 22% of product yield detected in aqueous medium under same reaction condition and remaining substrate produces hydroxy naphthaldehyde (**B78**) upon hydrolysis (Fig. 14.18B). Moreover, upon heating at 80°C the hexa-facial barrel **MOC12** with and without substrate, clearly portrayed no deformation which designates the thermal stability of the cage during the catalytic reaction. The proposed catalytic mechanism showed that guest encapsulated hexa-facial barrel undergo intermolecular rearrangement which restricted the conformational flexibility of the side chain. These constraints ended the reacting units, that is, diene and dienophile in a close proximity which leads to intermolecular [4+2] cycloaddition. Also, the enhanced reaction temperature (70–80°C) facilitates to overcome the activation energy barrier for the catalysis.

It is well recognized that Pt-N bonds are relatively more robust and stable compare to Pd-N bond formation which makes it tough to achieve large molecular cage structures using Pt(II) metal acceptors [80]. In most literature reports, a mixture of self-assembled products was experimentally perceived rather than one exclusive molecular structure formation due to the relative kinetic inertness of Pt-N bonds [81]. In this contrast, Mukherjee and co-workers presented a unique chiral tetrahedral architecture **MOC13** using Pt(II) metal acceptors [82]. Tetrahedral cage **MOC13** was prepared upon treatment of a triphenyl-based pyrimidium donor (**B80**) with chiral *cis*-Pt(II) metal acceptor (**B79**) in 1:1 water/methanol mixture at 45°C for 36 h (Fig. 14.19A). Further spectroscopic characterizations confirmed that cage **MOC13** was a [4+12] self-assembled tetrahedral structure where four faces are occupied by hexa-dentate donors (**B80**) and each corners are linked by three Pt(II) acceptors. Moreover, X-ray crystal structure portrayed that discrete cage **MOC13** embraces with around 860 $Å^3$ intrinsic hydrophobic cavity. Also, the chiral cage displayed excellent optical activity which was verified by circular dichroism.

Next, the large intrinsic cage cavity impelled authors to explore face-directed tetrahedral cage **MOC13** in supramolecular catalysis. Therefore, the cage compound was efficiently exploited as homogeneous catalyst to endorse the Michael addition reactions of various aromatic nitro-styrene derivatives with indole (**B81**). The catalytic reaction was carried out with nitro-styrene (**B72**) using 10 mol% of chiral cage at room temperature generated corresponding Michael adduct (**B82**) with 91% yield (Fig. 14.19B). As anticipated, a severe alteration in product yield (22%) was spotted in absence of molecular reactor **MOC13**. In

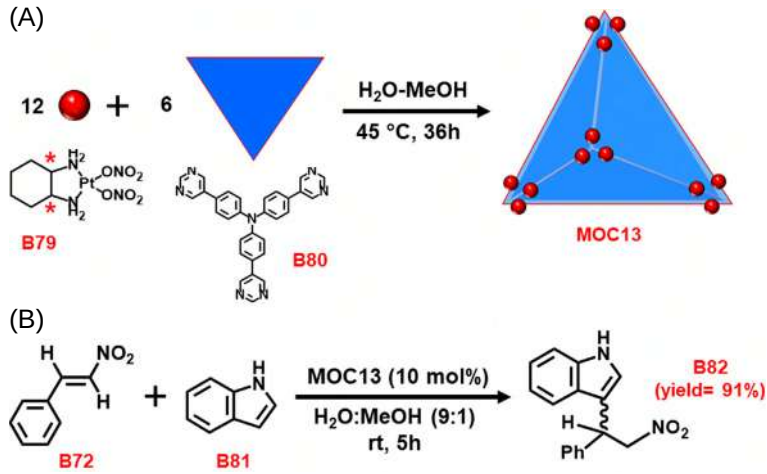

FIGURE 14.19 (A) Schematic representation for the preparation of face-directed tetrahedron cage **MOC13**. (B) Michael addition reaction within molecular tetrahedron **MOC13**.

the present catalysis, a series of β-nitro-styrene derivatives undergo nucleophilic addition reactions of electron rich indole and respective Michael adducts were attained with good to excellent yields. Therefore, the whole catalysis unveiled the robustness of Pt-N bonds in a molecular vessel can further improve the superiority of confined space for guest encapsulation as well as in catalysis.

Till now, octahedral transition metal-mediated various tetrahedral cages have been reported but owing to their solubility problems, their applications are limited in organic solvents [83,84]. In recent times, employing coordination-driven self-assembly approach, few tetrahedral molecular architectures were established using square planner metal ions such as Pd(II) acceptors [85]. In another report, Howlader et al. presented the Michael addition reaction applying face-directed (**MOC14**) and edge-directed (**MOC15**) tetrahedron cage compounds as catalyst in water medium [86]. Both the molecular tetrahedrons were developed employing di-topic (**B84**) and tri-topic (**B83**) tetrazole donors in presence of Pd(II) metal acceptor (Fig. 14.20A). The self-assembly reaction of di-topic donor (**B84**) with *cis*-Pd(II) acceptor (**B1**) in 1:2 stoichiometric ratio at 60°C temperature leads to generate [6+12] molecular cage **MOC15**. In analogous method, [4+12] self-assembled cage **MOC14** was prepared using tri-topic donor (**B83**) with identical metal acceptor in 1:3 stoichiometric ratio. Moreover, the x-ray crystal structure of cage **MOC14** displayed that it has a tetrahedron molecular architecture where four faces were blocked by tri-topic tetrazole donor (**B83**). Likewise, cage **MOC15** exhibited tetrahedron cage structure where six edges were connected by di-topic tetrazole donor (**B84**). In both cases, each vertex corner was connected by three Pd^{II} acceptors which forms a Pd_3 triangle.

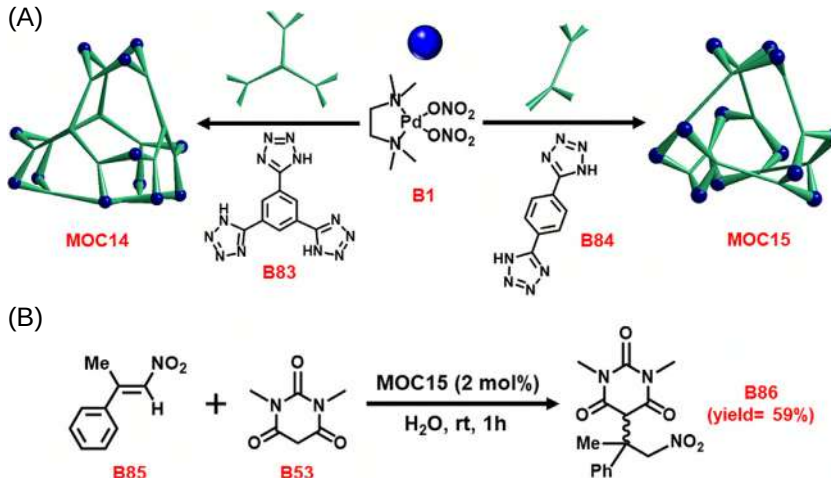

FIGURE 14.20 (A) Schematic representation for the preparation of face-directed (**MOC14**) and edge-directed tetrahedron cage (**MOC15**). (B) Michael addition reaction within molecular tetrahedron cage **MOC15**.

Although both discrete cages (**MOC14** and **MOC15**) were comparable in shape and size (6.8 Å X 6.9 Å), but their catalytic reactivity toward Michael addition reaction were reasonably diverse under identical conditions. In this regard, several water insoluble aromatic nitro-olefins were employed with active methylene substrate which generated their corresponding products in good yields (Fig. 14.20B). For example, model substrate (**B85**) reacts with 1,3-dimethylbarbituric acid (**B53**) at room temperature which resulted respective Michael adduct (**B86**) formation with 59% yield. Also, for all the catalytic substrates, 2 mol% of edge-directed tetrahedral cage **MOC15** was applied as homogeneous catalyst in the aqueous medium. In difference, using face-directed tetrahedral cage **MOC14** as catalyst, a drastic decline in corresponding products formation was noticed for all the nitro-olefins. Besides, no catalytic reactions were perceived for some substrates as compared to competitive reactions with cage **MOC15**. These experimental facts can be further attributed, the presence of large triangular windows for substrate encapsulation favors the catalysis for cage **MOC15** rather than cage **MOC14** (Fig. 14.20). These accounts further empower authors to recognize the noteworthy role of structural nature of molecular cage compounds on guests/substrates encapsulation as well as in catalytic performance.

Urea and thiourea functionalized organo-catalysts have seized superior attentions in researchers owing to the elevated thermal stability and high selective nature [87]. The urea and thiourea derivatives became an obvious choice for synthetic chemists. Previous literature reports experimentally demonstrated that urea and thiourea functional moieties were very sensitive toward the detection

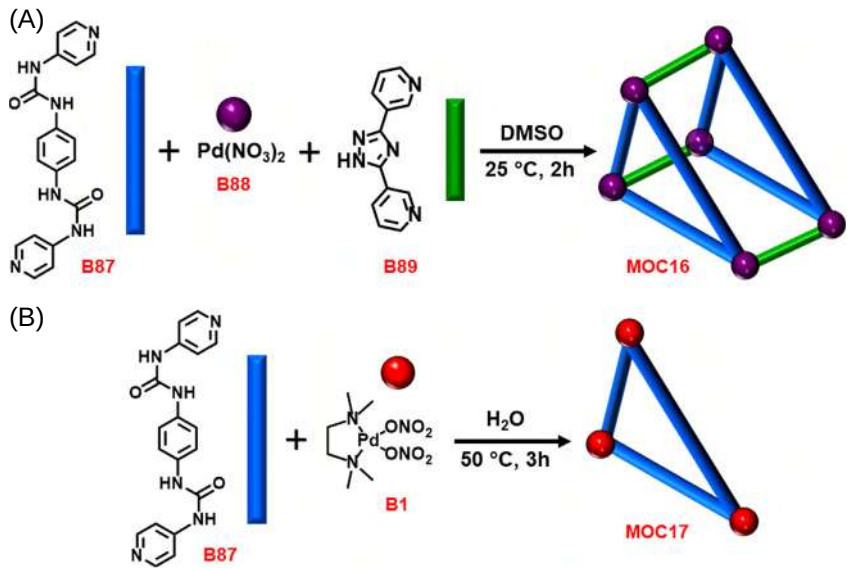

FIGURE 14.21 Schematic representation for the preparation of (A) molecular prism **MOC16** and (B) molecular triangle **MOC17**.

of various analytes [88]. Consequently, Mukherjee and co-workers developed a porous molecular prism **MOC16** via incorporating urea functionality for promoting the "turned-on" catalytic activity [89]. The novelty of this work was the urea functionalized cage **MOC16** appeared as unique heterogeneous catalyst for Michael addition and Diels–Alder reaction for various aromatic substrates in water. In a multicomponent reaction, urea decorated bidentate donor **B87** was treated with $Pd(NO_3)_2$ along with 'clip type' linker **B89** in 1:1:1 stoichiometric ratio which leads to produce trigonal molecular prism **MOC16** (Fig. 14.21A). Further structural analyses of molecular prism **MOC16** revealed that Pd atoms were occupied the six corner positions which were linked by urea- and triazole-based donors (**B87** and **B89**). Similarly, another two-component self-assembly reaction by treating urea-based ligand (**B87**) with *cis*-block Pd(II) acceptor (**B1**) in aqueous medium produced [3+3] molecular triangle **MOC17** (Fig. 14.21B).

Subsequently, to examine the substrate recognition ability of molecular cage **MOC16**, several nitro-olefin compounds were used as guest. As expected, intermolecular hydrogen bonding between urea moieties and nitro-olefins was detected from the absorption spectral change of molecular prism **MOC16**. Therefore, authors have explored the Michael addition reaction of aromatic nitro-olefins with 1,3-dimethylbarbituric acid (**B53**) in water using 5 mol% of cage **MOC16** (Fig. 14.22A). Although the cage **MOC16** exhibited excellent catalytic activity for nitro-styrene (**B72**) but a major decline in Michael adduct (**B90**) yield were observed applying molecular triangle **MOC17** (10 mol%) in same

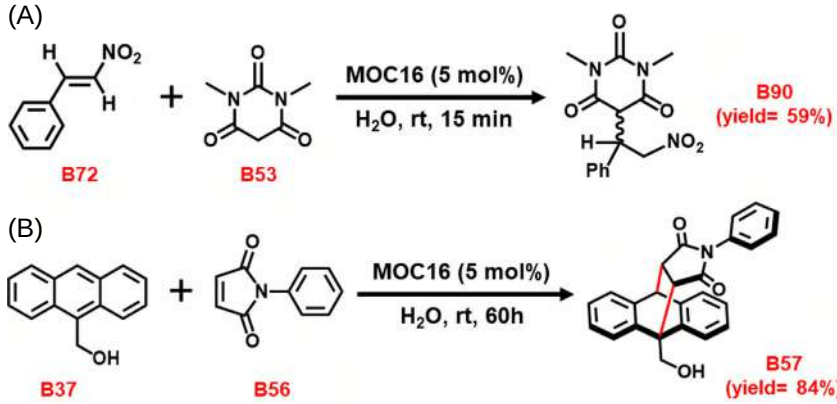

FIGURE 14.22 (A) Michael addition and (B) Diels–Alder reactions using molecular prism **MOC16**.

conditions as heterogeneous catalyst. Moreover, the proposed reaction pathway revealed that the urea moieties of cage **MOC16** helped to bind nitroolefins inside the confined cavity which was absence in triangle **MOC17** owing to intermolecular self-quenching effect. These experimental analyses further emphasized the pivotal role of 3D confined space of molecular prism **MOC16** which makes it free from intermolecular self-hydrogen bonding.

Previous literature report by Fujita et al. demonstrated porous **MOCs** as efficient catalyst for [4+2] Diels–Alder reaction in homogeneous condition [90]. In the present report, authors employed cage **MOC16** as heterogeneous catalyst which portrayed a significant rate enhancement due to the strong substrate-cage complexation inside the 3D confined cavity. The catalysis was performed using 5 mol% of cage **MOC16** at room temperature in water medium. Various N-substituted maleimides as dienophiles with 9-hydroxymethyl-anthracene (**B37**) as diene were examined in presence and absence of cage catalyst (Fig. 14.22B). All the catalytic reactions displayed greater product formation respective to absence of porous cage compound. Furthermore, the molecular prism **B7** was used for several catalytic cycles and exhibited easy recovery without any structural distortion.

In recent times, Sun and co-workers developed a unique molecular structure cationic building blocks rather than employing usual neutral ligands. The motivation of using charged precursor to prepare cage compound was the higher water solubility. Therefore, the coordination cage **MOC18** was successfully synthesized by treating the di-cationic ligand (**B91**) with [(2,2′-bipyridine)$Pd(NO_3)_2$] (**B4**) in 1:2 stoichiometric ratio [91]. The self-assembly reaction was carried out in D_2O medium for 12 h at 70°C and further spectroscopic characterizations demonstrated that molecular cage was a Pd_4L_2 species (Fig. 14.23). X-ray crystal structure of [2+4] cage **MOC18** confirmed that two charged pyridinium donors

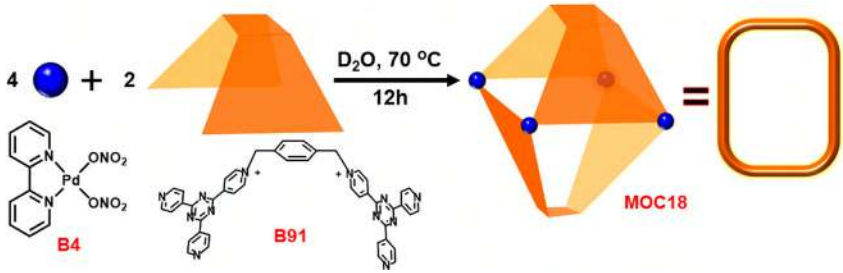

FIGURE 14.23 Schematic representation for the preparation of **MOC18**.

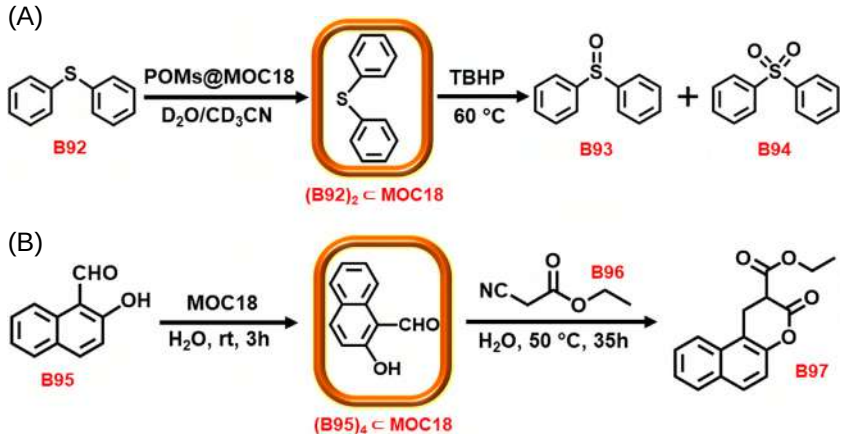

FIGURE 14.24 (A) Example of the desulfurization reaction within cage **MOC18**. (B) Preparation of functionalized coumarins in presence of cage **MOC18**.

(**B91**) were linked by four Pd(II) acceptors (**B4**) which were cis-capped by bipyridine ligands. Also, the present cage **MOC18** is quite similar to previously reported cage **MOC1** by Fujita et al. but a drastic 82% volume expansion was observed. Further, highly redox active cage displayed efficient host–guest complexation with various anionic polyoxometalates (**POMs**) clusters and neutral aromatic compounds.

Subsequently, porous cage **MOC18** was applied for the desulfurization reaction of various aromatic sulfides in presence of **POMs. POMs** are well known as powerful oxidants for organic substrates like alkanes, alkenes, and hetero-atoms containing ligands, but their product selectivity is low [92]. The combination of **POMs** and **MOC18** as hybrid catalyst revealed the reactivity improvement of catalytic desulfurization reactions in both conversion and product selectivity (sulfoxide over sulfone). For example, diphenyl sulfide (**B92**) was stirred with 10 mol% of **POMs@MOC18** catalyst in D_2O/CD_3CN (v/v=5:1) for 5 h at room temperature (Fig. 14.24A). Afterward, the mixture was heated overnight at 60°C in presence of tert-butyl hydroperoxide (TBHP). Further, ^1H NMR

analyses displayed 100% sulfide (**B92**) conversion and 95% product selectivity of sulfoxide (**B93**) over sulfone (**B94**). This work strongly provided a beneficial policy for improving product conversion and selectivity employing conventional transition-metal catalysts in water.

In another report, same authors explained the beneficial usage of cage **MOC18** as homogeneous catalyst for the preparation of functionalized coumarins in water media [93]. Hence, applying 20 mol% of cage catalyst **MOC18,** Knoevenagel condensation of several salicylaldehyde derivatives was performed with active methylene compounds such as malononitriles or cyanoacetates (Fig. 14.24B). The model substrate salicylaldehyde (**B95**) undergo condensation reaction with cyanoacetates (**B96**) which displayed four molecules of guest encapsulation inside the cage cavity confirmed from X-ray crystal structure. Further, Michaelis–Menten kinetic analysis showed that the condensation catalytic product (**B96**) was 23-fold improvement in comparison with control reaction without cage **MOC18**. Furthermore, upon employing other similar type Pd_6L_4 cages, the Knoevenagel condensation reaction demonstrated a mixture of products with lower yields. This report established that the fine-regulation of the size and symmetry of the molecular cage cavity is essential for the cage-mediated reactivity in supramolecular catalysis.

Metal-ligand mediated coordination cages established its strong potential as porous supramolecular hosts as conveyed by numerous discussed reports. But the key negatives associated with **MOCs** are the fragile nature of coordination bonds in presence of acids, bases, nucleophiles and other additives. Apart from that, in some cases the self-assembly leads to mixture of products or supramolecular sol–gel formation. As a result, several new types of porous organic materials such as covalent cages and frameworks have drawn significant interest of researchers as budding catalysts [94–97]. These organic compounds not only exhibited solution-phase processibility but also comprised with robust structural backbones which promote them as efficient homo- and hetero-geneous catalysts. Recently, various organic transformations are performed employing such discrete organic molecules as photocatalysts [98–100].

14.3 Conclusion and future prospects

Nature is the master of self-assembly by inventively exploiting a multitude of weak and noncovalent interactions. Therefore, the perception of chemical conversions inside the confined molecular space is not new. Over millions of years, mother nature demonstrated numerous biological reactions that occur in confined molecular pockets. By the virtue of various enzyme molecules present in the system, many conversions are so selective and specific that they are hard to be attained in bulk reaction. Till date different classes of porous molecular vessels (discrete and extended) are designed and developed to achieve high catalytic activity and stereo-selectivity. The prime motivation of supramolecular

chemists to develop molecular cages with inherent porosity and robust structural backbones, so it can mimic the complex functions like natural enzymes. In this regard, various unique design strategies are established to induce enantioselectivity within reactants and products via supramolecular catalysis. The significant feature of such enantiopure **MOCs** is the generation of chiral catalytic products followed by their selective separation. This Book Chapter mainly highlights the selective and efficient catalytic ability of supramolecular host molecules to function as reaction flasks in diverse solvent mediums.

Supramolecular chemistry has emerged as a foundation stone in organic self-assembly process after the trailblazing findings by Lehn, Cram, and Pedersen. Afterward, Fujita and co-workers initiated the coordination-driven self-assembly exploiting various organic ligands with suitable metal counterparts. For the first time, various two- and three-dimensional water-soluble molecular assemblies were developed with different shapes and sizes. These porous and discrete **MOC** compounds were further explored not only in host–guest chemistry but also in many challenging stereoselective organic transformations in water. Later, Raymond, Bergman, Toste and co-workers have established the negatively charged coordination molecular systems, which competently demonstrate the cationic mediated cyclization reactions in the aqueous medium. Despite such upgraded catalytic efficiency with excellent regioselectivity, in several cases the final product exhibited better host–guest interactions compare to the reactant molecules due to their spatial orientations. As a result, the key drawback associated with these catalytic organic transformations is the usage of desired host molecules in stoichiometric amounts. Subsequently, Mukherjee and co-workers developed various barrel-shaped molecular assemblies employing suitable square planar metal counterparts with functionalized organic donors to address this catalytic issue. The reported molecular barrels are comprised with two open windows for facile entry/exit of substrates and products effectively. In recent times, several other research groups demonstrated the impactful roles of attached auxiliary functional moieties inside the confined nanoreactor which exhibited enhanced catalytic turn-over number both in organic and aqueous medium. In this chapter, several unique strategies and drawbacks associated in supramolecular catalysis are elaborately discussed.

Metal-ligand coordination-driven self-assembly process for the design and synthesis of numerous 3D molecular architectures is currently a vibrant area of research. These richly diverse array of supramolecular host structures delivers a strong viewpoint for the development of various catalytic transformations in confined space. Notably, with the rise of water-soluble discrete molecular vessels, supramolecular catalysis in confined cavity heading toward the green chemistry. Moreover, it well established that the high effective concentrations and restricted degree of freedom of the substrates inside the confined cavity generate unusual and unique catalytic products which is irrational in bulk medium reaction. Also, we expect chiral molecular cages will display new reactivity during intermediates or transition states stabilization which enhances

the enantiomeric excess of catalytic products. In this regard, such coordination cage systems can be further improved to execute asymmetric supramolecular catalysis with high chemo- and stereo-selectivity. Likewise, these porous **MOCs** can be combined with various solid supports to formulate hybrid heterogeneous catalyst which will display higher durability and reusability. Similarly, larger host molecules can easily be employed for multicomponent catalytic reactions and can offers enhanced substrate scope in the confined cavity. In recent times, incorporation of active transition metal complexes in MOCs becomes an exciting area of reaction mechanism study and their potentials in modern era of catalysis is till unexplored.

In this regard, it can be presumed that the interplay between supramolecular catalysis and organometallic chemistry will apparently create a fertile ground for the modern artificial catalysts in near future. In short, supramolecular catalysis is a prosperous research area with several persuasive parameters, which will offer cutting-edge tools for emerging applied areas of industrial, environmental, chemical, and biological synthesis.

Acknowledgments

I sincerely grateful to Central Library, Guru Ghasidas Vishwavidyalaya, Bilaspur (India) for the access of various research journals and books. I also thankful to Dr. Rupak Saha and Dr. S. Shanmugaraju for their valuable comments and supports.

References

[1] J.W. Szostak, D.P. Bartel, P.L. Luisi, Synthesizing life, Nature 409 (2001) 387–390.
[2] P. Egan, R. Sinko, P.R. LeDuc, S. Keten, The role of mechanics in biological and bio-inspired systems, Nat. Commun. 6 (2015) 1–12.
[3] B. Kuhlman, P. Bradley, Advances in protein structure prediction and design, Nat. Rev. Mol. Cell Biol. 20 (2019) 681–697.
[4] R. Gatenby, B.R. Frieden, Investigating information dynamics in living systems through the structure and function of enzymes, PLoS One 11 (2016) e0154867.
[5] W. Tong, Analyzing the biology on the system level, Genom. Proteom. Bioinform. 2 (2004) 6–14.
[6] R. Wolfenden, Degrees of difficulty of water-consuming reactions in the absence of enzymes, Chem. Rev. 106 (2006) 3379–3396.
[7] A. Radzicka, R. Wolfenden, A proficient enzyme, Science 267 (1995) 90–93.
[8] N.S. Punekar, Enzymes: Catalysis, Kinetics and Mechanisms, Springer, India, 2018.
[9] S.J. Benkovic, S. Hammes-Schiffer, A perspective on enzyme catalysis, Science 301 (2003) 1196–1202.
[10] J. Dundas, L. Adamian, J. Liang, Structural signatures of enzyme binding pockets from order-independent surface alignment: a study of metalloendopeptidase and NAD binding proteins, J. Mol. Biol. 406 (2011) 713–729.

[11] M. Gao, J. Skolnick, A comprehensive survey of small-molecule binding pockets in proteins, PLoS Comput. Biol. 9 (2013) e1003302.
[12] S.-i. Shoda, H. Uyama, J.-i. Kadokawa, S. Kimura, S. Kobayashi, Enzymes as green catalysts for precision macromolecular synthesis, Chem. Rev. 116 (2016) 2307–2413.
[13] M. Raynal, P. Ballester, A. Vidal-Ferran, P.W.N.M. van Leeuwen, Supramolecular catalysis. Part 1: non-covalent interactions as a tool for building and modifying homogeneous catalysts, Chem. Soc. Rev. 43 (2014) 1660–1733.
[14] M. Raynal, P. Ballester, A. Vidal-Ferran, P.W.N.M. Van Leeuwen, Supramolecular catalysis. Part 2: artificial enzyme mimics, Chem. Soc. Rev. 43 (2014) 1734–1787.
[15] M.J. Wiester, P.A. Ulmann, C.A. Mirkin, Enzyme mimics based upon supramolecular coordination chemistry, Angew. Chem. Int. Ed. 50 (2011) 114–137.
[16] C.J. Brown, F.D. Toste, R.G. Bergman, K.N. Raymond, Supramolecular catalysis in metal–ligand cluster hosts, Chem. Rev. 115 (2015) 3012–3035.
[17] T.S. Koblenz, J. Wassenaar, J.N.H. Reek, Reactivity within a confined self-assembled nanospace, Chem. Soc. Rev. 37 (2008) 247–262.
[18] D.M. Vriezema, M. Comellas Aragonès, J.A.A.W. Elemans, J.J.L.M. Cornelissen, A.E. Rowan, R.J.M. Nolte, Self-assembled nanoreactors, Chem. Rev. 105 (2005) 1445–1490.
[19] M.D. Nothling, Z. Xiao, A. Bhaskaran, M.T. Blyth, C.W. Bennett, M.L. Coote, L.A. Connal, Synthetic catalysts inspired by hydrolytic enzymes, ACS Catal. 9 (2018) 168–187.
[20] J. Meeuwissen, J.N.H. Reek, Supramolecular catalysis beyond enzyme mimics, Nat. Chem. 2 (2010) 615–621.
[21] M. Morimoto, S.M. Bierschenk, K.T. Xia, R.G. Bergman, K.N. Raymond, F.D. Toste, Advances in supramolecular host-mediated reactivity, Nat. Catal. 3 (2020) 969–984.
[22] R. Chakrabarty, P.S. Mukherjee, P.J. Stang, Supramolecular coordination: self-assembly of finite two-and three-dimensional ensembles, Chem. Rev. 111 (2011) 6810–6918.
[23] D. Zhang, T.K. Ronson, J.R. Nitschke, Functional capsules via subcomponent self-assembly, Acc. Chem. Res. 51 (2018) 2423–2436.
[24] S.R. Seidel, P.J. Stang, High-symmetry coordination cages via self-assembly, Acc. Chem. Res. 35 (2002) 972–983.
[25] A.K. Bar, R. Chakrabarty, G. Mostafa, P.S. Mukherjee, Self-assembly of a nanoscopic Pt12Fe12 heterometallic open molecular box containing six porphyrin walls, Angew. Chem. 120 (2008) 8583–8587.
[26] E.G. Percástegui, T.K. Ronson, J.R. Nitschke, Design and applications of water-soluble coordination cages, Chem. Rev. 120 (2020) 13480–13544.
[27] M.D. Pluth, K.N. Raymond, Reversible guest exchange mechanisms in supramolecular host–guest assemblies, Chem. Soc. Rev. 36 (2007) 161–171.
[28] S. Yadav, P. Kannan, G. Qiu, Cavity-based applications of metallo-supramolecular coordination cages (MSCCs), Org. Chem. Front. 7 (2020) 2842–2872.
[29] H. Sepehrpour, W. Fu, Y. Sun, P.J. Stang, Biomedically relevant self-assembled metallacycles and metallacages, J. Am. Chem. Soc. 141 (2019) 14005–14020.
[30] I. Sinha, P.S. Mukherjee, Chemical transformations in confined space of coordination architectures, Inorg. Chem. 57 (2018) 4205–4221.
[31] J.W. Steed, J.L. Atwood, Supramolecular Chemistry, John Wiley & Sons, United Kingdom, 2013.
[32] S.J. Benkovic, S. Hammes-Schiffer, A perspective on enzyme catalysis, Science 301 (2003) 1196–1202.

[33] A. Schmid, J.S. Dordick, B. Hauer, A. Kiener, M. Wubbolts, B. Witholt, Industrial biocatalysis today and tomorrow, Nature 409 (2001) 258–268.

[34] X. Chen, H. Jiang, B. Hou, W. Gong, Y. Liu, Y. Cui, Boosting chemical stability, catalytic activity, and enantioselectivity of metal–organic frameworks for batch and flow reactions, J. Am. Chem. Soc. 139 (2017) 13476–13482.

[35] O.I. Kolodiazhnyi, Multiple stereoselectivity and its application in organic synthesis, Tetrahedron 32 (2003) 5953–6018.

[36] C.S. Wood, T.K. Ronson, A.M. Belenguer, J.J. Holstein, J.R. Nitschke, Two-stage directed self-assembly of a cyclic [3]catenane, Nat. Chem. 7 (2015) 354–358.

[37] T.K. Ronson, S. Zarra, S.P. Black, J.R. Nitschke, Metal–organic container molecules through subcomponent self-assembly, Chem. Commun. 49 (2013) 2476–2490.

[38] N. Mittal, M.L. Saha, M. Schmittel, A seven-component metallosupramolecular quadrilateral with four different orthogonal complexation vertices, Chem. Commun. 51 (2015) 15514–15517.

[39] S.J. Dalgarno, N.P. Power, J.L. Atwood, Metallo-supramolecular capsules, Coord. Chem. Rev. 252 (2008) 825–841.

[40] M. Fujita, M. Tominaga, A. Hori, B. Therrien, Coordination assemblies from a Pd (II)-cornered square complex, Acc. Chem. Res. 38 (2005) 369–378.

[41] J.-M. Lehn, Towards complex matter: supramolecular chemistry and self-organization, Euro. Rev. 17 (2009) 263–280.

[42] S. Leininger, B. Olenyuk, P.J. Stang, Self-assembly of discrete cyclic nanostructures mediated by transition metals, Chem. Rev. 100 (2000) 853–908.

[43] D. Philp, J.F. Stoddart, Self-assembly in natural and unnatural systems, Angew. Chem. Int. Ed. Engl. 35 (1996) 1154–1196.

[44] X. Yan, X. Chi, P. Wei, M. Zhang, F. Huang, [n] Pseudorotaxanes (n= 2, 3) from Self-Assembly of Two Cryptands and a 1, 2-Bis (4-pyridinium) ethane Derivative, Eur. J. Org. Chem. 2012 (2012) 6351–6356.

[45] F. Reichel, J.K. Clegg, K. Gloe, K. Gloe, J.J. Weigand, J.K. Reynolds, C.-G. Li, J.R. Aldrich-Wright, C.J. Kepert, L.F. Lindoy, Self-assembly of an imidazolate-bridged FeIII/CuII heterometallic cage, Inorg. Chem. 53 (2014) 688–690.

[46] S.M. Jansze, G. Cecot, M.D. Wise, K.O. Zhurov, T.K. Ronson, A.M. Castilla, A. Finelli, P. Pattison, E. Solari, R. Scopelliti, Ligand aspect ratio as a decisive factor for the self-assembly of coordination cages, J. Am. Chem. Soc. 138 (2016) 2046–2054.

[47] N.B. Debata, D. Tripathy, D.K. Chand, Self-assembled coordination complexes from various palladium (II) components and bidentate or polydentate ligands, Coord. Chem. Rev. 256 (2012) 1831–1945.

[48] M. Fujita, D. Oguro, M. Miyazawa, H. Oka, K. Yamaguchi, K. Ogura, Self-assembly of ten molecules into nanometre-sized organic host frameworks, Nature 378 (1995) 469–471.

[49] M. Yoshizawa, Y. Takeyama, T. Kusukawa, M. Fujita, Cavity-directed, highly stereoselective [2+ 2] photodimerization of olefins within self-assembled coordination cages, Angew. Chem. Int. Ed. 41 (2002) 1347–1349.

[50] Y. Nishioka, T. Yamaguchi, M. Yoshizawa, M. Fujita, Unusual [2+ 4] and [2+ 2] cycloadditions of arenes in the confined cavity of self-assembled cages, J. Am. Chem. Soc. 129 (2007) 7000–7001.

[51] T. Murase, S. Horiuchi, M. Fujita, Naphthalene Diels− Alder in a self-assembled molecular flask, J. Am. Chem. Soc. 132 (2010) 2866–2867.

[52] S. Horiuchi, Y. Nishioka, T. Murase, M. Fujita, Both [2+ 2] and [2+ 4] additions of inert aromatics via identical ternary host–guest complexes, Chem. Commun. 46 (2010) 3460–3462.
[53] S. Horiuchi, T. Murase, M. Fujita, Diels–Alder reactions of inert aromatic compounds within a self-assembled coordination cage, Chem. Asian J. 6 (2011) 1839–1847.
[54] Y. Fang, T. Murase, M. Fujita, Cavity-promoted Diels–Alder reactions of unsubstituted naphthalene: fine reactivity tuning by cavity shrinkage, Chem. Lett. 44 (2015) 1095–1097.
[55] M. Yoshizawa, M. Tamura, M. Fujita, Diels-Alder in aqueous molecular hosts: unusual regioselectivity and efficient catalysis, Science 312 (2006) 251–254.
[56] T. Murase, H. Takezawa, M. Fujita, Photo-driven anti-Markovnikov alkyne hydration in self-assembled hollow complexes, Chem. Commun. 47 (2011) 10960–10962.
[57] T. Murase, Y. Nishijima, M. Fujita, Unusual photoreaction of Triquinacene within self-assembled hosts, Chem. Asian J. 7 (2012) 826–829.
[58] T. Murase, Y. Nishijima, M. Fujita, Cage-catalyzed Knoevenagel condensation under neutral conditions in water, J. Am. Chem. Soc. 134 (2012) 162–164.
[59] B. Roy, A.K. Ghosh, S. Srivastava, P. D'Silva, P.S. Mukherjee, A Pd8 tetrafacial molecular barrel as carrier for water insoluble fluorophore, J. Am. Chem. Soc. 137 (2015) 11916–11919.
[60] P. Howlader, B. Mondal, P.C. Purba, E. Zangrando, P.S. Mukherjee, Self-assembled Pd (II) barrels as containers for transient merocyanine form and reverse thermochromism of spiropyran, J. Am. Chem. Soc. 140 (2018) 7952–7960.
[61] R. Saha, A. Devaraj, S. Bhattacharyya, S. Das, E. Zangrando, P.S. Mukherjee, Unusual behavior of donor–acceptor Stenhouse adducts in confined space of a water-soluble PdII8 molecular vessel, J. Am. Chem. Soc. 141 (2019) 8638–8645.
[62] I.A. Bhat, R. Jain, M.M. Siddiqui, D.K. Saini, P.S. Mukherjee, Water-soluble Pd8L4 self-assembled molecular barrel as an aqueous carrier for hydrophobic curcumin, Inorg. Chem. 56 (2017) 5352–5360.
[63] D. Samanta, S. Mukherjee, Y.P. Patil, P.S. Mukherjee, Self-assembled Pd6 open cage with triimidazole walls and the use of its confined nanospace for catalytic Knoevenagel-and Diels–Alder reactions in aqueous medium, Chem. Eur. J. 18 (2012) 12322–12329.
[64] K. Ono, M. Yoshizawa, T. Kato, M. Fujita, Three-metal-center spin interactions through the intercalation of metal azaporphines and porphines into an organic pillared coordination box, Chem. Commun. (2008) 2328–2330.
[65] J. Lee, K. Ghosh, P.J. Stang, Stoichiometric control of multiple different tectons in coordination-driven self-assembly: preparation of fused metallacyclic polygons, J. Am. Chem. Soc. 131 (2009) 12028–12029.
[66] A.K. Bar, G. Mostafa, P.S. Mukherjee, A Pd6 molecular Cage via multicomponent self-assembly incorporating both neutral and anionic linkers, Inorg. Chem. 49 (2010) 7647–7649.
[67] D. Samanta, P.S. Mukherjee, Multicomponent self-sorting of a Pd 7 molecular boat and its use in catalytic Knoevenagel condensation, Chem. Commun. 49 (2013) 4307–4309.
[68] R.N. Dsouza, U. Pischel, W.M. Nau, Fluorescent dyes and their supramolecular host/guest complexes with macrocycles in aqueous solution, Chem. Rev. 111 (2011) 7941–7980.
[69] S. Ray, A. Bhaumik, M. Pramanik, R.J. Butcher, S.O. Yildirim, C. Mukhopadhyay, Binary conjugate Brønsted–Lewis acid supported on mesoporous silica nanoparticles for the domino

addition/elimination/addition and addition/elimination/addition/cyclization cascade, Catal. Commun. 43 (2014) 173–178.

[70] P. Das, A. Kumar, P. Howlader, P.S. Mukherjee, A self-assembled trigonal prismatic molecular vessel for catalytic dehydration reactions in water, Chem. Eur. J. 23 (2017) 12565–12574.

[71] Y. Kim, W. Li, S. Shin, M. Lee, Development of toroidal nanostructures by self-assembly: rational designs and applications, Acc. Chem. Res. 46 (2013) 2888–2897.

[72] B. Roy, A. Devaraj, R. Saha, S. Jharimune, K.W. Chi, P.S. Mukherjee, Catalytic intramolecular cycloaddition reactions by using a discrete molecular architecture, Chem. Eur. J. 23 (2017) 15704–15712.

[73] L.F. Tietze, Domino reactions in organic synthesis, Chem. Rev. 96 (1996) 115–136.

[74] R. Saha, A. Devaraj, S. Bhattacharyya, S. Das, E. Zangrando, P.S. Mukherjee, Unusual behavior of donor–acceptor Stenhouse adducts in confined space of a water-soluble PdII8 molecular vessel, J. Am. Chem. Soc. 141 (2019) 8638–8645.

[75] M. Amireddy, K. Chen, Organocatalytic synthesis of spirocyclohexane indane-1, 3-diones via a chiral squaramide-catalyzed Michael/aldol cascade reaction of γ-nitro ketones and 2-arylideneindane-1, 3-diones, Tetrahedron 71 (2015) 8003–8008.

[76] H. Duan, Z. Chen, L. Han, Y. Feng, Y. Zhu, S. Yang, Palladium-catalyzed chemoselective synthesis of indane-1, 3-dione derivatives via tert-butyl isocyanide insertion, Org. Biomol. Chem. 13 (2015) 6782–6788.

[77] W. Meng, A.B. League, T.K. Ronson, J.K. Clegg, W.C. Isley Iii, D. Semrouni, L. Gagliardi, C.J. Cramer, J.R. Nitschke, Empirical and theoretical insights into the structural features and host–guest chemistry of M8L4 Tube Architectures, J. Am. Chem. Soc. 136 (2014) 3972–3980.

[78] G. Cecot, M. Marmier, S. Geremia, R. De Zorzi, A.V. Vologzhanina, P. Pattison, E. Solari, F. Fadaei Tirani, R. Scopelliti, K. Severin, The intricate structural chemistry of MII2 n L n-Type assemblies, J. Am. Chem. Soc. 139 (2017) 8371–8381.

[79] I.A. Bhat, A. Devaraj, E. Zangrando, P.S. Mukherjee, A Discrete self-assembled Pd12 triangular orthobicupola cage and its use for intramolecular cycloaddition, Chem. Eur. J. 24 (2018) 13938–13946.

[80] F. Ibukuro, T. Kusukawa, M. Fujita, A thermally switchable molecular lock. Guest-templated synthesis of a kinetically stable nanosized cage, J. Am. Chem. Soc. 120 (1998) 8561–8562.

[81] N. Takeda, K. Umemoto, K. Yamaguchi, M. Fujita, A nanometre-sized hexahedral coordination capsule assembled from 24 components, Nature 398 (1999) 794–796.

[82] I.A. Bhat, A. Devaraj, P. Howlader, K.-W. Chi, P.S. Mukherjee, Preparation of a chiral Pt 12 tetrahedral cage and its use in catalytic Michael addition reaction, Chem. Commun. 54 (2018) 4814–4817.

[83] T.K. Ronson, S. Zarra, S.P. Black, J.R. Nitschke, Metal–organic container molecules through subcomponent self-assembly, Chem. Commun. 49 (2013) 2476–2490.

[84] T.K. Ronson, D.A. Roberts, S.P. Black, J.R. Nitschke, Stacking interactions drive selective self-assembly and self-sorting of pyrene-based MII4L6 architectures, J. Am. Chem. Soc. 137 (2015) 14502–14512.

[85] J.-P. Bourgeois, M. Fujita, M. Kawano, S. Sakamoto, K. Yamaguchi, A cationic guest in a 24+ cationic host, J. Am. Chem. Soc. 125 (2003) 9260–9261.

[86] P. Howlader, P.S. Mukherjee, Face and edge directed self-assembly of Pd 12 tetrahedral nano-cages and their self-sorting, Chem. Sci. 7 (2016) 5893–5899.

[87] Z. Zhang, P.R. Schreiner, Thio) urea organocatalysis—What can be learnt from anion recognition? Chem. Soc. Rev. 38 (2009) 1187–1198.
[88] D. Samanta, P.S. Mukherjee, Pt II 6 nanoscopic cages with an organometallic backbone as sensors for picric acid, Dalton Trans. 42 (2013) 16784–16795.
[89] P. Howlader, P. Das, E. Zangrando, P.S. Mukherjee, Urea-functionalized self-assembled molecular prism for heterogeneous catalysis in water, J. Am. Chem. Soc. 138 (2016) 1668–1676.
[90] M. Yoshizawa, J.K. Klosterman, M. Fujita, Functional molecular flasks: new properties and reactions within discrete, self-assembled hosts, Angew. Chem. Int. Ed. 48 (2009) 3418–3438.
[91] L.-X. Cai, S.-C. Li, D.-N. Yan, L.-P. Zhou, F. Guo, Q.-F. Sun, Water-soluble redox-active cage hosting polyoxometalates for selective desulfurization catalysis, J. Am. Chem. Soc. 140 (2018) 4869–4876.
[92] S.-S. Wang, G.-Y. Yang, Recent advances in polyoxometalate-catalyzed reactions, Chem. Rev. 115 (2015) 4893–4962.
[93] S.-C. Li, L.-X. Cai, L.-P. Zhou, F. Guo, Q.-F. Sun, Supramolecular synthesis of coumarin derivatives catalyzed by a coordination-assembled cage in aqueous solution, Sci. China Chem. 62 (2019) 713–718.
[94] S. Kandambeth, K. Dey, R. Banerjee, Covalent organic frameworks: chemistry beyond the structure, J. Am. Chem. Soc. 141 (2018) 1807–1822.
[95] Z. Wang, C.B. Reddy, X. Zhou, J.J. Ibrahim, Y. Yang, Phosphine-built-in porous organic cage for stabilization and boosting the catalytic performance of palladium nanoparticles in cross-coupling of aryl halides, ACS Appl. Mater. Interfaces 12 (2020) 53141–53149.
[96] S. Lu, Y. Hu, S. Wan, R. McCaffrey, Y. Jin, H. Gu, W. Zhang, Synthesis of ultrafine and highly dispersed metal nanoparticles confined in a thioether-containing covalent organic framework and their catalytic applications, J. Am. Chem. Soc. 139 (2017) 17082–17088.
[97] Y. Zhou, Z. Xiang, D. Cao, C.-J. Liu, Covalent organic polymer supported palladium catalysts for CO oxidation, Chem. Commun. 49 (2013) 5633–5635.
[98] B. Mondal, P.S. Mukherjee, Cage encapsulated gold nanoparticles as heterogeneous photocatalyst for facile and selective reduction of nitroarenes to azo compounds, J. Am. Chem. Soc. 140 (2018) 12592–12601.
[99] N. Sun, C. Wang, H. Wang, L. Yang, P. Jin, W. Zhang, J. Jiang, Multifunctional tubular organic cage-supported ultrafine palladium nanoparticles for sequential catalysis, Angew. Chem. 131 (2019) 18179–18184.
[100] B. Mondal, P. Bhandari, P.S. Mukherjee, Nucleation of tiny silver nanoparticles by using a tetrafacial organic molecular barrel: potential use in visible-light-triggered photocatalysis, Chem. Eur. J. 26 (2020) 15007–15015.

Chapter 15

Anion sensing applications of supramolecular coordination complexes

Muniyappan Boominathan and Murugan Arunachalam
Department of Chemistry, The Gandhigram Rural Institute (Deemed to be University), Gandhigram, Dindigul, India

15.1 Introduction

Supramolecular chemistry deals with complex molecular systems self-assembled from small molecular components *via* noncovalent interactions [1]. Supramolecular complexes exhibit entirely different properties and due to the dynamic and reversible nature of supramolecular interactions, they are responsive to external stimuli. Fabrication of supramolecular nanoobjects for the selective and sensitive detection of analytes stands as a central objective in modern chemistry. Significant progress has been made in the past three decades in the area of molecular sensors for specific analytes [2]. From an environmental perspective, higher concentration of specific anions in drinking water, food, and beverages are of health concern whereas pollutant anions have been linked to carcinogenesis and are also a matter of environmental concern [3,4]. Though anions are ubiquitous in the natural world and play vital role in chemistry and biology, their binding features went unrecognized as to the extent of metal ions and great deal of attention has been recently made to develop artificial receptors and sensors for anions [5].

15.2 Anion receptors

Synthetic anion receptors were developed toward their applications in removal of pollutants from drinking water, as sensors for environmental and biologically relevant anions [6]. The design of anion receptors is particularly challenging when compared to the design of receptors for cations. Despite the early discovery of the katapinands [7], noncovalent anion coordination chemistry is relatively slow to develop in comparison with the development of hosts

Supramolecular Coordination Complexes: Design, Synthesis, and Applications.
DOI: https://doi.org/10.1016/B978-0-323-90582-4.00003-8

for cations and even neutral molecules. Anions are pH sensitive, larger than the isoelectronic cations and they have low charge-to-radius ratio and hence the electrostatic interactions are less effective compared to their isoelectronic cations. Among anion binding interactions, electrostatic interactions play key role in stabilizing anions in solution. Anion receptor has to compete with the polar protic solvation shell surrounding the target anions to stabilize them. In general, anion binding by neutral receptors *via* hydrogen bonding interactions is comparatively weaker in polar protic solvents than anion recognition by charged receptor *via* electrostatic interactions. Charged receptors are capable to compete effectively with polar solvents and stabilize anion by means of electrostatic interactions.

15.3 Anion sensors

Biological and environmental significance of anions has led to the development of chemosensors for the selective detection of anions, and this has emerged as an important area of research in supramolecular chemistry [8–11]. Luminescent anion sensors possess appealing advantages as diagnostic tool in biological systems over other chemosensors in terms of their sensitivity [12]. The role of a chemical sensor is to convert the binding event of an analyte to spectroscopic signal transduction to detect through optical, fluorescent, and electrochemical responses. The essential characteristics of anion sensors are selectivity, that is, the preferential binding of a particular anion over the broad range of anions of different size and geometry. A typical chemosensor is designed in such a way that the signaling unit is linked to the anion binding site which translates the anion binding event to sensory response.

Efforts have been made to integrate metal ions with organic receptors to make use of metal ion to build receptor frameworks or as anion binding element in more competitive environment [13]. This chapter is meant to give an overview on applications of anion sensors based on supramolecular coordination complexes. A variety of chemosensors have been developed so far with different ways of operation. In this chapter, anion sensors are broadly classified into different categories as follows: (1) metal extrusion assays, (2) ternary anion-coordination complexes, (3) indicator displacement assays, (4) luminescent metal complex-based anion receptors, (5) luminescent lanthanide complexes, (6) mechanically interlocked anion sensors. Anion sensors are categorized in this chapter based on the role of metal ions, the mode of binding of anion to the metal center as well as the molecular architecture of the chemosensor.

15.3.1 Metal extrusion assays

In addition to the contribution of metal ions in organizing the supramolecular self-assembly, the anion's ability to form coordination bond with metal ions

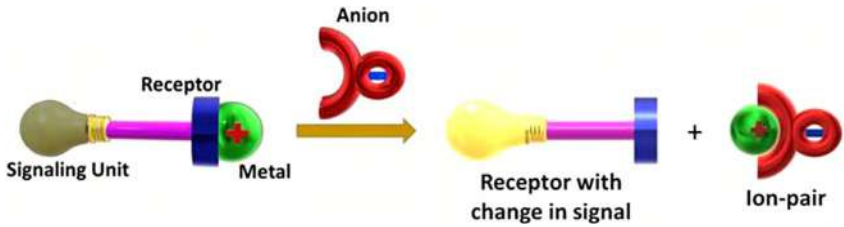

FIGURE 15.1 Cartoon showing the mechanism of metal extrusion assays.

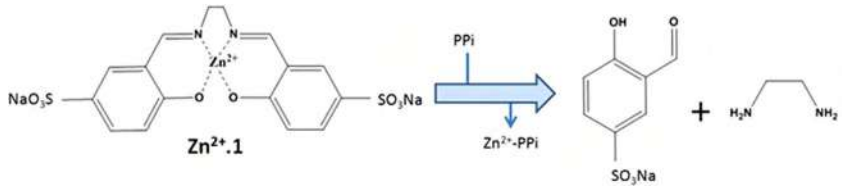

FIGURE 15.2 Scheme showing metal extrusion mechanism in **Zn^{2+}.1** by pyrophosphate (PPi) anion [15].

make use of them as versatile anion binding site. The previously coordinated metal ion to the ligand is displaced from the binding site of the ligand. The change from the coordinated to noncoordinated state of the supramolecular complex upon binding of anion to the metal ion induces signal transduction and display colorimetric/fluorometric response to detect the respective anions. In this type of chemosensors, the association constant for the binding of anion to the metal should be more than that of the binding of metal ion to ligand. Changes in colorimetric and fluorescent sensory output were detected when anions coordinate with metal ions in coordination complexes. The selectivity of the receptor mainly relies on the preorganization of the receptor, position of the anion binding site, and cavity size of the receptor molecules. Upon coordination with metal ion, the anion may displace the metal ion and free-up the ligand by forming metal salt which result the free ligand to regenerate its sensory response, as shown in Fig. 15.1.

Zelder et al. demonstrated a Zn^{II}-salen complex (**Zn^{2+}.1**) as a locked fluorescent phosphate anion probe by novel disassembly strategy, as shown in Fig. 15.2 [14]. This approach utilized the high affinity of phosphates toward Zn(II) ion and the instability of free salen ligand (**1**) under physiological conditions. Upon displacement of Zn(II) by anions, the unstable free base salen ligand (**1**) disassemble by fast hydrolysis into its corresponding salicylaldehyde subunits which under physiological pH "turn-ON" green fluorescence.

Chen and co-workers demonstrated benzothiazole-based fluorescent probe **2** for the selective detection of Zn^{2+} ion in living cell and further they explored **Zn^{2+}.2** complex for selective pyrophosphate (PPi) sensing in HEPES buffer

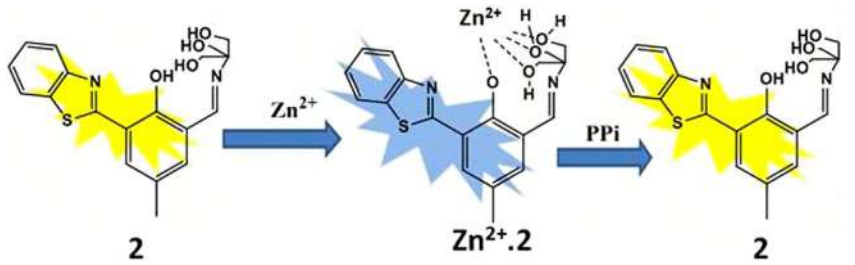

FIGURE 15.3 Mechanism showing the operation of metal extrusion-based fluorescence ON-OFF-ON probe [15].

solution (Fig. 15.3) [15]. The main advantage of this probe is that it could detect pyrophosphate anion in a solution with a concentration as low as 60 nM and hence can be used to monitor enzyme-catalyzed degradation of pyrophosphate anion in the biological system.

15.3.2 Ternary anion-coordination complexes

The tendency of anions to coordinate with metal ions is used to detect through colorimetric or fluorometric response of the coordination complex. Anion sensors where anions coordinated with metal ions have been nicely reviewed [16]. Characteristic colors of metal complexes are changed due to the perturbances of the electronic structures of metal complexes upon coordination of anions to the vacant binding site of metal ion. The sensitivity of anion sensors of this type are mainly determined by the sensitivity of the receptors toward a particular cation. This can be tuned by the appropriate choice of metal ion, the basicity of the ligand, and size of the anion binding pocket. Among various metal complexes, Zn(II)-dipicolylamine metal–ligand systems are the most commonly studied metal ions for the binding and sensing of anions especially biologically relevant phosphate derivatives [17]. Pioneering work by Hamachi and co-workers [18] on of dipicolylamine ligand-based fluorescent Zn(II) complexes explored their utility as selective sensors for phosphates and its derivatives (Fig. 15.4) with very high binding affinity.

As a representative of Zn(II)-dipicolylamine complexes based anion sensors, only selected examples are shown in Fig. 15.4 [19]. The tridendate dipicolylamine ligand selectively complex with Zn(II) ion and leave the fourth coordination vacant for the binding of anion or labile solvent molecules. In **2Zn^{2+}.3**, the fluorescence of anthracene motif is quenched by photoinduced electron transfer (PET) mechanism. The cancelling of PET mechanism upon binding with zinc metal ions enhances the fluorescent output of anthracene unit in **3**. The binding of the second zinc metal ion is facilitated by the phosphate anion present in the solution (Fig. 15.5). Zn(II)-dipicolylamine complexes **Zn^{2+}.4,**

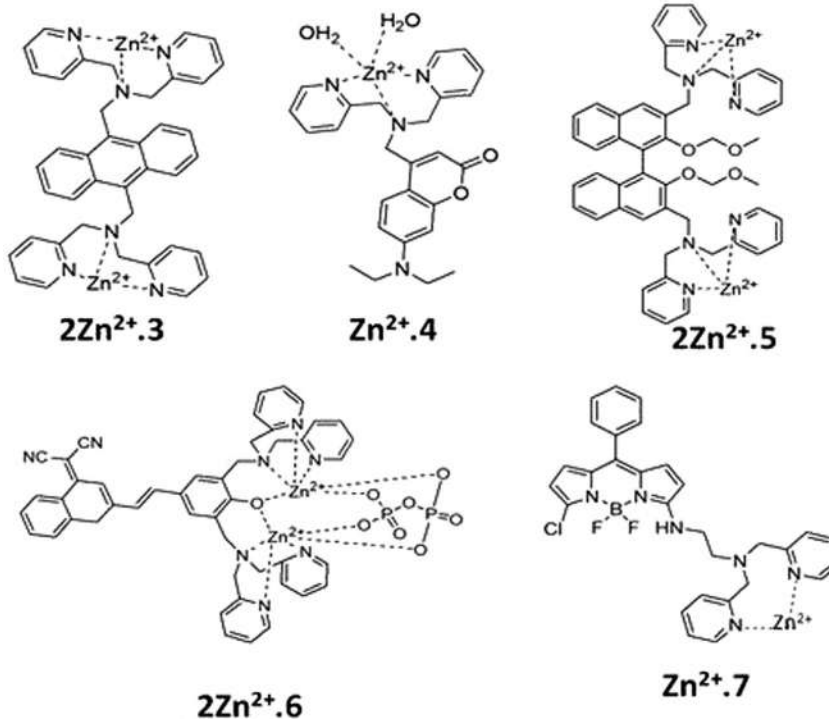

FIGURE 15.4 Reperesentative Zn^{2+}-dipicolylamine-based chemosensors for anions [19].

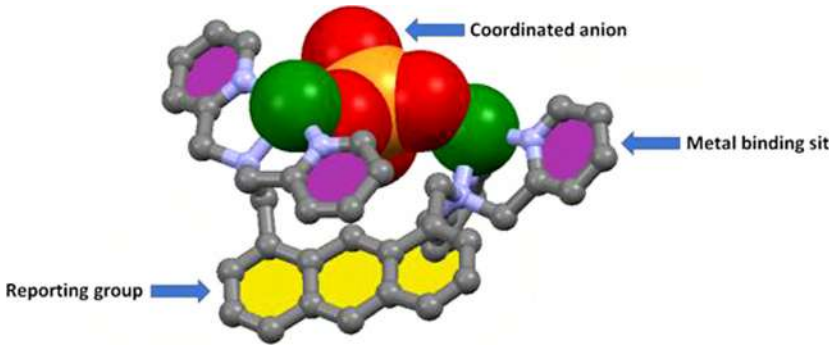

FIGURE 15.5 Graphics showing the ligand-metal-anion ternary complex formation in **$2Zn^{2+}$.3.** Color code: C, grey; N, blue; Zn, green, P, orange and O, red.

$2Zn^{2+}$.5, $2Zn^{2+}$.6, and **Zn^{2+}.7** (Fig. 15.4) showed selectivity toward biological phosphates in aqueous media [19]. Convenient synthesis and easy incorporation on the suitable scaffold facilitated the development of anion sensors based on dipicolylamine ligands.

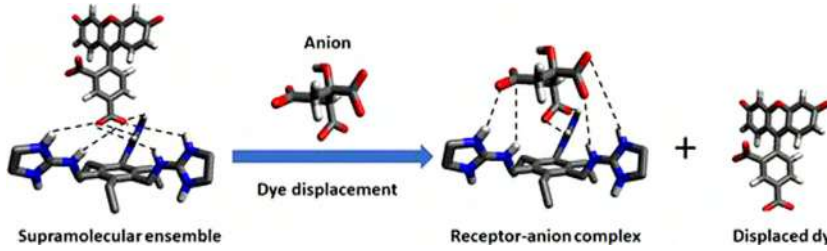

FIGURE 15.6 Schematic diagram showing the mechanism of indicator displacement approach [22].

15.3.3 Indicator displacement assays

Indicator displacement assay is nothing but a supramolecular ensemble consisting of noncovalently connected optical/fluorescent guest molecule [20]. Unlike traditional anion sensors, this strategy offers a unique approach for the sensing of anionic analytes of biological and environmental significance [21]. The anion binding unit and the signal transducers such as dye molecules are assembled in the form of ternary complex involving metalloreceptor, metal(s), and anionic dye. Upon complexation with the targeted anion, the anion might displace the indicator which could be visualized by the original optical/fluorescent signals of the uncomplexed dye molecule (Fig. 15.6) [22]. The indicator displacement approach has several advantages over the conventional chemosensors. The first and foremost advantage is that this approach does not require extensive synthesis to covalently connect the dye onto the anion receptor. The selectivity and sensitivity of the detection could be fine-tuned by choosing suitable dye molecule. The dyes employed in the indicator displacement approach could be colorimetric or fluorimetric in nature. Anion sensors based on the indicator displacement assay approach have been extensively reviewed [21].

15.3.4 Luminescent metal complex-based anion receptors

Incorporation of metal complexes as signaling unit on to the anion receptor is another attractive strategy to develop anion sensors. Coordination complexes linked to the anion binding functional groups could act as a signal transducer and show colorimetric and fluorescence response upon binding with anions. Luminescent metal complexes with strong metal–ligand coordination and are functionalized with anion-binding elements comes under this category of anion sensors. Compound **8** represents one of the first metal-centered anion receptor in which terpyridyl ligands coordinate with Ru(II) and thiourea functional group act as a anion-binding element for dicarboxylate anions especially pimelate ion (Fig. 15.7) [23].

Ru(II)-polypyridyl complexes have been extensively utilized for the development of chemosensors for anions due to their luminescent and electrochemical

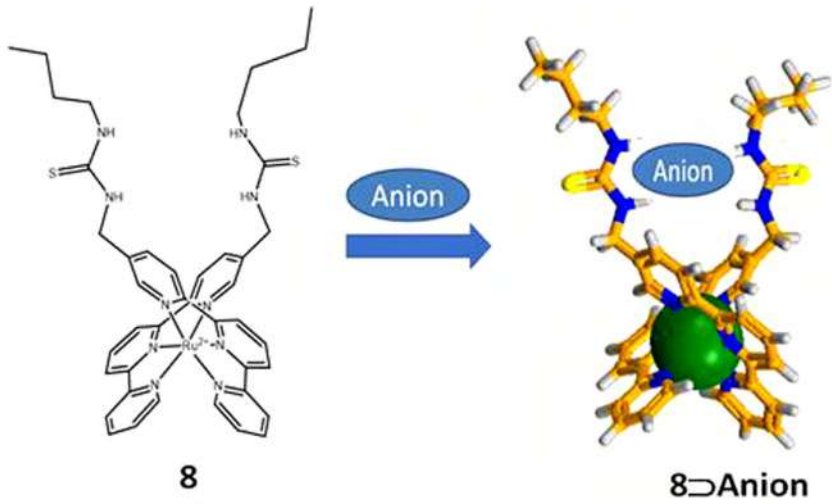

FIGURE 15.7 Schematic diagram showing the recognition of anions by Ruthenium(II)-polypyridyl complex-based luminescent metallo-receptor **8** [23].

characteristics [24–26]. The photophysical characteristics of these complexes are often modified by manipulating the ligand structures and by the introduction of coligands in the complexes. Ruthenium complexes derived from rigid and preorganized bidendate chelating ligands such as bipyridine, terpyridine, and phenanthroline-type form complexes which absorb visible light, form long-lived excited states, and display good photochemical stability [24–26]. Incorporation of anion binding functional groups on to the Ru(II)-polypyridyl complexes have make them as a receptor for anion. Anion binding event is reflected on the photophysical properties of Ru-polypyridyl complexes. Good illustrations are compounds depicted in Fig. 15.8. Ghosh et al. developed chemosensors based on bisheteroleptic Ru(II) complexes (Fig. 15.8) by incorporating anion binding elements to recognize anions *via* –C-H…anion [27,28], and –C-X…anion [29,30] interactions. Complexation of triazole units with Ru(II) enhances the acidity of the trazole –C-H proton in $\mathbf{Ru^{2+}.9}$ and $\mathbf{Ru^{2+}.10}$ which make them as effective hydrogen bond donors for anion binding [27,28]. Moreover, substituents attached to the triazole motifs also influence the anion binding ability. The second sphere anion binding event readily reflected on the photophysical properties of the metal complex. Ghosh et al. also explored Ru(II) bisheteroleptic complexes $\mathbf{Ru^{2+}.11}$ and $\mathbf{Ru^{2+}.12}$ for second sphere anion binding *via* halogen bonding interactions [29,30]. Direct attachment of halogen bonding motif to the Ru(II) metal center in $\mathbf{Ru^{2+}.11}$ and $\mathbf{Ru^{2+}.12}$ effectively transform the anion binding event to the reporter group. Efforts have also been made [31] to develop efficient sensors $\mathbf{Ru^{2+}.13}$ $\mathbf{Ru^{2+}.14}$, $\mathbf{Ru^{2+}.15}$ and $\mathbf{Ru^{2+}.16}$ by systematically integrating –C-H…anion and –C-X…anion binding motifs along

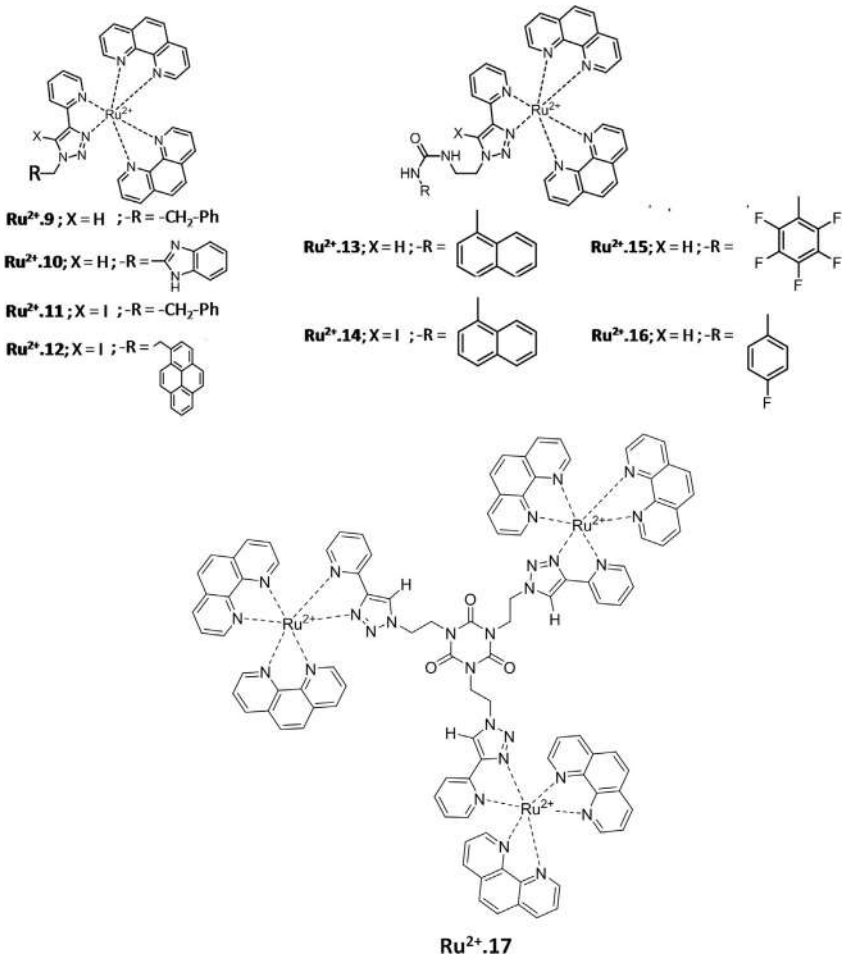

FIGURE 15.8 Molecular structures of chemosensors based on Ru(II)-bis-heterpleptic complexes.

with anion-π and urea functionality in the receptors [31–33]. Among these sensors, a chemosensor amalgamated with urea- and iodotriazole binding motifs coupled with naphthyl probe showed efficicient sensing capability in terms of binding constant, excited state life-time, and lower detection limit toward phosphate anions. They have also synthesized the trazine-based tripodal bis-heteroleptic Ru-complex **Ru^{2+}.17** and demonstrated its selective sensing toward phosphates [34].

Similar to Ru(II) complexes, cyclometallated iridium(III) complexes have been widely demonstrates as chemosensors for environmentally and biologically important anions [35]. Selected examples of cyclometallated iridium(III) complexes used as chemosensors for anions are listed in Fig. 15.9. Hong

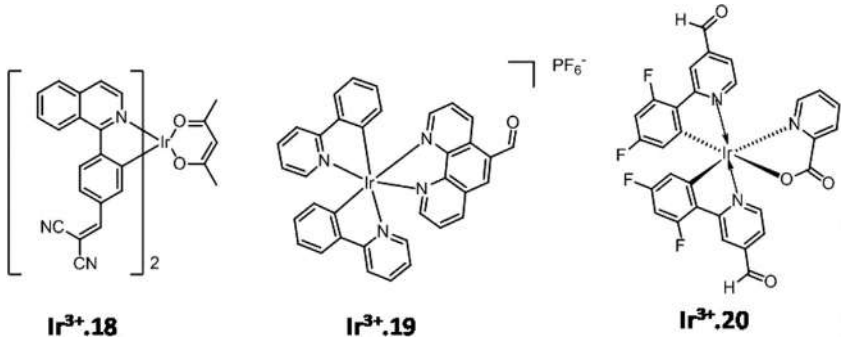

FIGURE 15.9 Molecular structures of cyclometallated Ir(III) complexes $\mathbf{Ir^{3+}.18}$, $\mathbf{Ir^{3+}.19}$ and $\mathbf{Ir^{3+}.20}$ for cyanide anion in aqueous media.

and co-workers explored electrochemiluminescence approach for the selective detection of cyanide anion from tap water using Ir(III) complex $\mathbf{Ir^{3+}.18}$ [36]. Cyanide anion undergoes addition reaction with the dicyanovinyl motif attached to the ligand which omits the interference of other anions including sulfides and biothiols in real samples. Similarly, formyl-functionalized cyclometallated iridium (III) complexes $\mathbf{Ir^{3+}.19}$ [37] and $\mathbf{Ir^{3+}.20}$ [38] displayed good sensitivity toward cyanide anion in aqueous solvent media. The addition of cyanide anion illuminated the luminescence of the probe via the formation of cycnohydrin.

15.3.5 Luminescent lanthanide complexes

The necessity to create imaging and sensor probes for biological and clinical applications opened a new area of luminescent Ln(III)-based anion sensors. Compared to transition metal complexes, lanthanide, and heavy metal complexes exhibit relatively high Stokes shift which inhibit the background interference. This enables them to use for bioimaging applications. Ln(III) complexes generally show sharp line-like emission spectra which facilitate the ratiometric analysis of emission intensity before and after the binding of anions. Several multidendate ligands have been developed to complex with Ln(III) ions wherein the vacant coordination site(s) is/are generally occupied by water molecule in aqueous media, as the case shown in Fig. 15.10 for $\mathbf{Eu^{3+}.21}$ [39]. Upon replacement of the coordinated water molecule by anions, the binding alters the photophysical characteristics such as the luminescent intensity, spectral shape, and life-time and exhibit their sensing capabilities to discriminate nucleoside phosphates such as adenosine triphosphate (ATP), adenosine diphosphate (ADP), and adenosine monophosphate (AMP). Moreover, $\mathbf{Eu^{3+}.21}$ was also used as universal assay for real-time monitoring of enzymes that generate nucleoside phosphates [40].

Luminescence of Ln(III) complexes, particularly Eu(III) and Tb(III) complexes which emit red and green spectral regions are long-lived due to the Laporte forbidden f–f transitions. The unique photophysical properties of Ln(III)

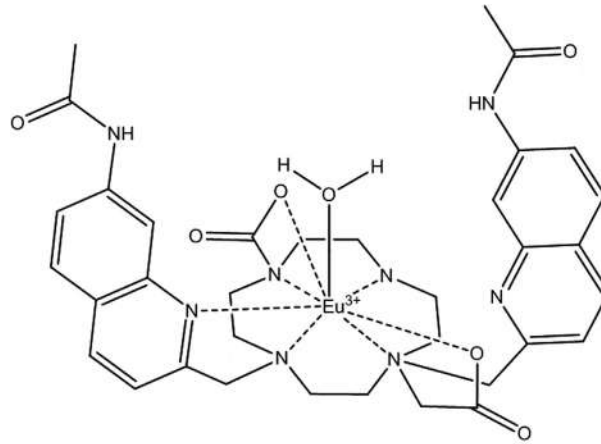

Eu^{3+}.21

FIGURE 15.10 Molecular structure of **Eu^{3+}.21** capable of discriminating nucleoside phosphates in mitochondria of living cells.

complexes make them suitable to probe anions in complex biofluids via time-resolved luminescence measurements. Enhanced signal-to-noise and sensitive detection are the two main advantages of time-gating methods. The binding affinity of the receptor is modulated by changing the structure of the ligand and their conformational flexibility. Ln(III) complexes responsive to the changes in chemical composition of biofluids have been fabricated and reported in the literature. For instance, the reversible binding of HCO_3^- anion at Ln(III) centers has been used to estimate equilibrium HCO_3^- concentration in mitochondria and in human serum [41]. Luminescent Ln(III) complexes have been devised in recent years for their utility as sensors for anions in aqueous media and they have been comprehensively reviewed recently by Butler and co-workers [42].

15.3.6 Mechanically interlocked anion sensors

Anions were utilized as templates for making mechanically interlocked molecules such as rotaxanes and catenanes [43]. Mechanically interlocked molecules have displayed excellent selectivity toward guests compared to their analogous noninterlocked molecular systems. Unique three-dimensional binding cavities that mimic proteins and the microenvironment created by the mechanically interlocked molecules facilitated their utility as selective supramolecular hosts for a variety of guests including anions, as shown in Fig. 15.11. The incorporation of reporter groups onto the anion binding mechanically interlocked molecular components such as rotaxanes and catenanes revealed their sensing capabilities for anion-sensing applications [44–46]. Optical and fluorescent reporter groups in these mechanically interlocked molecules can be brought

FIGURE 15.11 Cartoon showing the function of rotaxne-based turn-ON fluorescent sensor.

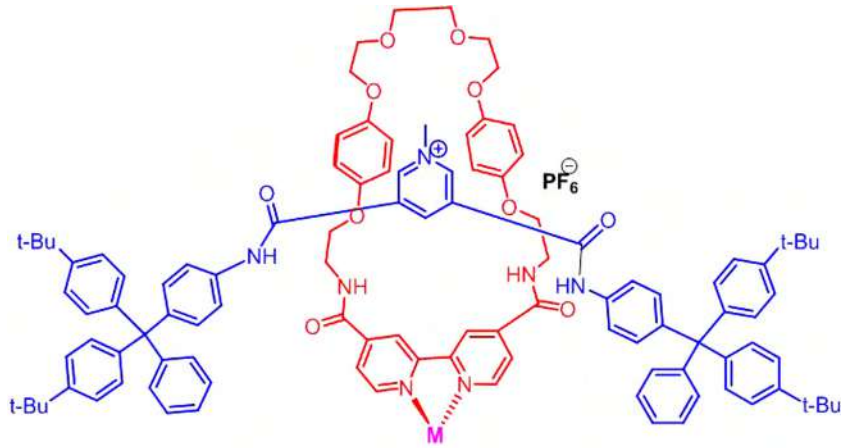

22 M = $[Ru(bipy)_2(PF_6)_2]$

23 M = $[Re(CO)_3(Cl)]$

FIGURE 15.12 Molecular structures of rotaxane-based chemosensors for Cl^-.

together or separated upon anion coordination to the binding site which interfere the sensory response. In 2012, Beer and co-workers [47] synthesized photo-active ruthenium(II) and rhenium(I) bipyridylrotaxanes **22** and **23**, respectively (Fig. 15.12) *via* chloride anion templation. They demonstrated the ability of these rotaxanes to selectively sense chloride anion in aqueous media containing upto 10% water. To further exploit the use of rotaxanes as anion sensor in 100% water, β-cyclodextrins were functionalized as stoppers and iodotriazolium moieties were incorporated to facilitate the anion binding *via* halogen bonding interactions [48].

Though anion receptor chemistry has been extensively explored by utilizing hydrogen bonding interactions, charge-assisted halogen bonding is employed as yet another anion binding motifs. Receptors capable of recognizing and sensing anions *via* halogen bonding interactions got momentum and gained enormous interest [49]. Halogen bonding is a directional noncovalent interaction in which

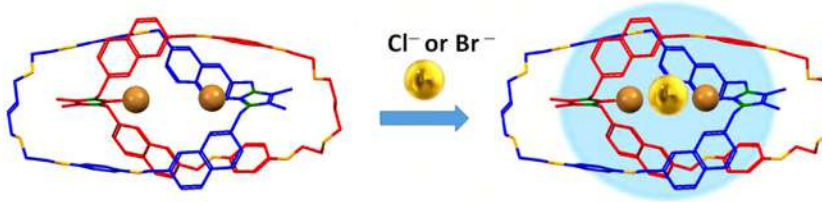

FIGURE 15.13 Cartoon showing the anion binding by **24**.

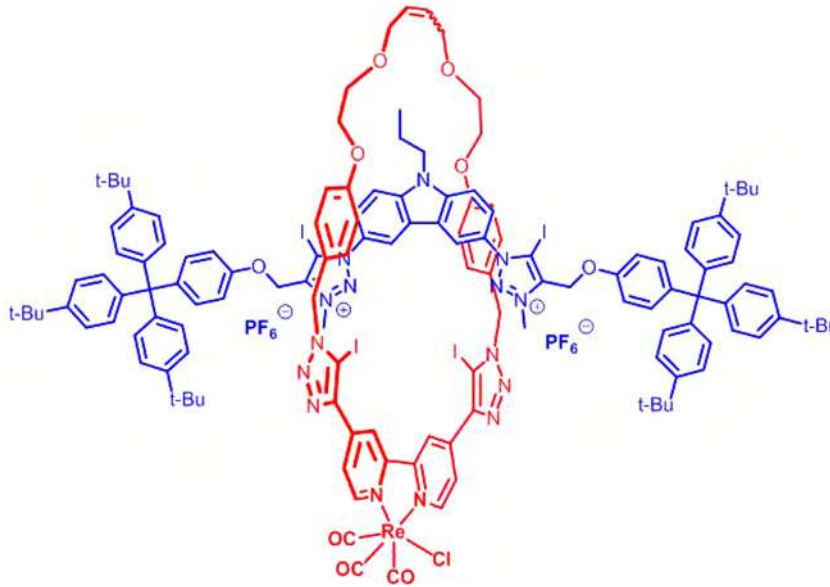

FIGURE 15.14 Molecular structure of first all halogen bonding rotaxane-based chemosensor **25**.

the halogens interact with anions *via* sigma hole formation between polarizable electron-deficient halogen and electron-rich anions. Generally, halogen bonding interactions preferentially exist between the electrophilic region of halogen atom and halide anions over oxyanions. Beer et al. reported their first halogen-bonding catenane without any strong hydrogen bonding sites in the catenane **24**. Naphthalene was introduced as the signaling unit in **24** and demonstrated the receptor as a chemosensor for the selective sensing of chloride and bromide anion *via* halogen bonding interactions (Fig. 15.13) [50]. In **24**, naphthalene unit not only act as a rigid spacer but also play its role as luminescent reporter unit in the catenane host for anion sensing. Beer and coworkers demonstrated the ability of rotaxanes as chemosensors for anions using a series of rotaxanes and **25** is the first all halogen bonding rotaxane in which photoactive rhenium(I) bipyridyl motif is attached to the wheel component of the [2] rotaxane (Fig. 15.14) [51].

Binding of halide anions especially iodide anion to the binding pocket of the rotaxane *via* multiple halogen bonding interactions resulted in the quenching of metal–ligand charge transfer (MLCT) emission band of rhenium(I) bipyridine unit in aqueous solvent mixtures.

15.4 Conclusions and future perspectives

This chapter intended to showcase anion sensing applications of supramolecular coordination complexes with a special emphasis on sensor probe design. As we have illustrated, coordination complexes contributed enormously for the development of chemosensors for anions which function through various supramolecular mechanisms. Strategical functionalization of reporter groups on the supramolecular complexes allows to sense anionic analytes with high sensitivity and selectivity. Anion binding affinity is strong in cases where anions coordinate directly to metal ions even in highly polar biological fluids. To be more selective and sensitive, the chemosensor has to be designed in such a way that the microenvironment created by the receptor should avoid direct interaction with the bulk solution. It is envisaged that supramolecular chemists could fabricate sensor probes to fully address biologically relevant anions in their native environment to overcome hydration energy with high selectivity and sensitivity. Immobilization of mechanically interlocked molecule-based anion receptors would be a promising strategy to construct anion-responsive advanced functional devices. It is also necessary to develop chemosensors that are harmless and capable to sense biological analytes in complex cellular environment so as to use them in vivo for diagnostic and medicinal applications. The development of anion sensors continues to be the hot area of research and we foresee further progress in real-world applications of anion sensors over the coming years.

References

[1] F. Huang, E.V. Anslyn, Introduction: supramolecular chemistry, Chem. Rev. 115 (15) (2015) 6999–7000.

[2] T.L. Mako, J.M. Racicot, M. Levine, Supramolecular luminescent sensors, Chem. Rev. 119 (1) (2019) 322–477.

[3] S. Kubik, Anion recognition in water, Chem. Soc. Rev. 39 (2010) 3648–3663.

[4] M.J. Langton, C.J. Serpell, P.D. Beer, Anion Recognition in Water: Recent Advances from a Supramolecular and Macromolecular Perspective, Angew. Chem. Int. Ed. 55 (6) (2016) 1974–1987.

[5] L. Chen, S.N. Berry, X. Wu, E.N.W. Howe, P.A. Gale, Advances in anion receptor chemistry, Chem. 6 (1) (2020) 61–141.

[6] P.A. Gale, E.N.W. Howe, X. Wu, M.J. Spooner, Anion receptor chemistry: highlights from 2016, Coord. Chem. Rev. 375 (2018) 333–372.

[7] H.E. Simmons, C.H. Park, Macrobicyclic amines. I. Out-in isomerism of 1,(k+2)-diazabicyclo[k.l.m]alkanes, J. Am. Chem. Soc. 90 (9) (1968) 2428–2429.

[8] P.A. Gale, and C. Caltagirone, (2011). Anion Sensors. In Chemosensors (eds. B. Wang, B. Wang and E.V. Anslyn). https://doi.org/10.1002/9781118019580.ch19.

[9] P.A. Gale, C. Caltagirone, Anion sensing by small molecules and molecular ensembles, Chem. Soc. Rev. 44 (13) (2015) 4212–4227.
[10] H.M. Tay, P. Beer, Optical sensing of anions by macrocyclic and interlocked hosts, Org. Biomol. Chem. 19 (21) (2021) 4652–4677.
[11] T.D. Ashton, K.A. Jolliffe, F.M. Pfeffer, Luminescent probes for the bioimaging of small anionic species in vitro and in vivo, Chem. Soc. Rev. 44 (14) (2015) 4547–4595.
[12] J.L. Kolanowski, F. Liu, E.J. New, Fluorescent probes for the simultaneous detection of multiple analytes in biology, Chem. Soc. Rev. 47 (1) (2018) 195–208.
[13] P.D. Beer, S.R. Bayly, Anion sensing by metal-based receptors. In: Stibor I. (ed.) Anion Sensing. Topics in Current Chemistry, Vol. 255. Springer, Berlin and Heidelberg.
[14] N. Kumari, F. Zelder, Detecting biologically relevant phosphates with locked salicylaldehyde probes in water, Chem. Commun. 51 (96) (2015) 17170–17173.
[15] C. Chang, F. Wang, T. Wei, X. Chen, Benzothiazole-based fluorescent sensor for ratiometric detection of Zn(II) ions and secondary sensing PPi and its applications for biological imaging and PPase catalysis assays, Ind. Eng. Chem. Res. 56 (31) (2017) 8797–8805.
[16] M.V.R. Raju, S.M. Harris, V.C. Pierre, Design and applications of metal-based molecular receptors and probes for inorganic phosphate, Chem. Soc. Rev. 49 (4) (2020) 1090–1108.
[17] H.T. Ngo, X. Liu, K.A. Jolliffe, Anion recognition and sensing with Zn(ii)–dipicolylamine complexes, Chem. Soc. Rev. 41 (14) (2012) 4928–4965.
[18] A. Ojida, Y. Mito-oka, M. Inoue, I. Hamachi, First artificial receptors and chemosensors toward phosphorylated peptide in aqueous solution, J. Am. Chem. Soc. 124 (22) (2002) 6256–6258.
[19] S. Pal, T.K. Ghosh, R. Ghosh, S. Mondal, P. Ghosh, Recent advances in recognition, sensing and extraction of phosphates: 2015 onwards, Coord. Chem. Rev. 405 (2020) 213128 and references cited therein.
[20] I.A. Rather, R. Ali, Indicator displacement assays: from concept to recent developments, Org. Biomol. Chem. 19 (27) (2021) 5926–5981.
[21] A.C. Sedgwick, J.T. Brewster, T. Wu, X. Feng, S.D. Bull, X. Qian, J.L. Sessler, T.D. James, E.V. Anslyn, X. Sun, Indicator displacement assays (IDAs): the past, present and future, Chem. Soc. Rev. 50 (1) (2021) 9–38.
[22] S.L. Wiskur, J.J. Lavigne, A. Metzger, S.L. Tobey, V. Lynch, E.V. Anslyn, Thermodynamic analysis of receptors based on guanidinium/boronic acid groups for the complexation of carboxylates, α-hydroxycarboxylates, and diols: driving force for binding and cooperativity, Chemistry – A European Journal, 10 (15) (2004) 3792–3804.
[23] M.S. Goodman, V. Jubian, A.D. Hamilton, Metal templated receptors for the effective complexation of dicarboxylates, Tetrahedron Lett. 36 (15) (1995) 2551–2554.
[24] D.A. Jose, P. Kar, D. Koley, B. Ganguly, W. Thiel, H.N. Ghosh, A. Das, Phenol- and catechol-based ruthenium(II) polypyridyl complexes as colorimetric sensors for fluoride ions, Inorg. Chem. 46 (14) (2007) 5576–5584.
[25] P. Alreja, N. Kaur, Recent advances in 1,10-phenanthroline ligands for chemosensing of cations and anions, RSC Adv. 6 (28) (2016) 23169–23217.
[26] Q. Zhao, F. Li, C. Huang, Phosphorescent chemosensors based on heavy-metal complexes, Chem. Soc. Rev. 39 (8) (2010) 3007–3030.
[27] B. Chowdhury, S. Khatua, R. Dutta, S. Chakraborty, P. Ghosh, Bis-heteroleptic Ruthenium(II) complex of a triazole ligand as a selective probe for phosphates, Inorg. Chem. 53 (15) (2014) 8061–8070.

[28] S. Mondal, K. Sarkar, P. Ghosh, Influence of Triazole Substituents of Bis-Heteroleptic Ru(II) Probes toward Selective Sensing of Dihydrogen Phosphate, Inorg. Chem. 60 (12) (2021) 9084–9096.
[29] S. Mondal, T.K. Ghosh, B. Chowdhury, P. Ghosh, Supramolecular self-assembly driven selective sensing of phosphates, Inorg. Chem. 58 (23) (2019) 15993–16003.
[30] B. Chowdhury, S. Sinha, P. Ghosh, Selective sensing of phosphates by a new Bis-heteroleptic RuII complex through halogen bonding: a superior sensor over its hydrogen-bonding analogue, Chem. Eur. J. 22 (50) (2016) 18051–18059.
[31] T.K. Ghosh, S. Mondal, S. Bej, M. Nandi, P. Ghosh, An integrated urea and halogen bond donor based receptor for superior and selective sensing of phosphates, Dalton Trans. 48 (14) (2019) 4538–4546.
[32] T.K. Ghosh, P. Ghosh, Balancing the acidity of the pendant urea arm of bis-heteroleptic ruthenium(ii) complex containing pyridyl triazole for improved oxyanion recognition, Dalton Trans. 47 (22) (2018) 7561–7570.
[33] T.K. Ghosh, S. Chakraborty, B. Chowdhury, P. Ghosh, Bis-heteroleptic Ruthenium(II) complex of pendant urea functionalized pyridyl triazole and phenathroline for recognition, sensing, and extraction of oxyanions, Inorg. Chem. 56 (9) (2017) 5371–5382.
[34] B. Chowdhury, R. Dutta, S. Khatua, P. Ghosh, A cyanuric acid platform based tripodal bis-heteroleptic Ru(II) complex of click generated ligand for selective sensing of phosphates via C–H···anion interaction, Inorg. Chem. 55 (1) (2016) 259–271.
[35] H. Shi, Y. Wang, S. Lin, J. Lou, Q. Zhang, Recent development and application of cyclometalated iridium(III) complexes as chemical and biological probes, Dalton Trans. 50 (19) (2021) 6410–6417.
[36] T. Kim, H.J. Kim, I-S. Shin, J.-I. Hong, Potential-dependent electrochemiluminescence for selective molecular sensing of cyanide, Anal. Chem. 92 (8) (2020) 6019–6025.
[37] L. N, H.-D. Ou, Q. Xu, Y. Jin, W. Deng, Z.-J. Yao, An efficient probe of cyclometallated phosphorescent iridium complex for selective detection of cyanide, ACS Omega 5 (9) (2020) 4636−4645.
[38] K.S. Bejoymohandas, A. Kumar, S. Sreenadh, E. Varathan, S. Varughese, V. Subramanian, M.L.P. Reddy, A highly selective chemosensor for cyanide derived from a formyl-functionalized phosphorescent iridium(III) complex, Inorg. Chem. 55 (7) (2016) 3448–3461.
[39] R. Mailhot, T. T.-Pollard, R. Pal, S.J. Butler, Cationic europium complexes for visualizing fluctuations in mitochondrial ATP levels in living cells, Chem. Eur. J. 24 (42) (2018) 10745–10755.
[40] S.H. Hewitt, R. Ali, R. Mailhot, C.R. Antonen, C.A. Dodson, S.J. Butler, A simple, robust, universal assay for real-time enzyme monitoring by signalling changes in nucleoside phosphate anion concentration using a europium(III)-based anion receptor, Chem. Sci. 10 (20) (2019) 5373–5381.
[41] D.G. Smith, R. Pal, D. Parker, Measuring equilibrium bicarbonate concentrations directly in cellular mitochondria and in human serum using europium/terbium emission intensity ratios, Chemistry – A European Journal 18 (37) (2012) 11604–11613.
[42] S.E. Bodman, S.J. Butler, Advances in anion binding and sensing using luminescent lanthanide complexes, Chem. Sci. 12 (8) (2021) 2716–2734.
[43] G.T. Spence, P.D. Beer, Expanding the scope of the anion templated synthesis of interlocked structures, Acc. Chem. Res. 46 (2) (2013) 571–586.

[44] M.J. Langton, P.D. Beer, Rotaxane and Catenane Host Structures for Sensing Charged Guest Species, Acc. Chem. Res. 47 (7) (2014) 1935–1949.
[45] J.E.M. Lewis, M. Galli, S.M. Goldup, Properties and emerging applications of mechanically interlocked ligands, Chem. Commun. 53 (2) (2017) 298–312.
[46] K.M. Bąk, K. Porfyrakis, J.J. Davis, P.D. Beer, Exploiting the mechanical bond for molecular recognition and sensing of charged species, Mater. Chem. Front. 4 (2020) 1052–1073.
[47] L.M. Hancock, E. Marchi, P. Ceroni, P.D. Beer, Anion sensing in aqueous media by photo-active transition-metal bipyridyl rotaxanes, Chemistry – A European Journal 18 (36) (2012) 11277–11283.
[48] M.J. Langton, I. Marques, S.W. Robinson, V. Félix, P.D. Beer, Iodide recognition and sensing in water by a halogen-bonding ruthenium(II)-based rotaxane, Chemistry – A European Journal 22 (1) (2016) 185–192.
[49] A. Caballero, F. Zapata, N.G. White, P.J. Costa, V. Félix, P.D. Beer, A halogen-bonding catenane for anion recognition and sensing, Angew. Chem. Int. Ed. 51 (8) (2012) 1876–1880.
[50] J.M. Mercurio, A. Caballero, J. Cookson, P.D. Beer, A Hhalogen- and hydrogen-bonding [2]catenane for anion recognition and sensing, RSC Adv. 5 (2015) 9298–9306.
[51] B.R. Mullaney, A.L. Thompson, P.D. Beer, An all-halogen bonding rotaxane for selective sensing of halides in aqueous media, Angew. Chem. Int. Ed. 53 (2014) 11458–11462.

Chapter 16

Supramolecular coordination complexes for fluorescence sensing of nitroaromatic explosives

Binduja Mohan, Ananthu Shanmughan and Sankarasekaran Shanmugaraju
Department of Chemistry, Indian Institute of Technology Palakkad (IITPKD), Palakkad, Kerala, India

16.1 Introduction

Increased use of chemical explosives is one of the threatening difficulties confronted by the national security system as well as the environment [1]. In recent years, the development of reliable sensor systems for selective identification of chemical explosives attracted significant research interest as it is beneficial for the safety of people and national security [2]. A proper and convenient detection method that could help to combat terrorism, and prevent environmental contamination and harmful health hazard to the living organism is an urgent need. Chemical explosives are substances that undergo a spontaneous chemical reaction upon exposure to heat or shock which produces stable gaseous species accompanied by the liberation of excess energy [3]. Based on their burning velocities, the chemical explosives are classified as weak and strong explosives. Weak explosives detonate with a burning velocity around the order cm/s; on the other hand, strong explosives explode with the burning velocity of km/s order, which is almost five times higher than weak explosives [4]. Because of the ease in production and transportation, nitroaromatic compounds (NACs) classified as secondary explosives are extensively used by humans for various activities, which then eventually contaminate and pollute the environment [5]. Therefore, quick and easy sensing of NACs even in trace quantity is a vital topic being explored in the present world. There are numerous non-optical techniques for NACs detection such as sniffer dogs, metal detectors, and instrumental techniques like GC-MS, surface-enhanced Raman spectroscopy, and ion-mobility spectroscopy which are currently available for NACs sensing. However, each of

Supramolecular Coordination Complexes: Design, Synthesis, and Applications.
DOI: https://doi.org/10.1016/B978-0-323-90582-4.00006-3

these techniques is limited by several drawbacks including high instrument cost, required skilled operators, high maintenance cost, tedious calibration, lack of portability, and not being easy to operate on-site [6]. Taking these limitations into consideration, scientists are focusing on fluorescence sensing which has the advantage of high sensitivity with excellent selectivity, quick response time, cost-effectiveness, ease of transportation, and visualization [7]. The π-electron-rich aromatic fluorophores can easily form charge-transfer complexes with π-electron-deficient NACs, making them a suitable sensor for the selective detection of chemical explosives [8]. There exist numerous electron-rich fluorescent sensors such as conjugated organic/inorganic polymers, luminescent metallacycles and cages, fluorescent dendrimers, small molecule fluorophores, luminescent nanomaterials, metal-organic frameworks, covalent organic frameworks [9–13]. Among these, luminescent metallacycles and metallocages act as efficient NACs sensors because of their facile synthesis in quantitative yields *via* metal-ligand coordination directed self-assembly, excellent selectivity, and enhanced sensitivity. In general, metallacycles and metallocages are built by the "self-assembly" process, that is, the self-association of predesigned molecular building units to generate electron-rich supramolecular coordination complexes (SCCs) [14]. Furthermore, the presence of large internal cavities help SCCs to easily accommodate electron-deficient NACs through multiple noncovalent interactions. Based on the dimension, the supramolecular architectures can be classified into two main categories; two-dimensional (2D) ensembles and three-dimensional (3D) cage-like structures [15]. In this chapter, we discuss the design, synthesis, and fluorescence sensing studies of various SCCs including a series of 2D metallacycles, and several 3D metallocages. A special mention is given to the sensing mechanism and mode of binding between the host and guest complexes. We believe that this chapter will be of interest to researchers working in the area of supramolecular chemistry, sensor chemistry, and photochemistry.

16.2 Two-dimensional (2D) metallacycles for sensing of nitroaromatic explosives

A wide variety of 2D metallacycles have been synthesized by the linear combination of appropriate predesigned building blocks with accurate bite angles [14,15]. In this section, various 2D SCCs are grouped into several categories according to their molecular geometry and their fluorescence sensing properties toward NACs have been reviewed in detail particularly focusing on the mechanism of fluorescence sensing.

16.2.1 Molecular rhomboid based fluorescent sensor for NACs

Stang and co-workers designed a molecular rhomboid (**SCC-1**) through [2+2] self-assembly of di-Pt(II) acceptor ($\mathbf{M_1}$) having a 60° bite angle with tetraphenyl ethylene (TPE)-containing donor ligand ($\mathbf{L_1}$) (Fig. 16.1A) [16]. The synthesized

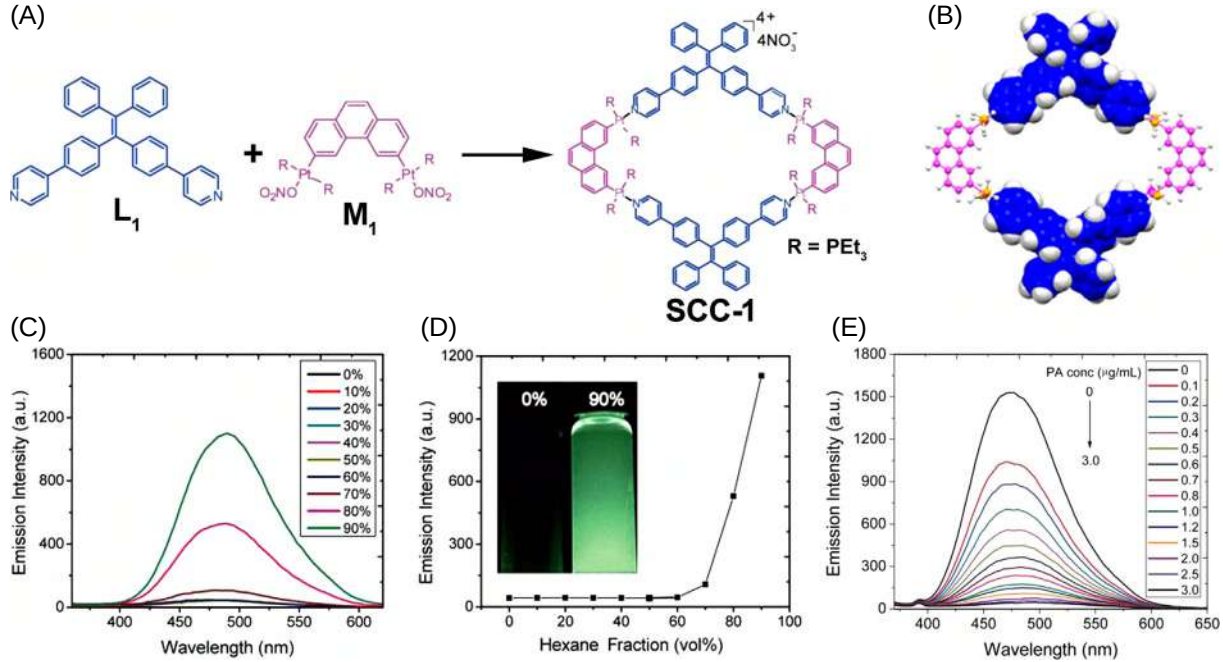

FIGURE 16.1 (A) Self-assembly formation of rhomboid **SCC-1** from the combination of donor $\mathbf{L_1}$ and acceptor $\mathbf{M_1}$; (B) simulated molecular model of **SCC-1**; (C) fluorescence emission changes of **SCC-1** in different hexane fractions, and (D) the corresponding plot of maximum emission intensity (Inset: photograph of **SCC-1** in CH_2Cl_2 and 10%/90% CH_2Cl_2/hexane mixture upon excitation at $\lambda = 365$ nm; (E) fluorescence emission changes of **SCC-1** in 10%/90% CH_2Cl_2/hexane mixture upon the increasing concentration of picric acid. Reprinted with permission from Ref. [16]. Copyright 2015 American Chemical Society.

rhomboid was characterized using ESI-TOF mass analysis, multinuclear NMR (^{1}H and ^{31}P NMR) analysis, and molecular simulation confirmed the well-defined rhomboidal architecture with the presence of a 2.4 × 2.0 nm internal cavity (Fig. 16.1B). The TPE-based supramolecular structures are known for their excellent aggregation-induced emission (AIE) properties and thus, the AIE properties of **SCC-1** were validated by measuring the change in the emission intensity in dichloromethane upon increasing the volume percentage of hexane. Dilute dichloromethane solution of the assembly **SCC-1** displayed a weak emission and upon incremental addition of hexane increased the emission intensity (Figs. 16.1C and D). As the macrocycle aggregate, the phenyl functionality rigidifies thus restricting nonradiative relaxation and enhancing fluorescence intensity. The as-synthesized rhomboid **SCC-1** aggregate in the CH_2Cl_2/hexane mixture and acts as an excellent fluorescent turn-off probe for picric acid (PA) (Fig. 16.1E). The **SCC-1** showed excellent selectivity for PA even up to 0.1 ppm and no notable fluorescence changes were observed for other NACs such as 4-nitrotoluene (4-NT), and nitrobenzene (NB), 2,4-dinitrotoluene (2,4-DNT), and 1,3-dinitrobenzene (1,3-DNB). Another distinctive feature of **SCC-1** is the ability to sense PA even in an aqueous medium, that is, by synthesizing an aggregate of **SCC-1** in acetone/H_2O with elevated water content (90%), sensing of PA was found to be feasible. The quenching constant and the detection limit was estimated to be 2.18 × 10^{6} M^{-1} and 0.13 ppb, respectively.

16.2.2 Molecular squares based fluorescent sensors for NACs

The finite supramolecular squares are a significant class of 2D molecular architectures because of their structural simplicity and easy synthesis from the preprogrammed building units and strong conformational stability [17]. In general, the supramolecular squares are prepared by the linear combination of four *cis*-blocked 90° acceptors and four complementary linear donor ligands or *vice versa* [18]. For instance, the self-assembly of four equivalent ferrocenes functionalized 1,1′-bis(diphenylphosphino)ferrocene (dppf) blocked 90° acceptors ($\mathbf{M_2}$ = (dppf)Pd$(OTf)_2$, $\mathbf{M_3}$ = (dppf)Pt$(OTf)_2$) with four equivalent of Pt(II)-ethynyl functionalized linear donor [$\mathbf{L_2}$ = *trans*-[(4-pyridylethynyl)$_2$Pt$(PEt_3)_2$] resulted in the formation of two unique [4+4] self-assembled heterometallic molecular squares (**SCC-2**) and (**SCC-3**), respectively in quantitative yields and in analytically pure form (Fig. 16.2A) [19]. The significant advantages of these molecular squares are (1) the presence of bulky -PEt_3 groups enhance the solubility of the metallacycles in all common organic solvents as well as prevents the self-quenching of fluorescence through molecular aggregation, (2) the rigid-ethynyl functionalities help to increase the π-electron density and stability of the fluorophores that results in the decrease of nonradiative decay in solution, (3) the ethynyl functional groups of Pt(II)/Pd(II) complexes improve the luminescent properties of the supramolecular architectures *via* metal-to-ligand charge transfer transition. The highly emissive characteristic and

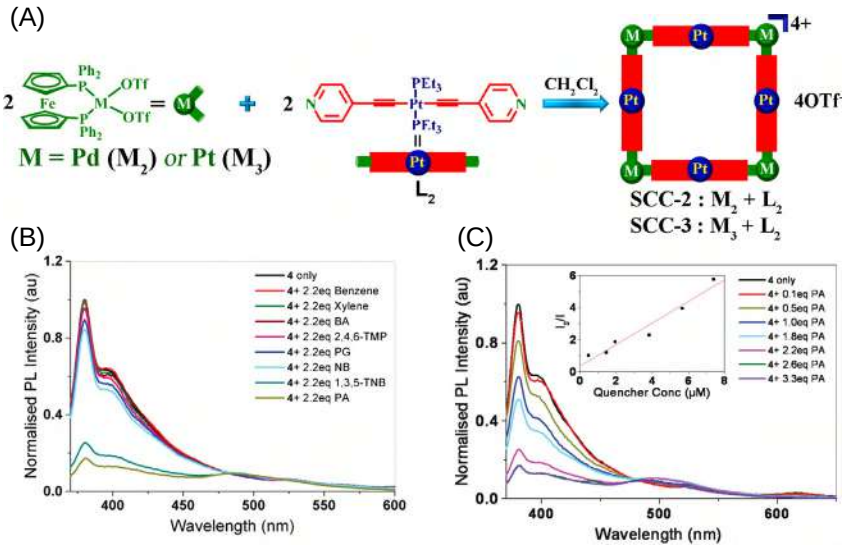

FIGURE 16.2 (A) Self-assembly formation of the heterometallic molecular squares **SCC-2** and **SCC-3**; (B) fluorescence emission quenching of **SCC-2** in THF upon the addition of the various analytes; (C) the extent of emission quenching of complex **SCC-2** upon the mixing of PA and the corresponding Stern–Volmer plot (inset). Reprinted with permission from Ref. [19]. Copyright 2011 Royal Society of Chemistry.

π-electron richness formulate **SCC-2** and **SCC-3** as suitable candidates for NACs sensing. The fluorescence intensity of the molecular squares was found to be readily attenuated upon the incremental addition of various NACs especially PA, 4-nitrobenzene (NB), and 1,3,5-trinitrobenzene (TNB) (Fig. 16.2B). Among these, PA displayed the highest quenching efficiency with quenching constants (K_{SV}) found to be 6.72×10^5 M^{-1} and 7.00×10^5 M^{-1} for **SCC-2** and **SCC-3**, respectively (Fig. 16.2C). The observed strong quenching for PA can be attributed to its high electron-deficient nature as well as high polarizability that facilitates the strong π–π interactions and subsequent energy transfer from metallacycles to NACs. Furthermore, in separate fluorescence titration studies, the donor ligand $\mathbf{L_2}$ exhibited a moderate fluorescence quenching with PA while the similar titration studies with acceptor $\mathbf{M_2}$ showed no noticeable changes in the emission intensity. This evidence of the importance of $\mathbf{L_2}$ to engender the metallacycles to be fluorescent confirms that acceptor $\mathbf{M_2}$ does not have any role in the fluorescence sensing properties except its structural role to hold the macrocycles intact.

In another report, Shanmugaraju et al. synthesized two novel homometallic octanuclear molecular squares (**SCC-4** and **SCC-5**) from a carbazole based shape-selective Pt(II) 90° acceptor [3,6-bis{trans-Pt$(PEt_3)_2(NO_3)$(ethynyl)}-carbazole, $\mathbf{M_4}$] and linear dipyridyl donors [$\mathbf{L_3}$ = 4,4'-bipyridine;

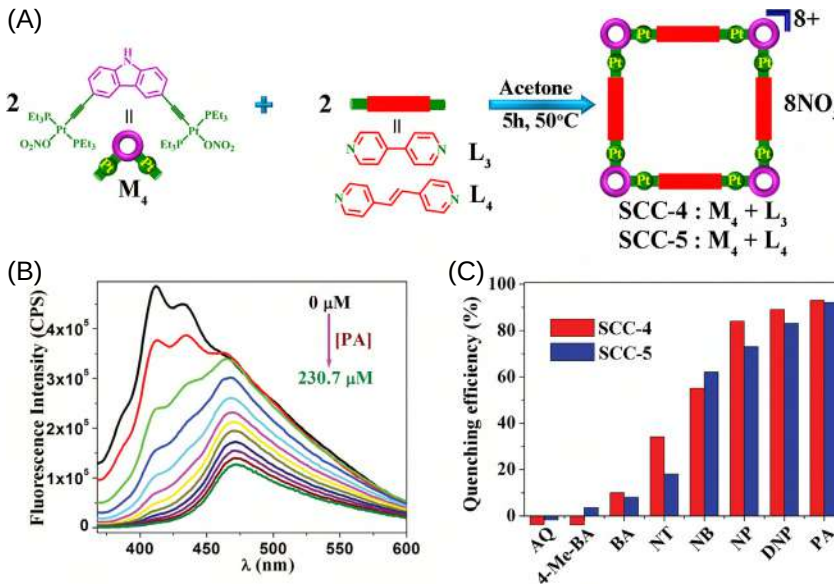

FIGURE 16.3 (A) Self-assembly formation of octanuclear homometallic molecular squares **SCC-4** and **SCC-5** by employing a Pt^{II} organometallic 90° acceptor $\mathbf{M_4}$ and linear ditopic donors $\mathbf{L_3}$ and $\mathbf{L_4}$; (B) observed fluorescence quenching of **SCC-5** upon the mixing of PA in DMF–methanol solution; (C) extent of fluorescence quenching of the squares (**SCC-4** and **SCC-5**) observed upon the addition of various analytes. Reprinted with permission from Ref. [20]. Copyright 2011 Royal Society of Chemistry.

$\mathbf{L_4}$ = *trans*-1,2-bis(4-pyridylethylene)] (Fig. 16.3A) [20]. Carbazole moiety plays an influential role in the characteristic properties of these metallacycles as it offers excellent photo-physics with robust electron-donating ability. Gratifyingly, both the molecular squares displayed high photoluminescence and excellent quenching affinity toward NACs. Amongst the various NACs, increment addition of PA showed an effective attenuation of fluorescence intensity which is accompanied by the appearance of a new low-energy band (Fig. 16.3B and C). The electron-deficient nature of PA facilitates ground state charge transfer complexation between π-electron-rich molecular squares and PA. The Stern–Volmer curve indicated that the fluorescence quenching of metallacycles by NACs exhibited both static and dynamic nature with a binding constant estimated to be $K_{SV} = 2.0 \times 10^4\ M^{-1}$ for **SCC-4** and $5.0 \times 10^4\ M^{-1}$ for **SCC-5**.

Similarly, the Mukherjee group has also developed a molecular square (**SCC-6**) through [4+4] self-assembly of the phenyl-substituted carbazole-derived diplatinum acceptor ($\mathbf{M_5}$) and divinylanthracene-based dipyridyl donor ligand, ($\mathbf{L_5}$) [21]. The as-synthesized molecular square **SCC-6** displayed an AIE effect which makes **SCC-6** highly emissive due to the restricted molecular rotation.

The morphology of the aggregate formation and other structural features were analyzed using SEM and TEM imaging techniques. Molecular modeling using the PM6 method supported the formation of a nearly planar molecular square **SCC-6** with the twisted phenyl ring of carbazole functionality (about 55.38° out of the plane). The emission intensity of **SCC-6** in solution gradually decreased upon the gradual addition of trinitrotoluene (TNT) and the initial fluorescent emission was attenuated by around 80% upon the addition of only 4 equivalents of TNT. Also, the observable change in the fluorescence lifetime with the addition of TNT confirmed the dynamic fluorescence quenching mechanism. Other interfering nitroaromatics such as 3,4-DNT, nitrotoluene (NT), trinitrobenzene (TNB), 1,3-dinitrobenzene (DNB), nitrobenzene (NB), nitromethane (NM), 3- nitrobenzoic acid (NBA) and benzophenone (BPH) showed no notable fluorescence responses whereas 2,4-dinitrotoluene (DNT) showed 30% fluorescence quenching efficiency. Further, solid-state sensing studies showed around 80% fluorescence quenching of freshly made thin film of **SCC-6** by nitrobenzene vapor when exposed for about 400 s. In addition, 60% quenching was observed upon exposure to DNT vapors for about 300 s. The solid-state quenching was reversible by water washing, the used thin film was washed with water followed by drying and subsequent studies showed similar quenching upon reusing the same film several times. This confirms the reversible sensing ability of **SCC-6** for NACs both in solution and vapor phases.

16.2.3 Molecular rectangles-based fluorescent sensors for NACs

Molecular rectangles are uncommon two-dimensional metallacycles because of the challenges faced in the self-assembly of cis-protected 90° metal acceptors with rigid linear donors. Generally, the reaction of 90° acceptor and linear donor results in the formation of molecular squares instead of a molecular rectangle. However, Stang and co-workers developed a unique two-component self-assembly strategy for the synthesis of molecular rectangles through [2+2] self-assembly interaction between linear ditopic metal unit and "clip" type donor ligand [22]. Following this strategy, Mukherjee's group designed a set of molecular rectangles with extended π-conjugation, and rectangles showed excellent luminescent properties and efficient sensing characteristics toward NACs [23]. Self-assembly of two linear 180° metal acceptors, [1,4-bis{trans-(ethynyl)Pd(PEt_3)$_2$(NO_3)}benzene] Pd(II) acceptor (**M_6**) and [4,4'-bis{trans-Pt(PEt_3)$_2$(O_3SCF_3)(ethynyl)}biphenyl] Pt(II) acceptor (**M_7**) with a "clip" type anthracene derived donor unit (**L_6**) separately result in the generation of two cationic supramolecular [2+2] molecular rectangular assemblies (**SCC-7**) and (**SCC-8**), respectively [23,24]. The molecular rectangles **SCC-7** and **SCC-8** in $CHCl_3$ showed strong binding affinity toward NACs even at very low concentrations. The incremental addition of PA into these molecular rectangles results in the gradual reduction of fluorescence intensity. The changes in electronic absorption and the linear Stern–Volmer plot with binding constant

in the range 1.9 × 10^4 M^{-1} for **SCC-7** and 5.0 × 10^4 M^{-1} for **SCC-8** affirm that the fluorescence quenching occurs through a static quenching mechanism via ground-state charge-transfer complex formation between rectangles and PA.

The same group reported another interesting example of the formation of [2+2] self-assembled molecular rectangle (**SCC-9**) from a chloro-bridged half-sandwich Ru(II) acceptor [Ru_2(m-Cl_2)(η^6-p-cymene)$_2Cl_2$] (**M_8**) and linear bipyridyl donor ligand (**L_4**) [25]. The XRD structure validates the strong coordination of each ruthenium unit to the N-atom of the bipyridyl ligand which results in the rectangular geometry having an overall dimension in the range of 3.24 × 13.51 Å. Along with this, the analysis revealed the robust π–π interactions between two parallel dipyridyl donor ligands and the inward inclination of two bridged chlorine atoms to obtain an octahedral arrangement. The aforementioned molecular rectangle **SCC-9** displayed selective fluorescence quenching toward phenolic nitroaromatics such as 4-nitrophenol, 2,4-dinitrophenol, and picric acid whereas no significant attenuation is observed with nonphenolic nitroaromatics like TNT, 2,4-DNT, 4-nitrobenzene (NB), 4-nitrotoluene(NT), and nitromethane (NM). This striking selectivity is attributed to the intermolecular hydrogen bonding between the phenolic -OH groups and bridging Cl atoms of the metallacycle (Fig. 16.4).

It is commonly observed that either catatonically or anionically charged molecular architectures hinder the smooth entrance of guest analytes into the internal cavity as the counter-ions usually fill the inner pore of the assemblies. In contrast, the neutral molecular assemblies often filled with only solvent molecules can act as the best host for guest inclusion through the easy displacement of entrapped solvent molecules [26]. In light of this, Mukherjee and his group designed a neutral Pd(II) [2+2] rectangle (**SCC-10**) *via* coordination driven self-assembly of [1,8-bis{trans-Pt(PEt_3)$_2$(NO_3)(ethynyl)}anthracene] Pd(II) acceptor (**M_9**) with linear Na_2–fumarate donor ligand (**L_7**) (Fig. 16.5A) [27].

Similarly, another rectangle (**SCC-11**) was obtained from [trans-Pd(PEt_3)Cl_2] Pd(II) acceptor (**M_{10}**) and 1,8-diethynylanthracene (**L_8**) using CuCl catalyst *via* trans-metalation [23]. The molecular rectangle **SCC-11** is the first known neutral molecular ensemble with Pd-C coordination-driven self-assembly (Fig. 16.5B). The solid-state packing analysis indicated the head-to-tail fashioned arrangement of rectangles to form one-dimensional chains *via* π–π stacking with neighboring anthracene units (Fig. 16.5C). Molecular rectangle **SCC-10**, and **SCC-11**, showed a prominent emission in which **SCC-10** is lesser emissive than **SCC-11** due to a lack of extended conjugation and delocalization of π-electron all over the system. Also, both these molecular rectangles showed selective sensing toward NACs especially PA and TNT even in micromolar solutions (Fig. 16.5D). The Stern–Volmer binding constant of both **SCC-10** and **SCC-11** with TNT and PA respectively is in the range of 10^4 M^{-1}, which implies a strong host–guest interaction (Figs. 16.5E and F).

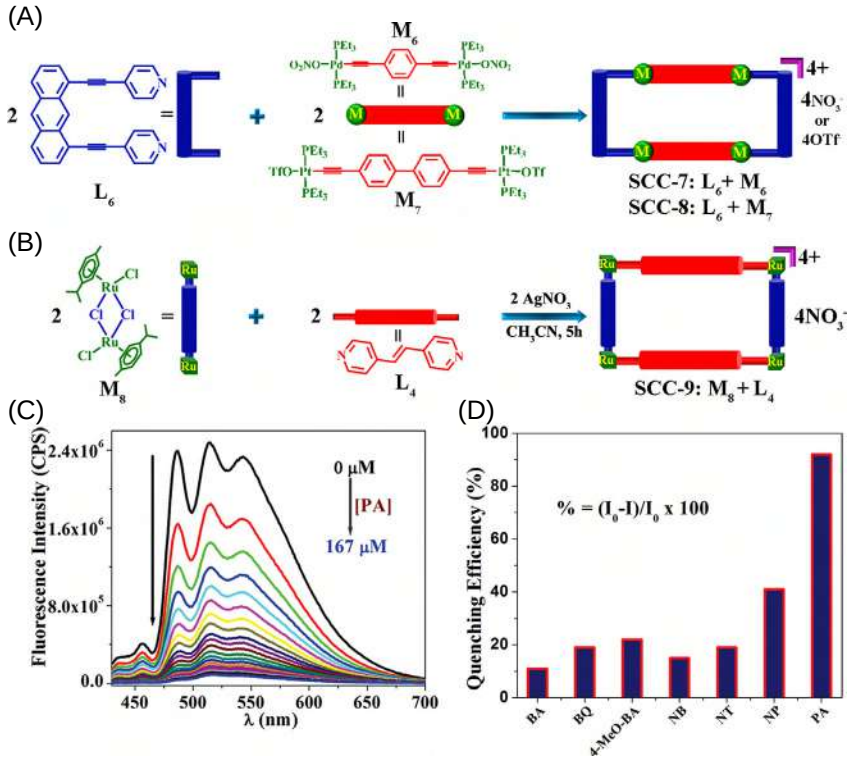

FIGURE 16.4 (A) Self-assembly of cationic molecular rectangles **SCC-7** and **SCC-8** by employing an anthracene-based "clip" donor $\mathbf{L_6}$ and linear organometallic acceptors $\mathbf{M_6}$ and $\mathbf{M_7}$; (B) the complementary design of Ru^{II}-based rectangle **SCC-9** using acceptor $\mathbf{M_8}$ and linear bipyridyl donor $\mathbf{L_3}$; (C) observed fluorescence quenching of **SCC-8** with picric acid in chloroform-methanol solution; (D) relative fluorescence quenching of **SCC-8** observed upon addition of different analytes. Reprinted with permission from Ref. [23–25]. Copyright 2011 American Chemical Society and Copyright 2011 Royal Society of Chemistry.

16.2.4 Molecular tweezer based fluorescent sensors for NACs

In 2011, Mukherjee group synthesized a Ru(II) molecular tweezer (**SCC-12**) *via* [2+2] self-assembly of $[Ru_2(\mu\text{-}\eta^4\text{-}C_2O_4)\text{-}(MeOH)_2(\eta^6\text{-}p\text{-cymene})_2][O_3SCF_3]_2$ ($\mathbf{M_{11}}$) and 1,3-bis(3-pyridylethynyl)benzene] bipyridyl donor ($\mathbf{L_9}$) [28]. The synthesized molecular tweezer shows excellent emission in methanol at $\lambda = 338$ nm. The self-quenching probability is negligible due to the presence of a bulky *p*-cymene capping unit on each Ru(II) metallic center. Upon the incremental addition of TNT into the fluorescence solution of molecular tweezer, **SCC-12** resulted in a significant quenching of fluorescence, whereas there is only a weak fluorescence attenuation observed with the addition of various other guest molecules such as BA, benzoquinone (BQ), 4-MeO-BA. On the other hand, electron-poor benzoquinone displayed notable fluorescence enhancement

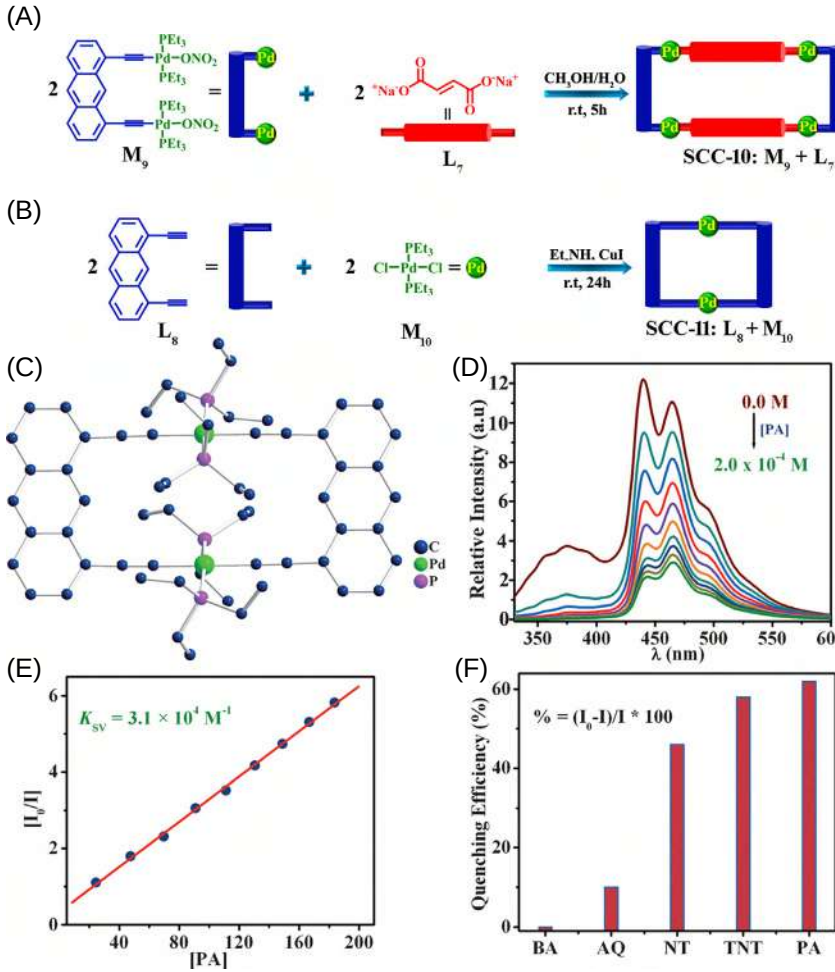

FIGURE 16.5 (A) Self-assembly formation of Pd^{II}-neutral molecular rectangle **SCC-10** through Pd-O coordination using sodium fumarate (**L_7**) and (B) the complementary design of rectangle **SCC-11** through Pd-C bond formation reaction using $[Pd(PEt_3)_2Cl_2]$; (C) Ball and stick model of the molecular structure of **SCC-11**; (D) the observed fluorescence quenching titration profile of **SCC-11** upon the gradual addition of picric acid and (E) its corresponding Stern–Volmer plot; (F) extent of observed fluorescence quenching of **SCC-11** upon the addition of various analytes. Reprinted with permission from Ref. [23,27]. Copyright 2009 Royal Society of Chemistry.

upon interacting with **SCC-12**. The formation of hydrogen bonding between the oxygen of bridging oxalate-moiety with -OH group of hydroquinone formed from the conversion of benzoquinone in solution might be the reason for this unusual behavior (Fig. 16.6).

Lu et al. created an alkoxybridged Re(I) "pincer'' macrocyclic complex (**SCC-13**) with AIEE (aggregation-induced emission enhancement) property

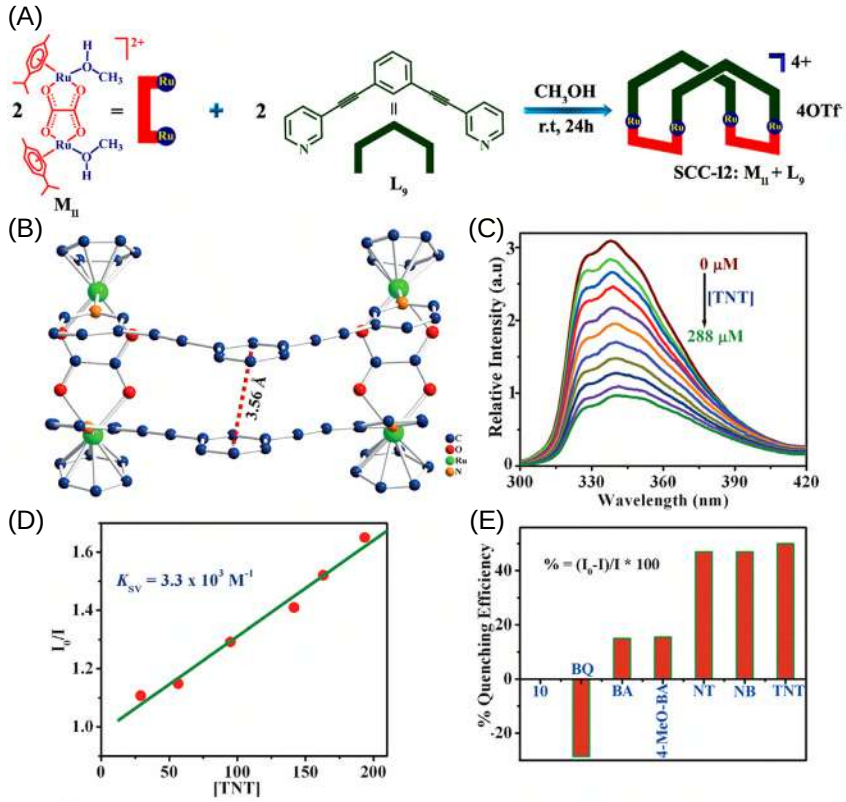

FIGURE 16.6 (A) Self-assembly of Ru^{II}-based molecular tweezer **SCC-12** by using Ru_2 acceptor $\mathbf{M_{11}}$ and bipyridyl "clip" donor $\mathbf{L_9}$; (B) ball and stick model of the molecular structure of **SCC-12**; (C) fluorescence quenching titration profile of **SCC-12** upon the gradual addition of TNT and (D) its corresponding Stern–Volmer plot and (E) extent of observed fluorescence quenching of **SCC-12** upon the addition of various analytes. Reprinted with permission from Ref. [28]. Copyright 2011 American Chemical Society.

[29]. This complex was designed by the one-pot facile self-assembly strategy under solvothermal conditions between a Re acceptor $[Re_2(CO)_{10}]$ ($\mathbf{M_{12}}$) and 4-(1-naphthylvinyl)-pyridine donor ligand ($\mathbf{L_{10}}$). This pincer complex exhibited week emission in DCM at $\lambda = 420$ nm whereas the gradual addition of polar solvent ACN to the solution resulted in a colossal enhancement of fluorescence up to an increase in the intensity by 20-fold. This might be attributed to the formation of nano aggregates *via* intermolecular interactions. In addition, the quantum yield of the complex was also enhanced upon the addition of around 90% of ACN into the **SCC-13** solution. This molecular pincer complex **SCC-13** selectively quenches PA with around 94% more efficiency than other NAC analytes and the binding constant was estimated to be $1.0 \times 10^5\ M^{-1}$.

16.2.5 Hexagonal macrocycles based fluorescent sensors for NACs

In 2016, Mukherjee and his team designed a hexagonal macrocycle (**SCC-14**) *via* [6+6] self-assembly of triphenylamine (TPA) based Pt(II) acceptor (**M_{13}**) and anthracene derived donor ligand (**L_5**) [21]. The synthesized hexagonal architecture **SCC-14** exhibited strong emission characteristics due to the AIE effect *via* restricted molecular motion. Upon incremental addition of TNT, the fluorescent intensity attenuated whereas other analytes such as nitrobenzene (NB), 3,4-dinitrotoluene (DNT), 1,3-dinitrobenzene (DNB), nitrotoluene (NT), trinitrobenzene (TNB), benzophenone, nitromethane (NM), and 3- nitrobenzoic acid (NBA) showed no significant changes in the luminescence nature of macrocycle **SCC-14**. The Stern–Volmer constant was determined to be 1.54×10^4 M^{-1} and the mechanism of quenching was analyzed to be dynamic quenching due to the changes observed in the fluorescence lifetime. Additionally, the freshly prepared thin film of macrocycle **SCC-14** showed about 64% quenching of fluorescence emission after exposure to DNT vapor for 200 s. Also, there occurs a significant quenching while exposing the film to NB vapors. The used-thin film can be recovered by washing several times with water followed by drying. This thin film exhibited excellent reusability, thus making it a good candidate for NACs sensing.

By using a TPE-based ligand (**L_1**), Stang and his group developed two different hexagons *via* coordination-driven self-assembly [16]. A 120° Pt acceptor (**M_{14}**) and a 180° Pt acceptor (**M_{15}**) in combination with **L_1** resulted in a [3+3] hexagon (**SCC-15**) and a [6+6] hexagon (**SCC-16**), respectively (Fig. 16.7A). Molecular simulation suggested a hexagonal structure with almost planar geometry having varying cavity sizes. Variations observed in the quantum yield as well as the formation of aggregate upon addition of hexane into the CH_2Cl_2 solution of the macrocycle **SCC-15** strengthened the presence of the AIE effect. Both the hexagons **SCC-15** and **SCC-16** in CH_2Cl_2/hexane mixture with 90% hexane content displayed an eminent fluorescence quenching upon the addition of PA (Figs. 16.7B and C). The Stern–Volmer constant for **SCC-15** and **SCC-16** was calculated as 1.13×10^6 M^{-1} for **SCC-15**, and 4.50×10^4 M^{-1} for **SCC-16**, and the detection limit was estimated to be 9.20 ppb for **SCC-15**, and 48.0 ppb for **SCC-16**. The quenching efficacy of **SCC-16** is higher compared to **SCC-15** due to the structural diversity between **SCC-15** and **SCC-16**. The initial emission intensity of **SCC-15** upon addition of 3.0 μg/mL PA concentration decreased by 93% whereas hexagon **SCC-16** decreased only up to 59%, and even increasing PA concentration to 40.0 μg/mL hiked the quenching only to 88% of the initial intensity (Figs. 16.7B and C). This is attributed to the largest structural skeleton of hexagon **SCC-16** which limits the tight and locked packing of the TPE group thus eventually affecting the quenching of fluorescence upon interacting with PA.

Generally, the synthesis of supramolecular metallacycle-based polymers *via* dynamic covalent bonds for NACs sensing is a rarely explored area of research

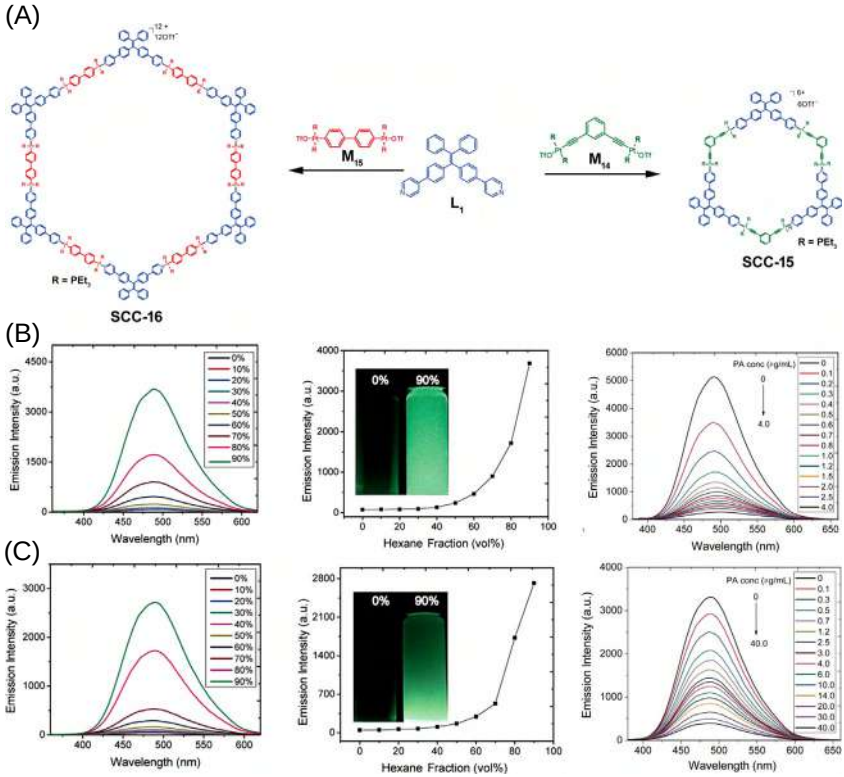

FIGURE 16.7 (A) Self-assembly formation of [3+3] molecular hexagon (**SCC-15**) and [6+6] molecular hexagon (**SCC-16**) *via* a two-component self-assembly process; (B) fluorescence emission changes of **SCC-15** in different hexane fractions (left), the corresponding plot of maximum emission intensity (Inset: photograph of **SCC-16** in CH_2Cl_2 and 10%/90% CH_2Cl_2/hexane mixture upon excitation at $\lambda = 365$ nm (middle) and fluorescence emission changes of **SCC-15** in 10%/90% CH_2Cl_2/hexane mixture upon the increasing concentration of picric acid (right); (C) fluorescence emission changes of **SCC-16** in different hexane fractions (left), the corresponding plot of maximum emission intensity (Inset: photograph of **SCC-16** in CH_2Cl_2 and 10%/90% CH_2Cl_2/hexane mixture upon excitation at $\lambda = 365$ nm (middle) and fluorescence emission changes of **SCC-16** in 10%/90% CH_2Cl_2/hexane mixture upon the increasing concentration of picric acid (right). Reprinted with permission from Ref. [16]. Copyright 2015 American Chemical Society.

because of the difficulty in synthesis. Zhang and his co-workers developed a hexagonal metallacycle (**SCC-17**) with AIE properties *via* the self-assembly of triphenylamine (TPA) derivative ($\mathbf{L_{11}}$) which acts as an AIE fluorophore and a diplatinum (II) acceptor ($\mathbf{M_{16}}$) (Fig. 16.8A) [30]. Further extended their design strategy to develop a supramolecular network (**SCC-18**) through a polymeric reaction between metallacycle **SCC-17** and amine-terminated polydimethylsiloxane (Fig. 16.8A). This supramolecular framework **SCC-18** displayed a great selectivity toward PA. The morphology and the structural features of the

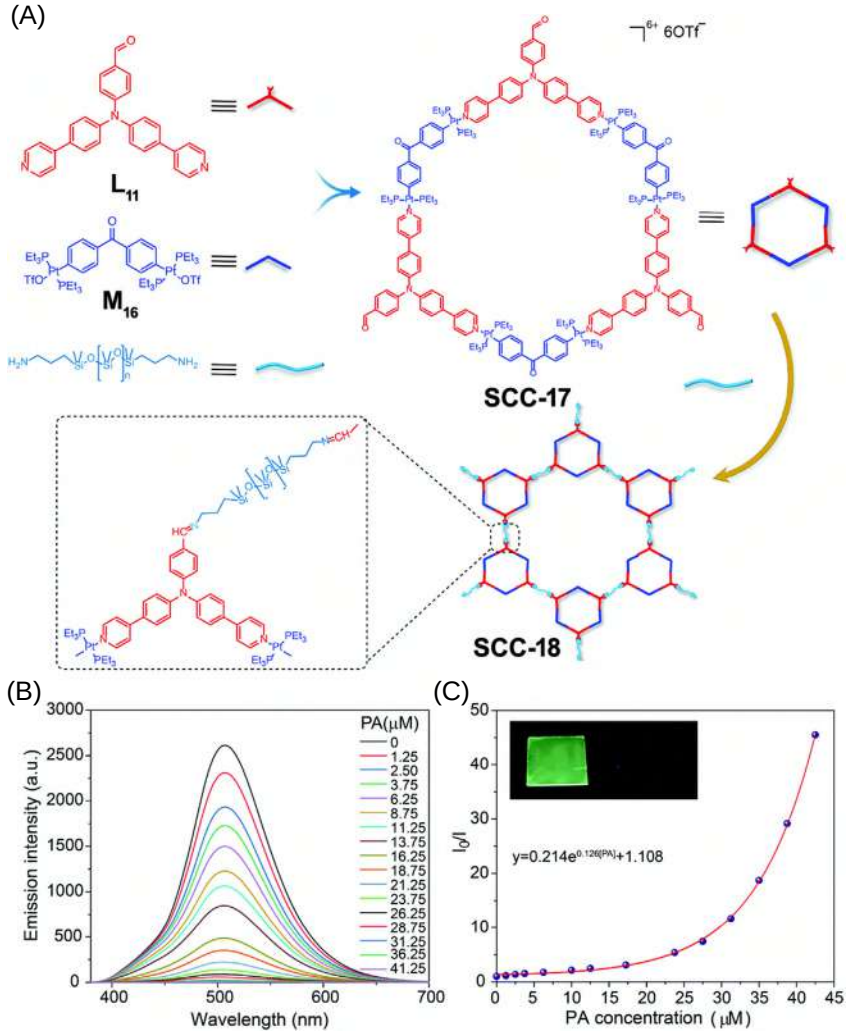

FIGURE 16.8 (A) Synthetic routes and graphical representations of molecular hexagon **SCC-17** and supramolecular network **SCC-18**; (B) the changes in emission intensity **SCC-18** on incremental addition of PA; and (C) the corresponding Stern–Volmer plot (Inset: photographs of **SCC-18** before and after the addition of PA). Reprinted with permission from Ref. [30]. Copyright 2020 Royal Society of Chemistry.

synthesized network were analyzed using scanning electron microscopy (freeze-drying method). It is observed that the quantum yield of the supramolecular network is high compared to the macrocycle **SCC-17** and the ligand $\mathbf{L_{11}}$ due to the restricted molecular motion of TPA functionality which resulted in the decrease of nonradiative decay and thus eventually increased the emission characteristics.

The fluorescence intensity of the network **SCC-18** decreased significantly upon the addition of PA. The emission intensity was almost completely quenched when 4 eq of PA was added to the supramolecular framework (Fig. 16.8B). By the nonlinear fitting method, the quenching constant was estimated to be 1.3×10^5 M^{-1} and the developed network **SCC-18** can detect the presence of PA up to 10^{-7} M concentration (Fig. 16.8C). In addition, freshly made thin film of supramolecular network system **SCC-18** showed a notable quenching efficiency upon adding a tiny drop of PA solution in dichloromethane (Fig. 16.8C). Therefore, the synthesized supramolecular network can act as a selective sensor for PA.

16.3 Fluorescence sensing by 3D metallocages

The self-assembly process of three-dimensional supramolecular architecture is intricate and challenging in comparison to two-dimensional ensembles. Usually, the development of 3D complexes requires more inventive and ingenious design pathways and thus, 3D molecular architectures are a keen topic of interest in modern research [22]. Three-dimensional cages show much more sensing characteristics compared to other systems as these architectures can not only interact with the guest *via* the surface of the cage systems but through encapsulation of the guest molecules in the internal cavities. The main design requirement for the synthesis of 3D molecular ensembles is the presence of building blocks with three or more reactive sites to generate a three-dimensional structure (Fig. 16.9).

16.3.1 Molecular trigonal prism based fluorescent sensors for NACs

In recent years, numerous trigonal prismatic three-dimensional metallocages with practical applications especially in the field of nitro-aromatic sensing were developed and examined. Generally, the top and bottom of these trigonal prismatic architectures are electron-rich to encapsulate the electron-poor NACs strongly snug inside the cavity [31]. Methodical analyses have been conducted to study the efficiency of these supramolecular assemblies for the construction of NACs sensing fluorescent probes. Mukherjee and his group devised a trigonal prism (**SCC-19**) *via* coordination driven [2+3] self-assembly of Pt(III) acceptor [4,4',4''-tris{trans-Pt(PEt_3)$_2$(NO_3)(ethynyl)}triphenylamine] (**M_{17}**) and an amide-derived "clip" type donor (**L_{12}**) [32]. The as-synthesized prism **SCC-19** showed exceptional binding affinity toward nitroaromatic systems especially, PA and TNT. For PA, the fluorescence quenching was observed at $\lambda = 413$ nm, whereas the intensity of fluorescence attenuated at 546 nm upon incremental addition of TNT into the metallocage architecture. In addition, the Stern–Volmer plots established the binding constant around 19.6×10^3 M^{-1} and 48.1×10^3 M^{-1} for TNT and PA, respectively. Later, various π-conjugated trigonal prismatic cages derived from triphenylbenzene were developed and their sensing ability toward NACs was investigated. The coordination-driven self-assembly

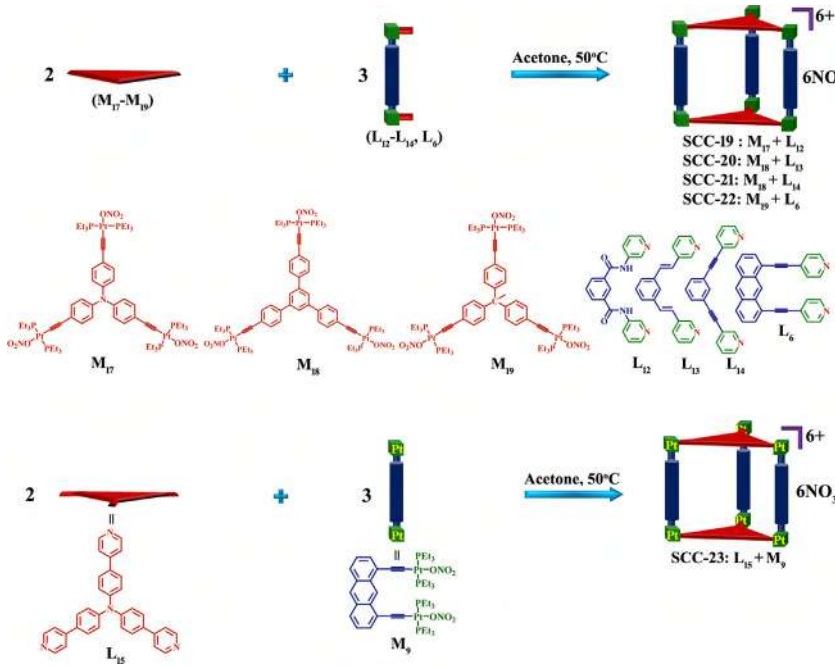

FIGURE 16.9 [2+3] Self-assembly formation of Pt^{II}-based trigonal prismatic cages **SCC-19** to **SCC-23** by employing tritopic Pt^{II} acceptors $\mathbf{M_{17}}$-$\mathbf{M_{19}}$ and $\mathbf{M_9}$ with a series of "clip" donors ($\mathbf{L_6}$, $\mathbf{L_{12}}$-$\mathbf{L_{15}}$). Reprinted with permission from Ref. [31]. Copyright 2015 Wiley.

process between a tritopic planar acceptor ($\mathbf{M_{18}}$) and two distinct donor ligands ($\mathbf{L_{13}}$, $\mathbf{L_{14}}$) leads to the generation of two different trigonal prisms (**SCC-20**) and (**SCC-21**), respectively [33]. Both these cage structures showed sufficient fluorescence quenching toward PA (98% efficiency for **SCC-20** and 93% for **SCC-21**). In addition, the Stern–Volmer binding constants were estimated to be $4.51 \times 10^4\ M^{-1}$ for **SCC-20** and $3.58 \times 10^4\ M^{-1}$ for **SCC-21**, and these trigonal prisms displayed remarkable sensing affinity even in ppb level concentration of PA. Also, a strong fluorescence attenuation (about 46%) was observed even upon the exposure of saturated vapors of PA on the freshly prepared thin film of cage **SCC-20**.

Further to this strategy, the same group designed a novel distorted trigonal prism (**SCC-22**) from the self-assembly of a rigid clip type anthracene donor ligand ($\mathbf{L_6}$) with a tripodal acceptor [1,3,5-tris{4-trans-$Pt(PEt_3)_2(NO_3)$(ethynyl)phenyl}benzene] ($\mathbf{M_{19}}$) generated by substituting the central phenyl in $\mathbf{M_{18}}$ and nitrogen in $\mathbf{M_{17}}$ with -$C(CH_3)$ group [34]. The synthesized distorted trigonal prism **SCC-22** displayed emissive nature in DMF around $\lambda = 400$–500 nm upon excitation at $\lambda = 400$ nm having a lifetime of 6.2 ns and quantum yield of 0.35. The fluorescence intensity of the cage was significantly attenuated in the presence of TNT with a binding constant of

1.73×10^2 M^{-1}. The binding affinity of the cage toward TNT was further confirmed by comparing the fluorescence changes of the precursors: acceptor $\mathbf{M_{19}}$ and donor $\mathbf{L_6}$ upon increasing the concentration of TNT. The metal acceptor $\mathbf{M_{19}}$ showed no quenching effect with TNT and the clip type donor ligand $\mathbf{L_6}$ showed extremely low fluorescent quenching which signifies the importance of the cage architecture. The cage structure facilitates a strong host–guest interaction with TNT inside the hydrophobic interior cavity. Additionally, upon exposure to saturated vapors of TNT on a spin-coated thin film of the cage **SCC-22** displayed gradual quenching of fluorescence. Another method complementary to the above designed by the same researchers involves the synthesis of a trigonal prism (**SCC-23**) from the self-assembly of platinum-based clip acceptor [1,8-bis{trans-$Pt(PEt_3)_2(NO_3)$(ethynyl)}anthracene] ($\mathbf{M_9}$) with triphenylamine-derived tritopic planar donor ligand 4,4',4''-tris(4-pyridylethynyl) triphenylamine ($\mathbf{L_{15}}$) [34]. The expected cage structure was precipitated as bright yellow powder upon reacting the donor and acceptor in acetone at 50°C. Cage **SCC-23** showed an eminent luminescent response at $\lambda = 472$ nm with a lifetime in the range of 8.0 ns and a quantum yield around 0.48. Also, this trigonal prism **SCC-23** displayed effective quenching upon incremental addition of DNT and TNT.

In addition to Pt^{II}-metallocages, several octahedral metal ions such as Re(I) and Ru(II) were utilized for the synthesis of metallocages and used for NAC sensing application. Mukherjee et al. developed two trigonal prismatic metallocages (**SCC-24**) and (**SCC-25**) from the self-assembly of half-sandwiched Ru(II) metal acceptors ($\mathbf{M_{11}}$ and $\mathbf{M_{20}}$) with an organic tritopic ligand 1,3,5-tris(4-pyridylethynyl)benzene ($\mathbf{L_{16}}$) in 2:3 molar ratio [35]. The face-to-face arrangement of two planar tritopic ligands in addition to the three ruthenium metal acceptors resulted in the generation of trigonal prismatic architecture with about 24 Å distance between adjacent edges and a height of around 7 Å. Methanolic solution of cages **SCC-24** and **SCC-25** displayed emissions at $\lambda = 349$, 361, and 380 nm with quantum yields of about 0.12 and 0.22 respectively. **SCC-24** exhibited a quenching of fluorescence for about 70% upon the addition of 149 μM TNT. The further addition of TNT presented a linear response up to 150 μM ($K_{SV} = 2.1 \times 10^4$ M^{-1}). However, the fluorescence intensity lowered completely upon the addition of about 45.8 μM PA ($K_{SV} = 1.0 \times 10^5$ M^{-1}) due to the higher electron-deficient nature of PA compared to TNT. No notable fluorescence quenching was observed when cages **SCC-24** and **SCC-25** were exposed to similar interfering compounds such as BQ, MeOBA, and BA. A similar kind of Re(I)-based neutral molecular cage (**SCC-26**) was synthesized by Lu and coworkers *via* one-pot self-assembly of Re(I) metal acceptor [$Re_2(CO)_{10}$] ($\mathbf{M_{12}}$) with triazine-based donor ligand 2,4,6-tri-4-pyridyl-1,3,5-triazine ($\mathbf{L_{17}}$) and indigo ($\mathbf{L_{18}}$) as a bridging unit, as given in Figure 16.10 [36]. The quantum yield and lifetime of the assembly were estimated to be 0.01 and 5.5 ns, respectively. The π–π^* excited state of indigo in **SCC-26** resulted in a strong emission of fluorescence around $\lambda = 392$ nm upon excitation around $\lambda = 350$ nm. A strong fluorescence attenuation along with the bathochromic shift from $\lambda = 392$ to

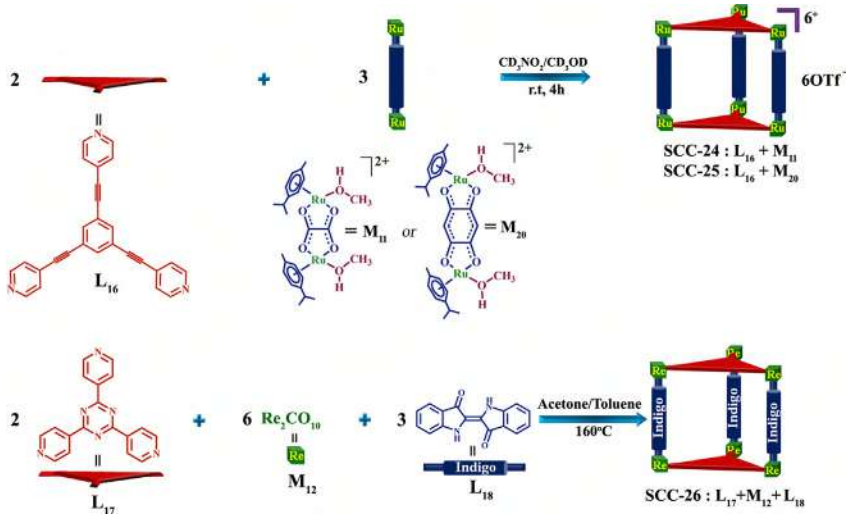

FIGURE 16.10 Two-component self-assembly of Ru^{II}-based trigonal prismatic cages **SCC-24, SCC-25** by employing the π-conjugated tritopic donor $\mathbf{L_{16}}$ with Ru_2^{II} acceptors $\mathbf{M_{11}}$ and $\mathbf{M_{20}}$, respectively, and in-situ generation of Re(I)-based prism **SCC-26** using triazine donor ($\mathbf{L_{17}}$) with indigo-bridging ligand ($\mathbf{L_{18}}$) and Re_2CO_{10} ($\mathbf{M_{12}}$). Reprinted with permission from Ref. [31]. Copyright 2015 Wiley.

397 nm was observed with the addition of nitrobenzene derivatives into the solution of cage **SCC-26** and the Stern–Volmer binding constant was estimated to be in the range of 2.0×10^2 M^{-1} to 4.2×10^3 M^{-1}.

16.3.2 Molecular tetragonal prism-based fluorescent sensors for NACs

Due to the synthetic complexity and suitable precursor selection, the development of tetragonal prisms seldom occurs. In 2012, Shanmugaraju et al. developed a unique tetragonal prism (**SCC-27**) through coordination-driven [2+4] self-assembly between tetratopic Pt(I) acceptor [1,3,6,8-tetrakis{trans-$Pt(PEt_3)_2$(I)(ethynyl)}pyrene] ($\mathbf{M_{21}}$) and a clip donor ligand unit ($\mathbf{L_{12}}$) (Fig. 16.11A) [37]. The internal diameter of the cage was about 2.02 nm and the distance between the top and bottom donor pyrene unit was estimated to be 1.41 nm from the energy-minimized structure of the tetragonal cage **SCC-27**. These values indicate the ability of the tetragonal prism **SCC-27** to encapsulate the guest species into their internal pores. The cage architecture showed selective fluorescence quenching upon the increase in the concentration of TNT with a binding constant $K_{SV} = 9.7 \times 10^5$ M^{-1}. An explicit shift in the color visualized under a UV lamp implies the occurrence of a static quenching mechanism through the formation of a ground state charge-transfer complex between the tetragonal prism **SCC-27** and TNT (Fig. 16.11B). Titration of **SCC-27** with nitroaromatics like PA and TNT showed a prominent quenching response while

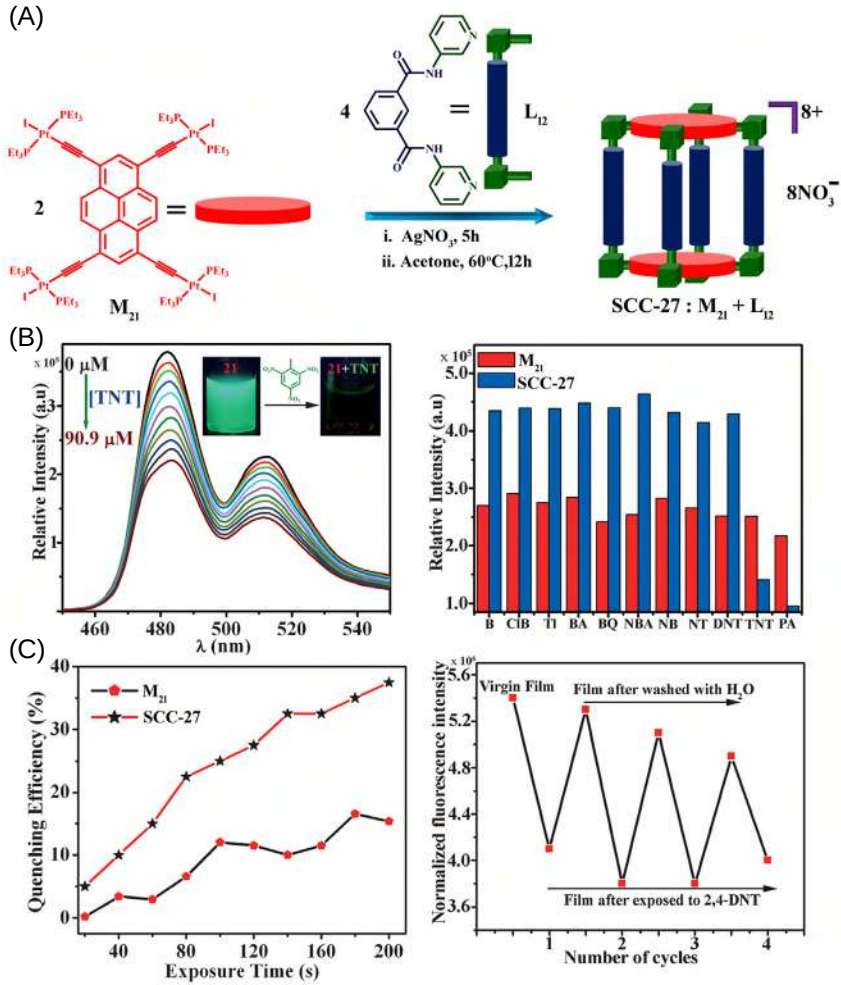

FIGURE 16.11 (A) Two-component [2+4] self-assembly formation of tetragonal prism **SCC-27** by employing a star-shaped Pt^{II}–pyrene acceptor (**M_{21}**) and amide-based "clip" donor (**L_{12}**). (B) Observed fluorescence quenching of prism **SCC-27** upon the addition of TNT (left, inset: visual color change under UV light) and relative changes in the emission intensity of **SCC-27** upon the mixing of different analytes (right). (C) The quenching efficiency of **SCC-27** and **M_{21}** as a function of the exposure time (left) and reproducibility of sensing ability of thin film of **SCC-27** to the saturated vapor of 2,4-DNT (right).

other competitive analytes such as benzene, benzoquinone, toluene, and benzoic acid displayed a weak quenching effect. Most importantly, the as-synthesized prism **SCC-27** senses TNT even below the permissible TNT level in drinking water. The acceptor **M_{21}** upon titration with TNT resulted in a binding efficacy lower than the porous tetragonal prismatic cage **SCC-27** which implies the

significance of the formation of cage architecture in sensing. The selective binding toward NACs was due to the host–guest interaction between the electron-rich nanocavity of the cage and the electron-poor NACs. Moreover, the freshly prepared thin film of cage **SCC-27** and the metal acceptor $\mathbf{M_{21}}$ displayed a decrease in the fluorescence intensity after the exposure of DNT to about 200s at standard temperature conditions. However, **SCC-27** showed attenuation in the intensity to about 40% whereas $\mathbf{M_{21}}$ quenched only up to 13% (Fig. 16.11C). In addition, the developed prism **SCC-27** showed reversible sensing affinity toward NACs in both solutions as well as vapor phases.

16.4 Conclusion

In summary, we have exemplified a plethora of discrete luminescent 2D metallacycles and 3D metallocages and demonstrated their fluorescence sensing properties toward secondary chemical explosives NACs. The high selectivity and strong binding affinity of SCCs toward electron-poor NACs were attributed to their π-electron-rich nature that facilitates a strong donor–acceptor type of interactions and the presence of confined internal cavity furthering sensing efficiency by forming a strong host–guest complexation through multiple noncovalent supramolecular interactions. The facile self-assembly procedure along with ease of functionalization make these metalloassemblies a suitable candidate for sensing. Despite all the advantages, most of these architectures exhibit limited practical applicability because of the lack of reversibility and in some cases low sensitivity. Increasing the link between discrete molecular entities *via* various supramolecular interactions would improve the sensitivity by promoting long-range exciton migration through the adjacent metallacycles and cages. In light of this, scientists are exploring the design and construction of extended polymeric networks such as supramolecular polymers, MOFs, COFs, POPs, and HOFs and studying their fluorescence sensing application along with the sequestration of hazardous pollutants.

Acknowledgment

We acknowledge the financial support received from the Science and Engineering Research Board (EMEQ Award EEQ/2018/000799 to SS), India, and the Indian Institute of Technology Palakkad (IITPKD).

References

[1] D. Banerjee, Z. Hu, Luminescent metal-organic frameworks as explosive sensors, Dalton Trans. 43 (2014) 10668–10685.

[2] Y. Salinas, R. Martnez-Manez, M.D. Marcos, F. Sancenon, A.M. Costero, M. Parraad, S. Gilad, Optical chemosensors and reagents to detect explosives, Chem. Soc. Rev. 41 (3) (2012) 1261–1296.

[3] L. Senesac, T.G. Thundat, Nanosensors for trace explosive detection, Mater. Today 11 (3) (2008) 28–36.

[4] S. Shanmugaraju, P.S. Mukherjee, π-Electron rich small molecule sensors for the recognition of nitroaromatics, Chem. Commun. 51 (89) (2015) 16014–16032.
[5] M. Brutschy, M.W. Schneider, M. Mastalerz, S.R. Waldvogel, Porous organic cage compounds as highly potent affinity materials for sensing by quartz crystal microbalances, Adv. Mater. 24 (45) (2012) 6049–6052.
[6] D.A. Moore, Instrumentation for trace detection of high explosives, Rev. Sci. Instrum. 75 (8) (2004) 2499.
[7] T.W. Bell, N.M. Hext, Supramolecular optical chemosensors for organic analytes, Chem. Soc. Rev. 33 (9) (2004) 589–598.
[8] M.E. Germain, M.J. Knapp, Optical explosives detection: from color changes to fluorescence turn-on, Chem. Soc. Rev. 38 (9) (2009) 2543–2555.
[9] K.K. Kartha, S.S. Babu, S. Srinivasan, A. Ajayaghosh, Attogram sensing of trinitrotoluene with a self-assembled molecular gelator, J. Am. Chem. Soc. 134 (10) (2012) 4834–4841.
[10] S. Rochat, T.M. Swager, Conjugated amplifying polymers for optical sensing applications, ACS Appl. Mater. Interfaces 5 (11) (2013) 4488–4502.
[11] S.J. Toal, W.C. Trogler, Polymer sensors for nitroaromatic explosives detection, J. Mater. Chem. 16 (28) (2006) 2871–2883.
[12] D.A. Olley, E.J. Wren, G. Vamvounis, M.J. Fernee, X. Wang, P.L. Burn, P. Meredith, P.E. Shaw, Explosive sensing with fluorescent dendrimers: the role of collisional quenching, Chem. Mater. 23 (3) (2011) 789–794.
[13] P.E. Shaw, S.S.Y. Chen, X. Wang, P.L. Burn, P. Meredith, High-generation dendrimers with excimer-like photoluminescence for the detection of explosives, J. Phys. Chem. C. 117 (10) (2013) 5328–5337.
[14] J.R. Nitschke, Construction, substitution, and sorting of metallo-organic structures via subcomponent self-assembly, Acc. Chem. Res. 40 (12) (2007) 103–112.
[15] R. Chakrabarty, P.S. Mukherjee, P.J. Stang, Supramolecular coordination: self-assembly of finite two- and three-dimensional ensembles, Chem. Rev. 111 (11) (2011) 6810–6918.
[16] X. Yan, H. Wang, C.E. Hauke, T.R. Cook, M. Wang, M.L. Saha, Z. Zhou, M. Zhang, X. Li, F. Huang, P.J. Stang, A suite of tetraphenylethylene-based discrete organoplatinum(II) metallacycles: controllable structure and stoichiometry, aggregation-induced emission and nitroaromatics sensing, J. Am. Chem. Soc. 137 (48) (2015) 15276–15286.
[17] F. Würthner, C.-C. You, C.R. Saha-Möller, Metallosupramolecular squares: from structure to function, Chem. Soc. Rev. 33 (3) (2004) 133–146.
[18] P.J. Stang, B. Olenyuk, Self-assembly, symmetry, and molecular architecture: coordination as the motif in the rational design of supramolecular metallacyclic polygons and polyhedra, Acc. Chem. Res. 30 (12) (1997) 502–518.
[19] V. Vajpayee, H. Kim, A. Mishra, P.S. Mukherjee, P.J. Stang, M.H. Lee, H.K. Kim, K.-W. Chi, Self-assembled molecular squares containing metal-based donor: synthesis and application in the sensing of nitro-aromatics, Dalton Trans. 40 (13) (2011) 3112–3115.
[20] S. Shanmugaraju, D. Samanta, B. Gole, P.S. Mukherjee, Coordination-driven self-assembly of 2D-metallamacrocycles using a shape-selective $Pt(II)_2$-organometallic 90° acceptor: design, synthesis and sensing study, Dalton Trans. 40 (45) (2011) 12333–12341.
[21] A. Chowdhury, P. Howlader, P.S. Mukherjee, Aggregation-induced emission of platinum(II) metallacycles and their ability to detect nitroaromatics, Chem. Eur. J. 22 (22) (2016) 7468–7478.
[22] P.J. Stang, B. Olenyuk, Self-Assembly, symmetry, and molecular architecture: coordination as the motif in the rational design of supramolecular metallacyclic polygons and polyhedra, Acc. Chem. Res. 30 (12) (1997) 502–518.

[23] A.K. Bar, S. Shanmugaraju, K.-W. Chi, P.S. Mukherjee, Self-assembly of neutral and cationic PdII organometallic molecular rectangles: synthesis, characterization and nitroaromatic sensing, Dalton Trans. 40 (10) (2011) 2257–2267.

[24] S. Shanmugaraju, S.A. Joshi, P.S. Mukherjee, Self-assembly of metallamacrocycles using a dinuclear organometallic acceptor: synthesis, characterization, and sensing study, Inorg. Chem. 50 (22) (2011) 11736–11745.

[25] S. Shanmugaraju, H. Jadhav, P.S. Mukherjee, Self-assembly of chloro-bridged arene–ruthenium-based rectangle: synthesis, structural characterization and sensing study, Proc. Indian Acad. Sci. Sect. A 84 (2) (2014) 197–203.

[26] P. Thanasekaran, C.-H. Lee, K.-L. Lu, Neutral discrete metal-organic cyclic architectures: opportunities for structural features and properties in confined spaces, Coord. Chem. Rev. 280 (2014) 96–175.

[27] A.K. Bar, B. Gole, S. Ghosh, P.S. Mukherjee, Self-assembly of a Pd(II) neutral molecular rectangle via a new organometallic Pd(II)2 molecular clip and oxygen donor linker, Dalton Trans. (34) (2009) 6701–6704.

[28] S. Shanmugaraju, A.K. Bar, S.A. Joshi, Y.P. Patil, P.S. Mukherjee, Constructions of 2D-metallamacrocycles using half-sandwich Ru^{II}_2 precursors: synthesis, molecular structures, and self-selection for a single linkage isomer, Organometallics 30 (7) (2011) 1951–1960.

[29] V. Sathish, A. Ramdass, Z.-Z. Lu, M. Velayudham, P. Thanasekaran, K.-L. Lu, S. Rajagopal, Aggregation-induced emission enhancement in alkoxy-bridged binuclear rhenium(I) complexes: application as sensor for explosives and interaction with microheterogeneous media, J. Phys. Chem. B 117 (46) (2013) 14358–14366.

[30] Y. Hou, S. Li, Z. Zhang, L. Chena, M. Zhang, A fluorescent platinum(II) metallacycle-cored supramolecular network formed by dynamic covalent bonds and its application in halogen ions and picric acid detection, Polym. Chem. (11) (2020) 254–258.

[31] S. Shanmugaraju, P.S. Mukherjee, Self-assembled discrete molecules for sensing nitroaromatics, Chem. Eur. J. 21 (18) (2015) 6656–6666.

[32] S. Ghosh, P.S. Mukherjee, Self-assembly of a nanoscopic prism via a new organometallic Pt_3 acceptor and its fluorescent detection of nitroaromatics, Organometallics 27 (3) (2008) 316–319.

[33] D. Samanta, P.S. Mukherjee, PtII6 nanoscopic cages with an organometallic backbone as sensors for picric acid, Dalton Trans. 42 (48) (2013) 16784–16795.

[34] S. Ghosh, B. Gole, A.K. Bar, P.S. Mukherjee, Self-assembly of molecular prisms via Pt_3 organometallic acceptors and a Pt_2 organometallic clip, Organometallics 28 (15) (2009) 4288–4296.

[35] M. Wang, V. Vajpayee, S. Shanmugaraju, Y.-R. Zheng, Z. Zhao, H. Kim, P.S. Mukherjee, K.-W. Chi, P.J. Stang, Coordination-driven self-assembly of M_3L_2 trigonal cages from preorganized metalloligands incorporating octahedral metal centers and fluorescent detection of nitroaromatics, Inorg. Chem. 50 (4) (2011) 1506–1512.

[36] J.Y. Wu, C.H. Chang, P. Thanasekaran, C.C. Tsai, T.W. Tseng, G.H. Lee, S.M. Peng, K.-L. Lu, Unusual face-to-face pi-pi stacking interactions within an indigo-pillared M3(tpt)-based triangular metalloprism, Dalton Trans. (44) (2008) 6110–6112.

[37] S. Shanmugaraju, H. Jadhav, Y.P. Patil, P.S. Mukherjee, Self-assembly of an octanuclear platinum(II) tetragonal prism from a new $Pt(II)_4$ organometallic star-shaped acceptor and its nitroaromatic sensing study, Inorg. Chem. 52 (24) (2012) 13072–13074.

Chapter 17

Metal ion sensing applications of finite supramolecular coordination complexes

Arivazhagan Chinnappa[a], **Jeyabalan Shanmugapriya**[b] **and Gandhi Sivaraman**[c]

[a] *Department of Chemistry, National Institute of Technology, Tiruchirappalli, Tamil Nadu, India,* [b] *Department of Chemistry, Madura College, Madurai, Tamil Nadu, India,* [c] *Department of Chemistry, Gandhigram Rural Institute-Deemed to be University, Dindigul, Tamil Nadu, India*

17.1 Introduction

Supramolecular chemistry has led to the discovery of stunning views and complex functional structures in varied sizes and shapes during the last few decades [1]. Within the supramolecular chemistry, the coordination-driven self-assembly of discrete supramolecular coordination complexes (SCCs), ranging from two-dimensional (2D) assemblies (rhomboids, squares, rectangles, triangles, and pentagons, etc.) to three-dimensional (3D) assemblies (trigonal pyramids, trigonal prisms, cubes, cuboctahedra, cages, double squares, adamantanoids, dodecahedra, and a variety of other cages and containers) has attracted considerable attention not only because of their beautiful structures of complexity but also their diverse applications in catalysis [2], sensing [3], separation [4], biomedical [5], and in host–guest chemistry [6], and other fields [7–11]. Synthetic advantages include fewer steps, fast and easy creation of the final products, one-pot synthesis, high yield, inherent self-correction, and defect-free assembly leading to the formation of thermodynamically stable products, compared to the classical covalent technique [12,13].

Self-assembly driven by coordination has shown to be a successful method for the formation of a wide variety of complex supramolecular structures, presented with the opportunity of cationic metal nodes with numerous coordination sites and multidentate Lewis base ligands to spontaneously self-assemble. Since the early pioneering work by Lehn [14] and Sauvage [15] coordination-driven self-assembly in the construction of infinite helicates, grids, ladders, rack, knots, rings, and related species has been studied by numerous groups on the feasibility

Supramolecular Coordination Complexes: Design, Synthesis, and Applications.
DOI: https://doi.org/10.1016/B978-0-323-90582-4.00009-9

and use those of Stang [16], Raymond [17], Fujita [18], Mirkin [19], Cotton [20], Shionoya [21], Nitschke [22], Newkome [23], and others [24,25]—various approaches have been used to construct well-defined shapes and dimensions for metallacycles and metallacages. In many ways, this research has been motivated by a desire to create stunning structures capable of accommodating ionic and molecular guests. In many of these SCCs, the metal ion and the organic linker provide a precise connectivity and geometry mandatory for the final product.

Conversely, we can add substantial functionality to the final assembly by simply introducing the required functionalities through various functional groups [26]. In particular, incorporation of transition metals into these assemblies often lead to the emergence of distinctive optical and electrochemical properties. As the properties of the final assemblies can also be manipulated by the functional groups, incorporation of different functional groups also challenging in the area of metallasupramolecular chemistry. In molecular-scale devices like sensors, the structural complexity of self-assembled systems can yield exciting features that can be easily exploited. This strategy has several advantages over conventional methods. Conventional methods of designing molecular-scale sensors are extremely demanding but time-consuming [27,28]. Metal-ligand coordination-driven self-assembly techniques, on the other hand, can lead to a vast and diverse number of structural motifs with high yields of structurally complex functional assemblies in a fewer step [29]. Thus, coordination-driven self-assembly is an effective tool for synthesizing metallamacromolecules of various sizes and shapes, which offers a promising platform for the sensing applications [30].

Supramolecular coordination chemistry was reviewed in several insightful review studies that focused on the design and synthesis of discrete SCCs where certain functional features were offered [31,32]. However, in this chapter, we focus on the journey of coordination-driven self-assembled SCCs of discrete 2D and 3D supramolecular ensembles for metal ion detection and isolation.

17.2 Alkali metal ion sensing by 2D and 3D supramolecular coordinaiton complexes

Metal ions play a vital role in fundamental processes of all living forms, which include osmotic regulation, catalysis, metabolism, biomineralization, and cell signaling [33]. Especially, Group I alkali metals such as Na^+ and K^+ are major ions present in our body fluid. Alkali metals Na^+ and K^+ play essential roles in many biological processes, such as they maintain the fluid and electrolyte balance, systemic blood pressure control, insulin metabolism and neurotransmission, and pH values [34]. Imbalances of these ions will result in Alzheimer's disease, anorexia, heart disease, and diabetes. Li^+ salts remain among the most important and habitually used drugs for the management of Alzheimer's disease, skin disease, amyotrophic lateral sclerosis and schizophrenia, and manic depression [35]. Therefore, the detection of these metal ions is quite important for both clinical diagnosis and biochemical applications.

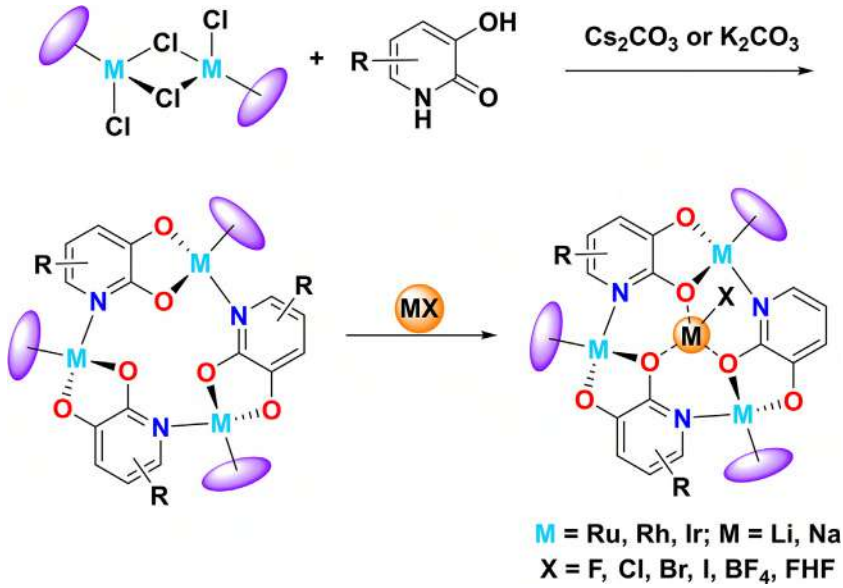

FIGURE 17.1 General synthetic scheme for the synthesis of trinuclear metallamacrocycles and their binding with alkali metals.

17.2.1 2D metallamacrocyclic receptors for alkali metals

Generally, metallacycles can be easily prepared with predictable sizes and shapes by the careful choice of complementary ligands to metals, through coordination-driven self-assembly under mild conditions to give quantitative yields of the final complex. Metallamacrocycles possess different kinds of cavities with well-defined sizes and shapes, which makes them excellent candidates for sensing applications.

The Severin and co-workers have carried out a wide range of research on the self-assembly of metallacrowns (MC) of the M-N-C-O series of 12-MC-3 complexes using half-sandwich organometallic fragments with rigid orthogal ligands [36–47]. The first structure of 12-MC-3 reported in this series is [Ru^{II}-N-C-O]$_3$ metallamacrocycle (1). The MC connectivity is provided by three tridentate dianion of 3-hydroxy-2-pyridone ligands occupying the bridging position and the coordination sphere of the Ru^{II} at the corners of the triangle. Synthesis of these metallamacrocycles is quite simple, for example, treatment of [(*p*-cymene)$RuCl_2$]$_2$ with 3-hydroxy-2-pyridone in the presence of base (Cs_2CO_3 or K_2CO_3) to give the [Ru^{II}-N-C-O]$_3$ metallamacrocycle.

The structure of these types of MC complexes has proven to be very common, with half sandwich metal corners such as Rh^{III} and Ir^{III}, wide range of derivatives of the 3-hydroxy-2-pyridone ligands used to create an assortment of 12-MC-3 complexes (Fig. 17.1).

Lithium and sodium ion receptors with great selectivity and sensitivity were discovered in several of these metallacycles, with binding constants based on the

TABLE 17.1 The number of host–guest complexes characterized X-ray crystallographically along with references.[a]

Entry	Ligand	Metal	Crystal structures isolated with		References
			Li^+ Salt	Na^+ Salt	
1	L1	(*p*-$MeC_6H_4{}^iPr$)Ru	LiCl	NaCl	[36]
2	L1	(*p*-$MeC_6H_4{}^iPr$)Ru	–	NaI	[37]
3	L1	(C_6H_6)Ru	LiCl	NaBr	
4	L1	(Me_5C_5)Rh	LiCl	–	
5	L1	($C_6H_4CO_2Et$)Ru	LiCl	NaCl	[38]
6	L1	(Me_5C_5)Ir	$LiBF_4$	–	[39]
7	L1	(Me_5C_5)Ir	LiF	–	
8	L1	(*p*-$MeC_6H_4{}^iPr$)Ru	$LiBF_4$	–	[40]
9	L1	(Me_5C_5)Rh	$LiBF_4$	–	
10	L1	(*p*-$MeC_6H_4{}^iPr$)Ru	LiF	–	
11	L1	(Me_5C_5)Rh	LiF	–	
12	L1	(*p*-$MeC_6H_4{}^iPr$)Ru	LiFHF	–	
13	L1	(Me_5C_5)Ir	LiFHF	–	
14	L1	(*p*-$MeC_6H_4{}^iPr$)Ru	–	$NaBF_4$	[41]
15	L1	(*p*-$MeC_6H_4{}^iPr$)Ru	–	Na_2SiF_6	
16	L2	(*p*-$MeC_6H_4{}^iPr$)Ru	LiCl	NaCl	[43]
17	L1	(C_6H_5Me)Ru	LiCl	–	[46]
18	L1	($C_6H_3{}^iPr_3$)Ru	LiCl	–	

[a] *(L1 = 2,3-dihydroxypyridine; L2 = 5-chloro-2,3-dihydroxypyridine).*

half-sandwich fragment type, ligand, and target concentration and pH. Binding constants were compared with various crown ethers and cryptands, and the stability of complex formed between MC and Li^+ or Na^+ and are in most cases three orders higher than that of crown ethers or cryptands. Due to the higher stability of these metallacrown alkali metal complexes, detection, and isolation of alkali metals in water were also carried out successfully. Among Li^+ and Na^+, the selectivity was higher for Li^+ than Na^+. NMR, electrochemistry, and colorimetry were used to measure the host–guest complex concentrations. In general, metal ion binding with MC induces peak potential to shift toward anodic region. In all complexes, the alkali metal is bound to the oxygen atoms of the MC ring, the halide anion is bound to the alkali metal, and the alkali metal and MC ring also form a 1:1 host–guest ratio, except Na_2SiF_6, where two MC rings ($12MC_{Ru}{}^{II}$-3) (1) encapsulate one Na^+ ion. [41] If the π-ligand attached on the metal is bulk, then that complex will be very selectively bind with Li^+ ions. Table 17.1 shows the number of host–guest complexes characterized

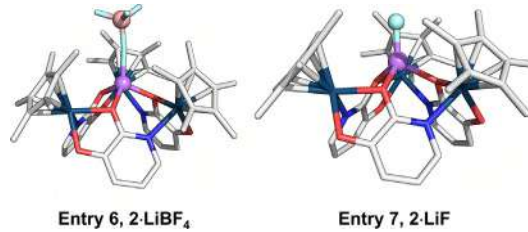

FIGURE 17.2 Crystal structures of alkali metal bound Ir-metallacrown complexes. This figure was reproduced using data downloaded from the Cambridge Crystallographic Data Centre (CCDC No. 175846 and 175845).

X-ray crystallographically along with references and Fig. 17.2 shows the crystal structures of few alkali metal-bound metallacrown Ir based complexes (2).

Interestingly, incorporation of pyrene, dansyl, and methoxycoumarin into the 12-$MC_{Ru}{}^{II}$-3 metallamacrocycle provided the opportunity to detect alkali metal through fluorescence sprectroscopy [47]. As shown in Fig. 17.3, the dansyl unit incorporated metallacycle (3) displayed a pronounced fluorescence peak at 547 nm when excited at 360 nm. Upon addition of LiCl the signal intensity was increased due to a 'turn-on' response of the receptor upon binding of Li^+. They ascribed the binding of Li^+ reducing the ability of Ru centers to quench the fluorescence of dansyl groups. Methoxycoumarin appended macrocycle has been used to detect Li^+ ions in human serum with high specificity and selectivity over Na^+ ions.

17.2.2 3D metallacage receptors for alkali metals

Severin and co-workers synthesized a hexanuclear coordination cage (4) based on the reaction of [(cymene)$Ru(NO_3)_2$] with 3,5-pyridinedicarboxylic acid [48]. The cage is a neutral structure that functions as an exo-receptor for alkali metals. Here O-atoms of carbonyl group constitute a metal receptor site, very alike toward what was detected for 12-MC-3 metallamacrocyles. Excess concentrations remained required to discern the change in NMR spectroscopy and single crystals with KOAc and CsOAc stood investigated by X-ray crystallography. The results indicate that an overabundance of M+ ions results in the reorganisation of the octahedral cage into dodecanuclear coordination cages with an icosahedral geometry, with all eight metal receptor sites occupied by K^+ or Cs^+ ions.

Extending the same strategy, four hexanuclear coordination cages created on half sandwich organometallic fragments of cyclopentadienyl Rh(III) and (IrIII) with pyridine-3,5-dicarboxylate ligands were synthesized by the same group [49]. The cages act as ditopic excoreceptors for the large alkali metals K^+ and Cs^+, however, display low affinity for Na^+. Stoichiometric ratio of Cp^*Rh/K^+ stood established through a Job plot with 1:2 host–guest ratio and again this was confirmed with high-resolution ESI-MS spectra of the adducts. The ability of these coordination cages to bind alkali metal ions is

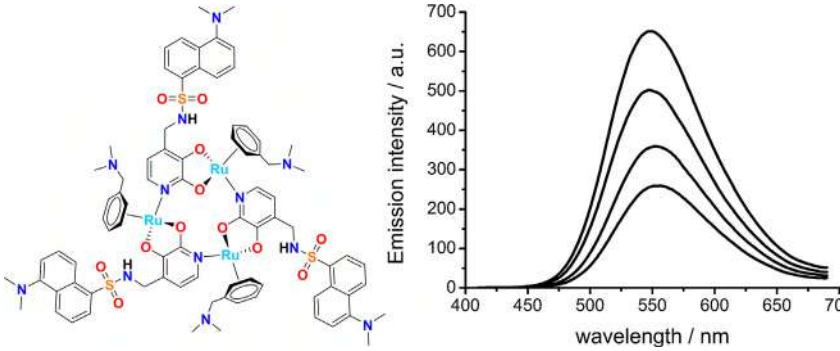

FIGURE 17.3 Trinuclear 12-$MC_{Ru}{}^{II}$-3 metallamacrocycle (3) for high affinity and selective binding of Li^+ and Na^+ ion (left) and Increase in the fluorescence of macrocycle 3 (2.0 mM) in methanol/water (9:1, pH 7.0, 10 mM phophate buffer) upon the addition of LiCl (0.0, 0.5, 1.5 and 3.0 mM). Excitation wavelength: 360 nm. (right) (*Reproduced from Ref. [47] with permission from Royal Society of chemistry, Copyright © 2009.*)

similar to that of 2,3-dihydroxy-pyridine based macrocycles of 12-MC-3 metallacrown complexes having the general formula [(π-ligand)$M(C_5H_3NO_2)_3$] ((π-ligand)M = (arene)Ru, (cyclopentadienyl)Rh, and (cyclopentadienyl)Ir: three (π-ligand)M fragments constitutes the bonding site that contains three oxygen atoms of the pyridine ligands. Whereas the coordination cages are very selective for the larger cations such as K^+ and Cs^+

Recently, the same research group synthesized an imine-based molecular cage with distinct binding sites for small and large alkali metal cations [50]. Condensation reaction of aldehyde containing metallacrown with amine-containing Ru dimer leads to the formation of hexa nuclear cylindrical cage (5). The crystal structure analysis revealed that the cage has inner and outer cavities for binding the alkali metals of different sizes (Fig. 17.4). Upon addition of Cs^+ ions to the solution of cage changed the color from orange to yellow. UV/Vis titration displayed the band at 520 nm decreased and the band at 400 nm increased with increasing amounts of CsO_2CCF_3. Binding studies through diverse metal cations (Li^+, Na^+, K^+, Rb^+, and Cs^+) suggest that 1:1 binding for larger cations like Rb^+ and Cs^+ and 1:2 binding for smaller cations like Li^+, Na^+, and K^+. However, NMR data suggest that only one binding site remains strongly preferred over the other, and 1:1 host–guest model was selected as a good approximation.

Puddephatt and co-workers have synthesized several Pd(II) based "lantern complexes" using bispyridyl amide ligands which act as efficient hosts for cations [51] (Fig. 17.5). This cationic dipalladium(II) lantern complexes were prepared from the reaction of $[PdCl_2(PhCN)_2]$ with 2 equiv of bispyridyl amide ligands in the presence of $[AgO_2CCF_3]$ or $[AgO_3SCF_3]$ to abstract chloride to give corresponding lantern complexes (6 and 7). Encapsulation of cations by the lantern complexes was confirmed by single crystal X-ray structures and ESI-MS

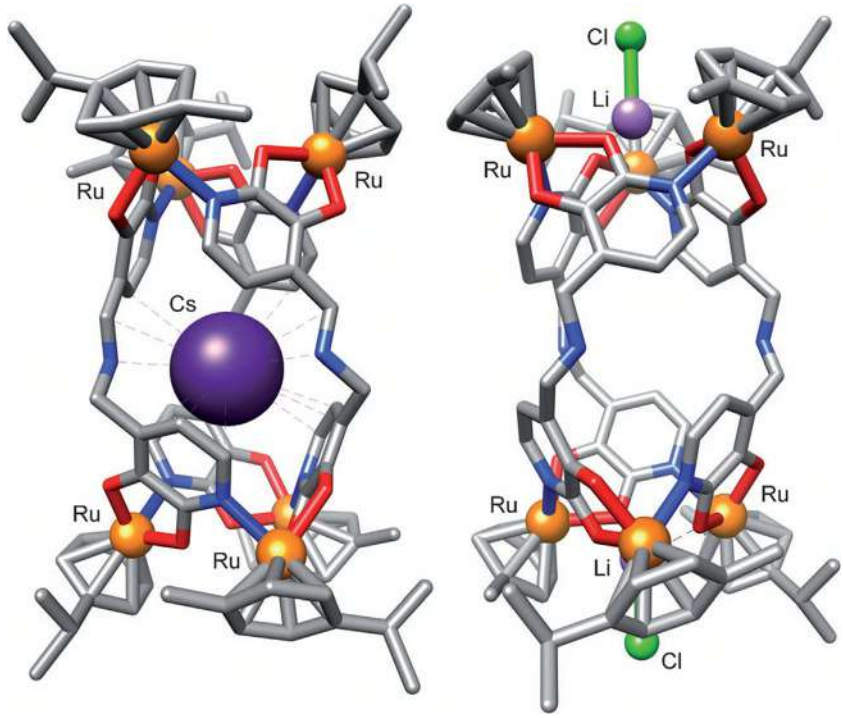

FIGURE 17.4 Molecular structures of the Cs^+ (left) and the bis-LiCl (right) adducts of cage 5 in the solid state. Solvent molecules and hydrogen atoms have been omitted for clarity. (*Reproduced from Ref. [50] with permission from John Wiley and Sons, Copyright © 2013WILEY-VCH Verlag GmbH, Weinheim, Fed. Rep. Of Germany.*)

studies. Cations encapsulation occurring through easy conformational change of amide ligands and the selectivity of lantern complexes for alkali metals in the sequence $Na^+ >> K^+ >> Li^+$.

Beer and co-workers have synthesized several bimetallic cryptands containing polyether cavities of various sizes for Group I metal cations sensing applications [52] (Fig. 17.6). Metal cation binding studies were supported by electrospray mass spectrometry, cyclic, and square wave voltammetry. Addition of alkali metal cations to 1:1 DCM:MeCN solutions of the cryptands led to significant anodic shifts in the receptors's metal-based oxidation through the destabilization of cobalt by complexed metal cation. Significantly, the magnitude of anodic shift and complementary metal cation: cryptand cavity size were correlated. For example, with the large cryptand 10, Cs^+ produces the largest electrochemical shift of 45 mV, whereas Li^+ induces no change in the electrochemical shift. The situation is reversed in the case of smaller cryptands 8 and 9, which show the maximum electrochemical shift for smaller alkali metal cations.

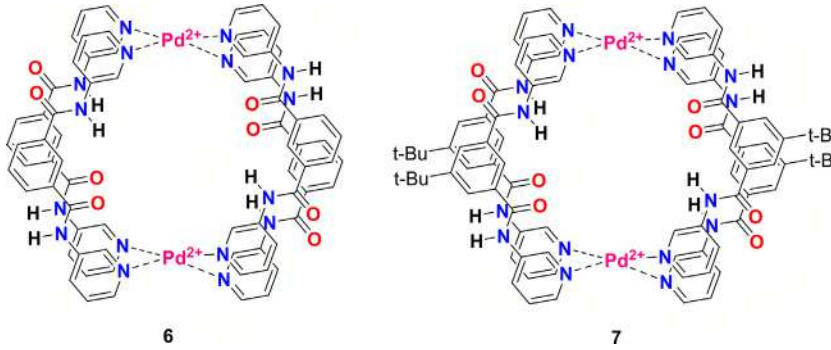

FIGURE 17.5 Chemical structures of dipalladium lantern complexes 6 and 7.

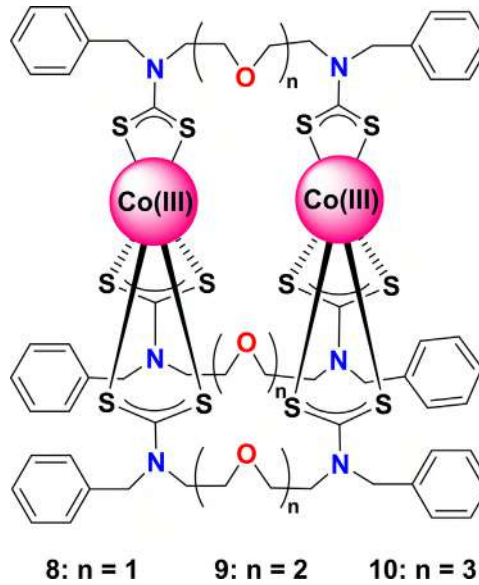

FIGURE 17.6 Chemical structures of bimetallic cryptands containing polyethers for alkali metals.

17.3 Transition metal ion sensing by 2D and 3D supramolecular coordination complexes

Transition metals play a vital role in many biological processes such as oxygen transport, energy production, neurotransmission, etc [34]. The metals that are important for biological processes include Fe, Zn, Cu, Mn, Co, Ni, Cr, and so on. However, some metal ions for example Hg^{2+}, Cd^{2+}, and Pb^{2+} are highly toxic and cause detrimental effects on our health [27]. Recognition of such metal ions are very important in our day-to-day life.

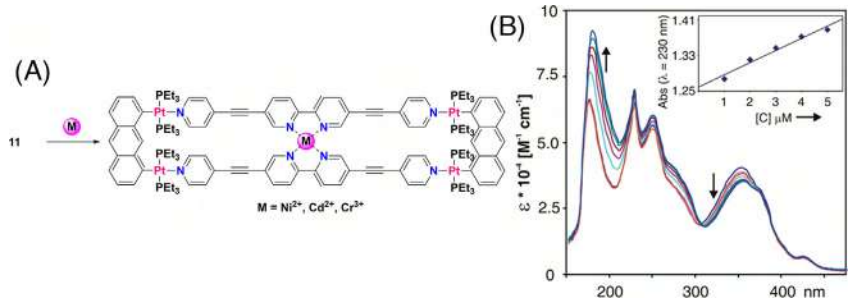

FIGURE 17.7 (A) Binding mechanism of rectangle 11 with 3d transition metal ions. (B) Titration of rectangle 11 in MeOH with $Ni(NO_3)_2 \cdot 6H_2O$. (*Reprinted with permission from Ref. [53]. Copyright (2004) American Chemical Society.*)

17.3.1 2D metallamacrocyclic receptors for transition metals

Stang and colleagues synthesized a self-assembled rectangle using a platinum-based organometallic clip with two parallel donor sites oriented in the same direction and a linear ditopic ligand [53]. The [2+2] self-assembly of diplatinum (II) molecular acceptor 1,8-bis[trans-$Pt(PEt_3)_2(NO_3)$]anthracene with rigid bispyridyl bridging ligand-3,8-bis-pyridin-4-yl-ethynyl-[1,10]-phenanthroline led to the formation of cationic molecular rectangle 11. Methonolic solutions of molecular rectangles exhibited a variety of absorbance bands in the ultraviolet region at 350, 280, and 230 nm and have been used as optical sensors for Ni(II), Cd(II), and Cr(III) ions up to a 1:1 host–guest ratio (Fig. 17.7). Titration with $Ni(II)(NO_3)_2 \cdot 6H_2O$ to a solution of 11 in methanol induced a drastic change in the UV-vis spectrum. Similar observation was made for other cations of Cd^{2+} and Cr^{3+}. The binding constants for 11 with Ni^{2+}, Cd^{2+}, and Cr^{3+} were calculated to be $2.01 \pm 0.05 \times 10^7$, $3.39 \pm 0.5 \times 10^4$, and $7.53 \pm 0.04 \times 10^3$, respectively. The presence of two phenanthroline units that contain N_4 pocket acts as binding site for 3d metal ions. Though the binding constants observed the same trend of affinity toward these metal ions with free 1,10-phenanthroline, rectangle 11 provides a supramolecular architecture for the phenanthroline group, endowing it with a preorganized structure for metal ion identification as well as new optical capabilities.

Extending the same strategy, Mukherjee and co-worker have constructed a di-Pd(II) molecular clip containing ethynyl functionality by bispyridyl linear linker *N,N'*-bis(4-pyridyl)ethylenediamine in a 1:1 ratio in acetone to acquire the self-assembled metallamacrocylce, 12 [54]. Incorporation of N_4 pocket that could act as recognition site for transition metals and ethylene functionality for enhanced fluorescent behavior. The addition of 3d transition metals such as Mn^{2+}, Fe^{3+}, Ni^{2+}, and Cu^{2+} ions in methanol solution significantly quenched the fluorescence intensity (Fig. 17.8). With Fe^{3+} ions, a solution of 10^{-5} stood adequate to illustration proficient fluorescence quenching. Interestingly, metal

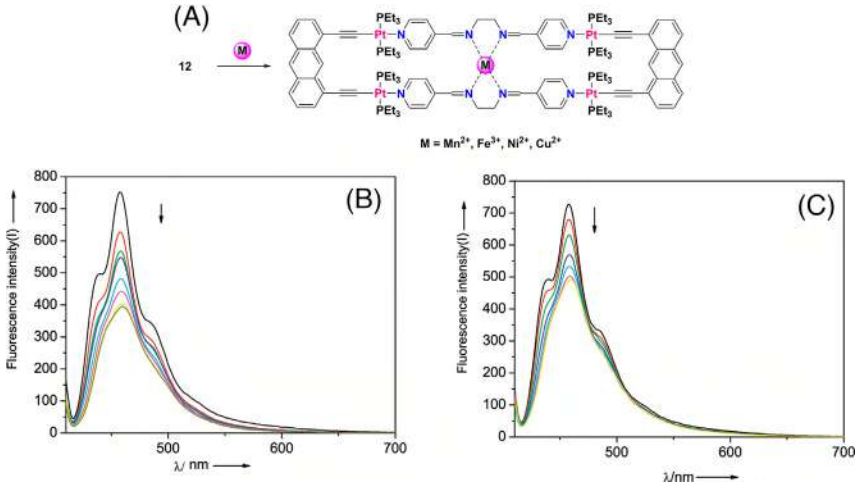

FIGURE 17.8 (A) Binding mechanism of 12 with 3d transition metal ions. Quenching of fluorescence intensity of 12 (3×10^{-5} M in methanol) by the gradual addition of (B) Cu^{2+}, 7.33×10^{-4} M to 6.39×10^{-3} M and (C) Ni^{2+}, 6.31×10^{-4} M to 2.77×10^{-3} M. (*Reprinted with permission from [54]. Copyright (2009) American Chemical Society.*)

ions having completely filled d orbital of d^{10} electronic configuration, such as Zn^{2+} or Cd^{2+} did not quench the fluorescence. The quenching of the fluorescence intensity was explained by photoinduced electron transfer (PET) mechanism. In the case of Zn^{2+}, PET does not occur because of the stable filled electronic configuration, so the fluorescence was not quenched. This nonresponsive nature of Zn^{2+} in the fluorescence titration might also owing to the soft-acid character of Zn^{2+}, which remains not seemly to bind in the hard donor N_4 pocket. This metallamacrocycle represents a unique example of fluorescence sensor for the detection of transition metal ions using diplatinum based organometallic clip with antharacene backbone and ethynyl functionalities.

Lu et al. have synthesized a gondola-shaped tetrarhenium metallacyclophane, which stood proficient of selectively recognize metal ions [55]. The synthesis of molecular rectangle 13 has been accomplished through the reaction of $Re_2(CO)_{10}$ with a ditopic hetercyclic clip 2,5-bis(5-*tert*-butyl-2-benzoxazolyl)-thiophene (tpbb) and 1,4-dihydroxy-9,10-anthraquinone (H_2-dhaq) in refluxing mesitylene through coordination-driven self-assembly (Fig. 17.9). This highly fluorescent cyclophane can able to selectively sense Hg^{2+} cations. The addition of other metal ions such as Li^{1+}, Sr^{2+}, Co^{2+}, Ni^{2+}, Cu^{2+}, Zn^{2+}, Pb^{2+}, and Ag^{1+} did not any significant effect on the absorption and emission of metallacyclophane. Nevertheless, the addition of Hg^{2+} ion, decreases the absorption maximum at 357 and 378 nm and the appearances of the new absorption peak at 425 nm increased. Likewise, quenching of the emission peak at 438 nm was observed with formation 1:1 host–guest complex. The well-defined binding site for metal ion recognition is formed by the sulfur atoms of the tpbb ligands.

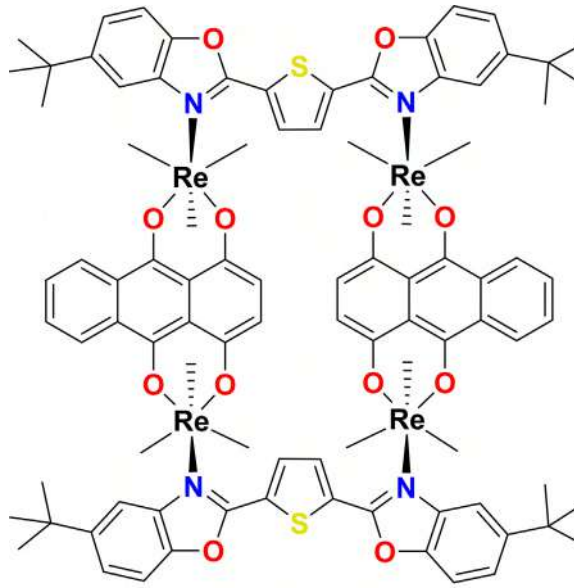

13

FIGURE 17.9 Chemical structure of Gondola shaped metallacycle 13.

Furthermore, this metallacyclophane can also be used for the recognition of anthracene.

Recently, Das and co-workers synthesized the Zn(II) metallamacrocycle (14) by the reaction of the cationic ligand 1,3-bis(2,6-diisopropyl-4-(pyridin-4-yl)-phenyl)-1*H*-imidazol-3-ium chloride/bromide with $ZnCl_2$ (anhydrous) in the presence of KO^tBu as base under an nitrogen atmosphere in anhydrous DMF solvent [56]. The fluorescence sensing of the metallamacrocycle 14 toward various biologically relevant cations such as Mg^{2+}, Ca^{2+}, Cr^{3+}, Mn^{2+}, Fe^{3+}, Fe^{2+}, Co^{2+}, Ni^{2+}, Cd^{2+}, Zn^{2+}, Ag^{+}, Pb^{2+}, Ru^{3+}, Sm^{3+}, Eu^{3+}, Gd^{3+}, Tb^{3+}, Dy^{3+}, and Er^{3+} was carried out in DMF. As shown in Fig. 17.10, 14 exhibited an emission at 400 nm, which was assigned to the emission of central imidazolium moiety. Upon addition of various cations does not change the fluorescence emission intensity, except for Fe^{3+}, which caused a pronounced decrease in emission intensity. The fluorescence intensity was completely quenched at higher concentrations of Fe^{3+} cations. The detection limit for Fe^{3+} ions calculated to be 2.5×10^{-6} M. Competitive experiments were carried out with other competing cations and there was no significant influence in the intensities of metallamacrocycle. Investigation of the binding mode of 14 and Fe^{3+} showed that lattice Cl^- ion in the cavity of metallamacrocycle remains accountable for the conversion of $FeCl_3$ to $FeCl_4^-$ and consequently capture of the $FeCl_4^-$ ion via a carbene-H $\cdots$ $FeCl_4^-$ interaction. Moreover, 14 displayed high selectivity toward IO^{4-} anions as well

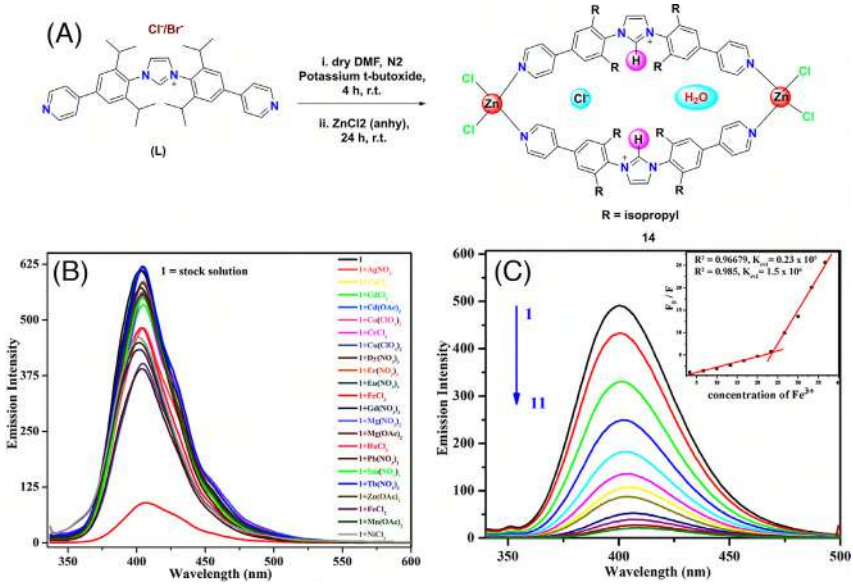

FIGURE 17.10 (A) Synthetic route for the Zn(II) metallamacrocycle (14) using imidazolium ligand (L). (B) Fluorescence spectra of metallamacrocycle 14 ($(1.0 \times 10^{-6}$ mol/L) upon addition of different cations (M^{n+}) (10 mL of a 5 mM solution of all guests was added to 3 mL of host 14) in DMF (λ_{ex} 300.7 nm). (C) Fluorescence titration of metallacycle 14 (2×10^{-3} mol/L) in DMF with increasing Fe^{3+} concentration (addition of 10 mL of Fe^{3+} ions per time; λ_{ex} 320 nm). (*Reprinted with permission from Ref. [56]. Copyright (2017) American Chemical Society.*)

even in the presence of other competitive anions. This study demonstrates an exclusive instance of the exploitation of an *N*-heterocyclic precursor established metallamacrocycle as a fluorescence-based dual sensor for the detection of Fe^{3+} and IO^{4-} ions.

Very recently, Hu and co-workers have prepared a Zn_6 metallamacrocycle (15) based on 4'-(4-carboxyphenyl)-2,2':6',2"-terpyridin ligand with $Zn(CH_3COO)_2$, $Pr(NO_3)_3 \times 6H_2O$ in water and DMF solvent at 160°C for 2 days [57]. Here, $Pr(NO_3)_3 \cdot 6H_2O$ serves as a template agent for the construction of metallamacrocycle. Cystallographic analysis of single crystals of 15 revealed the six Zn^{2+} ions are linked by six L^- anions, and resulting a hexanuclear Zn_6 metallamacrocycle. Sensing of 15 with different metal cations such as Na^+, Co^{2+}, Ni^{2+}, Cu^{2+}, Ag^+, Cd^{2+}, Hg^{2+}, Pb^{2+}, and Fe^{3+} was carried out in DMF solvent. The addition of metal cations induced a slight decrease in the luminescence intensity, except for Fe^{3+}, which almost completely quenched the intensity of 15 (Fig. 17.11). The Stern–Volmer quenching constant and the detection limit are calculated to be 1.68×10^5 M^{-1} and 5.36×10^{-8} M, respectively. The high quenching ability and lower detection limits of 15 demonstrate the high sensitivity toward Fe^{3+} cation and therefore 15 can be used as a potential sensor

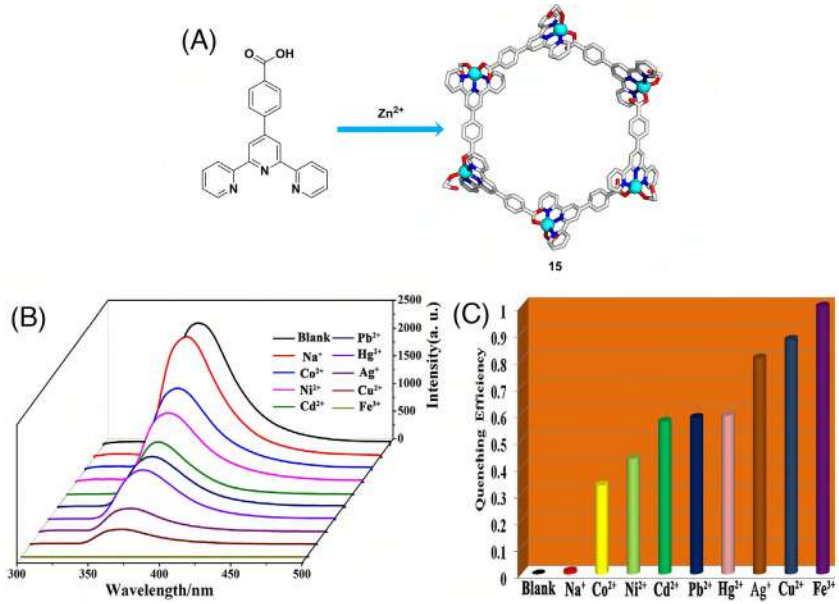

FIGURE 17.11 (A) Self-assembly and single crystal X-ray structure of Zn6 metallamacrocycle (15). X-ray structure figure was reproduced using data downloaded from the Cambridge Crystallographic Data Centre (CCDC No. 1058680). (B) The luminescence intensities of 15 on the addition of various metal ions in DMF solution (b) The quenching efficiencies of 15 on the addition of various metal ions in DMF solution. (*Adapted with permission from Ref. [57]* Copyright (2018) Elsevier Ltd.)

for detecting the Fe^{3+} cation. Further, this metallamacrocycle has also be used to detect CCl_4 molecules.

17.3.2 3D metallacage receptors for transition metals

Sun et al. described a bright photoactive Eu^{III} tetrahedral cages through high emission quantum yield, which was capable of detecting Cu^{2+} ions [58]. C3-symmetric oxazoline-based ligands by a 1,3,5-triazine core presenting sturdy "push-pull" character remained used as energy donor ligands for lanthanide corners, to indulgence the development of highly luminescent cages. Intraligand charge transfer (ILCT) from benzamide units to the triazine core in combination with coordination-driven self-assembly of Eu^{3+} ions resulted in the formation of bright Eu(III) tetrahedral cage. Efficient sensitization of the tetrahedral cage in CH_3CN or in the solid state stood established by discrete europium red emission peaks at 580, 594, 615, 649, and 693 nm. Transition metal ions sensing studies were carried out in CH_3CN solvent. Upon the addition of various divalent metal ions such Fe^{2+}, Co^{2+}, Ni^{2+}, Cu^{2+}, Zn^{2+}, Ca^{2+}, Cd^{2+}, Mn^{2+} the emission of the metallacage was slightly enhanced (Fig. 17.12). In the case of Cu^{2+}, 40 fold increase in intensity at 615 nm was observed over other metal cations. From

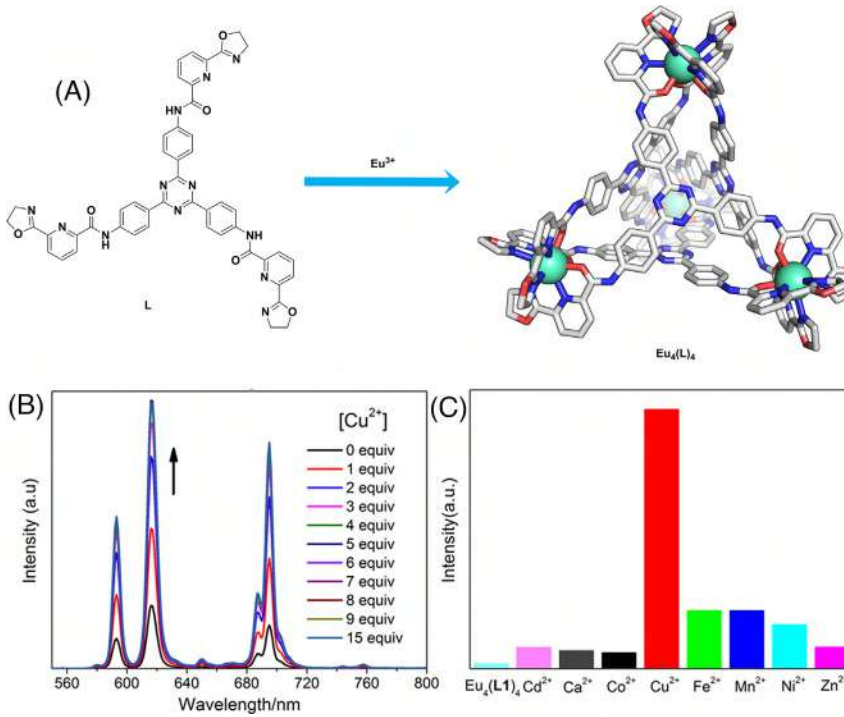

FIGURE 17.12 (A) Self-assembly and X-ray crystal structure of Eu_4L_4 metallamacrocycle. X-ray structure figure was reproduced using data downloaded from the Cambridge Crystallographic Data Centre (CCDC No. 1546602) (B) Fluorescence emission spectra of $Eu_4(L)_4$ ($c = 1' 10^{-5}$ M) containing different equiv of Cu^{2+} in CH_3CN. (C) Comparison of the emission intensity of $Eu_4(L)_4$ ($\lambda_{ex} = 365$ nm, $\lambda_{em} = 615$ nm) containing various transition metal cations (0.5 mM). (*Reprinted with permission from Ref. [57]. Copyright (2017) American Chemical Society.*)

the fluorescence titration experiments the stoichiometry was calculated to be 1:4 cage-to-Cu^{2+}. Weak cation-π interactions among Cu^{2+} and the triazine rings favors the LE→ILCT internal conversion thereby increasing the ILCT sensitization efficiency on the tetrahedral cage, resulting in fluorescence enhancement. This tetrahedral cage is a unique example where fluorescence enhancement was observed while sensing of Cu^{2+} cations over the disturbance of the ILCT sensitization alleyway.

17.4 Conclusions

This chapter systematically summarized the metal ion sensing applications of finite SCCs. This chapter focuses mainly on the sensing of alkali and transition metals through noncovalent interactions. The above examples suggest that the coordination-driven self-assembly remains an effective tool for synthesizing

supramolecular architecture by distinct shape and sizes. The cavities and voids present in these supramolecular systems allow the host to accommodate the guest either interior or exterior of the metallacycles or the cages. The functional properties of these SCCs can be easily tuned by the incorporation of the luminescent ligands or luminescent metals into the supramolecular architectures to achieve very sensitive detection of the metal ions. Some of the macrocyclic supramolecular structures have been used to detect the biologically important lithium ion in human serum.

References

[1] R. Chakrabarty, P.S. Mukherjee, P.J. Stang, Supramolecular Coordination: Self-Assembly of Finite Two and Three Dimensional Ensembles, Chem. Rev. 111 (2011) 6810–6918.

[2] Y. Fang, J.A. Powell, E. Li, Q. Wang, Z. Perry, A. Kirchon, X. Yang, Z. Xiao, C. Zhu, L. Zhang, F. Huang, H.C. Zhou, Catalytic reactions within the cavity of coordination cages, Chem. Soc. Rev. 48 (2019) 4707–4730.

[3] A. Kumar, S.S. Sun, A.J. Lees, Directed assembly metallocyclic supramolecular systems for molecular recognition and chemical sensing, Coord. Chem. Rev. 252 (2008) 922–939.

[4] D. Zhang, T.K. Ronson, Y.Q. Zou, J.R. Nitschke, Metal–organic cages for molecular separations, Nature Reviews Chemistry 5 (2021) 168–182.

[5] A. Casini, B. Woods, M. Wenzel, The Promise of Self-Assembled 3D Supramolecular Coordination Complexes for Biomedical Applications, Inorg. Chem. 56 (2017) 14715–14729.

[6] S. Goeb, M. Sallé, Electron-rich Coordination Receptors Based on Tetrathiafulvalene Derivatives: Controlling the Host–Guest Binding, Acc. Chem. Res. 54 (2021) 1043–1055.

[7] S. Datta, M.L. Saha, P.J. Stang, Hierarchical Assemblies of Supramolecular Coordination Complexes, Acc. Chem. Res. 51 (2018) 2047–2063.

[8] W.X. Gao, H.N. Zhang, G.X. Jin, Supramolecular catalysis based on discrete heterometallic coordination-driven metallacycles and metallacages, Coord. Chem. Rev. 386 (2019) 69–84.

[9] Y. Jin, Q. Zhang, Y. Zhang, C. Duan, Electron transfer in the confined environments of metal–organic coordination supramolecular systems, Chem. Soc. Rev. 49 (2020) 5561–5600.

[10] Y. Li, J. Zhang, H. Li, Y. Fan, T. He, H. Qiu, S. Yin, Metallacycle/Metallacage-Cored Fluorescent Supramolecular Assemblies with Aggregation-Induced Emission Properties, Adv. Opt. Mater. 8 (2020) 1902190.

[11] W. Tuo, Y. Xu, Y. Fan, J. Li, M. Qiu, X. Xiong, X. Li, Y. Sun, Biomedical applications of Pt(II) metallacycle/metallacage-based agents: From mono-chemotherapy to versatile imaging contrasts and theranostic platforms, Coord. Chem. Rev. 443 (2021) 214017.

[12] A. Schmidt, A. Casini, F.E. Kühn, Self-assembled M2L4 coordination cages: Synthesis and potential applications, Coord. Chem. Rev. 275 (2014) 19–36.

[13] J.A. Thomas, Metal ion directed self-assembly of sensors for ions, molecules and biomolecules, Dalton Trans. 40 (2011) 12005–12016.

[14] J.-M. Lehn, Supramolecular Chemistry: Concepts and Perspectives, VCH, Weinheim, 1995.

[15] J.P. Sauvage, C. Dietrich-Buchecker, Molecular Catenanes, Rotaxanes and Knots: A Journey Through the World of Molecular Topology, Wiley-VCH Verlag GmbH & Co, Weinheim, 2007, 1–368.

[16] S. Leininger, B. Olenyuk, P.J. Stang, Self-Assembly of Discrete Cyclic Nanostructures Mediated by Transition Metals, Chem. Rev. 100 (2000) 853–907.

[17] D.L. Caulder, C. Brückner, R.E. Powers, S. König, T.N. Parac, J.A. Leary, K.N. Raymond, Design, Formation and Properties of Tetrahedral M4L4 and M4L6 Supramolecular Clusters, J. Am. Chem. Soc. 123 (2001) 8923–8938.

[18] M. Fujita, Metal-directed self-assembly of two- and three-dimensional synthetic receptors, Chem. Soc. Rev. 27 (1998) 417–425.

[19] B.J. Holliday, C.A. Mirkin, Strategies for the Construction of Supramolecular Compounds through Coordination Chemistry, Angew. Chem. Int. Ed. 40 (2001) 2022–2043.

[20] F.A. Cotton, C. Lin, C.A. Murillo, Supramolecular Arrays Based on Dimetal Building Units, Acc. Chem. Res. 34 (2001) 759–771.

[21] T. Nakamura, H. Ube, R. Miyake, M. Shionoya, A C60-Templated Tetrameric Porphyrin Barrel Complex via Zinc-Mediated Self-Assembly Utilizing Labile Capping Ligands, J. Am. Chem. Soc. 135 (2013) 18790–18793.

[22] I.A. Riddell, M.M.J. Smulders, J.K. Clegg, Y.R. Hristova, B. Breiner, J.D. Thoburn, J.R. Nitschke, Anion-induced reconstitution of a self-assembling system to express a chloride-binding Co10L15 pentagonal prism, Nat. Chem. 4 (2012) 751–756.

[23] T.Z. Xie, S.Y. Liao, K. Guo, X. Lu, X. Dong, M. Huang, C.N. Moorefield, S.Z.D. Cheng, X. Liu, C. Wesdemiotis, G.R. Newkome, Construction of a Highly Symmetric Nanosphere via a One-Pot Reaction of a Tristerpyridine Ligand with Ru(II), J. Am. Chem. Soc. 136 (2014) 8165–8168.

[24] S. De, K. Mahata, M. Schmittel, Metal-coordination-driven dynamic heteroleptic architectures, Chem. Soc. Rev. 39 (2010) 1555–1575.

[25] G.Y. Wu, L.J. Chen, L. Xu, X.L. Zhao, H.B. Yang, Construction of supramolecular hexagonal metallacycles via coordination-driven self-assembly: Structure, properties and application, Coord. Chem. Rev. 369 (2018) 39–75.

[26] M.M.J. Smulders, I.A. Riddell, C. Browne, J.R. Nitschke, Building on architectural principles for three-dimensional metallosupramolecular construction, Chem. Soc. Rev. 42 (2013) 1728–1754.

[27] H. Na Kim, W. Xiu Ren, J. Seung Kim, J. Yoon, Fluorescent and colorimetric sensors for detection of lead, cadmium, and mercury ions, Chem. Soc. Rev. 41 (2012) 3210–3244.

[28] J.F. Zhang, Y. Zhou, J. Yoon, J.S. Kim, Recent progress in fluorescent and colorimetric chemosensors for detection of precious metal ions (silver, gold and platinum ions), Chem. Soc. Rev. 40 (2011) 3416–3429.

[29] H. Wang, Y. Li, N. Li, A. Filosa, X. Li, Increasing the size and complexity of discrete 2D metallosupramolecules, Nat. Rev. Mater. 6 (2020) 145–167.

[30] L. Xu, Y.-X. Hu, P.S. Mukherjee, Metallomacrocycles: From Structures to Applications, The Royal Society Of Chemistry (2019) 251–282.

[31] B. Li, T. He, Y. Fan, X. Yuan, H. Qiu, S. Yin, Recent developments in the construction of metallacycle/metallacage-cored supramolecular polymers via hierarchical self-assembly, Chem. Commun. 55 (2019) 8036–8059.

[32] L.J. Chen, H.B. Yang, Construction of Stimuli-Responsive Functional Materials via Hierarchical Self-Assembly Involving Coordination Interactions, Acc. Chem. Res. 51 (2018) 2699–2710.

[33] R.R. Crichton, Biological Inorganic Chemistry, Elsevier, Milan, 2007.

[34] K.P. Carter, A.M. Young, A.E. Palmer, Fluorescent Sensors for Measuring Metal Ions in Living Systems, Chem. Rev. 114 (2014) 4564–4601.

[35] B. Maloney, Y. Balaraman, Y. Liu, N. Chopra, H.J. Edenberg, J. Kelsoe, J.I. Nurnberger, D.K. Lahiri, Lithium alters expression of RNAs in a type-specific manner in differentiated

human neuroblastoma neuronal cultures, including specific genes involved in Alzheimer's disease, Sci. Rep. 9 (2019) 1–13.

[36] H. Piotrowski, K. Polborn, G. Hilt, K. Severin, A Self-Assembled Metallomacrocyclic Ionophore with High Affinity and Selectivity for Li+ +, J. Am. Chem. Soc. 123 (2001) 2699–2700.

[37] H. Piotrowski, G. Hilt, A. Schulz, P. Mayer, K. Polborn, K. Severin, Self-Assembled Organometallic [12] Metallacrown-3 Complexes, Chemistry - A European Journal 7 (2001) 3196–3208.

[38] H. Piotrowski, K. Severin, A self-assembled, redox-responsive receptor for the selective extraction of LiCl from water, Proc. Natl Acad. Sci. 99 (2002) 4997–5000.

[39] M.-L. Lehaire, R. Scopelliti, H. Piotrowski, K. Severin, Selective Recognition of Fluoride Anion Using a Li+–Metallacrown Complex, Angew. Chem. Int. Ed. 41 (2002) 1419–1422.

[40] M.L. Lehaire, R. Scopelliti, K. Severin, Stabilization of Molecular LiF and LiFHF inside Metallamacrocyclic Hosts, Inorg. Chem. 41 (2002) 5466–5474.

[41] M.L. Lehaire, R. Scopelliti, K. Severin, Encapsulation of molecular Na2SiF6 by two metallacrown complexes, Chem. Commun. 2 (2002) 2766–2767.

[42] Z. Grote, M.L. Lehaire, R. Scopelliti, K. Severin, Selective Complexation of Li+ in Water at Neutral pH Using a Self-Assembled Ionophore, J. Am. Chem. Soc. 125 (2003) 13638–13639.

[43] M.L. Lehaire, A. Schulz, R. Scopelliti, K. Severin, Electronic Effects in 12-Metallacrown-3 Complexes. A Theoretical and Experimental Study, Inorg. Chem. 42 (2003) 3576–3581.

[44] Z. Grote, R. Scopelliti, K. Severin, pH-Triggered Assembly of Organometallic Receptors for Lithium Ions, J. Am. Chem. Soc. 126 (2004) 16959–16972.

[45] I. Saur, K. Severin, Selection experiments with dynamic combinatorial libraries: the importance of the target concentration, Chem. Commun. (2005) 1471–1473.

[46] Z. Grote, H.D. Wizemann, R. Scopelliti, K. Severin, Lithium Isotope Separation by 12-Metallacrown-3 Complexes, ZAAC 633 (2007) 858–864.

[47] S. Rochat, Z. Grote, K. Severin, Ruthenium-based metallacrown complexes for the selective detection of lithium ions in water and in serum by fluorescence spectroscopy, Organic and Biomolecular Chemistry 7 (2009) 1147–1153.

[48] T. Brasey, R. Scopelliti, K. Severin, Guest-induced formation of an icosahedral coordination cage, Chem. Commun. (2006) 3308–3310.

[49] S. Mirtschin, E. Krasniqi, R. Scopelliti, K. Severin, Coordination Cages of Rhodium and Iridium as Exoreceptors for Alkali Metal Ions, Inorg. Chem. 47 (2008) 6375–6381.

[50] C. Schouwey, R. Scopelliti, K. Severin, An Imine-Based Molecular Cage with Distinct Binding Sites for Small and Large Alkali Metal Cations, Chem. Eur. J. 19 (2013) 6274–6281.

[51] N.L.S. Yue, D.J. Eisler, M.C. Jennings, R.J. Puddephatt, Macrocyclic and Lantern Complexes of Palladium(II) with Bis(amidopyridine) Ligands: Synthesis, Structure, and Host−Guest Chemistry, Inorg.Chem. 43 (2004) 7671−7681.

[52] P.D. Beer, N.G. Berry, A.R. Cowley, E.J. Hayes, E.C. Oates, W.W.H. Wong, Metal-directed self-assembly of bimetallic dithiocarbamate transition metal cryptands and their binding capabilities, Chem. Commun. 3 (2003) 2408–2409.

[53] M.J.E. Resendiz, J.C. Noveron, H. Disteldorf, S. Fischer, P.J. Stang, A Self-Assembled Supramolecular Optical Sensor for Ni(II), Cd(II), and Cr(III), Org. Lett. 6 (2004) 651–653.

[54] S. Ghosh, R. Chakrabarty, P.S. Mukherjee, Design, Synthesis, and Characterizations of a Series of Pt4 Macrocycles and Fluorescent Sensing of Fe3+/Cu2+/Ni2+ Through Metal Coordination, Inorg. Chem. 48 (2009) 549–556.

[55] M. Sathiyendiran, R.T. Liao, P. Thanasekaran, T.T. Luo, N.S. Venkataramanan, G.H. Lee, S.M. Peng, K.L. Lu, Gondola-Shaped Luminescent Tetrarhenium Metallacycles with Crown-Ether-like Multiple Recognition Sites, Inorg. Chem. 45 (2006) 10052–10054.

[56] G. Kumar, R. Guda, A. Husain, R. Bodapati, S.K. Das, A Functional Zn(II) Metallacycle Formed from an N-Heterocyclic Carbene Precursor: A Molecular Sensor for Selective Recognition of Fe3+ and IO4– Ions, Inorg. Chem. 56 (2017) 5017–5025.

[57] X. Liu, P. Gao, M. Hu, A novel hexanuclear Zn6 metallacycle as a luminescent sensor for the Fe3+ ion and CCl4 molecule, Polyhedron 144 (2018) 119–124.

[58] C.L. Liu, R.L. Zhang, C.S. Lin, L.P. Zhou, L.X. Cai, J.T. Kong, S.Q. Yang, K.L. Han, Q.F. Sun, Intraligand Charge Transfer Sensitization on Self-Assembled Europium Tetrahedral Cage Leads to Dual-Selective Luminescent Sensing toward Anion and Cation, J. Am. Chem. Soc. 139 (2017) 12474–12479.

Index

Page numbers followed by "*f*" and "*t*" indicate, figures and tables respectively.

T

W

X

Supramolecular Coordination Complexes

Design, Synthesis, and Applications

Edited by **Sankarasekaran Shanmugaraju**

An insightful guide to advanced topics within the domain of the synthesis and applications of supramolecular coordination complexes

Supramolecular Coordination Complexes: Design, Synthesis, and Applications goes in depth on the is an emerging area of supramolecular coordination chemistry that has provided invaluable opportunities to researchers in chemistry as well as in the interrelated areas of biology, materials science, and physics. Over the past several decades, a plethora of finite supramolecular complexes have been designed and successfully employed for diverse applications ranging from sensing and catalysis and biology. *Supramolecular Coordination Complexes* discusses the growth of the field and explores the advantages, opportunities and latest applications of supramolecular complexes. Beginning with an introduction to design principles, synthetic methods, and post-synthetic functionalization of supramolecular complexes, the book goes on to compile the different analytical and computational modeling methods used to understand the structure and functional properties of supramolecular structures. Applications of supramolecular complexes in biomedicine, sensing, catalysis, and materials are then explored in detail. Drawing on the knowledge of a global team of experts, *Supramolecular Coordination Complexes* provides a wealth of interesting information for students and researchers working in the design, synthesis, or application of such complexes.

Key Features

- Discusses cutting-edge approaches for the investigation of supramolecular coordination chemistry.
- Summarizes a varied range of supramolecular coordination complex design and applications.
- Highlights the interdisciplinary connections between supramolecular chemistry and the fields of biology and materials science.

Sankarasekaran Shanmugaraju
Indian Institute of Technology, Palakkad, India

Dr. Sankarasekaran Shanmugaraju received his B.Sc. and M.Sc. degrees in Chemistry from The American College, Madurai and he obtained his Ph.D. degree (honoured with a gold medal for the best thesis) in Inorganic Chemistry working with Prof. Partha Sarathi Mukherjee from Indian Institute of Science (IISc), Bangalore. After a short postdoctoral stint at IISc, in 2014 he moved to Trinity College Dublin, Ireland to work with Prof. Thorfinnur Gunnlaugsson as an IRC postdoctoral fellow. Since October 2018, he has been an assistant professor at the Indian Institute of Technology, Palakkad. The central theme of his group's current research interests is in the areas of supramolecular self-assembly formation of functional materials and porous polymers for their applications in biomedicine and environmental related issues. Dr. Shanmugaraju has published 34 high-quality publications in peer-reviewed international journals and a book chapter. His publications have been cited over 1773 times to date.

ISBN 978-0-323-90582-4

ELSEVIER elsevier.com/books-and-journals